

Durham E-Theses

The Role of Material Structure in Compacted Earthen Building Materials: Implications for Design and Construction

BECKETT, CHRISTOPHER, THOMAS, STONE

How to cite:

BECKETT, CHRISTOPHER, THOMAS, STONE (2011) *The Role of Material Structure in Compacted Earthen Building Materials: Implications for Design and Construction*, Durham theses, Durham University. Available at Durham E-Theses Online: <http://etheses.dur.ac.uk/3313/>

Use policy

The full-text may be used and/or reproduced, and given to third parties in any format or medium, without prior permission or charge, for personal research or study, educational, or not-for-profit purposes provided that:

- a full bibliographic reference is made to the original source
- a [link](#) is made to the metadata record in Durham E-Theses
- the full-text is not changed in any way

The full-text must not be sold in any format or medium without the formal permission of the copyright holders.

Please consult the [full Durham E-Theses policy](#) for further details.

Academic Support Office, Durham University, University Office, Old Elvet, Durham DH1 3HP
e-mail: e-theses.admin@dur.ac.uk Tel: +44 0191 334 6107
<http://etheses.dur.ac.uk>

Durham University

The Role of Material Structure in Compacted Earthen Building Materials: Implications for Design and Construction

Thesis by

Christopher Thomas Stone Beckett

Submitted as partial consideration towards
the degree of Doctor of Philosophy



Mechanics Group
School of Engineering & Computing Sciences
Durham University
United Kingdom

September 2011

The Role of Material Structure in Compacted Earthen Building Materials: Implications for Design and Construction

Christopher Thomas Stone Beckett

Rammed earth is an earthen construction material and an ancient construction technique. It is formed by compacting layers of moist sandy loam subsoil into formwork which is then removed, exposing the material and creating a freestanding, monolithic structure.

In this thesis, the behaviour of rammed earth is investigated in terms of unsaturated soil mechanics of compacted earthen materials. Basic unsaturated soil mechanics theory is discussed and a method for linking the behaviour and material structure of an unsaturated soil is presented through the development of a model for predicting a soil's water retention curve using the soil pore size distribution and capillary and adsorption phenomena.

A series of experiments is then performed in order to explain the behaviour of rammed earth in tension and compression under varying conditions in terms of the material micro- and macrostructures. An analysis of the sample manufacturing process is presented in order to understand formation of rammed earth's structure in both natural and laboratory-prepared materials. The effects of temperature and humidity, related to a number of sites around the world, on the compressive strength and of changing water content and clay flocculation on the tensile strength of rammed earth are then investigated and combined in order to determine the sources of strength in rammed earth. The pore networks of several rammed earth samples under compression and those of rammed earth samples comprising multiple compacted layers are then investigated using X-Ray computed tomography in order to determine the effects of loading and layering on the material macrostructure and to support results presented in previous chapters.

In the final chapter, implications for the design, construction and conservation of rammed earth structures are discussed based on the findings of investigations presented in the preceding chapters.

Declaration

The work in this thesis is based on research carried out in the Mechanics Group, School of Engineering and Computing Sciences, Durham University. No part of this report has been submitted elsewhere for any other degree or qualification and it all my own work unless referenced to the contrary in the text.

Copyright © 2011 by Christopher Beckett.

“The copyright of this thesis rests with the author. No quotations from it should be published without the authors prior written consent and information derived from it should be acknowledged.”

Thoroughly good stuff, mud... Give me a good stone wall to break down any day... But not mud. Not mud.

Colonel Gent discusses the merits of the defences of the city of Seringapatam with Colonel Wellesley. Bernard Cornwell. 1998. *Sharpe's Tiger*. Harper Collins, London (UK).

Contents

Nomenclature	xv
Acknowledgements	xvii
Publications	xviii
1 Introduction	1
1.1 The case for earthen construction	1
1.2 The rammed earth technique	3
1.2.1 Rammed earth wall construction	3
1.2.2 Development of the RE technique	3
1.2.2.1 China and South-East Asia	4
1.2.2.2 Europe and the Silk Route	5
1.2.2.3 Colonial expansion	7
1.2.2.4 RE in the 20 th and 21 st centuries	7
1.3 Thesis structure	11
1.4 References	12
2 Unsaturated soil mechanics theory	13
2.1 Introduction	13
2.2 Soil mineralogy	13
2.3 Soil phase relationships	15
2.4 Suction in unsaturated soils	16
2.4.1 Capillary suction	16
2.4.1.1 Surface tension and the contact angle	16
2.4.1.2 The Kelvin equation	17
2.4.1.3 Capillary rise	18
2.4.1.4 Liquid bridges	19
2.4.2 Matric suction	20
2.4.3 Osmotic suction	22
2.5 Soil structure	23
2.5.1 Aggregate and pore type classifications	24
2.5.2 Compaction	26
2.5.3 Pore size distribution measurement	29
2.5.3.1 Mercury intrusion porosimetry	29
2.5.3.2 Adsorption techniques	32
2.6 The soil water retention curve	34
2.7 Conclusion	38
2.8 References	39
3 Soil water retention curve estimation using cavitation and adsorption	43
3.1 Introduction	43
3.1.1 Experimentally-determined SWRCs	43
3.1.2 Predicting the SWRC using the soil pore size distribution	44
3.2 Combined capillary-adsorption model for the SWRC	45
3.2.1 Model overview	45
3.2.2 Soil solid skeleton assumptions	46

3.2.2.1	Particle shape approximations	46
3.2.2.2	Macro region particle size and separation	48
3.2.3	Main drying path suction calculations	50
3.2.3.1	Cavitation	50
3.2.3.2	Liquid bridges between spheres	52
3.2.3.3	Adsorbed films between cuboidal clay particles in the micro region	54
3.2.4	Main wetting path suction calculations	55
3.2.4.1	Pore snap-off in the macro region: liquid bridge coalescence	55
3.2.4.2	Pore snap-off in the micro region: thin film coalescence	56
3.2.5	Water content calculations	56
3.2.5.1	Main drying path macro-region water content	57
3.2.5.2	Main drying path micro-region water content	58
3.2.5.3	Main wetting path water content calculations	58
3.2.6	Summary of the CCA model calculation procedures	60
3.2.6.1	Solid skeleton assumptions	60
3.2.6.2	Main drying path calculations	60
3.2.6.3	Main wetting path calculations	60
3.3	Model performance	60
3.3.1	Comparison to measured data	60
3.3.2	Differences between measured and predicted data	66
3.3.2.1	Changing void ratio	66
3.3.2.2	Trapped Pores	67
3.4	Conclusion	70
3.5	References	71
4	The impact of sample production techniques on material structure	75
4.1	Chapter introduction	75
4.2	Mixing of dry granular materials	75
4.2.1	Introduction	75
4.2.2	Sandpile formation and phenomena of granular flow	76
4.2.2.1	Sandpile formation	76
4.2.2.2	Segregation and stratification	76
4.2.2.3	Effect of repose angle	77
4.2.2.4	Capture, percolation and amplification	78
4.2.2.5	Mechanism of layer formation	78
4.2.3	Material selection and preparation	79
4.2.4	Results and discussion	80
4.2.4.1	Effect of pouring direction	80
4.2.4.2	Effect of particle flow rate	81
4.2.5	Conclusions	83
4.3	Compaction of wet RE material	84
4.3.1	Introduction	84
4.3.2	Image analysis using particle image velocimetry	85
4.3.3	Development of the test procedure	88
4.3.3.1	Design of the compaction chamber	88
4.3.3.2	Development of “artificial rammed earth”	90
4.3.3.3	Parametric analyses	90
4.3.4	Results and discussion	92
4.3.5	Conclusions	94
4.4	Concluding remarks	94
4.5	References	100
5	The effect of humidity and temperature on the compressive strength of rammed earth	103
5.1	Introduction	103
5.1.1	Overview	103
5.1.2	Climates at RE sites	103
5.2	Experimental procedure	104

5.2.1	Humidity and temperature setpoint selection	104
5.2.2	Selection and preparation of raw materials	107
5.2.3	Sample manufacture	110
5.2.4	Sample compressive strength testing	111
5.3	Results and discussion	114
5.3.1	Sample density errors	114
5.3.2	Sample water contents on testing	114
5.3.3	Unconfined compressive strength results	116
5.3.4	Sources of compressive strength	121
5.4	Conclusion	126
5.5	References	127
6	The effect of changing salinity on the tensile strength of rammed earth	130
6.1	Introduction	130
6.2	The Brazilian test for testing the tensile strength of soils	130
6.3	Experimental procedure	132
6.3.1	Sample size selection	132
6.3.2	Soil mix preparation	133
6.3.3	Salinity values	136
6.3.4	Sample manufacture	138
6.3.5	Tensile strength testing	139
6.4	Results and discussion	140
6.4.1	Sample density errors	140
6.4.2	Failure mechanisms at different water contents	142
6.4.2.1	Griffith crack theory	142
6.4.2.2	Fracture of granular materials	143
6.4.3	Change in tensile strength with water content	146
6.4.4	Matric, osmotic and total suction determination	152
6.4.4.1	Matric suction	152
6.4.4.2	Osmotic suction	153
6.4.4.3	Total suction	156
6.4.5	Change in tensile strength with suction and CaCl_2 content	160
6.4.6	Comparison between tensile and unconfined compressive strengths	161
6.5	Conclusion	163
6.6	References	164
7	Macrostructural investigation of rammed earth using X-ray computed tomography	168
7.1	Introduction	168
7.2	X-ray computed tomography	168
7.3	Fractal analysis	169
7.4	Experimental procedure	171
7.4.1	Soil mix selection and raw material preparation	171
7.4.2	Sample preparation and testing	172
7.5	Results and discussion	173
7.5.1	Image processing	173
7.5.2	Preliminary fractal analysis	174
7.5.3	Effect of loading on material macrostructure	175
7.5.4	Effect of compaction on the material macrostructure	185
7.6	Conclusions	194
7.7	References	195
8	Conclusions and implications for rammed earth design and construction	197
8.1	Analytical and experimental investigation conclusions	197
8.1.1	Linking internal structure to retention behaviour	197
8.1.2	Comparison between laboratory- and construction-prepared material	197
8.1.2.1	Mixing processes	197
8.1.2.2	Layer compaction	198
8.1.2.3	Effect of multiple layers	198
8.1.3	The effect of material structure on strength	198

8.2	Implications and recommendations for design, construction and conservation	199
8.2.1	New-build structures	199
8.2.1.1	Design	199
8.2.1.2	Construction	200
8.2.1.3	Conservation	201
8.2.2	Ancient structures	202
8.3	Further work	203
8.3.1	Trapped pores and pore constriction	203
8.3.2	Stratification and segregation	203
8.3.3	Sources of strength in RE	203
8.3.4	Types of failure of RE	204
8.3.5	RE structures	204
8.4	Concluding remarks	205
8.5	References	206
References		209

List of Figures

1.1	Examples of RE construction variations (Villafeliche, Zaragoza, Spain, c. 12 th century): a) use of brickwork (<i>chained</i> RE) ; b) use of <i>lunetos</i> . Photographs by Paul A. Jaquin. Used with permission.	2
1.2	Method of construction for an RE wall, after (Jaquin, 2008)	4
1.3	12 th century RE wall (Castle of la Atalaya, Villena, Spain). Note the damaged material to the right of the photograph. Photograph by Paul A. Jaquin. Used with permission. . .	5
1.4	Han Dynasty pottery tower	6
1.5	Roman RE box rampart and defensive ditch (from Webster (1969))	6
1.6	RE sites in Asia and Europe	9
1.7	RE sites in the Americas (top) and Australia (middle) and a sketch showing the locations of RE sites pre- and post-19 th century (bottom)	10
2.1	Sketch of a soil element (a) and a simplified phase diagram (b)	15
2.2	Water meniscus trapped between two walls	17
2.3	Associated water pressures during capillary rise	19
2.4	ESEM images of a liquid bridge between sand particles (Lourenço et al., in press)	19
2.5	Meridional (κ) and azimuthal (l) radii in a liquid bridge	20
2.6	Capillary condensation and adsorption between two contacting particles	21
2.7	Osmosis and osmotic suction, after Hillel (2004)	23
2.8	Particle assemblage types as defined by Collins and McGown (1974) (figure reproduced from that work): a-c) connectors; d) irregular aggregations linked by connector assem- blages; e) irregular aggregations forming a honeycomb arrangement; f) regular aggre- gations interacting with silt or sand grains; g) regular aggregation interacting with the particle matrix; h) interweaving bunches of clay; i) interweaving bunches of clay with silt inclusions; j) clay particle matrix; k) granular particle matrix.	25
2.9	Pore size terminology as defined by Collins and McGown (1974) (figure reproduced from that work)	26
2.10	Example compaction curves for a sandy-clay soil. Reproduced from Proctor (1933)	27
2.11	The change in dry density and OWC with increasing compactive effort. Reproduced from Diamond (1971).	27
2.12	PSD of Speswhite kaolin compacted at different water contents. e_{MIP} is the void ratio according to MIP testing, as discussed in Section 2.5.3.1. Reproduced from Tarantino and De Col (2008).	28
2.13	Suction measurement during compaction. Reproduced from Gens et al. (1995).	29
2.14	Compaction of Speswhite kaolin at different compactive efforts. Reproduced from Tarantino and De Col (2008).	30
2.15	Inter- and intra-aggregate pore size and volume data as determined by MIP intrusion and extrusion, after Tarantino and De Col (2008)	31
2.16	PSD curves for Leda clay: a) critical-region dried; b) oven-dried (figure reproduced from Diamond (1970))	32
2.17	Sketch showing example wetting and drying paths for a monomodal (solid line) and bi- modal (dashed line) material. S_{r_d} and S_{r_w} are the saturation ratios for the drying and wetting materials respectively.	35
2.18	Sketch showing example monomodal drying paths for clayey (solid), silty (dot-dashed) and sandy (dashed) soils and corresponding AEV values	36
2.19	Illustrative example of wetting and drying contact angles	36

2.20	ESEM images showing the effect of wetting and drying on the contact angle between water and silica particles. Scales, where available, are shown on the diagrams (Lourenço et al., in press).	37
2.21	Bursting of concave water menisci on the increase of RH: a) 80.1%; b) 82.3%; c) >82.3%. θ indicates the contact angle (equivalent to θ_{slv}) (Lourenço et al., 2008a)	37
2.22	PSDs for a glacial till tested at suctions of 0, 1400 and 2500 kPa (Simms and Yanful, 2001)	39
3.1	The relationship between the BCC model and the SWRC (potential is a function of z in this formalism)	45
3.2	Sketch of the size of the inscribed spheres (dashed) between tetrahedrally- and cubically-packed spheres. Note that the 3-D inscribed sphere has a larger diameter than the 2-D inscribed sphere.	46
3.3	CCA model calculations procedure for one pore size using a tetrahedral packing system.	47
3.4	SEM micrographs for: a) sand particles (Lourenço et al., 2008a); and b) clay particles (Hattab and Fleureau, 2010) and corresponding shape approximations.	48
3.5	Specific surface area data (sources given in the figure) compared to spherical and cuboid shape approximations	49
3.6	Inner, outer and apparent particle diameters	50
3.7	Unit cell for the cubic packing of spheres	51
3.8	Enlarged (for ease of subsequent calculations) unit cell for the tetrahedral packing of spheres. Dotted lines show the shape of a single tetrahedral unit cell.	51
3.9	Formation of liquid bridges and adsorbed films between cubically-packed spheres on the cavitation of a soil pore	53
3.10	Change in κ and l with filling angle for different separation distances for $R = 1\text{mm}$.	53
3.11	Two parallel adsorbed films, facing each other across an intervening vapour (after Iwamatsu and Horii (1996))	54
3.12	Invasion of a capillary wedge into a slit-shaped pore	55
3.13	Liquid bridge configurations between cubically-packed spheres at cavitation (left) and snap-off (right)	56
3.14	Sketch of the smoothing function used to account for the ‘step’ between the macro- and micro region wetting suction calculations	59
3.15	Pore size distribution for soil CL, data from Zhang and Li (2010)	61
3.16	Pore size distribution for soil ML, data from Zhang and Li (2010)	62
3.17	Pore size distribution for soil SC, data from Zhang and Li (2010)	62
3.18	Pore size distribution for soil SM, data from Zhang and Li (2010)	63
3.19	Pore size distribution for soil GW-GM, data from Zhang and Li (2010)	63
3.20	Predicted SWRC for soil CL compared to experimental data from Zhang and Li (2010)	64
3.21	Predicted SWRC for soil ML compared to experimental data from Zhang and Li (2010)	64
3.22	Predicted SWRC for soil SC compared to experimental data from Zhang and Li (2010)	65
3.23	Predicted SWRC for soil SM compared to experimental data from Zhang and Li (2010)	65
3.24	Predicted SWRC for soil GW-GM compared to experimental data from Zhang and Li (2010)	66
3.25	Assumed linear relationship between V_v and applied suction for data shown in Figure 2.22	67
3.26	Predicted drying SWRCs (in terms of water content) using the CCA and BCC models for a glacial till compacted at 18% water content	68
3.27	Predicted drying SWRCs (in terms of saturation ratio) using the CCA and BCC models for a glacial till compacted at 18% water content	68
3.28	2-D representation of a pore with different throat diameters	70
4.1	Typical shape of a sandpile. θ_{xx} is the repose angle of species x .	76
4.2	(a) Results for spontaneous stratification of a bidisperse mixture of smaller smooth grains (light) and larger rougher grains (dark). (b) Results for a segregating mixture of smaller rougher (light) grains and larger, smoother grains (dark) (Cizeau et al., 1999)	77
4.3	The generalised repose angles for: (a) small, smooth particle rolling down a surface of rough particles, θ_{12} ; (b) rough, large particle rolling down a surface of small, smooth particles, θ_{21} ; (c) small, smooth particle rolling down a slope of the same species, θ_{11} ; (d) large, rough particle rolling down a slope of the same species, θ_{22} (Cizeau et al., 1999)	77

4.4	Diagrammatic process of kink formation and propagation (after Makse et al. (1998)): (a) initial avalanche at velocity $v(y)$; (b) formation of the kink; (c) profile and propagation of the kink up the sandpile (slope angle θ_0) with kink angles θ_{11} , θ_{21} and θ_{22}	79
4.5	Particle grading curves for fine and coarse sand	79
4.6	Silo pouring directions	81
4.7	(a)-(d) Stratification results for PDs 1, 2, 4 and 5 respectively (all using manual pouring)	82
4.8	Experimentally observed patterns for a mixture of dark sand (rough particles) and glass spheres (smooth particles). Classification of “stratification”, “continuous segregation” or “segregation” determined by observation. Reproduced from (Herrmann, 1999).	82
4.9	(a)-(b) Stratification pattern for low flow rate; (c)-(d) Stratification pattern for high flow rate	83
4.10	The formation of a coarse band due to a pause in material deposition	83
4.11	Image manipulation during PIV analysis, after White et al. (2003)	86
4.12	Sketch of the compaction chamber, showing principal dimensions in mm.	89
4.13	Photograph of the compaction chamber with scanner in place. Principal dimensions are shown in Figure 4.12.	89
4.14	Particle grading curves for sharp sand and modified gravel	91
4.15	Initial particle displacements after two strikes (scaled by a factor of 5 with the rammer striking between 200 and 300 mm in the silo length dimension) during compaction of the first ARE layer (units in mm)	95
4.16	Initial particle displacements after two strikes (scaled by a factor of 5 with the rammer striking between 200 and 300 mm in the silo length dimension) during compaction of the second ARE layer (units in mm).	95
4.17	Particle displacements after 11 strikes (scaled by a factor of 5 with the rammer striking between 200 and 300 mm in the silo length dimension) half way through the compaction of the second ARE layer (units in mm).	96
4.18	Particle displacements after 33 strikes (scaled by a factor of 5 with the rammer striking between 200 and 300 mm in the silo length dimension) at the end of the compaction of the second ARE layer (units in mm).	96
4.19	Contour plot of initial particle displacements after two strikes (with the rammer striking between 200 and 300 mm in the silo length dimension) during the compaction of the first ARE layer (units in mm).	97
4.20	Contour plot of initial particle displacements after two strikes (with the rammer striking between 200 and 300 mm in the silo length dimension) during the compaction of the second ARE layer (units in mm).	97
4.21	Contour plot of particle displacements after 11 strikes (with the rammer striking between 200 and 300 mm in the silo length dimension) during the compaction of the second ARE layer (units in mm).	98
4.22	Contour plot of particle displacements after 31 strikes (with the rammer striking between 200 and 300 mm in the silo length dimension) at the end of the compaction of the second ARE layer (units in mm).	98
5.1	Locations of RE sites compared to KGCC categories (Peel et al., 2007). Pre-19 th century sites are shown as light markers and post-19 th century are shown as dark markers. Larger markers represent a greater number of RE sites within a given area. KGCC global map used with permission.	105
5.2	Flow chart showing principal testing procedure stages, stage durations and environmental chamber (EC) use	105
5.3	Environmental data for 91 RE sites around the world: a) minimum temperatures; b) maximum temperatures; c) minimum humidities; and d) maximum humidities.	106
5.4	Raw material particle grading curves	108
5.5	Particle grading curves for virgin and re-used soil mix material	109
5.6	Water content against dry density for light Proctor compaction tests on soil mixes: a) 5-1-4; and b) 7-1-2.	109
5.7	Variation in recorded temperatures during cube equilibration period	111
5.8	Variation in recorded humidities during cube equilibration period	112
5.9	Water content against drying time for mix 5-1-4 cubes	112
5.10	Water content against drying time for mix 7-1-2 cubes	113

5.11	Errors in sample densities for soil mixes: a) 5-1-4; and b) 7-1-2	115
5.12	ECEP water contents for soil mix 5-1-4 cubes. Marker numbers correspond to the cube humidity setpoint.	116
5.13	ECEP water contents for soil mix 7-1-2 cubes. Marker numbers correspond to the cube humidity setpoint.	117
5.14	Effect of relative humidity on sample ECEP water content	117
5.15	Compressive strength against humidity and temperature for mix 5-1-4	118
5.16	Compressive strength against humidity and temperature for mix 7-1-2	119
5.17	Comparison of the compressive strengths of mixes 5-1-4 and 7-1-2 cubes against humidity and temperature	119
5.18	Compressive strengths of mix 5-1-4 against cube water content on testing. Marker numbers correspond to test number.	120
5.19	Compressive strengths of mix 7-1-2 against cube water content on testing. Marker numbers correspond to test number.	121
5.20	Calculated wetting and drying SWRCs for mixes 5-1-4 and 7-1-2	124
5.21	Compressive strengths of mixes 5-1-4 and 7-1-2 against calculated suction	124
5.22	Compressive strengths of mixes 5-1-4 and 7-1-2 against water content on testing	125
5.23	Compressive strengths of mixes 5-1-4 and 7-1-2 against water content on testing	125
6.1	Example Brazilian test apparatus	131
6.2	Deformation of a Brazilian test sample under loading, after Frydman (1964)	132
6.3	Cracking in an RE structure compared to the Brazilian test	133
6.4	Cracking in: a) 50 mm diameter Brazilian test sample; b) 100 mm diameter Brazilian test sample.	133
6.5	Raw material particle grading curves	134
6.6	Particle grading curves for mixes 5-1-4 and 7-1-2 showing recommended grading limits (Houben and Guillaud, 1996)	135
6.7	Water content against dry density for light Proctor compaction tests on soil mixes: a) 5-1-4; and b) 7-1-2.	135
6.8	Comparison between pre- and post-testing mix 5-1-4 material, showing the effect of additional silty clay on the grading curve of post-test material	136
6.9	Comparison between pre- and post-testing mix 7-1-2 material	137
6.10	Relationship between electrical conductivity and % content by mass for CaCl_2 dissolved in pure water at 18°C (SmartMeasurement, 2001)	138
6.11	Sketch of the cylindrical mould used for sample production showing principal dimensions	139
6.12	Errors in cube densities for soil mixes: a) 5-1-4; and b) 7-1-2	142
6.13	Griffith crack energy (Gordon, 1991)	143
6.14	Comparison of load against displacement profiles for samples tested at 0 dSm^{-1}	144
6.15	Comparison of load against displacement profiles for samples tested at 20 dSm^{-1}	145
6.16	Comparison of load against displacement profiles for samples tested at 40 dSm^{-1}	145
6.17	Logarithmic relationship for tensile strength against water content for mix 5-1-4. a and b are as defined in Eqn 6.7.	147
6.18	Logarithmic relationship for tensile strength against water content for mix 7-1-2. a and b are as defined in Eqn 6.7.	147
6.19	Change in tensile strength with water content as observed by various authors: a) and b) Ajaz and Parry (1975c); c) (Utomo and Dexter, 1981); d) and e) (Mullins and Panayiotopoulos, 1984); f) to i) (Young and Mullins, 1991).	148
6.20	Change in tensile strength with water content as observed by various authors: a) and b) Causarano (1993); c) (Ibarra et al., 2005); d) to f) (Panayiotopoulos, 1996); g) and h) Wang et al. (2007); i) Jaquin et al. (2008); j) Nahlawi et al. (2004).	149
6.21	Mesured SWRC for mix 6-1.5-2.5 at zero applied load (Jaquin et al., 2009)	154
6.22	Estimated SWRC (matric suction) for mixes 5-1-4 and 7-1-2	154
6.23	Change in CaCl_2 (saturated) vapour pressure with changing temperature and solution concentration (Dow, 2008)	157
6.24	Approximated change in CaCl_2 (saturated) vapour pressure with changing solution concentration (Dow, 2008)	158
6.25	Estimated SWRC (total suction) for mix 5-1-4	159
6.26	Estimated SWRC (total suction) for mix 7-1-2	159

6.27	Change in tensile strength with estimated ψ_m and CaCl_2 content for mixes 5-1-4 and 7-1-2	161
6.28	Change in tensile strength with estimated ψ_m and CaCl_2 content for mixes 5-1-4 and 7-1-2	162
7.1	Parallel method for determining particle profile fractal dimension	170
7.2	Box-counting method for determining particle profile fractal dimension. Hatching indicates those boxes that contain segments of the particle profile.	171
7.3	Sketch describing lacunarity and fractal dimension	172
7.4	Sketch of the mould (left) and presses (middle and right) used for sample preparation . .	173
7.5	Example of XRCT images: a) sample axes; b) XY-slice pre-processing; c) XY-slice post-processing. Outlines of particles seen in (b) have been outlined in (c).	175
7.6	Flowchart of image processing algorithm (using ImageJ software)	176
7.7	Calculated box-counting fractal dimensions for images 1 to 5 for sample 2s	177
7.8	Calculated minimum cover fractal dimensions for images 1 to 5 for sample 2s	177
7.9	Linear fit to minimum cover box-counting results (on logarithmic axes) for the image 1 for sample 2s	178
7.10	3-D reconstructions of the pore network of sample 2s: a) total pore space; b) view of internal XZ plane; c) view of internal YZ plane.	179
7.11	3-D reconstructions of the pore network of sample 9s: a) total pore space; b) view of internal XZ plane; c) view of internal YZ plane.	179
7.12	3-D reconstructions of the pore network of sample 10s: a) total pore space; b) view of internal XZ plane; c) view of internal YZ plane.	179
7.13	Change in pore area fraction with depth for samples 2s, 9s and 10s	180
7.14	Change in minimum cover fractal dimension with depth for samples 2s, 9s and 10s	180
7.15	Change in lacunarity with depth for samples 2s, 9s and 10s	181
7.16	XRCT images taken at: a) 16500 μm ; and b) 17379 μm	181
7.17	Change in calculated PAF with depth for different threshold intensity values	183
7.18	Change in calculated D_f with depth for different threshold intensity values	183
7.19	Change in calculated L with depth for different threshold intensity values	184
7.20	Large particle present in sample 10s at 13090 μm : a) XRCT image; b) threshold intensity of 50; c) threshold intensity of 75; d) threshold intensity of 114 (IsoData value).	185
7.21	Change in calculated relative PAF with depth for different threshold intensity values . . .	185
7.22	Change in calculated relative D_f with depth for different threshold intensity values	186
7.23	Change in calculated relative L with depth for different threshold intensity values	186
7.24	3-D reconstructions of the pore network of the top lift of sample 13d: a) total pore space; b) view of internal XZ plane; c) view of internal YZ plane.	188
7.25	3-D reconstructions of the pore network of the bottom lift of sample 13d: a) total pore space; b) view of internal XZ plane; c) view of internal YZ plane.	188
7.26	3-D reconstructions of the pore network of the top lift of sample 15d: a) total pore space; b) view of internal XZ plane; c) view of internal YZ plane.	188
7.27	3-D reconstructions of the pore network of the bottom lift of sample 15d: a) total pore space; b) view of internal XZ plane; c) view of internal YZ plane.	189
7.28	Change in pore area fraction with depth for samples 13d and 15d	189
7.29	Change in minimum cover fractal dimension with depth for samples 13d and 15d	190
7.30	Change in lacunarity with depth for samples 13d and 15d	190
7.31	Effect of changing the threshold value on the resulting binary images for sample 13d: a) original image (1100 μm depth); b) analysed using threshold value of 60; c) analysed using threshold value of 141; d) original image (17600 μm depth); e) analysed using threshold value of 60; f) analysed using threshold value of 141.	191
7.32	Change in pore area fraction with depth for samples 13d and 15d for different threshold intensity values	191
7.33	Change in minimum cover fractal dimension with depth for samples 13d and 15d for different threshold intensity values	192
7.34	Change in lacunarity with depth for samples 13d and 15d for different threshold intensity values	192
8.1	Simple detailing sketch of the use of a stem wall and overhanging eaves for RE wall protection. Note that additional details, for example roof and foundation detailing, are not shown.	207

8.2	Moulding of earthen render in Villafeliche, Zaragoza. Photographs by Paul A. Jaquin. Used with permission.	207
8.3	Concrete patches: a) the Asslim Kasbah, Morocco; b) Villafeliche, Zaragoza. Photographs by Paul A. Jaquin. Used with permission.	208
8.4	Earthen repairs made to Castillo Cox, Valencia. Photograph by Paul A. Jaquin. Used with permission.	208
8.5	Tension cracks: a) watchtower in Namgyal Tsembo, Leh; b) Villafeliche, Zaragoza; c) crack repaired using an earthen staple, Basgo, Ladakh. Photographs by Paul A. Jaquin. Used with permission.	208

List of Tables

3.1	Particle size values (Powrie, 2008)	46
3.2	Boundary particle radii (r_{lim}), boundary cavitation suction $\psi_{m_{cav}}$, boundary water content (WC_{lim}), saturated water content (WC_{sat}), boundary saturation ratio, residual water content (WC_{res}) and residual saturation ratio for soil types CL, ML, SC, SM and GW-GM.	61
5.1	Summary of minimum and maximum annual temperatures and relative humidities (RHs) for RE sites by region	106
5.2	Relative particle size category amounts for soil mixes 5-1-4 and 7-1-2.	108
5.3	OWC, $\rho_{d_{max}}$ and $\rho_{b_{max}}$ for soil mixes 5-1-4 and 7-1-2.	110
5.4	Humidity (RH) and temperature (temp.) combinations and corresponding test numbers. The number of batches required to test each combination are also given.	113
5.5	Equivalent pore diameters (EPDs), adsorbed film thicknesses and adsorbed water contents (AWCs) for suction values calculated at used humidity values and 20°C	123
6.1	Relative particle size category amounts for soil mixes 5-1-4 and 7-1-2.	134
6.2	OWC, $\rho_{d_{max}}$ and $\rho_{b_{max}}$ for soil mixes 5-1-4 and 7-1-2.	136
6.3	Sample density errors and water contents at testing. Numbers in parentheses correspond to sample numbers. Grey entries correspond to rejected samples.	141
6.4	Fitting parameters used with Eqn 6.4 to estimate the change in tensile strength with saturation ratio for mixes 5-1-4 and 7-1-2 at different $CaCl_2$ contents	146
6.5	van Genuchten fitting parameters used to estimate ψ_m in mixes 5-1-4 and 7-1-2	153
6.6	Comparison between osmotic suction prediction methods given in Rao and Shivananda (2005), Lang (1967) and Dao et al. (2008)	157
6.7	ψ_o values determined using Eqn 2.29 for different mix solution concentrations	157
6.8	van Genuchten fitting parameters used to estimate ψ in mixes 5-1-4 and 7-1-2	158
6.9	Tensile (TS) and equivalent compressive strength (ECS) values at equilibrium water contents for soil mixes 5-1-4 and 7-1-2 at 0 dSm ⁻¹ for 20°C and 45%RH	162
7.1	OWC, $\rho_{d_{max}}$ and $\rho_{b_{max}}$ for RE soil mix 6-1-3	172
7.2	Sample thresholding values	174

Nomenclature

For convenience, the nomenclature has been split into *abbreviations* and *symbols*.

Abbreviations

AEV	Air entry value
ARE	Artificial rammed earth
AWC	Adsorbed water content
BET	Brunauer-Emmett-Teller method
BJH	Barret-Joyner-Halenda method
CCA	Combined capillary-adsorption (soil pore model)
CT	Computed tomography
ECEP	Environmental chamber equilibration period
EPD	Equivalent pore diameter
ESEM	Environmental scanning electron microscopy
GP	Grid position
IEP	Initial equilibration period
IUPAC	International Union of Pure and Applied Chemistry
KGCC	Köpper-Geiger climate classification
LL	Liquid limit
MIP	Mercury intrusion porosimetry
OWC	Optimum water content
PAF	Pore area fraction
PD	Pouring direction
PI	Plasticity index
PIV	Particle image velocimetry
PL	Plastic limit
PSD	Pore size distribution
RE	Rammed earth
RH	Relative humidity
SAR	Sodium adsorption ratio
SIM	Semi-impermeable membrane
SSA	Specific surface area
SWRC	Soil water retention curve
TCD	Trinity College Dublin (transparent clay material)
USDA	United States Department of Agriculture
XRCT	X-ray computed tomography

Symbols

α	Fitting parameter (van Genuchten, 1980)
----------	---

δ	Stratification control parameter
d^*	Characteristic length
η	Attenuation coefficient (XRCT)
Γ	Tabulated Gamma function (Utomo and Dexter, 1981)
γ_{lv}	Liquid-vapour surface tension
γ_{Hg}	Liquid-vapour surface tension of mercury
γ_{sl}	Solid-liquid surface tension
γ_{sv}	Solid-vapour surface tension
κ	Meniscus radius
κ_{mod}	Modified liquid bridge meridional radius
λ	Element length
ψ_{cap}	Capillary suction
ψ_{capLB}	Liquid bridge capillary suction
ϕ'	Friction angle
ψ_m	Matric suction
ψ_{mADcav}	Slit-shaped pore drainage matric suction
ψ_{mAD}	Thin film matric suction
ψ_{mADSO}	Adsorbed film snap-off matric suction
ψ_{mLBSO}	Liquid bridge snap-off matric suction
ψ_o	Osmotic suction
ρ	Particle density
ρ_b	Bulk density
ρ_{pixel}	PIV error
$\rho_{b_{max}}$	Maximum bulk density
$\rho_{d_{max}}$	Maximum dry density
ρ_w	Density of water
σ_t	Tensile strength
σ_{t_0}	Tensile strength of basic soil elements (Utomo and Dexter, 1981)
σ_c	Unconfined compressive strength
θ_{xx}	Repose angle of species x
σ_t	Tensile strength
θ	Water content
θ_{slv}	Solid-liquid contact angle
A	Adsorption component of matric suction
A	Adsorption potential
A	Fitting parameter (Mata <i>et al.</i> , 2002)
A	Fitting parameter (Utomo and Dexter, 1981)
A	Lang (1967) fitting parameter
A	Pore cross-sectional area
A	Surface area
a	Fitting parameter (Causarano, 1993)
a	Half-width of sample deformation (Frydman, 1964)
A_{llv}	Hamaker constant for liquid-liquid interactions through an intervening vapour
A_{svl}	Hamaker constant for solid-vapour interactions through an intervening liquid
B	Fitting parameter (Mata <i>et al.</i> , 2002)
B	Lang (1967) fitting parameter
b	Fitting parameter (Causarano, 1993)
C	BET constant
C	Capillary component of matric suction
C	Lang (1967) fitting parameter

C	Smoothing function	r_c	Pore radius of interest (BJH method)
c	Solution concentration	r_d	Drainage radius (Tuller et al. (1999))
D	Lang (1967) fitting parameter	r_{imb}	Imbibition radius (Tuller et al. (1999))
D	Particle separation distance	r_{lim}	Pore radius separating the macro and micro regions
D	Sample diameter (Brazilian test)	R_{mod}	Modified particle radius
d	Pore diameter	R_{mod}^*	Modified particle radius for two similar particles
d	Silo width	r^*	Bubble cavitation radius
d_A	Adsorbant atom diameter	R_u	Universal gas constant
d_a	Adsorbate diameter	$S_f d_0^{0.5}$	Lang (1967) fitting parameter
D_{mod}	Modified particle separation distance	S_r	Saturation ratio
D_f	Fractal dimension	S_{r_d}	Saturation ratio during drying
ΔS	Pore surface area (BJH method)	S_{r_w}	Saturation ratio during wetting
ΔV	Pore volume (BJH method)	T	Absolute temperature
ΔE	Bubble formation energy barrier	t	Adsorbed film thickness
e	Void ratio	t	Sample thickness (Brazilian test)
ec	Electrical conductivity	t_c	Adsorbed film critical thickness
e_m	Microstructural void ratio	u_a	Air pressure
e_{MIP}	Void ratio according to MIP testing	u_w	Water pressure
e_w	Water ratio	V	Aggregate volume (Utomo and Dexter, 1981)
$F(\Gamma)$	Angularity factor	V	Amount (volume) adsorbed
g	Acceleration due to gravity	V	Total volume
H	Hydrostatic pressure	V_0	Volume of basic soil elements (Utomo and Dexter, 1981)
h	Height of the capillary column	$V(A)$	Adsorption curve
I	Intensity of attenuated radiation (XRCT)	v_{film}	Volume of water in an adsorbed film
i	Van't Hoff factor	V_{gas}	(Ideal) gas volume
I_o	Intensity of incident radiation (XRCT)	V_{Hg}	Volume of mercury (intruded or extruded)
$J(r)$	Adsorption-determined PSD	V_{m_l}	Liquid molar volume
K	Stress intensity factor	V_{m_v}	Vapour molar volume
k	Constant (used to find D_f)	$v_p(r)$	Volume contained within pores of radius r
k	Fitting parameter (Utomo and Dexter, 1981)	V_s	Volume of solids
L	Crack length	V_{sM}	Volume of solids in the macro region
l	Liquid bridge azimuthal radius	V_v	Volume of voids
L_g	Critical Griffith crack length	$V_{v_{cell}}$	Volume of voids in a unit cell
l_{mod}	Modified liquid bridge azimuthal radius	V_{vM}	Volume of voids in the macro region
M	Griffith factor of safety	$V_{w_{film}}$	Volume water in adsorbed films in a unit cell
M	Solution molarity (molL^{-1})	$V_{w_{LB}}$	Volume of water in a single liquid bridge
m	Fitting parameter (van Genuchten, 1980)	W	Weight of gas adsorbed (BET method)
m	Gradient used to determine D_f	WC_{AD}	Water content of slit-shaped pores
n	Fitting parameter (van Genuchten, 1980)	WC_{film}	Water content of adsorbed films
n	Number of moles (for a perfect gas)	WC_{LB}	Water content of liquid bridges
n	Porosity	WC_{res}	Residual water content
n_{cub}	Porosity of cubically-packed spheres	WC_{sat}	Saturation water content
n_{tet}	Porosity of tetrahedrally-packed spheres	WC_{totalM}	Total macro region water content
P	Applied load (Brazilian test)	WC_{totalm}	Total micro region water content
P	Applied load	W_m	Weight of adsorbate as monolayer (BET method)
P	Applied pressure during MIP	x	Distance travelled through a material (XRCT)
P	Perfect gas pressure	y_1	Half-height of deformed sample (Frydman, 1964)
P	Pore cross-sectional perimeter		
p_{ads}	Applied equilibrium pressure		
P_{gas}	(Ideal) gas pressure		
p_{sol}	Vapour pressure of a solution		
p^*	Saturated vapour pressure		
p_{sol}^*	Saturated vapour pressure of a solution		
R	Particle radius		
r	Pore radius		

Acknowledgements

I would firstly like to thank Dr. Charles Augarde for supervising this project and for offering me the chance to undertake this PhD. I would also like to thank him for the careful and inspiring supervision of my final undergraduate year, which pointed me firmly in the direction of rammed earth research, and for the many hours spent reading and providing feedback and input for this thesis and various publications. I would also like to thank Dr. Paul Jaquin, without whose enthusiasm and dedication to the subject the opportunity to continue rammed earth research would likely not have been available.

This PhD has involved a large number of laboratory investigations, which could not have been completed without the patience, expertise and experience of Mr. Steve Richardson, Mr. Charles McEleavey and Mr. Frank Davies. Their assistance has been invaluable both during this PhD and during my final undergraduate year.

I would like to thank Dr. Matthew Hall for all of the work that we have been able to do together and for hosting several trips to the University of Nottingham. I would also like to thank Prof. David White of the University of Western Australia for providing the software “geoPIV” and assistance and encouragement during its use.

I would like to thank the Royal Academy of Engineering for the award of an International Travel Award (£400), which enabled me to attend the Fifth International Conference on Unsaturated Soils in Barcelona, Spain in September 2010 and University College, University of Durham, for the award of a Travel Scholarship (£100), which enabled me to attend the Young Geotechnical Engineer’s Symposium in Bristol, England, in July 2010.

During this PhD I have had the opportunity to discuss various aspects of rammed earth and unsaturated soils with fellow postgraduate students. I would like to thank Mr. Jonathan Asquith and Mr. Jack Barnard for lively debates concerning the behaviour of unsaturated soils and Mr. William Coombs for providing advice, assistance and friendly competition during our undergraduate and postgraduate years.

Finally, I would like to thank my wife, Harriet, and my parents, Lesley and Paul (Ma and Pa if they are reading this), for their unwavering support. I could not have completed nor even started this PhD if it were not for them.

Publications

Aspects of the work presented in this thesis have been published, submitted or presented in the following papers:

- Beckett, C.T.S. and Augarde, C.E., 2011. Structure creation in earthen construction materials: information from dry soil mixtures. *Frontiers of Architecture and Civil Engineering in China*, 5(2):151–159.
- Beckett, C.T.S. and Augarde, C.E., 2011. A novel image-capturing technique for the experimental study of soil deformations under compaction. *Geotechnical Testing Journal*, 34(6):571–578.
- Beckett, C.T.S. and Augarde, C.E. Soil water retention curve estimation using cavitation and adsorption. Under review for *Géotechnique*.
- Beckett, C.T.S., Hall, M.R. and Augarde, C.E. Macrostructural changes in compacted earthen construction materials under loading. Under review for *Géotechnique*.
- Beckett, C.T.S. and Augarde, C. E., September 2010. Development of microstructure in compacted earthen building materials. In: Alonso, E., Gens, A. (Eds.), *Unsaturated Soils. Fifth International Conference on Unsaturated Soils*, CRC Press, pp. 139-144.
- Beckett, C.T.S., July 2010. The microstructures of compacted earthen materials: implications for design and conservation. In: Ibraim, E., Diambra, A., Bhattacharya, S., Nash, D.F.T. (Eds.), 11th BGA Young Geotechnical Engineer’s Symposium, University of Bristol, pp. 101-102.
- Beckett, C.T.S. and Augarde, C.E., 2012. The effect of humidity and temperature on the compressive strength of rammed earth. Under review for the *Second European Conference on Unsaturated Soils*, Naples, Italy.

Chapter 1

Introduction

1.1 The case for earthen construction

Climate change, growing energy costs and the impact of human activities on the environment have all become key concerns for future development in recent years. As major sources of carbon dioxide and energy consumption, alternative methods are beginning to be explored in order to reduce the environmental impact of construction and infrastructure, in order to comply with government targets to reduce carbon dioxide (CO₂) emissions (for example in the U.K., CO₂ emissions need to be reduced by one-third of the 1990 value by 2020). Examples of low-carbon materials being currently investigated include: hemp-based materials, due to their low carbon cost and rapid growth; lime-based mortars, due to their ability to absorb carbon dioxide during curing; straw-bale construction; and earthen construction.

Earthen construction techniques can be broadly divided into three main categories: *adobe*; *cob*; and *rammed earth* (Houben and Guillaud, 1996; Walker and Maniatidis, 2004; Keefe, 2005; Jayasinghe, 2009):

- Adobe structures are built using unburnt sun-dried bricks. The soil used can be of a range of types, however it must have a high enough clay content to have a malleable consistency when wet, which is necessary to fill the brick moulds, but not one so high as to cause excessive shrinkage.
- Cob structures are formed from a wet mixture of clayey subsoil which is placed onto stone foundations in courses prior to being trampled (a process known as “cobbing”) and left to dry. Again, a range of soil types can be used but with similar clay content restrictions as adobe. Fibres (for example straw or hair) can be added to the mix to improve its strength and to prevent shrinkage cracking during drying.
- Rammed earth (RE) structures are formed by compacting moist subsoil between formwork. Like cob, the material dries after it has been formed into the wall, rather than prior to construction as it does for adobe. Straw or other fibres can also be introduced into the soil mix, depending on local practices, however the material is sufficiently strong to not require these additions (King, 1996).

RE construction can be further divided into a number of sub-categories (Jaquin et al., 2007):

- *Mud RE* has a high water content and can have fibres added to the mix to prevent cracking during drying.
- *Strengthened RE* has a low water content and uses careful soil grading to ensure a strong material.
- *Chained RE* is a construction technique where fired bricks are used to line either the whole face of the wall or the breaks between lifts and blocks, as shown in Figure 1.1(a)).



Figure 1.1: Examples of RE construction variations (Villafeliche, Zaragoza, Spain, c. 12th century): a) use of brickwork (*chained* RE) ; b) use of *lunetos*. Photographs by Paul A. Jaquin. Used with permission.

- *Stabilised RE* uses chemical stabilising agents (for example cement or lime) to improve the strength of the soil mix. An example of a combination of strengthened and stabilised RE is shown in Figure 1.1(b), where lime is packed into the corners of the formwork forming *lunetos* (“moon” in Spanish), into which the earth is compacted, in order to increase the strength and durability of the corners of the walls (Delgado and Guerrero, 2006; Jaquin et al., 2007). Stabilised materials have significantly higher strengths and durabilities than unstabilised materials, so that walls can be made thinner, however this form of RE is significantly less environmentally friendly if cement (typically 5–10% by mass) is used as the stabiliser (Webb, 1994; Venkatarama Reddy and Prasanna Kumar, 2009).

RE offers several significant advantages over cob and adobe. Firstly, it requires significantly less water and has faster mixing and drying times (20%, 25% and 2% of that required by adobe, respectively), making it more suitable for locations where water is scarce and rapid construction is required (Easton, 2007). Furthermore, it does not involve materials that are difficult to handle (i.e. very wet clayey soil, as is required for adobe bricks or cob walls) and does not require mortar or the drying and laying of bricks. It can also be argued that, as RE walls can be left un-rendered, RE is the most aesthetically pleasing of the earthen construction techniques. RE can be used as both an internal and an external construction material without the need for stabilisation. Therefore, it is the most suitable earthen material to replace traditional construction materials, for example fired brick.

Unfortunately, modern RE construction suffers from a number of disadvantages, for example: a lack of a regulatory framework and national guidelines for design and construction; higher costs due to a labour-intensive construction process and the use of specially-designed formwork; and, perhaps the most damaging, a perceived reputation for poor quality and durability. Unstabilised and stabilised RE have lower strengths than other modern construction materials, for example concrete, steel and fired brick, so that they must either be used in conjunction with other materials or in significantly larger quantities. RE construction is therefore suitable for small structures, for example housing or panelling, but not for larger structures due to the unrealistic material quantities required.

This thesis concentrates on RE as a material and construction technique. The RE investigated in this thesis is more correctly referred to as strengthened RE, however from this point on it is referred to simply as “rammed earth” for convenience.

1.2 The rammed earth technique

1.2.1 Rammed earth wall construction

The process of constructing a typical RE wall is shown in Figure 1.2. The soil used is predominantly what is available on site, however modern practices have stricter guidelines on the suitability of soils so that additional material, for example sand or clay, might be added to the soil prior to ramming (Houben and Guillaud, 1996). A typical RE soil mix is well-graded and contain between 50–80% sand and gravel, 10–30% silt and 5–20% clay (Walker et al., 2005). Walls are constructed in blocks, with each block formed by filling the formwork in layers, which are then compacted, to its maximum height. Blocks are compacted in contact with each other, so that the final structure is continuous, rather than in discrete elements as it the case for brickwork.

The formwork comprises sturdy boards held in place by vertical supports and determines how tall a single block can be. The first lift is built either onto an earthen foundation or onto a concrete stem wall, depending on the building codes that are being used, so that the formwork boards can be wedged in place at their base and held together at the top with ties (Easton, 2007). For all subsequent lifts, the bases of formwork boards rest on horizontal supports (these are shown as boards in Figure 1.2, but could easily be scaffolding poles or some such equivalent). These supports can either sit underneath or through the formwork boards depending on the builder's preference. To ease their removal, bridging stones can be placed on top of the supports so that earth is not rammed directly onto them. These stones stay in place after the supports are removed. The use of horizontal supports leads to the formation of characteristic holes in the wall called *putlogs* (or *mechinales* in Spanish) on their removal (Jaquin et al., 2007). These putlogs can either be filled with additional soil mix which is compacted into place, as is the case where the holes are small, or left open, as is observed in surviving historic structures. By leaving the putlogs open, builders ensure that even very large walls can dry throughout their thickness, thereby increasing their durability. In the case of very thick structures, for example city walls, putlogs are not present due to the use of externally-supported scaffolding (this is also beneficial as the putlogs could be a structural weakness in the event of an attack). After filling the formwork it is removed and reconstructed further along the wall, ready to be filled again as shown in Figure 1.2. The rough sides of the blocks (shown as an over-emphasised sloping face in Figure 1.2) improve the contact between them, preventing the formation of cracks or other discontinuities between blocks which might lead to water ingress (Betts and Miller, 1937; Middleton, 1953; Keable, 1996; Maniatidis and Walker, 2003; Walker and Maniatidis, 2004).

An example of an RE structure constructed using the method described above is shown in Figure 1.3. Although built during the 12th century (Jaquin et al., 2007), the putlogs, delineations between blocks, individual rammed layers and the horizontal breaks between the lifts are still plainly visible. Note that the putlogs sit *below* the bottommost layer of the block (as also shown in Figure 1.2), so that the material in between the horizontal supports must be rammed after they have been put in place; it might be that the formwork used had notches in its upper part to accommodate the horizontal supports whilst still being able to ram the extra material.

1.2.2 Development of the RE technique

An understanding of RE's heritage is necessary if it is to be successfully recognised as a viable modern building material. RE construction has survived by its methods being passed on from one generation to the next and has spread as populations have migrated. Therefore, RE construction has, until recently, been based far more on experience and cultural preferences than on established building regulations.

A detailed description of the development and spread of the RE technique is given in Jaquin et al. (2008). This section presents a summary of that work, with additions where new evidence has become

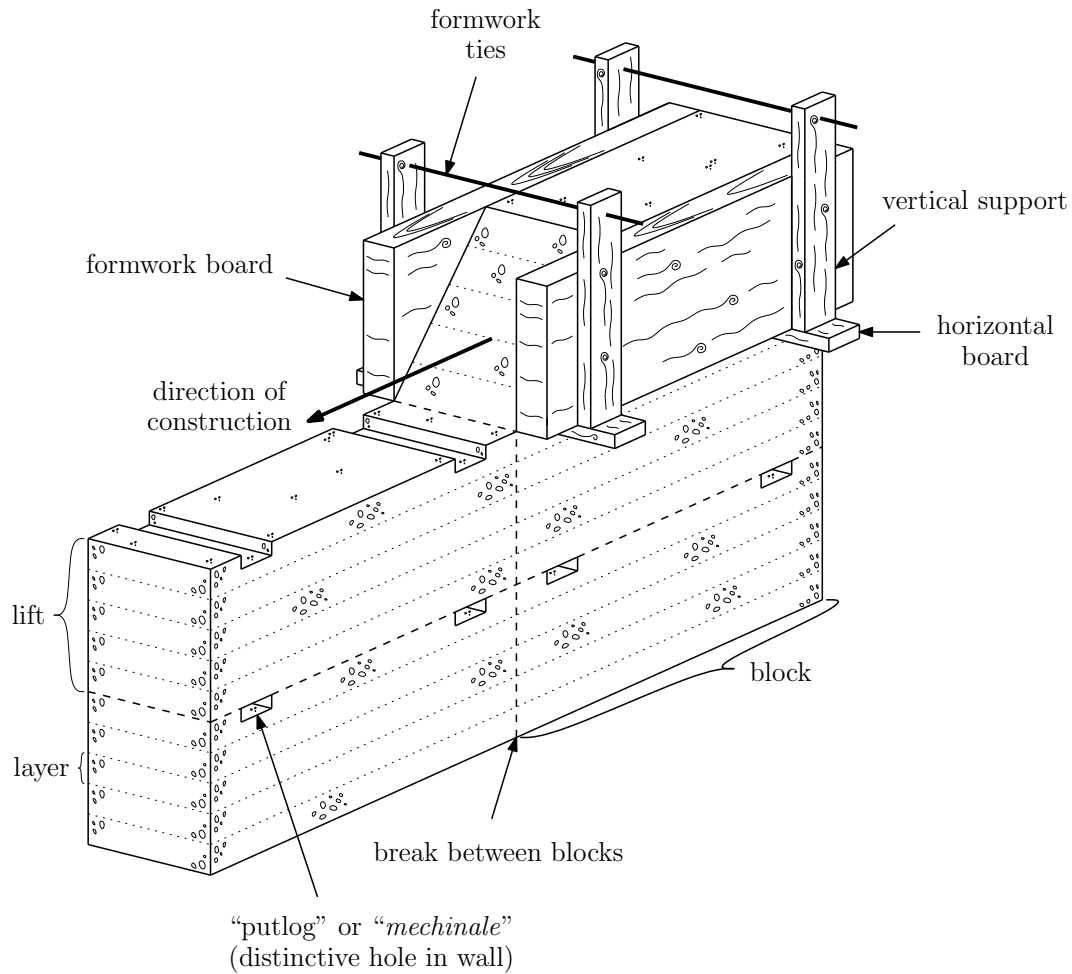


Figure 1.2: Method of construction for an RE wall, after (Jaquin, 2008)

available, as well as updated maps for key RE regions.

1.2.2.1 China and South-East Asia

RE sites in China and South-East Asia are shown in Figure 1.6. The earliest RE sites in China are in Taosi, Xi'an and Pingliangtai in the Henan province, and in Lianyunguan, in the nearby Jiangsu province, dating from the late Neolithic period (3000–2000 B.C.). At these sites, RE was principally used for the construction of defensive walls and remains show a progression from using no formwork (compacted heap walls) to using formwork as shown in Figure 1.2. Records suggest that RE buildings from this period used wide eaves to prevent rain from damaging the earthen walls; although the materials used for wall construction have changed, the practice of using wide eaves supported by ornate brackets (*dougong*) is still a characteristic feature in traditional Chinese and Japanese architecture today (Chambers, 1968; Steinhardt et al., 1984).

More RE sites appeared in the Henan province during the Shang Dynasty (1600–1046 B.C.), including at their capital city, Anyang. RE sites continued to spread throughout the Henan and Shandong provinces during the Western and Eastern Zhou dynasties (1045–221 B.C.) and the Qin Dynasty (220–206 B.C.). It was also during these periods that large sections of what would become the Great Wall were built, although little remains of these sections today. Sections of the Great Wall were also constructed in the Western and Eastern Han Dynasties (206 B.C.–220 A.D.). Figure 1.4 shows an example of a pottery tower, created as a funerary item, dating from this period; the model can be identified as one of an RE



Figure 1.3: 12th century RE wall (Castle of la Atalaya, Villena, Spain). Note the damaged material to the right of the photograph. Photograph by Paul A. Jaquin. Used with permission.

house due to the presence of putlogs and wide eaves (Liu et al., 2005).

The Hakka people migrated to southern China (Guangdong, Jiangxi and Fujian provinces) from the Henan and Shaanxi provinces during the Western and Eastern Jin Dynasties (265–420 A.D.), constructing village-sized *tulou* (fortifications capable of housing hundreds of people (Boyd, 1962)) using RE. The largest sections of the Great Wall were also built during the Jin Dynasty, however these fortifications were subsequently lost to raiders so that the later Ming Dynasty wall, the most famous of the Great Wall sections, lies well south of this line. Although short-lived, the Sui Dynasty (581–618 A.D.) saw the unification of Southern and Northern China and the creation of a centralised government, as well as significant economic reforms. Regulated trade might have seen the RE technique spread to Japan, as potentially shown by the Buddhist monastery in Horyuji (607 A.D., the earliest example of RE in Japan). Evidence of continued RE construction in China can be seen in Xi'an during the Tang Dynasty (618–907 A.D.).

The earliest RE site in Mongolia (Khar Balgas) dates from the Mongol Dynasty (750–1368 A.D.), which immediately predates the Mongol invasion of China and the beginning of the Ming Dynasty (1368–1644 A.D.). It is therefore likely that trade with China also led to a spreading of the RE construction technique beyond China's borders, leading to these early Mongolian sites. The largest and most well-known sections of the Great Wall were built during the Ming Dynasty as a response to the continued conflict with nearby tribes, spreading the RE technique to much of the northern Chinese border. Examples of Ming Dynasty RE structures can be seen at the wall forts at Hexibao and Jiayuguan. Xi'an was the capital city during the Ming Dynasty and so also saw extensive reconstruction in RE. RE structures continued to be constructed by the Hakka people during the Qing Dynasty (1644–1911 A.D.) and during the Empire of China period (1912–1916 A.D.), however these are the only examples of continued RE use during these times (Jaquin et al., 2008).

1.2.2.2 Europe and the Silk Route

RE sites in Europe and North Africa are shown in Figure 1.6. The earliest RE structures in Europe were built by the Phoenicians (1200–539 B.C.). Remains of these structures can be found stretching around the coast of the western half of the Mediterranean from the ancient site of Carthage (814 B.C.)



Figure 1.4: Han Dynasty pottery tower

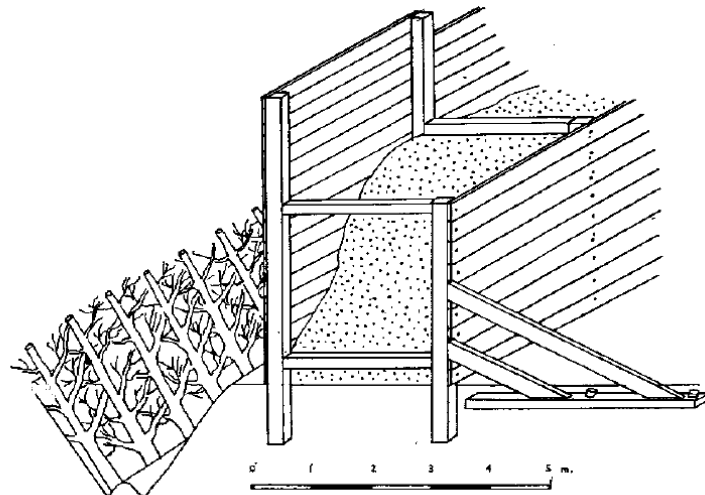


Figure 1.5: Roman RE box rampart and defensive ditch (from Webster (1969))

through to modern day Lyon (Houben and Guillaud, 1994). Hannibal also built RE fortifications along this route as he marched on Italy via the Straights of Gibraltar during the Second Punic War (218 B.C.), as was reported by Pliny the Elder (23–79 A.D.). RE was also recorded as being used before 23 B.C. in Marseilles. The Imperial Roman Army (30 B.C.–284 A.D.) used RE “box ramparts”, as shown in Figure 1.5, as defensive structures if more permanent or sturdy defences were not required, for example as have been excavated at Clawdd Coch fort in southern Wales (Webster, 1969).

Land-based trade between Europe and Asia was established c.100 B.C. and led to the growth of the Silk Route. Fortifications were constructed along its length in order to protect the trade; RE was used in these cases due to the availability of the materials, the remoteness of the locations traversed and the familiarity with the technique of the local craftsmen. Cities were constructed along the route in order to profit from the trade caravans, for example at Yerevan, again using RE as the principal building material. Yerevan was captured by Muslim forces in 658 A.D., who then reintroduced the RE technique as their territories spread across northern Africa, reaching the Iberian Peninsula in 756 A.D.. Continued conflict in the region led to further RE construction in the Iberian peninsula during the tenth, eleventh

and twelfth centuries; the castle of al Atalaya in Villena, built in 1172, shows evidence of both Muslim and Christian style RE construction. The peninsula was conquered by Christian forces in 1492, who used Muslim craftsmen to build (and repair) military and civilian RE structures.

RE was ‘rediscovered’ by Francois Cointeraux in the 18th century following the French Revolution (1789) as a material for the common man, however its use was never adopted on a large scale due to the growing availability of fired bricks and other more modern construction materials (Lee, 2007).

1.2.2.3 Colonial expansion

RE sites in North and South America and Australia and New Zealand are shown in Figure 1.7. Interestingly, no colonial-period RE structures have been identified in Africa despite the construction of multiple settlements. A sketch of the global expansion of RE sites after the turn of the 19th century is also shown in Figure 1.7, where pre- and post-19th century sites are shown as light and dark markers respectively. Larger markers represent a greater number of RE sites within a given area. This rapid expansion was due to improvements in technology, transport and communication associated with the period of the industrial revolution and with the growing popularity of emigrating to the colonies.

No RE sites have been discovered in the Americas dating from before the arrival of Christopher Columbus’ expedition in 1492, with the earliest (surviving) RE structures being built around 1556 A.D. in St. Augustine, Florida. The use of RE spread as colonists migrated north with the formation of the thirteen colonies, established between 1607 and 1703, and then west. Settlers also took the RE technique with them as they spread south to the northern regions of South America and with the foundation of New Spain (1535–1821). Both European and Chinese immigrants brought their RE techniques to the western United States in the 18th and 19th centuries, as seen in the Chew Kee Store (a Chinese-owned herbalists) in California (c.1850).

The first European explorers and settlers arrived in Australia and New Zealand in 1770, with no RE structures having been discovered from before this time. RE was recommended for the construction of buildings following the expansion of British territories into Van Diemen’s land (Tasmania) in 1803. As in the Americas, the RE technique spread as populations moved to new areas, as RE allowed for the rapid construction of houses and facilities in the new territories.

1.2.2.4 RE in the 20th and 21st centuries

Despite its rich and globe-spanning heritage, RE construction went into decline during the 20th century due to the growing availability of modern building materials and a consequent reputation for RE to be unreliable and of low durability (Conti, 2009). Several factors contributed to the development of this reputation; one might be that RE’s own popularity with new settlers gave people the perception that RE was only ‘good enough’ for rough colonial living. Another potential cause is that part of the cultures of peoples who lived and used RE structures was regular maintenance and repair of buildings; as modern building materials do not require this, people began to use these new materials in preference to RE. The lack of passing knowledge of RE construction on to younger generations and the subsequent presence of abandoned structures would therefore create an impression of RE being unsuitable and inferior to the more modern materials.

RE was suggested for the reconstruction of houses in the UK following damage suffered during the two World Wars, however, although some houses were built, it was not adopted on a large scale. Following the work of Betts and Miller (1937) several RE houses were also constructed in the United States, although no large-scale construction projects took place, and it is also suggested that RE was considered for housing projects in the Soviet Union prior to World War Two, again without success. RE was however used for the construction of houses in Germany following World War Two (Houben and Guillaud, 1994). Several

test houses were also constructed in the 1950s in Australia but again were met with little enthusiasm (Middleton, 1953).

RE has gained popularity in the late 20th and early 21st centuries due to the growing interest in the use of environmentally-friendly materials in construction. Ironically, the need to comply with building regulations, combined with a lack of knowledge about the behaviour of RE, means that RE materials are usually stabilised, reducing the environmental advantage despite using raw materials mostly available on-site. The argument over whether the increased performance offered by stabilisation outweighs the environmental cost is still ongoing. Examples of unstabilised RE construction in the UK include: the visitor's centre at the Eden Centre, Cornwall; the Autonomous Environmental Information Centre (AtEIC) at the Centre for Alternative Technologies (CAT) in Powys, Wales; the Genesis project in Somerset; the Rivergreen Centre in Aykley Heads, Durham; and Pines Calyx conference centre in Dover. These examples are showcases for applications of unstabilised RE as an environmentally-friendly material; stabilised RE structures are also seen in the UK, however these are by design more low-key and so less well known, for example a stabilised RE stable block in Northamptonshire and parts of the experimental post-World War One houses in Amesbury.



Key to map markers			
Asian		European and expansion	
● Western to Eastern Han Dynasties (206 BC – 220 AD)	● Mongol Dynasty (750-1368 AD)	● Empire of China (1912-1916 AD)	● 20 th Century
○ Silk Route (c.100 BC)	● Asian Muslim (8 th – 10 th Century)	● Qing Dynasty (1644-1911 AD)	● 19 th Century
● Qin Dynasty (220-206 BC)	● Tang Dynasty (618-907 AD)	● Buddhist (15 th Century)	● 18 th Century
● Western & Eastern Zhou Dynasties (1045-221 BC)	● Japanese Buddhist (607 AD)	● Ming Dynasty (1368-1644 AD)	● Spanish Structures (16 th Century)
● Shang Dynasty (1600-1046 BC)	● Sui Dynasty (581-618 AD)		● Berber Muslim (c.700 AD)
○ Late Neolithic (3000-2000 BC)	● Western & Eastern Jin Dynasties (265-420 AD)		○ Phoenician (1200-539 BC)

Figure 1.6: RE sites in Asia and Europe



Figure 1.7: RE sites in the Americas (top) and Australia (middle) and a sketch showing the locations of RE sites pre- and post-19th century (bottom)

1.3 Thesis structure

The aim of this thesis is to determine how the structure of RE, defined as the distribution of pores, particles and water within RE, affects its behaviour in a number of applications and environments, in order to improve confidence in its use and viability as a modern construction material. The work presented uses both analytical and experimental techniques to analyse RE as a geotechnical material.

An introduction to unsaturated soil mechanics is presented in Chapter 2 in order to describe the procedures which contribute to the formation of RE's material structure. Chapter 3 then investigates the relationship between the soil pore size distribution and its water retention properties, through the creation of a new modelling procedure, in order to demonstrate the link between material structure and behaviour.

The link between material structure and behaviour established in Chapter 3 is used to interpret experimental results presented in Chapters 4 to 7 in order to explain certain aspects of RE's behaviour. The processes used to manufacture RE samples in the laboratory are investigated in Chapter 4 in order to determine whether samples are representative of materials used in construction, focusing on the manufacture of dry soil mixes and the compaction process using new experimental procedures.

The effects of relative humidity and temperature on the compressive strength of RE are investigated in Chapter 5, in order to determine how RE materials behave in different climates. Humidities and temperatures are selected according to those conditions currently prevalent at RE sites around the world. This is an important issue when considering how and why existing structures have survived and when selecting suitable materials for construction.

Chapter 6 investigates the effects of changing water content on the tensile strength of RE, as well as the effects of dissolved ions in the pore water. The latter is an important factor when considering the water used to wet RE material during construction. The results from Chapters 5 and 6 are then used to determine the sources of tensile and compressive strength in RE in terms of its material structure.

In Chapter 7, X-ray computed tomography is used to observe the effect of compressive loading on RE's macrostructure, an important consideration when interpreting the likely effect of damage on RE structures. Samples comprising single and multiple layers are analysed in order to determine how layering and layer thickness affects the macrostructure and to support results found in Chapter 4 for the compaction of RE.

Conclusions arising from the research presented in Chapters 3 to 7, as well as implications and recommendations for RE design, construction and conservation which are presented in Chapter 8.

1.4 References

- Betts, M. C., Miller, T. A. H., 1937. Rammed earth walls for buildings. Farmers Bulletin No. 1500. U.S. Department of Agriculture, Washington D.C. (U.S. Govt. Printing Office).
- Boyd, A., 1962. Chinese architecture and town planning. Alec Tiranti Ltd, London (UK).
- Chambers, W., 1968. Design of Chinese buildings, furniture, dresses, machines and utensils. Benjamin Blom, Inc., New York (USA).
- Conti, A. P., 6-9 September 2009. Earth building today, a renewed use of an ancient technology. In: Proceedings of the 11th International Conference on Non-Conventional Materials and Technologies (NOCMAT). Bath University.
- Delgado, M. C. J., Guerrero, I. C., 2006. Earth building in Spain. *Construction and Building Materials* 20 (9), 679–690.
- Easton, D., 2007. The Rammed Earth House, Completely Revised Edition. Chelsea Green Publication Company, Vermont (USA).
- Houben, H., Guillaud, H., 1994. Earthen architecture: A comprehensive guide. Intermediate Technology Development Group, London (UK).
- Houben, H., Guillaud, H., 1996. Earth construction - a comprehensive guide., Second Edition. Intermediate Technology Publications, London (UK).
- Jaquin, P. A., 2008. Analysis of historic rammed earth construction. PhD Thesis, Durham University.
- Jaquin, P. A., Augarde, C. E., Gerrard, C., 22-24 August 2007. Historic rammed earth structures in Spain, construction techniques and a preliminary classification. Bangalore: Interline Publishing.
- Jaquin, P. A., Augarde, C. E., Gerrard, C. M., 2008. A chronological description of the spatial development of rammed earth techniques. *International Journal of Architectural Heritage: Conservation, Analysis and Restoration* 2 (4), 377–400.
- Jayasinghe, C., 2009. Structural design of earth buildings. Eco Ceylon Pvt. Ltd., Colombo.
- Keable, J., 1996. Rammed earth structures: a code of practice. Intermediate Technology Publications, London (UK).
- Keefe, L., 2005. Earth Building: Methods and materials, repair and conservation. Taylor & Francis, Oxford UK.
- King, B., 1996. Buildings of Earth and Straw: Structural Design for Rammed Earth and Straw-Bale Architecture. Ecological Design Press, Sausalito, California (USA).
- Lee, P., 2007. Francois Cointeraux and the school of "agriculture" in eighteenth-century France. *Journal of Architectural Education* 60 (4), 39–46.
- Liu, C. Y., Nylan, M., Barbieri-Low, A., 2005. Recarving China's Past: Art, Archaeology, and Architecture of the 'Wu Family Shrines'. Princeton University Art Museum, Princeton, New Jersey.
- Maniatidis, V., Walker, P., 2003. A Review of Rammed Earth Construction. University of Bath.
- Middleton, G. F., 1953. Build your house of earth. Commonwealth Experimental Building Station, Melbourne, Australia.
- Steinhardt, N. S., Xinian, F., Glahn, E., Throp, R. L., Juliano, A. L., 1984. Chinese Traditional Architecture. China Institute in America.
- Venkatarama Reddy, B. V., Prasanna Kumar, P., 6-9 September 2009. Role of clay content and moisture on characteristics of cement stabilised rammed earth. In: Proceedings of the 11th International Conference on Non-Conventional Materials and Technologies (NOCMAT). Bath University.
- Walker, P., Keable, R., Martin, J., Maniatidis, V., 2005. Rammed Earth: Design and Construction Guidelines. BRE Bookshop, Watford (UK).
- Walker, P., Maniatidis, V., 2004. Rammed earth: a natural option for walling. *Proceedings of the Institution of Civil Engineers-Civil Engineering* 157 (1), 5–5.
- Webb, D. J., 1994. Stabilised soil and the built environment. *Renewable Energy* 5, 1066–1080.
- Webster, G., 1969. The Roman Imperial Army. A. and C. Black, London.

Chapter 2

Unsaturated soil mechanics theory

2.1 Introduction

Rammed earth is effectively a manufactured, highly unsaturated soil, so that its behaviour can be understood by considering it in terms of unsaturated soil mechanics (Jaquin, 2008). In this chapter, an overview of the basics of soil mechanics and unsaturated soil mechanics is presented which will provide a foundation for work conducted in subsequent chapters.

The study of soil mechanics arguably began with the work of Terzaghi (1925) and grew out of a demand for better practices for the design in and with soil and to give engineers “a set of theoretical concepts which covered all important aspects of soil behaviour” Gens (2010). In classical soil mechanics, soils are viewed as collections of particles contacting at their boundaries and inundated with water; whether the water is free to flow (*drained*) or contained within the sample (*undrained*) affects the behaviour of the combined material. Terzaghi (1936) was the first to relate the roles of the solid soil structure and water content in the principle of *effective stress*, where the effect of an applied stress is divided between the structure and the pore water, depending on the drainage conditions.

Classical soil mechanics does not consider the behaviour of soil that is at water contents lower than saturation. However, the effects of reduced water contents on the properties of soils are now recognised for being responsible for a number of phenomena, for example collapse, shrinking and swelling, which cannot be explained using classical soil mechanics, and for being potentially beneficial in terms of reducing high costs resulting from overly-conservative designs (Lu and Likos, 2004; Gens, 2010). This has therefore led to the study of *unsaturated* soil mechanics, the basics of which are discussed in this chapter.

2.2 Soil mineralogy

Soils are formed by the physical, chemical and biological weathering of the Earth’s crust. As such, they comprise a vast range of particle sizes, the smallest being clay particles of the order of 10 nm across and the largest being boulders of sizes larger than 200 mm (BS 1377:1999). The uppermost layers of a natural soil (the *topsoil*) comprise organic material in various states of growth or decomposition, as well as burrowing organisms which aid in the breakdown of the material. “Soils” in geotechnical terms do not include the topsoil due to its variability and myriad of unknown properties and because it is a valuable resource that is usually removed from a construction site prior to any work being started. As such, geotechnical engineers are primarily concerned with properties of the sub-soil which comprises clay, silt, sand, gravel and boulder-sized particles (Craig, 2004; Powrie, 2008).

Physical erosion includes wind, freeze-thaw, water and glacial processes, to name but a few. Physical

erosion of rocks results in a wide range of particle sizes, from large boulders down to the fine “rock flour” formed by the grinding action of glaciers. However, all of these particles retain the chemical properties of the parent rock. Particles formed by physical weathering can be rounded, angular, flat or elongated in shape and are usually referred to as *grains*. Hence, soils that mainly comprise these particles are referred to as *granular soils* (Craig, 2004).

“Clays” in a geotechnical context can be used to describe both a class of particle sizes and materials which have a high plasticity when mixed with water and a high resistance to weathering. They are often referred to as *fine-grained soils* (sometimes shortened to just *fine soils*). Clay particles are aluminosilicates, formed from the chemical weathering of rocks (predominantly feldspars). Their planar structure grants them a large surface-area-to-mass ratio (specific surface area, SSA), resulting in their structure being highly influenced by surface forces. All soil particles have an associated surface charge due to their constituent molecules, however these are extremely weak for particles larger than clays due to their low SSAs (Craig, 2004; Powrie, 2008).

The basic “building blocks” of clays are the silicon-oxygen tetrahedron and the aluminium-hydroxyl or magnesium-hydroxyl octahedron, which have a net negative charge due to the valency imbalance of the individual atoms. These molecules combine to form strong sheet-like structures of silica $[\text{SiO}_4]_n$, *gibbsite* $[\text{Al}_2(\text{OH})_6]_n$ or *brucite* $[\text{Mg}_3(\text{OH})_6]_n$, where n denotes a large number of molecules. Cations within these sheets (i.e. Si^{4+} , Al^{3+} and Mg^{3+}) can be substituted for other cations depending on the conditions. As a result of cation substitution, sheet surface charges can become imbalanced so that additional cations are adsorbed onto the surface or held in suspension with water around the sheet. The tendency to adsorb or exchange cations is called the *cation exchange capacity* (Hillel, 1998, 2004; Powrie, 2008).

Clay minerals are formed by the combinations of two or more sheets and the type of clay mineral is determined by how combinations of these sheets are arranged. Although the intra-sheet bonding is strong, the inter-sheet bonding is relatively weak, and it is this which gives the individual clay minerals their distinct properties (Powrie, 2008). The most common clay minerals are *kaolinite*, *illite* and *montmorillonite*:

Kaolinite

Comprises a silica and a gibbsite sheet stacked one on top of the other and forms the largest particles of the clay mineral types. As it has strong inter-layer bonding it shows the least amount of swelling on the addition of water and has few or no exchangeable cations (Mitchell and Soga, 2005).

Illite

Comprises two sheets of silica either side of a sheet of gibbsite, separated by a layer of potassium ions due to its formation process. Aluminium ions in the gibbsite sheet may be exchanged by iron or magnesium (but not a complete replacement of the aluminium with magnesium, i.e. brucite).

Montmorillonite

Comprises two sheets of silica either side of a sheet of gibbsite, separated by a layer of cations in water (solvated cations), so that they are similar in structure to illites. However, the presence of water between the sheets means that montmorillonites swell to a much greater degree if additional water is added. Weak inter-layer bonding also means that montmorillonites are the smallest of the clay mineral particles. Silicon ions in the silica sheets can be extensively replaced by aluminium ions. Aluminium ions in the gibbsite sheets can be replaced by a range of other cations, so that montmorillonites have the highest cation exchange capacity of all the clay minerals.

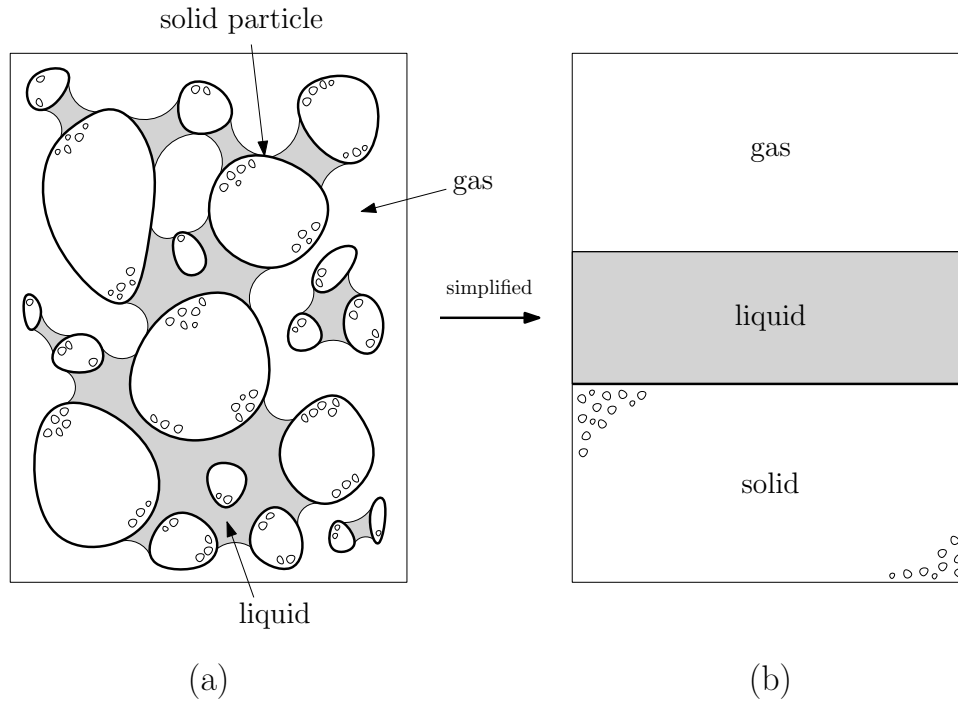


Figure 2.1: Sketch of a soil element (a) and a simplified phase diagram (b)

2.3 Soil phase relationships

An element of soil, as illustrated in Figure 2.1(a), comprises solid (particles of all sizes), liquid (water) and gas (air) phases. Soil phase relationships are determined by assuming that phases can be combined into bulk forms as shown in Figure 2.1(b) and are useful in expressing bulk soil properties. A selection of these phase relationships is described below.

1. The void ratio, e , is the ratio of the volume of voids present in the soil, V_v , to the volume of solids, V_s :

$$e = \frac{V_v}{V_s} \quad (2.1)$$

2. The porosity, n , is the ratio of the volume of voids to the total volume, $V = V_v + V_s$:

$$n = \frac{V_v}{V} = \frac{e}{1 + e} \quad (2.2)$$

3. The saturation ratio, S_r , is the ratio of the volume of water, V_w , to the volume of voids:

$$S_r = \frac{V_w}{V_v} \quad (2.3)$$

4. The water ratio, e_w , is the ratio of the volume of water to the volume of solids and is useful if the volume of voids in a sample is not constant, for example during compression (Tarantino, 2009):

$$e_w = \frac{V_w}{V_s} \quad (2.4)$$

2.4 Suction in unsaturated soils

“Suction” refers to the chemical potential of the pore water in unsaturated soils and is so named due to it invariably being negative (i.e. the pore water has a lower potential than free, pure water under the same conditions). However, suctions are quantified as positive in unsaturated soils practice for convenience. When discussing the suction present in an unsaturated soil, the quantity is more appropriately referred to as the *total suction*, as it is the combination of suctions from a number of sources. Although traditionally referred to in units of pressure, suction is more appropriately thought of as a variable that expresses the “degree of attachment” of the liquid to the solid phase, rather than as a physical negative pressure, as suctions can often be of considerable magnitude (Fredlund and Xing, 1994; Vanapalli and Fredlund, 1997; Gens, 2010). Suction acts to increase the bonding between particles and is considered to be one of the independent stress variables necessary to characterise unsaturated soils (Alonso et al., 1990; Gallipoli et al., 2003; Sun et al., 2007; Tarantino, 2007). This section investigates the contributions made by various suction sources to the total suction, as well as clarifying the terminology used for these suctions in unsaturated soils literature.

2.4.1 Capillary suction

2.4.1.1 Surface tension and the contact angle

Surface tension is a property which expresses the work required to change the surface area of a sample (Atkins and De Paula, 2006). For water, the surface tension can be estimated using

$$\gamma_{lv} = 0.1171 - 0.0001516T \quad (2.5)$$

where T is the absolute temperature in Kelvin (Edlefsen and Anderson, 1943).

The *contact angle* is the angle of the interface made between two phases in the presence of a third phase. In unsaturated soils, it is taken to be the angle between a line tangent to the air-water interface and the water-solid interface. If a solid makes a contact angle with water of $\leq 90^\circ$ then it is said to be “wetting” or hydrophilic. Similarly, contact angles of $> 90^\circ$ represent hydrophobic or “non-wetting” materials (Lu and Likos, 2004). Contact angles arise due to the balance of forces between the solid-vapour, γ_{sv} , solid-liquid, γ_{sl} , and liquid-vapour, γ_{lv} , surface tensions as

$$\cos(\theta_{slv}) = \frac{\gamma_{sv} - \gamma_{sl}}{\gamma_{lv}} \quad (2.6)$$

where θ_{slv} is the contact angle between a liquid and a solid in the presence of a vapour, as shown in Figure 2.2 (Atkins and De Paula, 2006). In the case of water, the contact angle with soil particles is usually assumed to be zero degrees (perfectly wetting), whilst in the case of mercury it can be as large as 140° (i.e. non-wetting) (Romero, 1999).

The Helmholtz energy is the difference between the internal energy of a system and the product of the temperature and the entropy. Surfaces have a natural tendency to contract, due to a reduction in the Helmholtz energy with reducing surface area, which can lead to the formation of curved surfaces (Atkins and De Paula, 2006). An example of a curved water surface trapped in a cylinder is shown in Figure 2.2. The difference between the pressures above, p_o , and below, p_i , the curved surface due to the

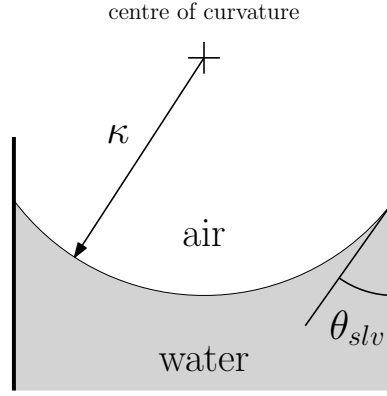


Figure 2.2: Water meniscus trapped between two walls

action of surface tension is given by the Young-Laplace equation

$$p_o - p_i = -\frac{2\gamma_{lv} \cos(\theta_{slv})}{\kappa} \quad (2.7)$$

where γ_{lv} is the surface tension and κ is the radius of the meniscus. Note that although Figure 2.2 shows a two-dimensional section through the meniscus, Eqn 2.7 is also the three-dimensional solution for the pressure of the liquid due to the curved surface (Atkins and De Paula, 2006). For an air-water interface, Eqn 2.7 can be re-written as

$$u_a - u_w = -\frac{2\gamma_{lv} \cos(\theta_{slv})}{\kappa} \quad (2.8)$$

where $u_a - u_w$ is the difference between the air and water pressures (u is traditionally used to denote pressure in soil mechanics literature). Therefore for air at atmospheric pressure, the water pressure is negative under a curved surface. If given positive units, this negative pressure is called the *capillary suction* (Volkwein, 1993; Mu and Su, 2007).

2.4.1.2 The Kelvin equation

As air is present in unsaturated soils, the liquid phase, considered above to be pure water, should be taken to be water containing dissolved air, and similarly, the gaseous phase as air containing water vapour (Gens, 2010). Thompson (1871) (Lord Kelvin) related the curvature of a liquid meniscus to the relative vapour pressure of the vapour of that liquid in the gas above the liquid, also known as the *relative humidity* (RH). The effects of RH are of particular importance to RE, as its large surface area means that it can easily equilibrate to ambient conditions throughout its bulk (Jaquin et al., 2008).

At equilibrium, the chemical potentials of a liquid, μ_l , and its vapour, μ_v , are equal ($\mu_l = \mu_v$). If the pressure of the liquid is increased by dP the potential of the liquid changes by $d\mu_l = V_{m_l} dP$ where V_{m_l} is the molar volume of the liquid. Similarly, the potential of the vapour changes by $d\mu_v = V_{m_v} dp$ where dp is the change in vapour pressure and V_{m_v} is the molar volume of the liquid. If the vapour is assumed to behave like a perfect gas, so that $PV = nR_u T$ can be applied (where P is the pressure of the gas, V is the volume, n is the number of moles and R_u is the universal gas constant (8.314 J/molK)), then

$$d\mu_v = \frac{R_u T dp}{p}. \quad (2.9)$$

In order to maintain equilibrium (i.e. assuming that the process is not instantaneous) the changes in the

potentials of the liquid and the vapour are therefore related by

$$V_{m_l} dP = \frac{R_u T dp}{p}. \quad (2.10)$$

Assuming that the effect of an increase in liquid pressure on the vapour pressure is small, the following integrations can be made:

$$\int_{p^*}^{p^* + \Delta P} V_{m_l} dP = RT \int_{p^*}^p \frac{dp}{p} \quad (2.11)$$

where p^* is the saturated vapour pressure of vapour of the liquid above the surface of and in equilibrium with a free body of that liquid (i.e. no external effects are present, such as curved surfaces) and which simplifies to Eqns 2.13 and 2.13:

$$\ln \frac{p}{p^*} = \frac{V_{m_l}}{R_u T} \Delta P \quad (2.12)$$

$$p = p^* \exp \left(\frac{V_{m_l} \Delta P}{R_u T} \right). \quad (2.13)$$

where $\frac{p}{p^*}$ closely approximates the relative humidity (Dao et al., 2008). If the change in liquid pressure $\Delta P = -\frac{2\gamma_{lv}}{\kappa}$ (i.e. Eqn 2.7 with $\theta_{slv} = 0$) then Eqn 2.13 can be rewritten as

$$p = p^* \exp \left(-\frac{2\gamma V_{m_l}}{\kappa R_u T} \right) \quad (2.14)$$

$$-\frac{2\gamma}{\kappa} = \frac{R_u T}{V_{m_l}} \ln(\text{RH}) \quad (2.15)$$

which are expressions for the *Kelvin equation* for droplets of radius κ (Thompson, 1871; Atkins and De Paula, 2006). Note that γ is the liquid-vapour surface tension; as capillarity only rely on the liquid-vapour surface tension, the subscripts have been dropped for convenience.

2.4.1.3 Capillary rise

A phenomenon associated with the drop in water pressure below a concave meniscus is *capillary rise*. If a tube of radius r_{tube} is placed in a free reservoir of liquid, the formation of a meniscus in the tube due to the contact angles between the liquid and the solid causes a column of water to rise until the water pressure at the level of the surface is equilibrated, as shown in Figure 2.3. If the atmospheric pressure is P , the height of the water column h is found using

$$h = \frac{2\gamma \cos(\theta_{slv})}{\kappa \rho_w g} \quad (2.16)$$

where ρ_w is the density of water and g is the acceleration due to gravity. If it is assumed that the contact angle is zero then the radius of the capillary tube equals the radius of the meniscus ($r_{tube} = \kappa$) so that the change in water pressure due to the presence of the meniscus, equivalent to the additional pressure at the surface datum due to the weight of the water column, $h\rho_w g$, is given by $u_a - u_w = -\frac{2\gamma}{r_{tube}}$. This result can be combined with Eqn 2.15 to relate the change in water pressure in capillary tubes to the relative humidity and temperature of the vapour as

$$u_a - u_w = -\frac{2\gamma}{r_{tube}} = -\frac{R_u T}{V_{m_l}} \ln(\text{RH}). \quad (2.17)$$

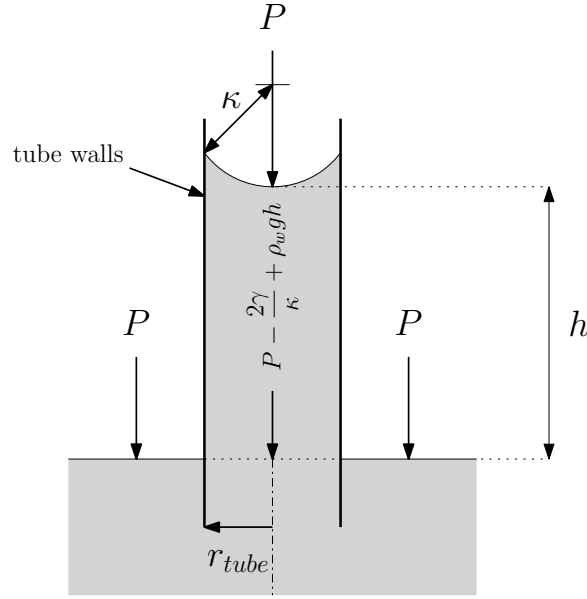


Figure 2.3: Associated water pressures during capillary rise

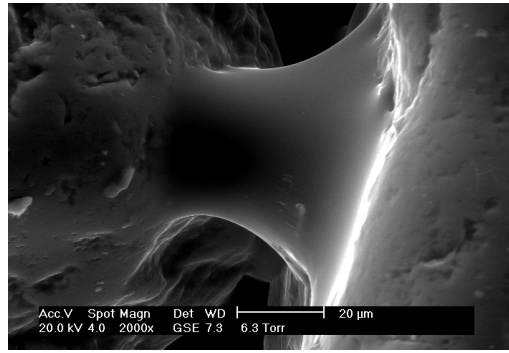


Figure 2.4: ESEM images of a liquid bridge between sand particles (Lourenço et al., in press)

In order to remove the negative sign from the right hand side of Eqn 2.17, the substitution $\psi_{cap} = -u_w$ is made, where ψ_{cap} is the capillary suction, so that

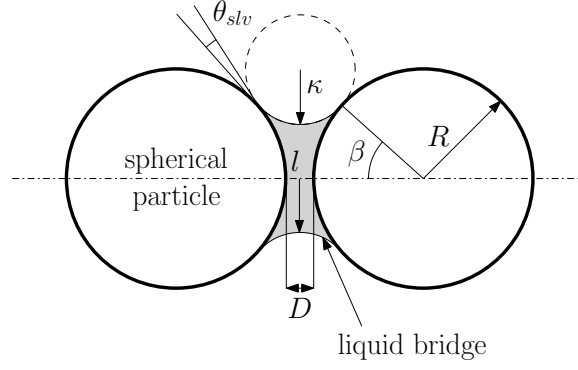
$$\psi_{cap} = \frac{R_u T}{V_{m_l}} \ln(RH). \quad (2.18)$$

which is another common form of the Kelvin equation when discussing capillary effects. Note that Eqn 2.18 has made the assumption that the air pressure is atmospheric, so that $u_a = 0$.

2.4.1.4 Liquid bridges

Water in unsaturated soils can be in either a *funicular* (continuous) and *pendular* (discontinuous) regime. In the pendular regime, water exists as menisci between soil particles, an example of which is shown in Figure 2.4 for a meniscus between two sand particles (Lourenço et al., in press). Such a configuration is referred to as a *liquid bridge*. The particles need not be in contact for a liquid bridge to be present, again as shown in Figure 2.4.

The capillary suction arising due to the curved surfaces of a liquid bridge, $\psi_{cap_{LB}}$, held between two

Figure 2.5: Meridional (κ) and azimuthal (l) radii in a liquid bridge

spherical particles of radius R at a separation distance D as shown in Figure 2.5 is given by

$$\psi_{capLB} = \gamma \left(\frac{1}{\kappa} - \frac{1}{l} \right) \quad (2.19)$$

where κ and l are the meridional (i.e. it remains the radius of the concave surface) and azimuthal (i.e. the radius of the convex surface) radii of the liquid bridge respectively (as shown in Figure 2.5), given by Butt and Kappl (2009) as

$$\kappa = \frac{2R(1 - \cos(\beta)) + D}{2 \cos(\theta_{slv} + \beta)} \quad (2.20)$$

$$l = R \sin(\beta) - \kappa (1 - \sin(\theta_{slv} + \beta)) \quad (2.21)$$

where β is the “filling angle” and θ_{slv} is normally considered to be zero for ease. The terms in the main bracket of Eqn 2.19 are subtracted as κ is concave with respect to the liquid whereas l is convex. ψ_{capLB} can be substituted into the Kelvin equation directly, giving

$$\psi_{capLB} = -\gamma \left(\frac{1}{\kappa} - \frac{1}{l} \right) = -\frac{R_u T}{V_{ml}} \ln(RH) \quad (2.22)$$

which allows the capillary suction in a liquid bridge to be related to the relative humidity.

2.4.2 Matric suction

Matric suction is the component of total suction that arises due to the combination of the curvature of water menisci between particles and the adsorption of a film of water molecules onto particle surfaces, according to

$$\psi_m = C(\kappa) + A(t) \quad (2.23)$$

where ψ_m is the matric suction, C is the capillary component described in its simplest form by Eqn 2.7 and is a function of the liquid-gas curvature, κ , and A is the adsorptive component which is a function of the film thickness, t (Philip, 1977). Figure 2.6 shows two particles in contact at point A where the adsorption of a film of water around the two particles results in the dominance of capillary effects at A as the films coalesce into a curved meniscus and of adsorption on surfaces remote from A (Edlefsen and Anderson, 1943).

Adsorption is the mechanism whereby soil particles readily acquire a layer of water molecules on their surfaces and can be attributed to short-range electrostatic and long range van der Waals forces (Tuller et al., 1999). Adsorbed water is present both in isolation as films adsorbed onto the surfaces of particles and as a region covering the surfaces of particles in the presence of bulk water or liquid bridges.

Electrostatic forces arise from the short-ranged electrical fields that emanate from charged surfaces of soil particles, predominantly clays, influencing the structure of nearby water molecules. The effect of the electric field is to attract and align water molecules on the particle surface due to the bipolar nature of the water molecule, changing the local density of the adsorbed water. Van der Waals forces arises due to long-range forces which influence the surrounding water molecules. As such, the effect is very similar to that of the electrostatic force in that the orientation and distribution of water molecules is altered (Lu and Likos, 2004; Israelachvili, 2005). Adsorption, electrostatic and van der Waals forces are often described as independent sources of suction, however it is perhaps more appropriate to combine their effects into one adsorptive term.

The effects of electrostatic and van der Waals forces increase as the distance between the water molecules and the particle surface decreases. Therefore, the suction due to these phenomena increases with reducing separation distance. However, as the number of water molecules near the surface increases with reducing separation distance, the pressure of the water increases with reducing separation distance in order to maintain equilibrium with the bulk water phase (Lu and Likos, 2004). Therefore, the suction at any point in the liquid is the same under equilibrium conditions.

If it is assumed that $R \gg t$, then the thickness of the adsorbed films at a given total suction, $t(\psi)$, is given by

$$t(\psi) = \sqrt[3]{\frac{-A_{svl}}{6\pi\psi}} \quad (2.24)$$

where $A_{svl} = -6 \times 10^{-20} \text{J}$ is the Hamaker constant for solid-vapour interactions through an intervening liquid (Iwamatsu and Horii, 1996; Tuller et al., 1999). Note the inclusion of a negative sign on the numerator to account for the positive definition of ψ .

Although it appears from Eqn 2.24 that thin films form as a response to, rather than in conjunction with, suction, the presence of thin films surrounding a particle will influence the shape of the liquid bridge so that capillary and adsorptive effects cannot be separated. If thin films are present then Eqns 2.20 and 2.21 need to be modified to incorporate the film thickness, becoming

$$\kappa_{mod} = \frac{2R_{mod}(1 - \cos(\beta)) + D_{mod}}{2 \cos(\theta_{slv} + \beta)} \quad (2.25)$$

$$l_{mod} = R_{mod} \sin(\beta) - \kappa_{mod}(1 - \sin(\theta_{slv} + \beta)) \quad (2.26)$$

where κ_{mod} and l_{mod} are the modified meridional and azimuthal radii respectively, $R_{mod} = R + t(\psi)$ and $D_{mod} = D - 2t(\psi)$ (where $t(\psi)$ is found from Eqn 2.24 using ψ_{capLB}). Note that as $t(\psi_{capLB})$ influences ψ_{capLB} an iterative process is now required to solve Eqn 2.19. Also note that Eqns 2.25 and 2.26 assume that both particles have the same radius. As adsorbed films are assumed to be present, θ_{slv} is the contact angle between the water in the liquid bridges and the adsorbed water in the films which can be assumed to be zero as the surface can be considered to be perfectly wetting.

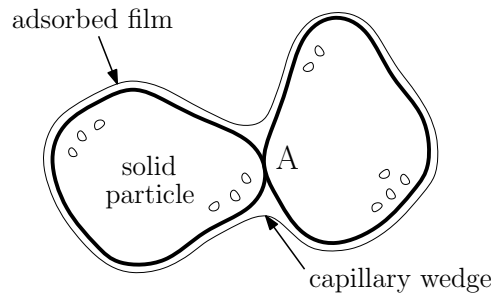


Figure 2.6: Capillary condensation and adsorption between two contacting particles

As ψ_{capLB} found using Eqn 2.19 now incorporates thin film adsorption through Eqns 2.25 and 2.26, it is more correct to refer to the calculated suction as ψ_m , i.e. the matric suction. A similar correction is required for Eqn 2.22, becoming

$$\psi_m = -\gamma \left(\frac{1}{\kappa_{mod}} - \frac{1}{l_{mod}} \right) = -\frac{R_u T}{V_{m_i}} \ln(RH) \quad (2.27)$$

which also incorporates a corrected version of Eqn 2.19.

The terms *matric suction* and *capillary suction* are often synonymous in the unsaturated soils literature, due to the similarity between Eqns 2.22 and 2.27 where the only difference is the presence of adsorbed films. However, the lack of the final clarification (i.e. the consideration of an adsorbed phase) has led to confusion over the two terms. To summarise, capillary suction is that suction which arises from curved air-water interfaces only, whilst matric suction incorporates an adsorptive term the function of which is to change the shape of the air-water interfaces. Both capillary and matric suction are therefore due to changes in the liquid pressure.

In the case of large particles (sands and silts), environmental scanning electron microscopy (ESEM) suggest that water droplets condense in discrete locations on the surfaces of large particles and then grow as the amount of water available (i.e. the relative humidity) increases (Lourenço et al., in press), so that adsorbed films surrounding the particles are not present. However, the water in contact with the particle surface is still in the adsorbed phase, so that Eqn 2.27 still applies for liquid bridges between large particles.

2.4.3 Osmotic suction

Figure 2.7 shows two solutions separated by a semi-impermeable membrane (SIM). Solution A has a lower solute concentration than solution B and solvent is free to diffuse across the SIM. As solution B has a higher concentration, there is a net diffusion of solvent from solution A into solution B due to the higher probability of solvent particles successfully crossing the SIM from solution A than from solution B (i.e. osmosis). This causes solution B to be driven up the column until the hydrostatic pressure H is sufficient to counter the diffusion. If a pressure equal to H is applied, the diffusion across the SIM in each direction becomes equal. This additional pressure is equal to the *osmotic suction* (Hillel, 2004).

It should be noted that the SIM in Figure 2.7 is vertical in order to eliminate any gravitation effects on the flow of solvent across the membrane. Gravitational effects are ignored when considering osmotic flow; it is only for clarity in Figure 2.7 that the hydrostatic pressure is described in terms of a water column. Gravitation is sometimes accredited with being an independent source of suction due to water being held at a higher elevation possessing a greater potential than the same water at a lower elevation (Buckingham, 1907). However, gravitational suction is often ignored in constitutive models as samples and bodies of water, for example liquid bridges, are considered to be small and flow between the different water bodies is assumed to be negligible. Although SIMs do not exist in real soil structures, the very small pores between and surface charges of clay particles can lead to membrane properties so that the movement of some solutes becomes restricted (Mitchell, 1991). Although osmotic suction values in soils are relatively unknown, osmotic suctions of up to 0.5 MPa have been measured in cement mortars immediately after mixing (in the absence of additives), showing that osmotic suctions can have a significant effect on the behaviour of a material (Dao et al., 2008).

Solutes lower the potential of the pore water and so consequently its vapour pressure (Eqn 2.13), so that the Kelvin equation in terms of relative humidity (Eqn 2.27) is no longer valid. Instead, the Kelvin equation must be modified to relate to the saturated vapour pressure of the solution, p_{sol}^* , rather than

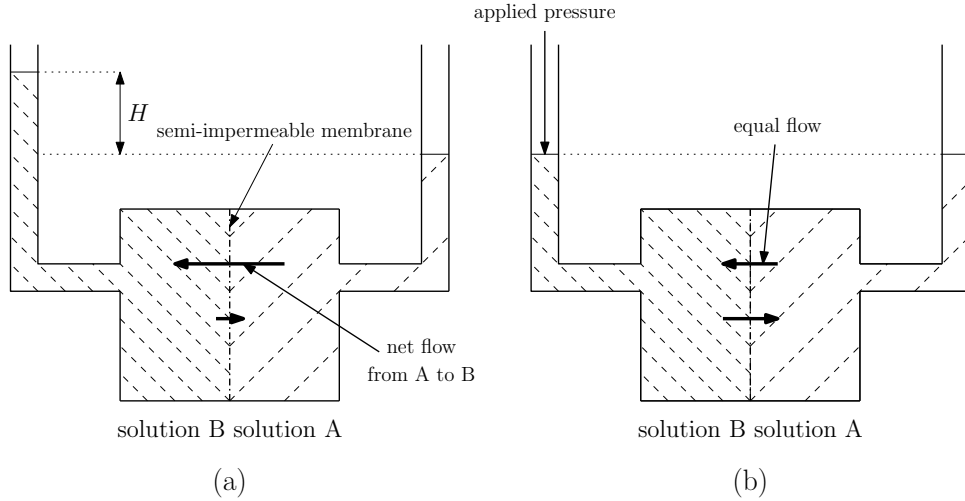


Figure 2.7: Osmosis and osmotic suction, after Hillel (2004)

pure water:

$$\psi_m = \frac{R_u T}{V_{m_l}} \ln \left(\frac{p_{sol}}{p_{sol}^*} \right) \quad (2.28)$$

where p_{sol} is the vapour pressure of the vaporised solution above the liquid solution. An expression similar to the Kelvin equation for the osmotic suction, ψ_o , was given in Dao et al. (2008) as

$$\psi_o = \frac{R_u T}{V_{m_l}} \ln \left(\frac{p_{sol}^*}{p^*} \right) \quad (2.29)$$

where p^* is the saturated vapour pressure of vapour of the solvent above the surface of and in equilibrium with the free solvent (i.e. no solutes are present), as before. Excellent agreement has been obtained between Eqn 2.29 and experimentally-determined osmotic suctions for a wide range of concentrations and temperatures (Dao et al., 2008). The combined effects of the matric and osmotic suctions can then be found using

$$\psi_{combined} = \psi_m + \psi_o = \frac{R_u T}{V_{m_l}} \ln \left(\frac{p_{sol}}{p_{sol}^*} \right) + \frac{R_u T}{V_{m_l}} \ln \left(\frac{p_{sol}^*}{p^*} \right) \quad (2.30)$$

which simplifies to

$$\psi_{combined} = \frac{R_u T}{V_{m_l}} \ln \left(\frac{p_{sol}}{p^*} \right) \quad (2.31)$$

i.e. similar to Eqn 2.18 but now in terms of combined suction and the vapour pressure of the solution, not pure water (i.e. not the relative humidity). As $\psi_{combined}$ incorporates matric (which includes capillary, adsorptive, electrostatic and van der Waals components) and osmotic terms it is instead an expression for the *total suction*, ψ (Fredlund and Rahardjo, 1993; Fredlund and Xing, 1994; Tuller et al., 1999; Tarantino and De Col, 2008; Arifin and Schanz, 2009; Tarantino, 2009; Baker and Frydman, 2009).

2.5 Soil structure

The structure of a soil is conventionally divided into the *microstructure* and the *macrostructure*; the former refers to the arrangement of individual particles, their associated pores and the water that resides within them and the latter refers to the arrangement of particle aggregates, the larger pores that can be found between them and the larger bodies of water that reside within those pores. In this section, the particle configurations and corresponding pore types which form the soil structure are described. The effect of compaction on the structure is then discussed, as are the methods for measuring the pore size

distribution.

2.5.1 Aggregate and pore type classifications

Although a soil might contain a known distribution of particle sizes, the addition of water to soil particles causes them to group together and form aggregates due to suction; water therefore plays a key role in the formation of a soil's material structure. A consideration of this structure is an important difference between unsaturated and classical soil mechanics.

Soil aggregate properties and features were thoroughly investigated in Collins and McGown (1974), in which two general size classes of aggregate were identified: *elementary particle arrangements*; and *particle assemblages*. Elementary particle arrangements consist of single forms of particles, be they clay, silt or sand or small groups of clay platelets (as clay particles are not seen in isolation in the presence of water (Diamond, 1970)). Particle-to-particle contacts for the larger particle size classes (silts and sands) become rarer as the clay content increases due to clay particles coating the surfaces of the larger particles.

Particle assemblages are combined units of elementary particle arrangements of any type and which have defined boundaries so that they act as one body. A number of different particle assemblages were identified as shown in Figure 2.8 and discussed below. Combinations of particle assemblages are present in any given soil (Diamond, 1971; Delage et al., 1996; Romero et al., 1999).

- *Connectors* are assemblages which form between silt and sand grains and are sometimes referred to as *clay bridges* (e.g. Casagrande (1932), Hall and Djerbib (2006)), as shown in Figure 2.8(a) to (c). Silt particles can be contained within the connecting material if space allows.
- *Aggregations* are assemblages which are of variable size and shape and which effectively act as individual units within the soil structure. In Collins and McGown (1974), aggregations are classified as “irregular” or “regular”. Irregular aggregations comprise a “confused” mixture of elementary particle arrangements, as shown in Figure 2.8(d) and (e). Regular aggregations are roughly equidimensional and can contain combinations of elementary particle arrangements or silt grains connected by a clay matrix, as shown in Figure 2.8(f) and (g).
- *Interweaving bunches* are groups of elementary particle assemblages as shown in Figure 2.8(h) and (i).
- *Particle matrices* are assemblages which form the “background” of the structure and which can act as a binder, depending on the size of the assemblage. Clay particle matrices comprise clay and small silt particles with mixtures of clay particle arrangements. Granular particle matrices comprise silt and sand particles.

Pore spaces were defined according to the structural elements which formed their boundaries, i.e. within and between the elemental particle arrangements and particle assemblages. Note that the terms “voids”, as used in Section 2.3 and “pores” are synonymous, however “pores” is preferred in unsaturated soils literature. The four classes of pore type identified are shown in Figure 2.9 and discussed below:

- *Intra-elemental* pores are those pores that occur within the elementary particle arrangements i.e. between individual particles or small groups of clay particles.
- *Intra-assemblage* pores occur within those particle assemblages identified above and are those pores that are present between elementary particle arrangements or between smaller particle assemblages within the larger assemblage.

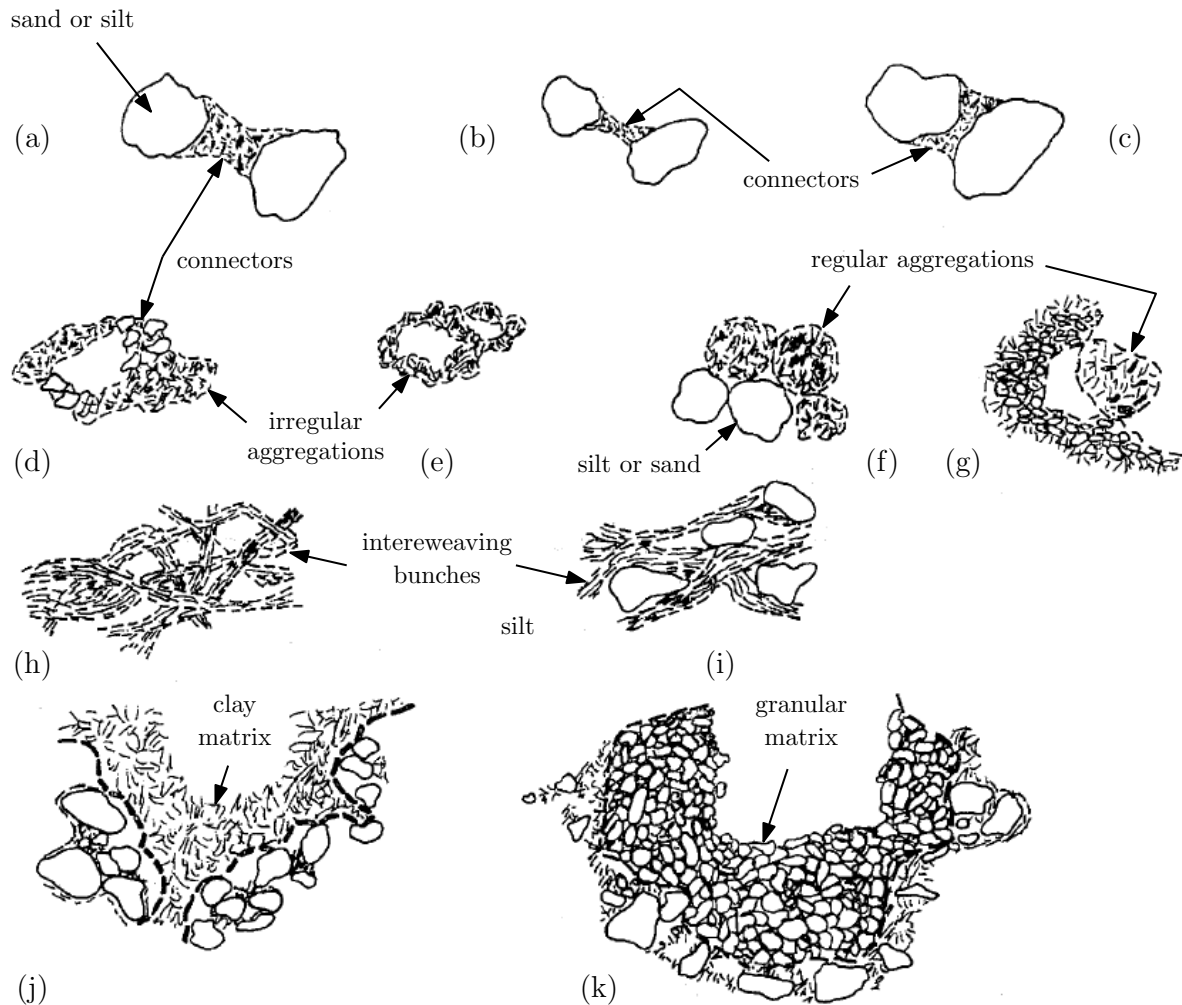


Figure 2.8: Particle assemblage types as defined by Collins and McGown (1974) (figure reproduced from that work): a-c) connectors; d) irregular aggregations linked by connector assemblages; e) irregular aggregations forming a honeycomb arrangement; f) regular aggregations interacting with silt or sand grains; g) regular aggregation interacting with the particle matrix; h) interweaving bunches of clay; i) interweaving bunches of clay with silt inclusions; j) clay particle matrix; k) granular particle matrix.

- *Inter-assemblage* pores are those that occur between particle assemblages.
- *Trans-assemblage* pores occur between groups of particle assemblages or elementary particle arrangements or combinations of the two, so that their boundaries are not defined by the aggregate type.

In general, pore sizes increase from the intra-elemental to the trans-assemblage classes, however some pores will not follow this trend due to the structures between which the pores occur being formed from different sized particles.

In more recent unsaturated soils literature, pore sizes are defined as either *intra-aggregate* or *inter-aggregate*, replacing the intra-assemblage and inter-assemblage classes respectively. A critical pore size forms the boundary between the two, the size of which being material dependent, although a significant size difference is implied when discussing intra- and inter-aggregate pores. *Intra-particle* and *intra-domain* pores are also mentioned in a small number of works (e.g. Alonso et al. (1987), Tarantino (2010)) and both fall within the Collins and McGown (1974) intra-elemental class. The use of the intra- and inter-aggregate pore size definitions has led to soils being described as having a *double structure* (Toll, 1990; Alonso et al., 1999). Pores can also be defined as *micropores* and *macropores*, although this

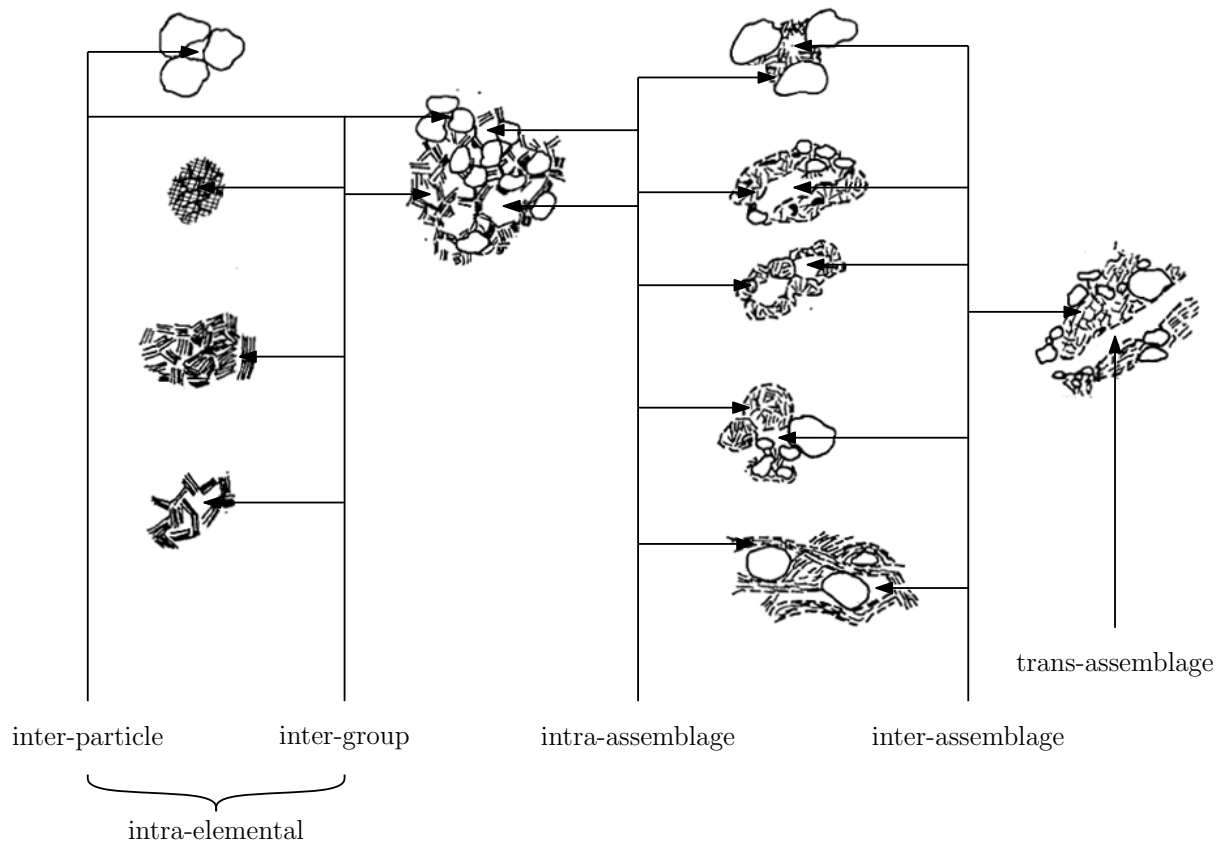


Figure 2.9: Pore size terminology as defined by Collins and McGown (1974) (figure reproduced from that work)

terminology does not relate the pore to the structure in which it resides. The International Union of Pure and Applied Chemistry (IUPAC) defines a *macropore* as a pore of diameter ≥ 50 nm (Everett, 1972), however in unsaturated soils literature the terms intra-aggregate pore and micropore and inter-aggregate pore and macropore are usually synonymous. Trans-assemblage pores are not commonly referred to, their presence either being included in the inter-aggregate or macropore class or being attributed to cracking.

2.5.2 Compaction

Compaction plays a significant role in the manufacture of RE and was originally investigated by Proctor (1933) as a response to a need to be able to improve the design of earthfill dams. Results for the compaction of a sandy clay soil are given in Figure 2.10 showing the change in bulk density (“compacted weight”), dry density (“dry weight”) and volume of voids (by % of total volume) for a range of water contents.

Figure 2.10 shows that, at a certain water content, a maximum density and minimum volume of voids are achieved. This is known as the *optimum water content* (OWC), and changes according to the compactive effort applied, as shown in Figure 2.11 for the compaction of a kaolin clay.

The increase and subsequent decrease in density (dry or bulk) as water content increases towards and then exceeds the OWC, as shown in Figure 2.10, is due to the formation and distribution of aggregates. At low water contents particles group together to form large aggregates, resulting in a large inter-aggregate pore volume and thus a high volume of voids on compaction; the high suctions present due to the low aggregate water content prevent aggregate deformation. As water content increases, aggregate size increases so that the total pore volume reduces until the water content equals the OWC, at which

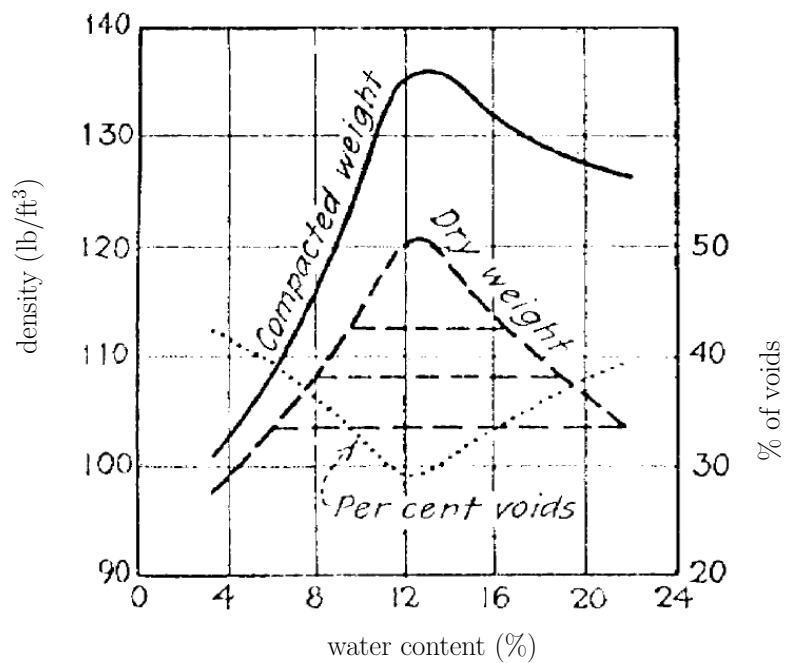


Figure 2.10: Example compaction curves for a sandy-clay soil. Reproduced from Proctor (1933)

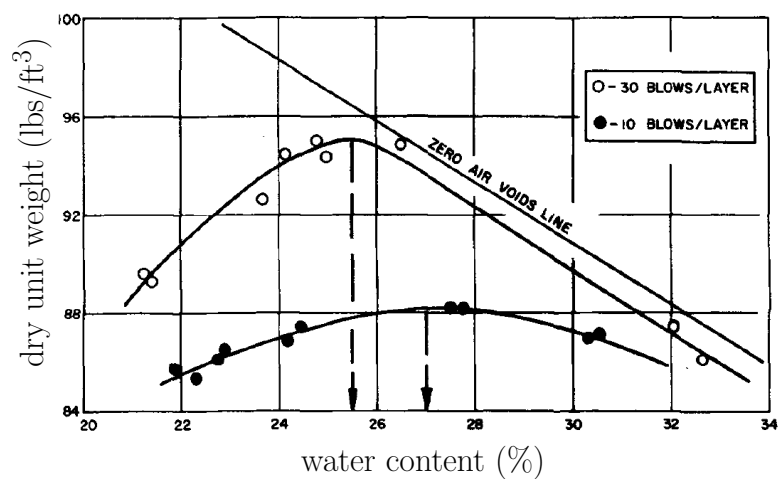


Figure 2.11: The change in dry density and OWC with increasing compactive effort. Reproduced from Diamond (1971).

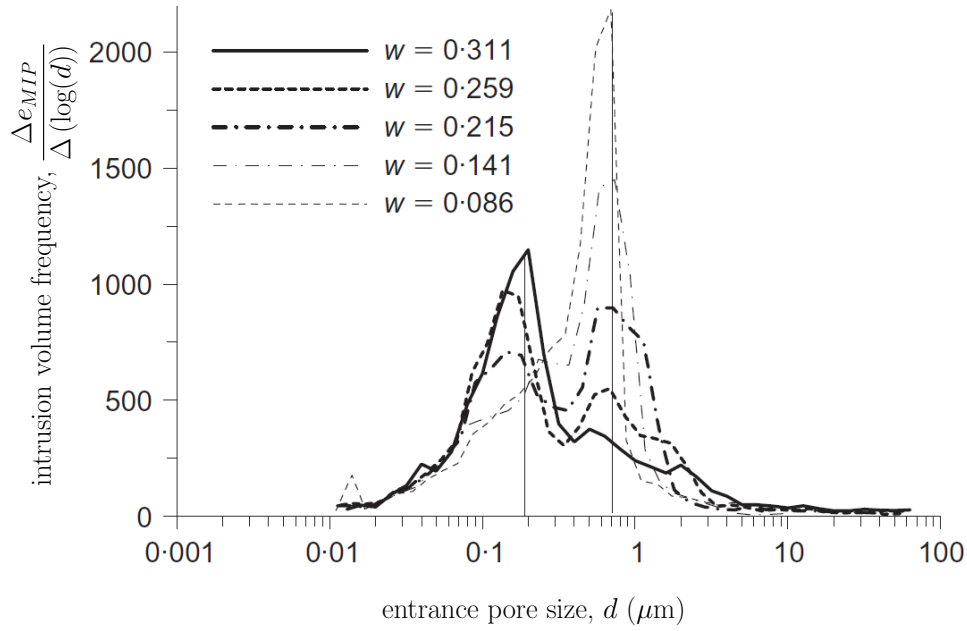


Figure 2.12: PSD of Speswhite kaolin compacted at different water contents. e_{MIP} is the void ratio according to MIP testing, as discussed in Section 2.5.3.1. Reproduced from Tarantino and De Col (2008).

point the most efficient packing of aggregates is achieved (minimum inter-aggregate pore volume). The OWC is the water content at which the air phase becomes discontinuous, existing as occluded bubbles as the water content increases above the OWC (Tarantino and Tombolato, 2005). A continued increase in water content results in a reduction in suction and the disruption of the aggregates so that the total volume of voids increases. As water contents reach saturation, the total volume of voids continues to increase as the water present in the pores prevents the solid structure from being compacted into a more efficient form, resulting in a reducing density (Cui, 1993; Vanapalli et al., 1999). At water contents lower than those examined in Figure 2.10, an increase in density and a decrease in the volume of voids is observed, due to the presence of smaller aggregates and a consequently improved packing arrangement on compaction (Hillel, 2004; Mitchell and Soga, 2005; Tarantino and Tombolato, 2005).

Soil structures are referred to as *monomodal* or *bimodal* depending on whether they show one or two main peaks in their pore size distributions (PSDs) respectively. In general, soils compacted at water contents less than the OWC exhibit bimodal properties, whereas those compacted above the OWC exhibit monomodal properties (this is characteristic of clayey soils (Tarantino, 2010)), as shown in Figure 2.12 for the compaction of Speswhite kaolin (plastic limit (PL) 0.32%, liquid limit (LL) 0.64%, plasticity index (PI) 0.32%, 20% silt 80% clay by mass) (Tarantino and De Col, 2008). Structural changes on compaction above and below the OWC were also investigated in Simms and Yanful (2004), however the results were not as clear as those given in Figure 2.12.

An analysis of the suction present at different water contents gives evidence for the presence of well-defined aggregates (i.e. a bimodal structure) below the OWC. Figure 2.13 shows suctions measured in samples of Barcelona silt (PL 0.16%, LL 0.32%, PI 0.16%, (Tarantino, 2009)) at varying levels of compacted effort. Suctions for water contents below the OWC are practically constant with changing compactive effort, suggesting that compaction only affects the distribution of the aggregates (and so the inter-aggregate pores) whilst water is present within the intra-aggregate pores. At water contents above the OWC, suctions are not constant as the division between intra- and inter-aggregate pores becomes less distinct (i.e. a monomodal structure) (Romero et al., 1999; Baker and Frydman, 2009). A comparison between the retention behaviours of compacted and “reconstituted” soils (those which are formed by

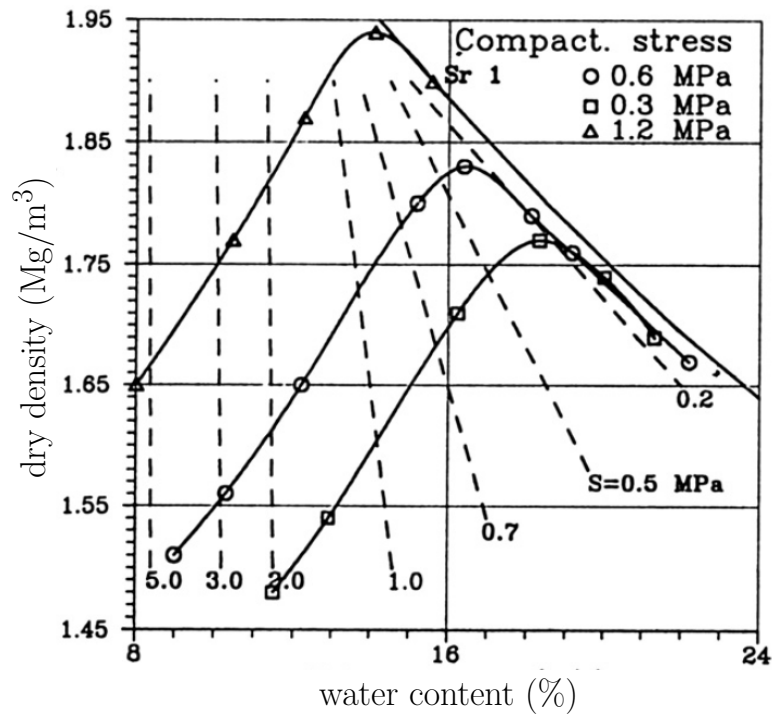


Figure 2.13: Suction measurement during compaction. Reproduced from Gens et al. (1995).

making a soil slurry which is then dried) also shows that the intra-aggregate pores are not affected by compaction and that compaction instead results in a change in the distribution of the inter-aggregate pores (Tarantino, 2009, 2010).

A well-defined OWC or peak density, as shown in Figures 2.10, 2.11 and 2.13, will not always be visible, as shown in Figure 2.14 for the compaction of Speswhite kaolin; in this case, higher compactive efforts are required in order to produce a ‘true’ OWC (Tarantino and Tombolato, 2005; Tarantino and De Col, 2008). Furthermore, soils which initially exhibit bimodal PSDs can develop monomodal PSDs on wetting (mechanical or hydraulic), whilst soils which are initially monomodal can develop bimodal PSDs on drying (Gens et al., 1995; Simms and Yanful, 2001; Tarantino, 2010). Therefore, it is necessary to measure the PSD of a given soil after any change that it undergoes; methods for doing this are discussed in the following section.

2.5.3 Pore size distribution measurement

The soil pore size distribution (PSD) shows the volumes occupied by pores of given sizes. As only size is shown, it is not possible to determine the type of pores according to the classifications specified by Collins and McGown (1974). Instead, the more general descriptions of intra- and inter-aggregate pores are used when referring to PSD properties. Several methods exist for determining the PSD, the most popular being mercury intrusion porosimetry (MIP) and nitrogen adsorption/desorption methods which are discussed below.

2.5.3.1 Mercury intrusion porosimetry

MIP works on the principle that a non-wetting fluid (i.e. one whose contact angle with a solid is $>90^\circ$) will not spontaneously intrude a solid porous material unless sufficient pressure is applied (Diamond, 1970). The pore radius r corresponding to the pressure required to intrude the measured volume of

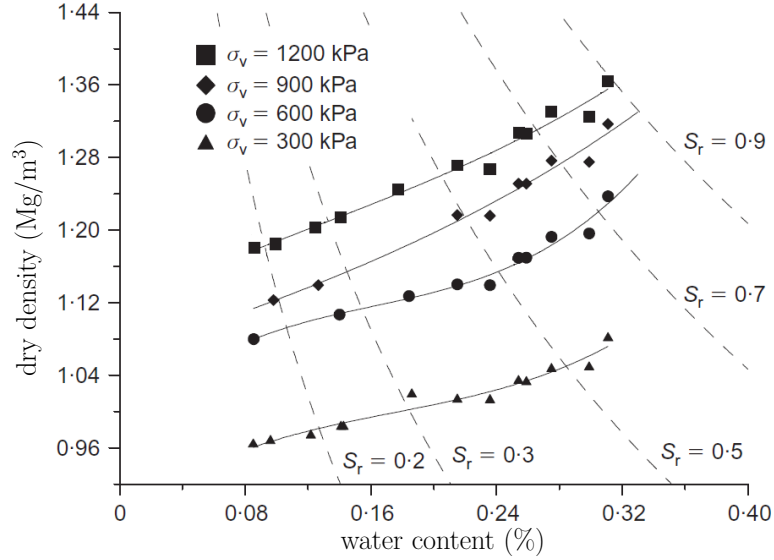


Figure 2.14: Compaction of Speswhite kaolin at different compactive efforts. Reproduced from Tarantino and De Col (2008).

mercury is determined using the Washburn equation

$$r = -\frac{2\gamma_{Hg} \cos(\theta_{slv})}{P} \quad (2.32)$$

where γ_{Hg} is the liquid-vapour surface tension of mercury, taken to be 0.484 N/m (more than four times that of water at this temperature as determined using Eqn 2.5), P is the applied pressure and θ_{slv} is the solid-liquid contact angle for mercury, taken to be between 139° and 147° depending on the clay mineral type (Washburn, 1921; Diamond, 1970; Delage and Pellerin, 1984; Romero and Simms, 2008). Therefore, Eqn 2.32 is equivalent to Eqn 2.7, except for being specific to mercury, so that pore sizes are related to theoretically-cylindrical channels. Note that in Eqn 2.32, pore and meniscus radii are assumed to be equal, despite the inclusion of the contact angle (which must be zero in cylindrical pores for this assumption to apply). As real soil pores are irregular in shape (as shown in Figure 2.9), pore radii determined using Eqn 2.32 are referred to as the “equivalent” radii (Diamond, 1970). MIP can be reliably used to determine the volumes of pores of equivalent sizes between 10 nm and 0.4 mm (Romero and Simms, 2008; d’Souza, 2008). MIP can also be used to determine both the inter- and intra-aggregate pore volumes by comparing the intruded and extruded volumes of mercury, as shown in Figure 2.15; e_{MIP} is found using Eqn 2.33, where V_{Hg} is the volume of mercury (either intruded or extruded), and e_m is the *microstructural void ratio*, i.e. that proportion of the total void ratio that is formed by the intra-aggregate pores (Romero and Vaunat, 2000).

$$e_{MIP} = \frac{V_{Hg}}{V_s} \quad (2.33)$$

MIP has several drawbacks, including a limited range of pore size detection due to a limited range of applicable pressures, a requirement that the pores be devoid of water prior to testing, the need to use very small sample sizes (of the order of 1 g), an inability to measure pores that are not directly accessible from the outside of the sample and an overestimation of the volumes of smaller pore sizes due to larger pores being blocked by smaller pores (known as the “ink bottle effect” or “pore trapping”), so that volumes of larger pores are associated with smaller pore sizes (Diamond, 1970; Willis et al., 1998; Kaufmann, 2009). However, it is nonetheless acknowledged as a reliable and useful tool for determining

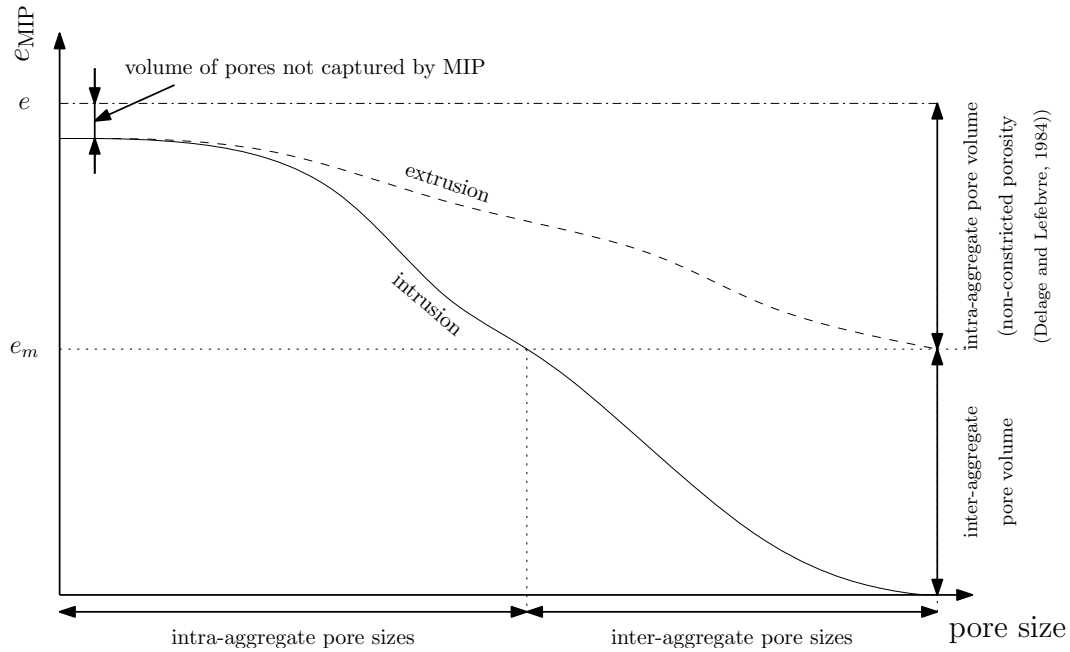


Figure 2.15: Inter- and intra-aggregate pore size and volume data as determined by MIP intrusion and extrusion, after Tarantino and De Col (2008)

the soil PSD.

Oven drying can be used to dry samples prior to MIP testing. However, Diamond (1970) demonstrated that this can lead to significant changes in the PSD, particularly in the presence of swelling clays for example illites and montmorillonites, due to the effect of desaturating clay particles. Instead, *freeze drying* or *critical region drying* are used to prepare samples prior to MIP testing as these methods have significantly less impact on the measured PSD (Acar and Olivieri, 1990; Delage and Pellerin, 1984; Simms and Yanful, 2004; Delage et al., 2006). In freeze drying, samples are rapidly frozen using liquid nitrogen. Water is then evacuated under vacuum at temperatures below the freezing point of water. Other cooling liquids can be used, however the use of nitrogen appears to be the simplest and most efficient method (Delage et al., 2006; Tarantino and De Col, 2008; Tarantino, 2010). Freezing prevents the creation of excess suction due to contracting menisci surrounding the particles, reducing any changes that might occur to the PSD. In critical region drying, temperatures and pressures are elevated to the point where water exists as a single homogeneous fluid phase (i.e. water vapour is not present in the surrounding air). Water is then distilled from the sample to a colder region without causing shrinkage (Diamond, 1970; Romero and Simms, 2008). Freeze-drying is the more common preparation method, however, due to its relative simplicity.

Examples of PSDs found for Leda clay (Crawford, 1968) using MIP on oven-dried and critical-region dried samples are shown in Figure 2.16. The total pore volume determined prior to testing was $0.67 \text{ cm}^3/\text{g}$. The total pore volume found using MIP after critical region drying was roughly $0.67 \text{ cm}^3/\text{g}$, whilst that after oven drying was only $0.28 \text{ cm}^3/\text{g}$. It should be noted that although it appears that the total pore volume of the oven-dried sample has significantly decreased, it is possible that the pores have contracted to a size smaller than the minimum size detectable by the MIP apparatus, however this is unlikely due to the almost constant intruded volume at the smallest pore sizes. Instead, it would appear that the effect of oven drying is to reduce the inter-aggregate pore volume ($0.1 \mu\text{m}$ to 1 mm in diameter) whilst maintaining a near-constant intra-aggregate pore volume, suggesting a coalescence of aggregates and pore constriction (Tarantino and De Col, 2008; Tarantino, 2009). This effect is not true for every clay, however, as similar tests on a halloysitic clay (a 1:1 aluminosilicate mineral similar to

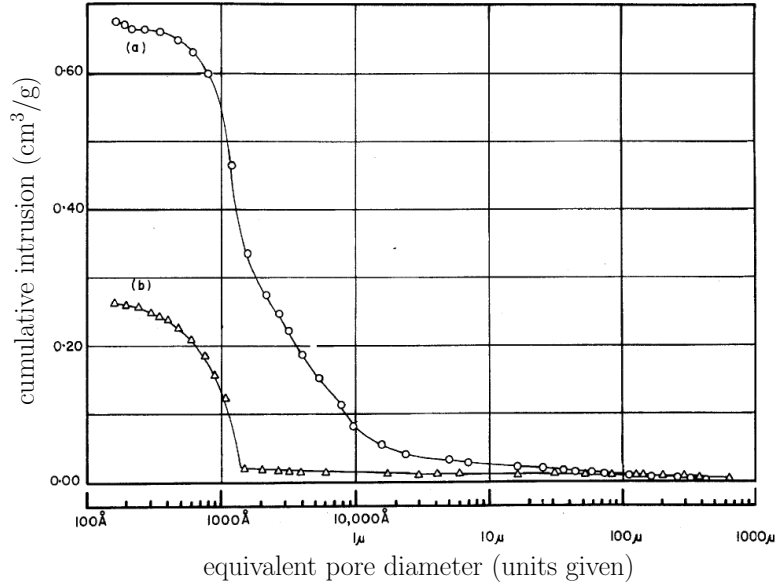


Figure 2.16: PSD curves for Leda clay: a) critical-region dried; b) oven-dried (figure reproduced from Diamond (1970))

kaolinite in composition but whose molecules form short cylinders) showed an increase in inter-aggregate pore volume on oven drying, potentially due to an ‘unrolling’ of the halloysite tubes (Diamond, 1970). It should also be noted that there is no definitive evidence that PSDs determined through freeze drying or critical region drying are identical to the pre-dried state of the soil, however it is clear that they produce significantly more representative results than are possible through oven drying.

A modification to MIP is the use of “Wood’s metal” in conjunction with mercury (Lange et al., 1998; Willis et al., 1998; Kaufmann, 2009). Wood’s metal has a chemical composition of 50.0% bismuth, 26.7% lead, 13.3% tin and 10.0% cadmium by weight, a freezing point of 65.5°C, a relative specific gravity of 9.7, liquid-air surface tension of 0.48 N/m and is insoluble in water, unlike mercury which is slightly soluble (Clever, 1985; Willis et al., 1998; Kaufmann, 2009). Wood’s metal has very similar properties to mercury above its melting point. Willis et al. (1998) substituted mercury for Wood’s metal for intrusion testing, using scanning electron microscopy and image analysis techniques to determine the pore size distribution (according to pore area and the pore major and minor axes) from sections cut from the intruded sample, taking advantage of Wood’s metal being solid at room temperature. In Kaufmann (2009) a sample was intruded using Wood’s metal which was then allowed to solidify in order to block ink-bottle pores and investigate the effects of pore connectivity on MIP results.

2.5.3.2 Adsorption techniques

The nitrogen adsorption/desorption method determines pore volumes from the amount of nitrogen vapour adsorbed at a certain pressure and at a temperature of 77°K (-196°C) and can measure pore sizes in the range of 0.5 to 500 nm (Willis et al., 1998). The method assumes that the pores are filled with liquid adsorbate. Increasing the partial pressure of the gas at a constant temperature then results in progressive desorption of nitrogen (Maria, 2010). The amount adsorbed, V , as a function of the applied (equilibrium) pressure p_{ads} is known as the *adsorption isotherm*. The adsorption potential, A , can be calculated as a function of the applied pressure according to

$$A = R_u T \ln \left(\frac{p^*}{p_{ads}} \right) \quad (2.34)$$

where p^* is the saturated vapour pressure as before (Jaroniec et al., 1996). A plot of the amount adsorbed against the adsorption potential is called the *adsorption curve*, $V(A)$. The PSD $J(r)$ is then determined from the derivative of $V(A)$ with respect to A and the derivative of A with respect to r , where r is the pore size, according to

$$J(r) = -\frac{dV(A)}{dA} \frac{dA}{dr} \quad (2.35)$$

which can be solved empirically using

$$J(r) = -\frac{dV(A)}{dA} \left(\frac{C_1}{r - d_a} \left(\frac{3C_2}{(r + \delta)^4} - \frac{9C_3}{(r + \delta)^1 0} \right) - \frac{C_1}{((r - d_a)^2} \left(\frac{C_3}{(r + \delta)^9} - \frac{C_2}{(r + \delta)^3} + C_4 \right) \right) \quad (2.36)$$

where d_a is the diameter of the adsorbate (i.e. the substance being adsorbed, in this case nitrogen), $\delta = \frac{d_A - d_a}{2}$, where d_A is the adsorbent atom diameter (e.g. that of carbon for carbonaceous pores) and C_1 to C_4 are constants specific to the adsorbant (e.g. nitrogen) and the shape of and material bounding the pores. For nitrogen in carbonaceous pores, $d_a = 0.3$ nm, $d_A = 0.26$ nm and $\delta = 0.02$ nm (Jaroniec et al., 1996).

The Barret-Joyner-Halenda (BJH) method can also be used to determine the PSD (Barret et al., 1951). In this method it is assumed that pores are cylindrical and that adsorption follows two sequential processes: adsorption of thin films followed by capillary condensation. An empirical relationship is used to relate the volume adsorbed at a given pressure, $V(p)$, to the adsorption potential at that pressure, $A(p)$, according to

$$V(p) = 0.0015468A(p) \quad (2.37)$$

allowing the PSD to be calculated using

$$V(p_k) = \sum_{i=1}^k \Delta V_i(r_i \leq r_c(p_k)) + \sum_{i=k+1}^n \Delta S_i t_i(r_i > r_c(p_k)) \quad (2.38)$$

where p_k is a given pressure, r is a pore radius, r_c is the pore radius of interest at pressure p_k (i.e. the pore radius that will appear on the PSD), ΔV is the pore volume and ΔS is the pore surface area (which are related to each other via a cylindrical pore approximation, allowing ΔV to be found). The first term of Eqn 2.38 accounts for those pores that are filled with water (i.e. smaller than r_c for a given pressure p_k) and the second for those pores in which adsorbed films are present on the surfaces (i.e. pores larger than r_c for pressure p_k).

An advantage of adsorption methods are that pore SSAs can also be determined. The Brunauer-Emmett-Teller (BET) method (Brunauer et al., 1938) is a common method for relating adsorbed quantities to the SSA:

$$\frac{1}{W \left(\frac{p^*}{p} \right) - 1} = \frac{1}{W_m C} + \frac{C - 1}{W_m C} \left(\frac{p}{p^*} \right) \quad (2.39)$$

where W is the weight of gas adsorbed, W_m is the weight of the adsorbate as a monolayer and C is the BET constant. A plot of $\frac{1}{W \left(\frac{p^*}{p} \right) - 1}$ against $\frac{p}{p^*}$ yields the gradient, s , and intercept, i , which are required to determine W_m and C according to

$$W_m = \frac{1}{s + i} \quad (2.40)$$

$$C = 1 + \frac{s}{i} \quad (2.41)$$

so that the total surface area can be found using

$$S = \frac{W_m N A_{cs}}{M} \quad (2.42)$$

where N is the Avogadro constant (6.023×10^{23}), M is the molecular weight of the adsorbate and A_{cs} is the cross-sectional area of the adsorbate (16.2 \AA^2 for nitrogen). SSA can then be found by dividing S by the mass of the sample.

2.6 The soil water retention curve

The relationship between the suction applied to a soil and its water content at that suction is referred to as the water retention function or *soil water retention curve* (SWRC). It can also be referred to as the *characteristic* curve, however here the term “retention” is preferred following the work of Nuth and Laloui (2008) who argue that “characteristic” suggests that a unique relationship exists between suction and water content for a given soil, which is not the case since it depends on the hydraulic and stress history of the specimen (Vatsala and Srinivasa Murthy, 2001; Tarantino and Tombolato, 2005; Tarantino, 2007; Likos, 2009). In this section, various properties of the SWRC are discussed and related to the structural properties of soils discussed in the previous sections.

A key feature of the SWRC is that hysteresis is shown between wetting and drying, so that the suctions required to dry a wet soil sample to a given water content are not the same as those required to wet a dry sample of the same material to the same water content (Nishimura and Fredlund, 2002; Huang et al., 2005; Rojas and Rojas, 2005; Liu and Zhao, 2007). As such, SWRCs are described as having *main drying* and *main wetting* paths. States that exist between these two limits, i.e. those obtained if a change in the wetting regime is applied (e.g. a sample that is drying is re-wetted), are said to belong to given *scanning curves*. Changes in the water content that occur along the main drying or wetting paths are irreversible, however changes in the water content that correspond to scanning-curve conditions are (roughly) reversible (Tarantino, 2009). A sketch of an example SWRC is shown in Figure 2.17, showing some of the common features seen when measuring SWRCs for materials with monomodal and bimodal properties:

- The *residual air content* is the difference between the saturated water contents prior to drying, $S_{rd} = 1$, and after wetting, $S_{rw} = 1$, and is associated with air that is trapped within pores as surrounding pores fill with water.
- The *residual water content* is that water which remains in the soil at very high suctions and is associated with water in the form of adsorbed films or trapped within the smallest intra-aggregate pores (Lu and Likos, 2004).
- The *air entry value* (AEV) is found from tangents drawn from the initial and central portions of the SWRC and is used as an indication of the largest pore sizes present in the sample. The AEV can be used to differentiate between different soil types, as shown in Figure 2.18, and indicates the strong relationship between the SWRC and the PSD due to materials containing smaller pores having higher AEVs (Hillel, 2004).
- The limit on suction of 1 GPa according to Croney et al. (1958) and Fredlund and Rahardjo (1993), amongst others, is due to this suction being associated with the emptying of the smallest pores present in soils, i.e. those between clay particles.
- If the material structure is bimodal, a flattening of the curve is seen due to the lack of pore sizes emptied in that suction region. This is not seen in monomodal material structures. For both

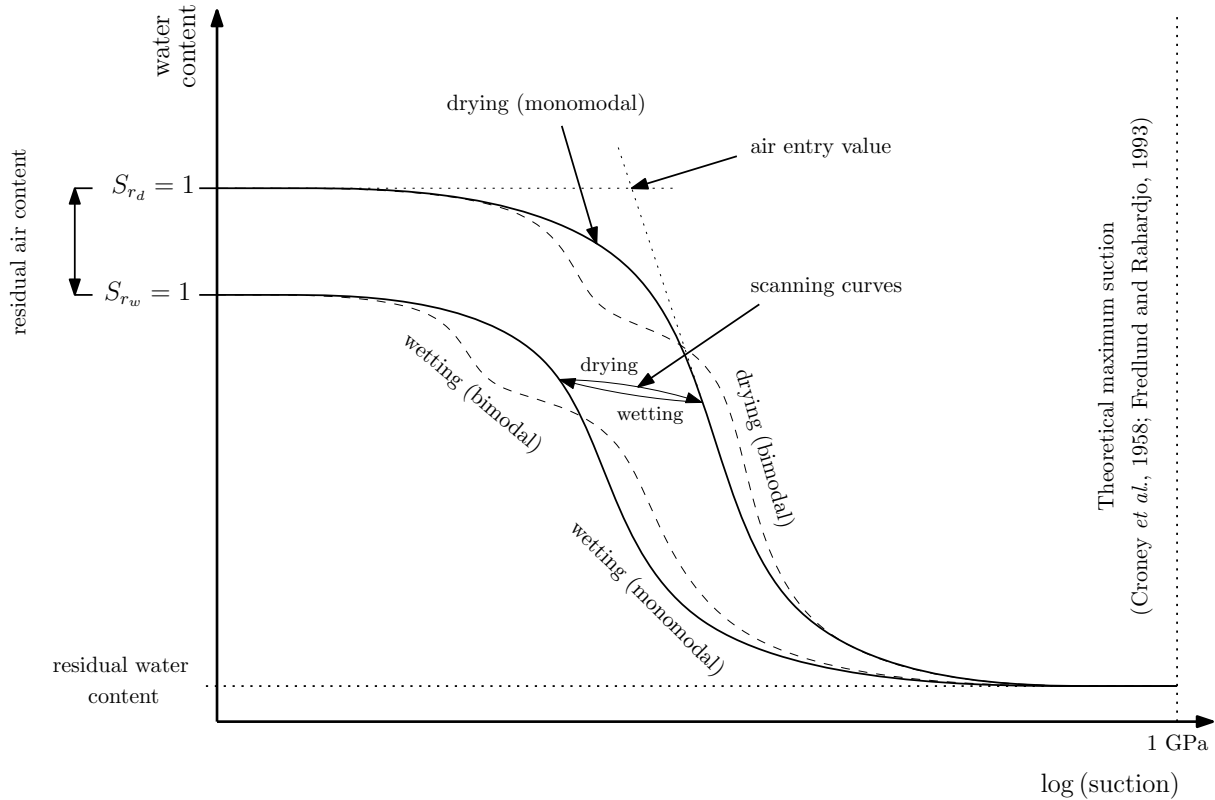


Figure 2.17: Sketch showing example wetting and drying paths for a monomodal (solid line) and bimodal (dashed line) material. S_{r_d} and S_{r_w} are the saturation ratios for the drying and wetting materials respectively.

monomodal and bimodal structures, the SWRC becomes more steep with reducing water content as those pore sizes that belong to the modal peak(s) are emptied.

Hysteresis in the SWRC has been attributed to an increase in the contact angle between drying and wetting. This is described in Figure 2.19 where a drop of liquid is travelling down a dry inclined solid surface; the surface is being wetted by the advancing drop and the retreating tail simulates drying. Eqn 2.7 shows that an increase in contact angle results in a reduction in suction for a given meniscus radius. This is also the case for Eqn 2.19 and, by extension, Eqn 2.27 for an increase in contact angle for a given filling angle.

Lourenço et al. (in press) investigated the effects of wetting and drying on the contact angles present in granular media. Environmental scanning electron microscopy (ESEM) was used to observe the shapes of menisci formed between monosized ($2 \mu\text{m}$ diameter) silica particles on a cycling of the RH between 35% and 100%, at a constant temperature of 5°C . Figures 2.20(a) to (d) show the process of wetting from an RH of 35% to 100% ((a) to (b)), drying to 35% ((b) to (c)) and re-wetting to roughly 80% ((c) to (d)). Figure 2.20(a) shows that, initially, both concave and convex menisci are present between the silica particles. This is likely to be due to different regions wetting or drying during equilibration to the initial RH of 35%. Wetting of the material to 100% produced *convex* menisci with large contact angles, apparently contravening the meniscus shapes predicted by Eqns 2.7 and 2.27. In the case of a convex meniscus, the pressure in the water is positive (i.e. compressive) due to the action of surface tension, suggesting that the meniscus is in fact forcing the particles apart rather than drawing them together. However, on a subsequent drying of the material to 35% RH followed by a re-wetting to roughly 80%, menisci remain concave as predicted by Eqns 2.7 and 2.27, so that suctions remain positive, as seen in experimentally-determined SWRCs (Fredlund and Xing, 1994; Romero and Vaunat, 2000; Fredlund et al., 2011). Results given in Lourenço et al. (2008b) show that menisci burst after the final wetting

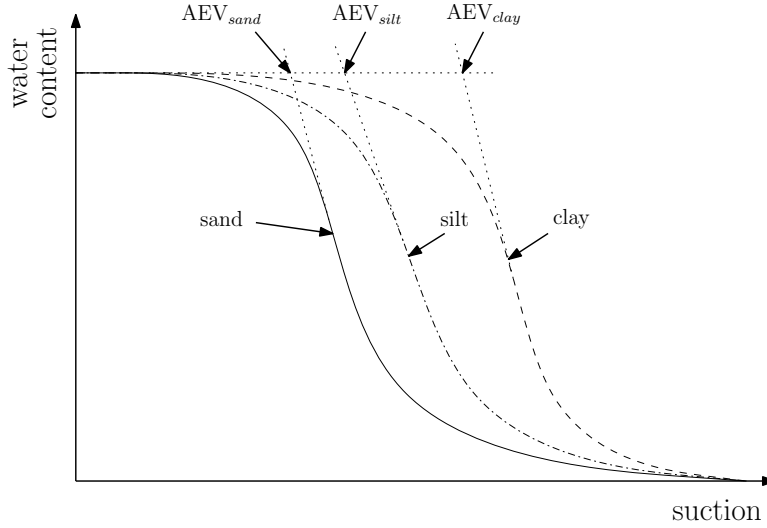


Figure 2.18: Sketch showing example monomodal drying paths for clayey (solid), silty (dot-dashed) and sandy (dashed) soils and corresponding AEV values

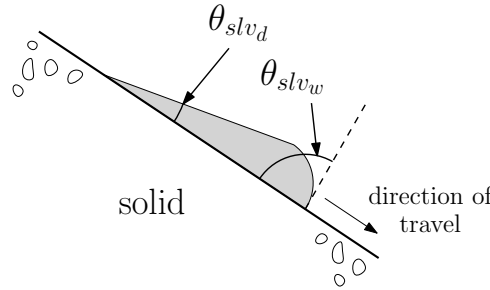


Figure 2.19: Illustrative example of wetting and drying contact angles

phase at an RH of 82.3% as menisci approach a convex shape due to geometrical restrictions. This is shown in Figure 2.21 (note that the water vapour pressure is shown in Torr: 1 Pa = 133.322 Torr).

The change from the formation of convex menisci during the initial wetting phase to the formation of concave menisci during the second wetting phase is due to the presence of adsorbed films on the particle surfaces, which are deposited by the retreating water menisci during the drying phase (Figures 2.20(b) to (c)). Therefore, Figures 2.20(c) and (d) show that, in the presence of adsorbed films, which are always present in soils if $RH > 0$ (Iwamatsu and Horii, 1996), the contact angle does not change considerably between wetting and drying so that a change in contact angle cannot be the cause of SWRC hysteresis.

Tuller et al. (1999) attributed SWRC hysteresis to different radii of imbibition, r_{imb} , and drainage, r_d , according to

$$r_{imb} = \frac{2A}{P} = \frac{P}{4(F(\Gamma) + \pi)} \quad (2.43)$$

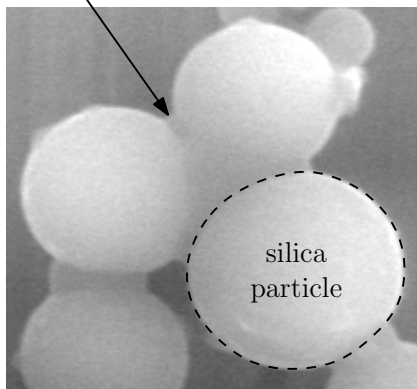
$$r_d = \frac{P}{2 \left((F(\Gamma) + \pi) + \sqrt{\pi(F(\Gamma) + \pi)} \right)} \quad (2.44)$$

where A and P are the pore cross-sectional area and perimeter respectively and $F(\Gamma)$ is the *angularity factor*, found using

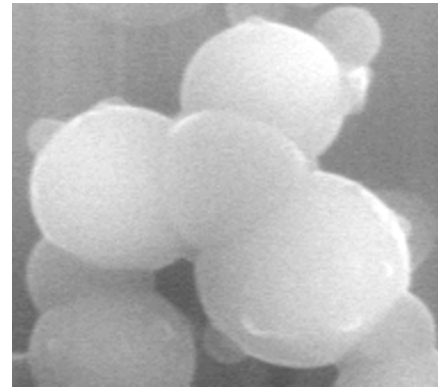
$$F(\Gamma) = \frac{P^2}{4A} - \pi \quad (2.45)$$

and is dependent on the shape of the pore cross section. Γ is the *angularity*, which is equal to the angle of the pore corners (i.e. 90° for pores with square cross-sections). r_{imb} is the radius of the inscribed circle

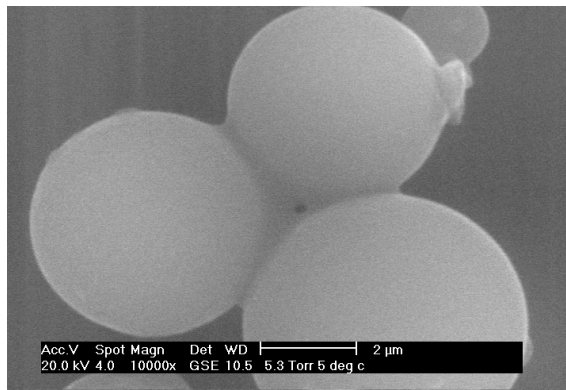
water meniscus



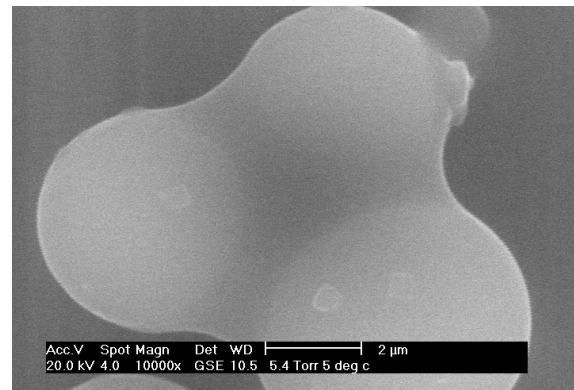
(a)



(b)



(c)



(d)

Figure 2.20: ESEM images showing the effect of wetting and drying on the contact angle between water and silica particles. Scales, where available, are shown on the diagrams (Lourenço et al., in press).

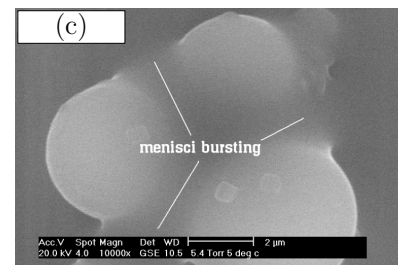
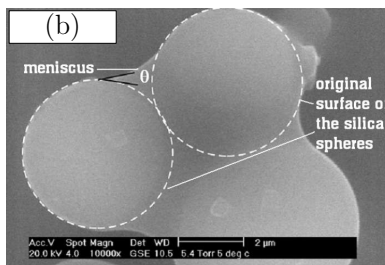
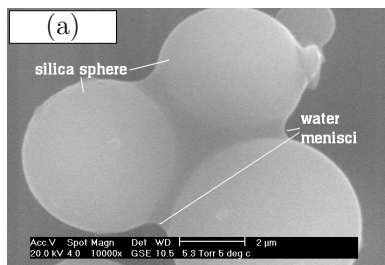


Figure 2.21: Bursting of concave water menisci on the increase of RH: a) 80.1%; b) 82.3%; c) >82.3%. θ indicates the contact angle (equivalent to θ_{slv}) (Lourenço et al., 2008a)

(which equals the pore radius for pores of circular cross sections i.e. cylinders), due to pores filling on the coalescence of any water films present (no films are present in pores of circular cross-section: imbibition is spontaneous) whilst r_d corresponds to the suction required to empty liquid from the centre of a pore, leaving liquid in the corners (again, for pores of circular cross-section emptying results in spontaneous draining of all of the water within the pore) (Mason and Morrow, 1991). Using r_{imb} and r_d , different values for wetting and drying suctions for a given pore can be found without requiring a change in θ_{slv} . However, information concerning the shape of pores is often not available due to their highly varied shape, so that the selection of an appropriate expression for $F(\Gamma)$ and the subsequent use of r_{imb} and r_d becomes an exercise in curve-fitting to measured data (Baker and Frydman, 2009).

PSDs found in Simms and Yanful (2001) for a glacial till (PL 18%, LL 27%, IP 9%, OWC 13.4%, 8% clay, 14% silt, 18% sand and 60% gravel by mass) compacted at 18% water content under different applied suctions are shown in Figure 2.22. Although compacted at water contents above the OWC, the initial PSD is bimodal for no applied suction, with modal peaks at roughly $0.1 \mu\text{m}$ and $3 \mu\text{m}$. Following the discussion given in Section 2.5.2, it is assumed that these values correspond to the modal intra- and inter-aggregate pore sizes respectively. Figure 2.22 shows that an increase in suction results in a significant increase and reduction in the intra- and inter-aggregate pore volumes respectively, suggesting that, on the application of a suction, either inter-aggregate pores constrict to intra-aggregate sizes, whilst pre-existing intra-aggregate pores are not affected, or that the application of a suction results in a coalescence of aggregates and a subsequent increase and decrease in intra- and inter-aggregate pore volumes respectively, depending on whether the data shown in Figure 2.22 is interpreted as a change in the modal pore size (moving to the left) (Simms and Yanful, 2001; ?) or a simultaneous decrease and increase in inter-aggregate and intra-aggregate pore volumes respectively (Tarantino and De Col, 2008). It is not known whether the modal intra-aggregate pore size reduces on a subsequent increase in suction once all of the inter-aggregate pores have constricted, however, due to a lack of data. Results also showed a significant reduction in sample porosity, from 0.32 at 0 kPa to 0.24 at 2500 kPa. As the total volume of voids decreased, a re-wetting of the sample would result in a reduced saturated water content compared to a pre-testing value. This, therefore, can account for the residual air content observed experimentally which was previously attributed to trapped air within the sample and can also account for the hysteresis observed between wetting and drying depending on the change that occurs in the PSD. Therefore, these results suggest that hysteresis is not a hydraulic phenomenon, as originally argued, but is in fact related to a change in the structure of the soil.

2.7 Conclusion

This chapter has discussed the basics of unsaturated soil mechanics and has shown how the behaviour of unsaturated soils can be related to the arrangements of particles and pores within the soil structure. In the following chapters, the topics discussed here will be used as a basis for the interpretation of findings of both analytical and experimental investigations in order to show how an appreciation of the structure of a material and the changes it undergoes is a powerful tool when considering unsaturated soil behaviour.

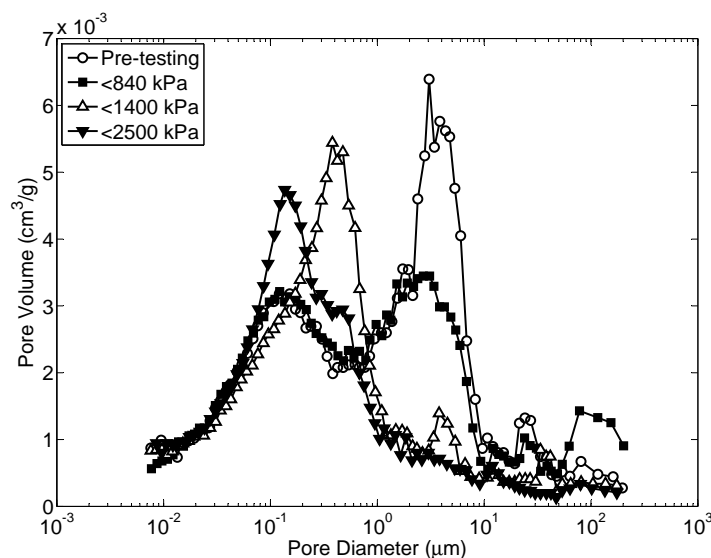


Figure 2.22: PSDs for a glacial till tested at suctions of 0, 1400 and 2500 kPa (Simms and Yanful, 2001)

2.8 References

- Acar, Y. B., Olivieri, I., 1990. Pore fluid effects on the fabric and hydraulic conductivity of laboratory-compacted clay. *Transportation Research Record* 1219, 144–159.
- Alonso, E., Gens, A., Hight, D. W., 1987. Special problems soils. General report. In: *Proceedings of the 9th European Conference on Soil Mechanics*. Dublin, pp. 1087–1146.
- Alonso, E., Vaunat, J., Gens, A., 1999. Modelling the mechanical behaviour of expansive clays. *Engineering Geology* 54, 173–183.
- Alonso, E. E., Gens, A., Josa, A., 1990. A constitutive model for partially saturated soils. *Géotechnique* 40 (3), 405–430.
- Arifin, Y., Schanz, T., 2009. Osmotic suction of highly plastic clays. *Acta Geotechnica* 4, 177–191.
- Atkins, P., De Paula, J., 2006. *Physical Chemistry*, 8th Edition. Oxford University Press, New York (USA).
- Baker, R., Frydman, S., 2009. Unsaturated soil mechanics: Critical review of physical foundations. *Engineering Geology* 106 (1-2), 26–39.
- Barret, E. P., Joyner, L. G., Halenda, P. P., 1951. The determination of pore volume and area distributions in porous substances. *Journal of the American Chemical Society* 73, 373–380.
- Brunauer, S., Emmett, P. H., Teller, E., 1938. Adsorption of gases in multimolecular layers. *Journal of the American Chemical Society* 60 (2), 309–319.
- Buckingham, E., 1907. *Studies on the movement of soil moisture*. Vol. 38. United States Department of Agriculture Bureau of Soils.
- Butt, H.-J., Kappl, M., 2009. Normal capillary forces. *Advances in Colloid and Interface Science* 146 (1-2), 48–60.
- Casagrande, A., 1932. The structure of clay and its importance in foundation engineering. *Journal of the Boston Society Civil Engineers* 19 (4), 168–209.
- Clever, H. L., 1985. Solubility of mercury. *Journal of Chemical Education* 62 (8), 720.
- Collins, K., McGown, A., 1974. Form and function of micro-fabric features in a variety of natural soils. *Géotechnique* 24 (2), 223–254.
- Craig, R. F., 2004. *Soil Mechanics*, 7th Edition. Spon Press, London (UK).
- Crawford, C. B., 1968. Quick clays of eastern Canada. *Engineering Geology* 2 (4), 239–265.
- Croney, D., Coleman, J. D., Black, W. P. M., 1958. Movement and distribution of water in soil in relation to highway design and performance. *Highway Research Board Special Report* 40, 226–252.
- Cui, Y. J., 1993. *Etude de comportement d'un limon compacté non saturé et sa modélisation dans un cadre élastoplastique*. Ph.D. thesis, CERMES-ENPC.
- Dao, V. N. T., Morris, P. H., Dux, P. F., 2008. On equations for the total suction and its matric and osmotic components. *Cement and Concrete Research* 38 (11), 1302–1305.
- Delage, P., Audiguier, M., Cui, Y. J., Howat, D., 1996. Microstructure of a compacted silt. *Canadian Geotechnical Journal* 33, 150–158.
- Delage, P., Lefebvre, G., 1984. Study of the structure of a sensitive Champlain clay and its evolution during consolidation. *Canadian Geotechnical Journal* 21 (1), 21–35.

- Delage, P., Marcial, D., Cui, Y. J., Ruiz, X., 2006. Ageing effects in a compacted bentonite: a microstructure approach. *Géotechnique* 56 (5), 291–304.
- Delage, P., Pellerin, F. M., 1984. Influence de la lyophilisation sur la structure d'une argile sensible du quebec. *Clay Minerals* 19 (2), 151–160.
- Diamond, S., 1970. Pore size distribution in clays. *Clays and Clay Minerals* 18, 7–23.
- Diamond, S., 1971. Microstructure and pore structure of impact-compacted clays. *Clays and Clay Minerals* 19, 239–249.
- d'Souzae, J. I., 2008. Mercury intrusion porosimetry: A tool for pharmaceutical particle characterisation. *Pharmainfo.net Latest Reviews* 6 (2).
- Edlefsen, N. E., Anderson, A. B. C., 1943. The thermodynamics of soil moisture. *Hilgardia* 16, 31–299.
- Everett, D. H., 1972. Manual of symbols and terminology for physicochemical quantities and units, appendix ii: Definitions, terminology and symbols in colloid and surface chemistry. *Pure and Applied Chemistry* 31 (4), 577–638.
- Fredlund, D., Rahardjo, H., 1993. *Soil Mechanics for Unsaturated Soils*. John Wiley & Sons Inc., New York (USA).
- Fredlund, D. G., Sheng, D., Zhao, J., 2011. Estimation of soil suction from the soil-water characteristic curve. *Canadian Geotechnical Journal* 48 (2), 186–198.
- Fredlund, D. G., Xing, A., 1994. Equations for the soil-water characteristic curve. *Canadian Geotechnical Journal* 31, 521–532.
- Gallipoli, D., Gens, A., Sharma, R., Vaunat, J., 2003. An elasto-plastic model for unsaturated soil incorporating the effects of suction and degree of saturation on mechanical behaviour. *Géotechnique* 53 (1), 123–135.
- Gens, A., 2010. Soil-environment interactions in geotechnical engineering. *Géotechnique* 60 (1), 3–74.
- Gens, A., Alonso, E. E., Suriol, J., Lloret, A., 1995. Effect of structure on the volumetric behaviour of a compacted soil. In: *First International Conference on Unsaturated Soils*. UNSAT '95, Paris, France, pp. 83–88.
- Hall, M., Djerbib, Y., 2006. Moisture ingress in rammed earth: Part 3 - sorptivity, surface receptiveness and surface inflow velocity. *Construction and Building Materials* 20 (6), 384–395.
- Hillel, D., 1998. *Environmental Soil Physics*. Academic Press, California (USA).
- Hillel, D., 2004. *Fundamentals of Soil Physics*. Academic Press, Inc., London (UK).
- Huang, H.-C., Tan, Y.-C., Liu, C.-W., Chen, C.-H., 2005. A novel hysteresis model in unsaturated soil. *Hydrological Processes* 19, 1653–1665.
- Israelachvili, J. N., 2005. Importance of pico-scale topography of surfaces for adhesion, friction, and failure. *MRS Bulletin* 30 (7), 533–539.
- Iwamatsu, M., Horii, K., 1996. Capillary condensation and adhesion of two wetter surfaces. *Journal of Colloid and Interface Science* 182 (2), 400–406.
- Jaquin, P. A., 2008. Study of historic rammed earth structures in Spain and India. *The Structural Engineer* 86 (2), 26–32.
- Jaquin, P. A., Augarde, C. E., Legrand, L., 2008. Unsaturated characteristics of rammed earth. In: Toll, D. G. (Ed.), *First European Conference on Unsaturated Soils*. Durham University, Durham, England, pp. 417–422.
- Jaroniec, M., Gadkaree, K. P., Choma, J., 1996. Relation between adsorption potential distribution and pore volume distribution for microporous carbons. *Colloids and Surfaces A: Physicochemical and Engineering Aspects* 118 (3), 203–210.
- Kaufmann, J., 2009. Characterization of pore space of cement-based materials by combined mercury and wood's metal intrusion. *Mercury* 216 (1), 209–216.
- Lange, D. A., Abell, A. B., Willis, K. L., Powell, S., 1998. Characterization of cement pore structure using wood's metal and mercury porosimetry. *Imaging Technologies*, 197–206.
- Likos, W. J., Jul 13-17 2009. Pore-scale model for water retention in unsaturated sand. *Amer Inst Physics, Golden, CO*, pp. 907–910.
- Liu, Y., Zhao, C. G., Nov 04-07 2007. Modeling the hysteresis for soil-water characteristic curves. *China Communications Press, Chongqing, China*, pp. 383–392.
- Lourengo, S. D. N., Gallipoli, D., Augarde, C. E., Toll, D., Evans, F., Medero, G., July 2008a. Studies of unsaturated soils by environmental scanning electron microscope using dynamic mode. In: Toll, D. G., Augarde, C. E., Gallipoli, D., Wheeler, S. J. (Eds.), *Unsaturated Soils: Advances in Geoengineering*. Proceedings of the 1st European Conference. First European Conference on Unsaturated Soils, Taylor & Francis.
- Lourengo, S. D. N., Gallipoli, D., Augarde, C. E., Toll, D. G., Fisher, P. C., Congreve, A., in press. Formation and evolution of water menisci in unsaturated granular media. *Géotechnique*.
- Lourengo, S. D. N., Toll, D. G., Augarde, C. E., Gallipoli, D., Congreve, A., Smart, T., Evans, F. D., July 2008b. Observations of unsaturated soils by environmental scanning electron microscopy in dynamic mode. In: Toll, D. G., Augarde, C. E., Gallipoli, D., Wheeler, S. J. (Eds.), *Unsaturated Soils: Advances in Geo-Engineering*. First European Conference on Unsaturated Soils, CRC Press.
- Lu, N., Likos, W. J., 2004. *Unsaturated Soil Mechanics*. John Wiley & Sons, Inc., New Jersey (USA).

- Maria, S., 2010. Methods for porosity measurement in lime-based mortars. *Construction and Building Materials* In Press, Corrected Proof, –.
- Mason, G., Morrow, N. R., 1991. Capillary behavior of a perfectly wetting liquid in irregular triangular tubes. *Journal of Colloid and Interface Science* 141 (1), 262–274.
- Mitchell, J. K., 1991. Conduction phenomena: From theory to geotechnical practice. *Géotechnique* 41 (3), 299–340.
- Mitchell, J. K., Soga, K., 2005. *Fundamentals of Soil Behaviour*, Third Edition. John Wiley & Sons Inc., Hoboken, New Jersey (USA).
- Mu, F., Su, X., Dec. 2007. Analysis of liquid bridge between spherical particles. *China Particuology* 5 (6), 420–424.
- Nishimura, T., Fredlund, D. G., March 2002. Hysteresis effects resulting from drying and wetting under relatively dry conditions. In: Juça, de Campos, Marinho (Eds.), *Unsaturated Soils. Third International Conference on Unsaturated Soils*, Swets and Zeitlinger, Lisse, Recife, Brazil.
- Nuth, M., Laloui, L., 2008. Advances in modelling hysteretic water retention curve in deformable soils. *Computers and Geotechnics* 35 (6), 835–844.
- Philip, J. R., 1977. Unitary approach to capillary condensation and adsorption. *Journal of Chemical Physics* 66, 5069–5075.
- Powrie, W., 2008. *Soil Mechanics: Concepts and Applications*, 2nd Edition. Spon Press.
- Proctor, R. R., 1933. Fundamental principles of soil compaction. *Engineering News Record* 111 (9), 245–248.
- Rojas, E., Rojas, F., 2005. Modeling hysteresis of the soil-water characteristic curve. *Soils and Foundations* 45 (3), 135–145.
- Romero, E., 1999. Characterisation and thermo-hydro mechanical behaviour of unsaturated boom clay: an experimental study. Phd thesis, Universitat Politècnica de Catalunya, Barcelona, Spain.
- Romero, E., Gens, A., Lloret, A., 1999. Water permeability, water retention and microstructure of unsaturated compacted boom clay. *Engineering Geology* 54 (1-2), 117–127.
- Romero, E., Simms, P., 2008. Microstructure investigation in unsaturated soils: A review with special attention to contribution a mercury intrusion porosimetry and environmental scanning electron microscopy. *Geotechnical and Geological Engineering* 26, 705–727.
- Romero, E., Vaunat, J., Apr 10-12 2000. Retention curves of deformable clays. In: Tarantino, A., Mancuso, C. (Eds.), *Experimental Evidence and Theoretical Approaches in Unsaturated Soils*. A A Balkema Publishers, Trent, Italy, pp. 91–106.
- Simms, P. H., Yanful, E. K., 2001. Measurement and estimation of pore shrinkage and pore measurement in a clayey till during soil-water characteristic curve tests. *Canadian Geotechnical Journal* 38, 741–754.
- Simms, P. H., Yanful, E. K., 2004. Estimation of soil-water characteristic curve of clayey till using measured pore-size distributions. *Journal of Environmental Engineering-Asce* 130 (8), 847–854.
- Sun, D. A., Sheng, D. C., Cui, H. B., Sloan, S. W., 2007. A density-dependent elastoplastic hydro-mechanical model for unsaturated compacted soils. *International Journal for Numerical and Analytical Methods in Geomechanics* 31 (11), 1257–1279.
- Tarantino, 2007. A possible critical state framework for unsaturated compacted soils. *Géotechnique* 57 (4).
- Tarantino, A., 2009. A water retention model for deformable soils. *Géotechnique* 59 (9), 751–762.
- Tarantino, A., 2010. Unsaturated soils: compaction versus reconstituted states. In: Alonso, E., Gens, A. (Eds.), *Unsaturated soils. Fifth International Conference on Unsaturated Soils*, CRC Press, pp. 113–136.
- Tarantino, A., De Col, E., 2008. Compaction behaviour of clay. *Géotechnique* 58 (3), 199–213.
- Tarantino, A., Tombolato, S., 2005. Coupling of hydraulic and mechanical behaviour in unsaturated compacted clay. *Géotechnique* 55 (4), 307–317.
- Terzaghi, K., 1925. Principles of soil mechanics. *Engineering News Records* 95 (19, 742–746; 20, 796–800; 21, 832–836; 22, 874–878; 23, 912–915; 25, 987–990; 26, 1026–1029; 27, 1064–1068).
- Terzaghi, K., 1936. The shearing resistance of saturated soils and the angle between the planes of shear. In: *Proceedings of the First International Conference on Soil Mechanics*. Vol. 1. Cambridge, MA (USA), pp. 54–56.
- Thompson, W., 1871. On the equilibrium of vapour at a curved surface of a liquid. *Phil. Mag.* 42(282).
- Toll, D. G., Mar 1990. A framework for unsaturated soil behaviour. *Géotechnique* 40 (1), 31–44.
- Tuller, M., Or, D., Dudley, L. M., 1999. Adsorption and capillary condensation in porous media: Liquid retention and interfacial configurations in angular pores. *Water Resour. Res.* 35 (7), 1949–1964.
- Vanapalli, S., Fredlund, D., 1997. Interpretation of undrained shear strength of unsaturated soils in terms of stress state variables. In: *3rd Brazilian Symposium on Unsaturated Soils*. pp. 278–289.
- Vanapalli, S. K., Fredlund, D. G., Pufahl, D. E., 1999. The influence of soil structure and stress history on the soil-water characteristics of a compacted till. *Géotechnique* 49 (2), 143–159.

- Vatsala, A., Srinivasa Murthy, B. R., 2001. Discussion: The influence of soil structure and stress history on the soil-water characteristics of a compacted till. *Géotechnique* 50 (0), 1–4.
- Volkwein, A., 1993. The capillary suction of water into concrete and the abnormal viscosity of the porewater. *Cement and Concrete Research* 23 (4), 843–852.
- Washburn, E. W., 1921. The dynamics of capillary flow. *Phys. Rev.* 17 (3), 273–283.
- Willis, K. L., Abell, A. B., Lange, D. A., 1998. Image-based characterization of cement pore structure using wood’s metal intrusion. *Cement and Concrete Research* 28 (12), 1695–1705.
-

Chapter 3

Soil water retention curve estimation using cavitation and adsorption

3.1 Introduction

Experimental evidence, for example that of Gallipoli et al. (2003), shows that the behaviour of an unsaturated soil is closely related to its water retention properties, which in turn depend on the material micro- and macrostructure, as shown in Chapter 2. In this chapter, the link between these properties is investigated in order to determine whether the one can be predicted from the other.

3.1.1 Experimentally-determined SWRCs

Several methods can be used to determine the SWRC including tensiometers (Lourenço et al., 2008a; Tarantino and De Col, 2008; Jaquin et al., 2009; Lourenço et al., 2010), hygrometers (Rodriguez et al., 2003; Fredlund, 2006) and filter paper testing (Jotisankasa et al., 2007; Nowamooz and Masrouri, 2010; Russell, 2010) and SWRCs are often determined using a combination of these. Fitting functions are then applied to the experimental data to determine the full SWRC. Some of the most popular are those of Brooks and Corey (Brooks and Corey, 1964), van Genuchten (van Genuchten, 1980) and the Fredlund and Xing (Fredlund and Xing, 1994). The advantage of the latter is that a limiting suction, usually taken to be 1 GPa, can be applied to prevent unrealistic suctions being predicted at low water contents (Croney et al., 1958; Fredlund and Rahardjo, 1993; Heath et al., 2004; Tarantino, 2009). The fits to experimental data afforded by these functions is often good for granular soils, however the quality of the fit deteriorates as the clay content of the soil increases due to a dependence on the saturation ratio of the material, rather than the water content, and a subsequent dependence on the material density at lower saturations (van Genuchten and Nielsen, 1985; Khaleel et al., 1995; Heath et al., 2004). To improve the fitting, a number of more complicated approximation approaches have been suggested, including work by Ahuja et al. (1998), Gallipoli et al. (2003), Huang et al. (2005), Nuth and Laloui (2008), Tarantino (2009), Fredlund and Gitirana (2011) and Pedroso and Williams (2011), however these suffer the drawback of requiring a greater number of fitting parameters to be determined in order to match the available dataset or become less accurate at suction values outside of those used to determine the fitting parameters due to implicit assumptions made about the soil structure (Tarantino, 2009). An improvement to these models would therefore involve a process whereby the use of fitting parameters or material assumptions could be avoided.

3.1.2 Predicting the SWRC using the soil pore size distribution

Several models have been proposed in order to relate the soil pore size distribution (PSD) and the SWRC. This is advantageous as PSD data can be obtained relatively easily from one sample, using for example mercury intrusion porosimetry (MIP), whereas SWRC data often requires a number of samples and combinations of testing methods. A disadvantage of predicting the SWRC from the PSD is, however, that the PSD represents a “snap-shot” of the structure of the soil under given conditions, whereas results from various authors (for example Simms and Yanful (2001)) show that the structure changes with changes in water content: this shall be discussed later in this chapter.

If a granular material containing only one pore size is considered, then it is clear that at a certain applied suction all of the pores would empty at once, resulting in an SWRC stepping between saturation ratios of $S_r = 1$ and $S_r = 0$ as that suction level is exceeded. Similarly, a granular material containing two distinct pore sizes would have an SWRC displaying two distinct steps, with their bounding S_r values determined by the relative proportion of the total pore space taken up by each pore size. This analogy can be extended to consider a material containing a large range of pore sizes, each contributing a small ‘step’ to the resulting SWRC according to their relative volumes. The shape of the PSD, therefore, must directly influence the shape of the SWRC (Vanapalli et al., 1999).

Improvements in the technology available to determine the PSDs of soils have shown that many unsaturated soils display a *bimodal* PSD, so that the SWRC predicted from the PSD should also be bimodal (Ahmed et al., 1974; Delage et al., 1996; Romero et al., 1999). A comparison between bimodal and monomodal SWRCs is shown in Figure 2.17. The fitting functions of Brooks and Corey, van Genuchten and the Fredlund and Xing produce monomodally-distributed SWRCs, so that they do not fully describe the behaviour of bimodally-distributed unsaturated soils (Collins and McGown, 1974; Toll, 1990; Gens and Alonso, 1992; Tarantino, 2010). Several modifications have therefore been made to these models to account for this bimodality, including work by Kutilek et al. (2009), Russell (2010) and Nowamooz and Chazallon (2011), however these suffer from the drawback of requiring additional fitting parameters which can be difficult to determine compared to the simpler requirements for monomodal approximations.

Several models have been suggested to link pore size to its drainage suction. The simplest of these models is the Bundle of Cylindrical Capillaries (BCC) model, where each pore size is considered to be a capillary tube of a certain diameter, as shown in Figure 3.1 (Millington and Quirk, 1961; Mualem, 1976). Eqn 2.8 relates the curvature of a water meniscus to the capillary suction; if the gas is air and the liquid water, then γ can be found using Eqn 2.5 assuming $\theta_{slv} = 0$.

The drawback with the BCC model is that the pores are either completely full or entirely empty; there can be no dual-occupancy of liquid and gas in a single pore (Or and Tuller, 1999; Tuller et al., 1999; Tuller and Or, 2004; Baker and Frydman, 2009). In essence, then, the BCC model does not model truly unsaturated soils, as the soil is divided into completely-saturated and completely-dry regions; this has consequences for hydraulic conductivity calculations as the water phase becomes discontinuous and hence the mechanism for maintaining hydraulic conductivity is lost (Tuller et al., 1999; Baker and Frydman, 2009).

An improvement to the BCC model was proposed in Tuller et al. (1999) where pores were considered to be angular in profile, rather than circular. The advantage of the angular pore space is that capillary wedges can exist in the corners of the pore whilst water can also be adsorbed onto the particle surfaces. The model used in Tuller et al. (1999) considers a square-shaped pore cross section with connecting narrow slit-shaped pores, although a range of other pore shapes could be accommodated. The capillary and adsorptive phases were separated for ease of calculation into capillary wedges present in the square-shaped pore and adsorbed films in the narrow slits. The disadvantage of this model was that calculations

were highly dependent on the “angularity factor” of the pores, as discussed in Section 2.6, which is information not usually available and which makes the matching of the predicted SWRC to available data largely arbitrary (Baker and Frydman, 2009). Furthermore, a capillary meniscus between two particles has both concave and convex curvatures in the meridional and azimuthal directions respectively, as shown in Figure 2.6, which are properties that are not included in the model of Tuller et al. (1999).

A more advanced model, then, is one where the arrangement of the particles is considered and menisci are allowed to form between them, for example those models proposed by Lu and Likos (2004), Mayer and Stowe (2006), Grof et al. (2008) and Likos (2009). For ease of calculation, soil particles in these models are considered to be spherical and the structure to be rigid (i.e. solid particles do not move relative to each other on the application of a suction), whilst the size of the interstitial voids is taken to be the diameter of the inscribed sphere as shown in Figure 3.2. Water either exists as a continuous phase or in the form of liquid bridges suspended between the particles. Adsorption is also included in the model developed in Likos (2009) in the form of thin films adsorbed onto the particle surfaces. A purely adsorptive model for determining the SWRC is presented in Frydman and Baker (2009), however the procedure used relates the final SWRC neither to the particle nor the pore sizes and so it can only be considered a fitting function at best.

A shortfall of the methods developed to date is that they either do not consider both the particles and the pores within a soil, or that they do not consider adsorption as a contribution to suction. In this chapter, a new method for predicting the SWRC from the PSD is presented that incorporates both adsorption and capillary effects. The advantages of this approach are that no curve fitting parameters are required and that the only input required is the PSD.

3.2 Combined capillary-adsorption model for the SWRC

3.2.1 Model overview

An overview of the proposed model is shown in Figure 3.3, showing the procedures necessary to calculate the main drying and wetting paths of the SWRC given a soil PSD and an assumed tetrahedral sphere packing system (for a cubic packing system, replace the appropriate equations with their cubic system counterparts). As the proposed model incorporates capillary and adsorption effects, it is referred to as

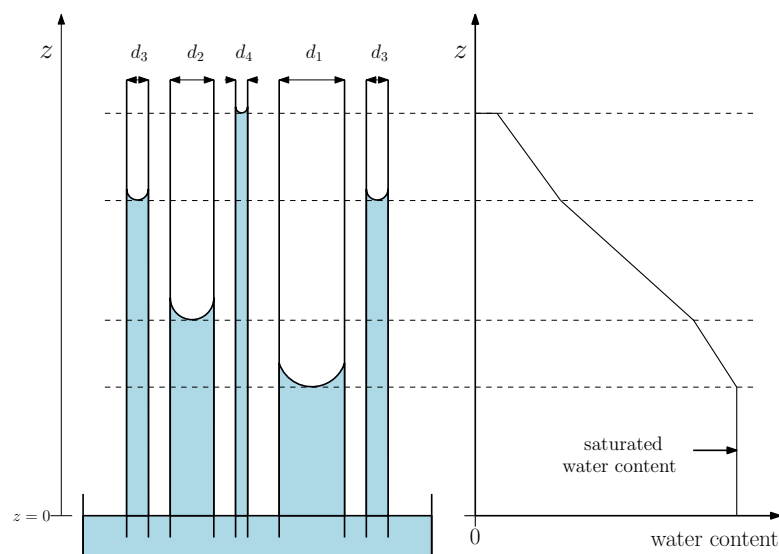


Figure 3.1: The relationship between the BCC model and the SWRC (potential is a function of z in this formalism)

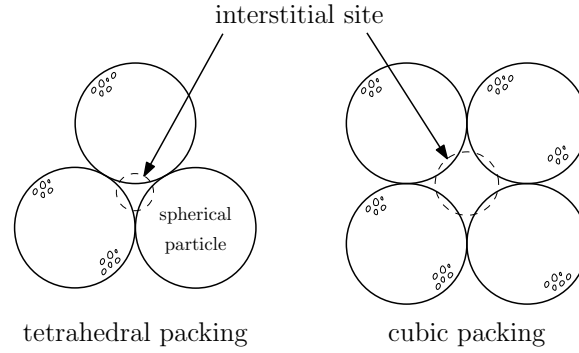


Figure 3.2: Sketch of the size of the inscribed spheres (dashed) between tetrahedrally- and cubically-packed spheres. Note that the 3-D inscribed sphere has a larger diameter than the 2-D inscribed sphere.

the *combined capillary-adsorption* (CCA) model from this point forward. Justifications, derivations and appropriate uses for the equations given in Figure 3.3 are given in the following sections.

3.2.2 Soil solid skeleton assumptions

3.2.2.1 Particle shape approximations

SEM/ESEM micrographs of soils have shown that large soil particles and soil aggregates are approximately round in shape (Lourenço et al., 2008b; Delage, 2009; Park, 2010), supporting the assumption that soil particles can be considered to be spherical made by previous authors. However, micrographs also show that clay particles are plate-like, so that a spherical approximation is not appropriate and will severely underestimate their specific surface area (Salem and Chilingarian, 1999; Tuller et al., 1999; Delage et al., 2006; Ouhadi and Yong, 2008; Frydman and Baker, 2009; Delage, 2010; Hattab and Fleureau, 2010; Monroy et al., 2010).

The first major feature of the CCA model is the adoption of different shape approximations for large and small particles; large particles (sand and silt) are modelled as spheres of radius R while small particles (clays) are modelled as cuboids of length and depth L and height αL , as shown in Figure 3.4. SSAs for the different shape approximations are calculated using

$$SSA_{sphere} = \frac{4\pi R^2}{\frac{4}{3}\pi R^3 \rho} = \frac{3}{\rho R} \quad (3.1)$$

$$SSA_{cuboid} = \frac{L^2(2 + 4\alpha)}{L^3 \alpha \rho} = \frac{2(1 + 2\alpha)}{L \alpha \rho} \quad (3.2)$$

where ρ is the particle density (taken to be 2.65 Mg/m^3).

Figure 3.5 shows experimental SSA data compared to Eqns 3.1 and 3.2, using particle size data given in Table 3.1. Particles $\geq 2 \mu\text{m}$ diameter (i.e. silts) are modelled as spheres, whilst smaller particles are modelled as cuboids. Where specific particle sizes have been given in the sources, results are shown as

Table 3.1: Particle size values (Powrie, 2008)

Mineral Group	Particle Length (μm)	Particle Thickness (μm)	α
Sand	1000 to 2000	1000 to 2000	N/A
Kaolinite	0.1 to 4	0.05 to 2	0.5
Illite	0.1 to 4	≥ 0.003	0.01
Montmorillonite	1 to 2	0.001 to 0.02	0.002

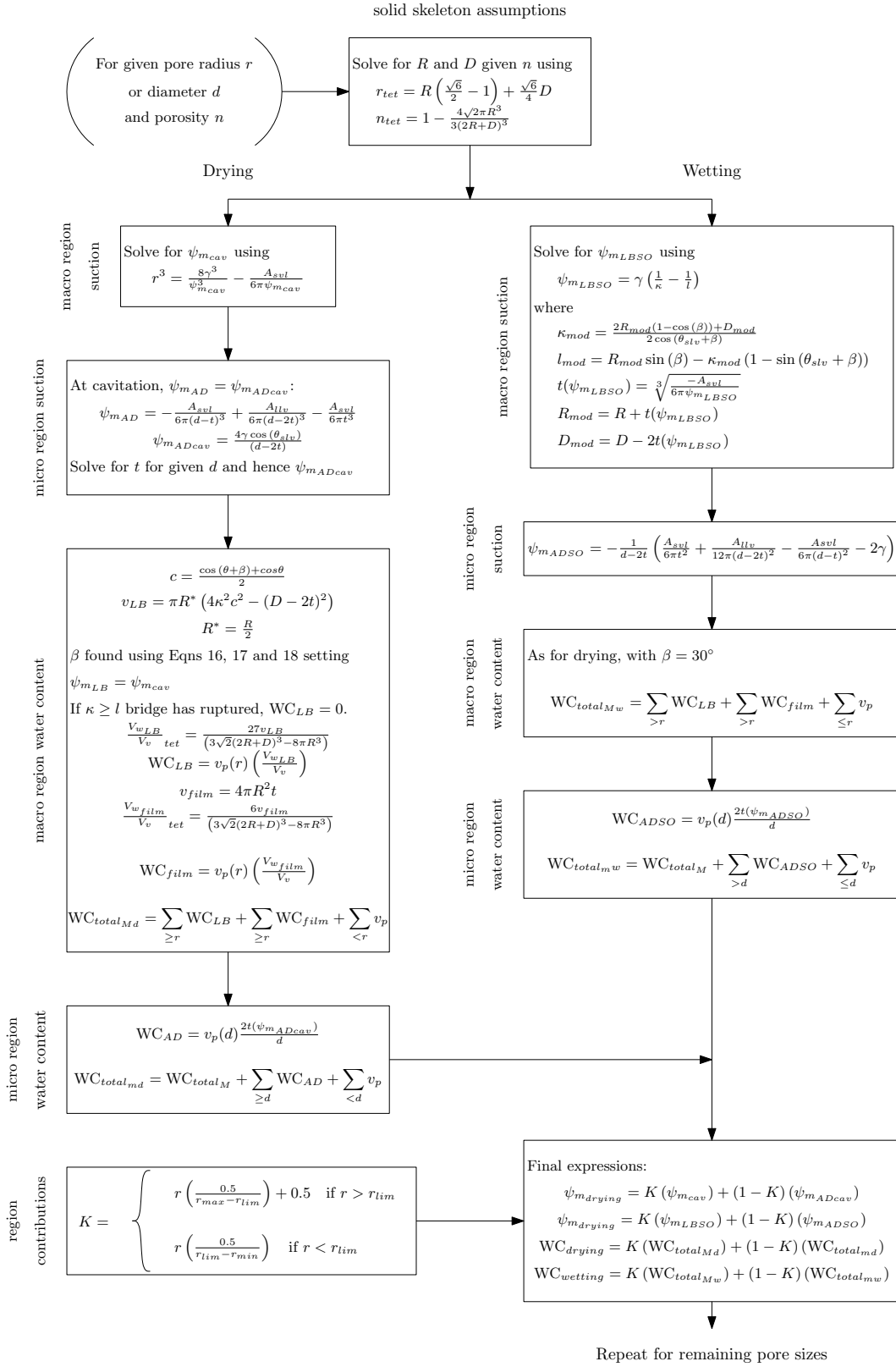


Figure 3.3: CCA model calculations procedure for one pore size using a tetrahedral packing system.

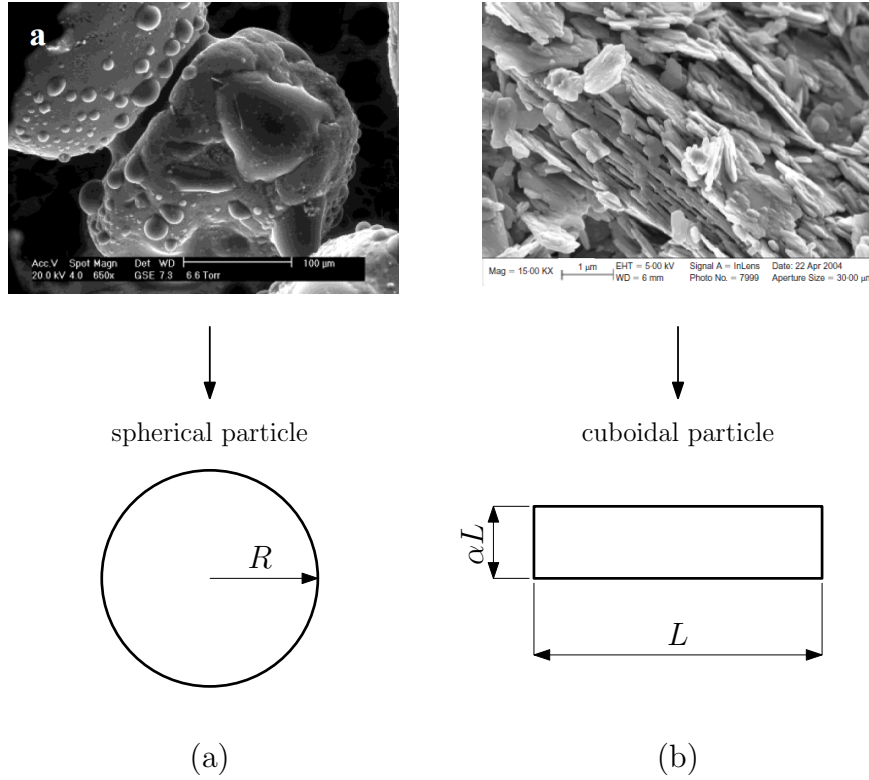


Figure 3.4: SEM micrographs for: a) sand particles (Lourenço et al., 2008a); and b) clay particles (Hattab and Fleureau, 2010) and corresponding shape approximations.

single points, for example data from Powrie (2008) and Likos (2009). If, however, only a size class has been given (e.g. “kaolinite” in Akbour et al. (2002)), the recorded SSA is attributed to the entirety of that class according to volumes calculated using the “particle length” entries in Table 3.1. Where both a particle size and SSA range is given (for example in Frydman and Baker (2009)), the corresponding bounding region is given in Figure 3.5; actual particle SSA values could therefore lie within any part of the regions specified in the model. A boundary pore radius, r_{lim} , found from the soil PSD defines the divide between the spherical and cuboidal approximations, representing the divide between the inter- and intra-aggregate pores. If a monomodal distribution, r_{lim} can easily be found as the pore size corresponding to the modal peak volume. If a bimodal distribution, the smaller of the modal sizes should be selected as r_{lim} . These two regions are referred to from this point on as the “macro” and “micro” regions respectively. Figure 3.5 shows that Eqns 3.1 and 3.2 produce good approximations to the data for the given α values.

3.2.2.2 Macro region particle size and separation

It is assumed that spherical macro region particles are either cubically or tetrahedrally packed, as shown in Figures 3.7 and 3.8 respectively. Particle asperities mean that the bulk of a particle’s surface is significantly further away from a contacting neighbour than would be the case if the particles were spherical and smooth (Mayer and Stowe, 2006; Grof et al., 2008; Likos, 2009); to account for this, a non-zero separation distance D is included between smooth particle surfaces so that the recorded particle diameter becomes the “apparent” diameter as shown in Figure 3.6 (Pietsch, 1968; Butt, 2008). The interstitial pore radii, r , (taken to be the radius of the largest possible interstitial sphere) for these

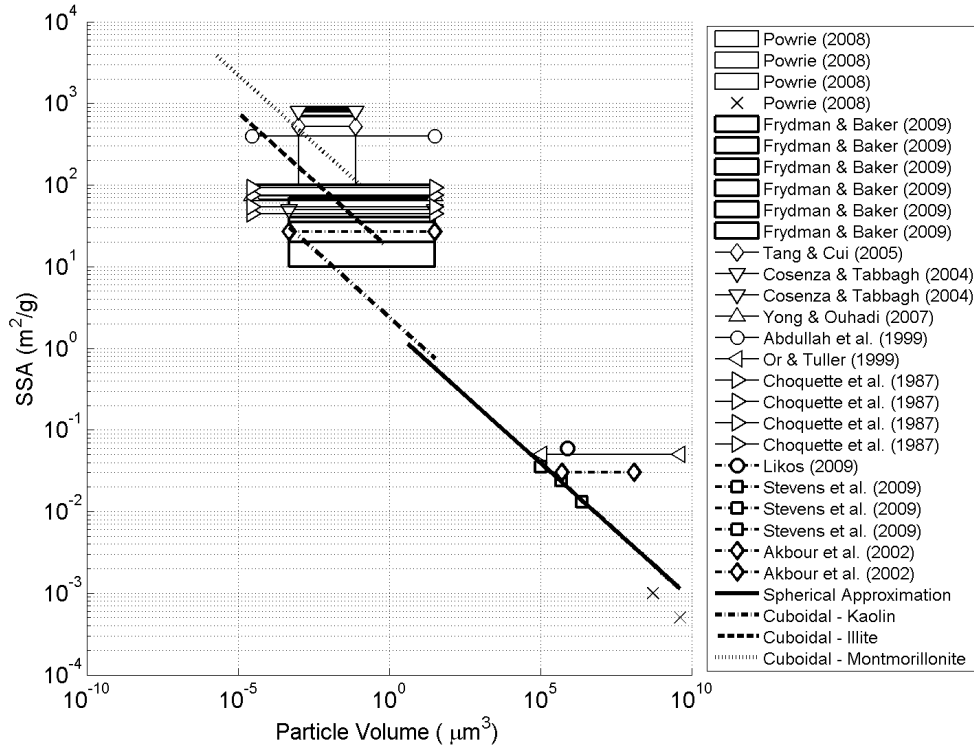


Figure 3.5: Specific surface area data (sources given in the figure) compared to spherical and cuboid shape approximations

packing arrangements are given by Eqns 3.3 and 3.4:

$$r_{cub} = R \left(\sqrt{3} - 1 \right) + \frac{\sqrt{3}}{2} D \quad (3.3)$$

$$r_{tet} = R \left(\frac{\sqrt{6}}{2} - 1 \right) + \frac{\sqrt{6}}{4} D \quad (3.4)$$

The inclusion of a separation distance allows materials of different porosities to be modelled depending on the packing method chosen for the spherical particles. Using the geometries given in Figures 3.7 and 3.8, expressions for the porosity of cubically-packed spheres, n_{cub} , and tetrahedrally-packed spheres, n_{tet} , can be found as

$$n_{cub} = 1 - \frac{4\pi R^3}{3(2R + D)^3} \quad (3.5)$$

$$n_{tet} = 1 - \frac{4\sqrt{2}\pi R^3}{3(2R + D)^3} \quad (3.6)$$

so that the minimum porosities for tetrahedral and cubic packing, found at $D = 0$, are 0.260 and 0.476 respectively. Soil porosity must be determined prior to finding the PSD and so is part of the PSD data. If V_{vM} and V_{sM} are the volume of voids and solids in the macro region respectively and n_M the porosity in the macro region, it can readily be shown that the porosity in the macro region is the same as the

bulk porosity, n , via

$$n_M = \frac{V_{vM}}{V_{vM} + V_{sM}} = \frac{V_{vM}}{V_{vM} + V_s \frac{V_{vM}}{V_v}} = \frac{1}{1 + \frac{V_s}{V_v}} = n \quad (3.7)$$

where V_v and V_s are the total volumes of voids and solids respectively. For a given value of r_{cub} , Eqns 3.3 and 3.5 can be used to solve for R and D for cubic packing; a similar process with Eqns 3.6 and 3.4 can be used for tetrahedral packing. It is assumed that the solid particle structure is rigid, i.e. the values of R and D do not change for a given r . Therefore, the values of $\frac{r}{R}$ and $\frac{r}{D}$ are constant in the macro region.

3.2.3 Main drying path suction calculations

The calculation of the SWRC main drying path is divided into:

1. Cavitation phenomena related to the emptying of macro-region pores;
2. Liquid bridges between spheres and the conditions that must be met in order for them to form;
3. Adsorbed films between cuboidal particles and the emptying of micro-region pores.

3.2.3.1 Cavitation

Cavitation is the process whereby bubbles of gas (or vapour in the absence of dissolved gas) form within a liquid when a certain critical negative pressure is reached; although perhaps similar, it is conceptually different to the mechanism of air entry due to the formation of a new liquid-gas interface rather than the movement of an existing interface (Or and Tuller, 2002). Here, however, it is assumed that the cavitation pressure corresponding to the largest pores present in the simulated material is equivalent to that at air entry. The largest negative pressure observed in pure water is currently -140 MPa, which is very close to the theoretical maximum negative pressure sustainable in water arising from intermolecular attractive forces. However, it is possible that negative water pressures can be significantly greater (i.e. more negative) in soils due to the presence of adsorbed water (as discussed in Section 2.4.2), which does not behave like pure water due to the influence of additional attractive forces (Maris and Balibar, 2000).

The energy cost of forming a bubble of radius r within the liquid is given by $\Delta E = 4\pi r^2 \gamma$ and the work done by the negative liquid pressure on the bubble by $\Delta E = \frac{4\pi}{3} r^3 P$, where P is the negative

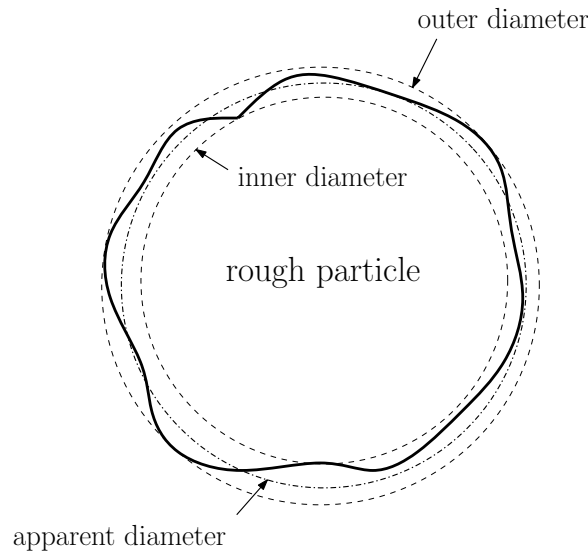


Figure 3.6: Inner, outer and apparent particle diameters

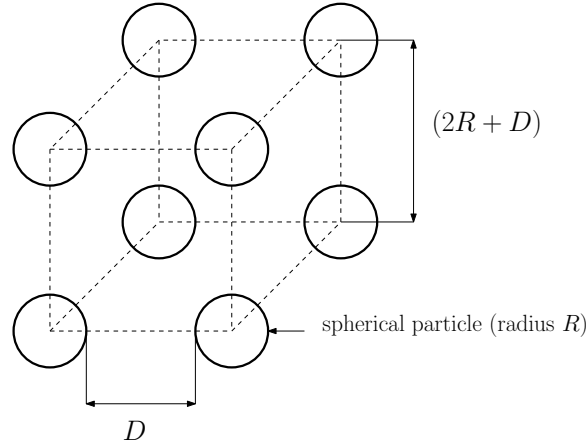


Figure 3.7: Unit cell for the cubic packing of spheres

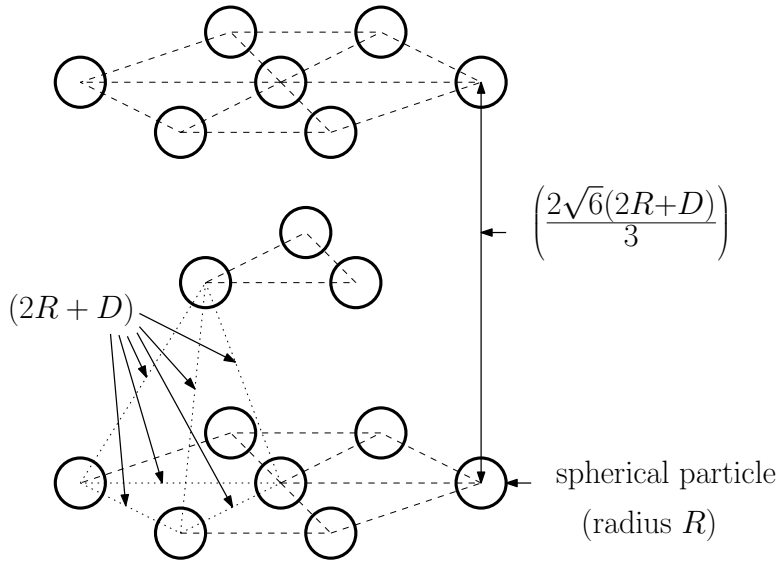


Figure 3.8: Enlarged (for ease of subsequent calculations) unit cell for the tetrahedral packing of spheres. Dotted lines show the shape of a single tetrahedral unit cell.

pressure of the liquid, so that the total energy cost of forming a bubble is given by

$$\Delta E = 4\pi r^2 \gamma - \frac{4\pi}{3} r^3 P. \quad (3.8)$$

which has a maximum value at the critical bubble radius, r^* , of

$$r^* = \frac{-2\gamma}{P} = \frac{2\gamma}{\psi_m} \quad (3.9)$$

which is the classical solution for the Young-Laplace equation (Eqn 2.7), showing that a continuity in suction exists between the liquid and the gas in the bubble (Or and Tuller, 2002). θ_{slv} is not present in Eqn 3.9 as the cavitation bubble does not require a liquid-solid contact in order to form: for completeness, it could be considered that θ_{slv} is now the liquid-liquid contact angle, which can be taken to be zero for the same liquid. It should also be noted that γ remains the liquid-gas surface tension, be the gas a previously-dissolved gas present in the liquid or the vapour of that liquid. Cavitation will not occur at positive water pressures due to the need for a negative P value in Eqn 3.9; therefore, if the air pressure is atmospheric then P can be assumed to be equivalent to the matric suction, ψ_m (Maris and Balibar,

2000). At low pressures, air and water vapour obey the perfect gas law, so that the volume of the bubble is inversely proportional to the gas pressure. Therefore, a bubble will grow to the maximum size afforded by the gas pressure on formation without the need for continued gas input.

At suctions lower than ψ_m , an input of energy is required in order for a bubble to form and grow, due to the contribution of surface tension and the need to work against the solid pore walls (in this formalism). Contrariwise, at suctions greater than ψ_m a bubble of radius r^* will spontaneously form and grow to the maximum size afforded by the pore space due to the overall reduction of the system energy (Or and Tuller, 2002). The size of the soil pore therefore determines the cavitation suction, so that cavitation offers a mechanism for the previously-described “spontaneous draining” (Bolton, 1991; Or and Tuller, 2003; Tuller and Or, 2004; Hillel, 2004; Lu and Likos, 2004) of pores of given size when a given value of suction is reached.

Bubbles in a liquid are unstable due to four main mechanisms: rise due to buoyancy; dissolution due to gas diffusion out of the bubble; contraction if the bubble radius becomes too large; and expansion if the negative liquid pressure reduces (becomes more negative). However, it is assumed here that bubbles, once formed, are stable, due to their being constrained by the rigid pore walls, so that they cannot expand or rise, and insufficient time for gas to diffuse out of the bubble (Young, 1989).

The cavitation radius given by Eqn 3.9 will not be the same as the interstitial pore radius due to the presence of adsorbed films. Here, it is assumed that the water in the adsorbed film does not contribute to the cavitation process, as shown in Figure 3.9. If t is the thickness of the adsorbed water film then

$$r = r^* + t \quad (3.10)$$

where r^* is the cavitation radius, calculated using Eqn 3.9 and r is the pore radius (i.e. half of the pore size given by the PSD). The thickness of a film adsorbed onto a spherical particle is given by Eqn 2.24. Substituting Eqns 3.9 and 2.24 into Eqn 3.10 and replacing ψ_m in Eqns 3.9 and 2.24 with the matric suction at cavitation $\psi_{m_{cav}}$ (for clarity in subsequent equations) therefore yields (after removal of the cubed root term)

$$r^3 = \frac{8\gamma^3}{\psi_{m_{cav}}^3} - \frac{A_{svl}}{6\pi\psi_{m_{cav}}} \quad (3.11)$$

which can be solved iteratively for $\psi_{m_{cav}}$ given a value of r from the PSD. The thickness of one water molecule is given in Hillel (2004) as 3.2 Å, so that $t \geq 3.2$ Å. At $t = 3.2$ Å, $\psi = 97.1$ MPa as calculated using Eqn 2.24 (in the absence of osmotic effects, it is assumed that $\psi = \psi_m$). It is therefore assumed that $t = 3.2$ Å for suctions higher than this value. $\psi_{m_{cav}}$ as found using Eqn 3.11 is therefore the suction required to cavitate the pore. Note that the osmotic suction is not included in these calculations for ease. If it is to be included then the total suction should be used in all expressions in place of the matric suction; this substitution can be done directly, with no additional changes to the equations being required.

3.2.3.2 Liquid bridges between spheres

It is assumed that, on cavitation of the pore, liquid bridges and adsorbed films form between and around the soil particles as shown in Figure 3.9. The suction arising due to the presence of the liquid bridge and adsorbed films is found using Eqns 2.25, 2.26 and 2.27. It should be noted that $\kappa < r^*$; this is due to the thin film thickness and any potential non-zero D value which depends on the value of n . The suction calculated using Eqn 2.27 is referred to as $\psi_{m_{LB}}$, i.e. the matric suction associated with liquid bridges, in order to distinguish it from $\psi_{m_{cav}}$. On the cavitation of the pore, $\psi_{m_{LB}} = \psi_{m_{cav}}$.

Figure 3.10 shows that for $D = 0$, $\kappa < l$ always. However, a range of filling angles exists where $\kappa > l$ for $D > 0$ so that $\psi_{m_{LB}} < 0$, which is undefined. A peak value of $\psi_{m_{LB}}$ therefore exists as β reduces to

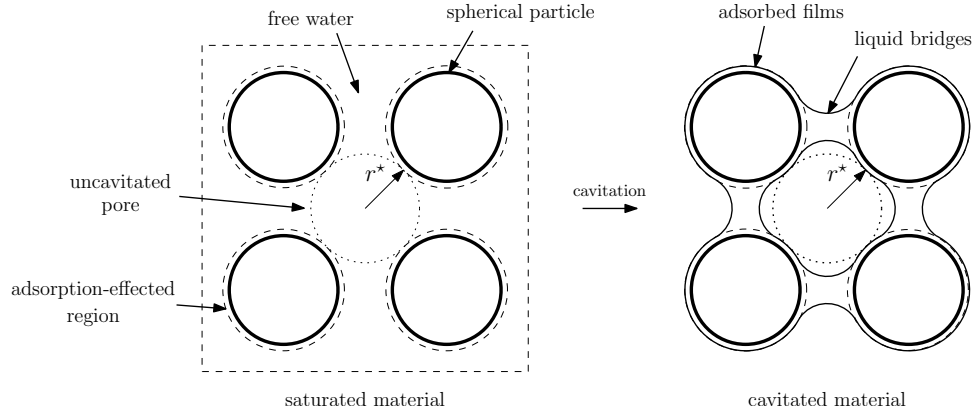


Figure 3.9: Formation of liquid bridges and adsorbed films between cubically-packed spheres on the cavitation of a soil pore

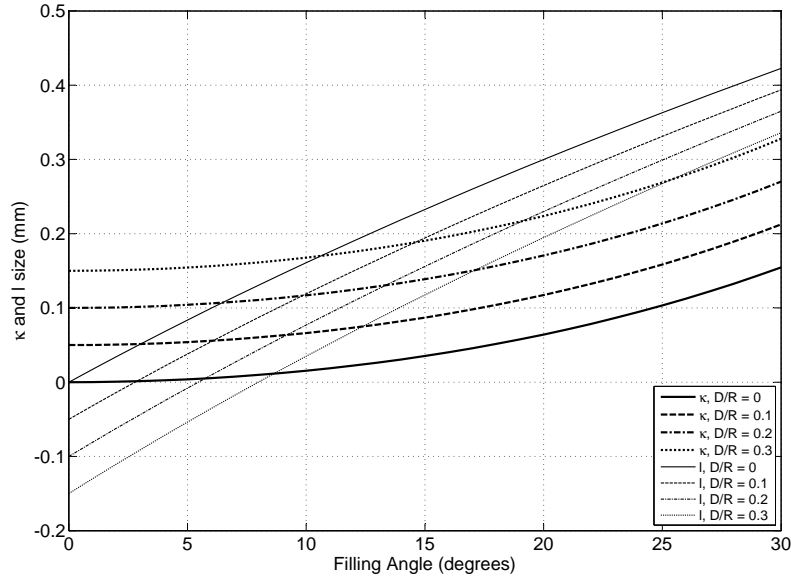


Figure 3.10: Change in κ and l with filling angle for different separation distances for $R = 1\text{mm}$.

the point where $\kappa = l$. The liquid bridges will rupture if $\psi_{m_{cav}}$ becomes greater than this peak $\psi_{m_{LB}}$ value. This can either occur at or after cavitation, depending on the values of R and D . The peak $\psi_{m_{LB}}$ value can be found either by differentiating Eqn 2.19 or by solving Eqn 2.19 for different values of β at given values of R and D . Furthermore, if $D \neq 0$ then the water trapped in the liquid bridges will cavitate if

$$\psi_{m_{LB}} \geq \frac{4\gamma}{D_{mod}} \quad (3.12)$$

so that the bridge will also rupture. As it is assumed that the water in the adsorbed films is not part of the liquid bridges, adsorbed films will remain after liquid bridge rupture. It is assumed that rupture is a slow process and that the particles are static with respect to each other; if the process happens quickly or if the particles are moving relatively to each other then the rupture suction will change (Pitois et al., 2000, 2001; Mu and Su, 2007).

Liquid bridges will coalesce if $\beta \geq 45^\circ$ in cubic packing and if $\beta \geq 30^\circ$ in tetrahedral packing. Equating Eqns 2.25 and 2.26 and setting β to either 45° or 30° for the type of packing required therefore

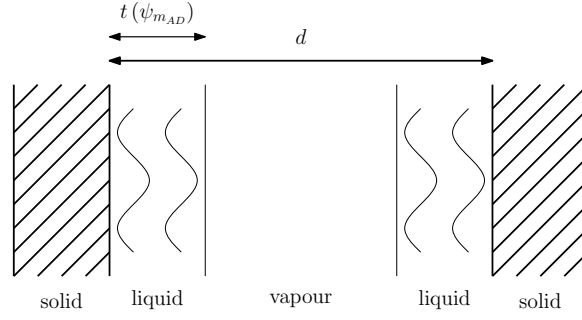


Figure 3.11: Two parallel adsorbed films, facing each other across an intervening vapour (after Iwamatsu and Horii (1996))

gives a value for D for the maximum porosity at which liquid bridges can be present for a given a value of R (as $\frac{D}{R}$ is constant for a given porosity, this calculation can be made easier by taking $R = 1$). Note that this is independent of r due to the scaling nature of the unit cells. The resulting maximum porosities are 0.600 for cubic and 0.519 for tetrahedral packing; at higher porosities water will only remain in the form of adsorbed films after cavitation. As cubic packing offers a slightly greater maximum porosity than tetrahedral packing, materials are modelled as tetrahedrally-packed if their porosity lies within the region $0.260 \leq n \leq 0.519$ and cubically-packed if $0.519 < n \leq 0.600$.

3.2.3.3 Adsorbed films between cuboidal clay particles in the micro region

Pores between cuboidal clay particles are modelled as slit-shaped, following the work of Or and Tuller (1999) and Tuller et al. (1999). Such a pore containing two adsorbed films with constant bulk densities and sharp interfaces is shown in Figure 3.11. It is assumed that the surfaces are completely wetted by the adsorbed films; if this were not the case then the surface tension terms would have to be modified by the inclusion of the contact angle. Suction is related to the film thickness, t , according to Iwamatsu and Horii (1996) as

$$\psi_{mAD} = -\frac{A_{svl}}{6\pi(d-t)^3} + \frac{A_{llv}}{6\pi(d-2t)^3} - \frac{A_{svl}}{6\pi t^3} \quad (3.13)$$

where d is the pore size (from the PSD, note that this is no longer halved as the radius is not required) and $A_{llv} = 3.7 \times 10^{-20} \text{J}$ is the Hamaker constant for liquid-liquid interactions through an intervening vapour (Iwamatsu and Horii, 1996). Figure 3.12 shows the cavitation of a slit-shaped pore between two cuboidal particles of size L by the invasion of a capillary wedge of curvature κ_{cap} . The cavitation suction required to drain the pore is given by

$$\psi_{mADcav} = \frac{2\gamma \cos(\theta_{slv})}{\kappa_{cap}} = \frac{4\gamma \cos(\theta_{slv})}{(d-2t)} \quad (3.14)$$

where again it is assumed that $\theta_{slv} = 0$. At cavitation, $\psi_{mAD} = \psi_{mADcav}$. Eqns 3.13 and 3.14 can be therefore be combined to solve for the unknown t and so ψ_{mADcav} .

At a critical vapour pressure, the slit-shaped pore will spontaneously fill due to the interaction and attraction of the two adsorbed films. The film thickness at which this occurs is given by

$$t_c = \frac{d}{2 + \left(\frac{-2A_{llv}}{A_{svl}} \right)^{\frac{1}{4}}} \quad (3.15)$$

so that the corresponding critical suction, ψ_{mADc} can be found by substituting t_c for t in Eqn 3.13 (Iwamatsu and Horii, 1996; Tuller et al., 1999). If $\psi_{mADc} < \psi_{mADcav}$ (i.e. $t > t_c$) then the pore will

remain filled at $\psi_{m_{ADcav}}$ rather than emptying. Therefore, pores below a certain critical diameter d_c will be permanently filled. If Eqn 3.15 is substituted into Eqns 3.13 and 3.14 and $\psi_{m_{ADcav}} = \psi_{m_{AD}}$ then d_c is found to be roughly 0.42 nm, corresponding to a suction of roughly 2 GPa. As the thickness of thin films is limited to $t \geq 3.2\text{\AA}$, the minimum value of d for a pore containing two adsorbed films is 6.4\AA (i.e. 0.64 nm), so that this condition should not be encountered. The current limit on pore sizes detectable using MIP is around 2 nm (d'Souzae, 2008), so that it can be expected that all pores detectable through MIP will cavitate. Furthermore, work conducted in Croney et al. (1958) and Vanapalli and Fredlund (1997), amongst others, suggests that the maximum suction attainable in soils is 1 GPa so that the limit of 2 GPa should never be reached. The use of slit-shaped pores is therefore appropriate for all pores in the micro region.

3.2.4 Main wetting path suction calculations

The next component of the model to be described is the calculation of the SWRC main wetting path. This is divided into:

1. Pore snap-off (i.e. filling) and liquid bridge coalescence;
2. Thin film coalescence.

3.2.4.1 Pore snap-off in the macro region: liquid bridge coalescence

Calculations for the suctions at pore snap-off are very similar to those for draining. Wetting from a completely dry state begins with the growth of adsorbed films on the particle surfaces. If it is assumed that $R \gg t$ then the film thickness at a given suction is given by Eqn 2.24. Films will continue to grow as suction reduces until a suction value is reached where a liquid bridge forms in the space between particles; the suction at which this occurs can be found using Eqns 2.24 to 2.27 using $\psi_{m_{LB}}$ found using Eqn 2.27 in the place of ψ in Eqn 2.24 (i.e. it is the film thickness at the liquid bridge suction).

If $R \gg t$ film coalescence occurs according to Eqn 3.15; however, this results in an unrealistic value for liquid bridge formation due to the very low suctions required to achieve t_c at larger values of D . It is therefore assumed that liquid bridges will form when the applied suction reduces to a value below the peak $\psi_{m_{LB}}$ for the given liquid bridge configuration.

Wetting continues as suction reduces via the growth of the liquid bridge until the liquid bridges coalesce at $\beta = 45^\circ$ in cubic and $\beta = 30^\circ$ in tetrahedral packing; this is the “pore snap-off” (or “instantaneous filling”) suction, $\psi_{m_{LBSO}}$. The suction at which this occurs can be found using Eqns 2.24 to 2.27 using $\psi_{m_{LB}}$ found using Eqn 2.27 in the place of ψ in Eqn 2.24, with the appropriate value of β for coalescence. Below this suction, the pore is assumed to be completely filled.

It should be noted that $\psi_{m_{LBSO}} < \psi_{m_{cav}}$ due to the former being derived from a geometric consideration of the liquid bridges and the latter from the cavitation radius as shown in Figure 3.13. This

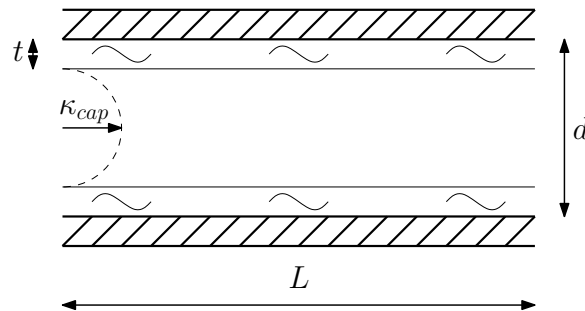


Figure 3.12: Invasion of a capillary wedge into a slit-shaped pore

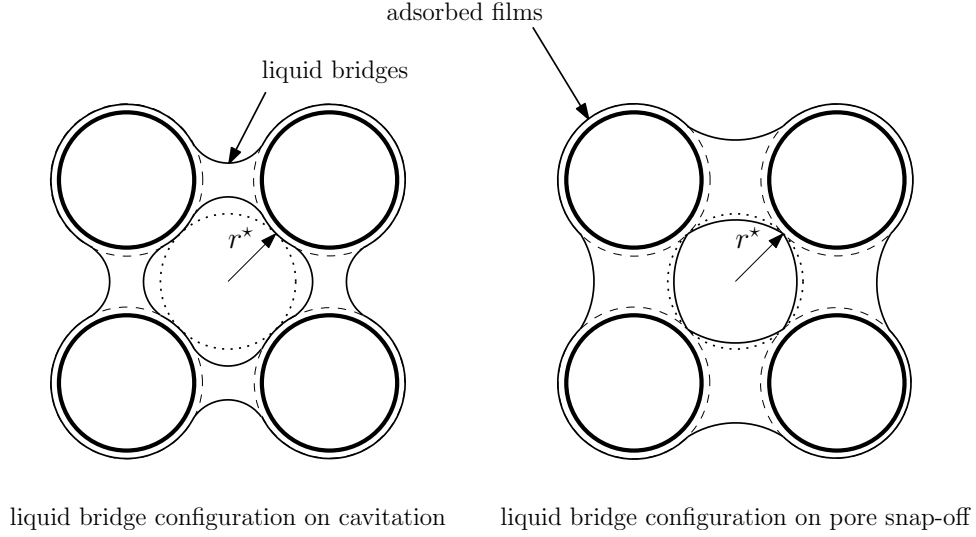


Figure 3.13: Liquid bridge configurations between cubically-packed spheres at cavitation (left) and snap-off (right)

is similar to the different drainage (r_d) and imbibition (r_{imb}) radii suggested by Tuller et al. (1999) but relies on simple pore-, particle- and water-phase geometry rather than complicated and perhaps arbitrary angularity factors.

3.2.4.2 Pore snap-off in the micro region: thin film coalescence

Pore snap-off in slit-shaped pores occurs either due to film coalescence (if the film thickness t exceeds the critical thickness t_c as given by Eqn 3.15) or through the invasion of a capillary wedge. It was shown in Section 3.2.3.3 that suctions greater than those expected to be found in soils are required in order for pores to fill due to film coalescence; therefore, it is assumed that pores fill due to capillary condensation. The suction present at the snap-off of a slit-shaped pore due to the invasion of a capillary wedge is given by Iwamatsu and Horii (1996) as

$$\psi_{mADSO} = -\frac{1}{d-2t} \left(\frac{A_{svl}}{6\pi t^2} + \frac{A_{llv}}{12\pi (d-2t)^2} - \frac{A_{svl}}{6\pi (d-t)^2} - 2\gamma \right) \quad (3.16)$$

where t is found using Eqns 3.13 and 3.14 (at snap-off, $\psi_{mAD} = \psi_{mADcav}$). Despite the similarities in the calculations, it can be seen that $\psi_{mADSO} < \psi_{mADcav}$. As it is for the invasion of a capillary wedge, Eqn 3.16 can be shown to be analogous of the Young-Laplace equation (Eqn 2.7) for menisci of radii of curvature $\frac{d}{2}$. A modified version of Eqn 3.16 is given in Iwamatsu and Horii (1996) which accounts for long-range van der Waals force effects between the surfaces of the slit-shaped pore; however, this equation is for use where $d \gg t$, so that it is assumed that it only applies to macro-region calculations, which are not governed by slit-shaped pore behaviour, so that Eqn 3.16 is sufficient.

3.2.5 Water content calculations

The volume of water present at a given suction is given by the volume of pores that remain saturated and the volume of water present in liquid bridges and adsorbed films in those pores that have cavitated. Calculations are presented for the main drying curve and are then related to the necessary calculations for the main wetting curves. The calculations for the water content are divided into:

- Liquid bridge and adsorbed film volume calculation in the macro region;

- Thin film volume in the micro region.

3.2.5.1 Main drying path macro-region water content

It is assumed that pores of radii smaller than $r(\psi_{m_{cav}})$, i.e. those smaller than those that cavitate at $\psi_{m_{cav}}$, are saturated, so that their water contents are given by the pore volume for that pore radius, $v_p(r)$, found directly from the PSD (i.e. there is no trapped air present in the pores).

Draining of a pore of radius r occurs when the suction reaches $\psi_{m_{cav}}(r)$ as stated in the above sections, whereafter water in the pores remains in the form of liquid bridges (if they have not already ruptured) and adsorbed films. The volume of a liquid bridge v_{LB} is given in Butt and Kappl (2009) as

$$c = \frac{\cos(\theta + \beta) + \cos \theta}{2} \quad (3.17)$$

$$v_{LB} = \pi R_{mod}^* (4\kappa^2 c^2 - (D_{mod} - 2t)^2) \quad (3.18)$$

where $R_{mod}^* = \frac{R_{mod}}{2}$ and β can be found using Eqns 2.25 to 2.27 by setting $\psi_{m_{LB}} = \psi_{m_{cav}}$ (i.e. it is the shape of the liquid bridge at the cavitation suction). For cubic unit cells (Figure 3.7), cavitation will lead to the formation of $(12 \times \frac{1}{4}) = 3$ liquid bridges. In the enlarged tetrahedral unit cell (Figure 3.8), cavitation results in $(6 \times \frac{1}{2}) + (6 \times \frac{1}{4}) + 9 = 27$ liquid bridges. The volume of water remaining in the two unit cells expressed as the ratio of water volume in the liquid bridges $V_{w_{LB}}$ to volume of voids in the cell $V_{v_{cell}}$ is given by

$$\frac{V_{w_{LB}}}{V_{v_{cell} \text{ cub}}} = \frac{3v_{LB}}{(2(2R + D)^3 - \frac{4}{3}\pi R^3)} \quad (3.19)$$

$$\frac{V_{w_{LB}}}{V_{v_{cell} \text{ tet}}} = \frac{27v_{LB}}{(3\sqrt{2}(2R + D)^3 - 8\pi R^3)} \quad (3.20)$$

for cubic and tetrahedral packing respectively. The corresponding water content for liquid bridges surrounding pores of size r is therefore given by

$$WC_{LB} = v_p(r) \left(\frac{V_{w_{LB}}}{V_{v_{cell}}} \right) \quad (3.21)$$

for the appropriate packing.

As, given appropriate values of R and D , liquid bridges can be present above $\psi_{m_{cav}}(r)$, the total liquid bridge water content at $\psi_{m_{cav}}(r)$ in the macro region is given by the liquid bridge water contents of those unit cells containing pores of radii $\geq r$. Given that $\psi_{m_{cav}}(r)$ is known, β and hence the appropriate $\frac{V_{w_{LB}}}{V_{v_{cell}}}$ expression can be solved for pores $\geq r$ using Eqns 2.25 to 2.27 using an iterative process. The total liquid bridge water content at that pore radius is then given by $\sum_{\geq r} WC_{LB}$ (i.e. the sum of liquid bridge water contents for pores of radius $\geq r$).

The volume of water contained within an adsorbed film on a spherical particle, assuming $R \gg t$, can be found using

$$v_{film} = 4\pi R^2 t \quad (3.22)$$

where t is calculated using $\psi_{m_{cav}}$ and Eqn 2.24 for all pore radii $\geq r$ (as film thickness does not depend on the pore or particle sizes). In the cubic cell the total surface area for adsorption is $(8 \times \frac{1}{8}) = 1$ sphere, whilst in the expanded tetrahedral cell it is $(12 \times \frac{1}{6}) + (2 \times \frac{1}{2}) + 3 = 6$ spheres, so that the total volume of water in the unit cell expressed as the ratio of water volume in the adsorbed films $V_{w_{film}}$ to volume

of voids is given by

$$\frac{V_{w_{film}}}{V_{v_{cell \text{ cub}}}} = \frac{v_{film}}{\left(2(2R + D)^3 - \frac{4}{3}\pi R^3\right)} \quad (3.23)$$

$$\frac{V_{w_{film}}}{V_{v_{cell \text{ tet}}}} = \frac{6v_{film}}{\left(3\sqrt{2}(2R + D)^3 - 8\pi R^3\right)} \quad (3.24)$$

so that

$$WC_{film} = v_p(r) \left(\frac{V_{w_{film}}}{V_{v_{cell}}} \right) \quad (3.25)$$

gives the adsorbed water content for that pore radius and selected packing type. As above, the total adsorbed water content is given by $\sum_{\geq r} WC_{film}$ (i.e. the sum of adsorbed film water contents for pores of radius $\geq r$). Note that it is assumed that Eqn 3.22 is applicable for $D \geq 0$; the slight error in calculated volume for $D < t$ is negligible.

The total water content in the macro region, WC_{total_M} , at $\psi_{m_{cav}}$ is therefore given by

$$WC_{total_M} = \sum_{\geq r} WC_{LB} + \sum_{\geq r} WC_{film} + \sum_{< r} v_p \quad (3.26)$$

where $\sum WC_{LB}$ and $\sum WC_{film}$ are calculated for all pores of radii $\geq r$ and $\sum v_p$ is calculated for all pores of radii $< r$.

3.2.5.2 Main drying path micro-region water content

$t(\psi_{m_{ADcav}})$ can be found for a given value of d using Eqn 3.14. The slit-shaped pore water content, WC_{AD} , for that pore diameter is then simply given by

$$WC_{AD} = v_p(d) \frac{2t(\psi_{m_{ADcav}})}{d} \quad (3.27)$$

so that the total adsorbed water content in the micro region is given by $\sum_{\geq d} WC_{AD}$ (i.e. the sum of adsorbed film water contents for pores of radius $\geq d$). As thin films and liquid bridges can still exist in the macro region at $\psi_{m_{ADcav}}$, the total water content in the micro region at $\psi_{m_{ADcav}}$ is given by

$$WC_{total_m} = WC_{total_M} + \sum_{\geq d} WC_{AD} + \sum_{< d} v_p \quad (3.28)$$

calculated at $\psi_{m_{ADcav}}$ and where $\sum WC_{AD}$ is calculated for all pores of diameters $\geq d$ (in the micro region, i.e. up to r_{lim}) and $\sum v_p$ is calculated for all pores of diameters $< d$.

3.2.5.3 Main wetting path water content calculations

The water content in the macro region during wetting is found using the same methods as stated above, using $\psi_{m_{LBSO}}$ instead of $\psi_{m_{cav}}$. However, the larger values of β (for the appropriate type of packing) in Eqns 3.17 and 3.18 result in reduced suctions for a given water content due to the ability to maintain liquid bridges to lower suctions than during drying. The total water content in the macro region during wetting is given by

$$WC_{total_M} = \sum_{> r} WC_{LB} + \sum_{> r} WC_{film} + \sum_{\leq r} v_p \quad (3.29)$$

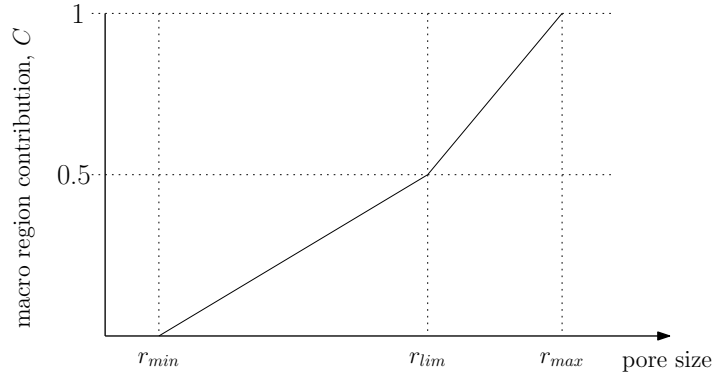


Figure 3.14: Sketch of the smoothing function used to account for the ‘step’ between the macro– and micro region wetting suction calculations

where $\sum WC_{LB}$ and $\sum WC_{film}$ are calculated for all pores of radii $> r$ and $\sum v_p$ is calculated for all pores of radii $\leq r$ as, unlike for drying, when suction equals $\psi_{m_{LBSO}}$ for that pore radius the pore is considered to be filled rather than empty.

During wetting of the micro region, it is assumed that the pore is completely filled at $\psi_{m_{ADSO}}$. The water content of pores with radii $> d$ is found using Eqn 3.28 in the same way as for drying, except that $t(\psi_{m_{ADSO}})$ is used in the calculation instead of $t(\psi_{m_{ADcav}})$. The total water content in the micro region on wetting is given by

$$WC_{total_m} = WC_{total_M} + \sum_{>d} WC_{ADSO} + \sum_{\leq d} v_p \quad (3.30)$$

where $\sum WC_{AD}$ is calculated for all pores of diameters $> d$ (in the micro region, i.e. up to r_{lim}) and $\sum v_p$ is calculated for all pores of diameters $\leq d$.

A ‘step’ exists in the main wetting curve predictions at the transition between the cavitation-based pore snap-off suction $\psi_{m_{ADSO}}$ in the micro region and the geometry-based liquid bridge coalescence snap-off suction $\psi_{m_{LBSO}}$ in the macro region. Such a step is also present in the drying calculations although it is significantly smaller as both the macro– and micro region drying suctions rely on cavitation. A simple linear smoothing function of the form shown in Figure 3.14 is applied to the wetting and drying curves shown in Figures 3.20 to 3.24 in order to remove this step. The contribution, C , of $\psi_{m_{LBSO}}$ to the main wetting suction is found using

$$C = \begin{cases} r \left(\frac{0.5}{r_{max} - r_{lim}} \right) + 0.5 & \text{if } r > r_{lim} \\ r \left(\frac{0.5}{r_{lim} - r_{min}} \right) & \text{if } r < r_{lim} \end{cases} \quad (3.31)$$

so that $0 \leq C \leq 1$ and where r_{max} and r_{min} are the maximum and minimum pore radii respectively. The contribution of $\psi_{m_{ADSO}}$ is simply given by $(1 - C)$ so that the total predicted main wetting suction $\psi_{m_{SO}}$ is given by

$$\psi_{m_{SO}} = C(\psi_{m_{LBSO}}) + (1 - C)(\psi_{m_{ADSO}}). \quad (3.32)$$

Such a function has the advantage of removing the step at the boundary pore radius r_{lim} whilst not over-emphasising any one pore size in particular. The application of a smoothing function means that the boundary between the macro– and micro regions is no longer an absolute transition, but rather where the major contribution to the predicted suction switches from $\psi_{m_{cav}}$ to $\psi_{m_{ADcav}}$ during drying or $\psi_{m_{LBSO}}$ to $\psi_{m_{ADSO}}$ during wetting. It is not clear however whether Eqn 3.31 is the most suitable for smoothing the predictions between the two regions: this is left to future study.

3.2.6 Summary of the CCA model calculation procedures

3.2.6.1 Solid skeleton assumptions

The particle geometry is calculated based on the assumption that large soil particles (those in the macro region) can be modelled as spheres whilst small particles (those in the micro region) can be modelled as cuboidal platelets. Particle sizes and separations in the macro region are calculated using the material porosity.

3.2.6.2 Main drying path calculations

The cavitation suction in the macro region, $\psi_{m_{cav}}$, for a given pore radius r (as given by the PSD) is calculated using Eqn 3.11. Pores smaller than this radius are considered to be saturated. Cavitated pores contain water either in the form of adsorbed films or both adsorbed films and liquid bridges depending on the values of $\psi_{m_{cav}}$, R and D . The water content corresponding to this suction is found via Eqn 3.26.

In the micro region, the cavitation suction $\psi_{m_{ADcav}}$ for a pore of diameter d is found using Eqns 3.13 and 3.14. Again, pores smaller than d are assumed to be saturated. The water content at $\psi_{m_{ADcav}}$ is found using Eqn 3.28.

3.2.6.3 Main wetting path calculations

Pore snap-off occurs in the macro region due to the coalescing of liquid bridges at either $\beta = 45^\circ$ or $\beta = 30^\circ$ for cubic- or tetrahedral packing respectively. The suction at snap-off, $\psi_{m_{LBSO}}$, can be found using Eqns 2.24 to 2.27 by equating $\psi_{m_{cav}}$ found using Eqn 2.24 with ψ in Eqn 2.19 and the appropriate value of β . The corresponding water content can again be found using Eqn 3.29, with a pore of radius r being considered filled at $\psi_{m_{LBSO}}(r)$.

In the micro-region, pore snap-off occurs either due to the invasion of a capillary wedge into the pore or due to thin film coalescence. The snap-off suction $\psi_{m_{ADSO}}$ can be found using Eqns 3.13, 3.14 and 3.16. The corresponding water content is found using Eqn 3.30. Wetting and drying suctions for a given water content are then corrected using a smoothing function.

3.3 Model performance

3.3.1 Comparison to measured data

Differential pore volumes found with MIP on freeze-dried samples are presented in Zhang and Li (2010) for five colluvial soil types CL, ML, SC, SM and GW-GM, mixed from a natural completely decomposed granitic soil from Hong Kong (the reader is referred to Zhang and Li (2010) for detailed information concerning the geotechnical properties of these soils). The range of pore diameters that could be identified was 6 nm to 146 μm ; results suggest that no pores smaller than 6 nm were present, which is consistent with the larger pores expected in kaolinitic clays (Diamond, 1970), and only soil GW-GM showed a significant volume of pores larger than 146 μm . The differential pore volume data was converted to a PSD via the numerical integration of the differential data; pore volume is expressed in cm^3/g in order to facilitate an easy comparison with water content (Diamond, 1970; Delage, 2009). A trapezoidal numerical integration method was used as data was in the form of discrete points, not a continuous curve, so that a more advanced integration approximation was not required. The resulting PSDs for the “compacted and saturated” data of Zhang and Li (2010) for the five soil types are shown in Figures 3.15 to 3.19. The modal peak corresponding to the smallest pore size was taken as r_{lim} ; these values and corresponding properties are shown in Table 3.2. The saturated water content (WC_{sat}) is assumed to equal the total

pore volume V_v for each soil, given in Figures 4 to 8 of Zhang and Li (2010). Soil GW-GM displays a *trimodal* PSD (see Figure 3.19); in this case the central peak was taken as the boundary value. $S_{r_{lim}}$ values (the saturation ratio at r_{lim}) given in Table 3.2 show that the majority of the water content in soils CL, ML, SC and SM resides in the micropores, so that suctions are dominated by the micro region, whilst the majority of the water in soil GW-GM can be found in the macropores with suctions correspondingly being dominated by the macro region.

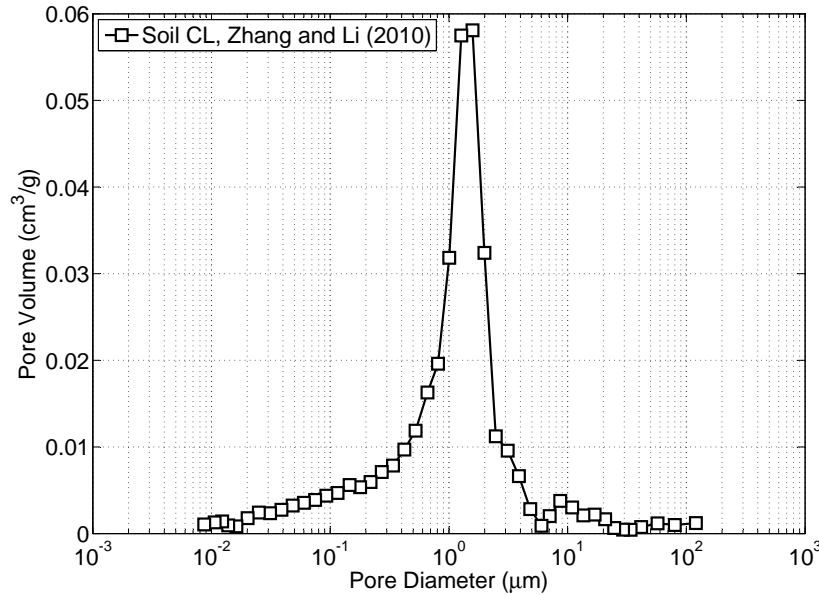


Figure 3.15: Pore size distribution for soil CL, data from Zhang and Li (2010)

Predicted SWRCs using the CCA model for soil types CL, ML, SC, SM and GW-GM are shown in Figures 3.20 to 3.24, alongside SWRCs predicted using the BCC model (i.e. Eqn 2.8) and experimental SWRC data found using the axis translation technique. As some pores could not be detected using MIP, the MIP-determined porosity, rather than bulk porosity, was used to predict the corresponding SWRCs for each soil. It should be noted that the axis translation technique has recently been called into question as a method for determining the SWRC due to its use of positive, rather than negative, water pressures, so that pore drainage cannot be due to cavitation according to Eqn 3.9 (Or and Tuller, 2002; Baker and Frydman, 2009; Frydman and Baker, 2009; Tarantino et al., 2011). However, it is assumed that the measured SWRC data given in Zhang and Li (2010) are acceptable for means of evaluating the performance of the CCA model.

For drying, the CCA model predicts a lower suction than the BCC model for a given water content

Table 3.2: Boundary particle radii (r_{lim}), boundary cavitation suction ψ_{mcav} , boundary water content (WC_{lim}), saturated water content (WC_{sat}), boundary saturation ratio, residual water content (WC_{res}) and residual saturation ratio for soil types CL, ML, SC, SM and GW-GM.

Soil	r_{lim} (μm)	ψ_{mcav} (kPa)	WC_{lim} (mL/g)	WC_{sat} (mL/g)	$S_{r_{lim}}$	WC_{res} (mL/g)	$S_{r_{res}}$
CL	0.8	181.7	0.34	0.379	0.89	0.0059	0.016
ML	0.4	363.4	0.18	0.221	0.80	0.0014	0.009
SC	0.6	242.2	0.17	0.198	0.86	0.0046	0.021
SM	1.0	145.4	0.12	0.176	0.68	0.0037	0.019
GW-GM	1.0	145.4	0.06	0.162	0.37	0.0027	0.016

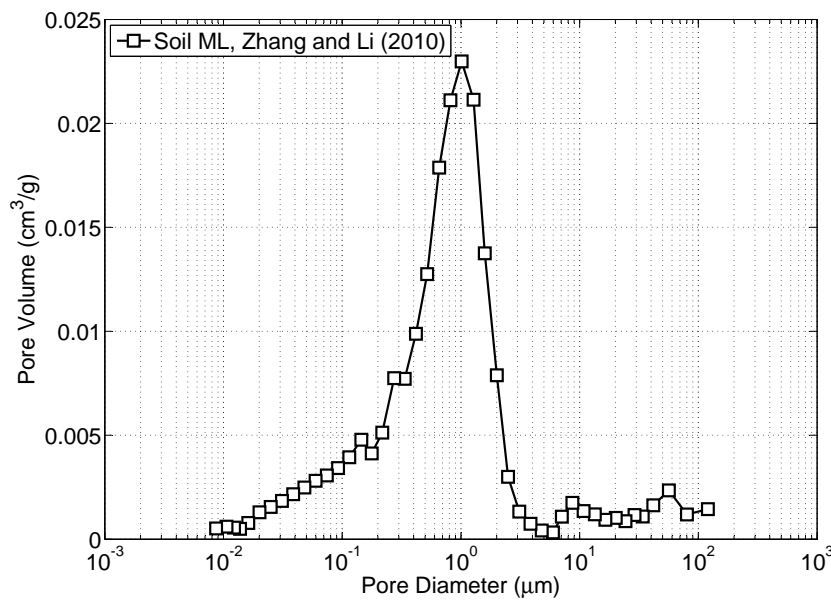


Figure 3.16: Pore size distribution for soil ML, data from Zhang and Li (2010)

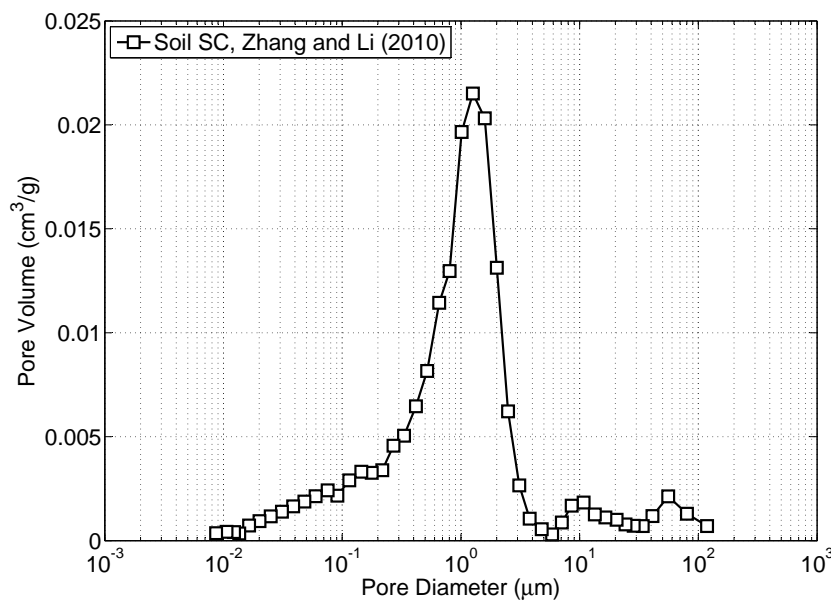


Figure 3.17: Pore size distribution for soil SC, data from Zhang and Li (2010)

and a lower water content for a given suction; this is due to the absence of any adsorption effects and the dual-occupancy of pores in the latter model. It should be noted that suctions do not reach the theoretical maximum suction of 1 GPa as pores emptied at that suction are too small to be captured by MIP. The fit to the measured data achieved by the CCA and BCC models appears to be of roughly equal quality, although the CCA model offers an improvement in predicting the SWRC at lower suctions as seen in Figures 3.20 to 3.23. The predicted suctions are lower than the measured values in the higher suction range, however the quality of the fit to the measured data is comparable to that of the BCC model. A distinct advantage of the CCA model, however, is that the water content corresponding to adsorbed films

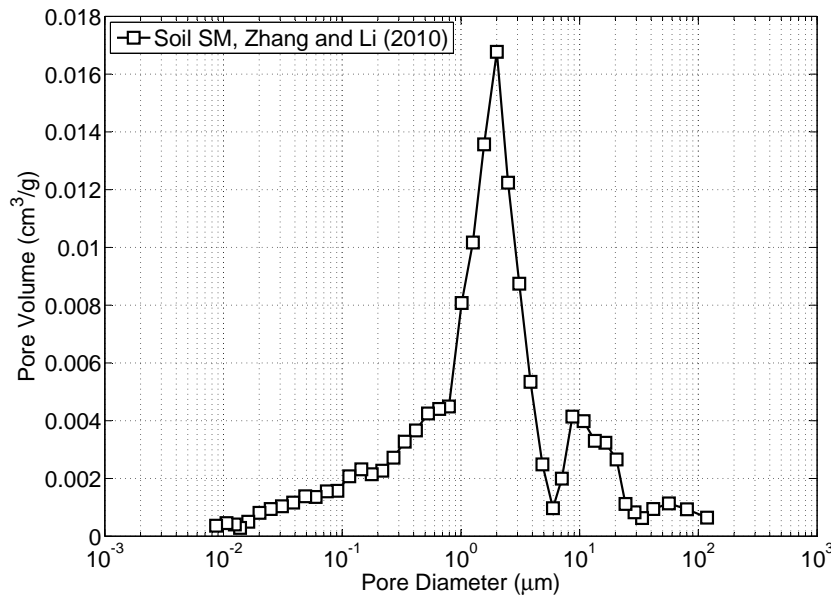


Figure 3.18: Pore size distribution for soil SM, data from Zhang and Li (2010)

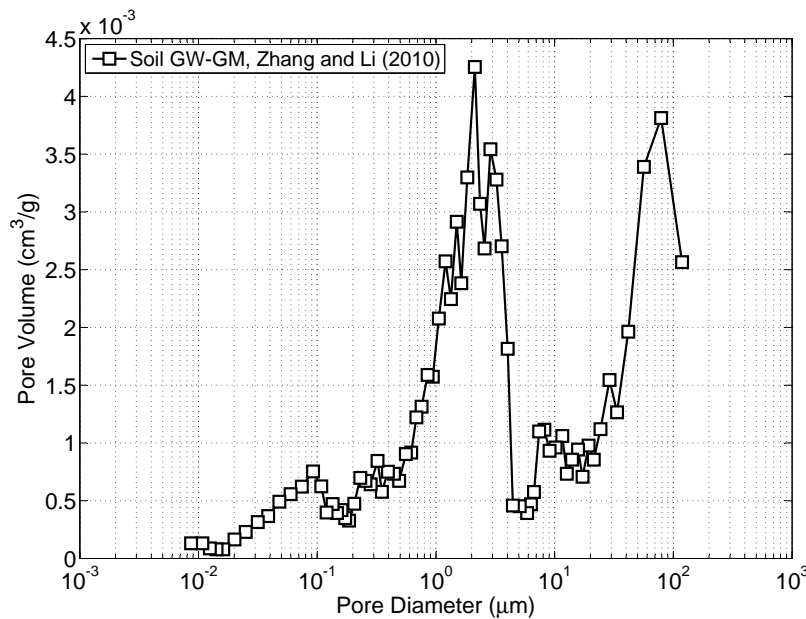


Figure 3.19: Pore size distribution for soil GW-GM, data from Zhang and Li (2010)

can also be investigated, as shown in Figures 3.20 to 3.24. For those pore sizes detectable by MIP this shows that capillary water is dominant (this is to be expected as the smallest pore diameters detected (roughly 6 nm) are roughly 20 times the size of a water molecule (0.32 nm) and the limit on the size of a body of water in which capillary effects can occur is currently believed to be around 1.4 nm (Butt and Kappl, 2009)) but that the proportion of adsorbed water to total water content is still significant and hence the difference between the two sets of model predictions.

Wetting SWRCs are shown in Figures 3.20 to 3.24 in order to show the different suctions predicted by the CCA model for drying and wetting. Although it would appear that the fit to the measured SWRC

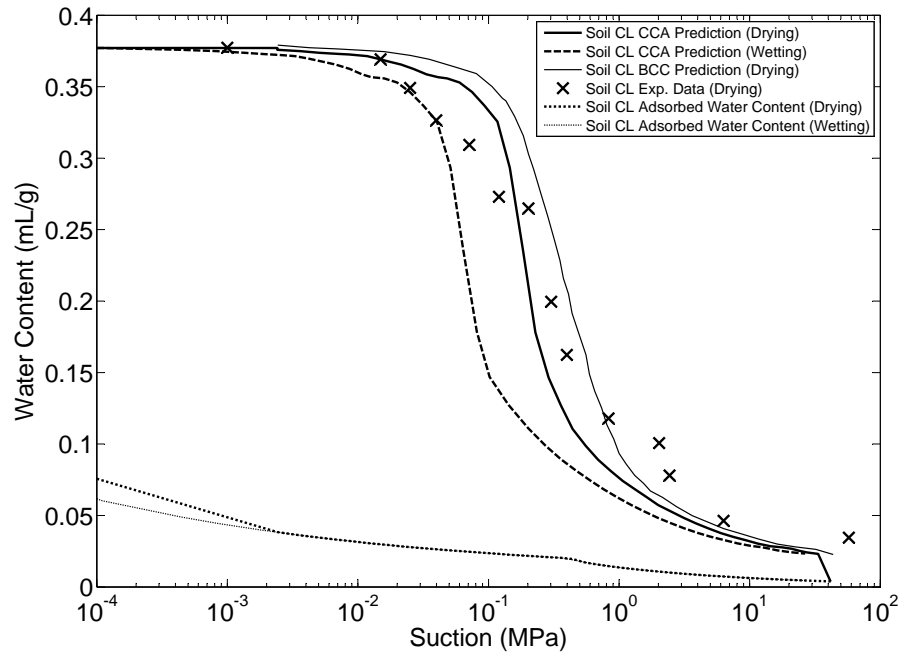


Figure 3.20: Predicted SWRC for soil CL compared to experimental data from Zhang and Li (2010)

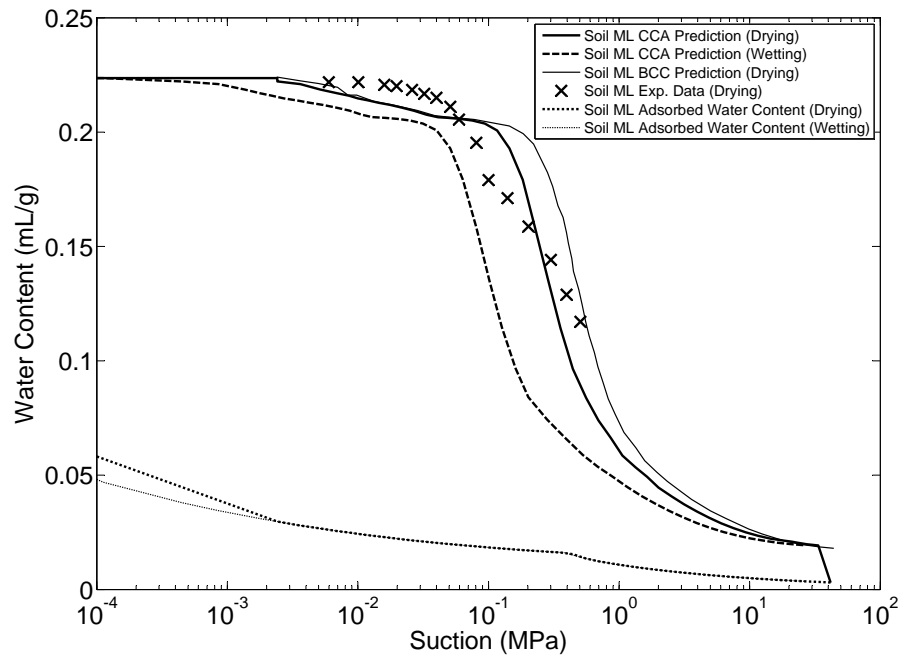


Figure 3.21: Predicted SWRC for soil ML compared to experimental data from Zhang and Li (2010)

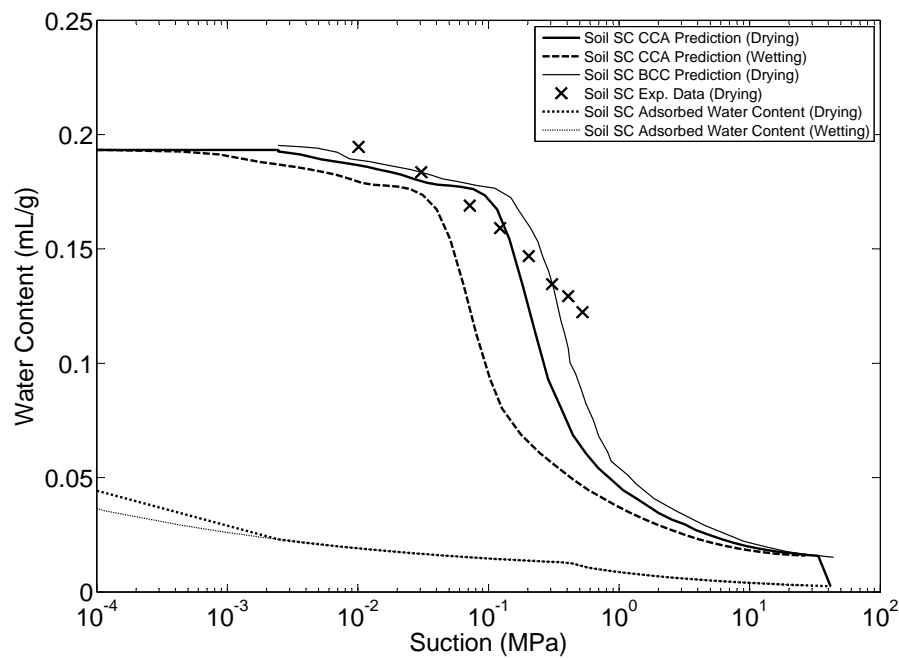


Figure 3.22: Predicted SWRC for soil SC compared to experimental data from Zhang and Li (2010)

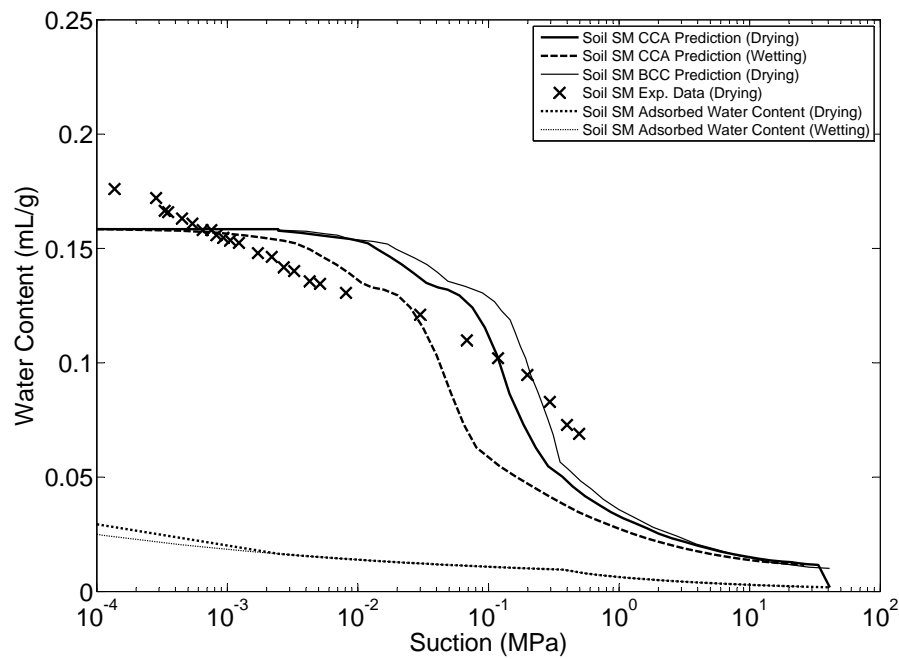


Figure 3.23: Predicted SWRC for soil SM compared to experimental data from Zhang and Li (2010)

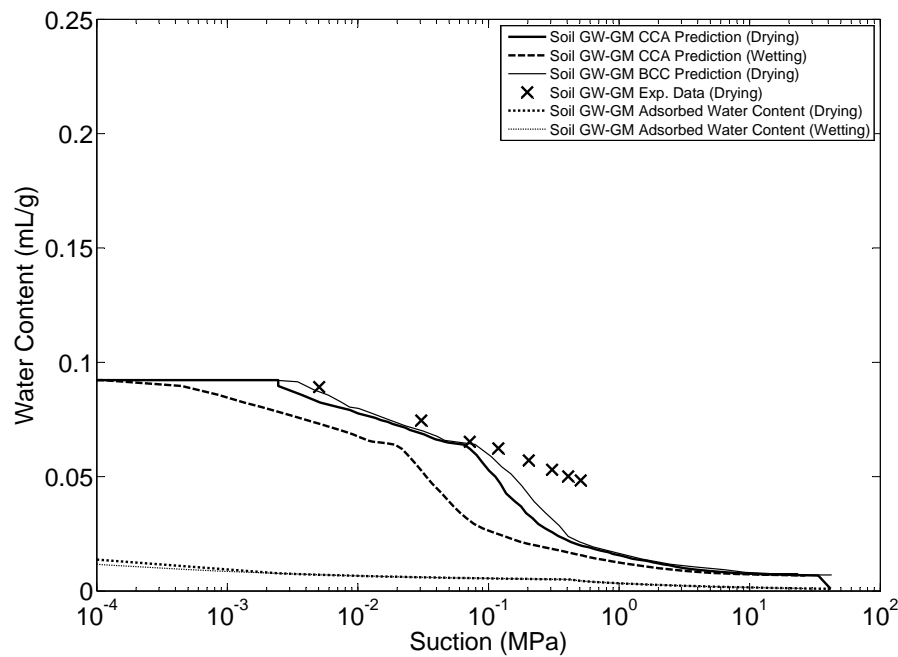


Figure 3.24: Predicted SWRC for soil GW-GM compared to experimental data from Zhang and Li (2010)

datapoints in the lower suction region is improved by means of using the wetting, rather than the drying, suction predictions for some soil types, it should be noted that the wetting SWRC is predicted using an unmodified PSD (i.e. the presence of any trapped or contracted pores has not been accounted for so that apparent fits to experimental drying data are arbitrary). However, it is clear that the CCA model can successfully predict hysteresis of the SWRC between wetting and drying as observed in numerous studies (Haines, 1930; van Genuchten, 1980; Dexter, 1997; Or and Tuller, 2003; Wheeler et al., 2003; Tamagnini, 2004; Nuth and Laloui, 2008).

3.3.2 Differences between measured and predicted data

3.3.2.1 Changing void ratio

The determination of an SWRC from the PSD assumes that the void ratio (e) of the material does not change during testing. However, progressive testing of samples during SWRC determination have shown that this is not the case and that e instead changes with changing applied suction, so that a changing water content is not necessarily a consequence of desaturation, but merely a reducing volume of voids. Furthermore, the nature of these changes is dependent on the rate at which the suctions are changing; rapidly changing suctions could result in force imbalances between the particles causing the structure to change. This is a key drawback of using the PSD to predict an SWRC as an SWRC calculated from a single PSD will not accurately match an experimentally-determined SWRC, depending on by how much e changes (Simms and Yanful, 2001; Urso et al., 2002; Simms and Yanful, 2004; Butt, 2008; Nuth and Laloui, 2008; Megias-Alguacil and Gauckler, 2010).

e values are not provided in Zhang and Li (2010) and so predictions made in Figures 3.20 to 3.23 cannot be converted to saturation ratio (which accounts for changes in e). However, PSDs, corresponding e values and measured SWRC data for a glacial till (OWC 13.7%, PL 18%, LL 27%, gravel content 60%, sand content 18%, silt content 14%, clay content 8%) under a range of applied suctions are given in

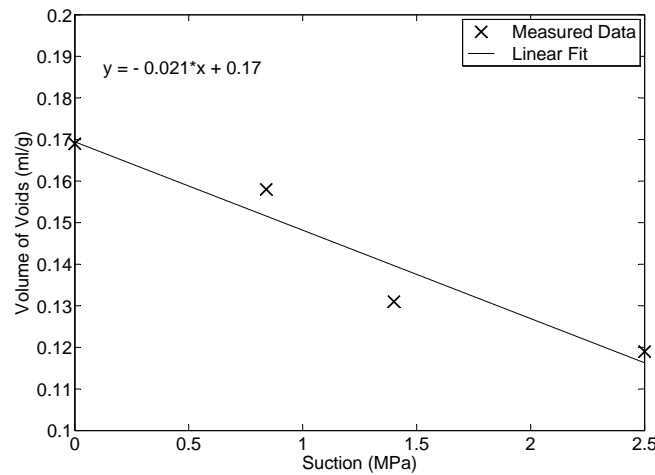


Figure 3.25: Assumed linear relationship between V_v and applied suction for data shown in Figure 2.22

Simms and Yanful (2001) and are reproduced in Figure 2.22. These data clearly show that, as suction increases, the volumes of inter- and intra-aggregate pores reduce and increase respectively, whilst the modal inter- and intra-aggregate pore sizes remain almost constant (the case for an applied suction of 1400 kPa is an exception and might be a result of experimental error: it is not commented on in Simms and Yanful (2001)).

SWRCs predicted using the CCA and BCC models are shown in Figures 3.26 and 3.27. A limiting value of $0.136 \mu\text{m}$ was used as r_{lim} for all suction values except for 1400 kPa, for which a value of $0.476 \mu\text{m}$ was used as the distribution appears monomodal. S_r values were calculated for corresponding measured suction values assuming a linear relationship between the volume of voids and applied suction, as shown in Figure 3.25. In both cases, the CCA model provides a closer approximation to the measured data than the BCC model, as found in Figures 3.20 to 3.23. It is not known why both the CCA and BCC models predict significantly lower suctions for a given water content or S_r value than was measured experimentally, however it might be an indication of further sample deformation that was not detected using MIP. The trend to the measured data formed by the envelope to the predicted SWRCs using the CCA model is, however, very similar in shape to the measured SWRC data, suggesting that the disparity between predicted and measured results is an additional experimental consideration (e.g. additional deformations or an error in the measurement of water content) and that the ‘true’ SWRC can be predicted by a function joining all of these individual, suction-dependent SWRCs (a similar procedure was suggested in Nuth and Laloui (2008)). Such a function has not been shown in Figures 3.26 and 3.27, however, as PSDs are not available for each measured data point. Figures 3.26 and 3.27 therefore indicate the importance of considering changing void ratio on SWRC prediction, as the considerable change in water content observed between suctions of 0 and 2500 kPa only results in a reduction in S_r from 1.0 to roughly 0.9; it is also therefore likely that, if additional PSDs and e values were available for data presented in Zhang and Li (2010), a significantly improved fit to the measured data could be achieved by the CCA model.

3.3.2.2 Trapped Pores

Another explanation for the disparity between the predicted and measured results is that the PSD used to predict the shape of the SWRC is unsuitable. Reasons for this might include: the specimen used for testing not being representative of the soil; the structure of the soil being changed prior to or during the

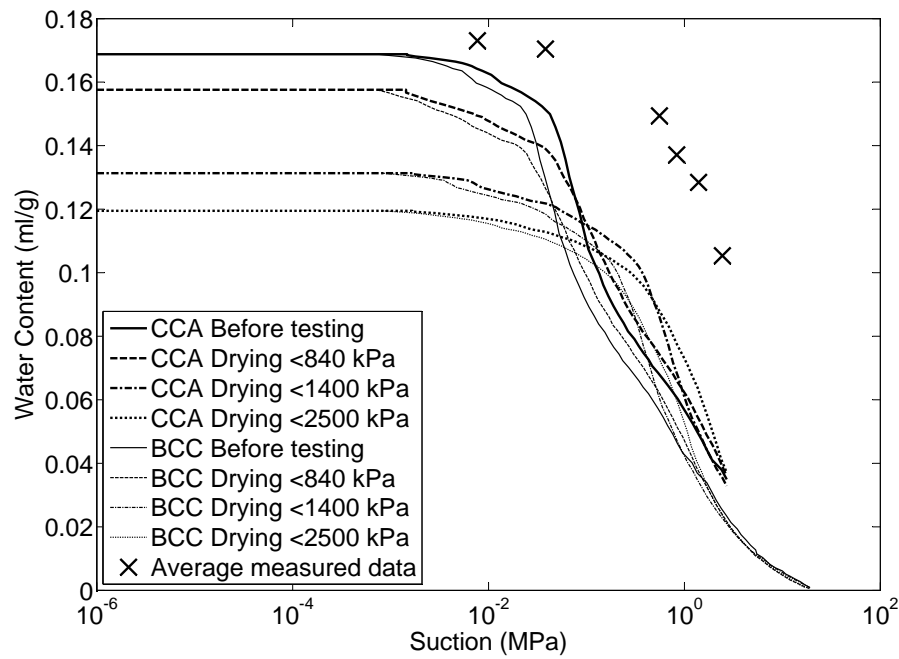


Figure 3.26: Predicted drying SWRCs (in terms of water content) using the CCA and BCC models for a glacial till compacted at 18% water content

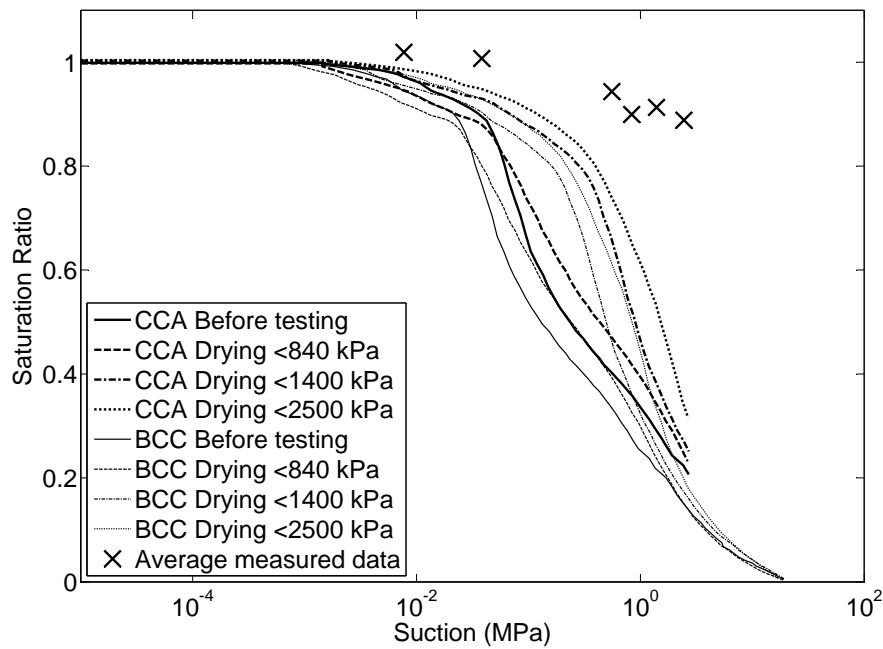


Figure 3.27: Predicted drying SWRCs (in terms of saturation ratio) using the CCA and BCC models for a glacial till compacted at 18% water content

mercury intrusion process, so that pore sizes are altered; and pores becoming trapped as mercury enters pores around them (Willis et al., 1998; Or and Tuller, 2003; Mayer and Stowe, 2006).

The predicted suction values for soil types CL, ML, SC and SM in the low suction range all display a similar overestimation, as seen in Figures 3.20 to 3.23. An overshoot is not observed in soil GW-GM, suggesting that the overshooting phenomenon is restricted to higher saturation ratios. This potentially suggests that larger pores empty at lower suctions than are predicted using cavitation theory. Eqn 2.32 relates the radius of a pore to the pressure required to intrude a known volume of mercury for use during MIP. Although for intrusion, MIP gives the main drying curve for a SWRC due to the $>90^\circ$ contact angle of mercury (Zhang and Li, 2010). Adsorption is not included in Eqn 2.32 as it is assumed that no adsorbed phase exists for mercury and soil solids. Eqn 2.32 also assumes that pores are columnar and cylindrical, so that calculated pore radii are the equivalent radii (see Section 2.5.3.1). This approximation might lead to a difference between the calculated and measured SWRCs. However, the similarities between Eqns 2.8 and 3.9 and the good fit to macro region data found in Figure 3.24 suggest that a cylindrical approximation is acceptable and that the error in prediction is not due to model assumptions (Vanapalli et al., 1999).

Samples in Zhang and Li (2010) were freeze-dried prior to being tested via MIP. The advantage of freeze-drying over oven drying is that it does not adversely effect the pore structure (again see Section 2.5.3.1). Although freeze-drying does not eliminate changes occurring to the pore structure, it is not expected that it could lead to the differences observed between the CCA-predicted and measured SWRC values. Furthermore, the similarity of the shape of the overshoot regions in Figures 3.20 to 3.23 again suggests that the error does not lie in the MIP experimental procedure, as it is unlikely that such a repetitive pattern could result. For this reason it is also not likely that samples were not representative of the soil types, as the resulting shapes of the overshoots would be expected to be much more varied due to structural variability.

“Trapped pores” are pores which are either not intruded (in MIP) or drained (during drying) at their associated draining suction and are thought to occur due to a smaller pore being present in the direction of drainage. Figure 3.28 shows an example columnar pore network consisting of pores (1) to (5) with radii r_i (with $1 \leq i \leq 5$), where $r_1 = r_5$, $r_2 = r_4$ and $r_3 < r_2 < r_1$ with corresponding drainage suctions $\psi(r_1) = \psi(r_5)$, $\psi(r_2) = \psi(r_4)$ and $\psi(r_3) > \psi(r_2) > \psi(r_1)$. Based on the BCC model, previous interpretations of a columnar pore of differing pore diameters subjected to drainage (by the application of a suction gradient) in the direction shown in Figure 3.28 were that pores (1) and (2) would drain as suction increased from $\psi(r_1)$ to $\psi(r_2)$ but pores (4) and (5) were “trapped” due to the water present in pore (3); when the suction reached $\psi(r_3)$ the water in pores (3), (4) and (5) would then spontaneously flow out of the system. However, the addition of cavitation and a continuous water phase due to adsorption leads to a different interpretation whereby as the suction increases both pores (1) and (5) drain at $\psi(r_1)$, with the displaced water from pore (5) flowing through pores (2), (3) and (4). At $\psi = \psi(r_2)$ pores (2) and (4) drain with water from pore (4) flowing through pore (3). Finally, pore (3) drains as suctions reach $\psi(r_3)$.

In the case of MIP, the lack of an adsorbed mercury phase suggests that pores can become trapped as described above using the BCC analysis, with the direction of intrusion opposite to the direction of draining shown in Figure 3.28. If trapped pores are present, therefore, volumes of mercury intruded at certain pressures do not correspond to one specific pore size, but to that size and those of pores that were previously trapped, underestimating the volume of larger pores and exaggerating that of smaller pores (Diamond, 1970; Simms and Yanful, 2001; Kaufmann, 2009). An example of this effect can be seen in Hajnos et al. (2006), where MIP testing consistently underestimated the volume of large pores as determined through water retention (Klute, 1986), nitrogen adsorption and water desorption methods. The effect of fewer large pores in the macro region would be an increase in the suction required to dry

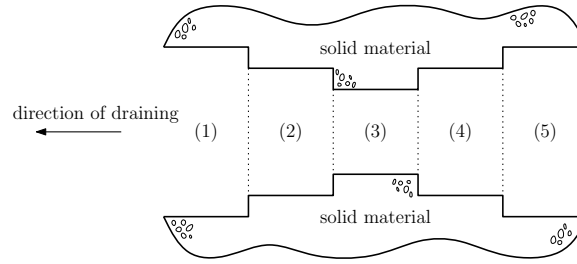


Figure 3.28: 2-D representation of a pore with different throat diameters

the soil to a given water content. Similarly, the effect of an exaggerated number of smaller pores in the micro region would be a reduction in the suction required to dry the soil to a given water content, so that the predicted SWRC would first overshoot and then undershoot measured data with reducing pore size as is seen in Figures 3.20 to 3.23. A method for correcting for trapped pores was put forward in Simms and Yanful (2001) and was used in Zhang and Li (2010) to predict the shape of the SWRC, making use of PSDs found for oven-dried material, although a significant improvement in the fit to the measured data was not seen. A robust method for correcting MIP-produced PSDs for trapped pores is a topic for future research.

3.4 Conclusion

The CCA model developed in this chapter offers a method for predicting a soil's SWRC directly from the PSD so that only one data source is required. This model offers several advantages over previous models for predicting the SWRC from the PSD:

- Particle shape is included in the prediction process. Particles are approximated as both spheres and cuboids depending on their size and particle surface areas are comparable to those of real particles;
- Soil double structure is included by splitting the PSD into macro and micro regions to represent the difference between macro and micropores;
- Capillary and adsorption effects are included through the use of liquid bridge and thin film equations respectively;
- Cavitation has been used to explain the drainage of macro and micropores and liquid bridge coalescence has been identified as a mechanism for pore filling, resulting in different wetting and drying suctions without the need for complicated angularity factors or separate definitions for radii of imbibition and drainage;
- A comparison with experimental data and predictions based on the work of Zhang and Li (2010) show that the CCA model more accurately predicts the SWRC in the macro region whilst providing an acceptable fit to measured data in the micro region.

The importance of considering changes in material void ratio when using PSDs to predict an SWRC have been discussed and identified as a mechanism by which predicted SWRCs differ from measured SWRCs. Trapped pores during MIP testing have also been suggested to be a cause of inaccuracies between measured and predicted data.

3.5 References

- Abdullah, W. S., Alshibli, K. A., Al-Zou'bi, M. S., 1999. Influence of pore water chemistry on the swelling behavior of compacted clays. *Applied Clay Science* 15 (5-6), 447–462.
- Ahmed, S., Lovell, C., Diamond, S., 1974. Pore sizes and strength of compacted clay. *ASCE J. Geotech Engng* 100(4), 407–425.
- Ahuja, L. R., Fiedler, F., Dunn, G. H., Benjamin, J. G., Garri-son, A., 1998. Changes in soil water retention curves due to tillage and natural reconsolidation. *Soil Science Society of America Journal* 62, 1228–1233.
- Akbour, R. A., Douch, J., Hamdani, M., Schmitz, P., Sep 2002. Transport of kaolinite colloids through quartz sand: Influence of humic acid, Ca^{2+} , and trace metals. *Journal of Colloid and Interface Science* 253 (1), 1–8.
- Baker, R., Frydman, S., 2009. Unsaturated soil mechanics: Critical review of physical foundations. *Engineering Geology* 106 (1-2), 26–39.
- Bolton, M., 1991. A guide to soil mechanics. M D & K Bolton.
- Brooks, R. H., Corey, A. T., 1964. Hydraulic properties of porous media. In: *Hydrology Paper No. 3*. Civil Engineering Dept., California State University, Fort Collins, Colorado.
- Butt, H.-J., 2008. Capillary forces: Influence of roughness and heterogeneity. *Langmuir* 24 (9), 4715–4721.
- Butt, H.-J., Kappl, M., 2009. Normal capillary forces. *Advances in Colloid and Interface Science* 146 (1-2), 48–60.
- Choquette, M., Brub, M.-A., Locat, J., 1987. Mineralogical and microtextural changes associated with lime stabilization of marine clays from eastern Canada. *Applied Clay Science* 2 (3), 215–232.
- Collins, K., McGown, A., 1974. Form and function of micro-fabric features in a variety of natural soils. *Géotechnique* 24 (2), 223–254.
- Cosenza, P., Tabbagh, A., 2004. Electromagnetic determination of clay water content: role of the microporosity. *Applied Clay Science* 26, 21–36.
- Croney, D., Coleman, J. D., Black, W. P. M., 1958. Movement and distribution of water in soil in relation to highway design and performance. Highway Research Board Special Report 40, 226–252.
- Delage, P., 2009. Discussion: Compaction behaviour of clay. *Géotechnique* 59 (1), 75–77.
- Delage, P., 2010. A microstructure approach to the sensitivity and compressibility of some eastern Canada sensitive clays. *Géotechnique* 60 (5), 353–368.
- Delage, P., Audiguier, M., Cui, Y. J., Howat, D., 1996. Microstructure of a compacted silt. *Canadian Geotechnical Journal* 33, 150–158.
- Delage, P., Marcial, D., Cui, Y. J., Ruiz, X., 2006. Ageing effects in a compacted bentonite: a microstructure approach. *Géotechnique* 56 (5), 291–304.
- Dexter, A. R., 1997. Physical properties of tilled soils. *Soil and Tillage Research* 43 (1-2), 41–63.
- Diamond, S., 1970. Pore size distribution in clays. *Clays and Clay Minerals* 18, 7–23.
- d'Souzae, J. I., 2008. Mercury intrusion porosimetry: A tool for pharmaceutical particle characterisation. *Pharmainfo.net Latest Reviews* 6 (2).
- Fredlund, D., Rahardjo, H., 1993. *Soil Mechanics for Unsaturated Soils*. John Wiley & Sons Inc., New York (USA).
- Fredlund, D. G., 2006. Unsaturated soil mechanics in engineering practice. *Journal of Geotechnical and Geoenvironmental Engineering* 132 (3), 286–321.
- Fredlund, D. G., Xing, A., 1994. Equations for the soil-water characteristic curve. *Canadian Geotechnical Journal* 31, 521–532.
- Fredlund, M., Gitirana, G., 2011. Probabilistic methods applied to unsaturated numerical modeling. *Geotechnical and Geological Engineering* 29, 217–223.
- Frydman, S., Baker, R., 2009. Theoretical soil-water characteristic curves based on adsorption, cavitation, and a double porosity model. *Int. J. Geomech.* 9 (6), 250–257.
- Gallipoli, D., Gens, A., Sharma, R., Vaunat, J., 2003. An elasto-plastic model for unsaturated soil incorporating the effects of suction and degree of saturation on mechanical behaviour. *Géotechnique* 53 (1), 123–135.
- Gens, A., Alonso, E. E., 1992. A framework for the behaviour of unsaturated expansive clays. *Canadian Geotechnical Journal* 29, 1013–1032.
- Grof, Z., Lawrence, C. J., Stepnek, F., 2008. The strength of liquid bridges in random granular materials. *Journal of Colloid and Interface Science* 319 (1), 182–192.
- Haines, W. B., 1930. Studies in the physical properties of soil. v. the hysteresis effect in capillary properties, and the modes of moisture distribution associated therewith. *The Journal of Agricultural Science* 20 (01), 97–116.
- Hajnos, M., Lipiec, J., Swieboda, R., Sokolowska, Z., Witkowska-Walczak, B., 2006. Complete characterization of pore size distribution of tilled and orchard soil using water retention curve, mercury porosimetry, nitrogen adsorption, and water desorption methods. *Geoderma* 135, 307–314, doi: DOI: 10.1016/j.geoderma.2006.01.010.
- Hattab, M., Fleureau, J.-M., 2010. Experimental study of kaolin particle orientation mechanism. *Géotechnique* 60 (5), 323–331.

- Heath, A. C., Pestana, J. M., Harvey, J. T., Bejerano, M. O., 2004. Normalizing behavior of unsaturated granular pavement materials. *Journal of Geotechnical and Geoenvironmental Engineering* 130, 896–904.
- Hillel, D., 2004. *Fundamentals of Soil Physics*. Academic Press, Inc., London (UK).
- Huang, H.-C., Tan, Y.-C., Liu, C.-W., Chen, C.-H., 2005. A novel hysteresis model in unsaturated soil. *Hydrological Processes* 19, 1653–1665.
- Iwamatsu, M., Horii, K., 1996. Capillary condensation and adhesion of two wetter surfaces. *Journal of Colloid and Interface Science* 182 (2), 400–406.
- Jaquin, P. A., Augarde, C. E., Gallipoli, D., Toll, D. G., 2009. The strength of unstabilised rammed earth materials. *Géotechnique* 59 (5), 487–490.
- Jotisankasa, A., Ridley, A., Coop, M., 2007. Collapse behavior of compacted silty clay in suction-monitored oedometer apparatus. *Journal of Geotechnical and Geoenvironmental Engineering* 133 (7), 867–877.
- Kaufmann, J., 2009. Characterization of pore space of cement-based materials by combined mercury and woods metal intrusion. *Mercury* 216 (1), 209–216.
- Khaleel, R., Relyea, J. F., Conca, J. L., 1995. Evaluation of van genuchten-mualem relationships to estimate unsaturated hydraulic conductivity at low water contents. *Water Resour. Res.* 31, 2659–2668.
- Klute, A. (Ed.), 1986. *Methods of Soil Analysis, Part 1. Physical and Mineralogical Methods*. ASA-SSSA Inc., Madison, Wisconsin, USA.
- Kutilek, M., Jendele, L., Krejca, M., 2009. Comparison of empirical, semi-empirical and physically based models of soil hydraulic functions derived for bi-modal soils. *Journal of Contaminant Hydrology* 104 (1-4), 84–89.
- Likos, W. J., Jul 13-17 2009. Pore-scale model for water retention in unsaturated sand. *Amer Inst Physics, Golden, CO*, pp. 907–910.
- Lourenço, S. D. N., Gallipoli, D., Augarde, C. E., Toll, D., Evans, F., Medero, G., July 2008a. Studies of unsaturated soils by environmental scanning electron microscope using dynamic mode. In: Toll, D. G., Augarde, C. E., Gallipoli, D., Wheeler, S. J. (Eds.), *Unsaturated Soils: Advances in Geoenvironmental Engineering*. Proceedings of the 1st European Conference. First European Conference on Unsaturated Soils, Taylor & Francis.
- Lourenço, S. D. N., Gallipoli, D., Toll, D. G., Augarde, C. E., Evans, F. D., September 2010. Advances in tensiometer-based suction control systems. In: Alonso, E., Gens, A. (Eds.), *Unsaturated Soils. Fifth International Conference on Unsaturated Soils*, CRC Press, pp. 695–700.
- Lourenço, S. D. N., Toll, D. G., Augarde, C. E., Gallipoli, D., Congreve, A., Smart, T., Evans, F. D., July 2008b. Observations of unsaturated soils by environmental scanning electron microscopy in dynamic mode. In: Toll, D. G., Augarde, C. E., Gallipoli, D., Wheeler, S. J. (Eds.), *Unsaturated Soils: Advances in Geo-Engineering*. First European Conference on Unsaturated Soils, CRC Press.
- Lu, N., Likos, W. J., 2004. *Unsaturated Soil Mechanics*. John Wiley & Sons, Inc., New Jersey (USA).
- Maris, H., Balibar, S., 2000. Negative pressures and cavitation in liquid helium. *Physics Today* 53 (2), 29–34.
- Mayer, R. P., Stowe, R. A., 2006. Packed uniform sphere model for solids: Interstitial access opening sizes and pressure deficiencies for wetting liquids with comparison to reported experimental results. *Journal of Colloid and Interface Science* 294 (1), 139–150.
- Megias-Alguacil, D., Gauckler, L. J., 2010. Analysis of the capillary forces between two small solid spheres binded by a convex liquid bridge. *Powder Technology* 198 (2), 211–218.
- Millington, R. J., Quirk, J. P., 1961. Permeability of porous media. *Nature* 183, 387–388.
- Monroy, R., Zdravkovic, L., Ridley, A., 2010. Evolution of microstructure in compacted London clay during wetting and loading. *Géotechnique* 60, 105–199.
- Mu, F., Su, X., Dec. 2007. Analysis of liquid bridge between spherical particles. *China Particuology* 5 (6), 420–424.
- Mualem, Y., 1976. A new model for predicting the hydraulic conductivity of unsaturated porous media. *Water Resour. Res.* 12, –.
- Nowamooz, H., Chazallon, C., 2011. Finite element modelling of a rammed earth wall. *Construction and Building Materials* 25 (4), 2112–2121.
- Nowamooz, H., Masrouri, F., 2010. Relationships between soil fabric and suction cycles in compacted swelling soils. *Engineering Geology* 114 (3-4), 444–455.
- Nuth, M., Laloui, L., 2008. Advances in modelling hysteretic water retention curve in deformable soils. *Computers and Geotechnics* 35 (6), 835–844.
- Or, D., Tuller, M., 1999. Liquid retention and interfacial area in variably saturated porous media: Upscaling from single-pore to sample-scale model. *Water Resour. Res.* 35, 3591–3605.
- Or, D., Tuller, M., 2002. Cavitation during desaturation of porous media under tension. *Water Resour. Res.* 38, 19–1–19–4.
- Or, D., Tuller, M., 2003. Capillarity. In: Hillel, D. (Ed.), *Encyclopedia of Soils in the Environment*. Vol. 1. Elsevier Ltd., Oxford, U.K., pp. 155–163.

- Ouhadi, V. R., Yong, R. N., 2008. Ettringite formation and behaviour in clayey soils. *Applied Clay Science* 42 (1-2), 258–265.
- Park, S.-S., 2010. Effect of wetting on unconfined compressive strength of cemented sands. *J. Geotech. and Geoenviron. Engrg.* 136 (12), 1713–1720.
- Pedroso, D. M., Williams, D. J., 2011. Automatic calibration of soil-water characteristic curves using genetic algorithms. *Computers and Geotechnics* 38 (3), 330–340.
- Pietsch, W. B., 1968. Tensile strength of granular materials. *Nature* 217, 736–737.
- Pitois, O., Moucheront, P., Chateau, X., 2000. Liquid bridge between two moving spheres: An experimental study of viscosity effects. *Journal of Colloid and Interface Science* 231 (1), 26–31.
- Pitois, O., Moucheront, P., Chateau, X., 2001. Rupture energy of a pendular liquid bridge. *The European Physical Journal B - Condensed Matter and Complex Systems* 23 (1), 79–86.
- Powrie, W., 2008. *Soil Mechanics: Concepts and Applications*, 2nd Edition. Spon Press.
- Rodriguez, R., Candela, L., Lloret, A., Nov 2003. Experimental system for studying the hydromechanical behavior of porous media. *Soil Sci Soc Amer*, Valladolid, Spain, pp. 345–353.
- Romero, E., Gens, A., Lloret, A., 1999. Water permeability, water retention and microstructure of unsaturated compacted boom clay. *Engineering Geology* 54 (1-2), 117–127.
- Russell, A. R., 2010. Water retention characteristics of soils with double porosity. *European Journal of Soil Science* 61 (3), 412–424.
- Salem, H. S., Chilingarian, G. V., 1999. Determination of specific surface area and mean grain size from well-log data and their influence on the physical behavior of offshore reservoirs. *Journal of Petroleum Science and Engineering* 22 (4), 241–252.
- Simms, P. H., Yanful, E. K., 2001. Measurement and estimation of pore shrinkage and pore measurement in a clayey till during soil-water characteristic curve tests. *Canadian Geotechnical Journal* 38, 741–754.
- Simms, P. H., Yanful, E. K., 2004. Estimation of soil-water characteristic curve of clayey till using measured pore-size distributions. *Journal of Environmental Engineering-Asce* 130 (8), 847–854.
- Stevens, N., Ralston, J., Sedev, R., 2009. The uniform capillary model for packed beds and particle wettability. *Journal of Colloid and Interface Science* 337 (1), 162–169.
- Tamagnini, R., Apr 2004. An extended cam-clay model for unsaturated soils with hydraulic hysteresis. *Géotechnique* 54 (3), 223–228.
- Tang, A.-M. e. a., 2005. Controlling suction by the vapour equilibrium technique at different temperatures and its application in determining the water retention properties of mx80 clay. *Canadian Geotechnical Journal* 42, 287–296.
- Tarantino, A., 2009. A water retention model for deformable soils. *Géotechnique* 59 (9), 751–762.
- Tarantino, A., 2010. Unsaturated soils: compaction versus reconstituted states. In: Alonso, E., Gens, A. (Eds.), *Unsaturated soils. Fifth International Conference on Unsaturated Soils*, CRC Press, pp. 113–136.
- Tarantino, A., De Col, E., 2008. Compaction behaviour of clay. *Géotechnique* 58 (3), 199–213.
- Tarantino, A., Gallipoli, D., Augarde, C. E., de Gennaro, V., Gomez, R., Laloui, L., Mancuso, C., el Mountasir, G., Munoz, J. J., Pereira, J., Peron, H., Pisoni, G., Romero, E., Raveendraraj, A., Rojas, J. C., Toll, D. G., Tombolato, S., Wheeler, S., 2011. Benchmark of experimental techniques for measuring and controlling suction. *Géotechnique* 61 (4), 303–312.
- Toll, D. G., Mar 1990. A framework for unsaturated soil behaviour. *Géotechnique* 40 (1), 31–44.
- Tuller, M., Or, D., 2004. Retention of water in soil and the soil water characteristic curve. In: Hillel, D. (Ed.), *Encyclopedia of Soils in the Environment*. Vol. 4. Elsevier Ltd., Oxford, U.K., pp. 278–289.
- Tuller, M., Or, D., Dudley, L. M., 1999. Adsorption and capillary condensation in porous media: Liquid retention and interfacial configurations in angular pores. *Water Resour. Res.* 35 (7), 1949–1964.
- Urso, M. E. D., Lawrence, C. J., Adams, M. J., 2002. A two-dimensional study of the rupture of funicular liquid bridges. *Chemical Engineering Science* 57 (4), 677–692.
- van Genuchten, M. T., 1980. A closed-form equation for predicting the hydraulic conductivity of unsaturated soils. *Soil Sci Soc Am J* 44 (5), 892–898.
- van Genuchten, M. T., Nielsen, D. R., 1985. On describing and predicting the hydraulic properties of unsaturated soil. *Annals of Geophysics* 3, 615–628.
- Vanapalli, S., Fredlund, D., 1997. Interpretation of undrained shear strength of unsaturated soils in terms of stress state variables. In: *3rd Brazilian Symposium on Unsaturated Soils*. pp. 278–289.
- Vanapalli, S. K., Fredlund, D. G., Pufahl, D. E., 1999. The influence of soil structure and stress history on the soil-water characteristics of a compacted till. *Géotechnique* 49 (2), 143–159.
- Wheeler, S. J., Sharma, R. S., Buisson, M. S. R., 2003. Coupling of hydraulic hysteresis and stress-strain behaviour in unsaturated soils. *Géotechnique* 53 (1), 41–54.

- Willis, K. L., Abell, A. B., Lange, D. A., 1998. Image-based characterization of cement pore structure using wood's metal intrusion. *Cement and Concrete Research* 28 (12), 1695–1705.
- Yong, R. N., Ouhadi, V. R., 2007. Experimental study on instability of bases on natural and lime/cement-stabilized clayey soils. *Applied Clay Science* 35 (3-4), 238–249.
- Young, F. R., 1989. *Cavitation*. McGraw-Hill Book Company (UK) Ltd.
- Zhang, L. M., Li, X., 2010. Microporosity structure of coarse granular soils. *J. Geotech. and Geoenviron. Engrg.* 136 (10), 1425–1436.
-

Chapter 4

The impact of sample production techniques on material structure

4.1 Chapter introduction

In the previous chapter, a method for relating the soil pore size distribution to the soil water retention curve was presented in order to demonstrate the role played by the material micro- and macrostructures in determining its behaviour. The following chapters build on this finding through several experimental investigations in order to explain the behaviour of rammed earth (RE) samples in terms of its micro- and macrostructures and to determine how these can be used to create desirable RE properties.

A comparison between laboratory- and field-compacted samples was made in Jommi and Sciotti (2003) and it was shown that the material had different material structures depending on the preparation method; following from the work presented in Chapter 3, it can therefore be surmised that the behaviour of the material is also affected by the compaction method. Therefore, this chapter investigates the effects of the processes used in the preparation of RE samples, based on those recommended by Hall and Djerbib (2004), on the final structure of the material, in order to determine whether samples produced in the laboratory are representative of material manufactured during the construction process. Two processes of interest have been identified: the mixing of dry granular materials during material preparation; and the compaction of wet RE into formwork.

4.2 Mixing of dry granular materials

4.2.1 Introduction

Material possessing a known particle grading curve can be prepared by combining dry constituent raw materials, as proposed by Hall and Djerbib (2004). Recommended limits on RE material particle grading curves, which are intended to produce materials with acceptable compressive strengths, are given in Houben and Guillaud (1996), so that the subsequent relative amounts of raw materials can be selected. RE mixes used in subsequent chapters are compared to these recommended limits by means of reference. As many natural soils do not fall within these boundaries, additional particle size fractions, for example silty-clay, need to be added in order to create a more suitable mix. Most soils used in RE construction, therefore, are more appropriately referred to as *soil mixes*, as the former suggests a natural, rather than a manufactured, material. However, although this production process results in a controlled particle size distribution, it might also impart some form of undesired structure on the material (Srebro and Levine,

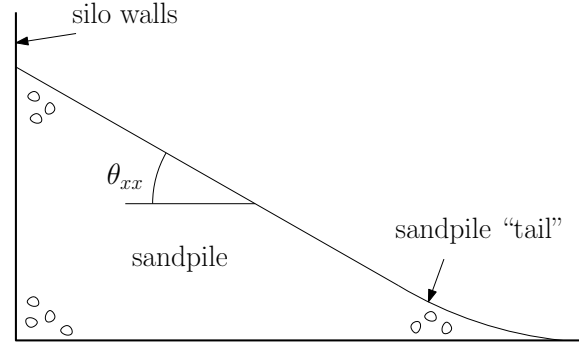


Figure 4.1: Typical shape of a sandpile. θ_{xx} is the repose angle of species x .

2003; Santamarina and Cho, 2004). In this investigation, the formation of patterns in dry granular mixes on pouring is analysed in order to determine whether similar phenomena can occur during the production of dry RE soil mixes.

4.2.2 Sandpile formation and phenomena of granular flow

4.2.2.1 Sandpile formation

In this chapter, “silo” is used to describe a cuboidal tank with vertical sides and a horizontal base which is open at the top. If a sand of species x is poured into a silo, then a characteristically-shaped sandpile will form as shown in Figure 4.1. The central, linear section of the slope lies at θ_{xx} , the repose angle for species x (which is equal to the friction angle if the sand is a Coulombic material, (Bolton, 1991)), whilst the tail of the slope adopts an exponentially-decaying profile due to particles losing energy as they strike the silo base (Grasselli and Herrmann, 1997, 1999; Herrmann, 1999, 2002; Haderler and Kuttler, 1999). It has been shown experimentally that the shape of the sandpile tail is affected by the particle drop height and flow rate; the greater the drop height and flow rate, the greater the particle energy and so the longer it takes for the energy to dissipate through collisions (Grasselli and Herrmann, 1998, 1999).

4.2.2.2 Segregation and stratification

Segregation is the phenomenon whereby a mixture of two dry granular materials spontaneously separate into two distinct regions on pouring. Such a pattern is shown in Figure 4.2(a). Segregation can be understood as the conflict between two competing effects: size segregation is where larger grains can roll more easily over smaller grains than smaller over larger, leading to a segregated pile with small grains at the top and large grains at the base; and shape segregation, where grains are of equal size but different shapes resulting in the rougher grains being at the top of the pile and the smoother at the bottom (Goyal and Tomassone, 2006).

If the larger grains are rougher than the smaller, therefore, the above two effects will compete, leading to *stratification*, where alternating layers of small and large particles are formed parallel to the surface of the sand pile with the smaller particles underlying the larger in a given layer (Cizeau et al., 1999). An example of a stratification pattern is shown in Figure 4.2(b). Stratification has also been identified in mixtures of more than two species, where the parallel layers are formed with the smallest (which are necessarily also the smoothest) particles on the bottom of the layer, with progressively rougher particles lying on top (Cizeau et al., 1999). As can be seen in Figure 4.2(b), an initial segregation regime exists in the bottom corner of the sandpile prior to the stratification zone; only size segregation is active in this initial zone, so that the larger particles are at the base of the pile (Cizeau et al., 1999).

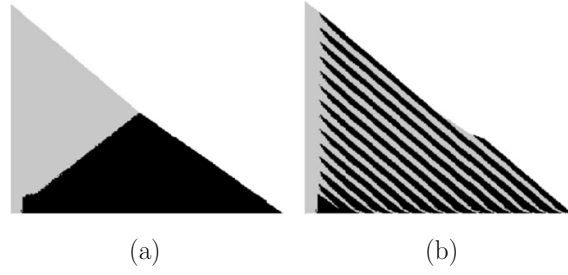


Figure 4.2: (a) Results for spontaneous stratification of a bidisperse mixture of smaller smooth grains (light) and larger rougher grains (dark). (b) Results for a segregating mixture of smaller rougher (light) grains and larger, smoother grains (dark) (Cizeau et al., 1999)

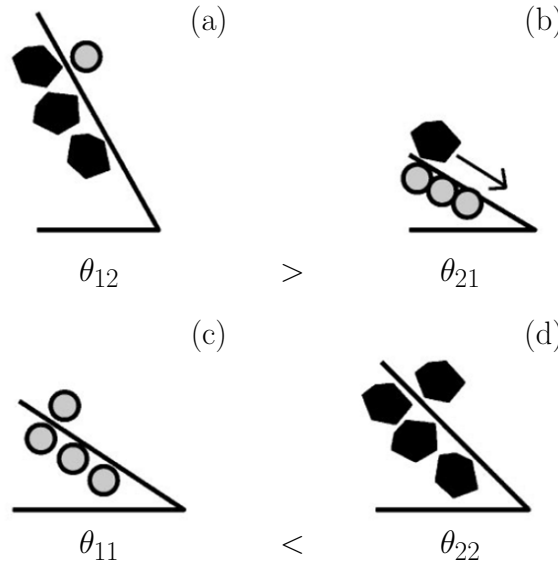


Figure 4.3: The generalised repose angles for: (a) small, smooth particle rolling down a surface of rough particles, θ_{12} ; (b) rough, large particle rolling down a surface of small, smooth particles, θ_{21} ; (c) small, smooth particle rolling down a slope of the same species, θ_{11} ; (d) large, rough particle rolling down a slope of the same species, θ_{22} (Cizeau et al., 1999)

4.2.2.3 Effect of repose angle

To understand stratification, a definition of the repose angles between the two sand species is required, showing the interactions between the individual grains (Cizeau et al., 1999). There are four generalised angles of repose for a combination of two granular species, as shown in Figure 4.3. In this formalism, the smaller species is denoted as “1” and the larger as “2”. ϕ'_x is the friction angle of a single granular species, whilst θ_{xx} and θ_{xy} are the repose angles for single species or a combination of two species respectively, with species x rolling down a surface of species y . The need to define both ϕ'_x and θ_{xx} for a material is because ϕ'_x can be considered a material property whilst the repose angle is affected by external influences as will be discussed in the following sections.

It can be assumed that $\theta_{21} < \theta_{11} < \theta_{22} < \theta_{12}$ (Makse et al., 1998; Cizeau et al., 1999), as the repose angle for a small grain rolling down a slope of large grains must be larger than for the opposite case. By defining the repose angles in this manner, both size and shape segregation are included ($\theta_{11} < \theta_{22}$ is due to the shapes of the species, $\theta_{21} < \theta_{12}$ is due to the sizes) (Cizeau et al., 1999). According to Makse et al. (1997), the control parameter for the stratification-segregation transition is the difference between the friction angles of the pure species

$$\delta = \phi'_2 - \phi'_1. \quad (4.1)$$

If $\delta > 0$ then stratification will occur (Goyal and Tomassone, 2006), otherwise the species will segregate. In addition, if the sizes of the two species are almost equal then segregation will only be partial (“continuous segregation”, Herrmann (1999)).

4.2.2.4 Capture, percolation and amplification

Three main mechanisms are present in determining stratification: “capture”; “percolation”; and “amplification” (Makse et al., 1998; Samadani and Kudrolli, 2001). Both occur in the “rolling phase”, where grains are in motion during an avalanche.

Capture is the trapping of rolling grains on the surface of the sandpile. As such, it is the smaller grains that are mostly affected, as they are the most sensitive to surface fluctuations.

Percolation is the effect of small grains filtering through the larger grains in the rolling phase, provided that the rolling phase is “thick” (five grains deep or more), (Makse et al., 1998). A large size ratio (i.e. the difference between the size of the largest and smallest grains) is necessary in order for percolation to function; in this case, a size ratio of 1.5 is necessary, below which the size segregation effect is very weak and the instability leading to stratification is not possible (Makse et al., 1998).

Amplification is the process of static grains on the sandpile surface becoming part of the rolling phase due to particle collisions. Amplification processes are of negligible importance if percolation is present as the small-grained rolling sublayer is in contact with a mostly large-grained static surface layer (Makse et al., 1998). As a result, amplification is restricted to thin flow conditions. An effect of amplification is that stratification does not stop when $\delta = 0$, but at some critical value $\delta_c < 0$, as smaller grains can roll over larger ones without being captured. However, the stratification is much weaker than when $\delta > 0$ (Cizeau et al., 1999).

4.2.2.5 Mechanism of layer formation

The process of layer formation can be divided into three stages: the avalanche of grains down the slope and the size segregation in the rolling phase due to percolation; the formation of a “kink”; and the uphill motion of the kink, with the formation of the dual-stratification layer (Makse et al., 1998). This process is shown in Figure 4.4.

Prior to an avalanche forming, the surface of the sandpile comprises mostly larger grains. When an incoming mass of grains avalanches down the sandpile, the small grains are captured whilst the large grains reach the base of the pile so that the larger particles form the avalanche head. These larger particles form the initial stages of the kink. Further flow continues to “smooth” the sandpile surface (without affecting the slope angle) until the smaller particles reach the base of the sandpile. The small grains stop as they reach the kink due to their increased ease of capture, followed by the larger grains, resulting in the stratification pattern of a layer of small grains underlying a layer of large grains. The kink moves up the slope with a constant shape as more material is added, with the process repeating when the kink reaches the top of the sandpile. The wavelength of the stratification layers is proportional to the thickness of the rolling layer and so to the grain flow rate. However, if the flow rate is too great then the kink mechanism is overwhelmed and the stratification pattern is replaced with mixing or weak segregation (Makse et al., 1998).

In a wide silo an avalanche might not contain sufficient mass to form a continuous layer reaching the silo base; instead, the avalanche halts partway down the sandpile, forming a “trapped kink”, with a coarse wedge at its head and the characteristic stratification pattern behind it. The upslope kink mechanism reinitiates once an avalanche reaches the silo base (Shimokawa and Ohta, 2007).

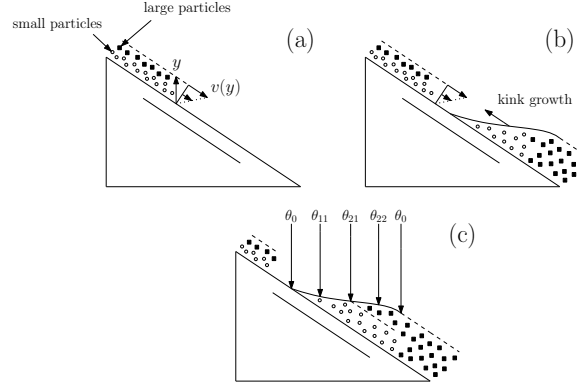


Figure 4.4: Diagrammatic process of kink formation and propagation (after Makse et al. (1998)): (a) initial avalanche at velocity $v(y)$; (b) formation of the kink; (c) profile and propagation of the kink up the sandpile (slope angle θ_0) with kink angles θ_{11} , θ_{21} and θ_{22}

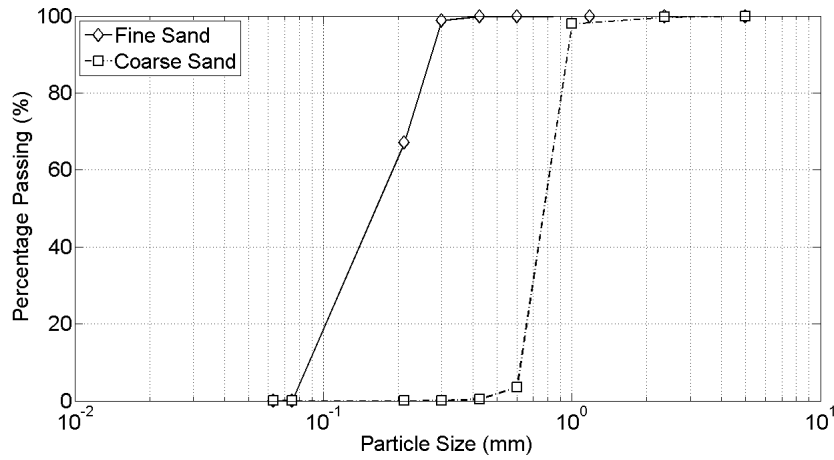


Figure 4.5: Particle grading curves for fine and coarse sand

4.2.3 Material selection and preparation

This section describes experiments that were conducted in order to determine whether segregation or stratification phenomena are introduced on the creation of dry RE soil mixes, which might be misrepresentative of natural RE-suitable soils.

Fine (average particle size $200\mu\text{m}$, $\phi'_{peak} = 26.0^\circ$, $\phi'_{ult} = 24.6^\circ$, $\theta_{11} = 33.1^\circ$) and coarse sand (average particle size $800\mu\text{m}$, $\phi'_{peak} = \phi'_{ult} = 35.1^\circ$, $\theta_{22} = 32.4^\circ$) of particle gradings given in Figure 4.5 were selected as both being suitable for inclusion in an RE mix and for stratification investigations ($\delta > 0$ using Equation 4.1 and near-uniform grading, increasing the likelihood of segregation phenomena occurring). ϕ'_{peak} is the largest friction angle found using shear box testing, whilst ϕ'_{ult} is the ultimate (or residual) value. Repose angle values were determined experimentally using the repose angles of free piles of the single species (i.e. no edge effects were present).

Although RE soil mixes contain at least 20% silty clay by mass (Houben and Guillaud, 1996), clay particles were not included in this investigation as they would coat the sand particles and thereby mask any patterns formed. The effect of clay might be to reduce interparticle friction due to a smoothing of particle surface features and so a disruption of the segregation or stratification processes due to a reduced value of δ . The silo used in these experiments was of dimensions 898 mm long by 446 mm high by 77 mm wide and was cleaned with an anti-static cleaner prior to each pouring experiment.

A relationship for determining the required width of a silo in order to prevent the walls affecting the

slope repose angle is given in Grasselli and Herrmann (1997) as

$$\theta(d) = \theta_{\infty} \left(1 + e^{\frac{-d}{d^*}} \right) \quad (4.2)$$

where d is the silo width and d^* is the “characteristic length” which is a function of the particle size and is the distance over which the confining walls have an effect on the angle of repose. It should be noted that Equation 4.2 originally appeared in Grasselli and Herrmann (1997) with an error (the second term in the bracketed expression was subtracted instead of added as above). Using results presented in Grasselli and Herrmann (1997) and assuming a linear relationship between d^* and average particle size, $d^* \approx 27$ mm for coarse sand and 10 mm for fine sand, suggesting that the repose angles found using the above-mentioned silo are free of wall effects.

As well as sand and silty-clay it is recommended that RE soil mixes contain at least 10% gravel by mass (Houben and Guillaud, 1996). Gravel was sieved to contain particles smaller than 10 mm to reduce the influence of large particles on structural behaviour (Hall and Djerbib, 2004); after sieving, the gravel investigated had an average particle size of roughly 6 mm, corresponding to $d^* = 175$ mm. It was therefore decided not to include gravel in the testing as the silo size (> 350 mm) and amount of material required were deemed unrealistic.

4.2.4 Results and discussion

4.2.4.1 Effect of pouring direction

Results of pouring from several directions using a constant particle flow rate (manually controlled using a large scoop) were compared in order to determine whether the direction of pouring influences the resulting segregation or stratification patterns. The pouring directions (PDs) used are shown in Figure 4.6 and the results in Figure 4.7. It can be seen that the stratification pattern initiates much closer to the silo wall for PD1 than for PD2 (Figure 4.7 (a) and (b)); this is because the initial slope can form much closer to the silo corner for PD1. It can also be seen that the initial pattern arising from PD2 is rounded; this is because of the initial pile not being close to the wall. As additional grains fill the gap between the initial pile and the wall, the stratification pattern becomes similar to that arising from PD1. Tests were conducted using PDs 4 and 5 to determine whether the shape of the initial pile influenced the stratification pattern (Figure 4.7 (c) and (d)). The general patterns obtained from PDs 4 and 5 can be described as the formation of an initial pile, the tip of which moves towards the grain source as the sandpile height increases due to the non-vertical particle flow arising from the use of a scoop. The stratification patterns are very similar (but mirrored) for both PDs, as would be expected. The final repose angle for all of the tests conducted was $32.2^\circ \pm 0.8^\circ$, i.e. very similar to the average repose (32.8°) and friction angles (29.9°) for the two species (although the friction angles for the two species should not strictly be combined in this manner as it assumes that there are no additional species interaction effects). The similarity between the average single-species and combined-species repose angles suggests that edge effects were not significant, supporting the linear approximation for determining characteristic lengths discussed in Section 4.2.3.

Variations in the stratification pattern with height are due to changes in the particle drop heights. As the drop height reduces, the inclination of the sandpile should approach the combined repose angle of the two species and the tail should shrink as the initial energy of the particles reduces, as seen in Figure 4.7 (a) and (b) (Grasselli and Herrmann, 1998, 1999). Results in Figure 4.7 also show that both stratification and segregation are present; this is due to the non-uniform particle sizes of the two species (i.e. for some particle combinations a size ratio of > 1.5 is not possible) and reducing particle energy as particles near the base of the sandpile after rolling. Therefore, although the average particle sizes and

friction angles suggest that stratification should occur, results resemble a combination of patterns arising in the “continuous segregation” and “stratification” regions of Figure 3 of Herrmann (1999), which is reproduced in Figure 4.8.

4.2.4.2 Effect of particle flow rate

It was found that segregation phenomena occurred on the pre-mixing of the two sands prior to filling the scoop, due to the formation of loose piles of material during the passage of the mixing paddle, so that material being added to the scoop was also not uniformly mixed. Furthermore, material left the scoop via an avalanche mechanism as it was tilted, suggesting that segregation occurred in the scoop prior to material being introduced to the silo. This also made control of the flow rate difficult. The scoop was therefore substituted for a mechanical funnel in order to reduce the effect of these segregation effects on the resulting sandpile patterns. The mechanical funnel also significantly improved control over the material flow rate.

Flow rates of $3.3 \times 10^{-2} \text{ ls}^{-1}$ and $6.4 \times 10^{-3} \text{ ls}^{-1}$, corresponding to the funnel being fully- and half-open respectively, were used to determine the effect of flow rate on the stratification pattern using PDs 3 and 6, as shown in Figure 4.6. Results are shown in Figure 4.9. The stratification pattern initiates much earlier (i.e. deeper) in the sandpile for both of the tested flow rates than for those sandpiles formed using manual pouring; this is likely due to an increased flow rate, combined with the vertical pouring direction, forming a steeper cone on impacting the silo base which immediately initiates the kink/trapped kink stratification mechanisms. The depth of the fine layers reduces with increasing flow rate due to an overwhelming of the percolation mechanism; the rolling layer is thicker and so fewer fine particles can percolate through successfully. This suggests that, with a sufficient flow rate, segregation of the material will no longer occur: this is an observation also made by Makse et al. (1998). The resulting repose angles were $31.6^\circ \pm 0.3^\circ$ for $3.3 \times 10^{-2} \text{ ls}^{-1}$ and $32.0^\circ \pm 0.7^\circ$ for $6.4 \times 10^{-3} \text{ ls}^{-1}$. As the error bands for each flow rate overlap, it is not possible to determine whether the flow rate affected the combined repose angle, however results from Grasselli and Herrmann (1998, 1999) and the general similarity of all repose angles found during this investigation suggest that flow rate does not affect the repose angle. Again, Figure 4.9 shows that both stratification and segregation are present in the sandpile; this is also assumed to be due to the non-uniform particle sizes of the two species.

Stratification on the emptying of a large silo was investigated in Samadani et al. (1999). To test whether stratification was occurring in the funnel (and hence a structure being imparted to the material prior to the formation of the sandpile) the material in the funnel was allowed to drain entirely and sandpile

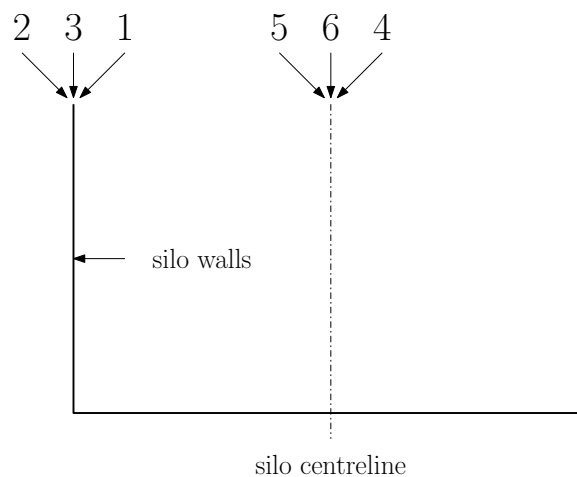


Figure 4.6: Silo pouring directions

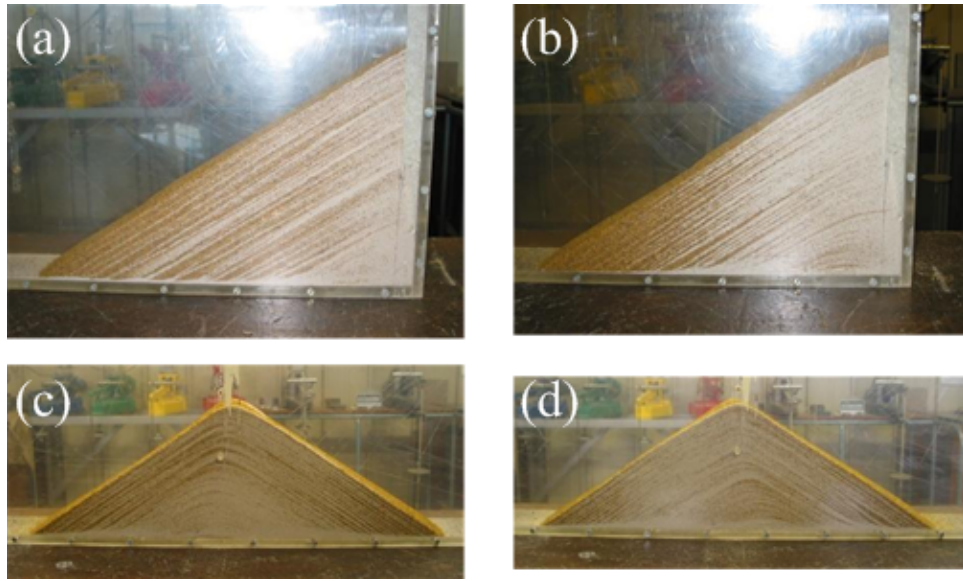


Figure 4.7: (a)-(d) Stratification results for PDs 1, 2, 4 and 5 respectively (all using manual pouring)

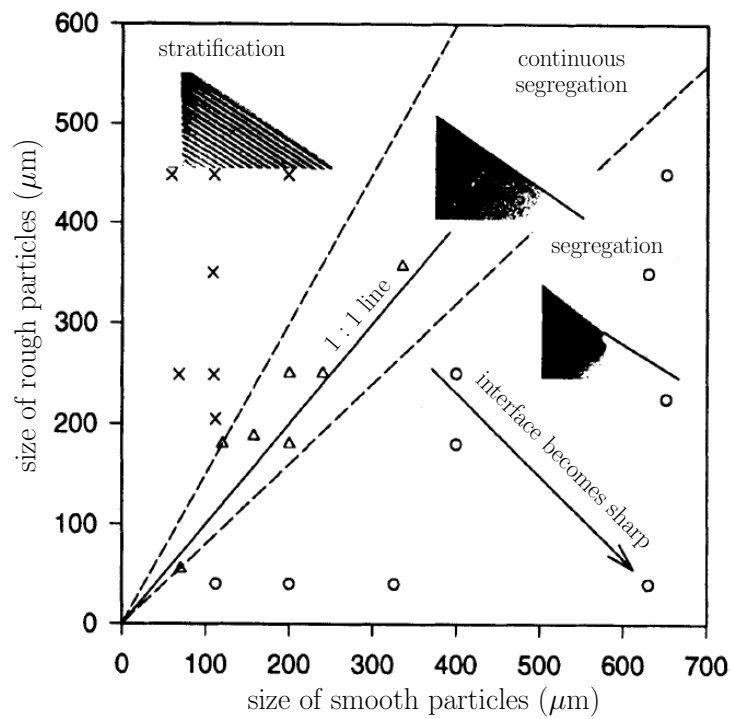


Figure 4.8: Experimentally observed patterns for a mixture of dark sand (rough particles) and glass spheres (smooth particles). Classification of “stratification”, “continuous segregation” or “segregation” determined by observation. Reproduced from (Herrmann, 1999).

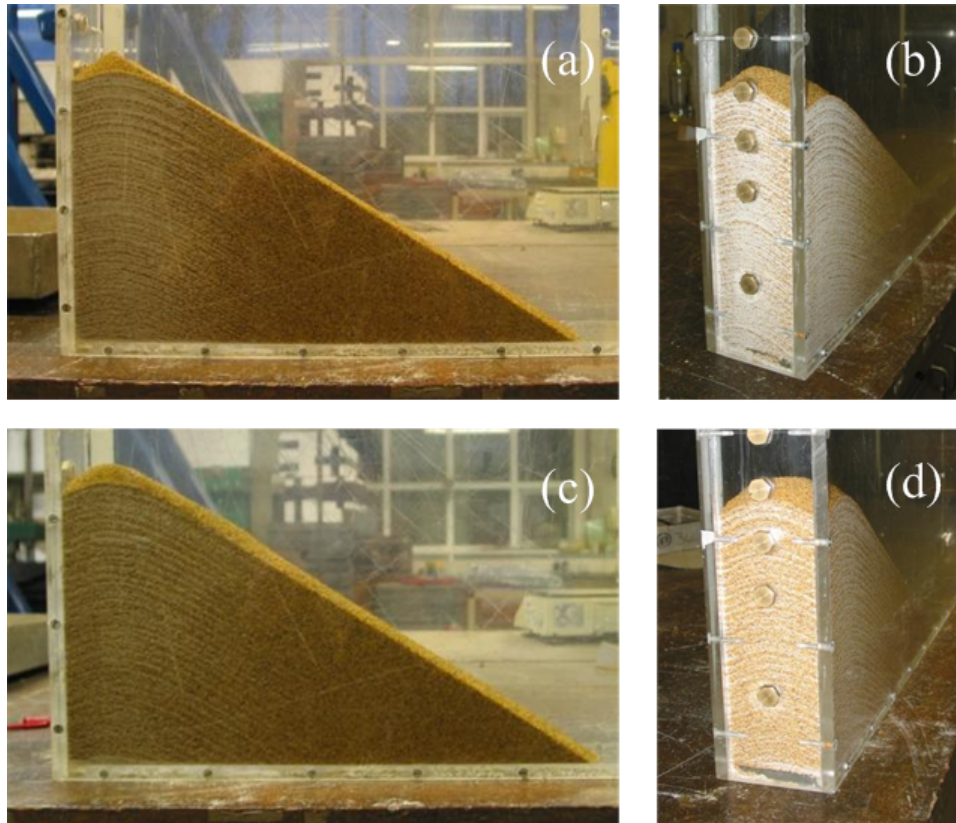


Figure 4.9: (a)-(b) Stratification pattern for low flow rate; (c)-(d) Stratification pattern for high flow rate

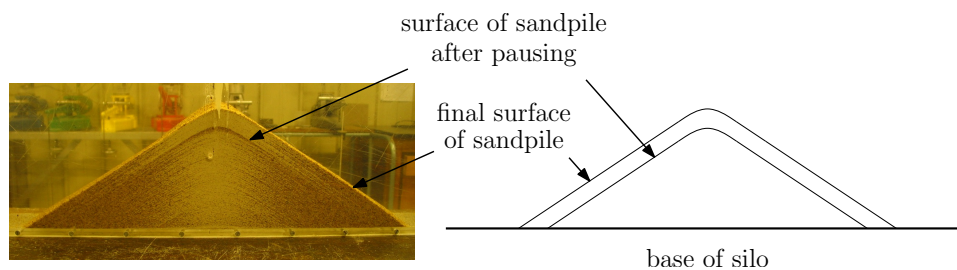


Figure 4.10: The formation of a coarse band due to a pause in material deposition

formation cease, before being reinitiated. The resulting stratification patterns given in Figure 4.10 clearly show a band of coarse material delineating where the flow ceased and restarted, suggesting that stratification does occur within the funnel. To avoid this, material was continually added to the funnel until the end of each test. Therefore, results show that a layered structure will form on the pouring of a mixture of two granular materials, so that these layered structures might be present in dry RE soil mixes prior to wetting.

4.2.5 Conclusions

The experimental work described above provides some insight into the mechanisms present in structure formation when mixing and pouring dry granular soil mixtures, and several general observations can be made:

- It has been determined that neither the flow rate nor the pouring direction influences the sandpile repose angle, the former supporting results found in Grasselli and Herrmann (1998), Grasselli and Herrmann (1999) and Ottino and Khakhar (2001).

- The presence of both segregation and stratification observed at the end of all of the tests suggests that a simple check on material friction angles in non-uniform particle size materials is not sufficient to determine whether segregation or stratification will occur. The final repose angle might be the average of the repose angles of the constituent species, however the use of the average friction angle should be avoided. The resulting patterns are different to the “continuous segregation” region given in Herrmann (1999), suggesting that a more gradual transition between segregation and stratification patterns exists.
- Segregation and stratification will occur on mixing if piles of material are allowed to form and within hoppers that are used to feed pouring experiments, confirming findings given in Samadani et al. (1999). Therefore, it is necessary to ensure that these hoppers do not empty before the sandpile is fully formed. The use of a high flow rate might prevent segregation phenomena from occurring, however this has not been investigated here.
- It has therefore been shown, given the above observations, that segregation phenomena can occur on the mixing of dry constituent materials during the preparation of an RE soil mix, creating a layered structure within the material prior to the addition of water. Caution should therefore be used during the preparation process so that segregated or stratified particle structures are not introduced into the material prior to wetting. The presence of a layered structure in the wetted material will affect both its strength and retention properties (by the formation of planes of weakness and preferred drainage paths respectively), thereby making it misrepresentative of a natural RE soil of the same particle grading.

4.3 Compaction of wet RE material

4.3.1 Introduction

An example RE structure is shown in Figure 1.3, showing the layered structure of the material. These layers are typical of RE structures and are similar to those that are formed when preparing RE samples; the behaviour and interaction of the material layers and their impact on the micro- and macrostructure of the final material is therefore of a key importance to understanding the properties of RE.

In this section, the deformations of a soil during compaction are investigated in order to ascertain how layers of RE interact with neighbouring layers and whether the layers present in RE samples prepared in the laboratory are representative of those seen in RE structures (Maniatidis and Walker, 2003; Jaquin et al., 2009). Firstly, a general discussion on the measurement of deformations in soils is given, following which an experimental procedure is developed to observe the deformations of two layers of soil, one above the other, on compaction. This method is designed to be flexible enough to be used for a number of potential geotechnical applications.

Understanding the processes and causes of deformations in soils is important in a number of geotechnical applications and phenomena, for example: compaction (Ajaz and Parry, 1975; Maniatidis and Walker, 2003; Tarantino and De Col, 2008; Tarantino, 2010); shearing (Jotisankasa et al., 2009); tunnelling (Take et al., 2005); installation of piles (White, 2002; Ni et al., 2010); and changes in water content (Wheeler and Sivakumar, 1995; Sivakumar et al., 2006; Gens, 2010). Such deformations are often difficult to monitor non-intrusively, although several advances have been made towards this goal. In the 1970s, Ajaz and Parry (1975) used lead shot target markers embedded in a regular pattern into the surface of a clay beam to evaluate bending strain in a compacting clay. The main drawback of the target marker method is, however, that the surface behaviour of the material is altered, so that the observed deformations may not be representative of the unaltered specimen. In Love et al. (1987), photographs

were used with small-scale laboratory models to track deformations of geogrid reinforcement placed at the base of a layer of granular fill on the surface of a soft clay. This technique relies on manually tracking areas of deforming material from one image to another and so is not suitable for large-scale or lengthy tests, where many images are required. More recently, Hall et al. (2010) used X-Ray micro Computed Tomography (XRCT) to observe deformations in a sand specimen subjected to a triaxial compression test. Although the use of XRCT offers a truly non-intrusive test, the size of samples currently able to be tested using XRCT machines are small (in the order of 20 cm^3), and tests are highly expensive, making parametric analyses unattractive. The XRCT process is described in Chapter 7, where it is used to observe changes in the macrostructure of RE under loading.

An analysis of existing techniques for deformation analysis shows that there is a need for techniques that can offer both quantitative and qualitative monitoring of deformations for use with medium-scale laboratory samples, of the order of thickness of RE walls. These techniques need to be inexpensive to run in order to encourage parametric testing.

4.3.2 Image analysis using particle image velocimetry

Image analysis techniques in geotechnical engineering are a family of methods which allow deformations of large specimens to be observed and recorded non-intrusively (Lee and Bassett, 2006; Zhang et al., 2006). Unobtrusive observation is necessary if results are to be reliable and comparable to the conditions experienced by the material *in situ*. Particle Image Velocimetry (“PIV”, also known as “digital image correlation” (Pan et al., 2009; Liu and Iskander, 2010)) is an example of a growing geotechnical image analysis technique whereby the motion of particles or collections of particles in a deforming medium are tracked by comparing digital images of the surface of that medium taken over several time intervals. PIV evolved from Laser Doppler Velocimetry (LDV), developed for use with fluid mechanics, where laser pulses are used to illuminate seed particles in a moving fluid at set time intervals. Assuming that the particles are travelling with the fluid, the fluid flow pattern at the location of the seed particle can then be evaluated (Adrian, 1986, 1991).

In PIV, a digital image of a deforming material is divided into “test patches” of pixels, and these are compared with corresponding (larger) “search patches” in a subsequent image after a known time interval. The location at which the highest correlation between the test and search patches is found indicates the displaced position of the patch so that full-field displacements and strains can then be determined (Adrian, 1991; White et al., 2003; Meguid et al., 2008; Pan et al., 2009) (Figure 4.11). The use of a patch of pixels creates a greater range of pixel intensities when compared to individual pixels which improves the match to that patch in the second image (White et al., 2003; Pan et al., 2009).

PIV has been extended for use with geotechnical materials and has been successful in measuring particle and pore size distributions and the movement and rotations of soil particles behind transparent viewing screens (Bhatia and Soliman, 1990; Guler et al., 1999; Zhang et al., 2006), in tracking large numbers of disc-shaped particles in order to approximate granular flow (Paikowsky and Xi, 2000) and in larger applications recording the displacements of a range of geogrid soil reinforcement products under tensile loading (Shinoda and Bathurst, 2004). In contrast to fluids or gases, intrusive markers often are not required for soils since the soil grains themselves serve as tracers (Slominski et al., 2007). Unlike in fluid mechanics, where each seed particle is interrogated individually (Adrian, 1986), the centroidal movement of the test patch between the two images is taken to be the average movement for all of the particles within that patch. Centroidal movement to sub-pixel accuracy can be calculated using iterative spatial domain cross-correlation or peak-finding fitting algorithms (to name two popular methods), with the former being the fastest and most accurate but the latter being the simplest (White, 2002; White et al., 2003; Zhang et al., 2006; Pan et al., 2009).

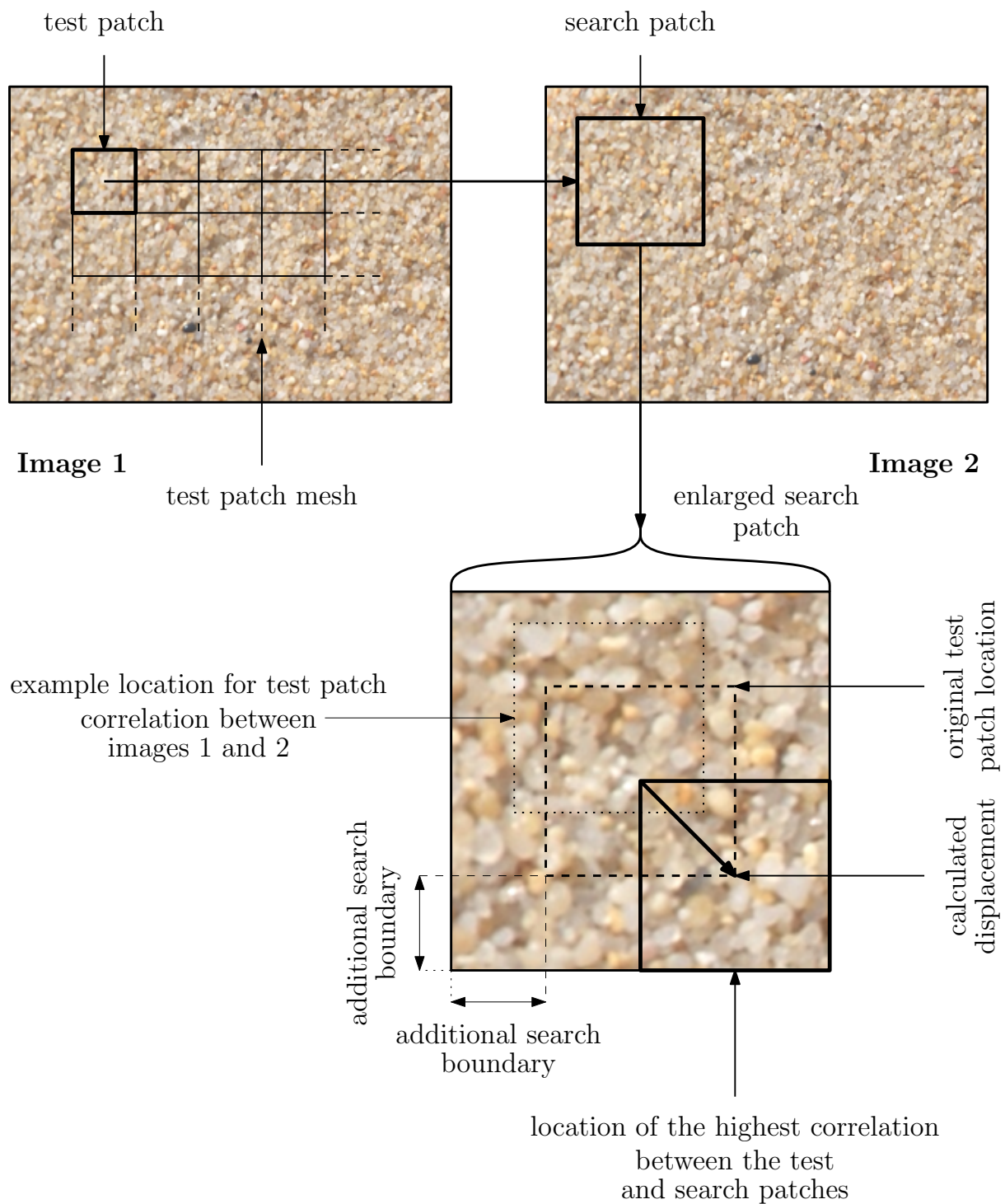


Figure 4.11: Image manipulation during PIV analysis, after White et al. (2003)

The accuracy of PIV depends on the quality of the image and the number of pixels used per test patch: the greater the number of pixels, the lower the error in finding the best match in the subsequent image but the longer the analysis time per patch (White, 2002; Pan et al., 2009). The disadvantage of using larger test patches is that fewer patches can be overlain on a given image, reducing the analysis resolution. Tracking accuracy is also affected by the magnitude of the displacements: if the displacement is an integer number of pixels, then the accuracy is increased, as less emphasis is placed on the fitting algorithm (White et al., 2003).

In fluid flow analyses, particles are tracked using an illuminated plane (the plane of the photograph). Particle displacements out-of-plane to the illuminated plane are therefore not recorded, which can lead to spurious results. A similar problem arises if particles move out-of-plane to the sampling window in geotechnical analyses: PIV is necessarily a 2-D procedure when used with geotechnical materials as no depth of field is provided, whereas it is likely that deformations occur in three dimensions unless tight control is maintained over the loading conditions. Three-dimensional “digital volume correlation” techniques can be used for tracking the three-dimensional displacements of particles in a solid volume, for example through the use of XRCT (Hall et al., 2010), however here it is assumed that the deformations monitored on the surface are constant with depth into the material (Pan et al., 2009).

PIV cannot be used to track large displacements as the patterns within the test patches as well as their locations will change (Slominski et al., 2007). Increasing the size of the search patch to accommodate larger deformations can also lead to multiple false matches for the test patch within the search limits, as well as increasing analysis time (White, 2002). PIV also cannot be used effectively on clayey materials due to their lack of surface definition. The surface of a clayey material can be modified, for example by embedding target markers as used in Ajaz and Parry (1975), however this will affect the resulting deformations and so cannot be considered a non-intrusive test (White, 2002; White et al., 2005). A textured flock was sprinkled over the surface of a kaolin clay in Teh et al. (2008) in order to monitor its displacements, following recommendations made in White (2002) and White et al. (2005); however, the flock can adhere to both the deforming material and the viewing screen, so that its movements are no longer representative of the deformations taking place (White, 2002).

A grid of control markers, placed over the viewing screen, is used in order to transform “image-space” displacements (in pixels) into “object-space” displacements (in millimetres or equivalent). These markers do not move with respect to the boundary of the deforming material, so that tracking of the control markers allows any movement of the capturing device to be eliminated: this is particularly important in geotechnical centrifuge modelling, where the motion of the centrifuge will cause a camera boom or arm to deflect, leading to an apparent movement of particles in an un-corrected image (White, 2002). A disadvantage of the use of control markers is that, in order to ensure the greatest accuracy, they must be placed close to areas of interest in the image, so that their presence can obscure some deformations.

Image distortion must be considered when converting between image- and object-space coordinates. This had previously been achieved by using a single scaling factor, however this is only valid if the camera obeys the pinhole model where the object plane is parallel to the image plane and the pixels on the camera’s CCD (Charged Couple Device) are square (White et al., 2003). Examples of corrections that are required include: non-coplanarity of image and object planes; lens distortion (radial and tangential); pixel non-squareness; and refraction through the viewing window. In total, sixteen additional numerical image correcting parameters were identified by White (2002) to accurately convert between image- and object-space coordinates.

In this study a flatbed scanner is used to capture images of a layer of material as it deforms during compaction. The scanner offers a number of advantages for use with PIV when compared to a digital camera. Firstly, the image size produced by a scanner is far larger; a modest flatbed scanner can achieve scans of 1200dpi, resulting in an A4-sized image (11.7×8.3 inches) of roughly 140 megapixels. The latest

generation commercial digital camera offers 21 Megapixels (model reference: Canon EOS-1Ds Mark III, correct at time of writing). The ability to select a scanning resolution without having to consider and accurately measure the distance between the image source and the viewing screen is also a significant advantage. Secondly, the plane of the scanned image is guaranteed to be parallel to the viewing screen, as the scanner's scanning glass can be placed in direct contact with the viewing screen. This not only eliminates non-coplanarity corrections, but also removes the need to consider refraction through the viewing window, as the scanning axis of the scanning bar remains perpendicular to the viewing window as the scan is taken. Thirdly, the cost of the equipment is significantly reduced: whereas a current generation digital camera could cost in the region of £4500 (model reference: Canon EOS-1Ds Mark III, correct at time of writing), a suitable flatbed scanner can cost as little as £25.

An apparent disadvantage of the scanner over the camera is the time required to capture the image; however, as long as no deformation occurs during the scanning process, this is not an issue. This is the case when considering deformations due to the compaction of an RE layer, as compaction is by means of discrete strikes, rather than being continuous. Another disadvantage of the scanner is the set viewing screen size: whereas a digital camera could capture a greater viewing area at a sacrifice of resolution (pixels/mm) by being moved away from the image plane, the scanner must remain in contact with the viewing screen. Therefore, the scanner is only suitable for tests that can fit within the scanning window. A scanner would therefore not be suitable for capturing fast-moving or large deformation processes, for example that occur in fluid or granular flow, but is excellently suited to the intermittent displacement that occurs in soils during operations such as compaction as long as the sample size is representative.

4.3.3 Development of the test procedure

4.3.3.1 Design of the compaction chamber

A compaction chamber was designed to accommodate multiple layers of soil so that deformations on compaction could be observed. A sketch of the compaction chamber showing principal dimensions is shown in Figure 4.12, and a photograph of the chamber with scanner fitted is shown in Figure 4.13. The chamber's viewing window is limited to the size of the flatbed scanner, in this case to an area of 300 mm wide by 250 mm high, or just larger than a landscape-orientated A4 piece of paper. This size allows for two layers of soil of 150 mm depth to be placed in the chamber and compacted (the final compacted depth being less than 100 mm on average for RE-suitable soils). The width of 300 mm is also representative of an internal or non-load bearing RE wall (Houben and Guillaud, 1996; King, 1996; Easton, 2007). The chamber is 100 mm wide to allow for a sufficiently-large rammer: this is the same rammer size as used in Hall and Djerbib (2004) for sample production. Two 10 mm thick Perspex panels form the front and rear of the chamber to allow the deforming material to be viewed. Two 15 mm thick steel panels form the chamber sides to prevent bulging. A 2.5kg "flat head" rammer is mounted above the chamber: its position can be changed by means of the rammer carriage and guide rails. The rammer is sufficiently long so that the drop height can be set to 300 mm above the surface of the soil for each strike. This is to maintain compaction consistency and to comply with the light Proctor test, chosen as it more closely approximates the conditions that would exist within the soil in a full-scale wall on construction (Hall and Djerbib, 2004; Walker et al., 2005; Bui and Morel, 2009). Two clamps mounted on the front of the chamber hold the scanner in place, in contact with the front panel. Although a number of rammer head shapes to improve the "kneading" of RE material on compaction are recommended in Betts and Miller (1937), only the flat head rammer will be investigated here; in order for deformations detected by the scanner to be representative of those occurring throughout the material, the ramming surface must be both flat and in contact with the Perspex panel to prevent greater deformations occurring in-depth and material spilling around the rammer head respectively.

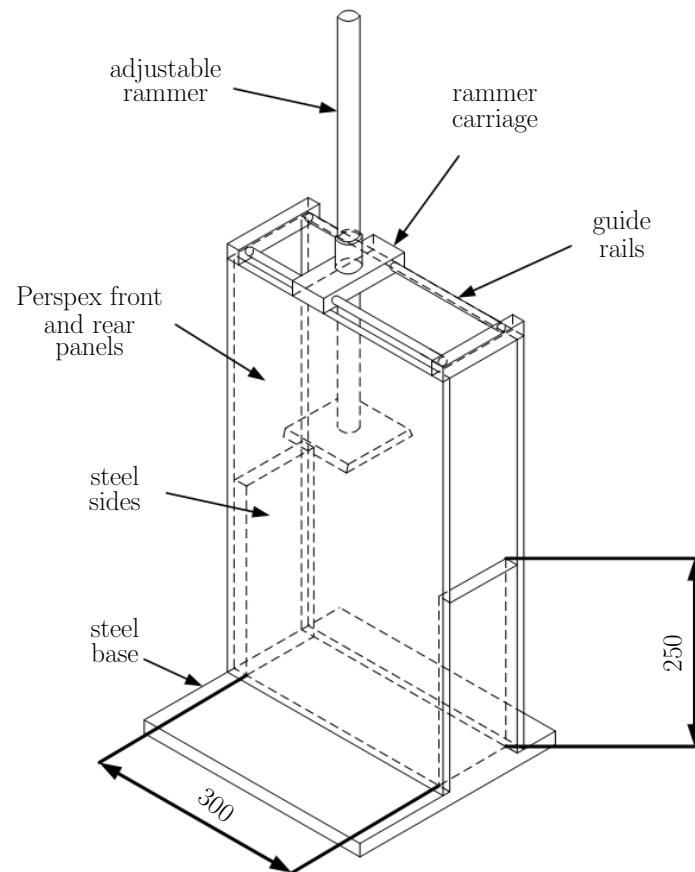


Figure 4.12: Sketch of the compaction chamber, showing principal dimensions in mm.



Figure 4.13: Photograph of the compaction chamber with scanner in place. Principal dimensions are shown in Figure 4.12.

4.3.3.2 Development of “artificial rammed earth”

As mentioned in Section 4.3.2, PIV cannot usually be used on clayey soils due to insufficient surface texture. However, as stated in Section 4.2.3, an RE soil mix must contain greater-than or equal-to 20% silty clay content by mass in order to perform adequately in compression and to produce an acceptable surface finish (Houben and Guillaud, 1996). In this study, rather than use the established techniques of tracking deformations in clayey materials using embedded target markers or texturing the surface with flock (Ajaz and Parry, 1975; Teh et al., 2008), which are unsuitable due to the large deformations on compaction, the clay in RE is substituted for an artificial, transparent medium. Transparent media can be used to model granular and clayey soils, depending on the application. In the former case, grains of a given refractive index are placed in a container and saturated with a fluid of the same refractive index (Allersma, 1982; Siemens et al., 2010). In the latter case, amorphous silica (or “fumed silica”) is mixed with a fluid of the same refractive index to form a solid, jelly-like clay substitute (Iskander et al., 2002; McKelvey et al., 2004; Liu et al., 2010). Iskander et al. (2002) found that the transparent material used in their tests had geotechnical properties that were consistent with a wide range of natural clays and the material used in McKelvey et al. (2004) (“Trinity College Dublin” or “TCD” material) had geotechnical properties consistent with normally consolidated alluvial clays. The use of transparent materials is a much safer method to monitor the deformations of structures in soils in the laboratory than other non-intrusive methods, for example radiography (Hughes and Withers, 1974). Furthermore, as testing is relatively quick and inexpensive, parametric analysis becomes more attractive.

In this work, the TCD material was combined with sharp sand (average particle size roughly 0.6 mm) and a modified gravel (average particle size roughly 5 mm) in the ratio of 5:1:4 (TCD:pea gravel:sand, by mass) in order to approximate a clayey RE soil. Particle grading curves for the sharp sand and pea gravel are shown in Figure 4.14. The gravel is a 1:1 mixture by mass of sieved gravel passing 10 mm (in order to prevent large particles interfering with the compaction process, following the procedures used in Hall and Djerbib (2004)) and sieved sharp sand passing 10 mm but not 2.36 mm, in order to ensure a well-graded material. The ratio of 5:1:4 was chosen as it contains the greatest clay content for RE-suitable soils as specified by Houben and Guillaud (1996). The TCD was not required to be transparent due to its being mixed with non-transparent materials; therefore, extensive testing to produce a truly transparent material was not required. Instead, the TCD produced here was translucent, which was sufficient for use in this experiment. The resulting combined material was dubbed “Artificial Rammed Earth” (ARE).

4.3.3.3 Parametric analyses

A series of preliminary tests was carried out to ensure that the scanned images would be adequate for PIV analysis, using a 1:1 mixture of coarse sand (particle grading curve shown in Figure 4.5) and sieved sharp sand (particle grading curve shown in Figure 4.14). A scanning resolution of 600 dpi was selected, producing a 35 megapixel image over an A4 size. The resulting images were sufficiently detailed to allow for accurate PIV analysis but not so large as to require too great a computational effort, determined using sample test patch sizes of 128×128 pixels at a central spacing of 128 pixels (i.e. the patches are in contact without overlapping) and the software “geoPIV”, developed by Prof. Dave White. geoPIV was used to perform all subsequent PIV analyses.

At 600 dpi, a sand grain of 2 mm average diameter would be represented by a bounding box of roughly 47×47 pixels, so that a test patch of 128×128 pixels would represent roughly 9 such grains. In the original work by White (2002), errors in displacement tracking for a number of materials were determined using a nominal resolution of 0.1 mm/pixel, so that the same sand grain would only occupy a bounding box of 20×20 pixels. The resulting empirical relationship between patch size and the error in displacement tracking (in pixels), determined through control experiments on a range of soil types for

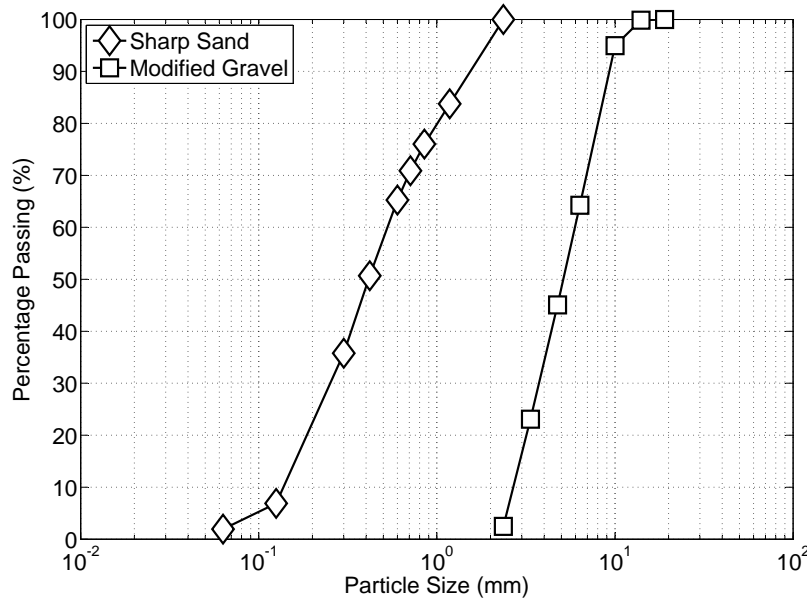


Figure 4.14: Particle grading curves for sharp sand and modified gravel

sub-pixel displacements, is given by (White et al., 2003) as

$$\rho_{pixel} = \frac{0.6}{L} + \frac{150000}{L^8}. \quad (4.3)$$

resulting in errors of 0.03 pixels for the 20 pixel bounding box and 0.01 pixels for the 47 pixel bounding box, or a threefold increase in accuracy for the 600 dpi setting.

Further tests were carried out to determine the optimum size (in pixels) for the test patches. Test patch sizes of 64×64 pixels at 64 pixel centres, 128×128 pixels at 128 pixel centres and 256×256 pixels at 256 pixel centres were considered. Results showed that test patches of 128×128 pixels produced the clearest data in an acceptable analysis time. It was found that the more-dense test patch mesh produced too many vectors for the displacement field to be legible, whilst the less dense mesh did not produce a sufficiently detailed displacement field. As geoPIV uses the Fast Fourier Transform method in order to determine the centroidal displacement of patches, it is recommended that patches should be of size 2^n pixels (where n is an integer) to reduce computational time (White, 2002). Therefore, no further patch sizes were investigated.

The “search boundary” is a border of pixels placed around the test patch to determine the size of the search patch (and so the maximum displacement that can be recorded, see Figure 4.11). Search boundary limits of 10, 30 and 50 pixels were tested with combinations of the above patch sizes: a 50 pixel boundary produced too many wild vectors, whilst a 10 pixel boundary could not adequately track particle displacements. 30 pixels was therefore selected as a compromise, creating a corresponding maximum displacement for tracking of roughly 1.8 mm (roughly 1.3 mm vertically or horizontally) at 600 dpi with a precision of 0.06 mm/pixel. Unlike the requirement for test patches to be 2^n pixels in size, no such restriction exists for the search patch, as only a test patch sized part of the search patch is interrogated to determine the correlation (see Figure 4.11).

Control markers were placed at known intervals on the surface of the viewing screen (the front Perspex panel). As image distortion is negated by having the scanning glass in contact and parallel with the viewing screen, only four control markers, placed at the four corners of the viewing window, were

required. This represents an advantage over the methods used by Iskander et al. (2002), White (2002) and White et al. (2003) as the control marker grid obscures as little of the deforming material as possible.

4.3.4 Results and discussion

Segregation and stratification of granular mixes on mixing and pouring is discussed in Section 4.2.3: as the ARE material did not show any signs of stratification or segregation, it can be said that it is not acting as a mixture of sands but instead as a cohesive ‘soil’ (Samadani and Kudrolli, 2001).

Compaction testing was conducted by placing a level, 110 mm deep layer of ARE material into the compaction chamber. A scan of the un-compacted material was taken to act as a starting point for the PIV analysis prior to compaction. The ARE was compacted by moving the rammer from the right of the chamber to the left (as viewed in Figures 4.15 to 4.22) in 50 mm intervals (i.e. five rammer strikes per pass) and then reversing the direction until a constant compacted level was achieved. A scan of the deformed material was taken after each strike of the rammer, once the rammer had been retracted. Although this can result in a greater compactive effort than that used in the light Proctor test, RE used in construction is (ideally) compacted until no further change in volume is observed; the compaction technique used here is therefore in keeping with construction practices. A second 110 mm deep layer of ARE material was then added on top of the first and the process of scanning and compacting repeated.

The average compacted depths of the first and second ARE layers were 67.1 mm and 73.7 mm respectively, corresponding to a 39% and 33% compaction (by volume): this is a favourable comparison to the expected compaction of an actual RE layer, which is roughly 33% (Walker et al., 2005), indicating that the ARE material is comparable to an actual RE soil for compaction testing.

Examples of results for the PIV analysis of the scanned images are shown in Figures 4.15 to 4.18: the displacement vectors show the centroidal movement of the test patches after a single rammer strike, scaled by a factor of five, so that a ‘dot’ represents no movement. Displacement fields are calculated using two consecutive images in order to prevent image distortion and the image behind the displacement field shows the material after compaction, i.e. the new particle positions. The axes show the size of the scanning window in millimetres (note that the units on the ordinate axis are inverted, as pixels are numbered from the top left corner of the image: displacements have been corrected for this). Figures 4.15 and 4.16 show the displacements after two strikes of the rammer, whilst Figure 4.17 shows particle displacements after eleven strikes (i.e. the first strike after two complete passes over the top of the material have been made). Figure 4.18 shows the displacements after 31 strikes of the rammer, at the end of the compaction process. Again, this is more than the 27 blows used for the light Proctor test, however it is necessary to ensure a uniform compaction across the layer. Deformation fields calculated from the captured PIV data corresponding to Figures 4.15 to 4.18 are shown in Figures 4.19 to 4.22 respectively. It should be noted that the vertical bands present in Figure 4.22 do not represent particle displacements, but instead are due to the scanning bar skipping whilst moving: this effect is present in all of the scans towards the end of the test. It is assumed that this is due to a combination of too great a force being applied by the clamps shown in Figure 4.13 and a slight bulging of the intervening Perspex panel, so that releasing the clamps would remove this effect. Unfortunately, it is an effect that can only be detected after the images have been processed.

As can be seen in Figures 4.15 to 4.22, compaction results in significant deformation underneath and around the rammer face, as expected. As this deformation is large (i.e. greater than 1.8 mm, the maximum displacement that can be detected by the 30 pixel search boundary) the displacement vectors in these regions are untrustworthy: their purpose is only to indicate those regions where deformations are the largest. Of interest is the apparent particle flow away from these regions into the more undisturbed material, showing that the action of compaction causes considerable horizontal as well as vertical

deformations, which may or may not be advantageous given the desired application. Figures 4.15 to 4.22 show that the effect of compaction is not restricted to the surface of the material, but that extensive deformations occur throughout the depth of the ARE layer: Figures 4.17, 4.18, 4.21 and 4.22 show that these deeper deformations continue throughout the compaction process, so that all of the material in the layer is affected by compaction.

The top of the first ARE layer is clearly visible in Figures 4.16 to 4.18 as a dark band running across the material at roughly 180 mm from the top of the silo, formed due to the forcing out of liquid paraffin and white spirit from the TCD material during compaction. This layer was observed to form towards the end of the compaction process, suggesting that the uppermost surface of the material has been compacted to a greater extent than the bulk of the layer. A reduced number of rammer strikes might prevent the formation of this layer. It is also possible that the use of a differently-shaped rammer head (for example a heart- or wedge-shaper rammer (Betts and Miller, 1937)) would produce a more uniform material density, due to a greater penetration. However, prior to the addition of a new RE layer to an RE structure, the surface of the underlying layer (if present) is scarified to improve layer bonding (Betts and Miller, 1937; Keable, 1996; Walker et al., 2005; Easton, 2007). It is therefore likely that the uppermost, potentially over-compacted material in the compacted layer would be removed so that the effect of its presence is negligible. Therefore, the use of a flat rammer head is suitable for RE construction, provided that the deformations during compaction occur throughout the layer. The effect of deeper layers on ARE compaction was not investigated here, however it is an easy extension of this investigation using the equipment and procedures discussed in this chapter.

Figures 4.16 to 4.18 and 4.20 to 4.22 show that the already-compacted material is not affected by the compaction of an overlying layer. A comparison of Figures 4.19 and 4.20 shows a very similar pattern for the deformations of the first and second layers, again suggesting that the first layer is acting as incompressible with respect to the second layer and that the compactive effort applied to the second layer is the same as that applied to the first. The slight increase in layer thickness between the first and second layers is therefore suggestibly caused by a larger amount of material being used for the second layer, rather than a change in density between the two, perhaps due to material settling prior to the layer depth being measured. This is an important result in terms of RE construction, as it suggests that the material properties of each layer are determined by compaction of that layer alone, and are not dependent on other layers in the structure. As RE walls are built on top of short concrete or masonry stem walls to protect the base of the wall from water damage (Betts and Miller, 1937; Keable, 1996; Walker et al., 2005; Easton, 2007), it can be assumed that the first (i.e. lowermost) layer is also compacted on top of an incompressible material so that all of the compacted layers have the same properties.

As the scanner is set to have a zero focal length (i.e. set to focus on items that are in contact with the scanning glass) the images of the deformed material are blurred due to the presence of the viewing screen. The separating of the scanner and the deforming material by the viewing screen is necessary to avoid scratching the scanning glass, which would lead to erroneous PIV results. It was shown in White et al. (2003) that the effect of test patches containing pixels of similar intensity, which is a result of blurring, reduces the precision of the calculated particle displacements. However, as the separation distance is constant (the scanner is not moved during the test), it can be assumed that the effect of blurring is also constant both along the length of the image (as the scanning bar traverses the scanning glass rather than capturing the entire image from one location) and for the duration of the test. The effect of blurring should therefore not influence particle tracking, as long as sufficient particle definition is maintained; the illuminated scanning bar should be enough to ensure this. The larger test patch size afforded by the use of the scanner also serves to reduce the impact of blurring due to the improved accuracy as predicted by Eqn 4.3. If a focused image is desired, then the front panel can be reduced in thickness; however, if it is made too thin then it will bulge on compaction, as discussed above, which might not only cause damage

to the scanner but will also result in a non-constant focal length, so that focusing effects will need to be considered when determining the final deformations. Using a smaller panel would also reduce bulging, however it also reduces the amount of material that can be viewed.

4.3.5 Conclusions

A new and novel experimental technique has been used to non-intrusively investigate the behaviour of ARE under compaction *in situ* in order to determine whether the internal structures of laboratory prepared RE samples are comparable to material found in RE structures. The technique has shown great potential for qualitative and quantitative analysis of soil deformations and it is anticipated that this idea could be employed to study a number of other geotechnical problems in the future.

It has been shown that the compaction of a layer of ARE is independent of the layers above it so that the material in one layer is representative of that in the structure as a whole: this result can be extended to RE due to the similar behaviour of ARE and RE under compaction. This result therefore justifies the use of small specimens for RE (of the order of one layer) as their behaviour can be extended to the material in bulk and suggests that the use of thin layers (of the order of 30 mm deep) in laboratory-prepared samples does not create a material that is misrepresentative of the material used in full-scale RE construction.

4.4 Concluding remarks

The aim of the investigations discussed in this chapter is to determine how processes that are involved in the creation of an RE sample, following the procedure recommended by Hall and Djerbib (2004), influence the formation of its material structure and to determine whether the resulting samples are representative of RE used in construction.

In Section 4.2, it was shown that the pouring of two dry sands leads to a partial segregation of the material, forming bands of the two sand species. This phenomenon occurs both during the mixing of the material, due to the formation of loose piles of material with the passage of a mixing paddle (or similar instrument), in the draining of a hopper and on the pouring of the material, i.e. under any process involving particle flow. Although the effect of the addition of dry clay particles was not investigated, for reasons discussed in Section 4.2.3, it is proposed that the effect of clay particles might be to reduce segregation effects, rather than eliminate them. The practice of combining and mixing dry constituent materials prior to the addition of water might therefore impart a segregated structure on the final material, which must be checked for if the sample material is to be comparable with natural RE materials.

The interaction of RE layers and the behaviour of RE as it is compacted was discussed in Section 4.3 by investigating the compaction of ARE material. The results given in Figures 4.15 to 4.22 show that compaction affects all of the material within the layer and that significant deformations occur throughout the compaction process, so that it is not just the uppermost material that is affected by the rammer strikes. Figures 4.15 to 4.22 show that material is pushed away from the rammer impact region due to the incompressibility of the underlying layer (be it the base of the formwork or an already-compacted RE layer), so that the material is mixed by the action of compaction. This mixing action might serve to mitigate any non-uniformity present due to segregation or stratification of the initial mix. Samples of compacted RE should therefore be comparable to the material used in construction and, perhaps more importantly, to each other, as concentrations of given particle sizes (with associated modifications to the material behaviour) should not occur. It is noted, however, that this is an extension of the results shown in Figures 4.15 to 4.22: further experimentation is required to determine the extent of material mixing

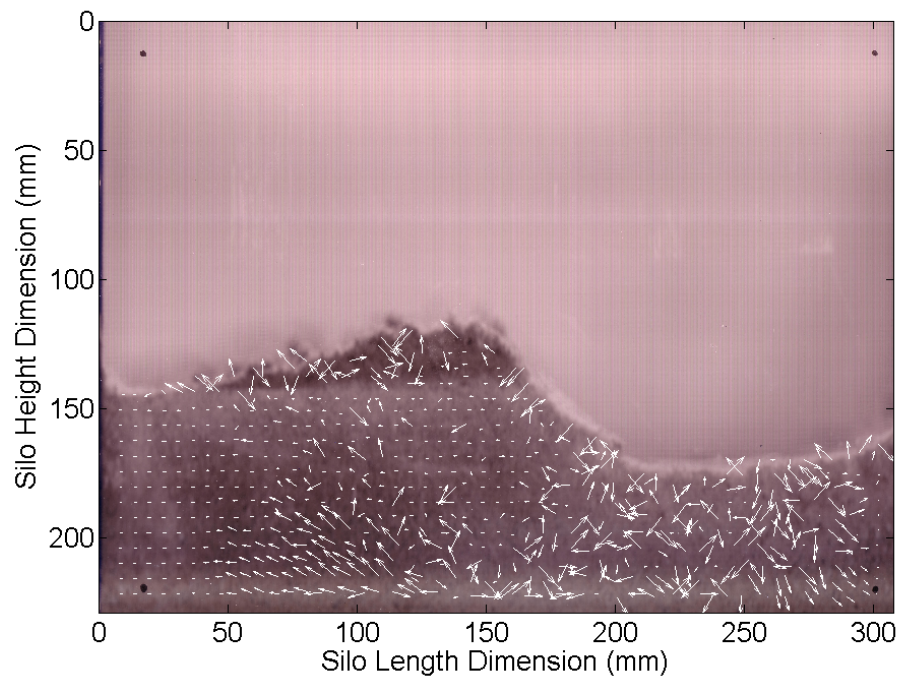


Figure 4.15: Initial particle displacements after two strikes (scaled by a factor of 5 with the rammer striking between 200 and 300 mm in the silo length dimension) during compaction of the first ARE layer (units in mm)

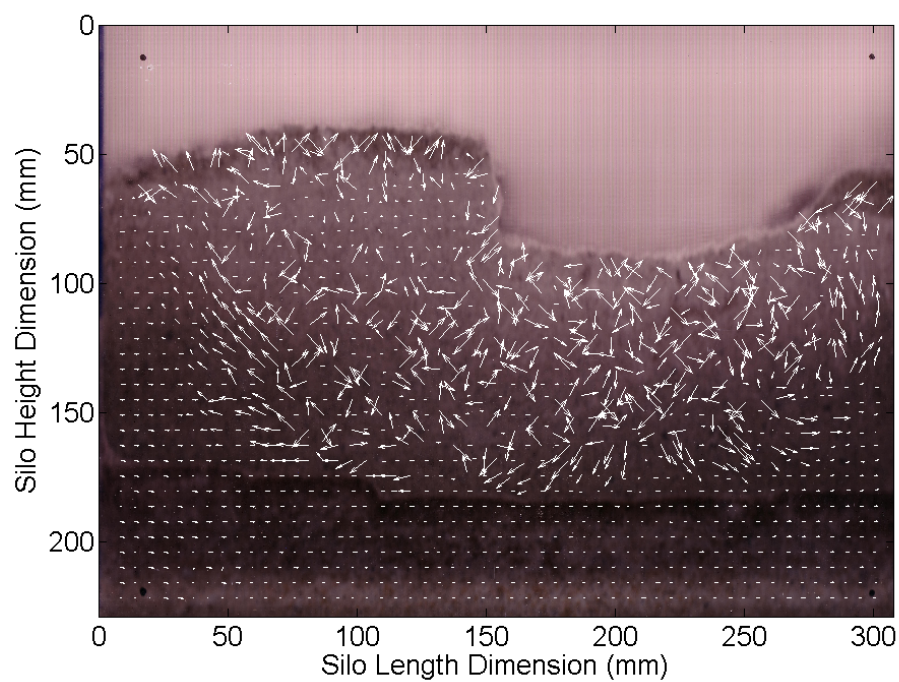


Figure 4.16: Initial particle displacements after two strikes (scaled by a factor of 5 with the rammer striking between 200 and 300 mm in the silo length dimension) during compaction of the second ARE layer (units in mm).

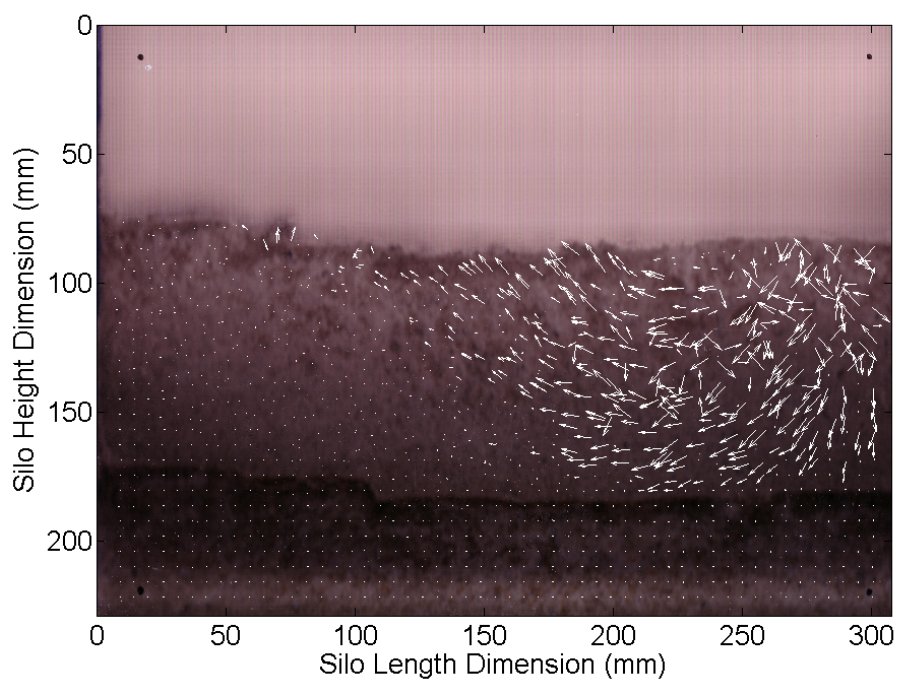


Figure 4.17: Particle displacements after 11 strikes (scaled by a factor of 5 with the rammer striking between 200 and 300 mm in the silo length dimension) half way through the compaction of the second ARE layer (units in mm).

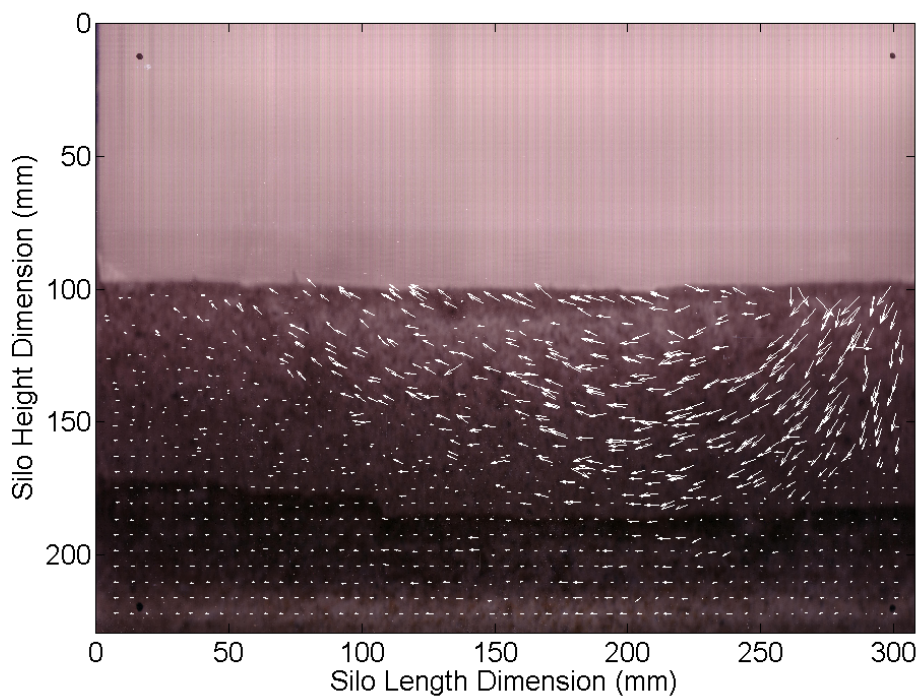


Figure 4.18: Particle displacements after 33 strikes (scaled by a factor of 5 with the rammer striking between 200 and 300 mm in the silo length dimension) at the end of the compaction of the second ARE layer (units in mm).

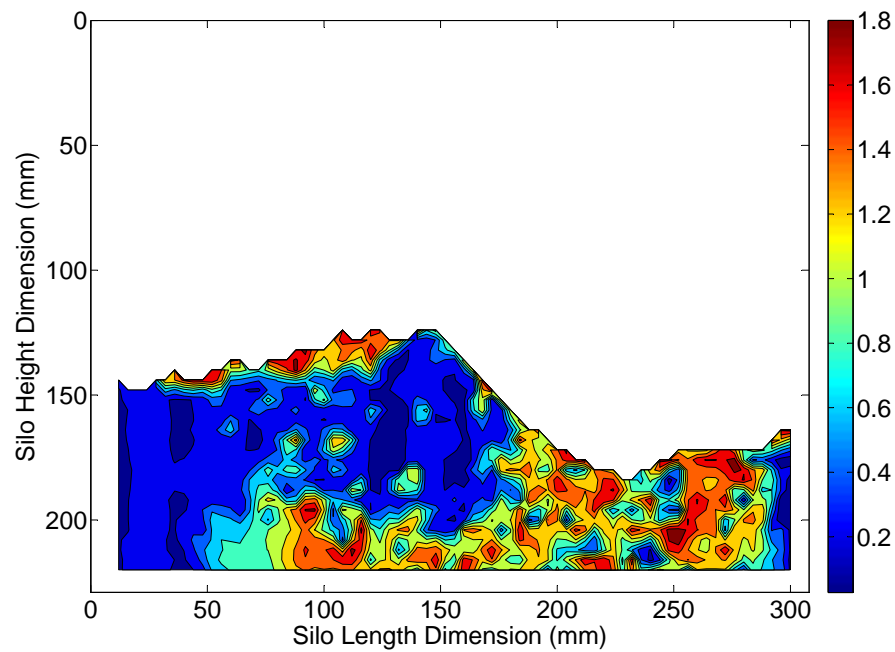


Figure 4.19: Contour plot of initial particle displacements after two strikes (with the rammer striking between 200 and 300 mm in the silo length dimension) during the compaction of the first ARE layer (units in mm).

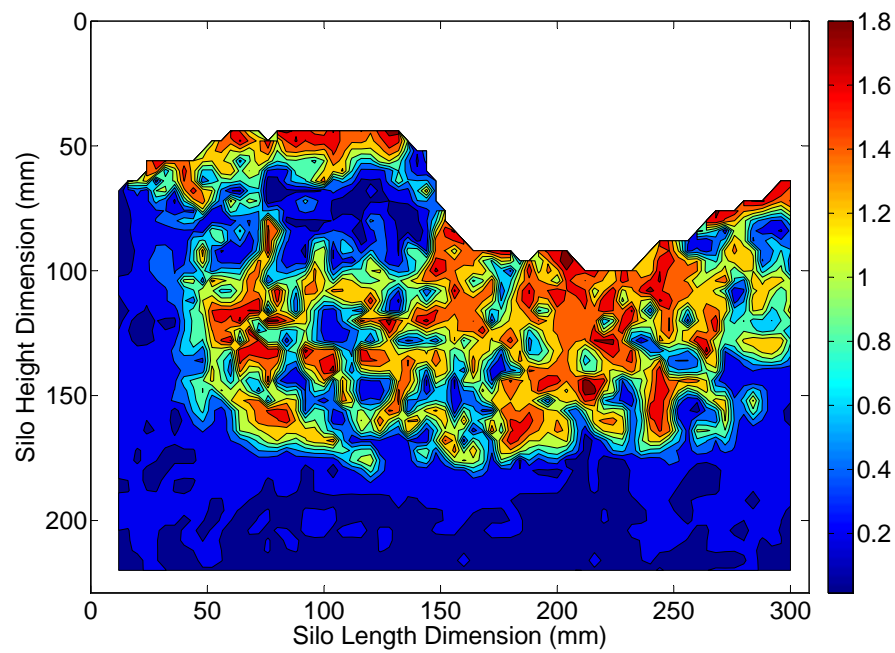


Figure 4.20: Contour plot of initial particle displacements after two strikes (with the rammer striking between 200 and 300 mm in the silo length dimension) during the compaction of the second ARE layer (units in mm).

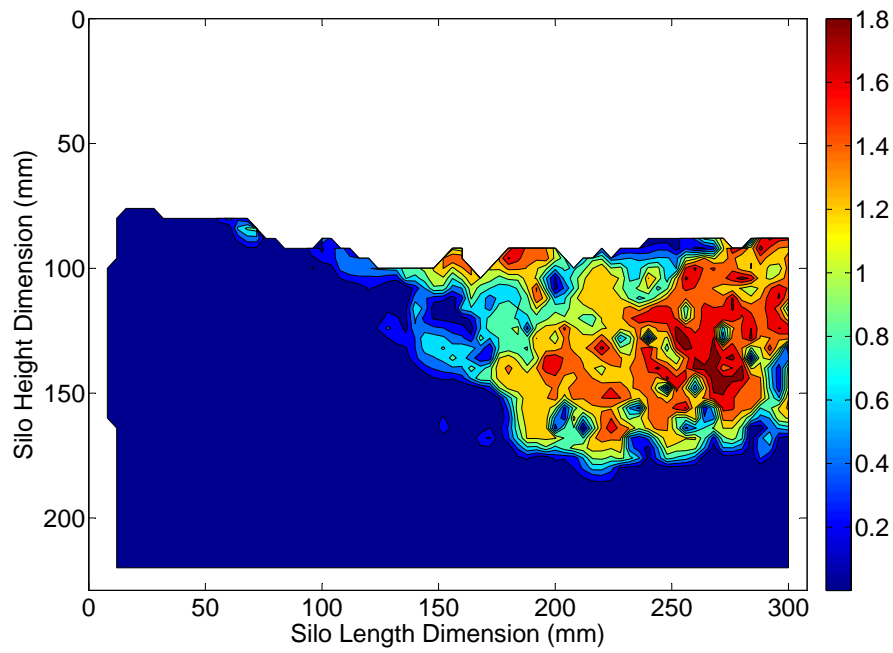


Figure 4.21: Contour plot of particle displacements after 11 strikes (with the rammer striking between 200 and 300 mm in the silo length dimension) during the compaction of the second ARE layer (units in mm).

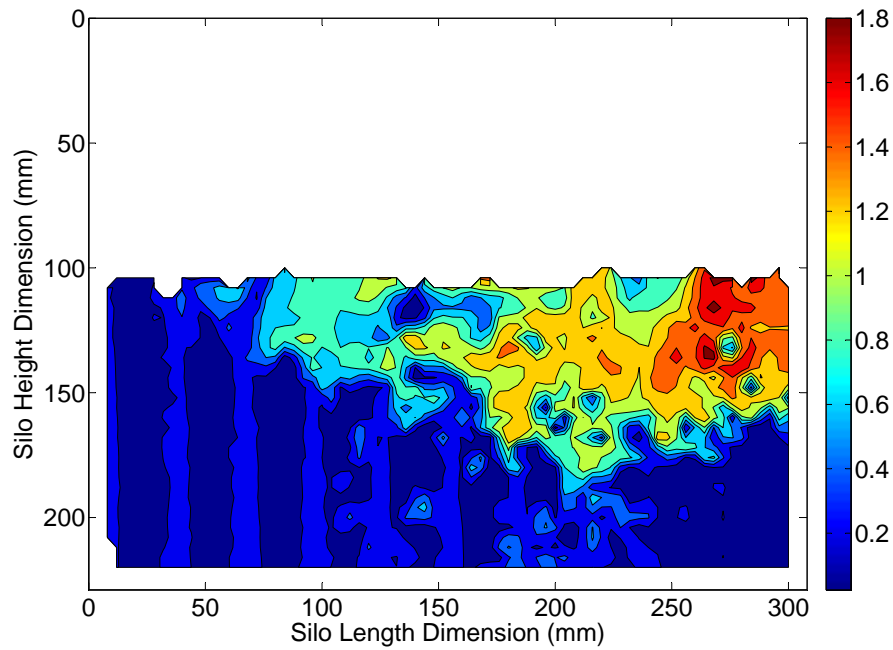


Figure 4.22: Contour plot of particle displacements after 31 strikes (with the rammer striking between 200 and 300 mm in the silo length dimension) at the end of the compaction of the second ARE layer (units in mm).

during compaction if the assumption that the particle distribution throughout the layer is uniform is to be justified.

Results given in Figures 4.15 to 4.22 show that, after compaction, the density of a layer is not affected by the compaction of a subsequent layer as shown by the lack of displacements. Therefore, single-layer specimens can be considered to be representative of much larger RE structures as long as deformations during compaction affect all of the material within the layer: again, the effect of compaction on a deep RE layer was not investigated and further research is required in this area. This is an important clarification as it means that tests performed on small samples can be used to predict the behaviour of much larger RE structures, so that parametric testing of small RE samples is now a much more powerful analysis tool.

Given the observations made in this chapter and summarised above, samples prepared using the production process recommended by Hall and Djerbib (2004) can be considered justified in terms of creating representative samples of RE used in construction. This result will now be used in the following chapters, where RE samples, made according to the procedures used in Hall and Djerbib (2004), are used to test RE's compressive and tensile strengths under a range of conditions in order to determine the effect of material micro- and macrostructure on RE's behaviour.

4.5 References

- Adrian, R., 1986. Multi-point optical measurements of simultaneous vectors in unsteady flow—a review. *International Journal of Heat and Fluid Flow* 7 (2), 127–145.
- Adrian, R. J., 1991. Particle imaging techniques for experimental fluid mechanics. *Annual Review of Fluid Mechanics* 23, 261–304.
- Ajaz, A., Parry, R. H. G., 1975. Stress-strain behaviour of two compacted clays in tension and compression. *Géotechnique* 25 (3), 495–512.
- Allersma, H., 1982. Photo-elastic stress analysis and strains in simple shear. In: Vermeer, P. A., Luger, H. J. (Eds.), *Proc., IUTAM Symposium on Deformation and Failure of Granular Materials*. A. A. Balkema, Rotterdam, pp. 345–353.
- Betts, M. C., Miller, T. A. H., 1937. Rammed earth walls for buildings. *Farmers Bulletin No. 1500*. U.S. Department of Agriculture, Washington D.C. (U.S. Govt. Printing Office).
- Bhatia, S. K., Soliman, A. F., 1990. Frequency distribution of void ratio of granular materials determined by an image analyzer. *Soils and Foundations* 30 (1), 1–16.
- Bolton, M., 1991. *A guide to soil mechanics*. M D & K Bolton.
- Bui, Q.-B., Morel, J.-C., 2009. Assessing the anisotropy of rammed earth. *Construction and Building Materials* 23 (9), 3005–3011.
- Cizeau, P., Makse, H. A., Stanley, H. E., 1999. Mechanisms of granular spontaneous stratification and segregation in two-dimensional silos. *Physical Review E* 59 (4), 4408–4421.
- Easton, D., 2007. *The Rammed Earth House, Completely Revised Edition*. Chelsea Green Publication Company, Vermont (USA).
- Gens, A., 2010. Soil-environment interactions in geotechnical engineering. *Géotechnique* 60 (1), 3–74.
- Goyal, R. K., Tomassone, M. S., 2006. Power-law and exponential segregation in two-dimensional silos of granular mixtures. *Physical Review E* 74 (5), 10.
- Grasselli, Y., Herrmann, H., 1998. tude sur la forme d'un tas de billes dans un silo bidimensionnel. *Comptes Rendus de l'Académie des Sciences - Series IIB - Mechanics-Physics-Chemistry-Astronomy* 326 (1), 61–67.
- Grasselli, Y., Herrmann, H., 1999. Shapes of heaps and in silos. *The European Physical Journal B - Condensed Matter and Complex Systems* 10, 673–679.
- Grasselli, Y., Herrmann, H. J., 1997. On the angles of dry granular heaps. *Physica A: Statistical and Theoretical Physics* 246 (3-4), 301–312.
- Guler, M., Edil, T. B., Bosscher, P. J., 1999. Measurement of particle movement in granular soils using image analysis. *Journal of Computing in Civil Engineering* 13 (2), 116–122.
- Hader, K. P., Kuttler, C., 1999. Dynamical models for granular matter. *Granular Matter* 2 (1), 9–18.
- Hall, M., Djerbib, Y., 2004. Rammed earth sample production: context, recommendations and consistency. *Construction and Building Materials* 18 (4), 281–286.
- Hall, S. A., Bornert, M., Desrues, J., Pannier, Y., Lenoir, N., Viggiani, G., Bésuelle, P., 2010. Discrete and continuum analysis of localised deformation in sand using x-ray μ ct and volumetric digital image correlation. *Géotechnique* 60 (5), 315–322.
- Herrmann, H. J., 1999. Shapes of granular surfaces. *Physica A: Statistical Mechanics and its Applications* 270 (1-2), 82–88.
- Herrmann, H. J., 2002. Granular matter. *Physica A: Statistical Mechanics and its Applications* 313 (1-2), 188–210.
- Houben, H., Guillaud, H., 1996. *Earth construction - a comprehensive guide.*, Second Edition. Intermediate Technology Publications, London (UK).
- Hughes, J. M. O., Withers, N. J., 1974. Reinforcing of soft cohesive soils with stone columns. *Ground Engineering* 3, 42–49.
- Iskander, M. G., Liu, J., Sadek, S., 2002. Transparent amorphous silica to model clay. *Journal of Geotechnical and Geoenvironmental Engineering* 128 (3), 262–273.
- Jaquin, P. A., Augarde, C. E., Gallipoli, D., Toll, D. G., 2009. The strength of unstabilised rammed earth materials. *Géotechnique* 59 (5), 487–490.
- Jommi, C., Sciotti, A., Sep 23-26 2003. A study of the microstructure to assess the reliability of laboratory compacted soils as reference material for earth constructions. In: Bontempi, F. (Ed.), *2nd International Conference on Structural and Construction Engineering*. A A Balkema Publishers, Rome, Italy, pp. 2409–2415.
- Jotisankasa, A., Coopy, M., Ridley, A., 2009. The mechanical behaviour of an unsaturated compacted silty clay. *Géotechnique* 59 (5), 415–428.
- Keable, J., 1996. *Rammed earth structures: a code of practice*. Intermediate Technology Publications, London (UK).
- King, B., 1996. *Buildings of Earth and Straw: Structural Design for Rammed Earth and Straw-Bale Architecture*. Ecological Design Press, Sausalito, California (USA).
- Lee, Y., Bassett, R., 2006. Application of a photogrammetric technique to a model tunnel. *Tunnelling and Underground Space Technology* 21 (1), 79–95.

- Liu, J., Hu, R., Wang, R., Yang, L., 2010. Regeneration of vernacular architecture: new rammed earth houses on the upper reaches of the yangtze river. *Frontiers of Energy and Power Engineering in China* 4 (1), 93–99.
- Liu, J., Iskander, M. G., 2010. Modelling capacity of transparent soil. *Canadian Geotechnical Journal* 47, 451–460.
- Love, J. P., Burd, H. J., Miligan, G. W. E., Houlsby, G. T., 1987. Analytical and model studies of reinforcement of a layer of granular fill on a soft clay subgrade. *Canadian Geotechnical Journal* 24 (4), 611–622.
- Makse, H. A., Ball, R. C., Stanley, H. E., Warr, S., 1998. Dynamics of granular stratification. *Physical Review E* 58 (3), 3357–3367.
- Makse, H. A., Havlin, S., King, P. R., Stanley, H. E., 1997. Spontaneous stratification in granular mixtures. *Nature* 386 (March), 379–381.
- Maniatidis, V., Walker, P., 2003. A Review of Rammed Earth Construction. University of Bath.
- McKelvey, D., Sivakumar, V., Bell, A., Graham, J., 2004. Modelling vibrated stone columns in soft clay. *Proceedings of the Institution of Civil Engineers-Geotechnical Engineering* 157 (3), 137–149.
- Meguid, M., Saada, O., Nunes, M., Mattar, J., 2008. Physical modeling of tunnels in soft ground: A review. *Tunnelling and Underground Space Technology* 23 (2), 185–198.
- Ni, Q., Hird, C., Guymer, I., 2010. Physical modelling of pile penetration in clay using transparent soil and particle image velocimetry. *Géotechnique* 60 (2), 121–132.
- Ottino, J. M., Khakhar, D. V., 2001. Fundamental research in heaping, mixing, and segregation of granular materials: challenges and perspectives. *Powder Technology* 121 (2–3), 117–122.
- Paikowsky, G., Xi, F., 2000. Particle motion tracking utilizing a high-resolution digital CCD camera. *Geotechnical Testing Journal* 23 (1), 123–134.
- Pan, B., Qian, K., Xie, H., Asundi, A., 2009. Two-dimensional digital image correlation for in-plane displacement and strain measurement: a review. *Measurement Science and Technology* 20 (6), 062001.
- Samadani, A., Kudrolli, A., 2001. Angle of repose and segregation in cohesive granular matter. *Physical Review E* 6405 (5), 9.
- Samadani, A., Pradhan, A., Kudrolli, A., 1999. Size segregation of granular matter in silo discharges. *Physical Review E* 60 (6), 7203.
- Santamarina, J. C., Cho, G. C., March 2004. Soil behaviour: The role of particle shape. In: *Proceedings of the Skempton Conference*. London.
- Shimokawa, M., Ohta, S., 2007. Dual stratification of a sand pile formed by trapped kink. *Physics Letters A* 366 (6), 591–595.
- Shinoda, M., Bathurst, R. J., 2004. Strain measurement of geogrids using a video-extensometer technique. *Geotechnical Testing Journal* 27 (5), 8p.
- Siemens, G., Peters, S., Take, W. A., 2010. Analysis of a drawdown test displaying the use of transparent soil in unsaturated flow applications. In: Alonso, E., Gens, A. (Eds.), *Unsaturated Soils. Fifth International Conference on Unsaturated Soils*, CRC Press.
- Sivakumar, V., Tan, W. C., Murray, E. J., McKinley, J. D., 2006. Wetting, drying and compression characteristics of compacted clay. *Géotechnique* 56 (1), 57–62.
- Slominski, C., Niedostatkiewicz, M., Tejchman, J., Apr. 2007. Application of particle image velocimetry (piv) for deformation measurement during granular silo flow. *Powder Technology* 173 (1), 1–18.
- Srebro, Y., Levine, D., 2003. Role of friction in compaction and segregation of granular materials. *Physical Review E* 68 (6), 9.
- Take, W. A., White, D. J., Bowers, K. H., Moss, N. A., Jun 15–17 2005. Remote real-time monitoring of tunnelling-induced settlement using image analysis. In: Bakker, K. J., Bezuijen, A., Broere, W., Kwast, E. A. (Eds.), *5th International Conference on Geotechnical Aspects of Underground Construction in Soft Ground*. Taylor & Francis Ltd, Amsterdam, pp. 771–777.
- Tarantino, A., 2010. Unsaturated soils: compaction versus reconstituted states. In: Alonso, E., Gens, A. (Eds.), *Unsaturated soils. Fifth International Conference on Unsaturated Soils*, CRC Press, pp. 113–136.
- Tarantino, A., De Col, E., 2008. Compaction behaviour of clay. *Géotechnique* 58 (3), 199–213.
- Teh, K. L., Cassidy, M. J., Leung, C. F., Chow, Y. K., Randolph, M. F., Quah, C. K., 2008. Revealing the bearing capacity mechanisms of a penetrating spudcan through sand overlying clay. *Géotechnique* 58 (10), 793–804.
- Walker, P., Keable, R., Martin, J., Maniatidis, V., 2005. *Rammed Earth: Design and Construction Guidelines*. BRE Bookshop, Watford (UK).
- Wheeler, S., Sivakumar, V., 1995. An elasto-plastic critical state framework for unsaturated soils. *Géotechnique* 45 (1), 35–53.
- White, D. J., 2002. An investigation into the behaviour of pressed-in piles. Thesis, University of Cambridge, UK.
- White, D. J., Randolph, M. F., Thompson, B., 2005. An image-based deformation measurement system for the geotechnical centrifuge. *International Journal of Physical Modelling in Geotechnics* 5 (3), 1–12.

- White, D. J., Take, W. A., Bolton, M. D., 2003. Soil deformation measurement using particle image velocimetry (PIV) and photogrammetry. *Géotechnique* 53 (7), 619–631.
- Zhang, G., Liang, D. F., Zhang, J. M., 2006. Image analysis measurement of soil particle movement during a soil-structure interface test. *Computers and Geotechnics* 33 (4-5), 248–259.
-

Chapter 5

The effect of humidity and temperature on the compressive strength of rammed earth

5.1 Introduction

5.1.1 Overview

The strength of a compacted soil has been attributed to by a number of factors including the clay content and cementation, water content, interparticle friction and suction, which can all be related to the material micro- and macrostructures (Utomo and Dexter, 1981; Abdullah et al., 1999; Rahimi et al., 2000; Fredlund, 2006; Gelard et al., 2007; Buscarnera and Nova, 2010; Chae et al., 2010). How important these contributions are to the strength of rammed earth (RE), however, is not yet known (Jaquin et al., 2008, 2009). In this chapter, the compressive strengths of two RE soil mixes are tested, at equilibrium water contents corresponding to a range of temperature and humidity combinations, in order to determine the effect of the micro- and macrostructures on the compressive strength of RE materials and to recommend suitable soil types for a range of climatic conditions.

5.1.2 Climates at RE sites

Suction can be linked to temperature and humidity through the Kelvin equation (Eqn 2.18 and Eqn 2.27 for liquid bridges). The climate at an RE site therefore has a critical effect on the strength of the material. The effect of relative humidity on RE is of particular importance, as its large exposed surface area means that material easily equilibrates to ambient humidity levels; an assessment of Eqn 2.15 shows that a drop in relative humidity from 100% to 90% represents an increase in suction from 0 to roughly 10 MPa (or an emptying of pores larger than roughly 1.4 nm effective radius as discussed in Chapter 3), so that suction in RE are likely to be much higher and the material much drier than unsaturated soils encountered in most geotechnical engineering applications.

The Köpper-Geiger climate classification (KGCC) was originally developed in 1900 but has proved to be a robust method to define different climate types around the world. KG classification is based on temperature, precipitation and seasonal variation in precipitation, with additional regional refinements

being made according to prevalent vegetation types. Five broad climate categories are identified: tropical (A); arid (B); temperate (C); cold (D); and polar (E), each with a range of sub-categories. For a detailed description of the governing parameters for each category and subcategory, the reader is referred to Table 1 of Peel et al. (2007).

In Peel et al. (2007), an updated version of the KGCC is presented in which weather station data for temperature and precipitation at a given location is used to determine the climate category and subcategory for that location. This approach is insensitive to temperature trends on the level of broad climate types (i.e. categories A to E) but variations due to trends are possible within each category as it is assumed that data from one period is directly comparable to that from another (Peel et al., 2007). It is acknowledged that an interpolation method which includes elevation as a third dimension would reduce irregularities associated with the effect of climates in mountainous regions being applied to those in lowland regions, however a 3-D interpolation method was not used due to the sparsity of data in mountainous areas (Peel et al., 2007).

Criticisms of the KGCC method (and the updated map given in Peel et al. (2007)) are that category B, which is the most prevalent (30.2% of total landmass), has very few subcategories compared to categories C and D (13.4% and 24.6% of total landmass respectively) which leads to misleading classifications when prevalent vegetation is considered. However, the approach is robust enough to provide an acceptable method to determine climate types around the world. Again, the reader is referred to Peel et al. (2007) for a more detailed description and discussion of the updated KGCC.

Selected RE sites shown in Figure 1.7 have been reproduced in Figure 5.1 to show the predominating climates according to the KGCC. It can be seen that pre-19th century sites reside within climate categories B and C according to the KGCC. Such structures are therefore subject to high temperatures (although not as high as in category A locations) and low annual rainfalls (and hence low annual humidities), for most of the year (Peel et al., 2007). However, it can also be seen that as the RE technique has spread, a greater range of climatic conditions have been encountered so that RE structures can now be subjected to any of the KGCC categories. An understanding of how RE behaves in a given climate is therefore necessary if confidence in its use is to be earned.

5.2 Experimental procedure

In this section, the procedures used to determine the unconfined compressive strengths of RE samples subjected to a range of humidity and temperature values are discussed. Unconfined compressive strengths are tested for as this is the property that is most commonly used to compare the performances of RE materials used for construction (King, 1996; Keable, 1996; Walker et al., 2005; Easton, 2007). A summary of the procedures used is shown in Figure 5.2, and they can be divided into the following steps:

- Humidity and temperature setpoint selection;
- Selection and preparation of raw materials;
- Sample manufacturing;
- Sample compressive strength testing.

5.2.1 Humidity and temperature setpoint selection

Minimum and maximum temperature and humidity data for 91 known RE sites shown in Figures 1.7 and 5.1 are given in Figure 5.3, with a summary for each major region given in Table 5.1. Data were found

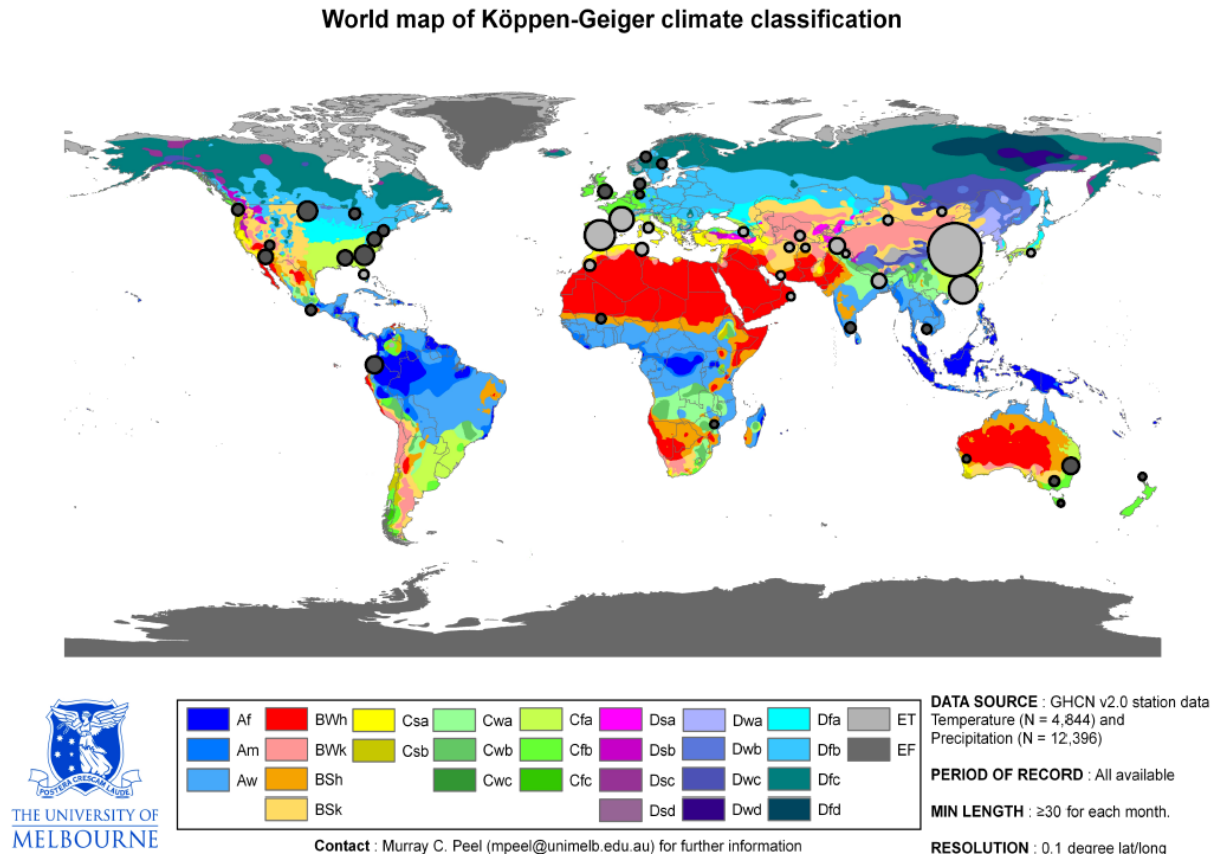


Figure 5.1: Locations of RE sites compared to KGCC categories (Peel et al., 2007). Pre-19th century sites are shown as light markers and post-19th century are shown as dark markers. Larger markers represent a greater number of RE sites within a given area. KGCC global map used with permission.

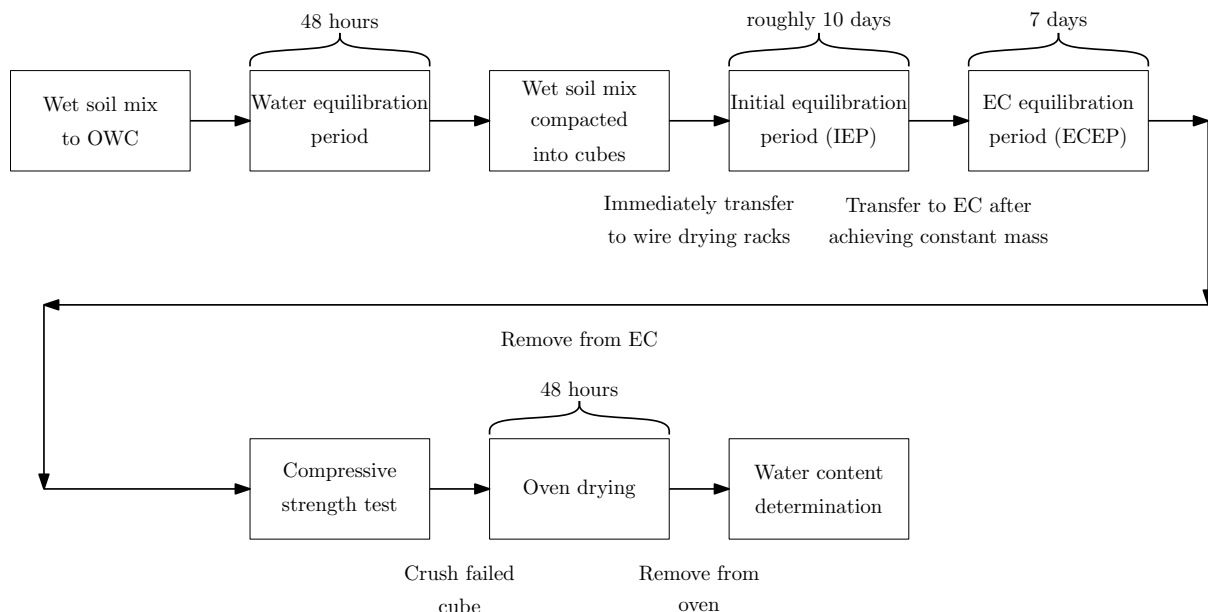


Figure 5.2: Flow chart showing principal testing procedure stages, stage durations and environmental chamber (EC) use

from a variety of sources, the largest being the EnergyPlus Simulation Software. Data are for the exact location for the RE site where possible, however in locations where meteorological information is sparse, data are for nearby locations: in these instances, values are for the nearest site both geographically and

meteorologically in order to remain realistic.

Figure 5.3 shows that most of the sites identified in this investigation reside in locations with temperatures between 0°C and 30°C and humidities between 40% and 100%. It is assumed that, as RE requires fine, dry weather for construction, no fresh RE material would be subjected to temperatures below 0 °C nor to humidities above 90%, so that conditions outside of these limits can be ignored. Therefore, humidity setpoints of 30%, 50%, 70% and 90% and temperatures of 15°C, 20°C, 30°C and 40°C (i.e. 16 possible setpoint combinations) were chosen for testing, which correspond to a suction range of 14.0 MPa to 173.9 MPa if suction is calculated using Eqn 2.15.

A Vötsch VC 4033 environmental chamber was used to control the humidity and temperature during cube equilibration (accuracy of $\pm 3\%$ and $\pm 4\%$ of the target value for combinations of humidities and temperatures above 15% and 15°C and 10% and 10°C respectively). The chamber could achieve temperatures between 10°C and 100°C and humidities between 10% and 100%, although it was noted that inaccuracies would occur as combinations of these limits were approached. The temperature and humidity ranges of 15°C to 40°C and 30% to 90% respectively are therefore within the operating range of the environmental chamber without encroaching on the operational limits.

Work conducted by Morton et al. (2005) suggests that the internal conditions in an earthen structure

Table 5.1: Summary of minimum and maximum annual temperatures and relative humidities (RHs) for RE sites by region

Region	Min Temp. (°C)	Max Temp. (°C)	Min RH (%)	Max RH (%)
Africa	4	38	36	90
Australia	3	32	23	91
Europe	-7	37	16	99
North America	-11	39	11	99
South America	8	31	15	97
South East Asia	-34	50	8	100

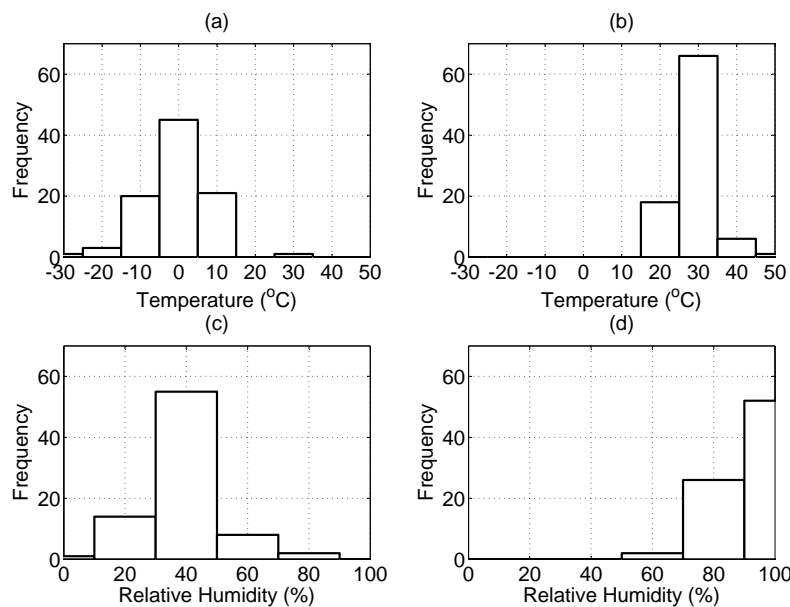


Figure 5.3: Environmental data for 91 RE sites around the world: a) minimum temperatures; b) maximum temperatures; c) minimum humidities; and d) maximum humidities.

are such that the humidity inside a house constructed from unfired clay bricks was roughly constant at 60% throughout the year at a temperature of 20°C. This is supported by results presented in Allinson and Hall (2010) for the hygrothermal analysis of stabilised RE structures which suggest that environmental conditions of 60% and 20°C are also representative of the conditions within RE structures. However, it should be noted that Morton et al. (2005) and Allinson and Hall (2010) monitored the conditions within mature earthen structures, not those that were in the process of drying. Despite this, these results suggest that testing of RE cubes at humidities above 90% and below 30% is not required so that the limits placed on humidity and temperature by the operating range of the environmental chamber are therefore acceptable. For convenience, setpoint combinations are referred to as two values in parentheses corresponding to the humidity and the temperature respectively, for example “(50%, 40°C)”, from this point forwards.

5.2.2 Selection and preparation of raw materials

It is noted in Hall and Djerbib (2004) that soils that are suitable for RE construction generally fall within the sandy-loam class of the United States Department of Agriculture (USDA) soil classification system. In order to differentiate more precisely between soil mixes, Hall and Djerbib (2004) proposed a method for naming soil mixes according to their relative sand-to-gravel-to-silty-clay components; for example, a soil mix of ‘5-1-4’ contains 50% sand, 10% gravel and 40% silty clay by mass. Soil mixes used in this and subsequent investigations have been named according to this system.

Soil mixes 5-1-4 and 7-1-2 were selected for compressive strength testing based on results from Hall and Djerbib (2004). Soil mix 7-1-2 was selected as it had the lowest compressive strength of those mixes tested and contains the smallest recommended clay content according to Houben and Guillaud (1996). Soil mix 5-1-4 was selected as it contains the largest recommended clay content; as the amount of clay contained within the soil mix has also been identified as a contributing factor to compressive strength, the use of mix 5-1-4 allows the role of the clay content to be investigated simultaneously with the effect of humidity and temperature.

Dried Birtley clay, sharp sand and pea gravel were combined in the appropriate proportions to form the two soil mixes. Birtley clay is a locally-available material which contains roughly 50% clay by mass (LL 58.8%, PL 25.7%, PI 33.1%). The primary mineral type is kaolinite, which displays the smallest amount of shrinkage or swelling on drying and wetting respectively and so is recommended for RE construction (Walker et al., 2005). It is also similar to the clay used in Hall and Djerbib (2004), allowing results to be compared to existing data. Dry silty-clay was prepared by pulverising lumps of the material which had been dried at 105°C for 48 hours, according to BS1377:1990, again following the procedures used in Hall and Djerbib (2004). An extra 24 hours was allowed in addition to the recommended 24 hours to ensure that the material was fully dry prior to pulverising. Pulverised material was passed through a 2.36 mm sieve; this sieve size was selected as particle aggregates were small enough to mix uniformly with the remaining mix fractions on the creation of the soil mixes whilst producing a sufficient quantity of material at an acceptable rate.

Sharp sand was prepared by passing it through a 2.36 mm sieve. This was to remove the gravel-sized fraction of particles (particles larger than 2.0 mm (BS1377:1990)), so that the gravel content of the soil mixes could be more accurately controlled.

The gravel component of the soil mix was sieved to pass 10 mm in order to prevent large particles interfering with the compressive strength testing. It was also found in Kirk (2009) that errors in determining the water content of an RE mix increase with increasing gravel content, so that the use of a low gravel content improves the control over the soil properties. It is noted that this process results in a less-representative soil mix as to what might be encountered during construction, however the use of

samples considerably smaller than full-scale RE walls (traditionally of >300 mm thickness (King, 1996; Maniatidis and Walker, 2003; Walker et al., 2005; Easton, 2007)) suggests that samples remain representative. To improve the particle grading, sieved gravel (<10 mm) and sieved sharp sand (>2.36 mm) were combined in a 1:1 ratio by mass.

Figure 5.4 shows the particle grading curves of the three raw materials. The particle grading curves for the combined soil mix material, along with the recommended limits on the particle grading specified by Houben and Guillaud (1996), are shown in Figure 5.5. The relative proportions of sand, gravel and silty-clay according to the limits on particle sizes as specified by BS1377:1990 in the final soil mixes (determined through wet sieving) are shown in Table 5.2, showing good agreement between the actual and theoretical constituent contents. Figure 5.5 shows that the grading curves for the two soil mixes lie on the limits recommended by Houben and Guillaud (1996), with mixes 5-1-4 and 7-1-2 containing the maximum and minimum recommended silty-clay content (particles smaller than $60\mu\text{m}$ (BS1377:1990)) respectively. As a result of sieving, the gravel component is skewed towards the smaller particle sizes in Figure 5.5, however it is still within the recommended limits.

The optimum water content (OWC), maximum dry and maximum bulk densities ($\rho_{d_{max}}$ and $\rho_{b_{max}}$ respectively) for the two soil mixes were determined using the results given in Figure 5.6 and are summarised in Table 5.3. Values were determined using the light Proctor test (BS1377:1990) which was used following the work of Hall and Djerbib (2004), Walker et al. (2005) and Bui and Morel (2009). A greater change in dry density with changing water content is found for mix 5-1-4 than for mix 7-1-2. This is due to mix 5-1-4's more-aggregated structure prior to compaction (i.e. it contains larger soil aggregates)

Table 5.2: Relative particle size category amounts for soil mixes 5-1-4 and 7-1-2.

Soil mix	Sand (0.06 to 2 mm) (%)	Gravel (>2 mm) (%)	Silty-Clay (<0.06 mm) (%)
5-1-4	52.7	10.2	37.1
7-1-2	70.6	10.0	19.4

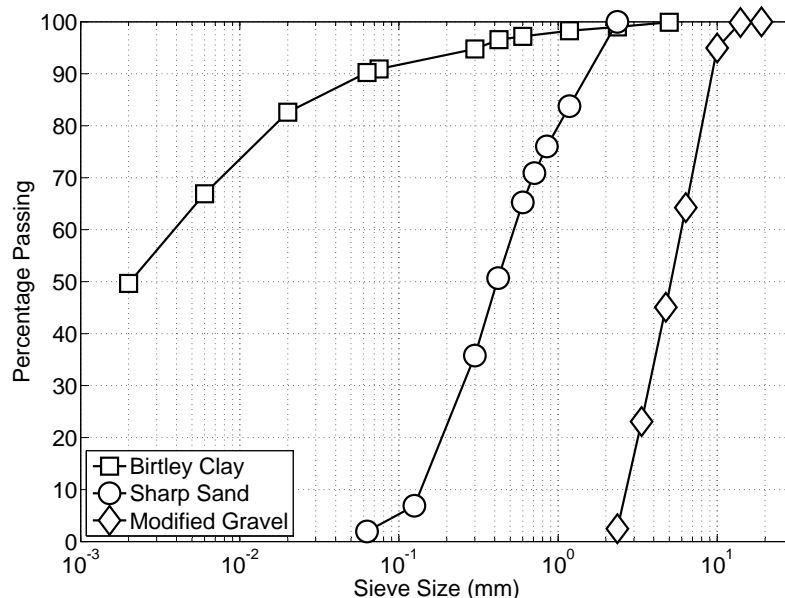


Figure 5.4: Raw material particle grading curves

which arises due to its higher clay content (Tarantino, 2010).

It was found in Beckett (2008) that the wetting of dry soil mixes results in fine material remaining in the container after the bulk of the material is removed so that the particle grading of the removed material is altered (this is termed *finer loss*, where “fine” material is the proportion of material passing a $63\mu\text{m}$ sieve (BS 1377:1990)). The effect of fines loss on the soil mixes was determined by comparing fresh soil mix material to material that had previously been wetted and then dried. Wet material was prepared in sealable polypropylene containers in three layers of 2.5 kg wetted to OWC using distilled

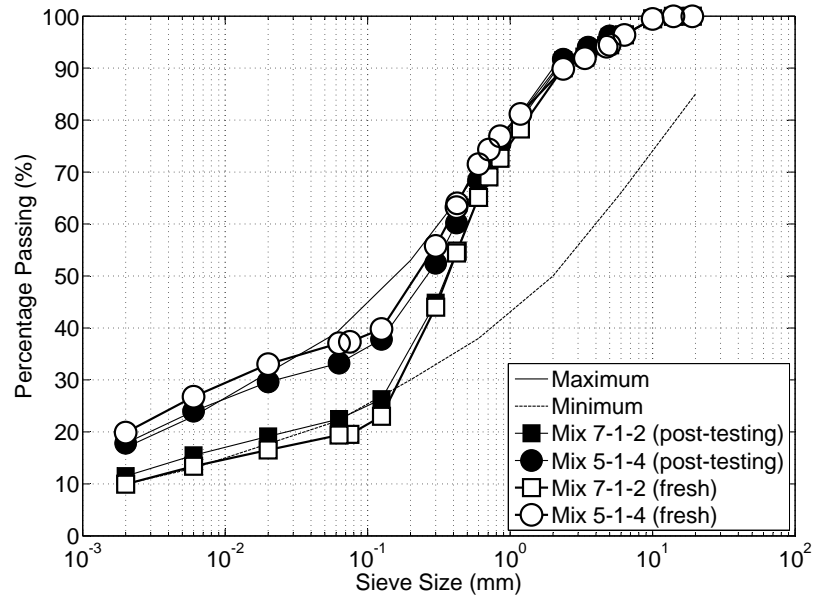


Figure 5.5: Particle grading curves for virgin and re-used soil mix material

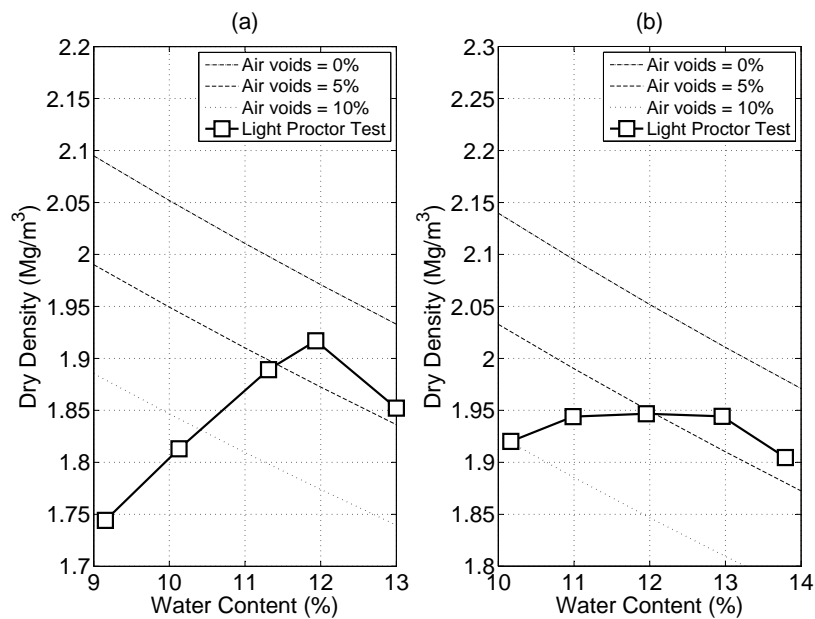


Figure 5.6: Water content against dry density for light Proctor compaction tests on soil mixes: a) 5-1-4; and b) 7-1-2.

water. Containers were treated with an anti-static cleaner prior to being filled with the dry soil mix to prevent dry clay particles from adhering to the container surfaces. The containers were sealed for 48 hours to allow the water to equilibrate. Material was extracted after 48 hours and dried at 105°C for 24 hours (BS1377:1990). Particle grading curves for the fresh and post-testing soil mixes, determined by wet sieving, are shown in Figure 5.5. The results show a reduction of 10.4% of the original fines content of mix 5-1-4 and an increase of 15.9% of the original fines content of mix 7-1-2. As no additional fine material is added during the testing procedure, it can be assumed that 15.9% represents the error in repeatability of the particle grading procedure; as the recorded fines loss in mix 5-1-4 is less than this amount it can be assumed that the effect of fines loss on the composition of the two soil mixes is negligible if material is prepared using this technique.

5.2.3 Sample manufacture

100 mm cube samples were selected for compressive strength testing following the work of Lilley and Robinson (1995), Hall and Djerbib (2004) and Jaquin et al. (2008). It is noted that it is usual in geotechnical engineering to use cylindrical samples of dimensions the order of 100 mm diameter and 200 mm height (Jaquin et al., 2009), however the large number of samples required for testing, a relatively short testing time and a limited quantity of available raw materials required the use of the smaller cube samples. Walker et al. (2005) indicates that the most commonly used measure of the strength of an RE material is its unconfined compressive strength, presumably due to the relative ease of testing; this is therefore also used here in order to allow for direct comparison of results and to stay in keeping with current RE literature (Jaquin et al., 2009).

Wet cube material was prepared in sealed containers following the procedure used for fines loss testing. Wet material was then removed from the containers and compacted into cube moulds, following the procedures recommended in Hall and Djerbib (2004), a procedure which has been justified through results presented and discussed in Chapter 4. The sides of the mould were treated with form release oil prior to introducing the wet material to prevent the cubes cracking on their removal. A 100 mm cube mould was used following the work of Hall and Djerbib (2004) so that results could be compared to those in the literature. Material limitations meant that larger cubes, for example those used in Lilley and Robinson (1995), could not be used. Material density was controlled by compacting the cubes in three layers of set mass with volume controlled using an adjustable rammer head. A removable guide collar was used to contain loose material whilst compacting and to ensure that layers were compacted vertically. Compaction was performed using a Milwaukee Tools Kango 900K electric rammer following work conducted in Jaquin (2008). Material was compacted at the OWC determined using the light Proctor test (Table 5.3); although a different compactive effort was used, it is assumed that the use of a set layer volume prevents the material from being over or under compacted, so that the OWC remains valid. A screed of soil mix material passing a 1.18 mm sieve was applied to the upper surface of the cube after compaction to ensure that a flat, level surface was present for compression testing. Unlike in concrete cube testing, this is a necessary requirement as cubes cannot be rotated to give two parallel faces for loading due to the orientation of the layers (Lilley and Robinson, 1995; Bui and Morel, 2009).

Table 5.3: OWC, $\rho_{d_{max}}$ and $\rho_{b_{max}}$ for soil mixes 5-1-4 and 7-1-2.

Soil mix	OWC (%)	$\rho_{d_{max}}$ (kg/m ³)	$\rho_{b_{max}}$ (kg/m ³)
5-1-4	12.0	1918.1	2147.0
7-1-2	12.0	1947.5	2197.0

Cubes were prepared in batches of six, with three cubes per soil mix. Completed cubes dried naturally on wire racks in controlled conditions until they had reached a constant mass, representing a water content equilibration with the atmospheric conditions, which took between 280 and 310 hours (11 to 12 days). This is referred to as the “initial” equilibration period (IEP). Figures 5.7 to 5.10 show the recorded temperatures and humidities during the IEP and the water contents against drying times respectively for both mixes. Marker numbers shown in these figures indicate the test number, as shown in Table 5.4. The temperature during the IEP varied by $\pm 2^\circ\text{C}$ (shown in Figure 5.7) whilst the humidity varied by greater than $\pm 15\%$ across the batches (Figure 5.8). The result of these variations is a range of 2% in the cube equilibrium water contents at the end of the IEP for both soil mixes; this has to be considered when interpreting cube compressive strengths.

5.2.4 Sample compressive strength testing

Samples were placed within the environmental chamber and allowed to equilibrate to the chosen humidity and temperature setpoints for seven days (the time required for a sample to reach a constant mass as shown by previous testing) (Jaquin et al., 2008; Tarantino and De Col, 2008; Tarantino, 2009). This is referred to as the environmental chamber equilibration period (ECEP). A longer equilibration period was not possible due to environmental chamber availability. The IEP was also necessary due to the limited availability of the environmental chamber: ideally, samples should have been placed in the environmental chamber immediately following manufacture. Temperatures (15, 20, 30 and 40°C) were combined with random humidities (any of 30, 50, 70 or 90%) in order to reduce any systematic errors that might arise due to chamber functionality. The order of tested setpoint combinations and corresponding test numbers are given in Table 5.4.

Samples were transported to and from the environmental chamber in a padded container and wrapped in clear plastic sheeting to prevent damage and water loss (Pradhan et al., 2005; Lu et al., 2007; Thom et al., 2007; Tarantino, 2009; Reynolds et al., 2009). Samples were tested within one hour of being removed from the environmental chamber, with samples remaining wrapped until being tested. Com-

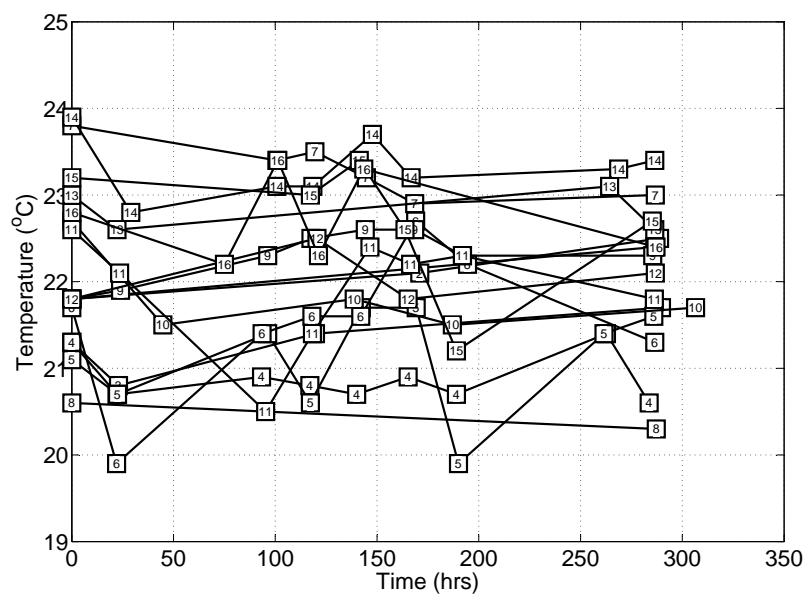


Figure 5.7: Variation in recorded temperatures during cube equilibration period

pression testing occurred in the same location as the IEP so that the compression testing environmental conditions were similar to those used for the initial equilibration. It is assumed that the water contents of the samples did not vary between being removed from the environmental chamber and the end of the compression test due to the short exposure to the atmosphere during this period.

Samples were crushed at a constant displacement rate of 0.5 mm/min based on previous testing conducted in Beckett (2008) and Jaquin et al. (2008), with cubes reaching compressive failure after roughly 6 minutes. Loads and displacements were recorded using “Triax” software (Toll, 1999) and failure

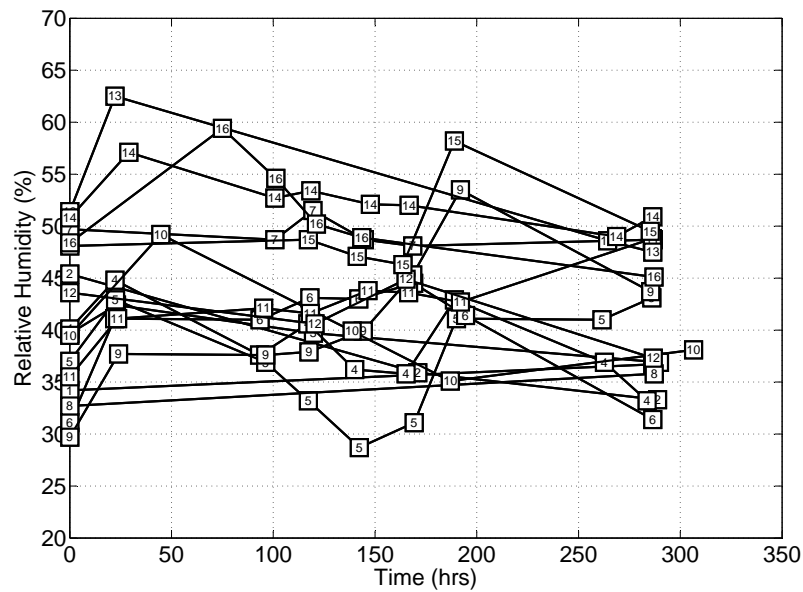


Figure 5.8: Variation in recorded humidities during cube equilibration period

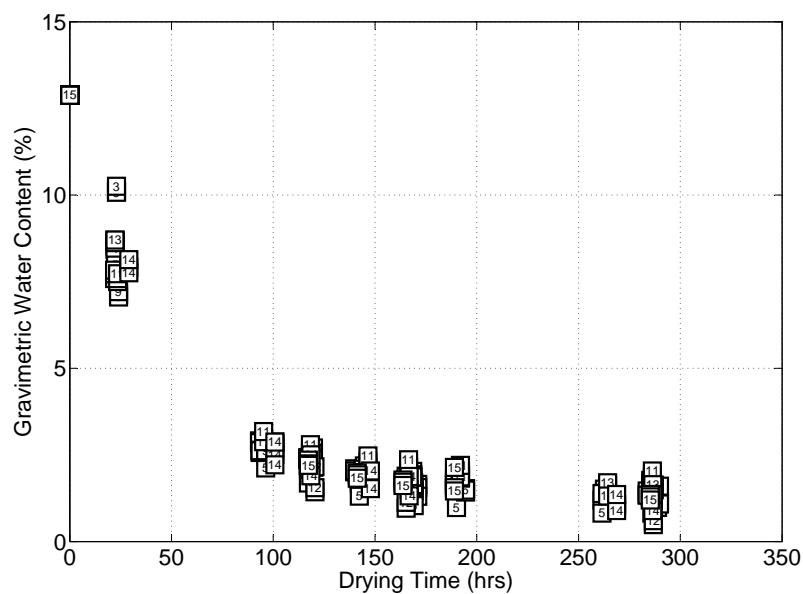


Figure 5.9: Water content against drying time for mix 5-1-4 cubes

was deemed to correspond to the maximum applied load. The average of three sample failure loads was used to determine the final failure load for that soil mix and setpoint combination. A 100×100 mm top plate (2015.3 g) was used to transfer the load to the sample, ensuring that the entirety of the top surface was loaded. A 100×100 mm plinth was used in order to provide a smooth underlying surface.

Young and Mullins (1991) found that the rate of deformation has a significant effect on the measured compressive and tensile strengths of soil samples. A loading rate of 0.05 MPa/s, equivalent of 30 kN/min for a sample of face 100 mm, was used in Heath et al. (2009b) to determine the compressive strength of unfired clay bricks (according to BS EN 772-1:2000 for materials of compressive strength below 10 MPa) and a rate of 20 kN/min was used in Hall and Djerbib (2004) for sample testing in order to compare RE compressive strengths to the standard test for concrete cubes (BS EN 12390-3:2002); however, it was deemed that these rates were too high for RE testing so that recorded results might be unrealistic (Azmatch et al., 2011). The use of 0.5 mm/min is, however, similar to the use of a rate of 0.1 mm/min in Jaquin et al. (2008), so that result trends can be compared. Furthermore, a displacement– rather than load-controlled test was selected in order to improve control over the sample loading.

After failure, samples were weighed and crushed before being dried in an oven at 105 °C for 48 hours; the extra 24 hours in addition to the recommended 24 hour drying period was allowed in order to ensure

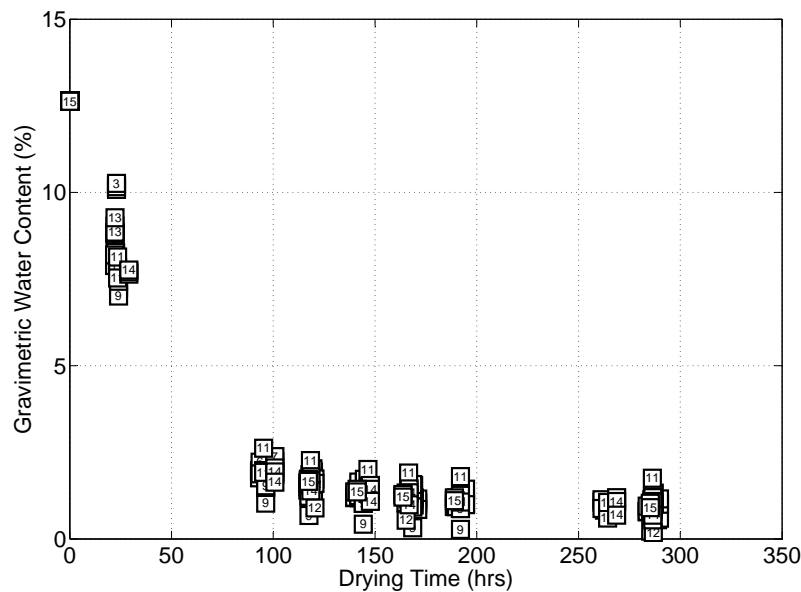


Figure 5.10: Water content against drying time for mix 7-1-2 cubes

Table 5.4: Humidity (RH) and temperature (temp.) combinations and corresponding test numbers. The number of batches required to test each combination are also given.

Test Number	RH (%)	Temp. (°C)	Batches	Test Number	RH (%)	Temp. (°C)	Batches
1	35	20	2	9	90	30	1
2	70	20	2	10	50	30	4
3	50	20	1	11	30	30	1
4	90	20	1	12	30	40	2
5	70	15	1	13	90	40	1
6	50	15	1	14	50	40	1
7	90	15	2	15	70	40	1
8	70	30	2	16	40	15	2

that the large amount of material placed within the ovens was fully dry. The mass of the dry material was then used to calculate the sample water content on testing.

5.3 Results and discussion

5.3.1 Sample density errors

The average initial mix water contents were 12.9% and 12.6% for mixes 5-1-4 and 7-1-2 respectively; it is assumed that the difference between these water contents and the target OWC (Table 5.3) is due to the soil mix material not being perfectly dry on the addition of water due to water adsorption during storage. Figure 5.6 shows that the effect of the additional 0.6% water content on the maximum dry density is not significant for mix 7-1-2, however the effect of the additional 0.9% water content produces a reduction in dry density of roughly 0.05 Mg/m^3 (i.e. reducing it to roughly 1.87 Mg/m^3) for mix 5-1-4.

The calculated errors in sample density, taken to be the relative difference between the measured sample density and the maximum bulk density found during Proctor testing for that soil mix, are shown in Figure 5.11. Positive errors represent lower densities than the target value. The relative density errors for samples of mix 5-1-4 peak around +2%, corresponding to an average dry density of 1.88 Mg/m^3 , which is in good agreement with that predicted from Figure 5.6 when accounting for the additional initial water content. Relative density errors for mix 7-1-2 peak around -1%, corresponding to an average dry density of 1.97 Mg/m^3 ; this is due to the overcompaction of the samples during manufacturing. Overcompaction occurs due to slipping of the adjustable plate on the rammer head, used to control the volume of each compacted layer. Slipping of the rammer head was overcome through design modifications which improved control over the layer volume; samples manufactured after these modifications were made show reduced density errors compared to those made prior to them.

In order to prevent under- or over-compacted samples from influencing the calculated compressive strengths, a limit of $\pm 3.5\%$ of the maximum bulk density was placed on sample densities. As a result, samples 10, 13, 16 and 38 from mix 5-1-4 were rejected, corresponding to setpoint combinations (70%, 15°C), (50%, 15°C), (90%, 15°C) and (90%, 40°C) respectively, so that failure loads for these setpoint combinations were determined from fewer results. All mix 7-1-2 samples fell within this limit. A narrower limit on sample density errors was not possible due to entire batches failing the criterion and an inability to retest batches due to limitations on the availability of the environmental chamber.

5.3.2 Sample water contents on testing

5-1-4 and 7-1-2 sample water contents after testing are shown in Figures 5.12 and 5.13 respectively. A total of 84 samples per mix were required to achieve a reliable set of results. It should be noted that not all 84 samples were tested to failure; some were rejected prior to compression testing due to errors in their manufacture. A comparison between ECEP water content and relative humidity is shown in Figure 5.14. Figures 5.12 to 5.14 show that water contents for given humidity setpoints fall within clearly defined bands, suggesting that the cube manufacturing process discussed in Section 5.2.3 produced consistent samples, but that the effect of temperature on water content was not consistent with Eqn 2.27, in that it is expected that an increase in temperature should produce a decrease in water content. Regardless, it would appear that relative humidity is the dominant factor in determining the equilibrium water content, which could provide a useful rule-of-thumb for predicting the water contents of RE mixes in given regions.

Of interest are the water contents of cubes 52, 53 and 54 (test 16, both mixes), which were nominally used with the setpoint combination (30%, 15°C), and cubes 79, 80 and 81 (test 1, both mixes), nominally used with the setpoints (30%, 20°C), as these tests appear to belong to the apparent 50% RH band. An

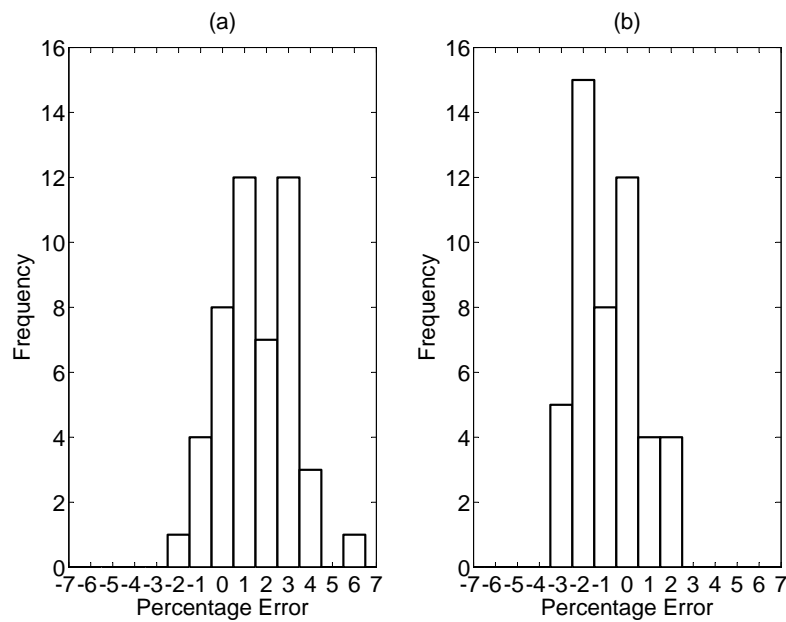


Figure 5.11: Errors in sample densities for soil mixes: a) 5-1-4; and b) 7-1-2

explanation for this lies in frequent malfunctions that occurred whilst using the environmental chamber, which occur whenever a low ($< 40\%$) humidity was required. As a result of these errors, the humidity for cubes 52, 53 and 54 (both mixes) was measured at 40% , whilst that for cubes 79, 80 and 81 (both mixes) was measured at 35% : these are the humidity values given in Figures 5.12 and 5.13. However, the corresponding water content for these corrected humidities is still higher than that suggested by the other results shown in Figures 5.12 and 5.13 for each mix; these errors are discussed further in the following sections. It was determined that these errors were due to the air conditioning fan housed within the environmental chamber blowing dry soil particles onto the chamber's internal wet bulb humidity sensor, causing an error in the sensor's readings and causing the internal humidity to change. The sensor could not be covered as it needed to be exposed to the environment within the chamber. Regular changing of the wet bulb sensor wick appeared to reduce the frequency of these failures. Humidity sensor measurements were verified by inserting a second humidity sensor into the chamber and sampling the humidity at regular intervals during testing.

Results for the effect of varying humidity on the compressive strength of commercially-produced unfired clay bricks are given in Heath et al. (2009a) and Heath et al. (2009b). Clay brick materials with clay contents 20% and 40% had water contents of 1.5% and 3.0% respectively under humidity and temperature conditions of 60% and 20°C . Heath et al. (2009b) assume that a linear relationship exists between the clay content and the water content at a given humidity for a standard temperature, in this case 60% and 20°C respectively as they are typical of the conditions present within a clay brick structure. Allinson and Hall (2010) showed that these conditions are also typical of RE structures, so that results for the two material types can be favourably compared. Figure 5.12 shows that the water content of mix 5-1-4 at 60% humidity and 20°C is roughly 1.5% , which is the same as that found for the 20% clay content clay brick in Heath et al. (2009b). The clay content of mix 7-1-2 as shown by Figure 5.5 is roughly 10% , resulting in a predicted water content at 60% RH and 20°C of 0.8% if the assumed-linear relationship between clay and water content is extrapolated. Figure 5.13 shows that the water content of mix 7-1-2 at 60% RH and 20°C is roughly 0.9% : the difference of 0.1% between the predicted and actual values falls within the standard deviation of the linear prediction, given in Heath

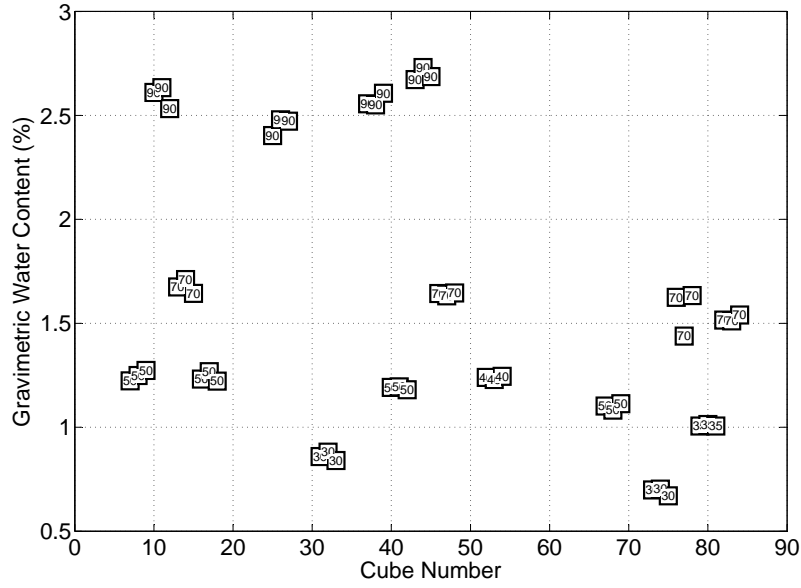


Figure 5.12: ECEP water contents for soil mix 5-1-4 cubes. Marker numbers correspond to the cube humidity setpoint.

et al. (2009b) as roughly 0.25%, therefore suggesting that the linear relationship is also valid for low-clay materials. This relationship cannot be confirmed using results presented in this investigation, however, as an insufficient range of RE soil mix clay contents has been tested, but it again offers a useful rule-of-thumb for predicting the equilibrium water content of an RE soil mix under standard internal humidity and temperature conditions.

5.3.3 Unconfined compressive strength results

Unconfined compressive strengths were calculated from the cube failure load using

$$\sigma_c = \frac{P}{A} \quad (5.1)$$

where σ_c is the unconfined compressive strength, P is the maximum applied load and A is the loaded surface area. It is assumed that the surface area does not change during testing and that the material behaves elastically (Hall and Djerbib, 2004), so that the net unconfined compressive strength is presented.

Results for calculated unconfined compressive strength against temperature and humidity are given in Figures 5.15 to 5.16. Surfaces have been determined via Delaunay triangulation using the available datapoints, which are also shown in Figures 5.15 and 5.16. Figure 5.17 shows a comparison between the compressive strengths of the two soil mixes; it can be seen that mix 7-1-2 is consistently stronger than mix 5-1-4 for a given combination of humidity and temperature. Following the work of Morel et al. (2007), an aspect ratio correction factor (e.g. Krefeld (1938) and Heathcote and Jankulovski (1992)), as used in Hall and Djerbib (2004), has not been applied to the compressive strength results as these correction factors are for homogeneous materials only. Mix 5-1-4 is apparently stronger than mix 7-1-2 for 50% humidity and 20 °C; however, this is assumed to be a result of experimental variability rather than being indicative of the material properties, so that it is expected that the unconfined compressive strength of mix 7-1-2 should be consistently greater than that of mix 5-1-4. This is perhaps a counter-intuitive result, as it is assumed in earthen construction literature that the addition of clay to a material

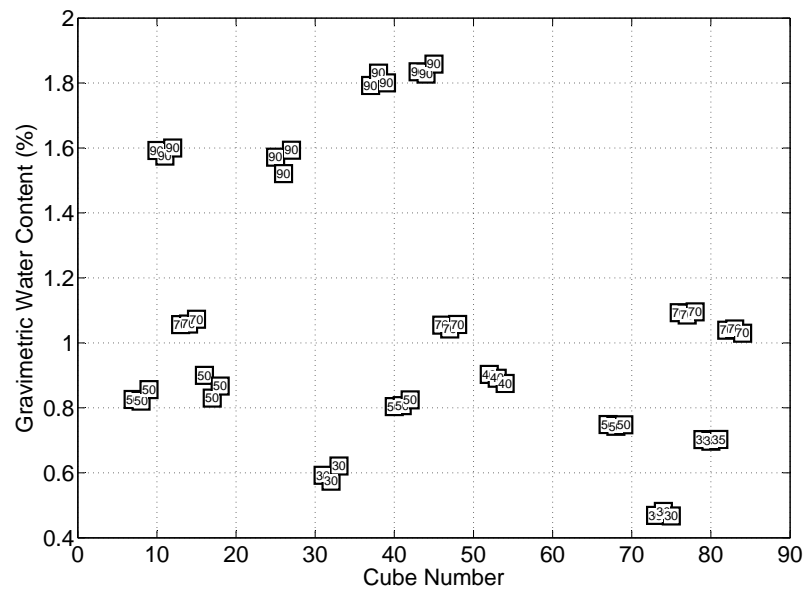


Figure 5.13: ECEP water contents for soil mix 7-1-2 cubes. Marker numbers correspond to the cube humidity setpoint.

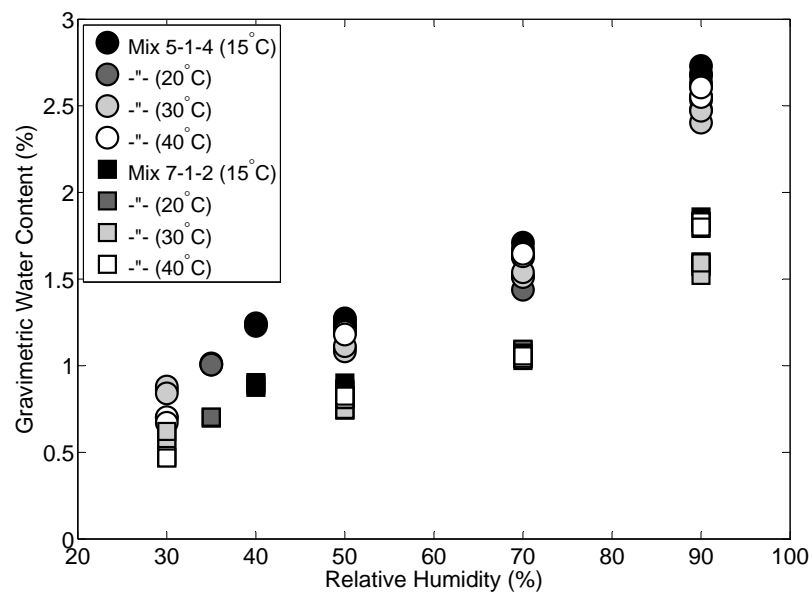


Figure 5.14: Effect of relative humidity on sample ECEP water content

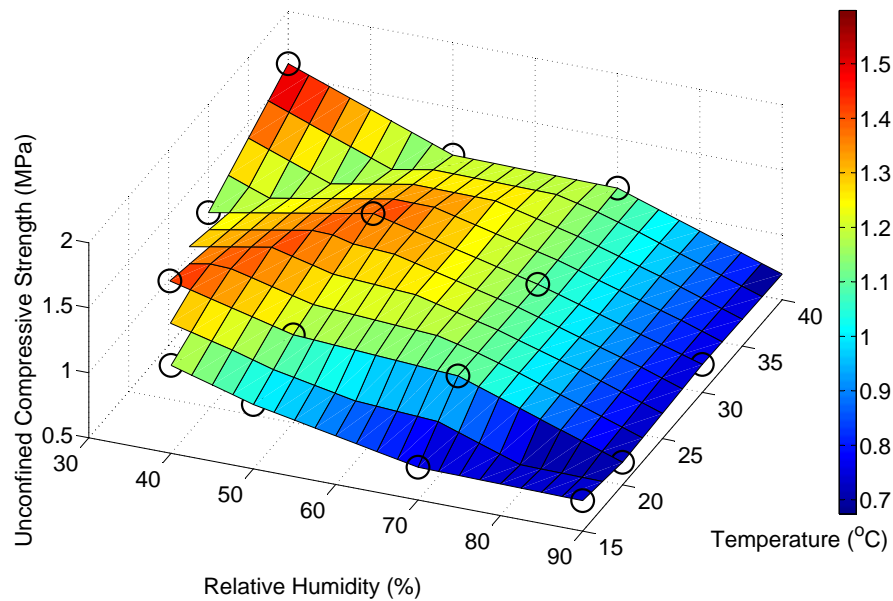


Figure 5.15: Compressive strength against humidity and temperature for mix 5-1-4

makes it stronger; this will be discussed in the following sections.

The maximum compressive strengths found for mixes 5-1-4 and 7-1-2 for the same sample size in Hall and Djerbib (2004), tested to failure after being allowed to stand in a sealed curing chamber for 28 days at 20°C ($\pm 1^\circ\text{C}$) and 75% humidity ($\pm 5\%$), were 1.1 MPa and 0.75 MPa respectively, in that mix 7-1-2 was the weaker, rather than stronger material. These results show good agreement with those found here for mix 5-1-4 (roughly 0.9 MPa for (75%, 20°C)), but not for mix 7-1-2 (roughly 1.0 MPa for (75%, 20°C)), suggesting that the latter was either tested under different conditions or was not manufactured using the same procedures as those used for the mix 5-1-4 samples. Therefore, a direct comparison between the compressive strengths found here and in Hall and Djerbib (2004) is not possible, although comparisons can be made between the result trends.

Samples either lost or gained water during the ECEP depending on the chosen combination of set-points and the sample water content after the IEP. Figures 5.18 and 5.19 show sample unconfined compressive strength against the ECEP water content, indicating whether the cubes were tested at lower (circular markers) or higher (bold square markers) water contents than the IEP value. The highest and lowest unconfined compressive strength values were achieved by samples which lost and gained water with respect to their IEP value respectively. Those samples that showed no appreciable change in water content ($\pm 0.3\%$ of the IEP water content, shown by small square markers) lie roughly between these two regions. This result is supported by those found in Nishimura and Fredlund (2002) for tests conducted on a compacted silty soil at high suctions (Khoury et al., 2010).

Samples of both soil mixes displayed an IEP water content range of roughly 2% due to variations in the equilibration conditions between tests. Therefore, some samples lost water even at the higher humidity values, whilst others may have gained water at the lowest humidity values; this is seen in Figures 5.18 and 5.19 in the large range of water content values (0.67% to 1.64% for mix 5-1-4 and 0.47% to 1.06% for mix 7-1-2) for those datapoints that represent no discernable change in water content between the IEP and ECEP values and in Figure 5.20 for the predicted material SWRCs, which shows both wetting and drying results residing on very similar curves; this is discussed in the following section. However, the overall distribution of the results shown in Figures 5.18 and 5.19 suggests that the effect of the large

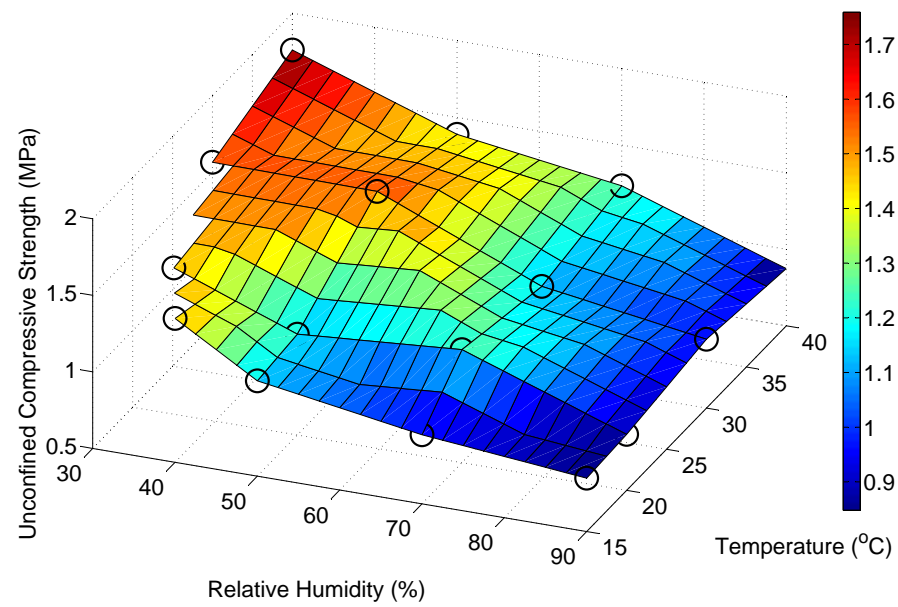


Figure 5.16: Compressive strength against humidity and temperature for mix 7-1-2

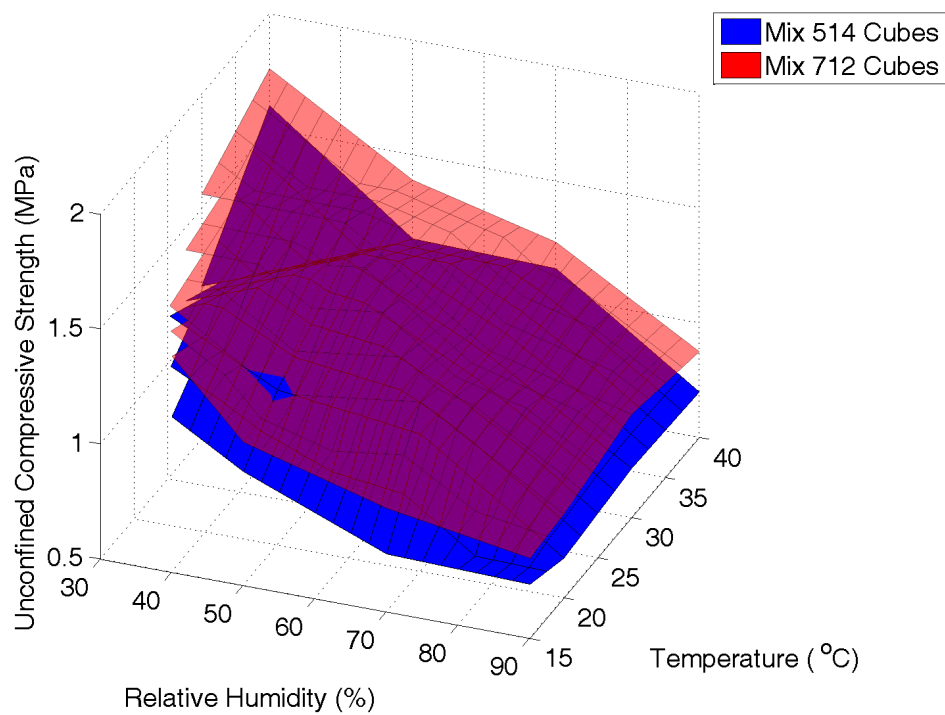


Figure 5.17: Comparison of the compressive strengths of mixes 5-1-4 and 7-1-2 cubes against humidity and temperature

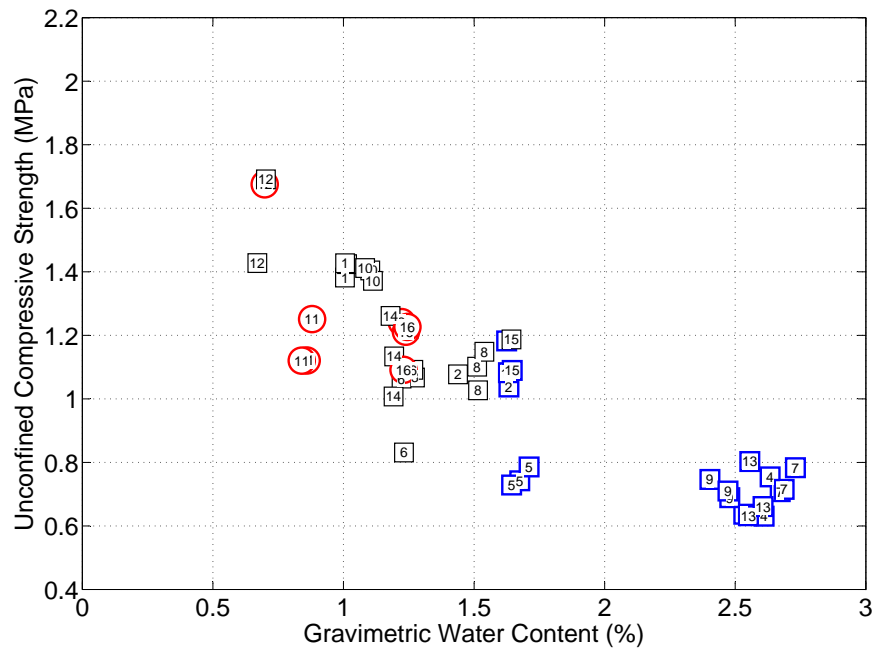


Figure 5.18: Compressive strengths of mix 5-1-4 against cube water content on testing. Marker numbers correspond to test number.

range of IEP water contents is negligible given the duration of the ECEP, so that an equilibration period of 7 days is acceptable for samples used in this investigation. The general trends of the results shown in Figures 5.18 and 5.19 conform well to those for RE samples found by previous investigations (Kirk, 2009; Jaquin, 2010).

The unconfined compressive strengths for setpoints (30%, 15°C) and (30%, 20°C) (test numbers 16 and 1 respectively) appear to conform to the general trend of results as shown in Figures 5.18 and 5.19. As the measured testing water contents for samples used in these tests (52, 53, 54, 79, 80 and 81 for both mixes) suggest that these samples should have failed at lower unconfined compressive strengths than were recorded, it is suggested that these samples were subjected to several wetting and drying cycles, so that their water contents are no longer indicative of the suction conditions present within the material. It is therefore suggested that data corresponding to these tests be ignored when interpreting the surfaces shown in Figures 5.15 to 5.17.

Results for setpoints (50%, 30°C) (test number 10) also appear to conform to the trend shown in Figures 5.18 and 5.19; however, on testing, a significantly greater unconfined compressive strength was found for these samples than for those samples tested at neighbouring setpoint combinations, suggesting that this batch was also in error due to being subjected to multiple wetting and drying cycles. The significantly larger number of batches required to achieve a successful result for this setpoint combination also suggests a protracted environmental chamber failure which could have influenced the test. Accordingly, it is suggested that data corresponding to this test also be ignored interpreting the surfaces shown in Figures 5.15 to 5.17.

It is recommended in New Zealand Standard NZS 4298:1998 that RE mixes have compressive strengths of ≥ 1.3 MPa (NZS 4298:1998 is used as a reference in this case following the work of Hall and Djerbib (2004)). Figures 5.15 to 5.17 show that both mixes achieve this criterion at high temperatures and low humidities (1.60 and 1.76 MPa at (30%, 40°C) respectively), but not at (60%, 20°C), which is more

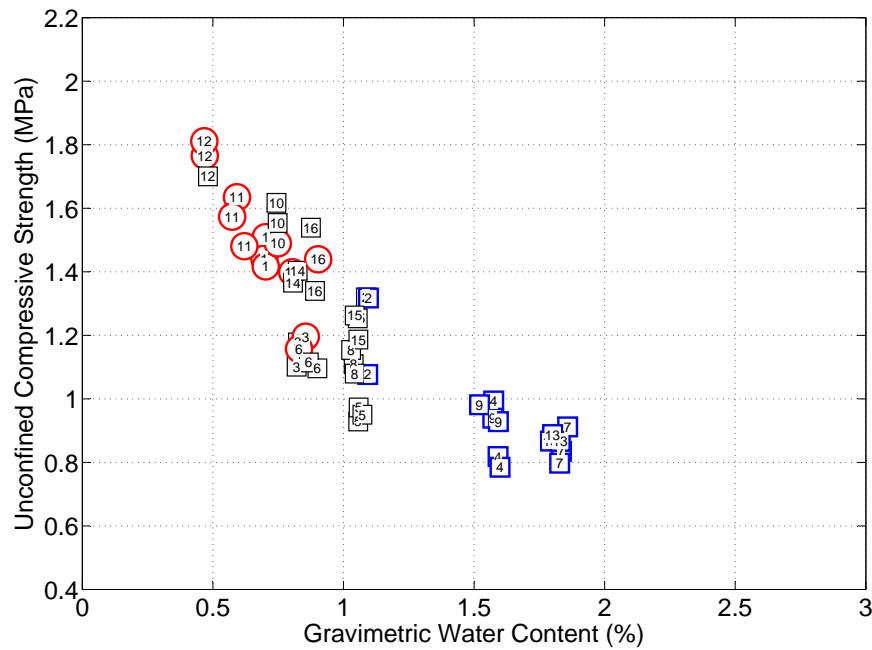


Figure 5.19: Compressive strengths of mix 7-1-2 against cube water content on testing. Marker numbers correspond to test number.

representative of the internal conditions in an RE structure. Care should therefore be taken in specifying compressive strength values as climatic conditions also need to be considered.

5.3.4 Sources of compressive strength

Suction is often cited as the primary source of strength for unsaturated earthen materials (Fisher, 1926; Mason and Clark, 1965; Fisher and Israelachvili, 1979; Mehrotra and Sastry, 1980; Jommi and Sciotti, 2003; Pitois et al., 2001; Kohonen et al., 2004; Rabinovich et al., 2005; Murase et al., 2008; Scholtès et al., 2009). As samples were equilibrated to given humidity and temperature values prior to testing, Eqn 2.18 can be used to determine the suction present in the samples for a given setpoint combination. Note that, in the absence of osmotic effects, the total suction predicted using Eqn 2.18 is equal to the matric suction (Dao et al., 2008). Figure 5.20 shows these calculated suction values against measured ECEP water contents for all of the tested samples (i.e. the SWRC for those water contents investigated). Wetting or drying was determined according to whether water content increased or decreased between the IEP and ECEP respectively. Figure 5.20 suggests that there is little difference between the wetting and drying suctions for both mixes; as suctions are very high (between 14.0 and 173.9 MPa for setpoint combinations (90%, 15°C) and (30%, 40°C) respectively), it is assumed that this is because the wetting and drying SWRC curves are converging, as shown in Figure 2.17. Figure 5.20 also shows that, for any given suction, samples of mix 5-1-4 (whether drying or wetting) have a higher water content than samples of mix 7-1-2; this is consistent with findings of previous authors who found that water contents were higher for given suctions for materials containing greater amounts of clay, due to the increased volume of smaller pores (which can remain filled with water at higher suctions) (Diamond, 1970; Vanapalli et al., 1999; Jaquin et al., 2008; Heath et al., 2009b; Tarantino, 2010; Zhang and Li, 2010).

Table 5.5 gives the equivalent pore diameters for suction values calculated using Eqn 2.18 at a temperature of 20°C (selected so that values can be compared easily). These data show that humidities

below 30% correspond to pore sizes around those thought to be the limit on the size of a body of water in which capillary effects can occur (1.4 nm, Butt and Kappl (2009)). Therefore, it is likely that adsorbed water plays an important role in determining the material strength and that suction is controlled by capillary invasion of the pores between clay particles (for example as idealised by Figure 3.12). Eqn 2.24 can be used to determine the thickness of adsorbed films at those suctions calculated above; these are also shown in Table 5.5. These values show that, at these suctions, films are of the order of one water molecule thick (0.32 nm); in the case of suction at 30% humidity, film thickness has been set to this limiting thickness.

It is possible to determine the amount of adsorbed water in samples of mixes 5-1-4 and 7-1-2 at those suctions given in Table 5.5, assuming that:

- the clay fraction accounts for 50% of the total silty-clay content (Figure 5.4);
- sample material is representative of the total mix proportions;
- the SSA for kaolin is $20 \text{ m}^2/\text{g}$ (based on the fitting to literature values achieved in Figure 3.5);
- adsorbed water content is given by total surface area multiplied by film thickness;
- film thickness is restrained to the critical film thickness (Eqn 3.15) at suctions below the drainage suction for given pore sizes;
- sample density was the optimum for that mix (Table 5.3);
- samples are 0.001 m^3 ;
- sample total water content at a given humidity is the average for that humidity value as given by Figure 5.14.

Results given in Table 5.5 suggest that a greater proportion of the water present in samples of mix 5-1-4 is in the adsorbed phase compared to samples of mix 7-1-2 due to the former's higher clay content, with quantities arguably becoming significant for both mixes as humidity approaches 30% and pore sizes 1.4 nm. Interestingly, although it is assumed that capillary effects become negligible around 1.4 nm, it appears that in both mixes capillary water still makes up the majority of the remaining water content in pores of that size; although the presence of a clay mineral with a higher SSA would significantly increase the adsorbed water content, this result suggests either that the limit on capillarity is smaller for kaolin clays or that adsorbed films in these tight pore spaces are thicker than those predicted by Eqn 2.24. This is, therefore, a topic for further research.

A plot of calculated unconfined compressive strength against total suction is shown in Figure 5.21. These results show that, for a given suction, samples of mix 7-1-2 generally achieve higher unconfined compressive strengths than samples of mix 5-1-4. Regressions of the form

$$\log(\text{UCS}) = 0.27 \log(\psi) - 1.07, R^2 = 0.72 \quad (5.2)$$

$$\log(\text{UCS}) = 0.23 \log(\psi) - 0.78, R^2 = 0.79 \quad (5.3)$$

where UCS is the unconfined compressive strength and ψ is the total suction appear to adequately describe the relationship between unconfined compressive strength and suction in the suction range investigated for mixes 5-1-4 and 7-1-2 respectively. Although the fit to the data achieved by these regressions is not particularly strong, it is suggested that is due to experimental variability and not the use of an inappropriate regression form, so that Eqns 5.2 and 5.3 can be used to roughly describe the change in unconfined compressive strength with total suction for these mixes. Given the values presented

Table 5.5: Equivalent pore diameters (EPDs), adsorbed film thicknesses and adsorbed water contents (AWCs) for suction values calculated at used humidity values and 20°C

Humidity	90%	70%	50%	30%
Suction (MPa)	14.25	48.23	93.72	162.79
EPD (nm)	20.40	6.03	3.10	1.79
Film thickness (nm)	0.607	0.404	0.324	0.320 (0.269)
Mix 5-1-4 AWC (cm ³)	4.66	3.10	2.49	2.46
Mix 5-1-4 AWC (%)	0.24	0.16	0.13	0.13
Mix 5-1-4 ECEP WC (%)	2.60	1.60	1.20	0.80
Mix 5-1-4 AWC (rough % of total WC)	9.2	10.0	10.8	16.3
Mix 7-1-2 AWC (cm ³)	2.36	1.57	1.26	1.25
Mix 7-1-2 AWC (%)	0.12	0.08	0.06	0.06
Mix 7-1-2 ECEP WC (%)	1.70	1.10	0.80	0.60
Mix 7-1-2 AWC (rough % of total WC)	7.1	7.3	7.5	10.0

in Table 5.5, results shown in Figure 5.21 suggest that the effect of an increased proportion of adsorbed water of the total water content is a reduction in the unconfined compressive strength achieved as, for a given suction, relatively less of the water present can contribute to capillarity; this is consistent with observations of many authors, who suggest that it is capillary water and not the adsorbed phase that contributes to strength and who observe that, at the lowest water contents where it is thought that all water is found in the adsorbed phase, material strengths become negligible (Bolton, 1991; Hillel, 1998; Gallipoli et al., 2003; Toll and Ong, 2003; Wheeler et al., 2003; Hillel, 2004; Lu and Likos, 2004; Mitchell and Soga, 2005).

Figures 5.22 and 5.23 show results for the unconfined compressive strength against sample ECEP water content (the former on linear and the latter on logarithmic axes). Again, relationships of the form

$$\log(\text{UCS}) = -0.61 \log(\text{WC}) + 9.46, R^2 = 0.75 \quad (5.4)$$

$$\log(\text{UCS}) = -0.56 \log(\text{WC}) + 9.37, R^2 = 0.83 \quad (5.5)$$

(where WC is the water content) suggestably describe the relationship between the unconfined compressive strengths and water content in the suction range investigated for mixes 5-1-4 and 7-1-2 respectively. It is assumed that Eqns 5.4 and 5.5 (and indeed Eqns 5.2 and 5.3) are very similar due to the use of the same raw materials and compaction regimes; clearly, if either of these were changed then the two functions would become dissimilar. However, a function of this type again appears to be appropriate for describing the change in unconfined compressive strength with water content for RE mixes under those conditions investigated. Although quite a similar quality of fit is achieved, Eqns 5.4 and 5.5 are of more use to earthen construction than Eqns 5.2 and 5.3 as water content is significantly easier to determine than suction and can be measured and monitored using equipment available on site. This is of particular importance to earthen construction as the strength of a material can be easily predicted if the required coefficients (which will vary depending on the material) are known. Although material strengths will not increase indefinitely with reducing water content as suggested by Eqns 5.4 and 5.5, earthen structures are not likely to ever experience conditions outside of the range of those tested (Figure 5.3) so that this is arguably not a concern when determining the suitability of these relationships, although caution should be exercised if extrapolating relationships to water contents outside of the investigated range.

The role of clay in compacted soils is often considered equivalent to that of a binding fraction in concrete, so that it is thought to be responsible for cementation phenomena between particles (Lambe,

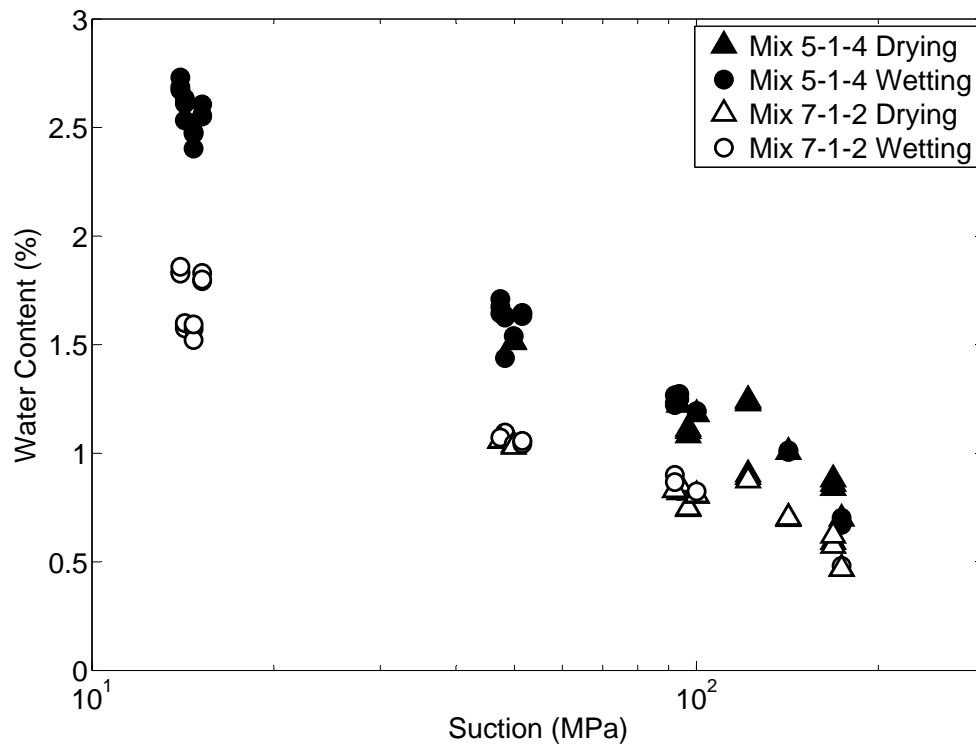


Figure 5.20: Calculated wetting and drying SWRCs for mixes 5-1-4 and 7-1-2

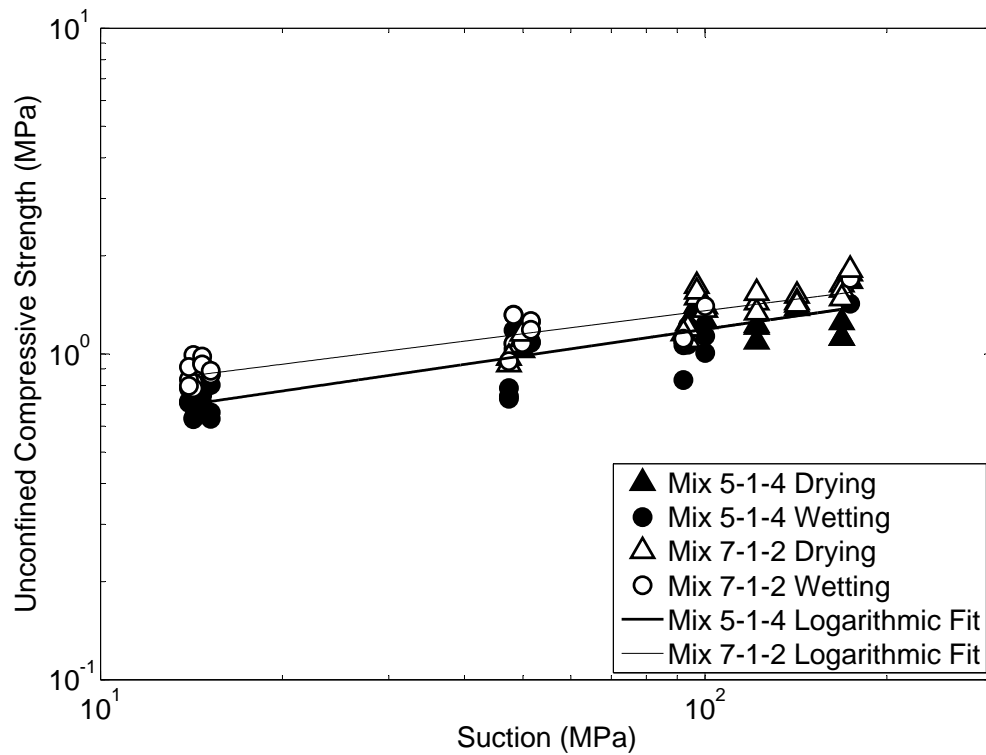


Figure 5.21: Compressive strengths of mixes 5-1-4 and 7-1-2 against calculated suction

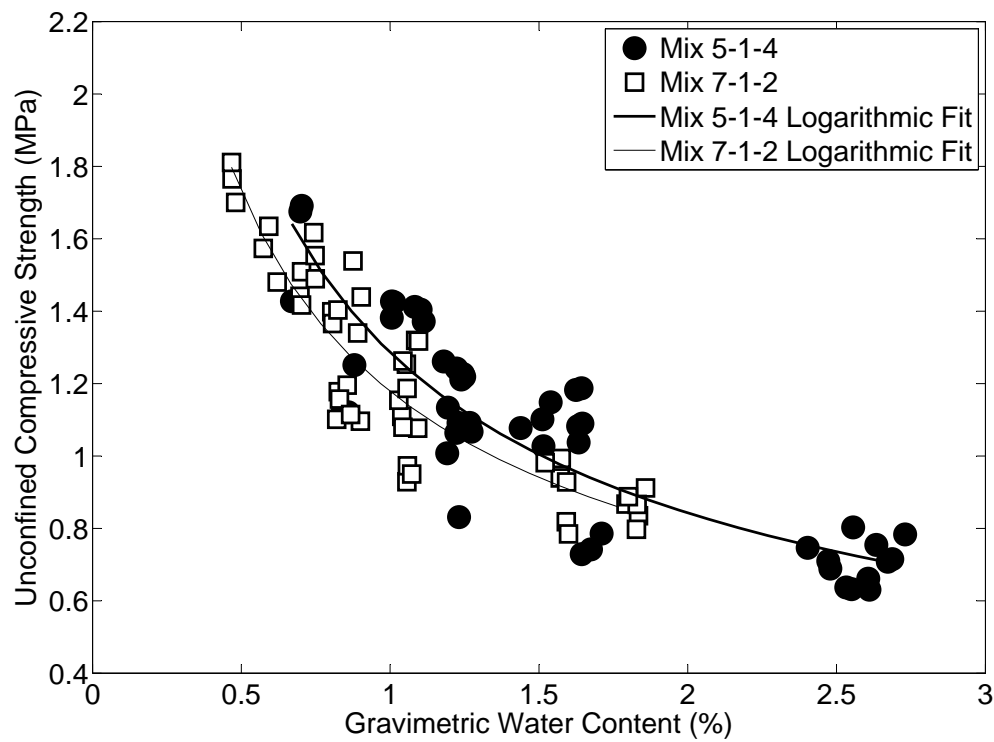


Figure 5.22: Compressive strengths of mixes 5-1-4 and 7-1-2 against water content on testing

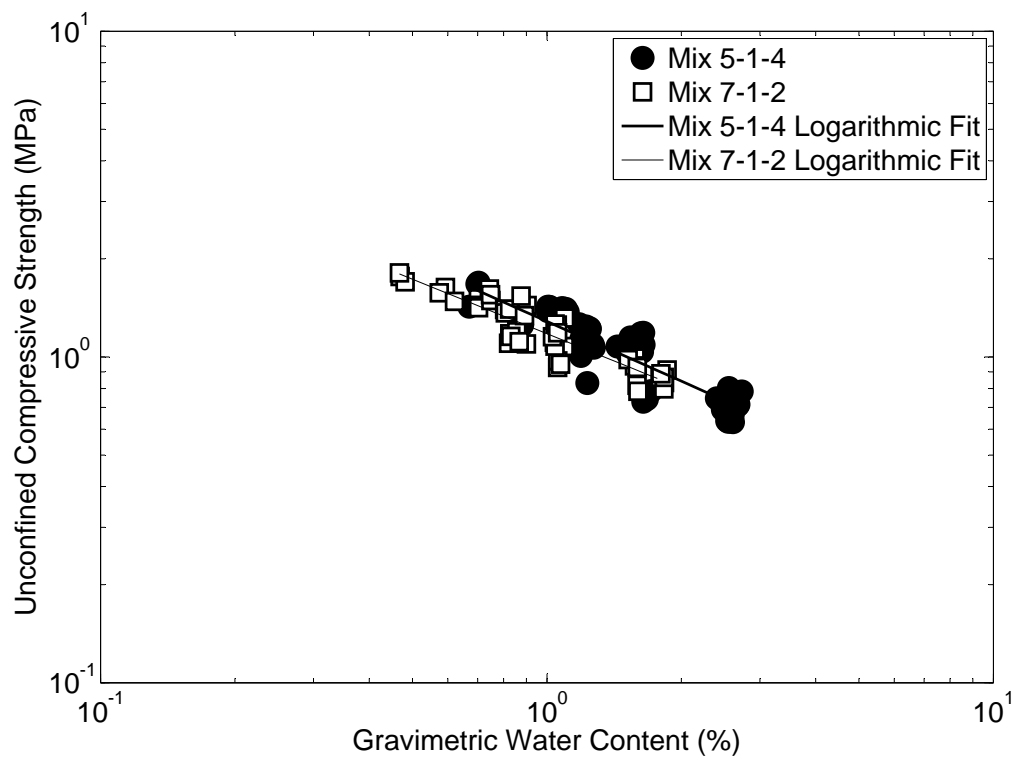


Figure 5.23: Compressive strengths of mixes 5-1-4 and 7-1-2 against water content on testing

1960; Barden et al., 1973; Keable, 1996; Morel et al., 2001; Maniatidis and Walker, 2003; Keefe, 2005; Bui and Morel, 2009; Quagliarini et al., 2010); indeed, in some RE literature, sample drying is referred to as “curing”, in order to emphasise the assumed similarity between the roles of the clay and cement fractions (Hall and Djerbib, 2004). The binding properties of the clay fraction are attributed to the high surface charge and specific surface area of the clay particles which gives them a high affinity for retaining water (Hillel, 1998, 2004; Mitchell and Soga, 2005). However, as discussed above an increase or a decrease in the clay content of a soil results in the increase or decrease in the volume of small pores, so that greater or lower suctions are required to achieve a given water content respectively. Therefore, a different interpretation of the role of clay would be that it influences the suction generated within the material (and its corresponding water content), so that cementation effects are, in fact, already accounted for by considering suction.

5.4 Conclusion

In this chapter, an experimental programme has been described to manufacture RE samples in order to investigate the effect of temperature and humidity on the unconfined compressive strength of RE.

An investigation into the locations of historic and modern (pre- and post-19th century) RE sites has shown that RE structures are now subjected to a significantly wider range of climatic conditions than they have been in the past. Therefore, an understanding of how these conditions affect the strength of the material and an appreciation of the need to incorporate climatic conditions into design practices are required.

Results suggest that a linear relationship exists between the water content on equilibration to a given humidity and temperature and the material clay content for those clay mineralogies investigated. Therefore, it should be possible to predict the final water content of an RE mix of known constituents, and so its unconfined compressive strength, given a known humidity.

Results show that samples of mix 7-1-2 achieve higher unconfined compressive strengths than those of mix 5-1-4 for a given suction, determined via the Kelvin equation and that, for a given suction, water contents are higher in mix 5-1-4 than in mix 7-1-2. A simplistic assessment of the quantity of adsorbed water present in samples of the two investigated mixes also suggests that the proportion of water present in the adsorbed phase in samples of mix 5-1-4 is greater than in those of mix 7-1-2, due to the higher clay content of the former material, and that an increase in the relative amount of adsorbed water produces a reduction in unconfined compressive strength due to a reduced quantity of capillary water. This also suggests that capillary effects are still present at very high suctions in those materials tested despite equivalent pore diameters being close to the assumed limit of capillarity of 1.4 nm; this is therefore a topic which requires further work in order to be fully understood.

It was found that the relationship between unconfined compressive strength and water content for both investigated mixes can be adequately described by an exponential regression; this is highly useful to earthen construction as water content is significantly easier to determine than suction and allows the strength of a given material to be predicted assuming that the required coefficients are known. Although material strengths will not increase indefinitely with reducing water content as suggested by such a relationship, it is likely that an exponential regression is suitable for all equilibrium water contents likely to be encountered in earthen structures.

It has been shown that the unconfined compressive strength of RE depends on the conditions in which it resides; therefore, the stating of a required material compressive strength for RE materials, for example as in NZS 4298:1998, should either be avoided or substantiated, as some materials that are deemed acceptable under some conditions might become unacceptable under others.

5.5 References

- Abdullah, W. S., Alshibli, K. A., Al-Zou'bi, M. S., 1999. Influence of pore water chemistry on the swelling behavior of compacted clays. *Applied Clay Science* 15 (5-6), 447–462.
- Allinson, D., Hall, M., 2010. Hygrothermal analysis of a stabilised rammed earth test building in the uk. *Energy and Buildings* 42, 845–852.
- Azmach, T. F., Sego, D. C., Arenson, L. U., Biggar, K. W., 2011. Tensile strength and stress-strain behaviour of devon silt under frozen fringe conditions. *Cold Regions Science and Technology* In Press, Corrected Proof, –.
- Barden, L., McGown, A., Collins, K., 1973. The collapse mechanism in partly saturated soil. *Engineering Geology* 7 (1), 49–60.
- Beckett, C. T. S., 2008. Cracking in rammed earth. MEng Dissertation, Durham University, Durham, UK.
- Bolton, M., 1991. A guide to soil mechanics. M D & K Bolton.
- BSI, 1990. BS 1377:1990. Methods of test for soils for civil engineering purposes.
- BSI, 2000. BS EN 772-:2000 Methods of test for masonry units. Determination of compressive strength.
- BSI, 2002. BS EN 12390-3:2002. Testing hardened concrete. Compressive strength of test specimens.
- Bui, Q.-B., Morel, J.-C., 2009. Assessing the anisotropy of rammed earth. *Construction and Building Materials* 23 (9), 3005–3011.
- Buscarnera, G., Nova, R., September 2010. Saturation induced instability on bonded geomaterials. In: Alonso, E., Gens, A. (Eds.), *Unsaturated Soils. Fifth International Conference on Unsaturated Soils*, CRC Press, pp. 771–777.
- Butt, H.-J., Kappl, M., 2009. Normal capillary forces. *Advances in Colloid and Interface Science* 146 (1-2), 48–60.
- Chae, J., Kim, B., Park, S.-w., Kato, S., 2010. Effect of suction on unconfined compressive strength in partly saturated soils. *KSCE Journal of Civil Engineering* 14 (3), 281–290.
- Dao, V. N. T., Morris, P. H., Dux, P. F., 2008. On equations for the total suction and its matric and osmotic components. *Cement and Concrete Research* 38 (11), 1302–1305.
- Diamond, S., 1970. Pore size distribution in clays. *Clays and Clay Minerals* 18, 7–23.
- Easton, D., 2007. *The Rammed Earth House, Completely Revised Edition*. Chelsea Green Publication Company, Vermont (USA).
- Fisher, L. R., Israelachvili, J. N., 1979. Direct experimental verification of the Kelvin equation for capillary condensation. *Nature* 277 (5697), 548–549.
- Fisher, R. A., 1926. On the capillary forces in an ideal soil; correction of formulae given by W. B. Haines. *The Journal of Agricultural Science* 16 (03), 492–505.
- Fredlund, D. G., 2006. Unsaturated soil mechanics in engineering practice. *Journal of Geotechnical and Geoenvironmental Engineering* 132 (3), 286–321.
- Gallipoli, D., Gens, A., Sharma, R., Vaunat, J., 2003. An elasto-plastic model for unsaturated soil incorporating the effects of suction and degree of saturation on mechanical behaviour. *Géotechnique* 53 (1), 123–135.
- Gelard, D., Fontaine, L., Maximilien, S., Olagnon, C., Laurent, J., Houben, H., Van Damme, H., 2007. When physics revisit earth construction: Recent advances in the understanding of the cohesion mechanisms of earthen materials. In: *Proc. International Symposium on Earthen Structures*, IIS Bangalore, 22-24 August 2007. pp. 294–302.
- Hall, M., Djerbib, Y., 2004. Rammed earth sample production: context, recommendations and consistency. *Construction and Building Materials* 18 (4), 281–286.
- Heath, A., Lawrence, M., Walker, P., Fourie, C., September 2009a. The compressive strength of modern earth masonry. In: *Proceedings of the 11th International Conference on Non-Conventional Materials and Technologies (NOCMAT)*. Bath University.
- Heath, A., Walker, P., Fourie, C., Lawrence, M., 2009b. Compressive strength of unfired clay masonry units. *Proceedings of the Institute of Civil Engineers: Construction Materials* 162 (3), 105–112.
- Heathcote, K., Jankulovski, E., 1992. Aspect ratio correction factors for soilcrete blocks. *Australian civil engineering transactions* CE34 (4: Australia: Institution of Engineers), 309–312.
- Hillel, D., 1998. *Environmental Soil Physics*. Academic Press, California (USA).
- Hillel, D., 2004. *Fundamentals of Soil Physics*. Academic Press, Inc., London (UK).
- Houben, H., Guillaud, H., 1996. *Earth construction - a comprehensive guide.*, Second Edition. Intermediate Technology Publications, London (UK).
- Jaquin, P. A., 2008. Analysis of historic rammed earth construction. PhD Thesis, Durham University.
- Jaquin, P. A., 2010. How mud bricks work - using unsaturated soil mechanics principles to explain the material properties of earth buildings - a year of research. In: *From small steps to giant leaps - putting research into practice*.
- Jaquin, P. A., Augarde, C. E., Gallipoli, D., Toll, D. G., 2009. The strength of unstabilised rammed earth materials. *Géotechnique* 59 (5), 487–490.

- Jaquin, P. A., Augarde, C. E., Legrand, L., 2008. Unsaturated characteristics of rammed earth. In: Toll, D. G. (Ed.), *First European Conference on Unsaturated Soils*. Durham University, Durham, England, pp. 417–422.
- Jommi, C., Sciotti, A., Sep 23-26 2003. A study of the microstructure to assess the reliability of laboratory compacted soils as reference material for earth constructions. In: Bontempi, F. (Ed.), *2nd International Conference on Structural and Construction Engineering*. A A Balkema Publishers, Rome, Italy, pp. 2409–2415.
- Keable, J., 1996. *Rammed earth structures: a code of practice*. Intermediate Technology Publications, London (UK).
- Keefe, L., 2005. *Earth Building: Methods and materials, repair and conservation*. Taylor & Francis, Oxford UK.
- Khoury, C. N., Miller, G. A., Hatami, K., Feb. 2010. Shear strength of unsaturated soil-geotextile interfaces. In: *ASCE Conf. Proc. Vol. 365*. ASCE, West Palm Beach, Florida, pp. 28–28.
- King, B., 1996. *Buildings of Earth and Straw: Structural Design for Rammed Earth and Straw-Bale Architecture*. Ecological Design Press, Sausalito, California (USA).
- Kirk, H., 2009. *The behaviour of low plasticity rammed earth soils*. Masters Thesis, Imperial College London.
- Kohonen, M. M., Geromichalos, D., Scheel, M., Schier, C., Herminghaus, S., 2004. On capillary bridges in wet granular materials. *Physica A: Statistical Mechanics and its Applications* 339 (1-2), 7–15.
- Krefeld, 1938. Effect of shape of specimen on the apparent compressive strength of brick masonry. In: *Proceedings of the American Society of Materials*, Philadelphia, USA. pp. 363–369.
- Lambe, T. W., 1960. A mechanistic picture of shear strength in clay. In: *Research Conference on the Shear Strength of Cohesive Soils*. ASCE, University of Boulder, Colorado (USA), pp. 555–580.
- Lilley, D. M., Robinson, J., 1995. Ultimate strength of rammed earth walls with openings. *Proceedings of the Institution of Civil Engineers-Structures and Buildings* 110 (3), 278–287.
- Lu, N., Likos, W. J., 2004. *Unsaturated Soil Mechanics*. John Wiley & Sons, Inc., New Jersey (USA).
- Lu, N., Wu, B., Tan, C. P., 2007. Tensile strength characteristics of unsaturated sands. *Journal of Geotechnical and Geoenvironmental Engineering* 133 (2), 144–154.
- Maniatidis, V., Walker, P., 2003. *A Review of Rammed Earth Construction*. University of Bath.
- Mason, G., Clark, W., 1965. Liquid bridges between spheres. *Chemical Engineering Science* 20 (10), 859–866.
- Mehrotra, V., Sastry, K., 1980. Pendular bond strength between unequal-sized spherical particles. *Powder Technology* 25 (2), 203–214.
- Mitchell, J. K., Soga, K., 2005. *Fundamentals of Soil Behaviour*, Third Edition. John Wiley & Sons Inc., Hoboken, New Jersey (USA).
- Morel, J. C., Mesbah, A., Oggero, M., Walker, P., 2001. Building houses with local materials: means to drastically reduce the environmental impact of construction. *Building and Environment* 36 (10), 1119–1126.
- Morel, J.-C., Pkla, A., Walker, P., 2007. Compressive strength testing of compressed earth blocks. *Construction and Building Materials* 21 (2), 303–309.
- Morton, T., Stevenson, F., Taylor, B., Charlton Smith, N., 2005. *Low cost earth brick construction*, 2 Kirk Park, Dalguise: Monitoring and Evaluation. Tech. rep., Arc Architects, Auchtermuchty, Fife.
- Murase, K., Mochida, T., Sagawa, Y., Sugama, H., 2008. Estimation on the strength of a liquid bridge adhered to three spheres. *Advanced Powder Technology* 19 (4), 349–367.
- Nishimura, T., Fredlund, D. G., March 2002. Hysteresis effects resulting from drying and wetting under relatively dry conditions. In: Juça, de Campos, Marinho (Eds.), *Unsaturated Soils*. Third International Conference on Unsaturated Soils, Swets and Zeitlinger, Lisse, Recife, Brazil.
- NZS, 1998. NZS 4298:1998. *Materials and workmanship for earth buildings incorporating amendment no. 1*.
- Peel, M. C., Finlayson, B. L., McMahon, T. A., 2007. Updated world map of the Köppen-Geiger climate classification. *Hydrology and Earth System Sciences* 11, 1633–1644.
- Pitois, O., Moucheron, P., Chateau, X., 2001. Rupture energy of a pendular liquid bridge. *The European Physical Journal B - Condensed Matter and Complex Systems* 23 (1), 79–86.
- Pradhan, B., Nagesh, M., Bhattacharjee, B., 2005. Prediction of the hydraulic diffusivity from pore size distribution of concrete. *Cement and Concrete Research* 35 (9), 1724–1733.
- Quagliarini, E., Lenci, S., Iorio, M., 2010. Mechanical properties of adobe walls in a Roman republican domus at Suasa. *Journal of Cultural Heritage* 11 (2), 130–137.
- Rabinovich, Y. I., Esayanur, M. S., Moudgil, B. M., 2005. Capillary forces between two spheres with a fixed volume liquid bridge: Theory and experiment. *Langmuir* 21 (24), 10992–10997.
- Rahimi, H., Pazira, E., Tajik, F., 2000. Effect of soil organic matter, electrical conductivity and sodium adsorption ratio on tensile strength of aggregates. *Soil & Tillage Research* 54 (3-4), 145–153.

- Reynolds, W. D., Drury, C. F., Tan, C. S., Fox, C. A., Yang, X. M., 2009. Use of indicators and pore volume-function characteristics to quantify soil physical quality. *Geoderma* 152 (3-4), 252–263.
- Scholtès, L., Hicher, P., Nicot, F., Chareyre, B., Darve, F., 2009. On the capillary stress tensor in wet granular materials. *International Journal for Numerical and Analytical Methods in Geomechanics* 33 (10), 1289–1313.
- Tarantino, A., 2009. A water retention model for deformable soils. *Géotechnique* 59 (9), 751–762.
- Tarantino, A., 2010. Unsaturated soils: compaction versus reconstituted states. In: Alonso, E., Gens, A. (Eds.), *Unsaturated soils. Fifth International Conference on Unsaturated Soils*, CRC Press, pp. 113–136.
- Tarantino, A., De Col, E., 2008. Compaction behaviour of clay. *Géotechnique* 58 (3), 199–213.
- Thom, R., Sivakumar, R., Sivakumar, V., Murray, E. J., Mackinnon, P., 2007. Pore size distribution of unsaturated compacted kaolin: the initial states and final states following saturation. *Géotechnique* 57 (5), 469–474.
- Toll, D. G., 1999. A data acquisition and control system for geotechnical testing. In: Toll, D. (Ed.), *Computing developments in civil and structural engineering*. Civil-Comp Press Ltd.
- Toll, D. G., Ong, B. H., 2003. Critical-state parameters for an unsaturated residual sandy clay. *Géotechnique* 53, 93–103.
- Utomo, W. H., Dexter, A. R., 1981. Soil friability. *Journal of Soil Science* 32 (2), 203–213.
- Vanapalli, S. K., Fredlund, D. G., Pufahl, D. E., 1999. The influence of soil structure and stress history on the soil-water characteristics of a compacted till. *Géotechnique* 49 (2), 143–159.
- Walker, P., Keable, R., Martin, J., Maniatis, V., 2005. *Rammed Earth: Design and Construction Guidelines*. BRE Bookshop, Watford (UK).
- Wheeler, S. J., Sharma, R. S., Buisson, M. S. R., 2003. Coupling of hydraulic hysteresis and stress-strain behaviour in unsaturated soils. *Géotechnique* 53 (1), 41–54.
- Young, I. M., Mullins, C. E., 1991. Factors affecting the strength of undisturbed cores from soils with low structural stability. *European Journal of Soil Science* 42 (2), 205–217.
- Zhang, L. M., Li, X., 2010. Microporosity structure of coarse granular soils. *J. Geotech. and Geoenviron. Engrg.* 136 (10), 1425–1436.

Chapter 6

The effect of changing salinity on the tensile strength of rammed earth

6.1 Introduction

Chapter 5 discussed the locations of several rammed earth (RE) sites around the world and showed that they are predominantly found in arid or semi-arid regions (see Figure 5.1). Soils in these regions potentially contain high concentrations of dissolved ions due to the use of deep water sources. Particle surface properties are strongly dependent on the presence of “exchangeable” ions (Dexter and Chan, 1991; Kay and Dexter, 1992; Barzegar et al., 1994a,b; Chorom et al., 1994; Barzegar et al., 1995a,b). The addition of cations which form large complex molecules in the presence of water (usually low-valency cations, for example solvated Sodium ions) to a clay will result in a deflocculated clay structure due to increased repulsion between the particles (i.e. larger interparticle pores). Conversely, the addition of cations which form small complex molecules (usually higher valency cations, for example solvated Calcium ions), will increase the attraction between clay particles, resulting in a flocculated clay structure (Dexter and Chan, 1991; Grant et al., 1992; Sivakumar and Wheeler, 2000; Hillel, 2004). These changes in the modal sizes of the soil micropores can have a profound influence on the mechanical behaviour of the soil and so are of particular concern to RE (Dexter and Chan, 1991; Barzegar et al., 1994b, 1995a; Rahimi et al., 2000; Prashant and Penumadu, 2007). In this chapter, tensile strength tests are conducted on RE samples containing varying concentrations of dissolved ions in order to determine their impact on RE construction. Although it is usual to compare RE materials according to their unconfined compressive strengths, the tensile strength is used here in order to determine how these materials behave in tension, a property that is regularly overlooked, and to determine whether any relation exists between the unconfined compressive and tensile strengths.

6.2 The Brazilian test for testing the tensile strength of soils

Direct and indirect methods exist for determining the tensile strength of soil specimens (e.g. Leonards and Narain, 1963; Ajaz and Parry, 1974; Krishnayya and Eisenstein, 1974; Ajaz and Parry, 1975b; Dexter and Kroesbergen, 1985; Tamrakar et al., 2005, 2007b,a). The “direct pull test” and “bending” tests are examples of direct testing methods and are capable of being interpreted to give stress-strain characteristics without the need to assume a preferred stress-strain law (Ajaz and Parry, 1975a). However, in the direct pull test stress concentrations at the specimen grips can lead to failure cracks developing close to the contact points and an early onset of failure. Furthermore, geometrical imperfections can lead

to a non-uniform stress distribution across the rupture plane at failure, resulting in misleading tensile strengths (Coviello et al., 2005). Stress concentrations also arise during bending tests (both three- and four-point tests), again leading to misleading results (Ajaz and Parry, 1975c). Furthermore, the bending test is sensitive to compaction planes, making it unsuitable for specimens of RE which are formed from multiple compacted layers (Krishnayya and Eisenstein, 1974, 1975).

Indirect testing methods require tensile strengths to be calculated from assumed stress-strain behaviours, but have the advantage of not requiring the specimen to be gripped. The Brazilian test is a popular test for determining the indirect tensile strength of soils and soft rocks due to the simplicity of the experimental apparatus and the ease with which samples can be prepared (Coviello et al., 2005; Aydin and Basu, 2006). In this test, compressive loads are applied diametrically to cylindrical samples, as shown in Figure 6.1, so that failure occurs in tension along the diameter contained in the plane formed by the two platens (Frydman, 1964). Note that in Figure 6.1, curved loading platens are shown; loading can be applied by either flat or curved platens with no effect on the accuracy of the resulting calculated tensile strengths, although curved platens are more common due to the increased ease in aligning the sample (Frydman, 1964; Coviello et al., 2005).

The applicability of the Brazilian test for determining the tensile strength of soils was investigated in Frydman (1964) and a simple criterion for acceptability was presented. As the compressive strength of soils is lower than that of soft rocks, deformation of the sample at the points where the platens contact the sample, which occurs if either flat or curved platens are used, must be taken into account, as shown in Figure 6.2 (Frydman, 1964). Deformations shown are those for the use of a flat platen; loading using flat platens initially places a point load on the contacted surface, whereas curved platens result in a distributed load. However, deformation of the sample leads to distributed loads being present in both cases so that the analysis is applicable to both platen types. It was found that if $\frac{a}{y_1} < 0.27$, where a and y_1 are as shown in Figure 6.2, the tensile stress σ_t along the central axis of the specimen is adequately described by

$$\sigma_t = \frac{2P}{\pi Dt} \quad (6.1)$$

where P is the applied compressive load, D is the diameter of the sample and t is the sample thickness.

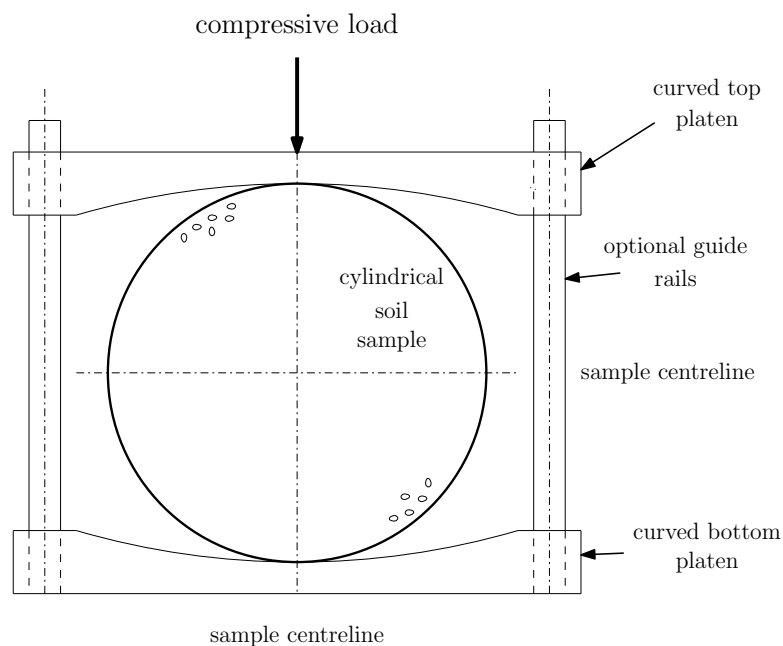


Figure 6.1: Example Brazilian test apparatus

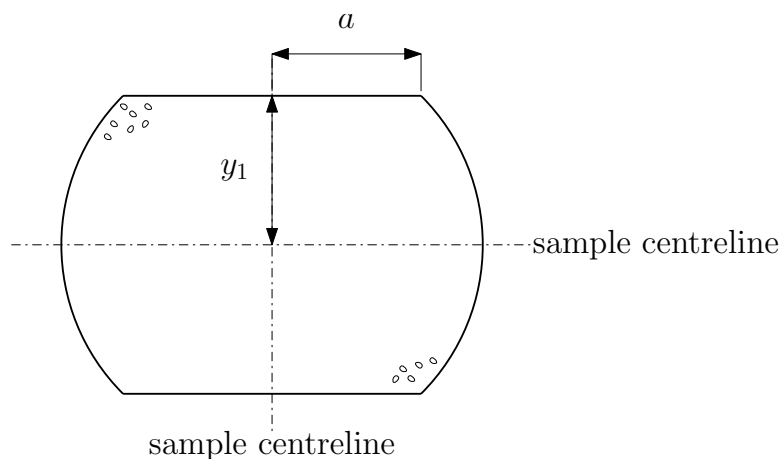


Figure 6.2: Deformation of a Brazilian test sample under loading, after Frydman (1964)

Failure of samples is indicated by the presence of a peak load which occurs prior to the formation of a tensile crack. Eqn 6.1 assumes that the material is behaving as an elastic material under a point load and that no deformation takes place (Carneiro and Barcellos, 1953) and is accurate to within the accuracy of the test method, given as a coefficient of variation of 10% by Frydman (1964). The applicability of Eqn 6.1 to soils was shown in Frydman (1964) through tests on various soil types. It was found that Eqn 6.1 adequately predicts the tensile strengths of all tested soils at a large range of water contents, except those which show very plastic behaviour, for example montmorillonitic clays. For a more detailed analysis of these results the reader is referred to Table 1 of Frydman (1964). As RE has a low clay content and hence a lower plasticity compared to samples tested in Frydman (1964), it can be assumed that the Brazilian test is appropriate for determining the tensile strength of RE samples.

A diagrammatic example of a tensile crack caused by a hogging structural displacement observed in an RE structure in Ambel, Spain is shown in Figure 6.3(a) (similar cracks are shown in Figure 8.5) (Jaquin, 2008). Cracking in a Brazilian test sample is analogous to a tension crack forming on the vertical surface of a wall and then propagating horizontally through the material, parallel to the compaction planes, as shown in Figure 6.3(b). It is assumed that the resistance to cracking in the horizontal direction (Figure 6.3(b)) is less than that in the vertical direction (Figure 6.3(a)) due to the orientation of the compaction planes, so that tensile strengths determined using the Brazilian test represent a conservative case for cracking in RE structures (Ajaz and Parry, 1975b; Krishnayya and Eisenstein, 1975; Bui and Morel, 2009).

6.3 Experimental procedure

This section describes the procedures used to prepare RE samples for testing, using the Brazilian method, at a range of water contents and dissolved ion concentrations.

6.3.1 Sample size selection

Brazilian tests on RE soil mixes were conducted in Jaquin et al. (2008), using samples of 50 mm diameter and 25 mm thickness. An investigation into the suitable size of RE samples for use with the Brazilian test was conducted in Beckett (2008) using mixes 5-1-4 and 7-1-2 and it was found that the use of sample sizes used in Jaquin et al. (2008) resulted a wide range of tensile strengths for given sample water contents. This was due to large particles in the soil mix (of the order of 10 mm in Beckett (2008) but roughly 14 mm in Jaquin et al. (2008)) interfering with the profile of the failure crack, as shown in Figure 6.4(a),

causing it to follow a more tortuous path and so changing the failure load. It was found that the use of 100 mm diameter by 50 mm thick samples reduced the influence of the larger particles on the profile of the failure crack, so that it lay roughly on a vertical plane between the two platens, as shown in Figure 6.4(b). 100 mm diameter by 50 mm thick samples are therefore used in this investigation.

6.3.2 Soil mix preparation

Soil mixes 5-1-4 and 7-1-2 were selected following work conducted in Beckett (2008) and to compare values for the measured tensile strengths to those for the compressive strengths found for the same soil mixes in Chapter 5. Dried silty-clay, sharp sand and pea gravel were combined in the appropriate proportions to form the two soil mixes.

The silty-clay used for soil mix preparation was obtained from the Newcastle University Biological and Engineering Impacts of Climate Change on Slopes (“BIONICS”) embankment project (LL 43.3%, PL 23.7%, PI 19.6%). The primary clay mineral type is kaolinite and the material contains roughly

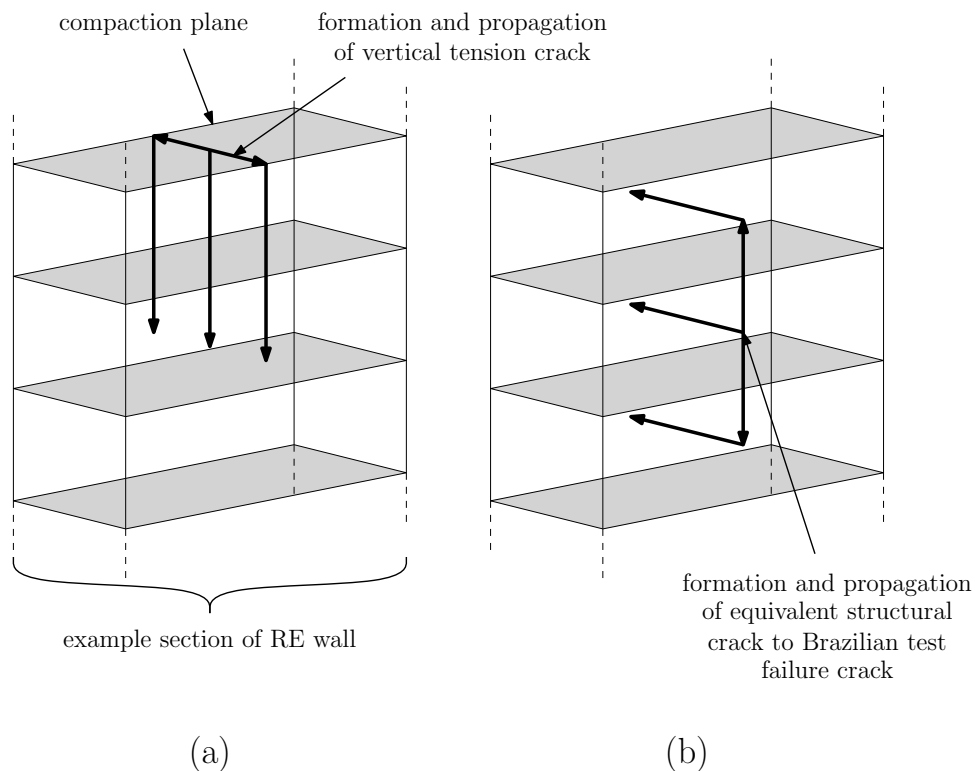


Figure 6.3: Cracking in an RE structure compared to the Brazilian test

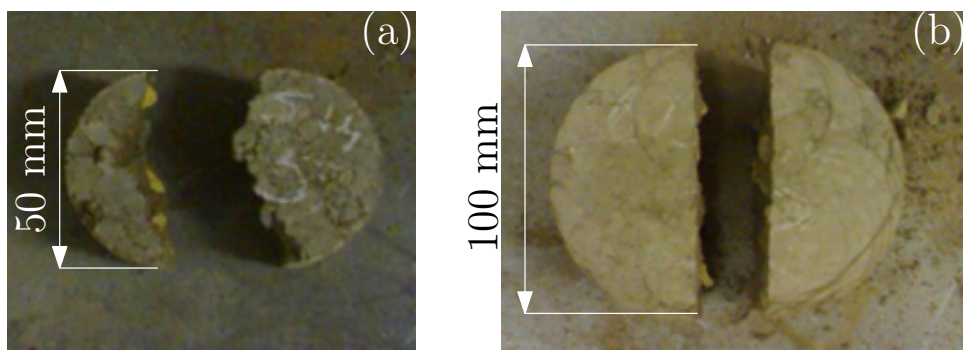


Figure 6.4: Cracking in: a) 50 mm diameter Brazilian test sample; b) 100 mm diameter Brazilian test sample.

50% clay particles by mass of silty-clay particles (i.e. those smaller than $60\mu\text{m}$ (BS1377:1990)) so that it is very similar to the Birtley clay used for sample manufacture in Chapter 5 (Mendes, 2011). The dried silty-clay, sand and gravel mix components were prepared according to the procedures given in Section 5.2.2. Figure 6.5 shows the particle grading curves of the three raw materials. The resulting particle grading curves for the freshly prepared soil mix material, along with the recommended limits on the particle grading specified by Houben and Guillaud (1996), are shown in Figure 6.6, showing that the grading curves for the two soil mixes lie roughly on those limits, with mixes 5-1-4 and 7-1-2 containing the maximum and minimum recommended silty-clay content respectively. The final relative proportions of sand, gravel and silty-clay (as determined by wet sieving) according to the limits on particle sizes as specified by BS1377:1990) in the final soil mixes are shown in Table 6.1, showing that the theoretical and measured mix constituent contents are in good agreement.

The optimum water content (OWC), maximum dry and maximum bulk densities ($\rho_{d_{max}}$ and $\rho_{b_{max}}$ respectively) for the two soil mixes were determined using the results given in Figure 6.7 and are summarised in Table 6.2. Values were determined using the light Proctor compaction test (BS1377:1990) in order to compare tensile strength results to compressive results found for the RE mixes used in Chapter 5. A greater change in dry density with water content is found for mix 5-1-4 than for 7-1-2; as discussed in Chapter 5, this is due to the more-aggregated structure of mix 5-1-4 prior to compaction (Tarantino, 2010). A clearly-defined peak dry density for mix 7-1-2 is not present, however a slight peak does exist at roughly 12% so that it has been selected as the OWC.

The effect of fines loss on the soil mixes was determined by comparing the particle grading curves of fresh soil mix material to those of material that had previously been wetted and then dried. Wet material

Table 6.1: Relative particle size category amounts for soil mixes 5-1-4 and 7-1-2.

Soil mix	Sand (0.06 to 2 mm) (%)	Gravel (>2 mm) (%)	Silty-Clay (<0.06 mm) (%)
5-1-4	52.6	10.0	37.4
7-1-2	75.4	7.3	17.3

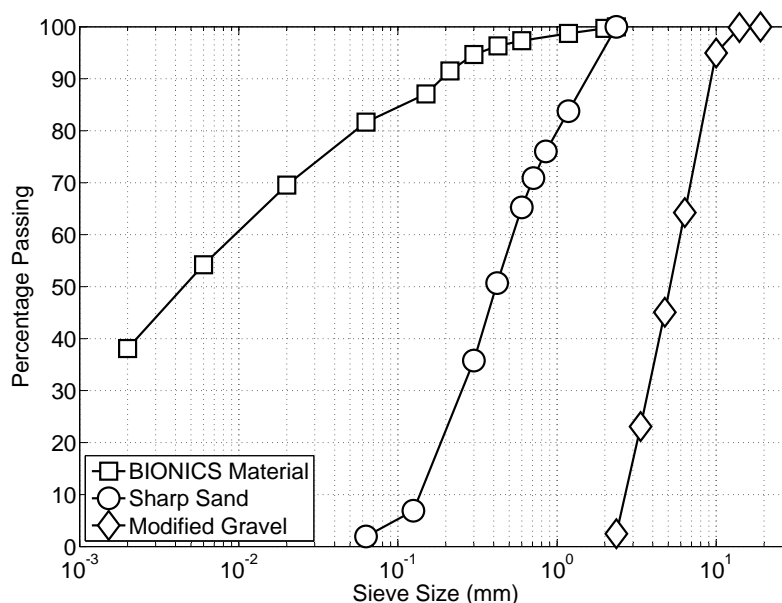


Figure 6.5: Raw material particle grading curves

was prepared in sealable polypropylene containers in three layers of 1.2 kg wetted to OWC using distilled water. The containers were sealed for 48 hours to allow the water to equilibrate. Material was extracted after 48 hours and dried at 105°C for 24 hours (BS1377:1990). Particle grading curves for the fresh and post-testing soil mixes, determined by wet sieving, are shown in Figures 6.8 and 6.9. Figure 6.8 shows that the silty-clay content of mix 5-1-4 reduces from 37.4% to 27.6%, so that the clay content of the mix needs to be increased if the material is to be re-used, as well as results for adding pulverised silty-clay,

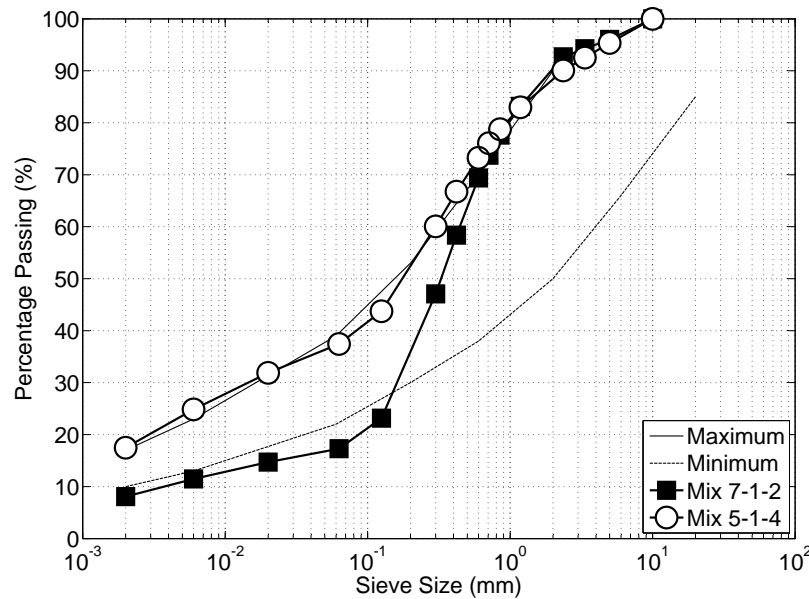


Figure 6.6: Particle grading curves for mixes 5-1-4 and 7-1-2 showing recommended grading limits (Houben and Guillaud, 1996)

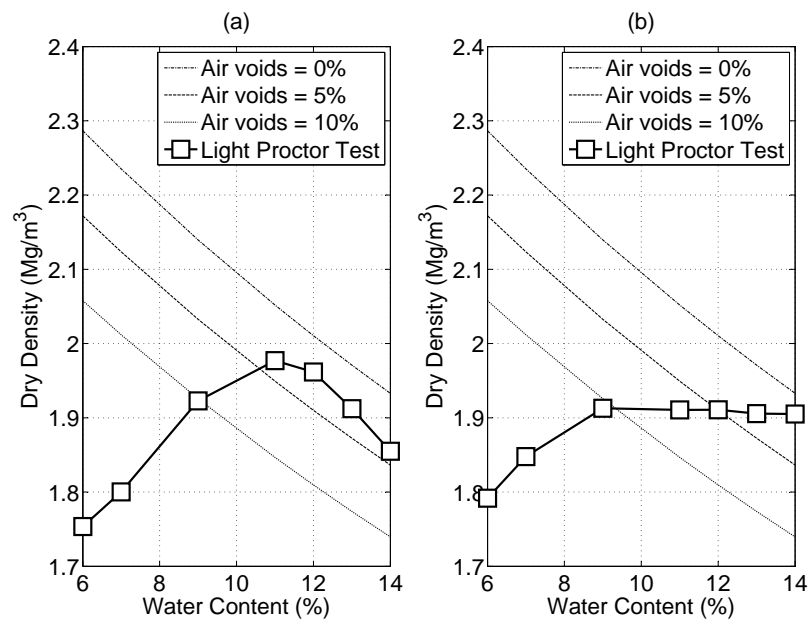


Figure 6.7: Water content against dry density for light Proctor compaction tests on soil mixes: a) 5-1-4; and b) 7-1-2.

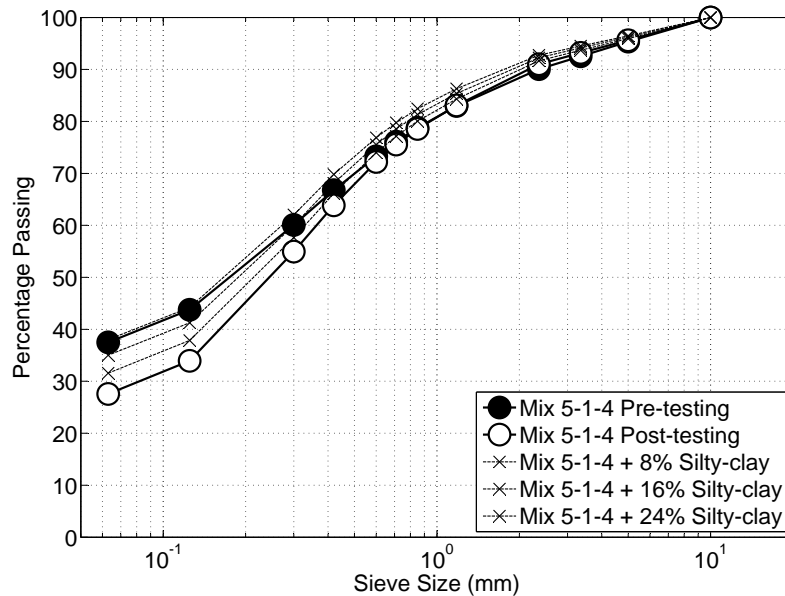


Figure 6.8: Comparison between pre- and post-testing mix 5-1-4 material, showing the effect of additional silty clay on the grading curve of post-test material

prepared using the same procedure as discussed in Section 5.2.2 and sieved to contain particles smaller than 2.36 mm, to the post-test soil mix. The effect of adding sieved silty clay is to increase all of the percentage passing values for particles smaller than 2.36 mm, however the effect on particles $<63 \mu\text{m}$ is the greatest due to the high $<63 \mu\text{m}$ particle content of the material. Results showed that an additional 22% (by mass) of silty clay would return the mix to its original clay content so that it could be reused. Figure 6.9 shows that mix 7-1-2 is not affected by the wetting process, so that it can be reused without any modifications.

6.3.3 Salinity values

The effect of the presence of dissolved ions on the tensile strength of RE mixes was investigated by adding various amounts of CaCl_2 powder to the pore water of mixes 5-1-4 and 7-1-2. CaCl_2 powder was chosen as it is readily available and is a compound that can be found in the water supplies of arid regions (Barzegar et al., 1994b; Barzegar, 1995; Olivella, 2010).

The lyotropic series can be considered to be the order of preference in which cations are absorbed, as is shown in Eqn 6.2. As Ca^{2+} is near the top of the scale, it is readily absorbed by clay minerals and so it is assumed that it will have a significant effect on the structure of the material (Hillel, 2004). The effect of Ca^{2+} ions is to cause clay flocculation and a reduction in the tensile strength of clay aggregates, an effect which is made use of in agriculture for aiding plant root growth (Dexter and Chan, 1991; Barzegar

Table 6.2: OWC, $\rho_{d_{max}}$ and $\rho_{b_{max}}$ for soil mixes 5-1-4 and 7-1-2.

Soil mix	OWC (%)	$\rho_{d_{max}}$ (kg/m ³)	$\rho_{b_{max}}$ (kg/m ³)
5-1-4	11.0	1977.1	2194.5
7-1-2	12.0	1920.9	2151.4

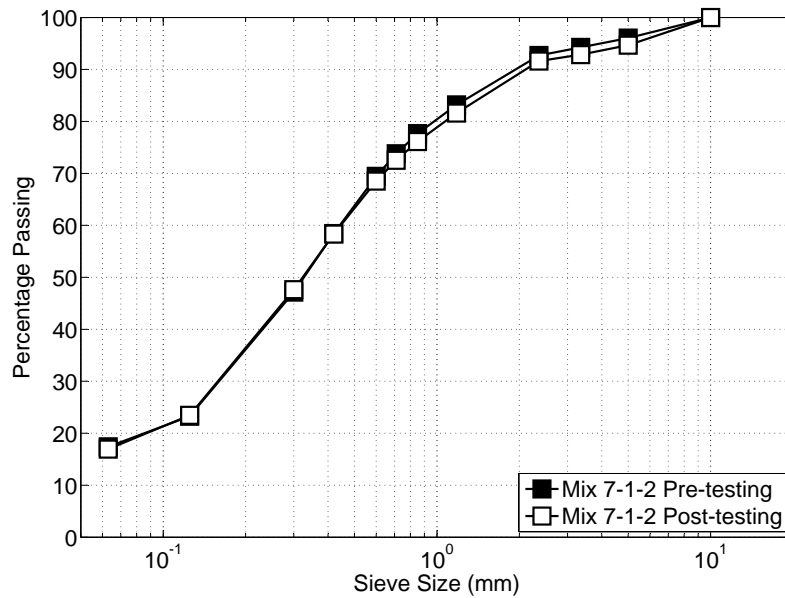


Figure 6.9: Comparison between pre- and post-testing mix 7-1-2 material

et al., 1995a). Therefore, it is likely that Ca^{2+} ions might be present in soils used for RE construction.

$$\text{Al}^{3+} > \text{Ca}^{2+} > \text{Mg}^{2+} > \text{NH}_4^+ > \text{K}^+ > \text{Na}^+ \quad (6.2)$$

Pore water electrical conductivity values of 0 (assumed value for pure water), 0.5 and 4.0 dSm^{-1} are used in Barzegar et al. (1994b) in order to determine the influence of electrolyte concentration and sodium adsorption ratio (SAR) on the tensile strength of soil samples. SAR is calculated using Eqn 6.3:

$$\text{SAR} = \frac{[\text{Na}^+]}{\left(\frac{([\text{Ca}^{2+}] + [\text{Mg}^{2+}])}{2} \right)^{\frac{1}{2}}} \quad (6.3)$$

where “[]” denotes a concentration. For $\text{SAR} \approx 0$, an increase in electrical conductivity from 0 to 4.0 dSm^{-1} resulted in a decrease in the tensile strength of roughly 10 kPa for all of the soil types tested. For more detailed information concerning these soil types, the reader is referred to Table 1 of Barzegar et al. (1994b). Information concerning the nature of the ions added to the pore water is not given in Barzegar et al. (1994b). However, the SAR depends on the relative concentrations of sodium, calcium and magnesium ions, so that a change in $[\text{Ca}^{2+}]$ and $[\text{Mg}^{2+}]$ with $[\text{Na}^+] \approx 0$ would vary the electrical conductivities of the pore water solution without changing the SAR value. This suggests that calcium or magnesium ions were present in the solutions used by Barzegar et al. (1994b). As Ca^{2+} and Mg^{2+} are high in the lyotropic series, electrical conductivities of 0, 0.5 and 4.0 dSm^{-1} suggestibly offer suitable guideline values for pore water electrical conductivities.

Results found in Beckett (2008) for the tensile strengths of RE soil mixes showed a maximum range of 50 kPa for sample tensile strengths at given water contents. Therefore, it is likely that the 10 kPa change in tensile strength observed in Barzegar et al. (1994b) on the increasing of the pore water electrical conductivity from 0 to 4.0 dSm^{-1} would be masked by the expected range of experimental values for given water contents using RE samples. A linear relationship between reducing tensile strength and increasing pore water electrical conductivity is suggested by data presented in Table 3 of Barzegar et al. (1994b),

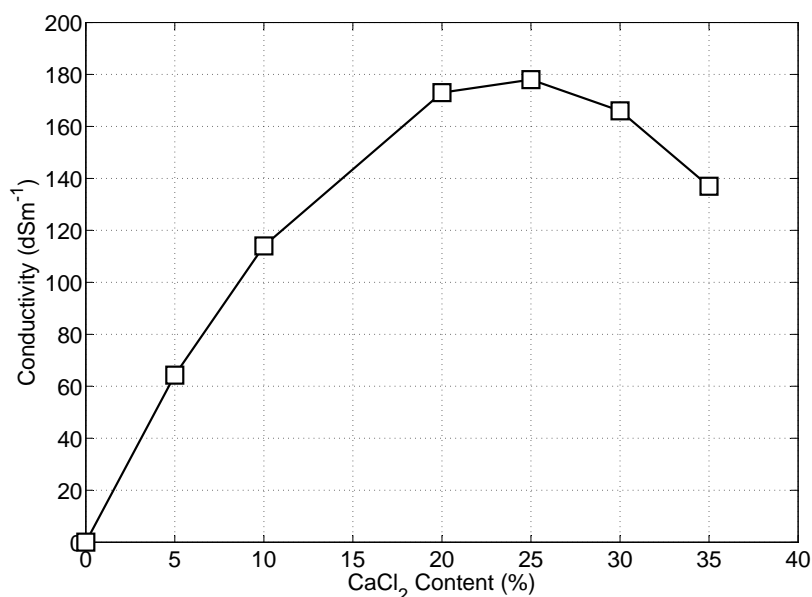


Figure 6.10: Relationship between electrical conductivity and % content by mass for CaCl_2 dissolved in pure water at 18°C (SmartMeasurement, 2001)

however it cannot be substantiated due to the small number of electrical conductivity values tested. This relationship suggests that, to ensure a change in tensile strength of 50 kPa, steps in the electrical conductivity need to be roughly 20 dSm^{-1} . Therefore, pore water electrical conductivity values of 0, 20 and 40 dSm^{-1} were selected for testing with RE samples.

The electrical conductivity of CaCl_2 in pure water is shown in Figure 6.10 (SmartMeasurement, 2001); Good agreement is achieved between this data and that found by Rao and Shivananda (2005) for concentrations below 10%. Using this data, electrical conductivities of 0, 20 and 40 dSm^{-1} correspond to 0, 1.6% and 3.1% CaCl_2 content by mass respectively. Figure 6.10 shows that electrical conductivities of 0, 20 and 40 dSm^{-1} lie in an approximately linear region of changing electrical conductivity with added mass of CaCl_2 , so that it is assumed that the effect on the tensile strength will also vary linearly. The CaCl_2 powder is added in addition to the mass of water added in order to wet the soil mixes to their OWC. Electrical conductivities were verified through testing of treated water using a Hanna Instruments HI9033 electrical conductivity meter. 1.6% and 3.1% CaCl_2 contents are equivalent to “brackish” and “saline” water respectively (UCAR, 2002), so that they are salinities that are found in natural ground water; this is important as it is necessary to test ion concentrations that might realistically be found in ground water and hence soils used for RE construction.

6.3.4 Sample manufacture

Wet material was prepared in sealed containers following the procedure used for fines loss testing discussed in Section 5.2.2. Powdered CaCl_2 was added to distilled water in the required quantities for each electrical conductivity and soil mix prior to wetting the material. Separate mixes were used for each electrical conductivity to prevent contamination. Only those mixes where no CaCl_2 was added to the pore water comprised corrected reused material as shown in Figure 6.8 so that CaCl_2 content could be accurately controlled.

Samples were prepared in three equal layers using a cylindrical mould, a sketch of which is shown in Figure 6.11. 27 blows of a 2.5 kg rammer dropped from a height of 300 mm were used to compact

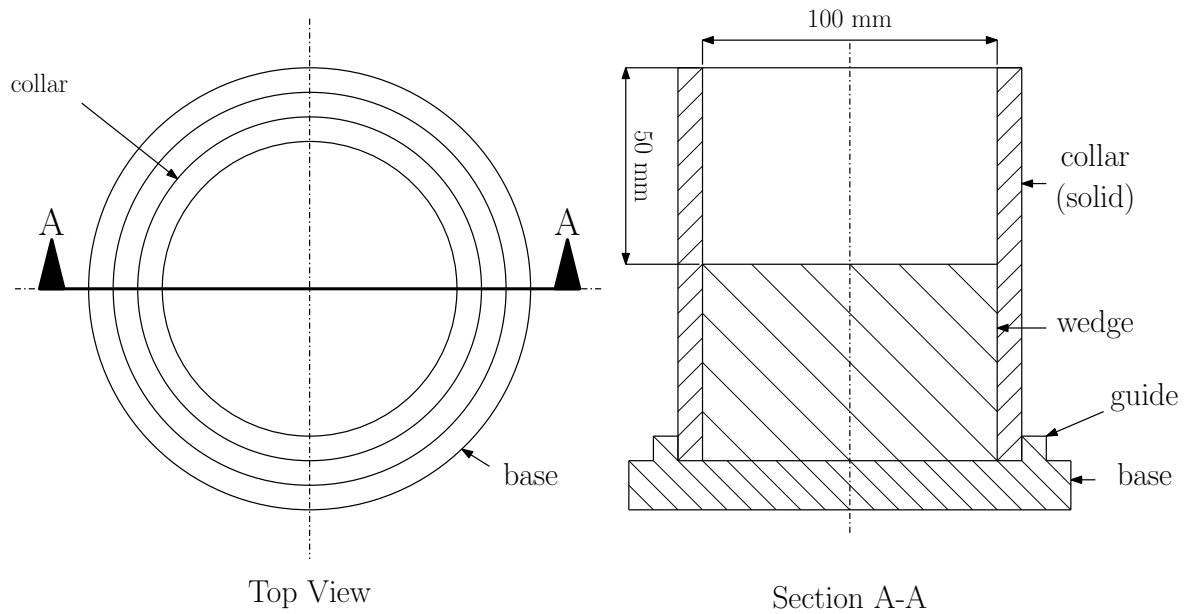


Figure 6.11: Sketch of the cylindrical mould used for sample production showing principal dimensions

each layer according to the light Proctor test (BS 1377:1990). The use of a Proctor compaction mould ensured that the compaction of each sample was consistent and that the maximum bulk density would be achieved using the soil mix OWC values found in Section 6.3.2. A loose-fitting wedge was added to the bottom of the split mould in order to produce samples of 50 mm thickness, as shown in Figure 6.11. The sides of the mould were treated with form release oil in order to prevent the sample from being damaged on extraction. As the compactive effort was the same as that used for OWC testing, no control over the layer volume was required, as was the case for the preparation of samples used in Chapter 5, as the final bulk densities were known. After compaction the upper surfaces of the samples were trimmed and any depressions filled; additional material was compacted manually using a hand-held Proctor rammer (2.5 kg, 300 mm drop height). A screed of soil mix material passing a 1.18 mm sieve was applied to the upper surface of the sample after compaction to ensure a flat, level surface for ease of crack identification. The samples were extracted by being pressed out of the mould collar from above by a hydraulic rammer; the cylindrical wedge was left in place in order to prevent damage on exiting the mould. Once extracted, samples were placed on wire racks in order to dry in a controlled environment of $20.0 \pm 0.3^\circ\text{C}$ and $45 \pm 5\%$ RH.

6.3.5 Tensile strength testing

Samples were tested at a range of water contents in order to determine the effect of water content on tensile strength. Water contents were chosen to provide a well-distributed range of results (Jaquin et al., 2009). On reaching the desired water content, samples were wrapped in clear plastic wrapping to allow water to equilibrate. Samples were not tested at their OWC due to the samples being too weak to be removed from the drying racks. As very wet RE is not subjected to loading, due to the presence of formwork, it was deemed that a lack of data for material strength at the OWC was acceptable (King, 1996; Walker et al., 2005; Easton, 2007). Sample diameters and thicknesses were measured prior to testing to account for any shrinkage and in order to determine a more accurate tensile strength.

Samples were tested by placing them in the Brazilian test cradle as shown in Figure 6.1 and crushing at a displacement rate of 0.12 mm/min, following work conducted in Young and Mullins (1991), Beckett

(2008) and Jaquin et al. (2008). It was found in Beckett (2008) that samples at 4% water content reached failure after roughly 10 minutes. This rate was therefore selected in order to test a large number of samples in a realistic time without a significant risk of them drying during testing. This rate is also similar to that used to determine compressive strengths of RE samples in Chapter 5, so that results found in that investigation and here can also be compared (Azmatch et al., 2011). A displacement– rather than load-controlled test was selected in order to improve control over the sample loading. Loads and displacements were recorded using “Triax” software (Toll, 1999) and failure was deemed to correspond to the maximum applied load. Two samples were tested for a given drying time in order to nominally test at the same water content. Sample water content was determined using the same procedures discussed in Section 5.2.4.

6.4 Results and discussion

6.4.1 Sample density errors

Sample material density errors (taken to be the relative difference between the measured sample density and the soil mix bulk density shown in Table 6.2), initial mix water contents and water contents at testing are shown in Table 6.3. As discussed in Chapter 5, the difference between these water contents and the target OWC is due to water adsorption during storage.

Measurements of the sample diameters and thicknesses taken prior to testing showed that shrinkage was negligible for all samples. The density errors for all samples given in Table 6.3 are shown in Figure 6.12, showing that samples of mix 5-1-4 were consistently less dense than the target maximum bulk density, whilst samples of mix 7-1-2 were consistently more dense than the target maximum bulk density with the exception of samples 1 to 6 at 20 dSm⁻¹, which showed lower bulk densities than the maximum. Despite these errors, however, Figure 6.12 shows that samples density errors are consistent within their mix and CaCl₂ content classes.

In order to prevent under- or over-compacted samples from influencing the calculated tensile strengths, a limit of $\pm 3.0\%$ of the maximum bulk density was placed on sample densities. Those samples whose density errors fell outside of this limit were rejected. Samples 1 to 6 for mix 7-1-2 at 20 dSm⁻¹ were rejected due to their density errors being inconsistent with all remaining mix 7-1-2 samples, as seen in Figure 6.12; this is presumably due to errors made during manufacture and not a consequence of the addition of CaCl₂. Samples 7 to 12 for mix 7-1-2 at 0 dSm⁻¹ were not tested due to errors that occurred during manufacture, hence their omission from Table 6.3. Rejected samples are shown in grey in Table 6.3. Samples 9 of mix 7-1-2 at 20 dSm⁻¹ and 6 of mix 7-1-2 at 40 dSm⁻¹ were retained despite a high density error (3.35% and 5.8% respectively) due to a lack of data at these water contents for 20 and 40 dSm⁻¹.

Table 6.3 shows that average initial mix water contents for both mixes at all electrical conductivities were within 0.3% of the calculated OWC values. Figure 6.7 shows that the effect of an additional 0.3% water content on the compacted dry and bulk densities is negligible for both mixes, so that the compacted density of the material should equal the maximum bulk density determined through the light Proctor compaction for both mixes at all CaCl₂ contents. The lower-than-target density found for all mix 5-1-4 samples is therefore not due to an initially-incorrect water content, as occurred in Chapter 5, but is instead due to an incomplete compaction of the sample, perhaps due to the use of the large Proctor rammer to manufacture thin sample layers. This suggests that mix 5-1-4 samples will be slightly weaker than if they were compacted to their optimum density; the limit on density errors, however, should reduce this effect. Due to the number of samples rejected, the average initial water contents for mixes 5-1-4 and 7-1-2 at 20 dSm⁻¹ is that found for samples 7-12 only.

Table 6.3: Sample density errors and water contents at testing. Numbers in parentheses correspond to sample numbers. Grey entries correspond to rejected samples.

Mix 5-1-4, 0 dSm ⁻¹ , average initial water content: 10.9%						
Density error (1-6)	-0.62	-0.48	-1.68	-1.45	-1.15	-1.67
Water content (1-6)	2.7	2.4	5.4	1.4	4.2	10.5
Density error (7-12)	-0.86	-2.39	-1.59	-0.76	-1.33	-2.28
Water content (7-12)	9.7	2.9	1.6	2.1	6.9	6.4
Mix 7-1-2, 0 dSm ⁻¹ , average initial water content: 11.7%						
Density error (1-6)	1.28	2.89	2.61	2.34	1.72	1.83
Water content (1-6)	10.3	1.0	5.5	1.9	7.3	2.0
Mix 5-1-4, 20 dSm ⁻¹ , average initial water content: 11.4%						
Density error (1-6)	-3.72	-2.59	-3.37	-2.8	-3.72	-2.61
Water content (1-6)	8.4	1.3	3.4	2.1	5.5	11.0
Density error (7-12)	-1.15	-0.49	-2.25	-2.21	-2.01	-2.4
Water content (7-12)	6.6	5.7	2.6	3.8	9.8	11.3
Mix 7-1-2, 20 dSm ⁻¹ , average initial water content: 12.3%						
Density error (1-6)	-3.3	-4.29	-3.37	-3.78	-2.61	-3.73
Water content (1-6)	1.2	0.7	7.4	4.7	0.8	3.5
Density error (7-12)	1.38	2.09	3.35	2.32	1.69	1.97
Water content (7-12)	3.9	3.5	1.7	2.2	6.9	8.1
Mix 5-1-4, 40 dSm ⁻¹ , average initial water content: 11.0%						
Density error (1-6)	-0.31	-2.62	-2.71	-3.01	-1.74	-1.99
Water content (1-6)	6.4	4.1	1.9	2.36	9.8	11.4
Density error (7-12)	-1.21	-1.94	-2.34	-3.64	-2.44	-2.72
Water content (7-12)	3.5	6.1	6.9	Not available	7.2	11.8
Mix 7-1-2, 40 dSm ⁻¹ , average initial water content: 11.9%						
Density error (1-6)	4.46	2.48	1.86	1.87	4.12	5.8
Water content (1-6)	4.5	2.9	1.4	1.7	6.9	9.2
Density error (7-12)	1.91	3.48	1.61	2.2	2.12	2.08
Water content (7-12)	3.4	Not available	6.5	4.5	6.9	7.6

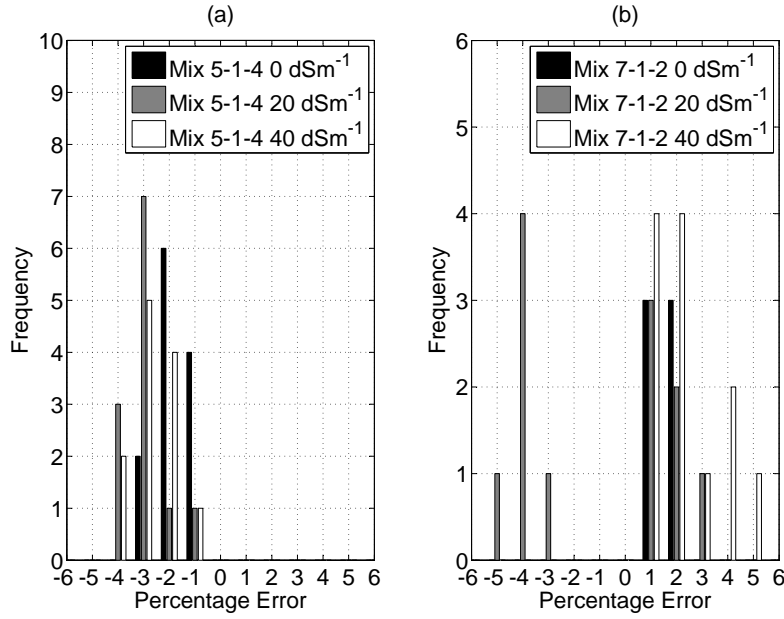


Figure 6.12: Errors in cube densities for soil mixes: a) 5-1-4; and b) 7-1-2

6.4.2 Failure mechanisms at different water contents

6.4.2.1 Griffith crack theory

Griffith crack theory (Griffith, 1921) is one of the simplest theories of crack formation and propagation, developed in order to explain the effect of defects on the rupture of elastic, homogeneous materials. Experiments by Griffith indicated that the actual strengths of *brittle* materials were much lower than those predicted by atomic theory; he attributed this to flaws in the material. Griffith crack theory is based on an energy balance between strain and surface energy. It follows from the First Law of Thermodynamics that there will be a net decrease in energy if a system moves from a state of non-equilibrium to one of equilibrium. Hence, a crack can only form (or an existing crack grow) if it causes the total energy in the system to decrease or remain constant. Therefore, a crack becomes unstable when the strain energy change that results from incremental crack growth is sufficient to equal the surface energy (the energy required to break the atomic bonds within a material and so create a new surface) of the material. The required local stress intensification for crack propagation is generated by flaws in the material. Figure 6.13 shows the required energies to initiate crack propagation, where M is the factor of safety (the amount of energy that needs to be fed into the system in order for the crack to propagate) and L_g is the corresponding critical length of crack required for crack propagation. The length of L_g depends on the material: the more brittle the material, the shorter L_g (Griffith, 1921; Gordon, 1991).

Irwin (1957) proposed an extension to the Griffith theory which used the “energy release rate” to incorporate the effect of plasticity in determining the fracture of *ductile* materials. The result of this addition is that ductile materials require more energy to initiate crack growth than in brittle materials (as was observed in Griffith (1921)). The *stress intensity factor*, K , was identified to quantify the amount of energy available for fracture. It is assumed that materials have a critical value of K , K_c , so that if conditions exist such that $K > K_c$ fracture will occur.

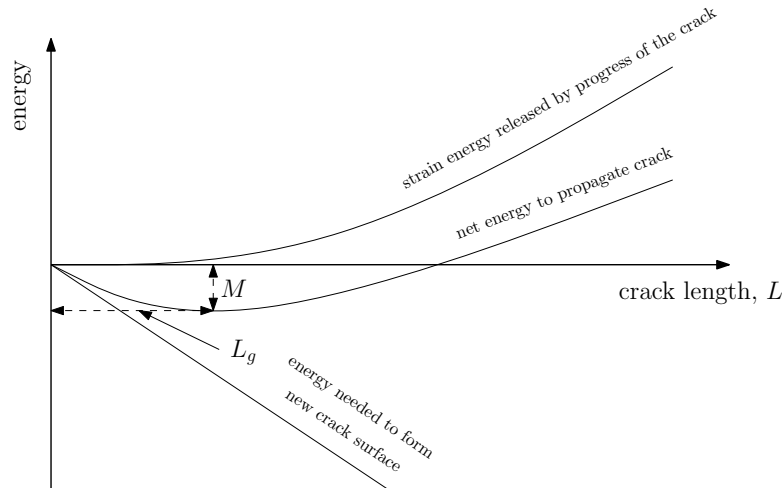


Figure 6.13: Griffith crack energy (Gordon, 1991)

6.4.2.2 Fracture of granular materials

The process of fracturing in rocks has been studied in some detail, however much less attention has been paid to uncemented sedimentary materials, for example soils and RE (Dehandschutter et al., 2004, 2005). An understanding of the fracturing process in soils has gained importance over recent years due to concerns associated with the burial of nuclear waste, for example, where heat-induced fracturing can lead to changes of permeability of the lining material and the escape of potentially-dangerous leachates (Gens et al., 2011).

Unlike the homogeneous materials investigated by Griffith (1921), unsaturated soils are *quasi-brittle* materials which derive their strength through sub-critical cracking, a process whereby crack growth is significant at conditions below K_c (Atkinson, 1987). Sub-critical cracking causes non-linear deformations to occur, so that the ideas of Irwin (1957) cannot be applied.

For dry soils, the application of a tensile or compressive load results in brittle failure through the formation, growth and joining of flaws within the soil structure. These flaws can either be the pores themselves or pre-existing cracks. Failure occurs through the formation of a *cataclastic zone* (i.e. a zone whose behaviour is governed by friction), that has little or no cohesion. Brittle failure of samples at low water contents is well documented and is due to frictional failure and the breaking of liquid bridges at the interparticle contacts (Braunack et al., 1979; Rondeau et al., 2003; Dehandschutter et al., 2005; Baltodano-Goulding, 2010; Hoyos et al., 2010). For wet soils, application of a compressive or tensile load results in the closure of the pre-existing flaws. Continued loading results in the formation of a shear plane within the material and subsequent shear failure (Vallejo, 2010). Note that the boundary between the “dry” and “wet” water contents will differ for any given soil. Subjecting a soil to drying and wetting cycles leads to the formation of tensile cracks within its structure (Dexter, 1988). Therefore, a soil which has been subjected to these cycles will have a lower failure load than one that has not, due to the increased amount of flaws.

Comparisons between typical failure plots for samples of both soil mixes tested at similar water contents are shown in Figures 6.14 to 6.16 for the three CaCl_2 contents. Samples tested at lower water contents exhibited brittle-like failures, as shown by the presence of a clearly-defined peak load and a high initial stiffness, whilst samples tested at higher water contents showed much more ductile-looking failure profiles with poorly-defined peak loads (Delage, 2009; Jaquin et al., 2009). A similar result was also found in Jaquin et al. (2008) for compressive tests on a similar RE soil mix with changing water content, with failure becoming more brittle as water content reduced. Figures 6.14 to 6.16 show that brittle and

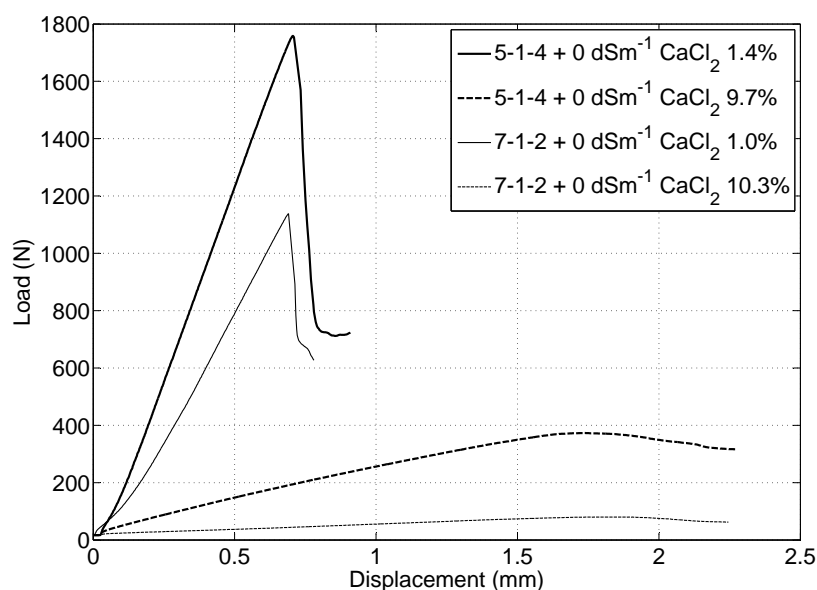


Figure 6.14: Comparison of load against displacement profiles for samples tested at 0 dSm^{-1}

ductile failures occur in samples of both mixes at all tested CaCl_2 contents, suggesting that comparisons between CaCl_2 contents are valid. A water content of roughly 7.5% separates the brittle and ductile-style failure patterns for both soil mixes. The transition from ductile to brittle failure can be linked to the amount of water present in the soil pores. For soils containing both water and air, Munkholm et al. (2002) suggest that stress concentrations occur in air-filled pores but not in water-filled pores, as the applied loads are distributed about the pore by the pore water. Therefore, crack propagation initiates from dry pores, so that crack propagation and subsequent brittle-like failures are much more prevalent under dry conditions. This observation is supported by experimental findings, for example those of Hallett et al. (1995).

A change from ductile to brittle failures with reducing water contents has been observed in a number of investigations. For example, similar profiles to those shown in Figures 6.14 to 6.16 for water contents below 7.5% were found in Wang et al. (2007) for clay specimens at water contents of 16.3% to 19.3% using the direct tension test. An OWC for the soil is not provided, however all of the tested water contents were below the soil's plastic limit (20.2%) so that it is assumed that the material is exhibiting brittle behaviour. The similarity between the direct tension testing results of Wang et al. (2007) and those shown in Figures 6.14 to 6.16 suggests that soil tensile strengths determined indirectly using the Brazilian test and directly using direct tension methods can be favorably compared (Ajaz and Parry, 1975b). Failure profiles for RE cylinder samples tested in compression over a range of water contents (5.5% to 10.2%) are given in Jaquin et al. (2008) and Kirk (2009). Although in compression the failure profiles are similar to those shown in Figures 6.14 to 6.16 for RE samples in tension. The change from ductile to brittle behaviour as water content reduces is linked to a critical suction value, above which the samples fail in a brittle manner. Although no suction measurements were made in this investigation, this description of sample failure agrees with the interpretation of sample strength being related to suction and suggests that the transitional water content of 7.5% could be linked to a critical suction value, perhaps representing the point at which the inter-aggregate pores are emptied of water so that water only resides in the intra-aggregate pores. Further work is required in order to investigate this.

Figures 6.14 to 6.16 show that samples of mixes 5-1-4 and 7-1-2 follow similar failure profiles for

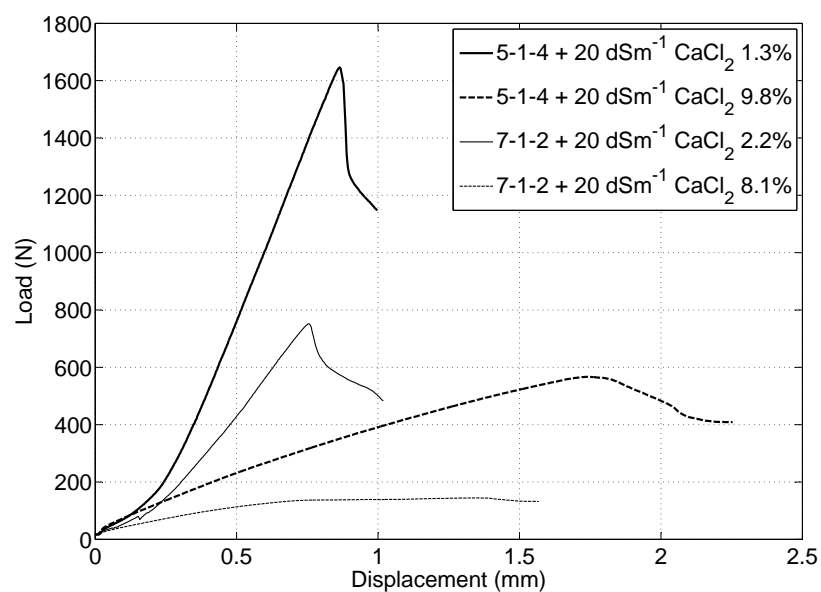


Figure 6.15: Comparison of load against displacement profiles for samples tested at 20 dSm^{-1}

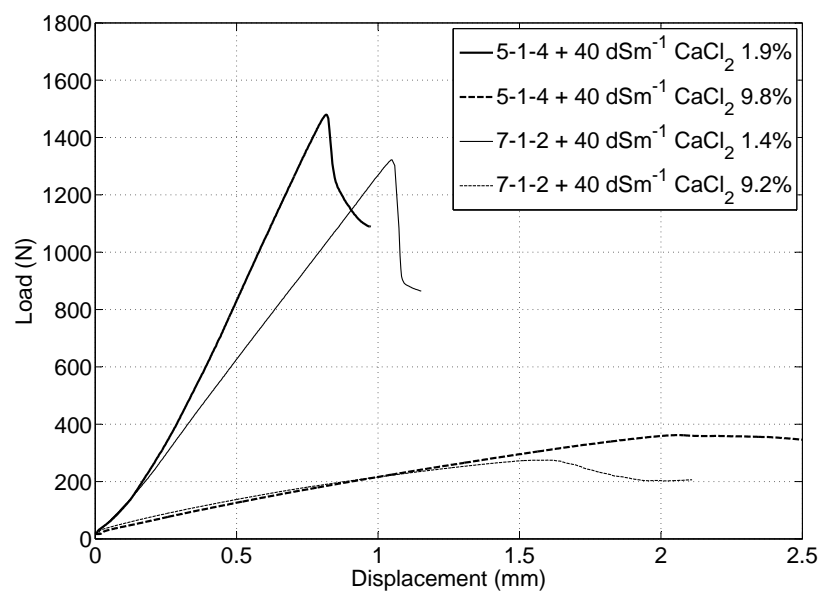


Figure 6.16: Comparison of load against displacement profiles for samples tested at 40 dSm^{-1}

Table 6.4: Fitting parameters used with Eqn 6.4 to estimate the change in tensile strength with saturation ratio for mixes 5-1-4 and 7-1-2 at different CaCl_2 contents

Mix	CaCl_2 content	a	b
5-1-4	0	-0.82	-2.41
5-1-4	20	-0.93	-2.42
5-1-4	20	-1.18	-2.61
7-1-2	0	-0.90	-3.33
7-1-2	20	-1.16	-3.41
7-1-2	40	-0.83	-2.72

similar water contents, with consistently higher loads present for mix 5-1-4 than for mix 7-1-2 for a given displacement. Therefore, the tensile strengths found for each mix at a given water content can be compared, as both materials behave in a similar manner. However, the transition from a ductile to a brittle failure with reducing water contents suggests that the tensile strengths of samples at significantly different water contents should not be compared, as it cannot be guaranteed that specimens are failing due to the same mechanism. As further work is required in order to investigate this observation and as it is the failure load and not the failure type that is of interest to RE construction, results will continue to be compared as if the material were behaving in a constant manner for the remainder of this chapter.

6.4.3 Change in tensile strength with water content

Calculated tensile strengths (Eqn 6.1) for a range of water contents (converted to saturation ratios) for samples of mixes 5-1-4 and 7-1-2 are shown in Figures 6.17 and 6.18 at pore water electrical conductivities of 0, 20 and 40 dSm^{-1} . Changes in the tensile strength in the central S_r region for a given S_r value are of the order of 10% of the unmodified material tensile strength per increase of the CaCl_2 content by 20dSm^{-1} ; although this is also of the order of the accuracy of the Brazilian test as determined by Frydman (1964), the result of a similar change in tensile strength at all S_r values in this range suggests that the measured results are representative of the material behaviour and not an error associated with experimental procedure. The result of reduced changes in tensile strength at higher and lower S_r values is discussed in the following sections.

Following similar work conducted in Chapter 5 (Eqns 5.2 to 5.5) and that of various authors, a regression of the form

$$\log(\sigma_t) = a \log(S_r) + b \quad (6.4)$$

(where a and b are fitting parameters) has been used to approximate the data trend, with parameters for each CaCl_2 content given in Table 6.4. Figure 6.18 shows that Eqn 6.4 results in a good approximation to the calculated data for mix 7-1-2 (correlation values of 0.87 to 0.94) for all CaCl_2 contents and values of S_r and that the results show a consistent change in tensile strength with S_r with changing CaCl_2 content. However, the fit to the data is poorer (correlation values of 0.64 to 0.77) for mix 5-1-4, with a significant underestimation of the tensile strengths in the middle of the S_r range and an apparently-inconsistent change in tensile strength with S_r for different CaCl_2 contents. Therefore, the appropriateness of the use of Eqn 6.4 to describe data of this type should be investigated.

Some examples of measured data and their approximations are shown in Figures 6.19 and 6.20 and are discussed below. The error in the scale on the ordinate axes in Figures 6.19(f) and (g) is as produced in the original article. The change in tensile strength with water content for samples of Gault (PL 34%, LL 73%, PI 39%, OWC 24.5%, 56% clay) and Balderhead (PL 20%, LL 34%, PI 14%, OWC 13.1%, 25% clay) clay soils are investigated in Ajaz and Parry (1975c) (Figure 6.19(a) and (b) respectively). Tensile

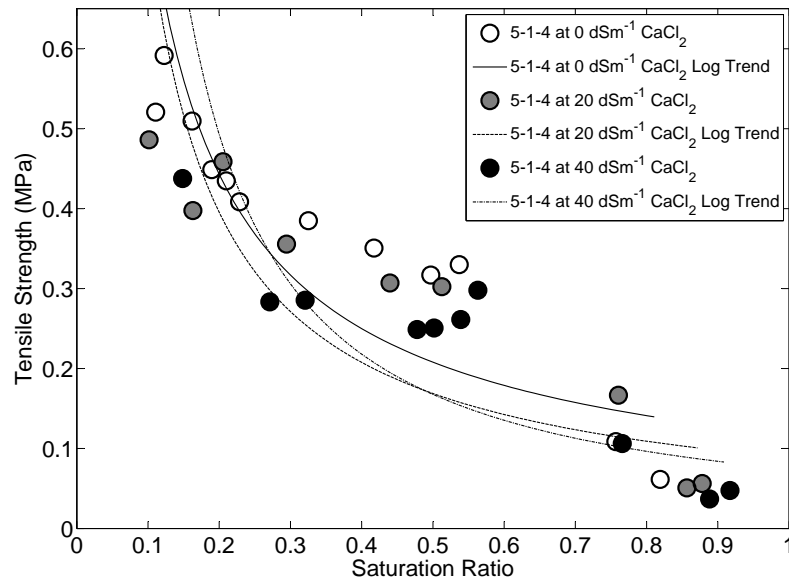


Figure 6.17: Logarithmic relationship for tensile strength against water content for mix 5-1-4. a and b are defined in Eqn 6.7.

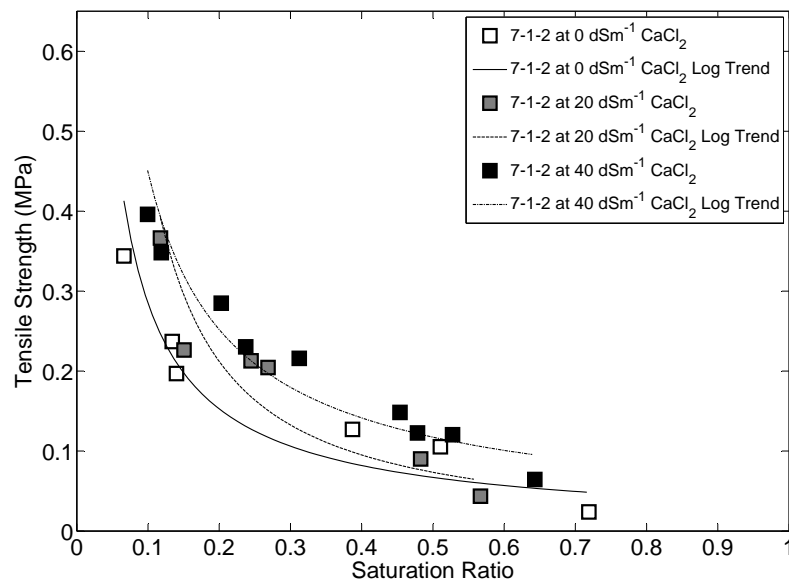


Figure 6.18: Logarithmic relationship for tensile strength against water content for mix 7-1-2. a and b are as defined in Eqn 6.7.

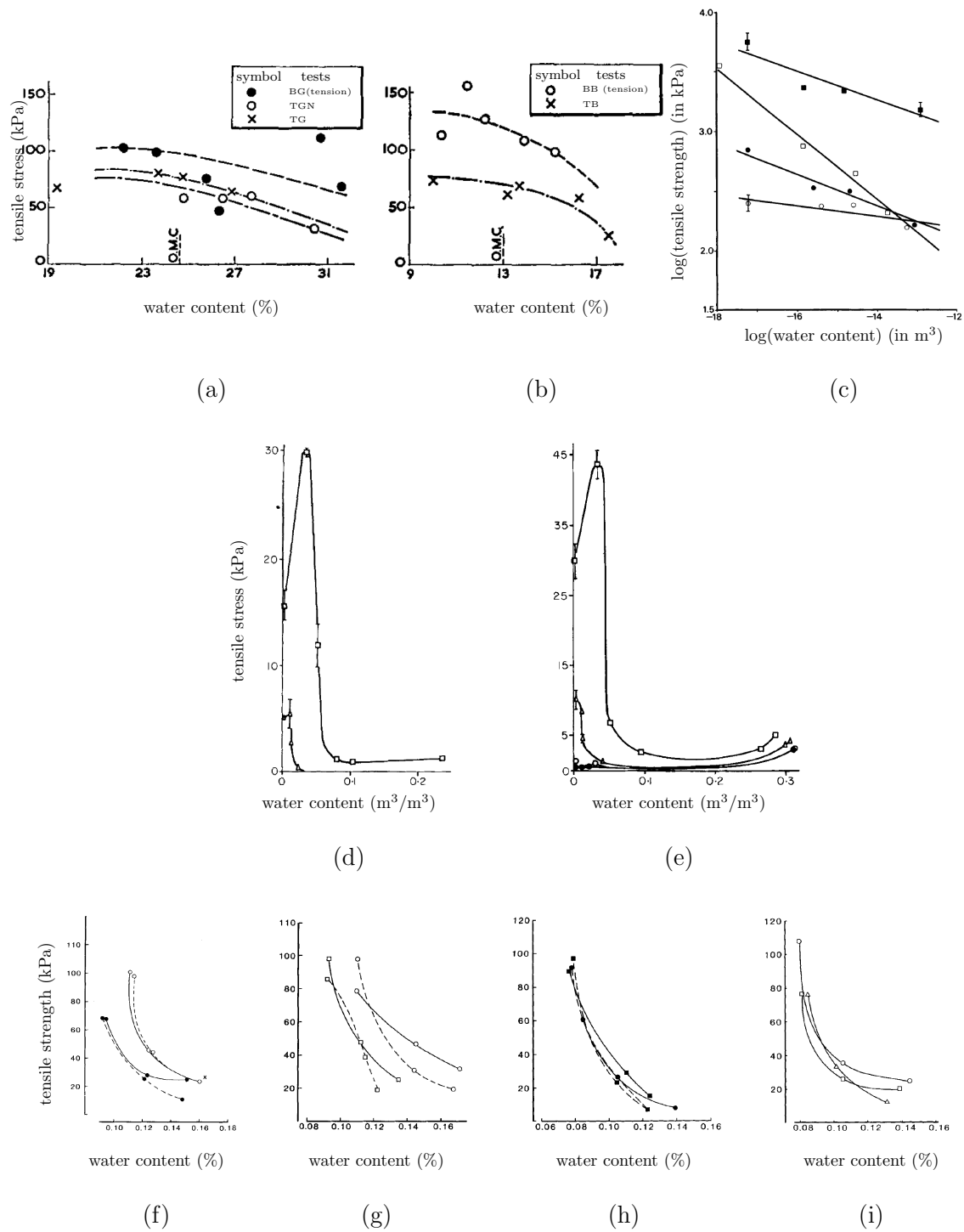


Figure 6.19: Change in tensile strength with water content as observed by various authors: a) and b) Ajaz and Parry (1975c); c) (Utomo and Dexter, 1981); d) and e) (Mullins and Panayiotopoulos, 1984); f) to i) (Young and Mullins, 1991).

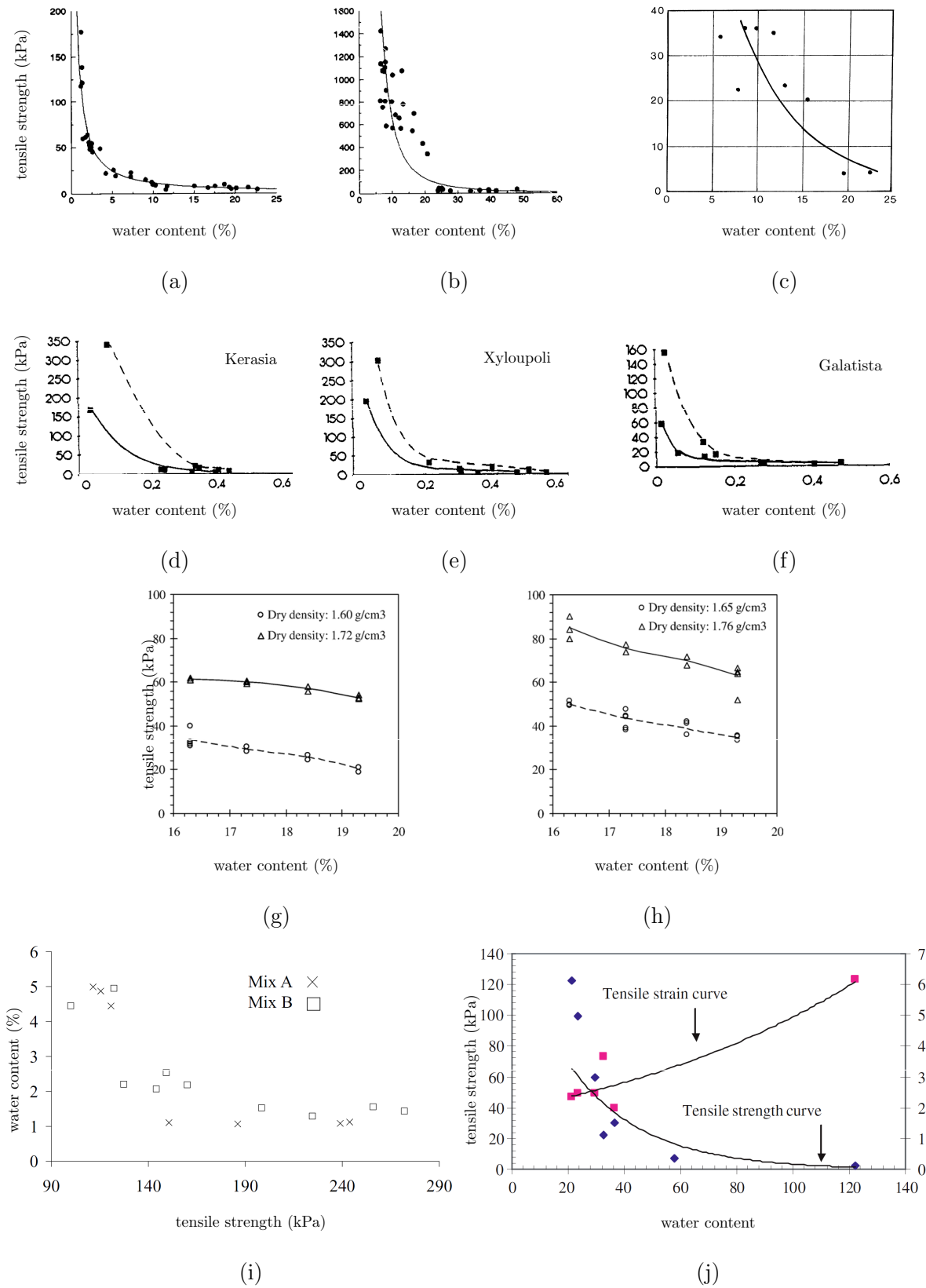


Figure 6.20: Change in tensile strength with water content as observed by various authors: a) and b) Causarano (1993); c) (Ibarra et al., 2005); d) to f) (Panayiotopoulos, 1996); g) and h) Wang et al. (2007); i) Jaquin et al. (2008); j) Nahlawi et al. (2004).

strengths were determined using bending tests and load- and strain-rate controlled direct tension tests, following the work of Ajaz and Parry (1974), for a water content range of roughly 19% to 32% and 10% to 18% for Gault and Balderhead clays respectively (i.e. values both above and below the OWCs for each soil). Regression lines are provided for each type of test used, however the type is not specified. Results suggest that the tensile strength increases to a constant level as water contents reduce for all test types, however this cannot be confirmed for lower water contents due to a lack of data.

In Utomo and Dexter (1981), a logarithmic relationship of the form

$$\ln(\sigma_t) = -k \ln(V) + A \quad (6.5)$$

$$A = \ln(\sigma_{t_0} V_0 \Gamma(1+k)) \quad (6.6)$$

is applied to the tensile strengths of spherical aggregates of Urrbrae (PL 19.5%, LL 26.5%, PI 12.6%) and Strathalbyn (PL 17.9%, LL 30.5%, PI 7.0%) sandy loam soils where A and k are fitting parameters, V is the aggregate volume, V_0 and σ_{t_0} are the volume and tensile strengths of the basic soil elements respectively and Γ is the Gamma function (e.g. Dodson (1994)), following the work of Braunack et al. (1979). Results for the Urrbrae soil are shown in Figure 6.19(c). Tensile strengths were determined indirectly using parallel plates, a similar method to the Brazilian test. Results suggest that tensile strength rises sharply with reducing water contents and a good fit to the calculated tensile strengths is achieved using Eqn 6.5. However, the data are sparse and for a wide water content range (12.3% to 30.2% for Urrbrae soil and 11.8% to 34.6% for Strathalbyn soil), so that any comment on the applicability of an exponential relationship to a smaller water content range cannot be justified.

Mullins and Panayiotopoulos (1984) investigated the tensile strengths of mixes of fine sand (particles passing 0.25 mm but >0.125 mm) and kaolin clay (95% kaolinite) in ratios of 0, 5, 20 and 80 g kaolin per kg of mixture for gravimetric water contents from 0% (nominal) to 30%, as shown in Figure 6.19(d) and (e). Samples of pure fine sand showed negligible tensile strength. Samples that contained kaolin showed a steady increase in tensile strength with reducing water content for water contents above 20%, except at very low water contents where tensile strengths rapidly reduced. Tensile strengths apparently reduced as water content reduced from 30% to roughly 20%, however this is difficult to substantiate due to a lack of data in this region. Tensile strength at a given water content increased with clay content. Lines joining the centres of the datapoints are used to describe the data trends. The method used to dry samples to the lowest water contents is not discussed, so that if oven drying was used, as is discussed in Chapter 2, the internal structure of the sample would not reflect that of a non oven-dried sample, creating exaggerated material strengths for given water contents (Diamond, 1970; Horn et al., 1994).

In Figures 6.19(f) to (i) (Young and Mullins, 1991), lines joining the centres of all of the datapoints have been used to describe the relationship between sample tensile strength, determined indirectly using the Brazilian test and Eqn 6.1, and water content for samples of sandy clay loam soils for water contents above roughly 8%. Note that the type of test has been inferred through the use of Eqn 6.1. The type of the regression lines is not given, however they appear to be polynomial of either second or third order. These data suggest that a rapid increase in tensile strength occurs with reducing water content, however the regression lines overestimate the increase in tensile strength with reducing water content and indeed in Figure 6.19(f) begin to double-back on themselves, so that their use is questionable.

A relationship between water content and tensile strength for soil aggregates of a sandy loam and a clay soil, shown in Figures 6.20(a) and (b), is given in Causarano (1993) as

$$\sigma_t = \frac{10^a}{\theta^b} \quad (6.7)$$

where a and b are fitting parameters. Eqn 6.7 results in a good fit to the data for both soil types,

although a better fit is afforded to the data for the sandy loam than for clay soil aggregates (assessed visually from Figure 6.20(a); no regression correlation values are provided). Eqn 6.7 offers an advantage over Eqn 6.5 as fewer material properties need to be determined for its use. A water content range of roughly 1% to 23% is investigated for sandy loam soil aggregates, whilst a larger range of roughly 6% to 48% is investigated for clay soil aggregates. However, in both cases, the presence of tests at higher water contents acts to extend the best fit approximation, making the approximated increase in tensile strength with reducing water contents more severe than it would be in the absence of these tests; if data corresponding to the highest water contents are removed, a far less severe approximation for the increase in tensile strength with reducing water content would be more appropriate.

The tensile strengths of samples of Kerasia (sandy clay loam), Xyloupoli (loam, sandy loam at depth) and Galatista soils (sandy loam, loam at depth) at water contents above roughly 1% were investigated in Panayiotopoulos (1996) using the Brazilian test (note that this is inferred: the type of test is not named but Eqn 6.1 is used to determine the tensile strength). Results for these tests are shown in Figures 6.20(d) to (f). The reader is referred to Table 1 of that work for detailed information concerning these soils. Although not specified in Panayiotopoulos (1996), a good fit to measured data is afforded by an apparently-exponential relationship similar to that given by Eqn 6.7. However, the relative sparsity of tensile strength data at lower water contents means that an assessment of the appropriateness of an exponential fit is not possible. Furthermore, data are for a large water content range (water contents $\leq 50\%$ volumetric water content, equivalent to $\leq 18.8\%$ gravimetric water content, assuming a soil density of 2.65 kg/m^3), so that the increase in strength as water contents reduce below 20% (7.5% gravimetric) is visually more severe than as might be the case, due to the very low tensile strengths of samples at water contents $\geq 20\%$.

Direct tension testing of samples of clayey soil (PL 26%, LL 127%, PI 101%, OWC 27.5%) was conducted in Nahlawi et al. (2004) and an exponential regression is used to approximate measured tensile strength against water content data, following the work of Krishnayya et al. (1974), Ajaz and Parry (1975c) and Tang and Graham (2000), as shown in Figure 6.20(j). For more information on the tests conducted in Nahlawi et al. (2004), the reader is referred to Table 1 of that article. However, once again the range of water contents tested is extensive (21.5 to 122.0% gravimetric) and data for tensile strengths at low water contents is not available, so that the increase in tensile strength at lower water contents ($< 60\%$ in this case) is exaggerated by the scale used. Furthermore, the fit provided by the exponential assumption underestimates the strengths at lower water contents whilst overestimating those at higher water contents, due to the presence of an outlying datapoint at 122% water content (its nearest neighbour is at 58% water content). Although this would suggest that a more, rather than a less severe approximation to the data would be more acceptable, a visual analysis of the data suggests that, with the omission of the datapoint at 122% water content, a less severe approximation would provide a much more acceptable description of the data trend.

Direct tension testing of samples of St. Benoit sandy loam soil (15.5% silty clay, 43.5% fine sand, 41% coarse sand by mass) at water contents between 5.9% and 22.6% is reported in Ibarra et al. (2005), following the work of Vomocil et al. (1961) and Farrell et al. (1967) and shown in Figure 6.20(c). For a constant bulk density, the regression line

$$\sigma_t = 109 \exp(-0.137\theta) \quad (6.8)$$

is used to approximate the increase in tensile strength with reducing water content, resulting in a regression coefficient of $R^2 = 0.889$. However, the regression line overestimates the tensile strength of the material at high water contents (around 20%) and suggests a higher tensile strength for samples at water contents lower than those tested than is suggested by the data. The effect of material density on tensile

strength is also investigated, showing a steady increase in tensile strength with increasing density for a given water content. A regression line of

$$\sigma_t = 0.0031 \exp(4.94\rho_b) \quad (6.9)$$

where ρ_b is the bulk density is fitted to the experimental data for a water content of 24%. However, it is not realistic to use Eqn 6.9 to predict the increase in tensile strength for samples made at lower water contents due to the significantly higher densities that can be expected.

The tensile strength of a clay loam soil (PL 20.2%, LL 29.1%, PI 8.9%), sieved to contain particles <2 mm, was investigated in Wang et al. (2007) using the uniaxial tensile test. Results for the tensile strength with changing water content are shown in Figure 6.20(g) and (h). The type of regression used is not specified, however a very gradual increase in tensile strength with reducing water content was found. Unfortunately, a very narrow range of water contents was investigated (16.3% to 19.3%), so that the behaviour of the material at lower water contents cannot be commented on.

Indirect tensile strength testing on two RE soil mixes (a loam and a silty-clay loam) were conducted in Jaquin et al. (2008) using the Brazilian test. Samples were made at the OWC (approximately 9%) and allowed to dry. Tests were conducted at a range of water contents between 1% and 5%. Results are shown in Figure 6.20(i); an approximation to the trend of the data is not provided, however the data presented for both mixes suggest sharply increasing tensile strengths with reducing water contents. It is not possible to comment on whether this trend would continue to lower water contents, however, due to a lack of data. The use of 50 mm diameter samples has been questioned for use with the Brazilian test in Section 6.3.1, however it is assumed that the trend of the data given in Jaquin et al. (2008) is representative of the strengths of the two soil mixes at different water contents.

These articles and corresponding results shown in Figures 6.19 and 6.20 show that the use of relationships of the form of Eqn 6.4 is commonplace to describe the change in tensile strength with water content (or S_r) despite a continually-incomplete fit to obtained experimental data. This therefore suggests that those trends shown in Figures 6.17 and 6.18 are not, in fact, representative of the material behaviour and that, instead, a more detailed investigation of the material behaviour is required; such an investigation is the topic of the following sections.

6.4.4 Matric, osmotic and total suction determination

6.4.4.1 Matric suction

Figure 6.21 shows the SWRC found in Jaquin et al. (2009) for RE mix 6-1.5-2.5 measured using tensiometers for samples under zero applied load. As tensiometers were used, suctions in that article are in terms of matric suction (Tarantino, 2009). Although for a different soil mix to those used in this investigation, it is assumed that suctions found at higher saturation ratios in that mix are similar to those present in mixes 5-1-4 and 7-1-2 due to the similar sand and gravel contents. Furthermore, as both materials are RE mixes, any changes in the material structure during drying should also be similar and represented by changing S_r values.

Matric suction (ψ_m) values for saturation ratios 0.83 and 0.76 from Jaquin et al. (2009) (calculated using $\rho_d = 2161.0 \text{ kgm}^{-3}$ at OWC of 7.65%) were combined with matric suction values for equilibrium conditions of 20°C and 45% RH for this investigation, calculated using Eqn 2.27, at the corresponding sample saturation ratios in order to estimate a rough SWRC for mixes 5-1-4 and 7-1-2 as shown in Figure 6.22. Although values for a higher saturation ratio (0.90) are available, they were not used in the estimation as it is assumed that the mix used in Jaquin et al. (2009) has a lower AEV to mixes 5-1-4 and 7-1-2 due to its higher gravel content. A modified van Genuchten expression was used to predict the

Table 6.5: van Genuchten fitting parameters used to estimate ψ_m in mixes 5-1-4 and 7-1-2

Mix	α	n
5-1-4	$10^{-4.66}$	1.29
7-1-2	$10^{-4.75}$	1.36

shape of the SWRC according to Eqn 6.10

$$S_r = \left(1 + \left(\frac{\log \left(1 + \frac{\psi_m}{10^9} \right)}{\log(2)} \right) \right) \times (1 + (\alpha \psi_m)^n)^{-m} \quad (6.10)$$

where α , m and n are fitting parameters, the values of which are given in Table 6.5 (for ψ_m in Pa) and where α controls the AEV and n (and, by extension, m) the gradient. m and n are related by

$$n = \frac{1}{1 - m} \quad (6.11)$$

following the work of Mualem (1976) (van Genuchten, 1980; Tarantino, 2009). The term in the first main pair of parentheses in Eqn 6.10 is a correction term which restricts the prediction to $S_r = 0$ at $\psi_m = 1$ GPa (Fredlund and Xing, 1994). Although a relatively crude fitting function, the use of a more complicated function was not deemed appropriate given the lack of datapoints and the roughness of the approximation. It can be shown that ψ_m does not change with solution concentration as, by the law of partial pressures,

$$\frac{\psi_m V_{m_l}}{R_u T} = \log \left(\frac{p_{sol}}{p_{sol}^*} \right) = \log \left(\frac{p_{sol}^* \frac{p}{p^*}}{p_{sol}^*} \right) = \log \left(\frac{p}{p^*} \right), \quad (6.12)$$

where the terms are as defined in Eqns 2.18 and 2.29, so that matric suction calculated using Eqn 2.27 can be used for all tested CaCl_2 contents. The result of higher S_r values for mix 5-1-4 than for mix 7-1-2 for given ψ_m values is consistent with the findings of many authors and is due to the larger volume of smaller pores present in samples of mix 5-1-4, due to its higher clay content (Diamond, 1970; Mullins and Panayiotopoulos, 1984; Vanapalli et al., 1999; Tarantino, 2010; Zhang and Li, 2010). Interestingly, Figure 6.22 suggests that mix 5-1-4 has a slightly lower AEV than mix 7-1-2, despite its higher clay content; this is a symptom of the use of the Fredlund and Xing (1994) correction factor and an indicator of the crudity of this estimation. It is assumed, however, that estimated ψ_m values are sufficient to investigate the role of ψ_m in determining tensile strength.

6.4.4.2 Osmotic suction

Several methods are available to predict the osmotic suction (ψ_o) given a dissolved ion content. In Rao and Shivananda (2005), the USDA calibration curve presented in Fredlund and Rahardjo (1993) was used to predict ψ_o based on the solution electrical conductivity according to

$$\text{ec} = 5.08c^{0.8658} \quad (6.13)$$

$$\psi_o = 31.92\text{ec}^{1.08} \quad (6.14)$$

where ec is the electrical conductivity of the pore water in μScm^{-1} , c is the solution concentration in mgL^{-1} and ψ_o is valid for suctions at 25°C (USDA, 1954). A subtle variation to Eqn 6.14 is used in Arifin and Schanz (2009):

$$\psi_o = 38.54\text{ec}^{1.0489} \quad (6.15)$$

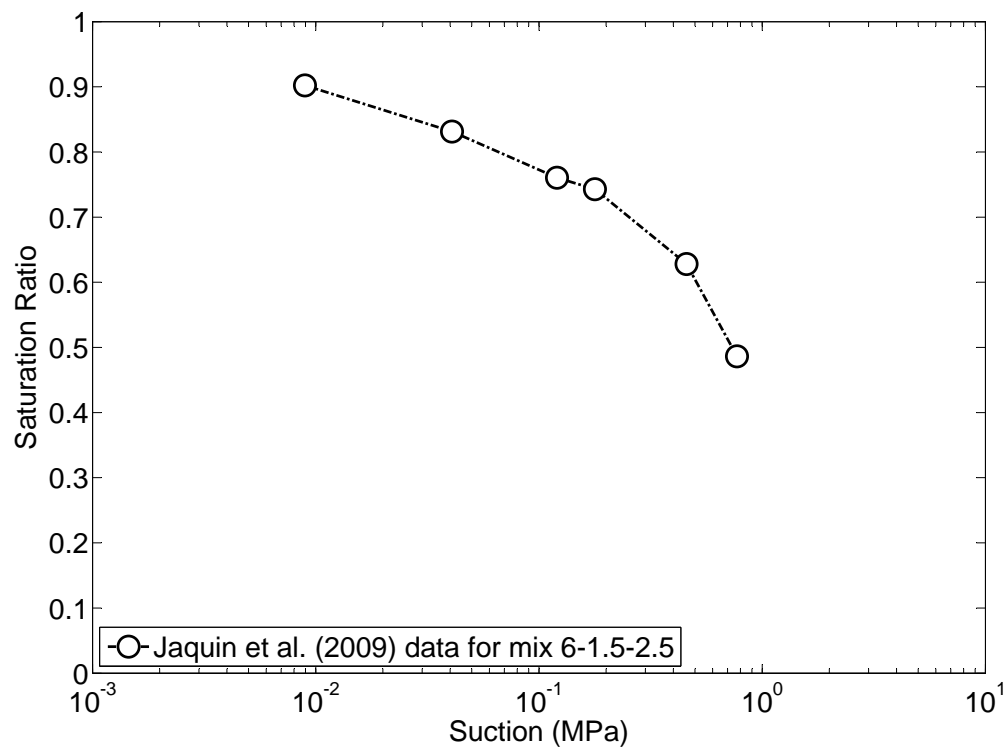


Figure 6.21: Mesured SWRC for mix 6-1.5-2.5 at zero applied load (Jaquin et al., 2009)

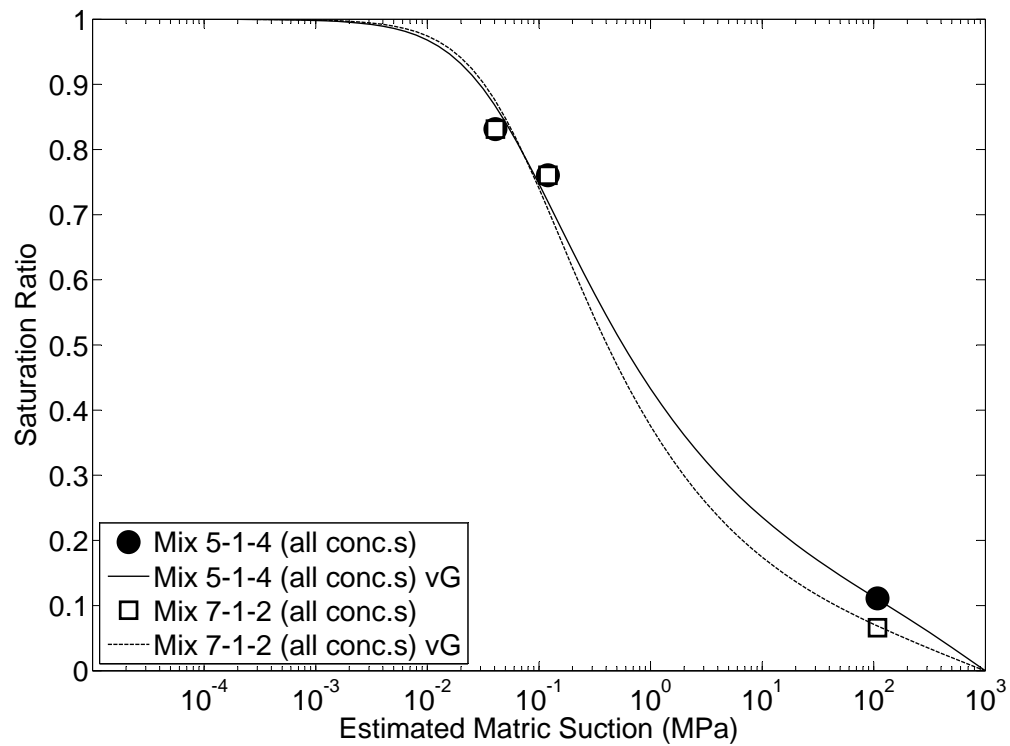


Figure 6.22: Estimated SWRC (matric suction) for mixes 5-1-4 and 7-1-2

as it provides an improved fit to the obtained data. A similar expression to Eqn 6.14 is also given in Mata et al. (2002):

$$\psi_o = A \left(\frac{ec}{1\mu\text{Scm}^{-1}} \right)^B \quad (6.16)$$

where $A = 0.019$ kPa and $B = 1.074$, again due to an improved fit to estimated data and which gives similar values for ψ_o to Eqns 6.14 and 6.15 in the range of ec values investigated in those articles.

A drawback of the use of Eqns 6.14 to 6.16 is that they are only validated for solutions of concentrations up to roughly 10%, i.e. in the roughly linear region of Figure 6.10; for concentrations above 10% the relationship between electrical conductivity and concentration becomes increasingly non-linear, so that the use of Eqns 6.14 to 6.16 becomes questionable. Instead of relying on the electrical conductivity, the Van't Hoff equation can be used to predict ψ_o from the solution molarity:

$$\psi_o = iMR_uT \quad (6.17)$$

where M is the molarity of the solution in molL^{-1} and i is the *Van't Hoff factor*, calculated via

$$i = 1 + (y - 1)x \quad (6.18)$$

where y is the number of molecules obtained from one molecule of the solute and x is the degree of ionisation of the solute, introduced to cover deviations from ideal solution behaviour (Mata et al., 2002; Rao and Shivananda, 2005). For CaCl_2 , $y = 3$ (one Ca^{2+} and two Cl^- ions) and $x = 1$, the latter due to the complete ionisation of the salt molecule, so that $i = 3$. However, tests conducted in Rao and Shivananda (2005) indicated that ψ_o values calculated using Eqn 6.17 were higher than those calculated using Eqn 6.14, so that a modified version is suggested for the rough prediction of ψ_o :

$$\psi_o = MR_uT \quad (6.19)$$

in that the Van't Hoff factor is set to 1.

Osmotic coefficients, ϕ_o , can also be determined for a given solution according to the procedure given in Lang (1967):

$$K = (1 + A(M^{0.5})) \quad (6.20)$$

$$\phi_o = 1 - \left(\frac{S_f d_0^{0.5}}{A^3 M} \right) \left(K - 2 \log(K) - \frac{1}{K} \right) + BM + CM^2 + DM^3 \quad (6.21)$$

$$\psi_o = -2MR_uT\phi_o \quad (6.22)$$

where $S_f d_0^{0.5}$, A , B , C and D are fitting parameters for a given salt type as given in Table 1 of Lang (1967) for NaCl . Although for NaCl rather than CaCl_2 , it was found in Rao and Shivananda (2005) and Arifin and Schanz (2009) that both salts produce almost identical ψ_o values for given concentrations/electrical conductivities. Due to the similarity between Eqns 6.17 and 6.22, the osmotic coefficient can be considered to be analogous to the Van't Hoff factor. As Eqns 6.17 to 6.22 are related to the solution molarity, rather than the electrical conductivity, they are arguably applicable to a greater range of solution concentrations.

An indirect method for predicting ψ_o from the solution concentration was also discussed in Section 2.4.3, whereby the difference between the saturated vapour pressures of the solution (p_{sol}^*) and pure, free water (p^*) can be used to determine the osmotic suction according to Eqn 2.29. Again, the advantage of Eqn 2.29 over Eqns 6.14 to 6.16 is that solution electrical conductivity is not required so that it can be applied to a greater range of solution concentrations. Note that, although the osmotic suction is conceptualised in Section 2.4.3 as the flow across a semi-impermeable membrane, no flow is

actually required in order to have an osmotic suction; the change in saturated vapour pressure due to the presence of a solute results in a change in the suction conditions regardless of flow.

A comparison between ψ_o predicted using Eqns 6.14 to 6.19 (omitting the very similar forms of Eqn 6.14 given by Arifin and Schanz (2009) and Mata et al. (2002)) and Eqn 2.29 for the initial solution CaCl_2 concentrations is given in Table 6.6. Where necessary, Figure 6.10 has been used to convert between electrical conductivity and solution concentration values. Note that predictions using Eqns 6.14 and 6.22 are determined at 25°C due to the lack of fitting data for 20°C. Despite the slight difference in temperature, these results show that predicted ψ_o values are not consistent between methods, regardless of whether the method relies on the electrical conductivity or the solution concentration. However, these results do show that large suctions exist even at relatively low solution concentrations, so that an evaluation of the osmotic suction present in CaCl_2 treated samples is necessary in order to describe observed results in terms of suction.

Drying of samples results in an increase in the concentration of the solution due to a decrease in the amount of water present per given volume of solution; this very basic process can be seen to occur on the evaporation of water from salt pans for the acquisition of salt from sea water. Therefore, initial concentrations are not representative of solution concentrations at low water contents. Due to the non-linearity of the concentration/electrical conductivity relationship shown in Figure 6.10, Eqns 6.14 to 6.16 are therefore not suitable for determining ψ_o at these higher concentrations. Furthermore, as Eqns 6.17 to 6.22 produce significantly different ψ_o predictions and rely on the use of arbitrary correction factors (be they the Van't Hoff factor or the osmotic coefficient), it is also suggested that they are not suitable for predicting ψ_o in this case. Therefore, Eqn 2.29 shall be used to evaluate ψ_o for the range of concentrations present in the tested samples.

The change in p_{sol}^* with solution concentration, necessary for the determination of ψ_o using Eqn 2.29, is shown in Figure 6.23 (Dow, 2008). Data for p_{sol}^* at 20°C were fitted with a quadratic regression of the form

$$p_{sol}^* = -0.46c^2 - 17.35c + 2396.28 \quad (6.23)$$

where c is the concentration of the solution in % CaCl_2 and p_{sol}^* is in Pa in order to determine intermediate vapour pressure values, as shown in Figure 6.24. As concentration changes with water content, a simple relationship between solution water content and concentration can then be determined as

$$\text{new concentration} = \left(\frac{\text{OWC}}{\text{WC}} \right) \times \text{initial concentration}, \quad (6.24)$$

where WC is the sample water content, so that the change in ψ_o with water content can be found assuming that drying results in the loss of water only. Note that, as concentrations of CaCl_2 of greater than 50% are not achievable at room temperature, this is the maximum solution concentration that can be used in conjunction with Eqn 6.23. ψ_o values found for various water contents for both mixes at different solution concentrations are given in Table 6.7, showing that ψ_o values for mix 7-1-2 at the lowest tested S_r values are significantly higher than those for mix 5-1-4, due to its higher OWC and lower equilibrium water content values and hence larger change in solution concentration between the two conditions. The effect of this significantly larger osmotic suction is discussed in the following sections.

6.4.4.3 Total suction

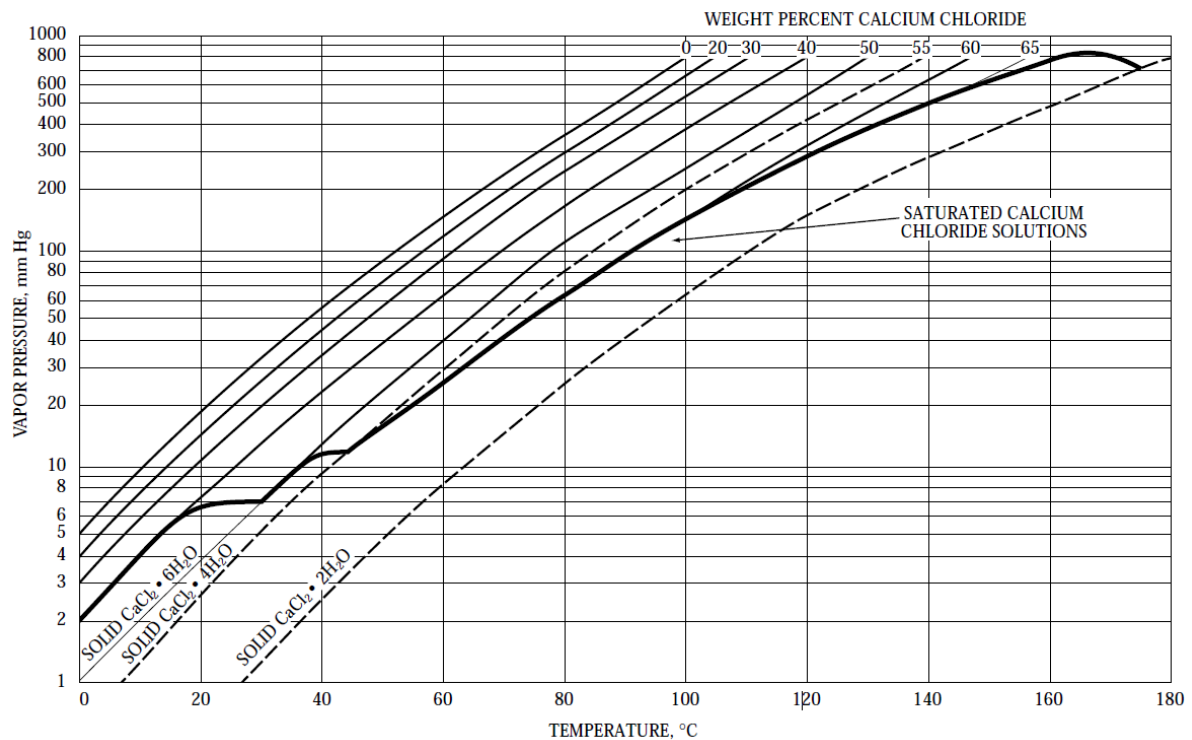
Total suction (ψ) can be found from $\psi = \psi_m + \psi_o$, as shown in Figures 6.25 and 6.26. As $\psi = \psi_m$ at 0 dsm^{-1} , these lines are identical to those in Figure 6.22. Also shown in Figures 6.25 and 6.26 is the best-fit van Genuchten prediction for ψ , found by fitting Eqn 6.10 to $\psi_m + \psi_o$ for the datapoints used to predict ψ_m in Section 6.4.4.1; corresponding parameter values are given in Table 6.8 (for ψ in Pa).

Table 6.6: Comparison between osmotic suction prediction methods given in Rao and Shivananda (2005), Lang (1967) and Dao et al. (2008)

ec	M	Conc. (%)	Eqn 6.14 (MPa)	Eqn 6.17 (MPa)	Eqn 6.19 (MPa)	Eqn 6.22 (MPa)	Eqn 2.29 (MPa)
0	0	0	0	0	0	N/A	0
20	1.44	1.6	0.88	10.52	3.51	7.11	1.50
40	2.88	3.1	1.79	21.05	7.02	14.94	3.18

Table 6.7: ψ_o values determined using Eqn 2.29 for different mix solution concentrations

Mix	S_r	ec	Conc. (%)	ψ_o (MPa)
5-1-4	0.86	20	1.60	1.50
5-1-4	0.83	20	1.65	1.55
5-1-4	0.76	20	1.80	1.72
5-1-4	0.11	20	12.35	16.96
5-1-4	0.86	40	3.10	3.18
5-1-4	0.83	40	3.19	3.29
5-1-4	0.76	40	3.49	3.64
5-1-4	0.11	40	23.92	44.95
7-1-2	0.84	20	1.60	1.50
7-1-2	0.83	20	1.61	1.51
7-1-2	0.76	20	1.76	1.67
7-1-2	0.07	20	20.31	34.61
7-1-2	0.84	40	3.10	3.18
7-1-2	0.83	40	3.12	3.21
7-1-2	0.76	40	3.42	3.55
7-1-2	0.07	40	39.35	118.37

Figure 6.23: Change in CaCl_2 (saturated) vapour pressure with changing temperature and solution concentration (Dow, 2008)

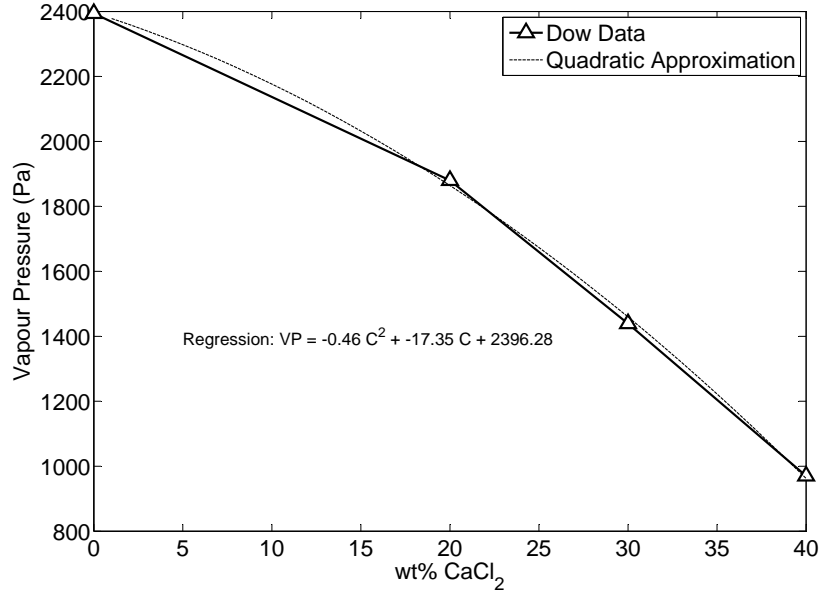


Figure 6.24: Approximated change in CaCl₂ (saturated) vapour pressure with changing solution concentration (Dow, 2008)

Table 6.8: van Genuchten fitting parameters used to estimate ψ in mixes 5-1-4 and 7-1-2

Mix	Concentration (dSm ⁻¹)	α	n
5-1-4	0	$10^{-4.66}$	1.29
5-1-4	20	$10^{-6.25}$	1.51
5-1-4	40	$10^{-6.60}$	1.57
7-1-2	0	$10^{-4.75}$	1.36
7-1-2	20	$10^{-6.28}$	1.61
7-1-2	40	$10^{-6.61}$	1.63

Although both $\psi_m + \psi_o$ and the modified van Genuchten expression pass through these datapoints (as expected), the trends described by each are different due to the former's dependence on the change in solution concentration. Therefore, although ψ_m is necessarily estimated using Eqn 6.10, ψ values used are those found using $\psi = \psi_m + \psi_o$ with ψ_o calculated using Eqn 2.29.

It is suggested in Arifin and Schanz (2009) that $\psi = \psi_m + \psi_o + \psi_H$, where ψ_H is the hydration force component of suction, attributed to clay swelling; however, it is assumed that a ψ_H term is not required here due to the use of mixes comprising low clay contents (both mixes 5-1-4 and 7-1-2 and that used by Jaquin et al. (2009)) and the use of low-swelling kaolinitic clays.

An interesting feature to note is that, around the sample equilibrium water content, the effect of ψ_o becomes negligible compared to that of ψ_m , so that the limit on total suction of 1 GPa appears to remain valid even at high solution concentrations. This is predominantly due to the effect of a significant increase in ψ_o as water contents reduce, however the limit on p_{sol}^* due to the inability to create solutions above 50% concentration at room temperature also limits the possible values of ψ_o at these water contents.

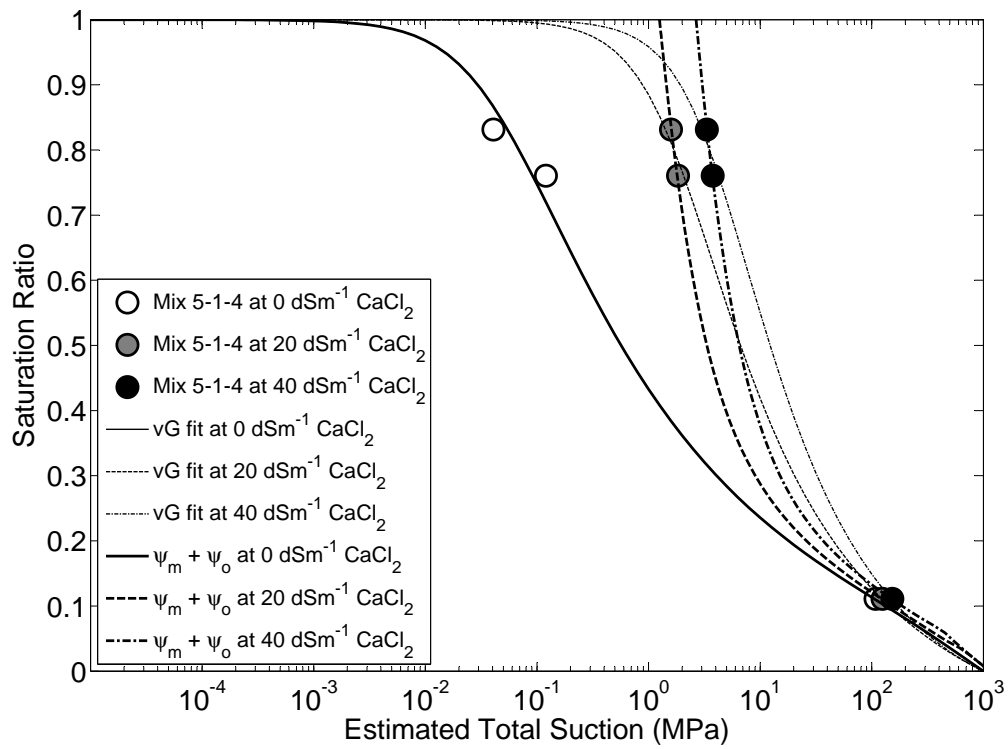


Figure 6.25: Estimated SWRC (total suction) for mix 5-1-4

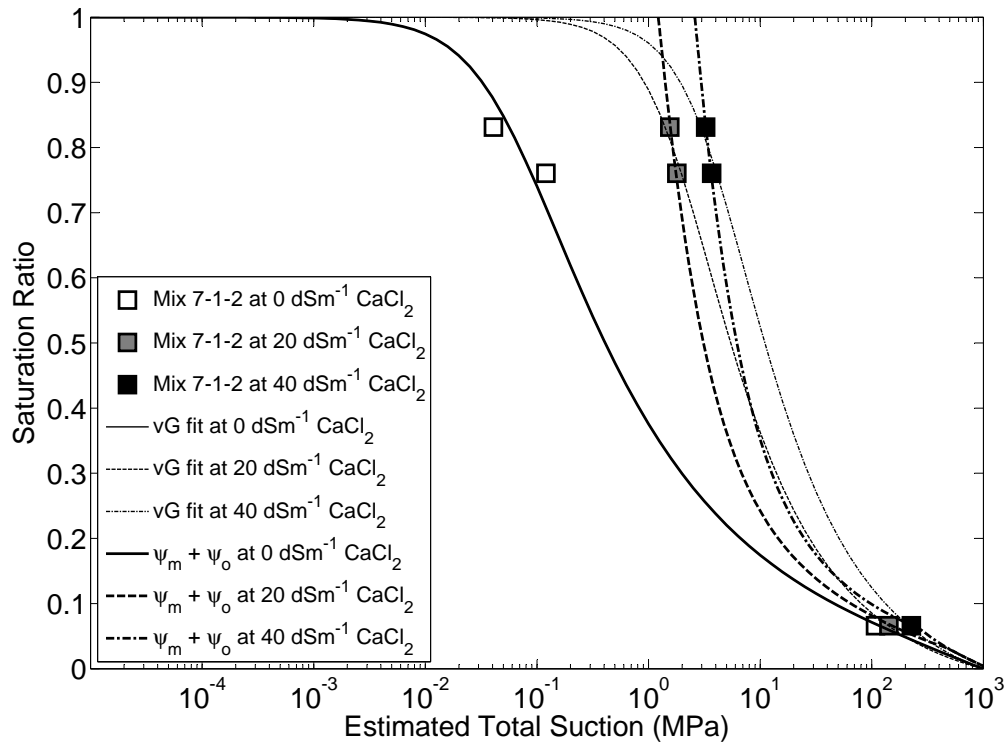


Figure 6.26: Estimated SWRC (total suction) for mix 7-1-2

6.4.5 Change in tensile strength with suction and CaCl_2 content

Measured tensile strength against estimated matric suction values are shown in Figure 6.27. Figures 6.17, 6.18 and 6.27 are quite similar, in that an increase in CaCl_2 concentration produces an apparent increase in the tensile strengths of samples of mix 7-1-2 and an apparent decrease in those of mix 5-1-4 in the central ψ_m value range, but little change at higher or lower ψ_m values, at least when considering the spread of the experimental data; this is to be expected, as ψ_m does not change with CaCl_2 content for a given value of S_r , Figure 6.27 is effectively a simple transformation of Figures 6.17 and 6.18. Although it is tempting to interpret results shown in Figure 6.27 as a converging of the results to a unique relationship between tensile strength and ψ_m as CaCl_2 content increases, this is not the case and is simply a result of the use of the one set of axes and the coincidence of similar tensile strength results for both mixes at 40 dSm^{-1} .

The result of reducing soil tensile strengths with the addition of Ca^{2+} ions has been observed by many previous authors (e.g. Albrecht (1940)) and is attributed to changes in the material structure caused by the breakdown of clayey aggregates due to clay flocculation and a corresponding increase in volume of larger pores present within the material (and so flaws capable of causing crack formation and propagation) due to the reduced packing efficiency of the aggregates (Dexter and Chan, 1991; Grant et al., 1992; Chorom et al., 1994; Barzegar et al., 1996; Dexter, 1997; Sivakumar and Wheeler, 2000). As the mechanism of flocculation is the formation of flocs (i.e. fragile structures), this would suggest that flocculation results in the formation of *larger*, rather than smaller aggregates; however, as these flocs are fragile, they are unable to act as bridging material between larger particles, so that aggregate size instead decreases. This effect was observed during material preparation as a reducing of the size of the clayey bodies which formed on wetting dry RE material with solutions of increasing CaCl_2 concentration. In Braunack et al. (1979) it was found that the tensile strength of aggregates increases as the size of the aggregate decreases, due to their being more dense and containing fewer surface cracks (Utomo and Dexter, 1981; Dexter, 1988; Causarano, 1993), suggesting that the breaking down of clayey aggregates on the addition of CaCl_2 should increase rather than decrease the tensile strengths of both mixes 5-1-4 and 7-1-2. However, as aggregate size is reducing due to changes in the material structure, it can be assumed that the findings of Braunack et al. (1979) do not apply in this case.

Tensile strength against total suction values are shown in Figure 6.28, showing the considerable difference between ψ_m and ψ values at higher CaCl_2 contents when compared to Figure 6.27. Note that, as $\psi = \psi_m$ for solutions of 0 dSm^{-1} , both figures show the same results for that concentration. Although data for mix 5-1-4 shows reducing tensile strengths with increasing CaCl_2 contents as it did in Figure 6.27, data for mix 7-1-2 appear to conform to an almost unique trend for changing tensile strength with ψ except for a few results at very low ψ values. This suggests that the effect of the significantly higher ψ_o values for a given S_r in samples of mix 7-1-2 is to counteract the weakening of the material structure due to clay flocculation. As the differences between ψ_m and ψ are relatively small at low S_r values and both ψ and ψ_m are small at high S_r values, this also suggests a reason for why the effect of changing CaCl_2 content on tensile strength appears to be restricted to the central range of S_r values.

The tensile failure of an unsaturated soil sample is assumed to be due to the breaking of liquid bridges between particles, so that it is analogous to the capillary forces present in the material (Dexter, 1997; Ghezzehei and Or, 2000; Vesga, 2008; Rojas et al., 2010); if this is the case, then a strong relationship should exist between ψ_m and tensile strength, as ψ_o has no capillary component (as discussed in Section 2.4.3). Figure 6.27 shows that this is arguably the case, however Figure 6.28 also shows that changing solution concentrations, and so ψ_o values, result in a change in tensile strength for a given ψ_m value. Tensile failure is therefore more appropriately described in terms of the total suction present in the material. Regardless, it would appear that the presence or introduction of dissolved ions to the soil

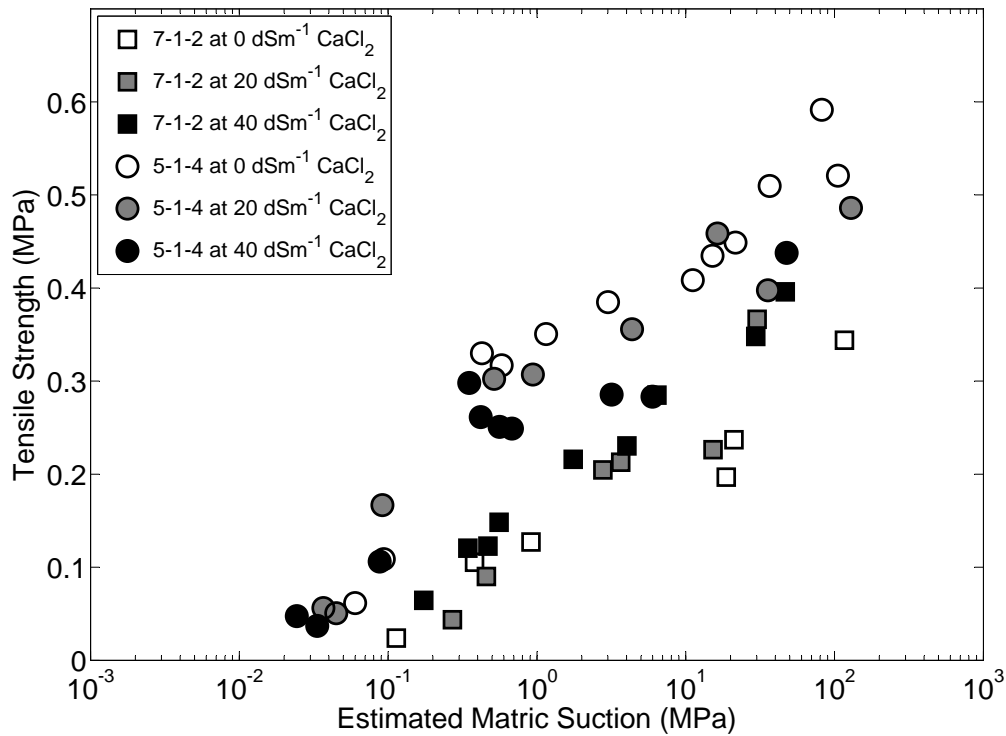


Figure 6.27: Change in tensile strength with estimated ψ_m and CaCl_2 content for mixes 5-1-4 and 7-1-2

water of RE mixes can have either a detrimental or beneficial effect on the material properties, so that the addition of dissolved ions might offer a method to improve the suitability of soils for RE construction. As this effect depends on both the species of dissolved ions and the clay content of the soil, however, practitioners should verify the effects of any added dissolved ions prior to construction.

6.4.6 Comparison between tensile and unconfined compressive strengths

A comparison between tensile and unconfined compressive strengths for mixes 5-1-4 and 7-1-2 at 20°C and 45% RH is given in Table 6.9. Results presented in Tarantino (2010) suggest that the method of compaction does not affect the resulting material structure, so that samples prepared to their optimum density using the light Proctor method in this investigation can be compared to samples prepared using an electric hammer to their optimum density in Chapter 5. Furthermore, mixes 5-1-4 and 7-1-2 used in this investigation at 0 dSm^{-1} showed equilibrium water contents around 1.4 and 1.0% respectively for $\psi_m \approx 105$ MPa (estimated); these agree well with data for 20°C and 45% RH for mixes used in Chapter 5, as given by Figures 5.14 and 5.20 (1.2 and 0.8% respectively, at $\psi_m \approx 130$ MPa, based on drying curve results), again suggesting that samples used in both investigations had similar structures and that comparisons between them are valid.

The unconfined compressive and tensile strengths, the latter determined using the Brazilian test, of two sandy-clay loam soils were compared in Young and Mullins (1991). It was found that compressive strengths were roughly 6.3 times those of the tensile strengths for both soils at a range of water contents tested at a deformation rate of 10 mm/min. This result agrees with those found by Tiwari and Ajmera (2011), who showed that an increase in the clay content of a material results in a reduced maximum shear stress for a given effective stress (for tests conducted on both kaolinitic and montmorillonitic soil

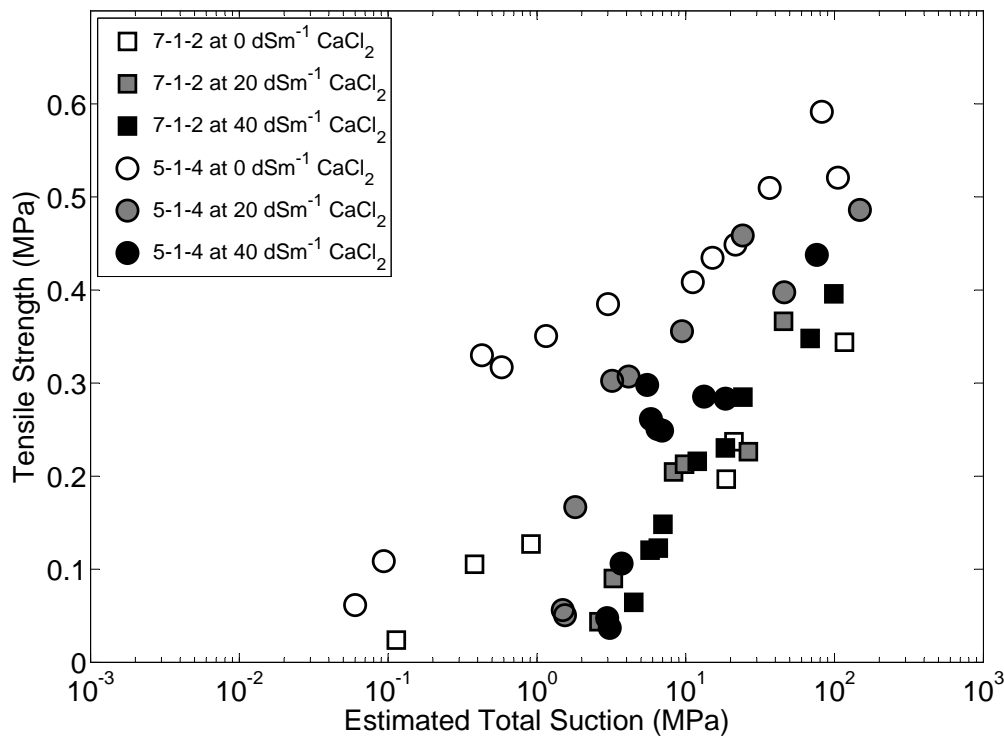


Figure 6.28: Change in tensile strength with estimated ψ_m and CaCl_2 content for mixes 5-1-4 and 7-1-2

Table 6.9: Tensile (TS) and equivalent compressive strength (ECS) values at equilibrium water contents for soil mixes 5-1-4 and 7-1-2 at 0 dSm^{-1} for 20°C and $45\%\text{RH}$

Soil mix	Sample number	Water content (%)	TS (MPa)	ECS (MPa)	TS % of ECS
5-1-4 at 0 dSm^{-1}	4	1.4	0.52	1.10	47.3
7-1-2 at 0 dSm^{-1}	2	1.0	0.34	1.25	27.2

mixes). Testing rates of 0.1 mm/min and 10 mm/min were compared in order to determine the effect of deformation rate on calculated compressive and tensile strengths, showing that the deformation rate did not significantly affect the calculated strengths given the variability inherent in the material. Mixes 5-1-4 and 7-1-2 are similar in composition to sandy clay loams (being loam and sandy loam soils respectively), however Table 6.9 shows that mix 5-1-4 only achieved equivalent unconfined compressive strength values of roughly 4 times those found in tension, whilst those for mix 7-1-2 were only roughly twice the tensile values. Reasons for this disparity, apart from the use of subtly different soil types, lie in the use of significantly smaller samples for strength testing in Young and Mullins (1991) (20 mm diameter, 40 mm in height for compressive and tensile testing) and a significantly higher deformation rate. These results therefore give an impression as to the variability inherent in unsaturated soils testing, as the selection of different sample sizes and testing rates for otherwise similar materials can significantly affect the results. It is suggested that the results presented in Table 6.9 are more representative of the behaviour of the material in bulk than those presented in Young and Mullins (1991) due to the use of significantly larger samples, however further work would be to assess the effect of deformation rates on the determined strengths.

6.5 Conclusion

The aim of the work conducted in this chapter was to investigate the tensile strengths of RE soil mixes and how this changes with S_r and the addition of dissolved ions in order to determine whether the presence of dissolved ions is a concern for RE construction.

Failure profiles for samples tested at high and low water contents were compared and it was found that samples display ductile-like failures at high water contents and brittle-like failures at low water contents, with a water content of roughly 7.5% dividing the two for both mixes. Failure profiles for samples tested using the Brazilian test have been shown to be similar to those found using direct tension testing methods, verifying the validity of the use of the Brazilian test with soil samples. It has been shown that the failure profiles for samples of both mixes at a given water content are similar, so that their calculated tensile strengths can be directly compared. However, it is suggested that a comparison of calculated tensile strengths between high and low water content samples of the same soil mix should be avoided due to the different failure mechanisms. This is an area which requires further research.

Tensile strength data was found for different S_r values and CaCl_2 contents using the Brazilian test. It was found that the addition of CaCl_2 had the greatest effect on tensile strength in the central range of S_r values, but that any change in sample tensile strengths at high or low S_r values were indiscernible from the variation in experimental results.

Matric, osmotic and total suction values were estimated for tested samples using available literature and experimental data. Matric suction was determined according to a modified van Genuchten approximation. Methods for determining the osmotic suction were compared, concluding that those methods which depend on the solution electrical conductivity were not suitable for solution concentrations used in this investigation due to the non-linearity of changing electrical conductivity with CaCl_2 content. Instead, osmotic suction was estimated from changing vapour pressure values. Total suction was then estimated from the sum of the matric and osmotic suction values. It was found that matric suction values were higher in samples of mix 5-1-4 than in those of mix 7-1-2 for solutions at 0 dSm^{-1} , so that the former consistently achieved higher tensile strengths at given water contents than the latter. It was argued that the effect of significantly higher osmotic suctions in mix 7-1-2 than in mix 5-1-4 for solution concentrations at 20 and 40 dSm^{-1} is to counteract the reduction in material strength caused by clay flocculation and to produce increasing tensile strengths with CaCl_2 content, in the central range of S_r values, rather than the decreasing strengths commonly observed by other authors. The relative significance of osmotic suction as compared to matric suction values in the central S_r value range as compared to those at high and low S_r values was then used to explain the significant effect of CaCl_2 addition on the tensile strength in that S_r value range.

A comparison between soil mix equilibrium water contents and matric suction values for mixes used in this investigation and those in Chapter 5 was made, showing a good agreement between the values. A comparison between the tensile strength and equivalent unconfined compressive strength for samples under equilibrium conditions showed that samples of mix 7-1-2 achieve unconfined compressive strengths roughly 4 times those in tension, whilst samples of mix 5-1-4 achieve unconfined compressive strengths only twice as high. A comparison to literature values indicates that the difference between these values changes significantly for different soils, so that the use of a single relation between them should be avoided.

6.6 References

- Ajaz, A., Parry, R. G. H., 1974. An unconfined direct tension test for compacted clays. *American Society for Testing and Materials Journal of Testing and Evaluation* 2 (3), 163–172.
- Ajaz, A., Parry, R. G. H., 1975a. Analysis of bending stresses in soil beams. *Géotechnique* 23 (3), 586–591.
- Ajaz, A., Parry, R. H. G., 1975b. Brazilian tensile test for soils: Discussion. *Canadian Geotechnical Journal* 12 (4), 542–544.
- Ajaz, A., Parry, R. H. G., 1975c. Stress-strain behaviour of two compacted clays in tension and compression. *Géotechnique* 25 (3), 495–512.
- Albrecht, W. A., 1940. Calcium-potassium-phosphorus relation as a possible factor in ecological array of plants. *Journal of the American Society of Agronomy* 32, 411–418.
- Arifin, Y., Schanz, T., 2009. Osmotic suction of highly plastic clays. *Acta Geotechnica* 4, 177–191.
- Atkinson, B. K. (Ed.), 1987. *Fracture mechanics of rock*. Academic Press Inc., London (UK).
- Aydin, A., Basu, A., 2006. The use of brazilian test as a quantitative measure of rock weathering. *Rock Mechanics and Rock Engineering* 39 (1), 77–85.
- Azmach, T. F., Sego, D. C., Arenson, L. U., Biggar, K. W., 2011. Tensile strength and stress-strain behaviour of devon silt under frozen fringe conditions. *Cold Regions Science and Technology* In Press, Corrected Proof, –.
- Baltodano-Goulding, R., September 2010. Deformation behavior in unsaturated soils. In: Alonso, E., Gens, A. (Eds.), *Unsaturated Soils*. Fifth International Conference on Unsaturated Soils, CRC Press, pp. 181–185.
- Barzegar, A., November 1995. Structural stability and mechanical strength of salt-affected soils. PhD Thesis, The University of Adelaide.
- Barzegar, A., Murray, R., Churchman, G., Rengasamy, P., 1994a. The strength of remolded soils as affected by exchangeable cations and dispersible clay. *Australian Journal of Soil Research* 32 (2), 185–199.
- Barzegar, A. R., Oades, J. M., Rengasamy, P., 1996. Soil structure degradation and mellowing of compacted soils by saline sodic solutions. *Soil Science Society of America Journal* 60 (2), 583–588.
- Barzegar, A. R., Oades, J. M., Rengasamy, P., Giles, L., 1994b. Effect of sodicity and salinity on disaggregation and tensile strength of an alfisol under different cropping systems. *Soil & Tillage Research* 32 (4), 329–345.
- Barzegar, A. R., Oades, J. M., Rengasamy, P., Murray, R. S., 1995a. Tensile strength of dry, remoulded soils as affected by properties of the clay fraction. *Geoderma* 65 (1-2), 93–108.
- Barzegar, A. R., Rengasamy, P., Oades, J. M., 1995b. Effects of clay type and rate of wetting on the mellowing of compacted soils. *Geoderma* 68 (1-2), 39–49.
- Beckett, C. T. S., 2008. *Cracking in rammed earth*. MEng Dissertation, Durham University, Durham, UK.
- Braunack, M. V., Hewitt, J. S., Dexter, A. R., 1979. Brittle fracture of soil aggregates and compaction of aggregate beds. *Journal of Soil Science* 30, 653–667.
- BSI, 1990. BS 1377:1990. Methods of test for soils for civil engineering purposes.
- Bui, Q.-B., Morel, J.-C., 2009. Assessing the anisotropy of rammed earth. *Construction and Building Materials* 23 (9), 3005–3011.
- Carneiro, F. L. L. E., Barcellos, A., 1953. Concrete tensile strength. *RILEM Bulletin Paris* 13.
- Causarano, H., 1993. Factors affecting the tensile strength of soil aggregates. *Soil & Tillage Research* 28 (1), 15–25.
- Chorom, M., Regasamy, P., Murray, R. S., 1994. Clay dispersion as influenced by ph and net particle charge of sodic soils. *Australian Journal of Soil Research* 32 (6), 1243–1252.
- Coviello, A., Lagioia, R., Nova, R., 2005. On the measurement of the tensile strength of soft rocks. *Rock Mechanics and Rock Engineering* 38 (4), 251–273.
- Dao, V. N. T., Morris, P. H., Dux, P. F., 2008. On equations for the total suction and its matric and osmotic components. *Cement and Concrete Research* 38 (11), 1302–1305.
- Dehandschutter, B., Vandycke, S., Sintubin, M., Vandenberghe, N., Gaviglio, P., Sizun, J. P., Wouters, L., 2004. Microfabric of fractured boom clay at depth: a case study of brittle-ductile transitional clay behaviour. *Applied Clay Science* 26 (1-4), 389–401.
- Dehandschutter, B., Vandycke, S., Sintubin, M., Vandenberghe, N., Wouters, L., 2005. Brittle fractures and ductile shear bands in argillaceous sediments: inferences from oligocene boom clay (belgium). *Journal of Structural Geology* 27 (6), 1095–1112.
- Delage, P., 2009. Discussion: Compaction behaviour of clay. *Géotechnique* 59 (1), 75–77.
- Dexter, A., 1988. Advances in characterization of soil structure. *Soil and Tillage Research* 11 (3-4), 199–238.
- Dexter, A. R., 1997. Physical properties of tilled soils. *Soil and Tillage Research* 43 (1-2), 41–63.

- Dexter, A. R., Chan, K. Y., 1991. Soil mechanical properties as influenced by exchangeable cations. *Journal of Soil Science* 42 (2), 219–226.
- Dexter, A. R., Kroesbergen, B., 1985. Methodology for determination of tensile strength of soil aggregates. *Journal of Agricultural Engineering Research* 31, 139–147.
- Diamond, S., 1970. Pore size distribution in clays. *Clays and Clay Minerals* 18, 7–23.
- Dodson, B., 1994. *Weibull Analysis*. ASQ Quality Press, Milwaukee (USA).
- Dow, 2008. *Calcium chloride handbook: A guide to properties, forms, storage and handling*. Dow Chemical Company (USA).
- Easton, D., 2007. *The Rammed Earth House, Completely Revised Edition*. Chelsea Green Publication Company, Vermont (USA).
- Farrell, D. A., Greacen, E. L., Larson, W. E., 1967. The effect of water content on axial strain in a loam soil under tension and compression. *Soil Society of America Proceedings* 32, 445–450.
- Fredlund, D., Rahardjo, H., 1993. *Soil Mechanics for Unsaturated Soils*. John Wiley & Sons Inc., New York (USA).
- Fredlund, D. G., Xing, A., 1994. Equations for the soil-water characteristic curve. *Canadian Geotechnical Journal* 31, 521–532.
- Frydman, S., 1964. The applicability of the Brazilian (indirect tension) test to soils. *Australian Journal of Applied Science* 15, 335–343.
- Gens, A., Valleján, B., Sánchez, M., Imbert, C., Villar, M. V., Van Geet, M., 2011. Hydromechanical behaviour of a heterogeneous compacted soil: experimental observations and modelling. *Géotechnique* 61 (5), 367–386.
- Ghezzehei, T. A., Or, D., 2000. Dynamics of soil aggregate coalescence governed by capillary and rheological processes. *Water Resour. Res.* 36, 367–379.
- Gordon, J. E., 1991. *Structures: Or why things don't fall down*, eleventh Edition. Penguin Group, London (UK).
- Grant, C. D., Dexter, A. R., Oades, J. M., 1992. Residual effects of additions of calcium compounds on soil structure and strength. *Soil & Tillage Research* 22 (3-4), 283–297.
- Griffith, A. A., 1921. The phenomena of rupture and flow in solids. *Philosophical Transactions of the Royal Society of London. Series A, Containing Papers of a Mathematical or Physical Character* 221, pp. 163–198.
- Hallett, P. D., Dexter, A. R., Seville, J. P. K., 1995. Identification of pre-existing cracks on soil fracture surfaces using dye. *Soil and Tillage Research* 33 (3-4), 163–184.
- Hillel, D., 2004. *Fundamentals of Soil Physics*. Academic Press, Inc., London (UK).
- Horn, R., Taubner, H., Wuttke, M., Baumgartl, T., 1994. Soil physical properties related to soil structure. *Soil and Tillage Research* 30 (2-4), 187–216.
- Houben, H., Guillaud, H., 1996. *Earth construction - a comprehensive guide.*, Second Edition. Intermediate Technology Publications, London (UK).
- Hoyos, L. R., Pérez-Ruiz, D., Puppala, A. J., 2010. Constitutive modeling of unsaturated soil behavior using a refined suction-controlled true triaxial cell: Preliminary observations. In: Alonso, E., Gens, A. (Eds.), *Unsaturated Soils. Fifth International Conference on Unsaturated Soils*, CRC Press.
- Ibarra, S. Y., McKyes, E., Broughton, R. S., 2005. Measurement of tensile strength of unsaturated sandy loam soil. *Soil and Tillage Research* 81 (1), 15–23.
- Irwin, G. R., 1957. Analysis of stresses and strains near the end of a crack traversing a plate. *Journal of Applied Mechanics* 24, 361–364.
- Jaquin, P. A., 2008. *Analysis of historic rammed earth construction*. PhD Thesis, Durham University.
- Jaquin, P. A., Augarde, C. E., Gallipoli, D., Toll, D. G., 2009. The strength of unstabilised rammed earth materials. *Géotechnique* 59 (5), 487–490.
- Jaquin, P. A., Augarde, C. E., Legrand, L., 2008. Unsaturated characteristics of rammed earth. In: Toll, D. G. (Ed.), *First European Conference on Unsaturated Soils*. Durham University, Durham, England, pp. 417–422.
- Kay, B. D., Dexter, A. R., 1992. The influence of dispersible clay and wetting drying cycles on the tensile-strength of a red-brown earth. *Australian Journal of Soil Research* 30 (3), 297–310.
- King, B., 1996. *Buildings of Earth and Straw: Structural Design for Rammed Earth and Straw-Bale Architecture*. Ecological Design Press, Sausalito, California (USA).
- Kirk, H., 2009. *The behaviour of low plasticity rammed earth soils*. Masters Thesis, Imperial College London.
- Krishnayya, A. V. G., Eisenstein, Z., 1974. Brazilian tensile test for soils. *Canadian Geotechnical Journal* 11 (4), 632–642.
- Krishnayya, A. V. G., Eisenstein, Z., 1975. Brazilian tensile test for soils: second reply. *Canadian Geotechnical Journal* 12 (4), 544–545.
- Krishnayya, A. V. G., Eisenstein, Z., Morgenstern, N. R., 1974. Behaviour of compacted soil in tension. *Journal of the Geotechnical Engineering Division, Proceedings of the American Society of Civil Engineers* 100 (GT9), 1051–1061.
- Lang, A. R. G., 1967. Osmotic coefficients and water potentials of sodium chloride solutions from 0 to 40°C. *Australian Journal of Chemistry* 20, 2017–2023.

- Leonards, G. A., Narain, J., 1963. Flexibility of clay and cracking of earth dams. *American Society of Civil Engineering Journal of Soil Mechanics and Foundation Engineering* 89 (SM2), 47–98.
- Mata, C., Romero, E., Ledesma, A., 2002. Hydro-chemical effects on water retention in bentonite-sand mixtures. In: Juco, J. F. T., De Campas, T. M. P., Marinho, F. A. M. (Eds.), *Proceedings of the 3rd International Conference on Unsaturated Soils*. Vol. 1. Swets and Zeitlinger, Rotterdam (NL), pp. 283–288.
- Mendes, J., 2011. The impact of climate change on an instrumented embankment: an unsaturated soil mechanics approach. PhD. Thesis, Durham University, Durham.
- Mualem, Y., 1976. A new model for predicting the hydraulic conductivity of unsaturated porous media. *Water Resour. Res.* 12, –.
- Mullins, C. E., Panayiotopoulos, K. P., 1984. The strength of unsaturated mixtures of sand and kaolin and the concept of effective stress. *European Journal of Soil Science* 35 (3), 459–468.
- Munkholm, L. J., Schjønning, P., Kay, B. D., 2002. Tensile strength of soil cores in relation to aggregate strength, soil fragmentation and pore characteristics. *Soil and Tillage Research* 64 (1-2), 125–135.
- Nahlawi, H., Chakrabarti, S., Kodikara, J., 2004. A direct tensile strength testing method for unsaturated geomaterials. *Geotechnical Testing Journal* 27 (4), 356–361.
- Olivella, S., September 2010. Geotechnical and environmental models involving unsaturated soils and rocks. In: Alonso, E., Gens, A. (Eds.), *Unsaturated Soils*. Fifth International Conference on Unsaturated Soils, CRC Press.
- Panayiotopoulos, K. P., 1996. The effect of matric suction on stress-strain relation and strength of three alfisols. *Soil and Tillage Research* 39 (1-2), 45–59.
- Prashant, A., Penumadu, D., 2007. Effect of microfabric on mechanical behaviour of kaolin clay using cubical true tri-axial testing. *Journal of Geotechnical and Geoenvironmental Engineering* 133 (4), 433–444.
- Rahimi, H., Pazira, E., Tajik, F., 2000. Effect of soil organic matter, electrical conductivity and sodium adsorption ratio on tensile strength of aggregates. *Soil & Tillage Research* 54 (3-4), 145–153.
- Rao, S. M., Shivananda, P., 2005. Role of osmotic suction in swelling of salt-amended clays. *Canadian Geotechnical Journal* 42, 307–315.
- Rojas, E., Gallegos, G., Leal, J., September 2010. A porous model based on porosimetry to simulate retention curves. In: Alonso, E., Gens, A. (Eds.), *Unsaturated Soils*. Fifth International Conference on Unsaturated Soils, CRC Press, pp. 927–932.
- Rondeau, X., Affolter, C., Komunjer, L., Clausse, D., Guigon, P., 2003. Experimental determination of capillary forces by crushing strength measurements. *Powder Technology* 130 (1-3), 124–131.
- Sivakumar, V., Wheeler, S., 2000. Influence of compaction procedure on the mechanical behaviour of an unsaturated compacted clay. part 1: Wetting and isotropic compression. *Géotechnique* 50 (4), 359–368.
- SmartMeasurement, 2001. Conductivity of calcium chloride. Online, accessed 25.05.2009.
- Tamrakar, S. B., Mitachi, T., Toyosawa, Y., Mar 07-09 2007a. Factors affecting tensile strength measurement and modified tensile strength measuring apparatus for soil. Weimar, Germany, pp. 207–218.
- Tamrakar, S. B., Mitachi, T., Toyosawa, Y., 2007b. Measurement of soil tensile strength and factors affecting its measurements. *Soils and Foundations* 47 (5), 911–918.
- Tamrakar, S. B., Toyosawa, Y., Mitach, T., Itoh, K., 2005. Tensile strength of compacted and saturated soils using newly developed tensile strength measuring apparatus. *Soils and Foundations* 45 (6), 103–110.
- Tang, G. X., Graham, J., 2000. A method for testing tensile strength in unsaturated soils. *Geotechnical Testing Journal* 23 (3), 377–382.
- Tarantino, A., 2009. A water retention model for deformable soils. *Géotechnique* 59 (9), 751–762.
- Tarantino, A., 2010. Unsaturated soils: compaction versus reconstituted states. In: Alonso, E., Gens, A. (Eds.), *Unsaturated soils*. Fifth International Conference on Unsaturated Soils, CRC Press, pp. 113–136.
- Tiwari, B., Ajmera, B., 2011. A new correlation relating the shear strength of reconstituted soil to the proportions of clay minerals and plasticity characteristics. *Applied Clay Science* 53 (1), 48–57.
- Toll, D. G., 1999. A data acquisition and control system for geotechnical testing. In: Toll, D. (Ed.), *Computing developments in civil and structural engineering*. Civil-Comp Press Ltd.
- UCAR, 2002. Salinity - dissolved salts, measuring salinity. University Corporation for Atmospheric Research, Online, accessed 25.05.2009.
- USDA, 1954. *Agriuculture handbook No. 60*, Diagenesis and improvement of saline and alkali soils. United States Salinity Laboratory, California (USA).
- Utomo, W. H., Dexter, A. R., 1981. Soil friability. *Journal of Soil Science* 32 (2), 203–213.
- Vallejo, L. E., 2010. Compressive strength of unsaturated fissured clays. In: Alonso, E., Gens, A. (Eds.), *Unsaturated soils*. Fifth International Conference on Unsaturated Soils, CRC Press, pp. 387–390.

-
- van Genuchten, M. T., 1980. A closed-form equation for predicting the hydraulic conductivity of unsaturated soils. *Soil Sci Soc Am J* 44 (5), 892–898.
- Vanapalli, S. K., Fredlund, D. G., Pufahl, D. E., 1999. The influence of soil structure and stress history on the soil-water characteristics of a compacted till. *Géotechnique* 49 (2), 143–159.
- Vesga, L., 2008. Equivalent effective stress and compressibility of unsaturated kaolinite clay subjected to drying. *Journal of Geotechnical and Geoenvironmental Engineering* 134 (3), 366–378.
- Vomocil, J. A., Waldron, L. J., Chancellor, W. J., 1961. Soil tensile strength by centrifugation. *Soil Society of America Proceedings* 25, 176–180.
- Walker, P., Keable, R., Martin, J., Maniatis, V., 2005. *Rammed Earth: Design and Construction Guidelines*. BRE Bookshop, Watford (UK).
- Wang, J. J., Zhu, J. G., Chiu, C. F., Zhang, H., 2007. Experimental study on fracture toughness and tensile strength of a clay. *Engineering Geology* 94 (1-2), 65–75.
- Young, I. M., Mullins, C. E., 1991. Factors affecting the strength of undisturbed cores from soils with low structural stability. *European Journal of Soil Science* 42 (2), 205–217.
- Zhang, L. M., Li, X., 2010. Microporosity structure of coarse granular soils. *J. Geotech. and Geoenviron. Engrg.* 136 (10), 1425–1436.
-

Chapter 7

Macrostructural investigation of rammed earth using X-ray computed tomography

7.1 Introduction

In Chapter 6, the failure of brittle materials was discussed and attributed to the formation and propagation of cracks, initiating in the pores. In this chapter, fractal analysis of binary threshold images obtained using XRCT is used to determine the extent of the effect of loading and the compaction of additional layers on the material structure. This is important to RE construction, as an understanding of the material changes will aid designers in predicting how the behaviour of the material will subsequently change and, if required, how best to repair damage in RE structures.

The effect of layering on the structure of RE was investigated in Chapter 4 through the use of particle image velocimetry to monitor the deformations of two layers of artificial RE material under compaction, and it was found that a layer of RE is not affected by the compaction of a layer above it. However, it was not determined whether the material structure changed or was constant throughout a single layer, due to the use of 2-D images of the material surface and the presence of deformations larger than those detectable. Results presented in Morel et al. (2007) and Bui and Morel (2009) suggest that the material density changes throughout the layer, so that the material properties might also change. As these changes in behaviour can be detrimental to the structure (e.g. reduced strength or increased permeability), it is necessary to understand how compaction of different layer thicknesses affects the material structure so that appropriate thicknesses can be used. XRCT can be used to non-destructively recreate detected pore networks, so that changes in material density can be determined. By using multi-layered samples, density changes across layer interfaces can also be investigated.

7.2 X-ray computed tomography

Computerised tomography (CT) was developed in order to create 2-D or 3-D reconstructions of internal features of objects non-destructively (Roscoe, 1970; Wellington and Vinegar, 1987). XRCT is an improvement over CT which significantly increases the scanning resolution: current generation XRCT devices are able to achieve maximum resolutions of roughly $0.05\text{ }\mu\text{m}$ and resolutions of $10\text{ }\mu\text{m}$ for objects that are a few millimetres across (Rigby et al., 2011). Due to this relatively large resolution, XRCT

is only able to provide information concerning the material *macrostructure*, namely the arrangement of differently-sized particle aggregates, and those pores surrounding them.

Attenuation is the loss of energy as a ray passes through a material. XRCT uses X-ray attenuation to reconstruct images of the interior of an object (Keller, 1998). Radiographic projections (i.e. 2-D images acquired using X-rays) of the object are taken from many angles by rotating the object relative to a stationary X-ray source and detector. The X-ray attenuation is then calculated at specific points and the 2-D image or *slice* constructed. 3-D reconstruction of the object can be achieved by converting slice pixels into voxels and then “stacking” several slices on top of each other. The reader is referred to Kruth et al. (2011) for a detailed description of the XRCT process. XRCT was first used with geotechnical materials to observe 2-D stress fields in sands (e.g. Roscoe (1970)). 3-D studies on strain localisation in sands have been conducted since the late 1980s, achieved using XRCT images and subsequent image analysis techniques (for example particle image velocimetry as discussed in Section 4.3.2) to track deformations during loading (Colliat-Dangus et al., 1988; Van Geet et al., 2000; Desrues and Gioacchino, 2004; Hall et al., 2010). XRCT has recently been used to characterise the hydration of clay pellets and powders (Van Geet et al., 2005; Gens et al., 2011).

Imperfections in the scanned objects or limitations of the equipment can lead to errors in XRCT scans (Van Geet et al., 2000):

- *Ring artifacts* are caused by inhomogeneities in the projector. They can be detected and accounted for by randomly moving the object relative to the detector.
- *Star artifacts* are caused by very dense inclusions within the object, radiating incident rays back out of the sample. Star artifacts can be reduced by placing different filters in front of the projector, depending on the material causing the error.
- Beer’s law (Wellington and Vinegar, 1987) is used to determine the size of features depending on the amount of attenuation according to Eqn 7.1:

$$\frac{I}{I_o} = \exp(-\eta x) \quad (7.1)$$

where I is the attenuated ray intensity, I_o is the incident intensity, x is the distance travelled through the material and η is the attenuation coefficient, which is a factor of the photoelectric effect (electrons emitting photons on the absorption of energy from incident rays), “Compton scatter” (a change in the ray’s wavelength due to its interacting with atoms), the wavelength of the incident rays and the density and atomic number of the object material (Keller, 1998; Van Geet et al., 2005). Eqn 7.1 is correct for monochromatic X-rays (i.e. only one energy). XRCT uses polychromatic X-rays and it is found that the lower-energy waves tend to be absorbed, so that the X-ray spectrum changes. This phenomenon is known as *beam hardening* or *shadowing* and appears to occur at the edges of objects, resulting in an apparent change in density at the edges. Again, the use of filters can prevent shadowing.

7.3 Fractal analysis

Fractal mechanics can be used to describe the shapes and arrangements of irregular objects (Mandelbrot, 1967). As opposed to Euclidean geometry, where objects are classified as one, two or three dimensional, the dimensionality of an irregular line can take any value between one and two, with more irregular lines having larger *fractal dimensions*.

As fractals quantify irregular structures, they have a range of applications in modelling particles and pore networks (Perfect et al., 1992; Lipiec et al., 1998; Perrier et al., 1999; Perrier and Bird, 2002; Atzeni

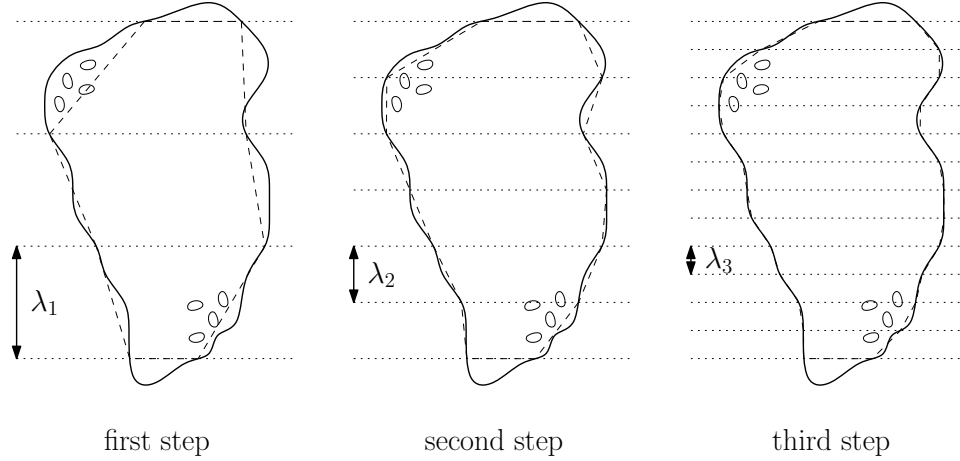


Figure 7.1: Parallel method for determining particle profile fractal dimension

et al., 2008) and their associated effects, for example permeability (Thevanayagam and Nasarajah, 1998; Xu and Sun, 2002; Xu, 2004a; Cihan et al., 2009; Jobmann and Billaux, 2010) and retention curve properties (Bird et al., 1996; Gimnez et al., 1997; Kravchenko and Zhang, 1998; Huang et al., 2006; Russell, 2010). Fractals have also been used to describe soil cohesive properties (Bonala and Reddi, 1999) and unsaturated shear strength (Xu, 2004b).

The fractal dimension of a line can be found by dividing it into elements of length λ (known as the *dividing method*) and finding the number of such elements, $P(\lambda)$, that are required to cover the line. $P(\lambda)$ and λ are related by

$$P(\lambda) = k\lambda^{-D_f} \quad (7.2)$$

where k is a constant and D_f is the fractal dimension (Ersahin et al., 2006). D_f is found by plotting λ on the abscissa axis against $P(\lambda)$ on the ordinate axis using a logarithmic scale and is the gradient of the resulting linear fit (necessary for the line to be considered fractal), m . The fractal dimension of a straight line or circular arc will always be 1 using this method (Vallejo, 1996).

The *parallel* method was used in Hyslip and Vallejo (1997) as an extension to the dividing method to quantify the roughness of sand grains. Parallel lines of separation distance λ were placed over the sand grain profiles (obtained through image analysis of high-resolution photographs) in order to determine the grain perimeter. The elements in this case were formed from lines joining the intersections of the grain profile and the parallel lines, as shown in Figure 7.1. The disadvantage of the parallel method is that the vertical and horizontal resolutions are different, so that the approximated lengths of horizontal features do not change whilst those of vertical features do, again as shown in Figure 7.1.

An improvement over the parallel method is the *box-counting method*, which overlays an object with parallel vertical *and* horizontal lines separated by a distance λ (Hirata, 1989). Each “box” formed by the intersecting lines forms one element and $P(\lambda)$ is found by counting the number of boxes which contain part of the object, as shown in Figure 7.2. Successively fine grids are used to determine D_f from a plot of λ against $P(\lambda)$ as before. The accuracy of the estimate of D_f can be improved by choosing an appropriate range of values for λ and by using multiple grid locations, using the average of the number of boxes filled for each location to find D_f (Foroutan-pour et al., 1999). The *minimum cover* value for D_f is the fractal dimension calculated using the grid which requires the least number of elements to cover the object (Tolle et al., 2003). Therefore, if only one grid location is used, the average and minimum cover D_f values are the same. Like the dividing method, the fractal dimension for a straight line or circular arc found using the box-counting method will always be 1.

The fractal dimension gives a measure of the size and dispersivity of objects: a low value of D_f means

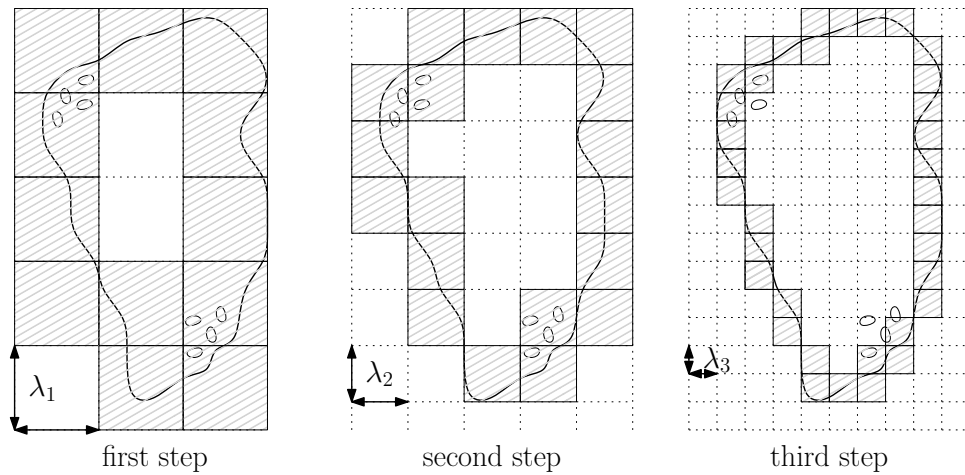


Figure 7.2: Box-counting method for determining particle profile fractal dimension. Hatching indicates those boxes that contain segments of the particle profile.

that the number of boxes required to cover the pattern increases slowly with decreasing box size, whilst a high value of D_f means that more smaller boxes are required. However, D_f cannot indicate the amount of objects present in the pattern as it is only the gradient of the λ against $P(\lambda)$ line (Pachepsky et al., 2000; Blair et al., 2007). Therefore, an additional parameter is required to describe fractal patterns. The *lacunarity*, L , represents the interconnectivity (or heterogeneity or *gappiness*) of the pattern, and can be considered to be the $P(\lambda)$ intercept of the linear fit to the plot of λ against $P(\lambda)$. A larger value of L therefore indicates that there are more gaps between the objects so that a greater number of boxes is required to cover the pattern (Zeng et al., 1996). Both the lacunarity and the fractal dimension are therefore required to describe a fractal pattern.

Fractal analysis can therefore be applied to pore networks to describe their arrangements (Bird et al., 2006; Atzeni et al., 2008). An example of materials with different lacunarities and fractal dimensions is shown in Figure 7.3. Material (a) has a more interconnected pore distribution than material (b), as it has a larger L value, however the pores are arranged in similar ways as both materials have the same value of D_f . Materials (c) and (a) have the same interconnectivity as they have the same value of L , but the pores in material (c) are more localised than those in material (a) as material (c) has a higher value of D_f and hence fewer larger boxes are required to cover the pattern at higher box sizes (Blair et al., 2007).

7.4 Experimental procedure

In this section, an experimental programme to manufacture and prepare RE samples for XRCT and fractal analysis is described, in order to determine the macrostructures of both loaded and unloaded RE samples. Samples were prepared in the laboratory at Durham University, however XRCT scanning was conducted at the University of Nottingham.

7.4.1 Soil mix selection and raw material preparation

Mix 6-1-3 (according to the naming system of Hall and Djerbib (2004)) was selected as a suitable soil as it represents an average of mixes 5-1-4 and 7-1-2, so that results could be interpreted to relate to those found in Chapters 5 and 6. Unfortunately, there was an insufficient number of tests available to analyse more than one mix. The dry mix was prepared according to the procedures discussed in Section 5.2.2. Once prepared, the mix was sieved to remove particles larger than 2.36 mm in order to prevent larger

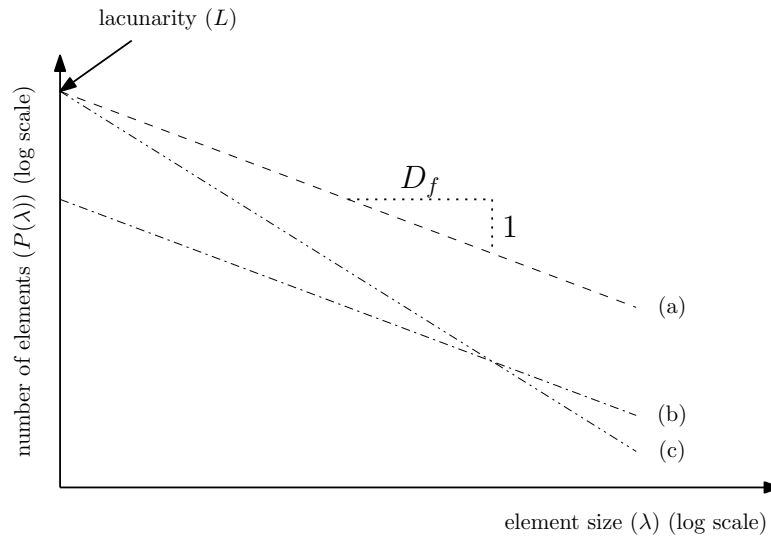


Figure 7.3: Sketch describing lacunarity and fractal dimension

particles interfering with compaction and obscuring the XRCT images (Tarantino, 2009). Sieved material maximum bulk and dry densities and OWC are given in Table 7.1, showing similar properties to mixes 5-1-4 and 7-1-2, determined using the light Proctor test. Wet mix material was prepared using the procedures discussed in Section 5.2.2.

7.4.2 Sample preparation and testing

It is recommended that samples be of the order of 1000 times larger than the desired resolution for XRCT scanning (Ketcham and Carlson, 2001). Samples of 20 mm height and 15 mm diameter were selected in order to use a high scanning resolution (1 pixel to 11 μm) whilst being large enough to be representative of material used in larger samples (for example those used in Chapters 5 and 6). Samples were manufactured using the apparatus shown in Figure 7.4. The mould shown in Figure 7.4 is open at both ends to facilitate extraction; during manufacture, the mould was secured to a removable steel base plate (not shown in Figure 7.4). The mould was not treated with form release oil, as was used in Chapters 5 and 6, due to possible contamination of the samples and a possible modification of the material macrostructure with respect to larger samples.

Single- and double-layer samples were prepared for XRCT scanning. Single-layer samples were manufactured using the single-layer press (Figure 7.4) and static compaction, with the amount of material required determined through the required density and known sample volume. Double-layer samples were manufactured by allocating half of the required material to each layer and compacting the first layer with the double-layer press and the second with the single-layer press. After manufacture, samples were extracted from the mould by pushing them from above using a 15 mm diameter steel rod. Twelve single-layer and three double-layer samples were prepared. Although dynamic compaction was used for sample manufacture in Chapters 5 and 6, results presented in Tarantino (2010) show that the method of compaction used does not affect the internal structure of the material so that samples prepared using

Table 7.1: OWC, $\rho_{d_{max}}$ and $\rho_{b_{max}}$ for RE soil mix 6-1-3

Soil mix	OWC (%)	$\rho_{d_{max}}$ (kg/m ³)	$\rho_{b_{max}}$ (kg/m ³)
6-1-3	12.0	1918.1	2147.0

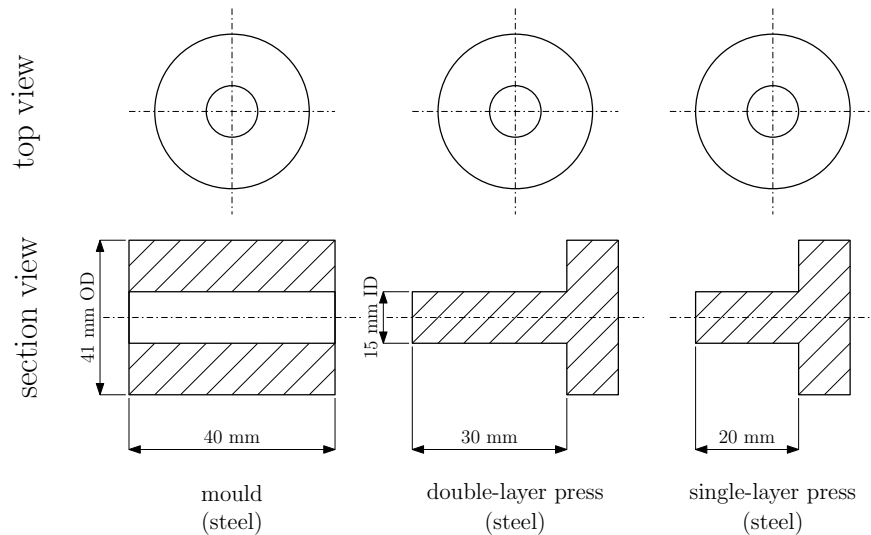


Figure 7.4: Sketch of the mould (left) and presses (middle and right) used for sample preparation

this method should be comparable to those used in previous chapters.

Samples were placed on wire racks to dry naturally to a constant mass at a temperature of $20^{\circ}\text{C} \pm 2^{\circ}\text{C}$ and a relative humidity of $40\% \pm 5\%$. The porosities of the single- and double-layer samples were 0.290 (standard deviation of 0.006) and 0.263 (standard deviation of 0.001) respectively, determined from the sample mass, dry density and volume on reaching a constant water content. Samples 2s, 9s, 10s, 13d and 15d were subsequently selected for XRCT testing (“s” and “d” denote single- and double-layer samples respectively) as they had similar dry masses and so, assumedly, similar internal structures, following the work presented in Section 5.3.4. The remaining samples were used to determine the compressive strength of the material and the corresponding failure loads. The average sample compressive failure load was 287.4 N, corresponding to a compressive stress of 1.63 MPa (calculated using Eqn 5.1 for a circular cross-section) i.e. in good agreement for compressive strengths found for samples in Chapter 5 (Figure 5.17) equilibrated under similar conditions. Following the work of Morel et al. (2007), a correction factor was not applied to calculated compressive strengths. Failure loads had a standard deviation of 10.1 N (57.2 kPa), indicating a good agreement between samples. Loads corresponding to 85%, 50% and 25% of the failure load were then applied to samples 2s, 9s and 10s respectively; these values were selected to provide a sufficient difference between their loaded macrostructures whilst not causing sufficient damage to prevent transportation. Samples 13d and 15d were not loaded. All samples were then wrapped in clear plastic film and bubble wrap and placed inside a rigid plastic tube for transportation to the University of Nottingham for scanning.

7.5 Results and discussion

7.5.1 Image processing

XRCT images were obtained using a Phoenix Nanotom 180NF XRCT system (GE Sensing and Inspection Technologies, GmbH, Wunsdorf, Germany) at a resolution of 1 pixel = $11 \mu\text{m}$. Each set of projection images was reconstructed using the back projection algorithm in the “datos|x rec” software. “ImageJ v.1.43u” software (Rasband, 2002) was then used to process the XRCT images. Figure 7.5(a) shows the sample axes as defined by the XRCT scanning software. Figures 7.5(b) and (c) show examples of a grayscale (as obtained from the XRCT analysis) image before and after processing; pores are shown as black pixels in the processed images, whilst solid material is shown as white. Example outlines of

particles seen in Figure 7.5(b) are shown in Figure 7.5(c). The image processing procedure is given in Figure 7.6.

Images are divided into pore spaces and solid material using a threshold intensity value; the lower the value, the lower the pixel intensity (i.e. the darker the shade) that corresponds to pores. In order to prevent shadowing, the upper and lower 100 images, corresponding to the upper and lower 1.1 mm, were removed from the image sequence. The removal of these images also reduces the chance of any damaged material, likely to be found at the ends of the sample, from influencing the analysis. Failure to remove these images results in a lower thresholding value being selected, so that fewer pores are identified. Roughly 1600 images in the XY plane were therefore subsequently available for analysis per sample, at 11 μm intervals. An area of 938×856 pixels was cropped from the centre of XY-orientated images to avoid shadowing at the sample surface and to provide a constant cross sectional area for the analysis. Due to the large number of images, only one in every ten images (i.e. one image every 110 μm) was processed in order to reduce the analysis time.

For thresholding, original image brightness values were modified whereby the lowest intensity present in the image was set to zero and the highest to 255 (the minimum and maximum possible intensity values respectively), in order to ensure the greatest contrast between pixels. A “median” filter was then applied in order to reduce the noise in the image by removing outlying intensity regions. This method replaces a pixel’s intensity with the median intensity of a region of a given size centred on that pixel (a region of a 2 pixel radius was used in this case). The brightness values were then corrected using the process described above to account for the filtering process. The ImageJ “IsoData” thresholding algorithm was applied to the modified images to determine a suitable thresholding value. The IsoData process divides the image into object (pores) and background (solids) using an initial threshold value. The average intensities of those pixels whose intensities are above and below the initial threshold value are then calculated and the average of those is used as a second threshold value. The process is repeated until the calculated threshold is larger than the average intensity for the entire image (Ridler and Calvard, 1978). Double-layer samples were analysed as one image sequence in order to compare one layer to another. IsoData threshold values are given in Table 7.2; the same thresholding value was applied to every image in the image sequence. Values differ between samples due to the manual brightness correction procedure and subtle differences in their structure which influence that correction.

7.5.2 Preliminary fractal analysis

The first five thresholded images (after removing the first 100 images) of sample 2s in the XY-plane were used to determine suitable values for the number of grid positions (GPs) and minimum box sizes for image analysis using the FracLac 2.5 plugin for ImageJ. Each combination was tested four times per image in order to assess repeatability. A greater number of GPs was not considered due to the increase in analysis time. Figures 7.7 and 7.8 show the results for the average box-counting and minimum cover fractal dimensions respectively; the number of GPs and minimum box sizes are shown in the figures.

Figure 7.7 shows that the use of the average value method leads to variations in calculated fractal dimensions of up to roughly 0.06 (4 GP, 2 pixel minimum box size). Furthermore, an increase in the number of grid positions and a decrease in minimum box size appears to have little impact on the

Table 7.2: Sample thresholding values

Sample	2s	9s	10s	13d	15d
Thresholding value	107	115	114	141	122

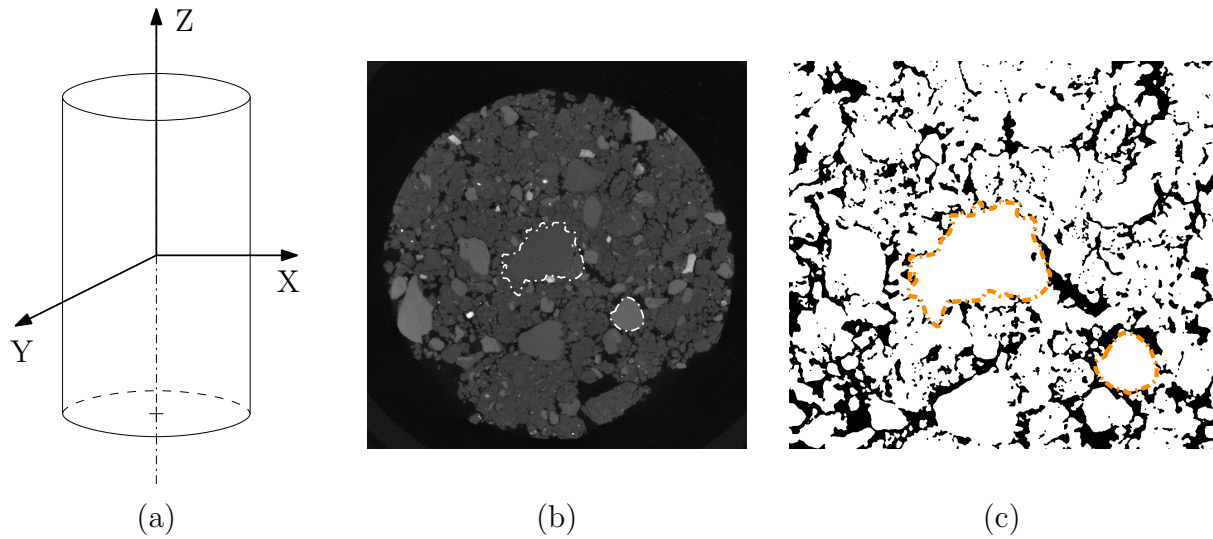


Figure 7.5: Example of XRCT images: a) sample axes; b) XY-slice pre-processing; c) XY-slice post-processing. Outlines of particles seen in (b) have been outlined in (c).

variation in the calculated fractal dimensions despite an associated significant increase in the analysis time. Figure 7.8 shows that the variation in the calculated minimum cover fractal dimension values is significantly less than that found for the average value method (roughly 0.02, i.e. a three-fold increase in consistency), although it could be argued that this is to be expected due to the use of only one value as opposed to the average of those found from the different grid positions. A slight improvement in reliability is seen on increasing GP and reducing the minimum box size. The minimum cover method was therefore selected for determining the fractal dimensions for the XRCT images, using 5 GPs and a 1 pixel minimum box size.

Figure 7.9 shows the minimum cover box counting results for the first image for sample 2s, showing the linear approximation to the data trend; the high value of R^2 (0.998) indicates that those pore networks identified by XRCT are fractally distributed, so that a fractal analysis of their various properties is valid.

7.5.3 Effect of loading on material macrostructure

This section investigates the effects of the application of a load on the macrostructure of RE. As XRCT can only give information about the macrostructure, due to its relatively low resolution with respect to the smallest pore sizes within a soil, those pores detected by XRCT are referred to here as *macropores*. 3-D reconstructions of the pore networks for samples 2s, 9s and 10s are shown in Figures 7.10 to 7.12 for pores identified using the IsoData threshold values given in Table 7.2, produced using the AvizoFire software (Visual Sciences Group, Burlington, USA). Axes are as defined in Figure 7.5. The pore area fraction (PAF, calculated by dividing the detected pore area by the total image area), fractal dimension, D_f , and lacunarity, L , calculated for each sample using the processed images are shown in Figures 7.13, 7.14 and 7.15 respectively. Depths have been calculated assuming a $110\ \mu\text{m}$ separation between images and have been corrected to account for the 1.1 mm of material removed from the top and bottom of the image sequence. To prevent the loss of loose particles from the base of the samples and to ensure a good seating within the scanner, samples were placed in the scanner with the compacted surface (which is the smoothest) facing downwards. Therefore, a depth of 0 in Figures 7.13, 7.14 and 7.15 corresponds to the base of the sample as samples were scanned from the uppermost surface downwards. Samples have been orientated with their base at the bottom of the image in Figures 7.10 to 7.12. A minimum pore size of 3×3 pixels (i.e. $\geq 1089\ \mu\text{m}^2$) was used to calculate the PAF in order to prevent anomalous features

thresholding process

- 1) delete first and last 100 images to prevent shadowing
- 2) import image sequence
- 3) analyse → set scale → 1 pixel = 11 microns
- 4) image → type → 8 bit (needed for thresholding to work)
- 5) edit → selection → specify (938 x 856 pixels, manually centre, check to see if all images OK)
- 6) image → crop
- 7) image → adjust → brightness/contrast (change min/max values to bracket intensity range)
- 8) process → filters → median (2 pixels)
- 9) image → adjust → brightness/contrast (change min/max values to bracket intensity range)
- 10) image → adjust → threshold (isodata, auto)
- 11) process → noise → remove outliers (2.0, 50, dark)
- if necessary —
- 12) process → binary → fill holes
- 13) file → save as → image sequence

analysis stages*pore area data*

- 14) analyse → set measurements (choose appropriate parameters)
- 15) analyse → analyse particles (1089-infinity, 0.00–1.00 circularity, display results, summarise)

fractal data:

- 16) plugins → fractal analysis → FracLac 2.5 release 1e

↓
 standard box count →

grid positions: 5
 binary or grayscale: use binary
 background colour: let program decide
 type of series: use default box sizes
 sizes per series: 0
 minimum size: 1
 maximum box size: 45% ROI
 find the minimum cover
 remaining options: ALL deselected

scan image stack
 or ROI ←

Figure 7.6: Flowchart of image processing algorithm (using ImageJ software)

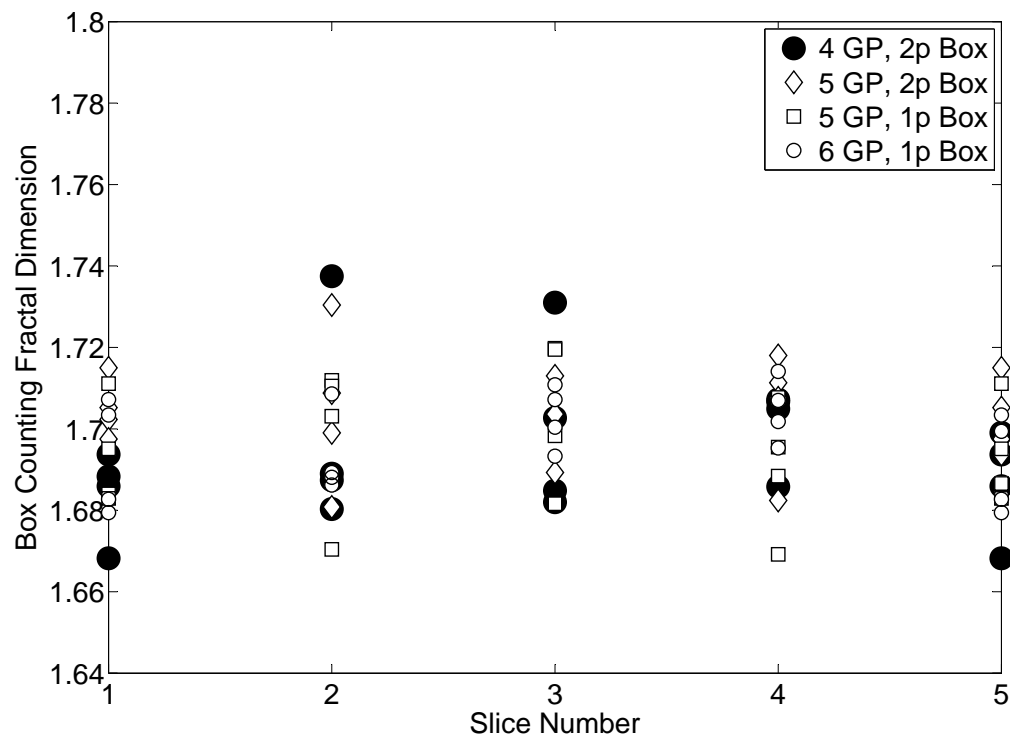


Figure 7.7: Calculated box-counting fractal dimensions for images 1 to 5 for sample 2s

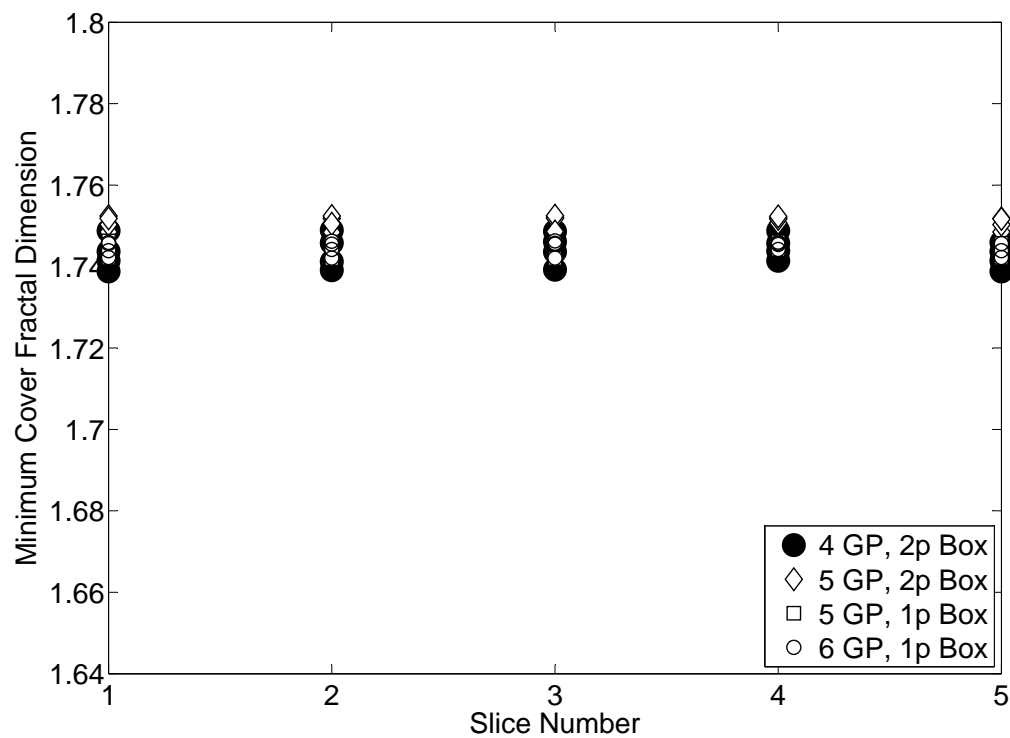


Figure 7.8: Calculated minimum cover fractal dimensions for images 1 to 5 for sample 2s

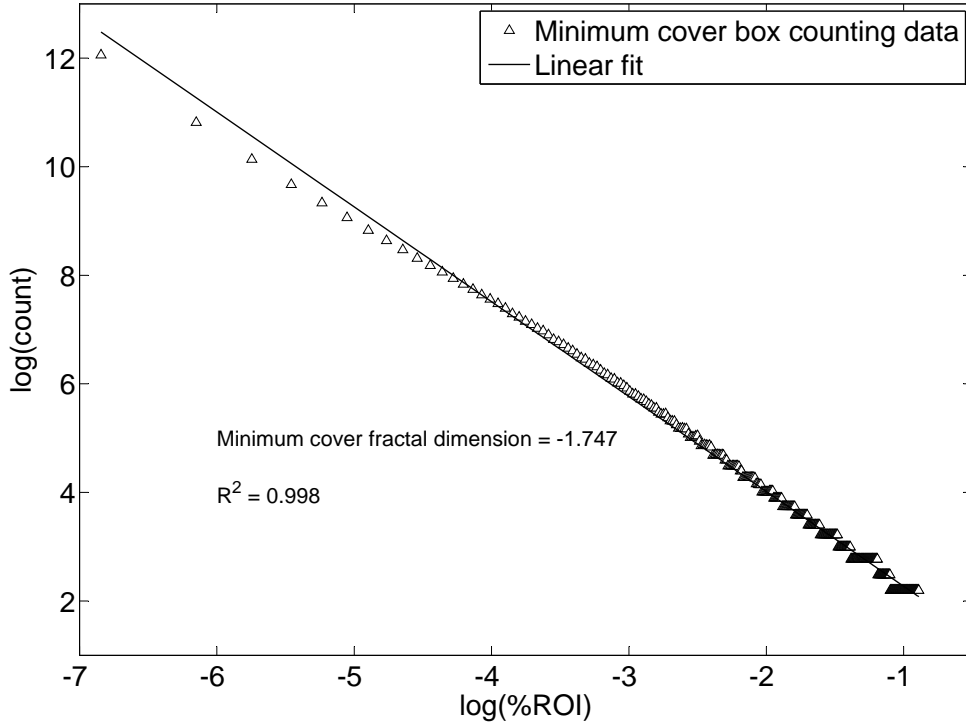


Figure 7.9: Linear fit to minimum cover box-counting results (on logarithmic axes) for the image 1 for sample 2s

(for example small pits on particle surfaces) from influencing the results, however a minimum box size of 1 pixel was used to determine D_f and L (i.e. features $\geq 121\mu\text{m}^2$ are included in the fractal analysis).

Figures 7.10 to 7.12 show that the layered structure thought to arise from segregation during the preparation of dry soil mixes, as discussed in Section 4.2.2, is not present, supporting the observation made in Section 4.3 that the action of compaction serves to create a more homogeneous mix.

Figures 7.13 and 7.14 show high values of PAF and D_f respectively for all samples at depths near 0 and 20 mm. However, XRCT images corresponding to depths prior to and at the tip of these “flicks” (for example Figures 7.16(a) and (b) for sample 2s) suggest that there is no significant change in the macrostructure of the samples in these regions. Therefore, it is assumed that these flicks are due to shadowing at the sample edges. Ignoring these, the maximum measured PAFs of samples 2s, 9s and 10s are roughly 0.16, 0.10 and 0.14 respectively, which are significantly smaller than their average bulk porosities of 0.29. This is due to the inability to detect pores smaller than $33\mu\text{m}$ in diameter and indicates how XRCT can only be used to gain information about the macrostructure.

Hall et al. (2010) used XRCT to measure the deformations that occurred in a sample of sand on the application and subsequent increase of a load. As only one sample was used, deformations observed for one load could be directly compared to those occurring at a different load, allowing highly detailed displacement fields to be determined. Unfortunately, a limit on the availability of the XRCT scanner and the need to transport samples meant that this approach was not possible for this investigation; instead, several samples loaded to different compressive loads had to be prepared, as discussed in Section 7.4.2. Therefore, the similarity of the initial sample macrostructures must be determined before any changes in the macrostructure due to loading can be investigated.

Figures 7.10 and 7.12 show that the macrostructures of samples 2s and 10s (respectively) are visually

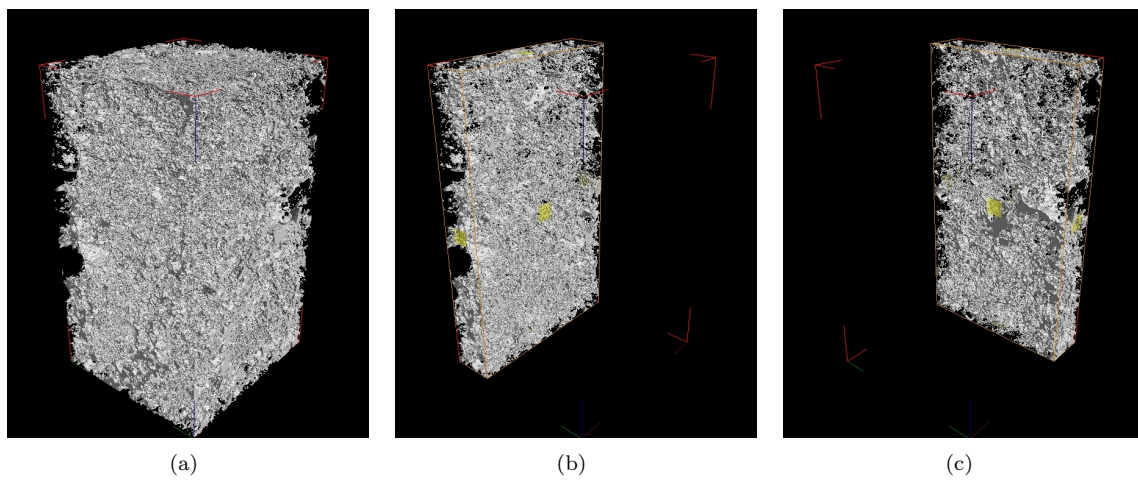


Figure 7.10: 3-D reconstructions of the pore network of sample 2s: a) total pore space; b) view of internal XZ plane; c) view of internal YZ plane.

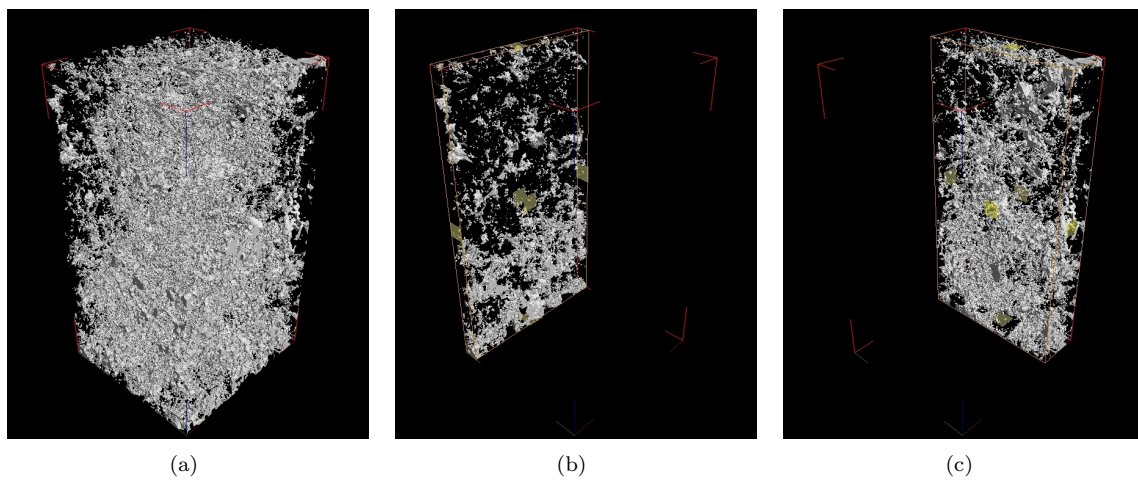


Figure 7.11: 3-D reconstructions of the pore network of sample 9s: a) total pore space; b) view of internal XZ plane; c) view of internal YZ plane.

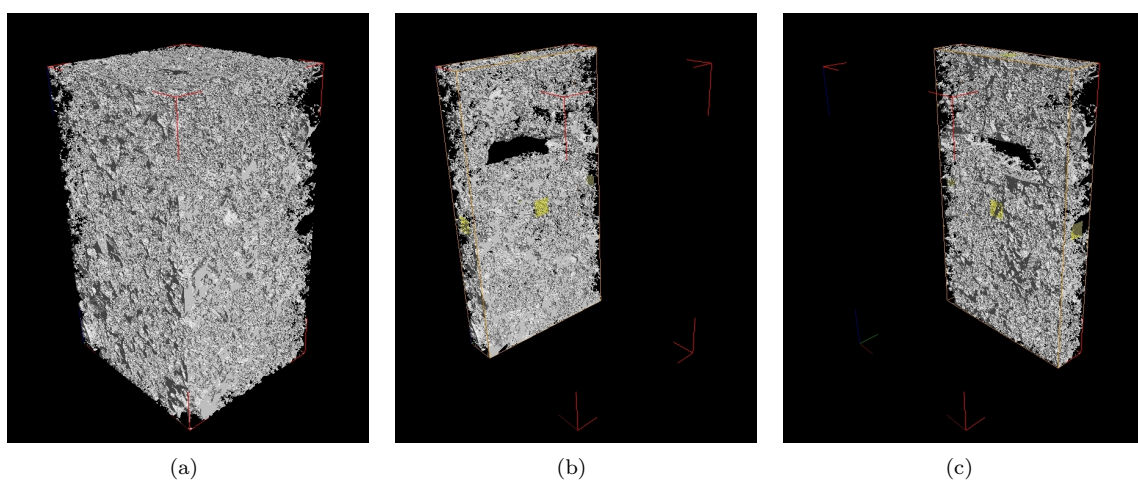


Figure 7.12: 3-D reconstructions of the pore network of sample 10s: a) total pore space; b) view of internal XZ plane; c) view of internal YZ plane.

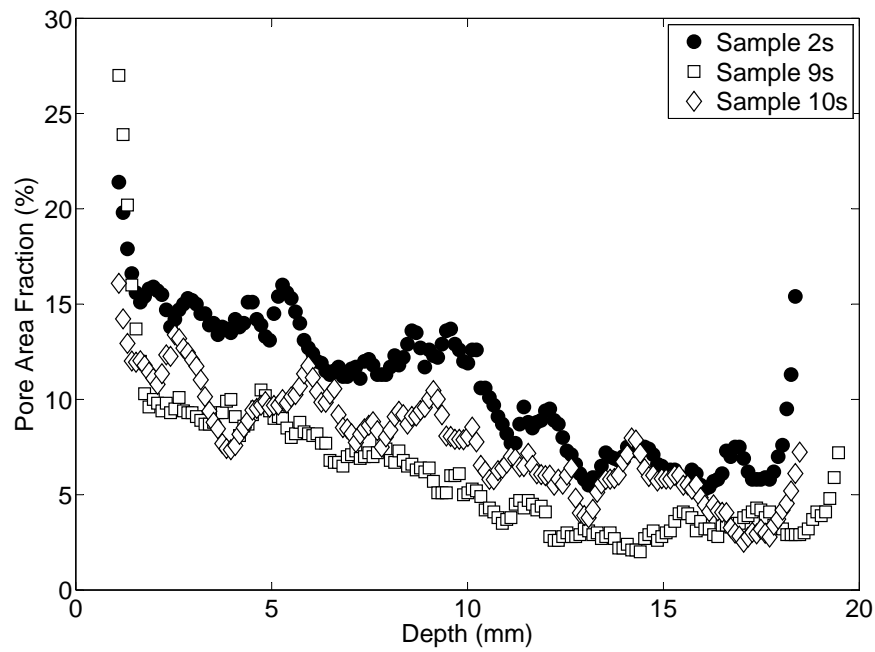


Figure 7.13: Change in pore area fraction with depth for samples 2s, 9s and 10s

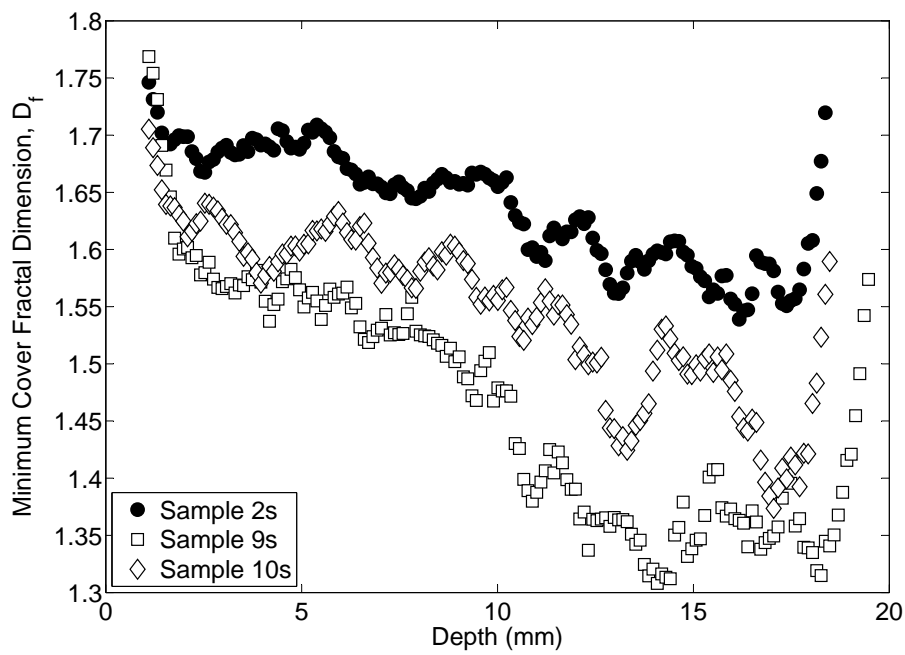


Figure 7.14: Change in minimum cover fractal dimension with depth for samples 2s, 9s and 10s

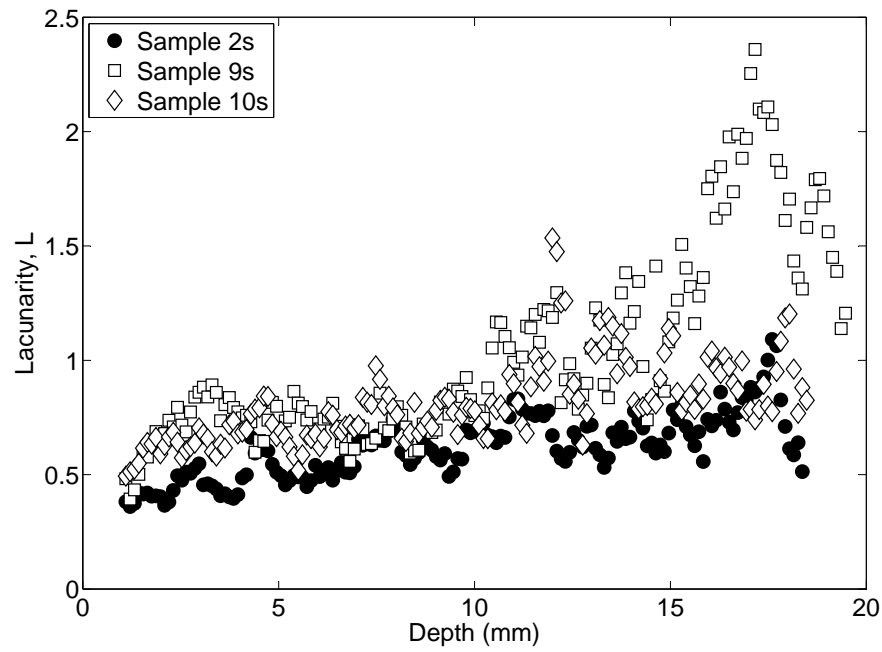


Figure 7.15: Change in lacunarity with depth for samples 2s, 9s and 10s

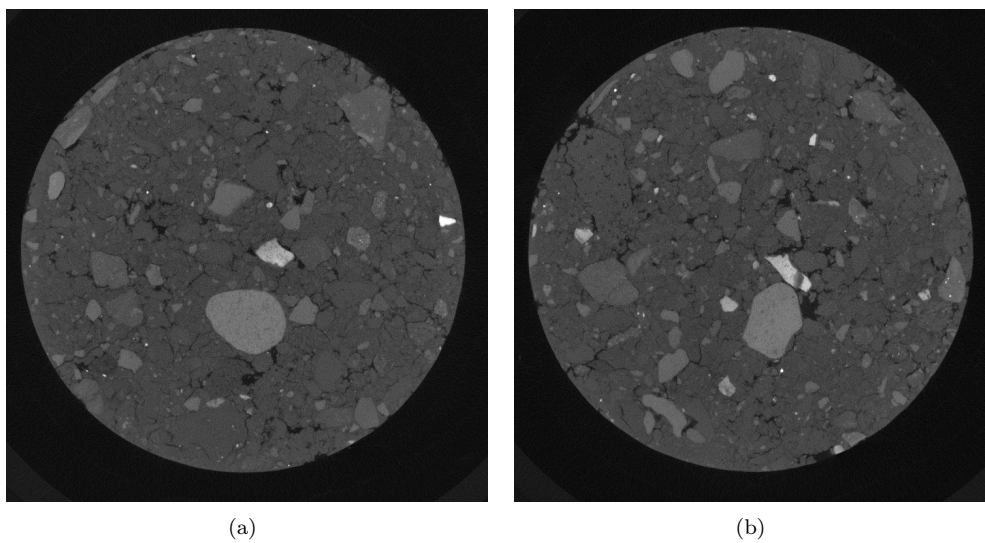


Figure 7.16: XRCT images taken at: a) 16500 μm ; and b) 17379 μm

very similar, whilst that of sample 9s (Figure 7.11) appears to contain significantly fewer macropores. It is assumed that the observed differences are not a result of comparing different thresholding results due to the use of similar thresholding values for each sample. According to Section 6.4.2.2, an increase in loading from sample 10s through sample 9s to sample 2s should produce a progressive change in internal structure due to cracking, so that, assuming that their internal structures were initially similar, the macrostructure of sample 9s should represent a condition between those of samples 2s and 10s. Figures 7.13 to 7.15 show that this is not the case, however, with sample 9s displaying lower PAF and D_f and greater L values than samples 2s and 10s, indicating a significantly different macrostructure. Therefore, results for sample 9s cannot be used to determine the effect of loading on the macrostructure. Samples 2s and 10s, however, appear to be consistent with the assumed theory and each other and so can be used to determine the effect of loading.

The macrostructures of samples 2s and 10s can be investigated in more detail by varying the threshold values. Low thresholding values detect the darkest pixels and so the centres of the largest pores, whilst smaller pores are detected as the value is increased (Taud et al., 2005). Figures 7.17, 7.18 and 7.19 show the effects of varying the threshold intensity on PAF, D_f and L respectively (selected intensities are shown in parentheses in the figure legends). Threshold values below 50 were not examined as no pores could be detected in some images. Similarly, values larger than the IsoData threshold values (Table 7.2) were not investigated as some images became completely populated by pores.

Figure 7.17 shows that the PAFs detected using the lowest threshold value in both samples 2s and 10s are very similar, although sample 2s shows slightly larger PAFs at low depths (i.e. towards the base of the sample), indicating a similar proportion of larger pores in both samples, with a slightly greater number towards the base of sample 2s. Larger PAFs are found for sample 2s than for sample 10s with increasing threshold value, suggesting that the change in porosity on the application of a load, attributed to crack formation and propagation, affects all of the detected pore sizes. Figures 7.17 and 7.18 show that trends of PAF and D_f values for a given threshold value are consistent between the samples at all threshold values with changing depth and that, in general, regions with higher initial PAFs will experience greater increases in PAF on the application of a load than those regions with lower initial PAFs.

Figure 7.19 shows that calculated L values reduce as threshold values increase for both samples 2s and 10s, indicating that pore interconnectivity increases with increasing threshold value, so that smaller pores lie between, and not in isolation of, larger pores. Figure 7.19 also shows that the trends of changing L with depth for both samples are similar at all threshold values, as found for the PAF and D_f . The similar trends for PAF, D_f and L for both samples suggest that their macrostructures were similar so that the differences between them are due to the application of a load and not due to structural differences.

Figures 7.21, 7.22 and 7.23 show the relative values of PAF, D_f and L , calculated using

$$\frac{\text{value 2s} - \text{value 10s}}{\text{value 2s}} \times 100 \quad (7.3)$$

respectively. The use of relative values removes the effect of shadowing. Figure 7.21 shows that measured relative PAF values appear to converge on those found using the IsoData threshold values as the threshold value increases, showing that greatest differences exist between those structures which only contain the largest pores rather than those which include smaller pores. This is consistent with the theory discussed in Section 6.4.2.2, as more cracks can form and propagate around larger pores than smaller pores.

Figure 7.21 shows that an increase from 25% to 85% of the failure load results in, on average, a roughly 30% relative increase in the detected pore space. Therefore, poorly-compacted material will experience a greater absolute increase in pore space than well-compacted material for the same applied load. This increase in pore space will significantly increase the material's permeability through the creation of preferential wetting paths, so that any incident water will readily be adsorbed, thereby weakening the

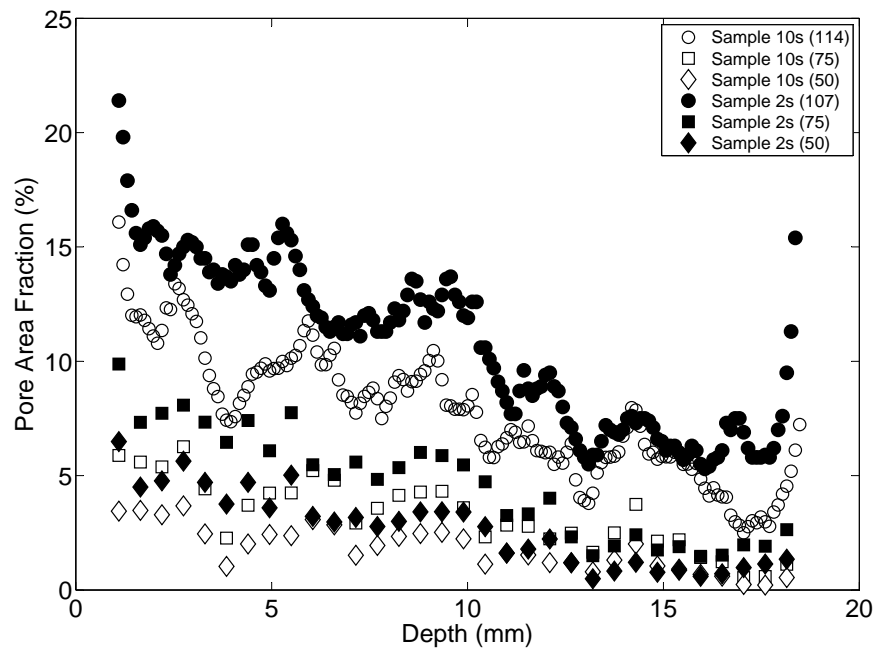


Figure 7.17: Change in calculated PAF with depth for different threshold intensity values

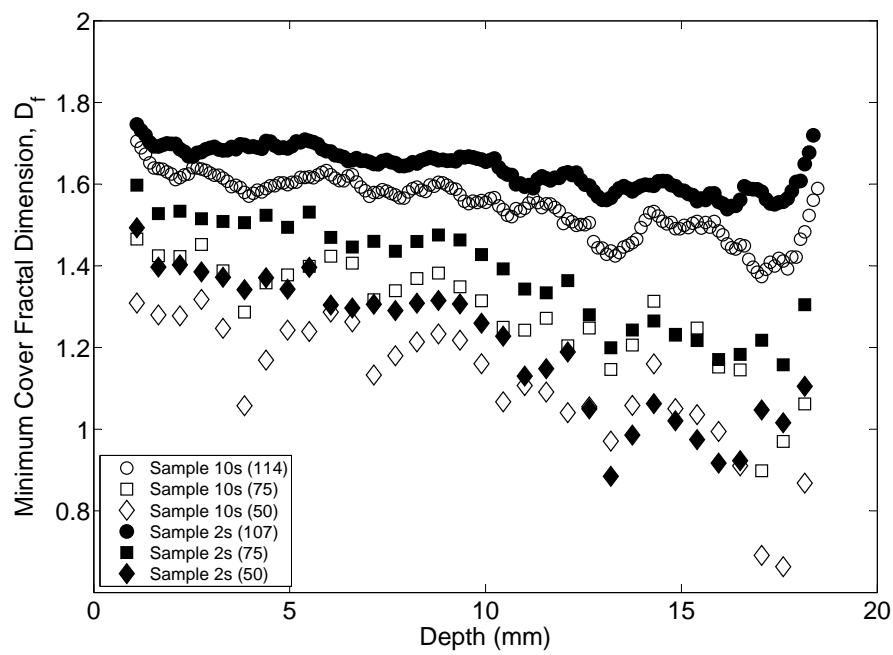


Figure 7.18: Change in calculated D_f with depth for different threshold intensity values

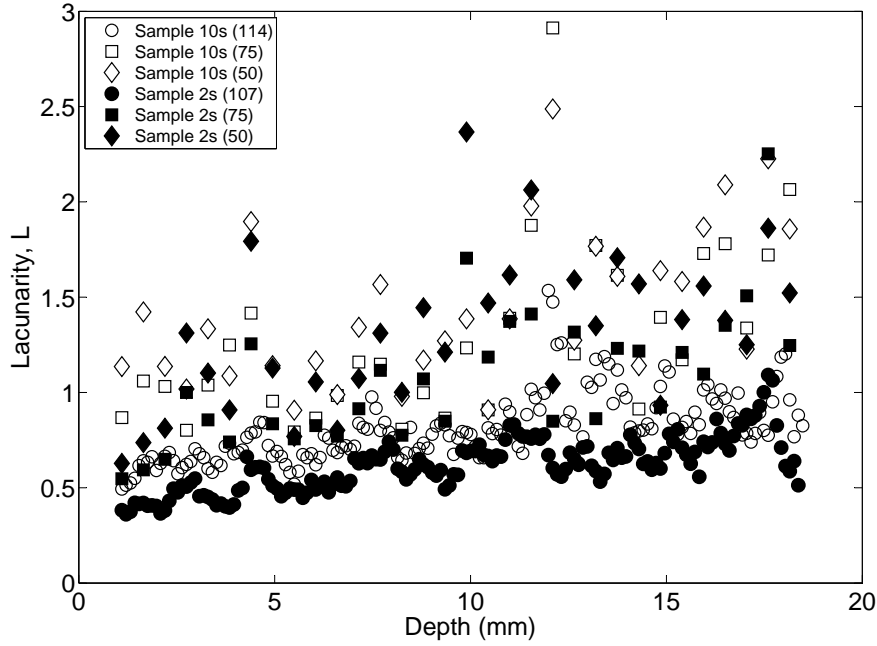


Figure 7.19: Change in calculated L with depth for different threshold intensity values

material and indicating the need to properly compact the material during construction (Jaquin et al., 2009). Although only tested on one RE soil mix, it is likely that a similar increase in pore space will occur on the loading of other mixes.

A convergence of results to those found at the automatic thresholding value is also seen in Figures 7.22 and 7.23 for relative D_f and L values respectively. Although initially quite large, relative D_f values converge to values between 5 and 10% and relative L values to values mostly between 0 and -50%, indicating that although the application of a load results in an increased PAF, the shape and interconnectivity of the macropores in each sample remain similar, showing that crack formation and propagation occurs according to similar mechanisms and, again, that the two samples had similar initial macrostructures.

Figures 7.21 and 7.22 show a region of negative relative PAF and D_f values between depths of roughly 13 mm and 17 mm, so that sample 2s has a lower PAF than sample 10s, apparently contradicting the theory discussed in Section 6.4.2.2. However, Figure 7.12 shows that a large particle (roughly 10 mm) is present at this depth which was not removed during sieving. This particle is shown in Figure 7.20, at a depth of 13090 μm . The effect of this particle is an increase in PAF and D_f , due to the reduced compaction of the surrounding material, and so negative relative PAF and D_f values. Furthermore, the presence of a rigid particle lying across the sample perpendicular to the direction of compaction would result in an increase in the compaction of the material above it, again leading to reduced PAF values above this depth, as seen in Figure 7.17, and hence a significant increase in relative PAF and D_f values on comparison with sample 2s, as seen in Figure 7.21. Similar patterns are seen in Figures 7.22 and 7.23, again due to the presence of the large particle; the D_f of sample 10s increases due to the increased pore area but L also increases, due to the presence of the large gap, resulting in negative values of both relative D_f and L between these depths. This demonstrates the importance of removing these particles from the samples prior to analysis. Therefore, results shown in Figures 7.21 to 7.23 again suggest that the macrostructures of samples 2s and 10s were similar (with the exception of the large particle) and that the effect of the application of a load is the creation of larger, more interconnected pores, due to

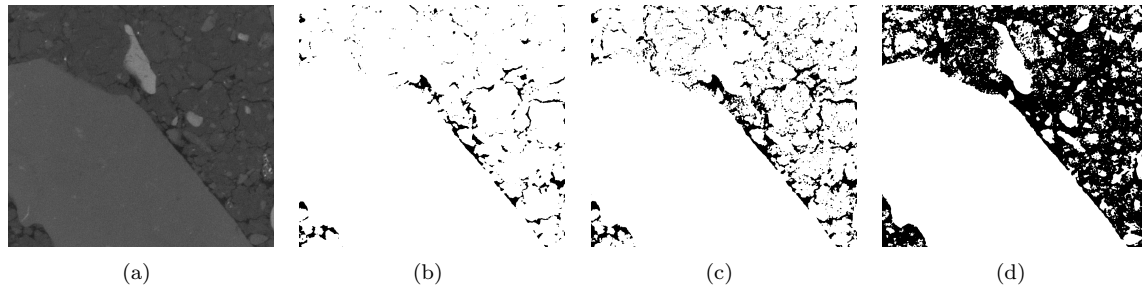


Figure 7.20: Large particle present in sample 10s at 13090 μm : a) XRCT image; b) threshold intensity of 50; c) threshold intensity of 75; d) threshold intensity of 114 (IsoData value).

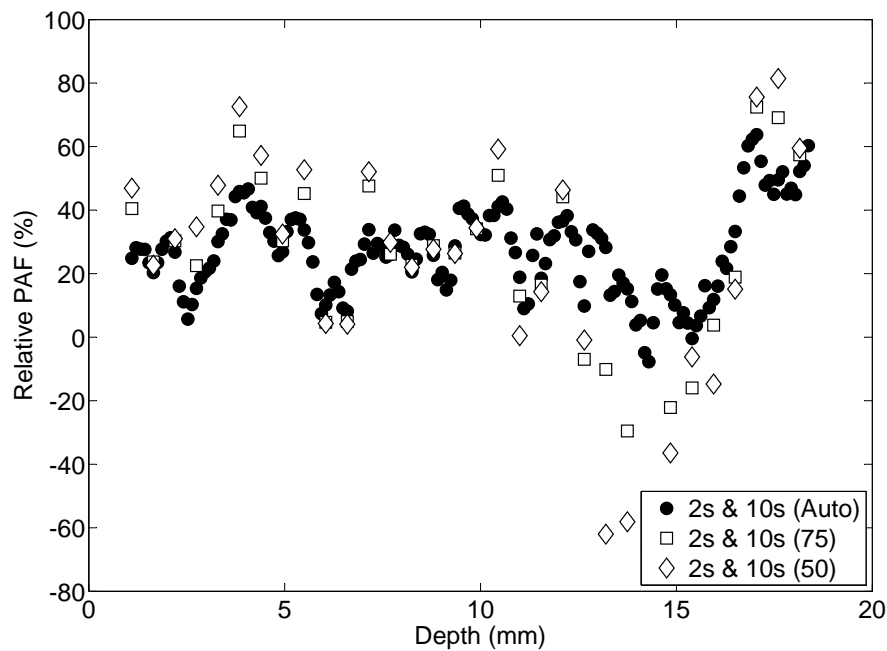


Figure 7.21: Change in calculated relative PAF with depth for different threshold intensity values

cracking.

In RE construction, blocks of roughly 1.5 m height are prepared before the formwork is removed and the material allowed to dry (King, 1996). If it is assumed that the wet density of the material is roughly 2.1 Mg/m^3 (following results from Sections 5.2.2 and 6.3.2) and a layer, once compacted, is roughly 100 mm deep, then it can be shown that the bottommost layer in a block is subjected to a load of roughly 29 kN/m^2 due to the material self weight, or roughly 2% of the sample failure load found in Section 7.4.2. As this is very small, it can be assumed that no significant cracking occurs due to material self weight. Therefore, the macrostructure of material comprising unloaded RE samples is nominally representative of material found in full-scale RE blocks.

7.5.4 Effect of compaction on the material macrostructure

This section investigates the change in macrostructure with the depth of a layer as a result of the compaction process. Compaction plays a significant role in RE construction, as it is through the building up of layers of material that RE structures are formed and gain their characteristic appearance.

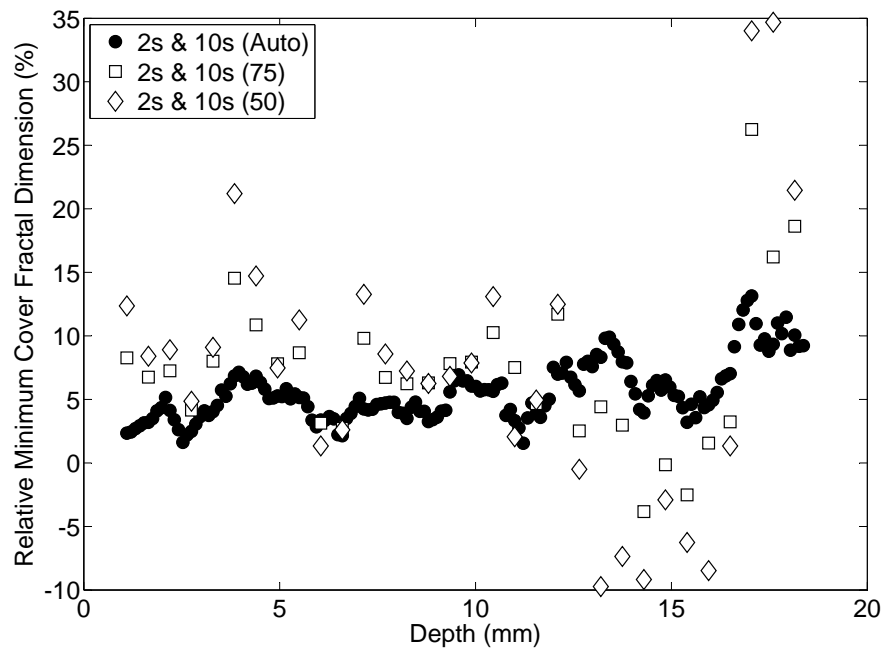


Figure 7.22: Change in calculated relative D_f with depth for different threshold intensity values

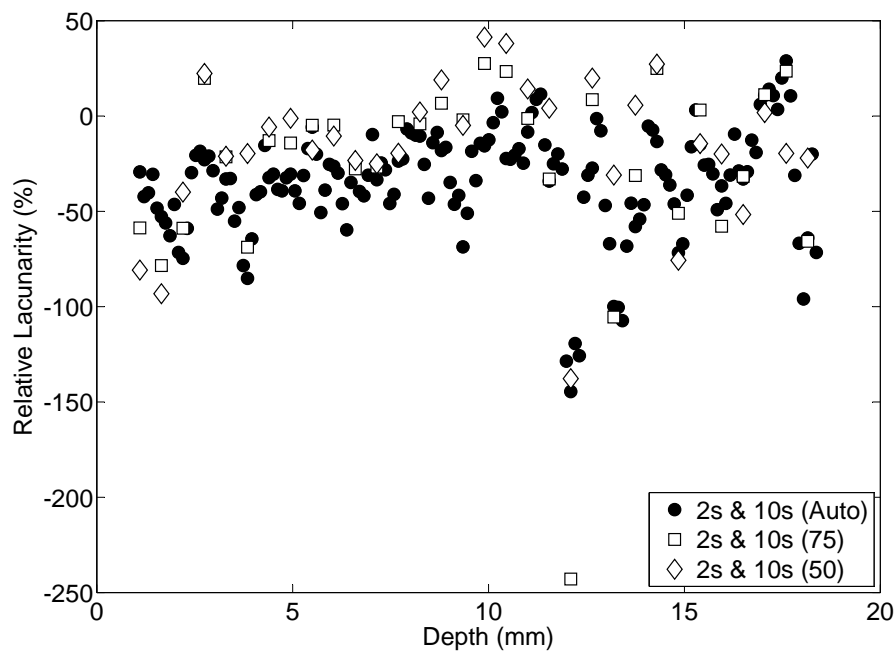


Figure 7.23: Change in calculated relative L with depth for different threshold intensity values

3-D reconstructions of the scanned pore spaces for samples 13d and 15d are shown in Figures 7.24 to 7.27 for pores identified using the IsoData threshold values (Table 7.2). Axes are as defined in Figure 7.5. PAF, D_f and L calculated for each sample are shown in Figures 7.28, 7.29 and 7.30 respectively. Again, the base of the sample is orientated towards the bottom of the image in Figures 7.24 to 7.27.

As was found for samples 2s and 10s (Figures 7.10 and 7.12 respectively), Figures 7.24 to 7.27 show that the measured pore networks of samples 13d and 15d are visually very similar. Figures 7.28 to 7.30 also show that the PAF, D_f and L trends are very similar for both layers of samples 13d and 15d, as well as a relatively good agreement between samples, indicating that they have similar macrostructures. However, Figure 7.28 shows that PAF values in sample 15d are significantly lower at all depths than those in sample 13d, either suggesting that sample 15d was more highly compacted than 13d or that fewer pores could be detected in the former using the IsoData threshold value. As the results trends and D_f values at all depths (Figure 7.29) are similar for both samples, it is assumed that the difference in detected PAF values is due to the image processing technique and not due to a change in material structure, so that a comparison between the two samples is valid. This supports results shown in Figures 7.17 to 7.23, as the initial structures of samples 2s and 10s can be assumed to be similar. Of interest is the apparent *reversed* shadowing seen in Figure 7.28, whereby detected PAF values reduce at the top and base of the sample, rather than increase as is the case for shadowing in Figure 7.13. The break between the layers is also indicated by a sudden reduction in PAF and D_f in Figures 7.28 and 7.29 respectively at a depth of roughly 9 mm, the magnitude of which is similar to that seen at the top and bottom edges and suggesting that ‘shadowing’ is also present at the layer interface, perhaps due to a slight discontinuity. As no significant change in L is seen at this depth (Figure 7.30), it is suggested that the layers are continuous away from the edges due to no change in the interconnectivity.

However, the reversal of the expected shadowing result and the very high PAFs and D_f values found in Figures 7.28 to 7.30 compared to those in Figures 7.13 and 7.14 suggest that the results of the initial image analysis are incorrect. Images were therefore re-analysed at a lower threshold value in order to remove some of the detected pore space. Figures 7.31(a) and (d) show example images from sample 13d corresponding to depths of 1100 μm and 17600 μm respectively. The resulting post-processing images corresponding to the initial (141) and reduced (60, chosen visually) threshold values are shown in Figures 7.31(b) and (c) for 1100 μm depth and Figures 7.31(e) and (f) for 17600 μm depth. Figures 7.31(a) to (c) show that a much more representative approximation to the pore network is achieved using the lower thresholding value. However, Figures 7.31(d) to (f) show that the IsoData thresholding value produces a better approximation at greater depths, indicating the importance of selecting representative thresholding values prior to the analysis. Both threshold values have therefore been used to describe the macrostructures of samples 13d and 15d; Figures 7.32 to 7.34 show a comparison between those PAF, D_f and L values calculated at threshold values of 141 and 60 for sample 13d and 122 and 60 for sample 15d respectively.

Figures 7.32 to 7.34 show good agreement between the PAF, D_f and L trends (and values for the latter for reasons discussed above) of samples 13d and 15d at both threshold values, again showing that samples manufactured using the procedure discussed in Section 7.4.2 are consistent in terms of density and material macrostructure. A break between the layers in samples 13d and 15d is clearly visible in Figures 7.32 and 7.33 at roughly 9 mm for both sets of threshold values. The effect of shadowing detected at the lower threshold values is also consistent with that found in Figure 7.13 (i.e. an increase in the number of detected pores at the edges), suggesting that the ‘reversed’ shadowing in Figures 7.28 to 7.30 was due to the use of too high a threshold value. The break between the sample layers is again clearly visible at a depth of roughly 9 mm from the base of the sample. A break between the layers at 9 mm, rather than the half-way point of 10 mm, suggests that the bottom layer is more highly compacted than the top layer; this can be seen in the lower PAF values found for the bottom layer than for the top layer

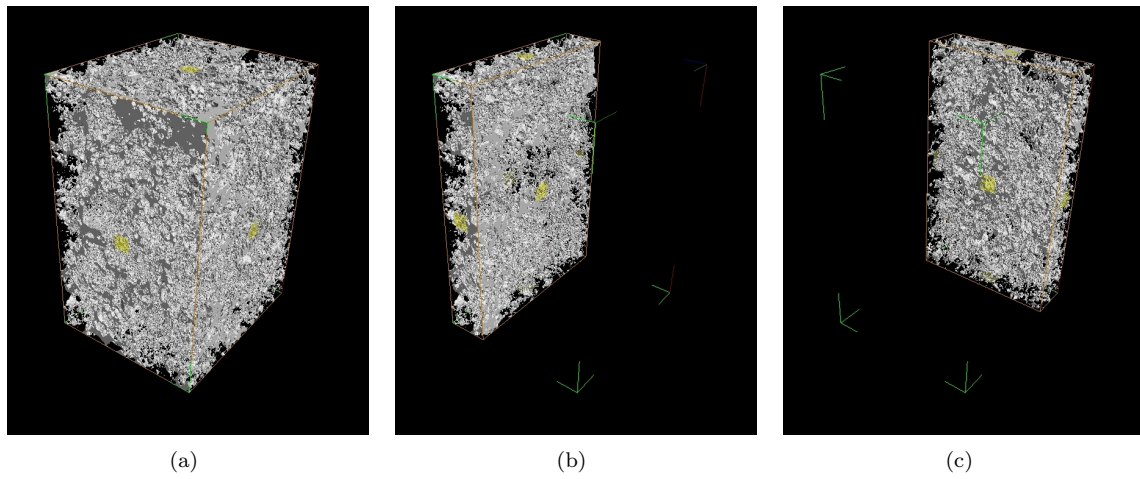


Figure 7.24: 3-D reconstructions of the pore network of the top lift of sample 13d: a) total pore space; b) view of internal XZ plane; c) view of internal YZ plane.

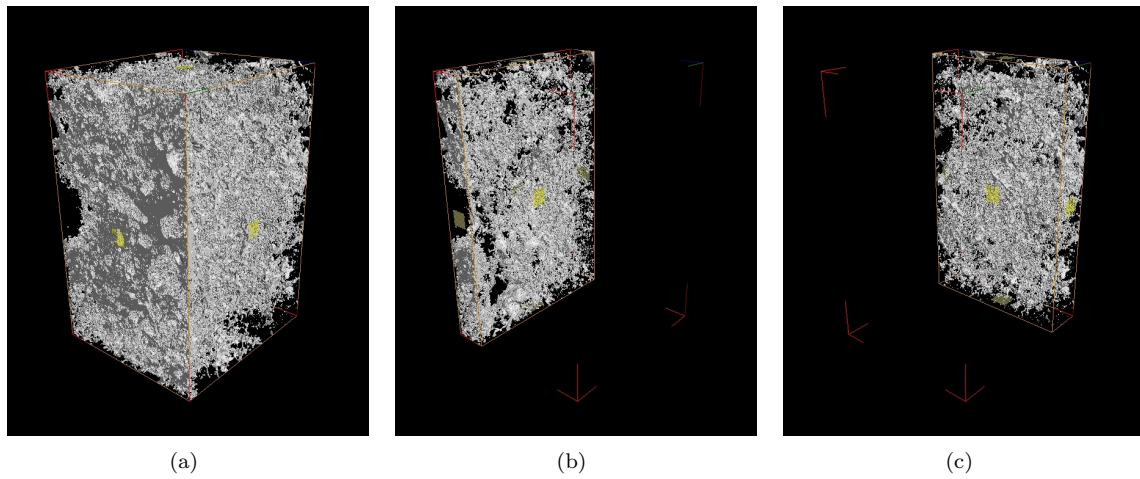


Figure 7.25: 3-D reconstructions of the pore network of the bottom lift of sample 13d: a) total pore space; b) view of internal XZ plane; c) view of internal YZ plane.

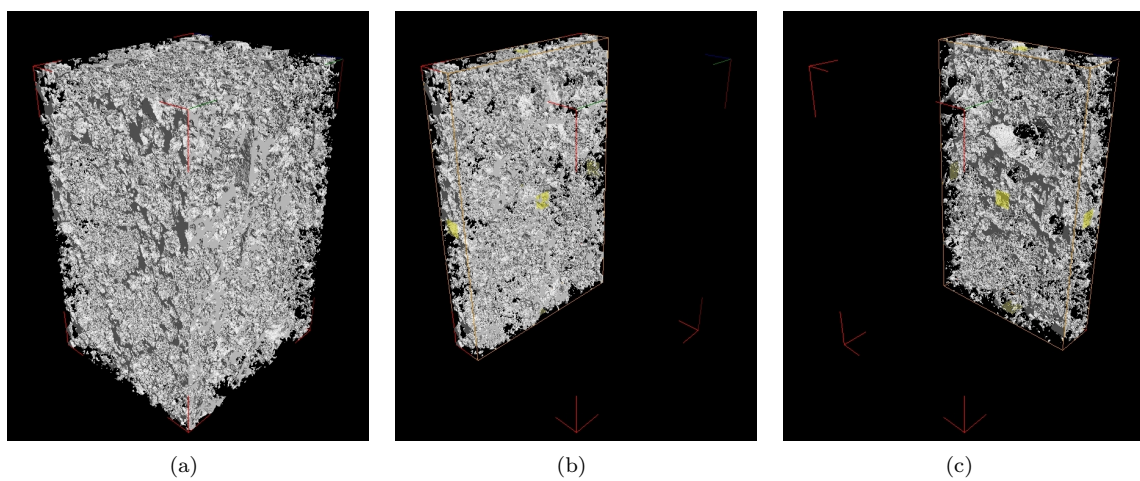


Figure 7.26: 3-D reconstructions of the pore network of the top lift of sample 15d: a) total pore space; b) view of internal XZ plane; c) view of internal YZ plane.

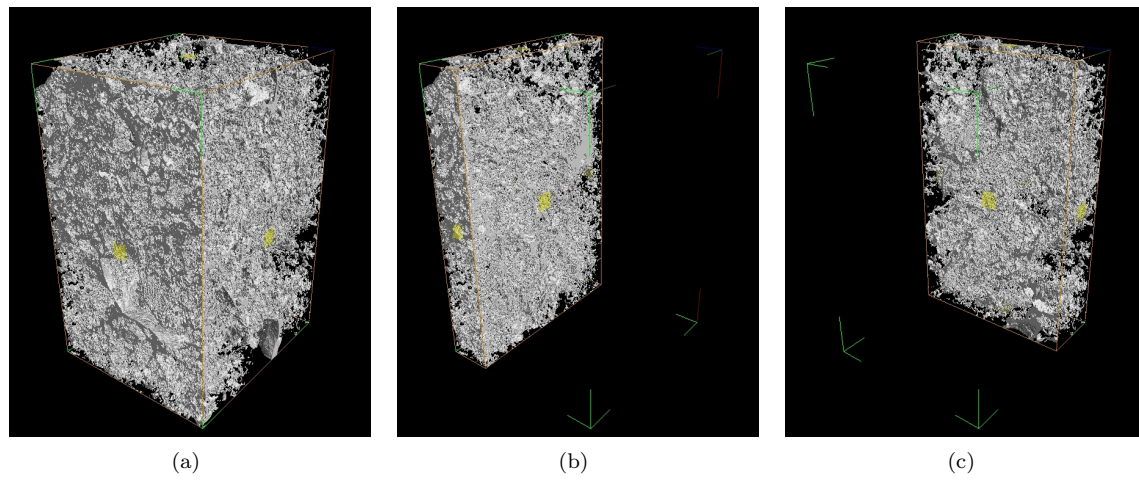


Figure 7.27: 3-D reconstructions of the pore network of the bottom lift of sample 15d: a) total pore space; b) view of internal XZ plane; c) view of internal YZ plane.

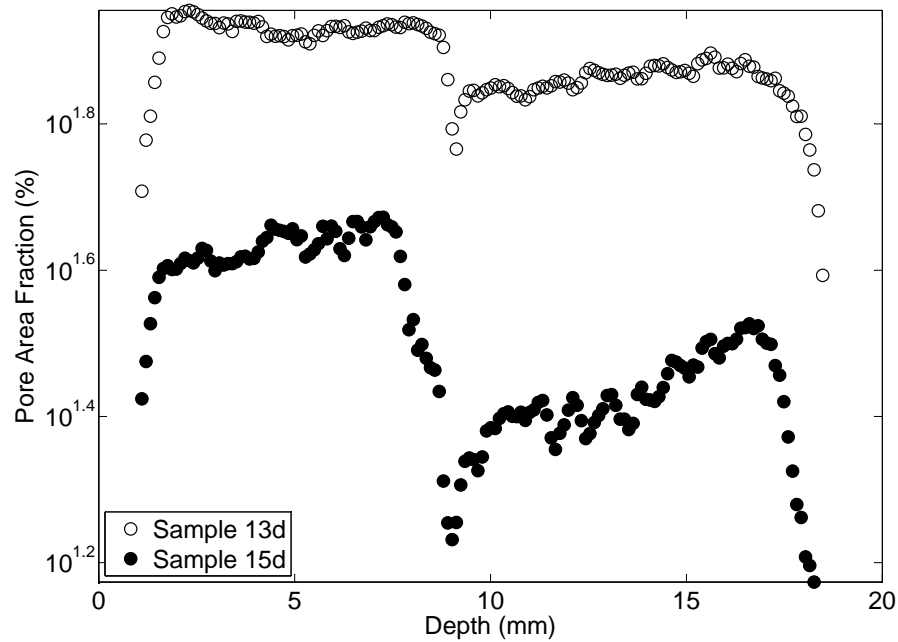


Figure 7.28: Change in pore area fraction with depth for samples 13d and 15d

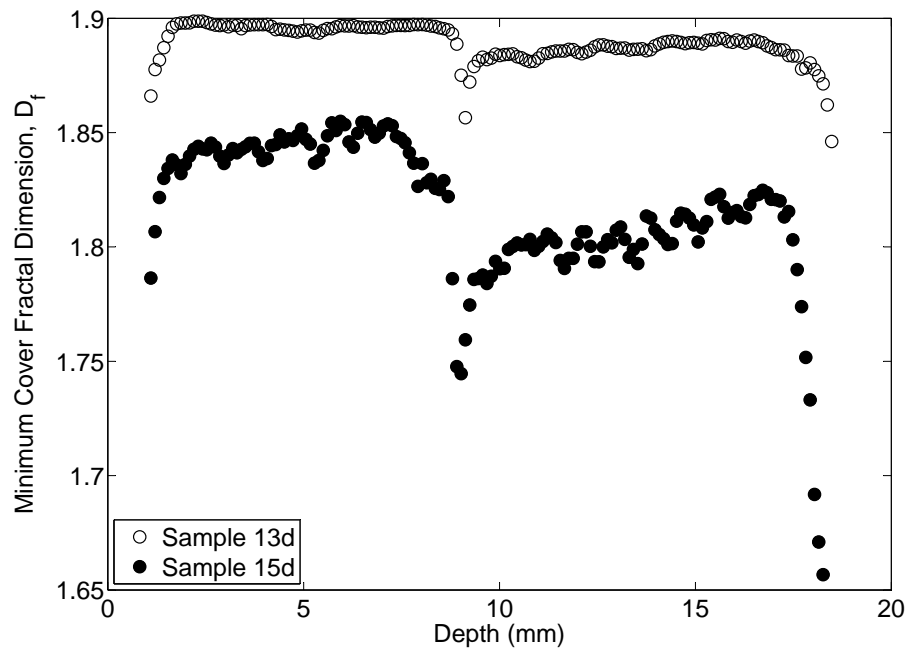


Figure 7.29: Change in minimum cover fractal dimension with depth for samples 13d and 15d

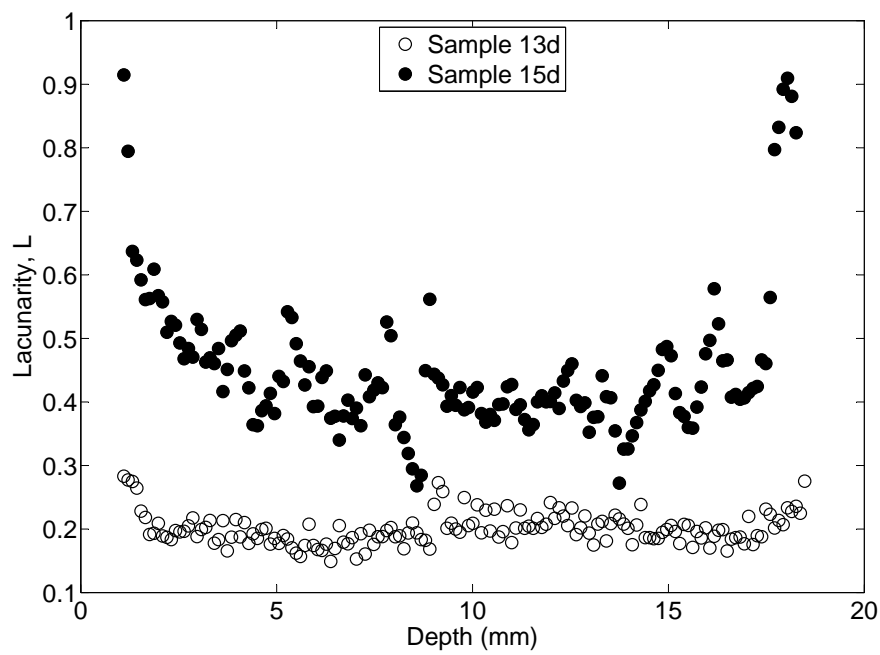


Figure 7.30: Change in lacunarity with depth for samples 13d and 15d

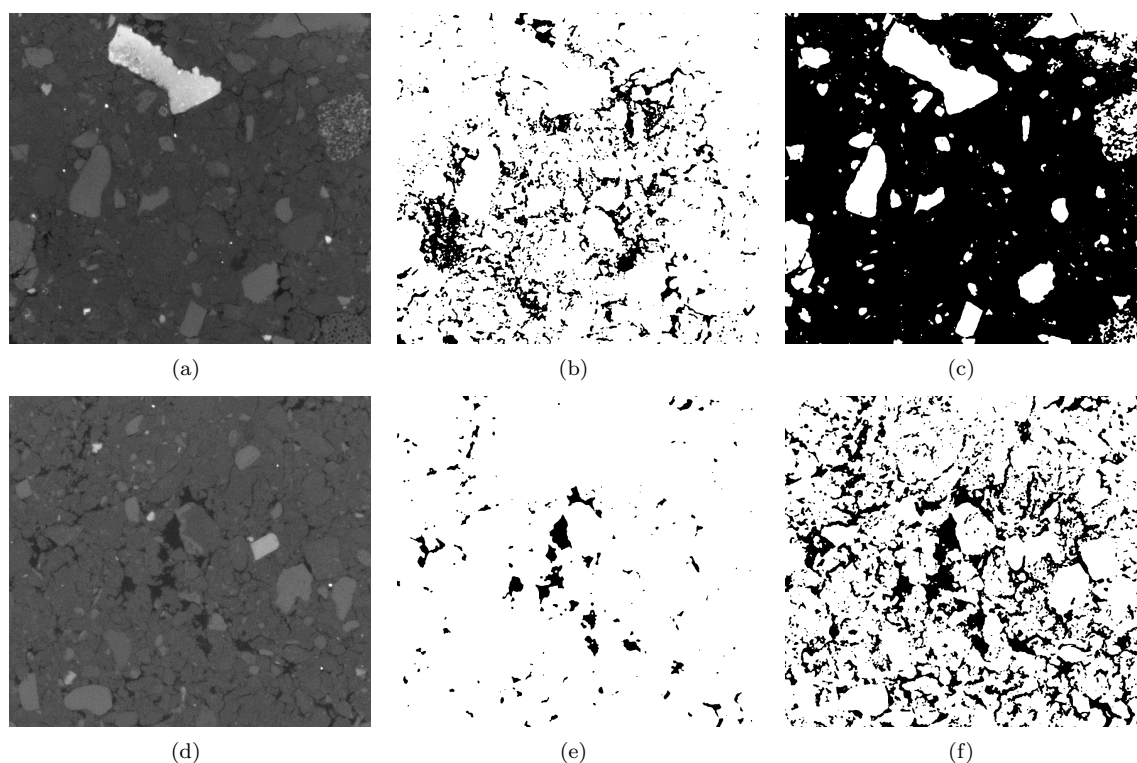


Figure 7.31: Effect of changing the threshold value on the resulting binary images for sample 13d: a) original image (1100 μm depth); b) analysed using threshold value of 60; c) analysed using threshold value of 141; d) original image (17600 μm depth); e) analysed using threshold value of 60; f) analysed using threshold value of 141.

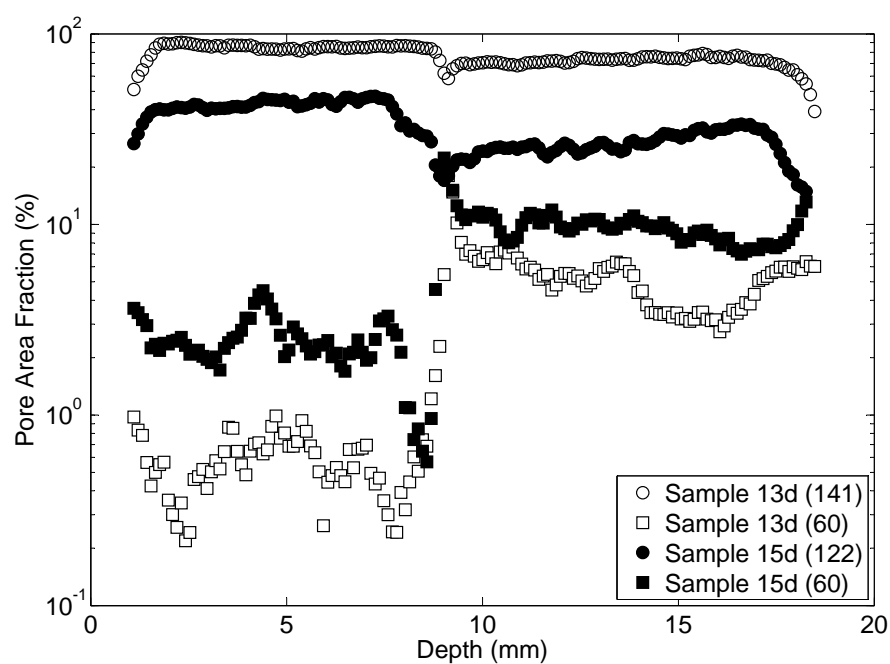


Figure 7.32: Change in pore area fraction with depth for samples 13d and 15d for different threshold intensity values

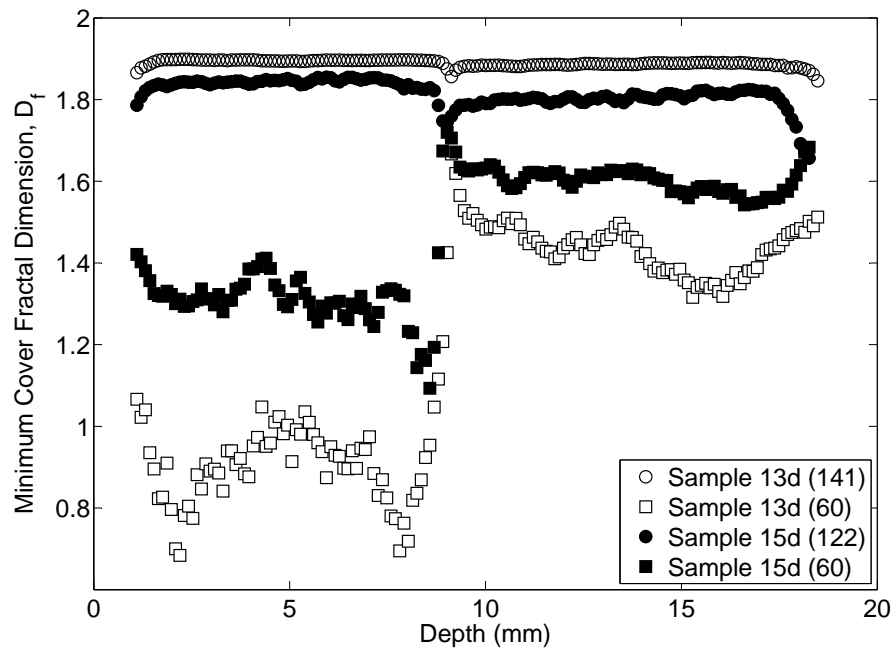


Figure 7.33: Change in minimum cover fractal dimension with depth for samples 13d and 15d for different threshold intensity values

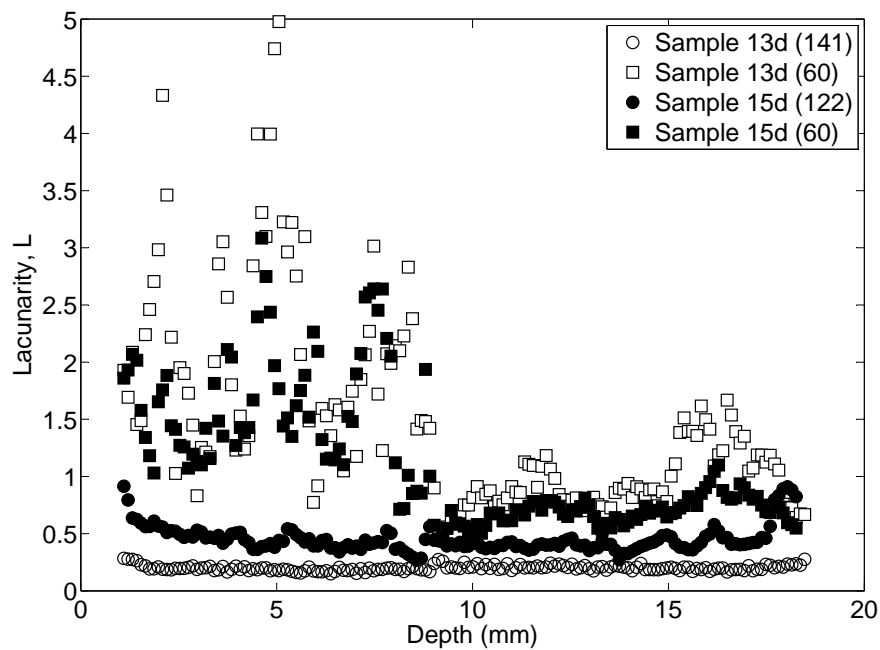


Figure 7.34: Change in lacunarity with depth for samples 13d and 15d for different threshold intensity values

(Figure 7.32). The magnitude of the change in PAF and D_f between the layers (as depth increases past 9 mm) is significantly larger than that corresponding to shadowing at the edges, indicating that a change in the material structure occurs across the layer boundary and that results are not the product of an analysis error.

Figures 7.32 and 7.33 show that PAF and D_f values calculated using the threshold value of 60 are lower for the lower layer than for the upper layer, whilst Figure 7.34 shows that, whilst quite erratic, L values are generally higher in the lower layer than in the upper layer, suggesting that macropores in the lower layer are smaller and have a lower interconnectivity (i.e. more gaps) than those in the upper layer. The good agreement between the results for samples 13d and 15d suggests that this result is not due to experimental error but is in fact representative of a change in the material macrostructure between layers. As results discussed in Section 4.3 showed that compaction of the upper layer does not affect the lower layer, an explanation for the change in macrostructure is an inaccuracy in the size of the press used to compact the lower layer (see Figure 7.4), in that the double-layer press was too long, resulting in a higher material density for a given mass of material. This is also suggested by the excellent agreement between the samples (at all threshold levels) for the depth of the layer break, which would not be seen if the reduced depth of the bottom layer was due to the compaction of the upper layer, due to the heterogeneity of the material mix. The generally constant trend of PAF results for the lower layer also supports this observation, as it would not be seen if it had been compressed by the upper layer; instead, the top of the lower layer would probably be more compact than the bottom of the layer, as seen for the single-layer samples. This observation was confirmed by careful measurement of the double-layer press shaft, showing that it was roughly 31 mm long (i.e. too long by 1 mm). Therefore, it is suggested that results found in Figures 7.32 and 7.33 support those found in Section 4.3, in that layers are not affected by the compaction of additional layers.

Figure 7.32 shows that PAF values appear to vary about a roughly constant value with depth for each layer. However, Figure 7.13 shows that PAF generally reduces with increasing depth (i.e. towards the top of the sample) for all three of the single-layer samples, supporting the observations made by Morel et al. (2007) and Bui and Morel (2009). It is suggested that the disparity between double- and single-layer samples is due to the layers in samples 13d and 15d being very thin (roughly 10 mm), so that material throughout the layer is subjected to the same compaction, whereas those in samples 2s, 9s and 10s are sufficiently thick for compaction to vary throughout the layer, due to friction with the mould (Morel et al., 2007). As RE layers used in construction are of the order of 100 mm thick after compaction (see Chapter 1), results shown in Figures 7.13 and 7.15 are therefore suggested to be more representative of the material comprising RE layers than those shown in Figures 7.32 to 7.34. Therefore, although compaction of one layer does not effect the structure of layers below it, the density of the material within the layer does reduce with depth, with a corresponding increase in the macropore sizes and interconnectivity of the pore network. Again, this demonstrates the need to properly compact material in order to avoid introducing detrimental material properties. Although only tested for one soil mix, it is again assumed that this effect occurs with all mixes during compaction. This effect can be observed in many existing RE structures, where the surface of an RE layer becomes smoother (indicating fewer pores) as it approaches the top of a lift. An example of this is shown in Figure 1.3, where regions of coarse material delineate the lifts.

The result of changing material density with layer depth supports the observation made by Morel et al. (2007) that compressive strength correction factors for different aspect ratios determined for masonry materials (e.g. Krefeld (1938) and Heathcote and Jankulovski (1992)) are not suitable for soils, as the material is not homogeneous throughout the layer. However, in Morel et al. (2007) it is assumed that the material comprising samples with aspect ratios below 1.5 can be considered homogeneous, so that existing correction factors might be acceptable, whereas results presented here show that the material

comprising the single-layer samples (aspect ratio $\frac{4}{3}$) is not, and that homogeneous material is only present, in large, in the double-layer samples (aspect ratio $\frac{2}{3}$). Furthermore, results found in Chapter 4 for tests on samples of different size but identical aspect ratio show that recorded material strengths are significantly affected by the size of the sample relative to the size of the largest particle contained within it, due to changes in the crack propagation paths. Therefore, it is suggested that layer thickness, rather than aspect ratio, should be considered when determining material homogeneity.

7.6 Conclusions

The aims of this chapter were to determine the effect of compaction, loading and layering on the macrostructure of RE, through the use of XRCT and fractal analyses.

The application of a load to an RE sample results in an increase in the size and interconnectivity of pores due to cracking, shown through the increase in PAF and D_f and a reduction in L for a given depth within a sample layer. Threshold intensity values were varied to show that the application of a load has a greater effect on larger pores than smaller pores, as the greater surface area allows for the formation and propagation of a greater number of cracks. PAF, D_f and L values also showed that the application of a load does not change the shape and distribution of the pores, but instead increases their size and interconnectivity. It was also shown that poorly-compacted material will suffer more cracking than well-compacted material for the same applied load, indicating the need to properly compact material during construction. Following the discussion presented in Chapters 5 and 6, the application of a compressive load to an RE structure might allow it to achieve lower equilibrium water contents and so a higher compressive strength for a given humidity and temperature than if it were not loaded, due to the presence of larger pores. However, as the application of a load creates cracks, rather than pores, it might be that a preferential failure mechanism is also created, so that an increase in strength is not seen. Further work is required to substantiate this observation, however, as XRCT data does not give information about the structure of material features smaller than the scanning resolution.

Single- and double-layer samples were used to investigate the effect of compaction on the material macrostructure with depth through an RE layer and across a layer boundary. Results showed that the PAF and D_f decrease whilst L increases with increasing depth, showing that pores become larger and more interconnected and, hence, that density reduces towards the base of a layer. Results for double-layered samples suggested that the macrostructure of an underlying layer is not affected by the compaction of a subsequent layer, as was suggested in Chapter 4, however this result is difficult to substantiate due to sample lower layers being compacted to a higher degree than upper layers.

Results for tests on single- and double-layered samples show that the material comprising RE layers is non-homogeneous, so that correction factors based on sample aspect ratios should be avoided, supporting the observations made by Morel et al. (2007). Instead, it is recommended that layer thickness and maximum particle size be considered when accounting for sample size. This, however, is a topic for future research.

7.7 References

- Atzeni, C., Pia, G., Sanna, U., Spanu, N., 2008. A fractal model of the porous microstructure of earth-based materials. *Construction and Building Materials* 22 (8), 1607–1613.
- Bird, N., Bartoli, F., Dexter, A., 1996. Water retention models for fractal soil structures. *European Journal of Soil Science* 47, 1–6.
- Bird, N., Daz, M. C., Saa, A., Tarquis, A. M., 2006. Fractal and multifractal analysis of pore-scale images of soil. *Journal of Hydrology* 322 (1–4), 211–219.
- Blair, J. M., Falconer, R. E., Milne, A. C., Young, I. M., Crawford, J. W., 2007. Modeling three-dimensional microstructure in heterogeneous media. *Soil Science Society of America Journal* 71 (6), 1807–1812.
- Bonala, M. V. S., Reddi, L. N., 1999. Fractal representation of soil cohesion. *Journal of Geotechnical and Geoenvironmental Engineering* 125 (10), 901–904.
- Bui, Q.-B., Morel, J.-C., 2009. Assessing the anisotropy of rammed earth. *Construction and Building Materials* 23 (9), 3005–3011.
- Cihan, A., Tyner, J. S., Perfect, E., 2009. Predicting relative permeability from water retention: A direct approach based on fractal geometry. *Water Resources Research* 45, 8.
- Colliat-Dangus, J. L., Desrues, J., Foray, P., 1988. Triaxial testing of granular soil under elevated cell pressure. In: Donaghe, R. T., Chaney, R. C., Silver, M. L. (Eds.), *Proceedings of a conference on advanced triaxial testing for soil and rocks*. American Society for Testing and Materials, Philadelphia (USA), pp. 290–310.
- Desrues, J., Gioacchino, V., 2004. Strain localization in sand: an overview of the experimental results obtained in grenoble using stereophotogrammetry. *International Journal for Numerical and Analytical Methods in Geomechanics* 28, 279–321.
- Ersahin, S., Gunal, H., Kutlu, T., Yetgin, B., Coban, S., 2006. Estimating specific surface area and cation exchange capacity in soils using fractal dimension of particle-size distribution. *Geoderma* 136 (3–4), 588–597.
- Foroutan-pour, K., Dutilleul, P., Smith, D. L., 1999. Advances in the implementation of the box-counting method of fractal dimension estimation. *Applied Mathematics and Computation* 105 (2–3), 195–210.
- Gens, A., Valleján, B., Sánchez, M., Imbert, C., Villar, M. V., Van Geet, M., 2011. Hydromechanical behaviour of a heterogeneous compacted soil: experimental observations and modelling. *Géotechnique* 61 (5), 367–386.
- Gimnez, D., Perfect, E., Rawls, W. J., Pachepsky, Y., 1997. Fractal models for predicting soil hydraulic properties: a review. *Engineering Geology* 48 (3–4), 161–183.
- Hall, M., Djerbib, Y., 2004. Rammed earth sample production: context, recommendations and consistency. *Construction and Building Materials* 18 (4), 281–286.
- Hall, S. A., Bornert, M., Desrues, J., Pannier, Y., Lenoir, N., Viggiani, G., Bésuelle, P., 2010. Discrete and continuum analysis of localised deformation in sand using x-ray μ ct and volumetric digital image correlation. *Géotechnique* 60 (5), 315–322.
- Heathcote, K., Jankulovski, E., 1992. Aspect ratio correction factors for soilcrete blocks. *Australian civil engineering transactions* CE34 (4: Australia: Institution of Engineers), 309–312.
- Hirata, T., 1989. Fractal dimension of fault systems in Japan: Fractal structure in rock fracture geometry at various scales. *Pure and Applied Geophysics* 131, 157–170.
- Huang, G.-H., Zhang, R.-D., Huang, Q.-Z., 2006. Modeling soil water retention curve with a fractal method. *Pedosphere* 16, 137–146.
- Hyslip, J. P., Vallejo, L. E., 1997. Fractal analysis of the roughness and size distribution of granular materials. *Engineering Geology* 48 (3–4), 231–244.
- Jaquin, P. A., Augarde, C. E., Gallipoli, D., Toll, D. G., 2009. The strength of unstabilised rammed earth materials. *Géotechnique* 59 (5), 487–490.
- Jobmann, M., Billaux, D., 2010. Fractal model for permeability calculation from porosity and pore radius information and application to excavation damaged zones surrounding waste emplacement boreholes in opalinus clay. *International Journal of Rock Mechanics and Mining Sciences* 47 (4), 583–589.
- Keller, A., 1998. High resolution, non-destructive measurement and characterization of fracture apertures. *International Journal of Rock Mechanics and Mining Sciences* 35 (8), 1037–1050.
- Ketcham, R. A., Carlson, W. D., 2001. Acquisition, optimization and interpretation of x-ray computed tomographic imagery: Applications to the geosciences. *Computers and Geosciences* 27, 381–400.
- King, B., 1996. *Buildings of Earth and Straw: Structural Design for Rammed Earth and Straw-Bale Architecture*. Ecological Design Press, Sausalito, California (USA).
- Kravchenko, A., Zhang, R., 1998. Estimating the soil water retention from particle-size distributions: a fractal approach. *Soil Science* 163 (3), 171–179.
- Krefeld, 1938. Effect of shape of specimen on the apparent compressive strength of brick masonry. In: *Proceedings of the American Society of Materials, Philadelphia, USA*. pp. 363–369.
- Kruth, J., Bartscher, M., Carmignato, S., Schmitt, R., Chiffre, L. D., Weckenmann, A., 2011. Computed tomography for dimensional metrology. *CIRP Annals - Manufacturing Technology* 60 (2), 821 – 842.

- Lipiec, J., Hatano, R., Slowinska-Jurkiewicz, A., 1998. The fractal dimension of pore distribution patterns in variously-compacted soil. *Soil and Tillage Research* 47 (1-2), 61–66.
- Mandelbrot, B. B., 1967. How long is the coast of Great Britain? Statistical self-similarity and the fractional dimension. *Science* 156, 636–638.
- Morel, J.-C., Pkla, A., Walker, P., 2007. Compressive strength testing of compressed earth blocks. *Construction and Building Materials* 21 (2), 303–309.
- Pachepsky, Y. A., Gimnez, D., Crawford, J. W., Rawls, W. J., 2000. Conventional and fractal geometry in soil science. In: Y. Pachepsky, J. C., Rawls, W. (Eds.), *Fractals in Soil Science*. Vol. Volume 27. Elsevier, pp. 7–18.
- Perfect, E., Rasiyah, V., Kay, B. D., 1992. Fractal dimensions of soil aggregate-size distributions calculated by number and mass. *Journal of the Soil Science Society of America* 56, 1407–1409.
- Perrier, E. M. A., Bird, N. R. A., 2002. Modelling soil fragmentation: the pore solid fractal approach. *Soil & Tillage Research* 64, 91–99.
- Perrier, E. M. A., Bird, N. R. A., Rieu, M., 1999. Generalizing the fractal model of soil structure: the poresolid fractal approach. *Geoderma* 88, 137–164.
- Rasband, W., 2002. NIH Image J.
URL <http://rsbweb.nih.gov/ij/index.html> (verified 02.08.2011)
- Ridler, T. W., Calvard, S., 1978. Picture thresholding using an iterative selection method. *Systems, Man and Cybernetics, IEEE Transactions on* 8 (8), 630–632.
- Rigby, S. P., Chigada, P. I., Wang, J., Wilkinson, S. K., Bateman, H., Al-Duri, B., Wood, J., Bakalis, S., Miri, T., 2011. Improving the interpretation of mercury porosimetry data using computerised x-ray tomography and mean-field dft. *Chemical Engineering Science* 66 (11), 2328–2339.
- Roscoe, K. H., 1970. The influence of strains in soil mechanics. *Géotechnique* 20 (2), 129–170.
- Russell, A. R., 2010. Water retention characteristics of soils with double porosity. *European Journal of Soil Science* 61 (3), 412–424.
- Tarantino, A., 2009. A water retention model for deformable soils. *Géotechnique* 59 (9), 751–762.
- Tarantino, A., 2010. Unsaturated soils: compaction versus reconstituted states. In: Alonso, E., Gens, A. (Eds.), *Unsaturated soils. Fifth International Conference on Unsaturated Soils*, CRC Press, pp. 113–136.
- Taud, H., Martinez-Angeles, R., Parrot, J., Hernandez-Escobedo, L., 2005. Porosity estimation method by x-ray computed tomography. *Journal of Petroleum Science and Engineering* 47 (3–4), 209–217.
- Thevanayagam, S., Nasarajah, S., 1998. Fractal model for flow through saturated soils. *Journal of Geotechnical and Geoenvironmental Engineering* 124 (1), 53–66.
- Tolle, C. R., Mcjunkin, T. R., J., G. D., 2003. Suboptimal minimum cluster volume cover-based method for measuring fractal dimension. In: *IEEE Transaction on Pattern Analysis and Machine Intelligence*. pp. 32–41.
- Vallejo, L. E., 1996. Fractal analysis of the fabric changes in a consolidating clay. *Engineering Geology* 43 (4), 281–290.
- Van Geet, M., Swennen, R., Wevers, M., 2000. Quantitative analysis of reservoir rocks by microfocus x-ray computerised tomography. *Sedimentary Geology* 132 (1-2), 25–36.
- Van Geet, M., Volckaert, G., Roels, S., 2005. The use of microfocus x-ray computed tomography in characterising the hydration of a clay pellet/powder mixture. *Applied Clay Science* 29 (2), 73–87.
- Wellington, S. L., Vinegar, H. J., 1987. X-ray computerized tomography. *Journal of Petroleum Technology*, 885–898.
- Xu, Y. F., 2004a. Calculation of unsaturated hydraulic conductivity using a fractal model for the pore-size distribution. *Computers and Geotechnics* 31 (7), 549–557.
- Xu, Y. F., 2004b. Fractal approach to unsaturated shear strength. *Journal of Geotechnical and Geoenvironmental Engineering* 130 (3), 264–273.
- Xu, Y. F., Sun, D. A., 2002. A fractal model for soil pores and its application to determination of water permeability. *Physica a-Statistical Mechanics and Its Applications* 316 (1-4), 56–64.
- Zeng, Y., Gantzer, C. J., Payton, R. L., Anderson, S. H., 1996. Fractal dimension and lacunarity of bulk density determined with X-ray computed tomography. *Soil Science Society of America Journal* 60 (6), 1718–1724.

Chapter 8

Conclusions and implications for rammed earth design and construction

8.1 Analytical and experimental investigation conclusions

The investigations presented in this thesis have demonstrated how various aspects of the behaviour of RE are determined by its corresponding micro- and macrostructures. In this chapter, the results of these investigations are collated in order to describe how the material structure is formed and how it affects its strength. These effects are then interpreted in terms of their implications for the design, construction and maintenance of RE structures.

8.1.1 Linking internal structure to retention behaviour

The link between the pore size distribution (PSD) and the water retention behaviour was investigated in Chapter 3 and it was shown that the soil water retention curve (SWRC) can be adequately predicted using information provided by the PSD alone, given sufficient information concerning the change in void ratio with applied suction, according to phenomena known to occur in porous material on changes in suction. This is an important result as it supports the validity of those processes and allows for the interpretation of subsequent experimental results in terms of changes which occur to the internal structure of the material.

8.1.2 Comparison between laboratory- and construction-prepared material

The effects of manufacturing processes used in construction and in the laboratory on the final material structure of RE can be assessed by considering the results presented in Chapters 4 to 7, in order to determine whether the latter is representative of the former.

8.1.2.1 Mixing processes

In construction, material is prepared to near its optimum water content (OWC) by mixing materials with water and, if required, additional material, for example sand or clay. In the laboratory, soil mixes are prepared by combining dry soil constituents, which can lead to the creation of a layered structure due to stratification and segregation (Section 4.2.2). The dry material is wetted to the OWC by adding

controlled amounts of water to the dry material, so that a layered structure might still be present in the wetted material.

8.1.2.2 Layer compaction

In construction, wet soil is heaped between formwork and compacted to form a layer (or a “lift” in RE terminology), as shown in Figure 1.2. Experimental results discussed in Section 4.3 show that all of the material in a layer is affected by the compaction process, however the material at the bottom of the layer is less dense than that at the top, as determined through the presence of larger macropores (Section 7.5.4). After compaction, the structure of materials which have higher clay contents, and so larger aggregates prior to compaction, comprise a larger number of smaller pores than materials containing less clay (Section 5.3.4).

The combination of heaping of wet material into sample moulds and mixing due to compaction results in a removal of any potential initially-layered structures within the wet material, as shown by results presented in Section 4.3 and in reconstructed 3-D pore networks shown in Sections 7.5.3 and 7.5.4. The internal structure of the material is dependent on its initial clay content, as described above for construction materials. Layers in laboratory samples are thinner than those used in construction so that the change in density between the top and bottom of a layer on compaction is reduced, as shown in Section 7.5.4 for double-layer samples, as compared to results for single-layer samples, as shown in Section 7.5.3.

8.1.2.3 Effect of multiple layers

In construction, a block of material is prepared by compacting layers of material on top of each other up to the height of the formwork (see Figure 1.2 and Section 1.2.1). The formwork is then removed and the block allowed to dry prior to the placing of another block above it. This is similar to the process used to manufacture samples in the laboratory, although the formwork (or mould) is significantly smaller. Results given in Sections 4.3 and 7.5.4 show that the density, and so the macrostructure, of a layer (thick or thin) is not affected by the compaction of layers above it. As compaction does not affect the intra-aggregate pores, this result also extends to the material microstructure. As discussed in Section 7.5.3, the self weight of overlying layers (in construction or in laboratory samples) is insufficient to cause significant cracking in the lowermost layers.

For a given compactive effort, laboratory samples are likely to achieve higher densities than the same material compacted during construction due to the former’s use of thinner layers. Therefore, care should be taken to control sample densities. Assuming that this is done, the final micro- and macrostructures of laboratory-prepared and construction materials should be the same for the same material, so that the results of tests conducted on laboratory samples can apply to full-scale structures.

8.1.3 The effect of material structure on strength

Results given in Sections 5.3.3 and Section 6.4.3 show that compacted materials containing a higher amount of clay achieve greater unconfined compressive and tensile strengths than materials containing less clay at a given water content. This effect is often attributed to clay cementation, i.e. a binding action caused by clay particles; however, as discussed in Section 5.3.4, materials with a higher clay content also have higher suctions for given water contents, due to the increased volume of smaller pores, so that it is instead suggested that the increase in compressive and tensile strength observed on the addition of clay is, in fact, due to this increase in suction.

It was shown in Section 5.3.4 that the proportion of adsorbed water is greater for a given suction in materials containing more clay, due to the increased surface area available for adsorption. It was argued that, as a result, unconfined compressive strengths are lower than those found in materials containing less clay for given suction values due to the reduced proportion of capillary water.

The change in tensile strength with solution content and concentration was investigated in Section 6.4.5. As for unconfined compressive strength in Chapter 5, a strong relationship was found between suction and tensile strength suggesting that suction is a key property in determining both material properties. The addition of CaCl_2 to the material resulted both in an increase in osmotic suction and a breakdown of soil aggregates due to clay flocculation and a subsequent increase in the volume of larger pores contained within the material. It was found that high osmotic suctions can counter the effect of the weakening of the structure due to flocculation, resulting in increasing tensile strengths with solution concentration in the central S_r value range. Tensile strengths at high and low S_r values were largely unaffected by solution concentration (when considering experimental variation) due to low total suctions in the former and the relatively low contribution of osmotic suction to total suction in the latter case.

8.2 Implications and recommendations for design, construction and conservation

8.2.1 New-build structures

8.2.1.1 Design

Location and climate

Results found in Chapter 5 show that temperature and humidity affect the strength of RE and that materials achieve their greatest strengths in hot, arid conditions; indeed, most surviving RE structures are found in such regions. Therefore, changing climatic conditions likely to occur at the proposed location for an RE structure should be considered when designing an RE structure, as the range of conditions present during design might not be present during construction or throughout its expected life: for example, if the region is to become wetter and cooler additional water protection and thicker walls (due to weaker material) should be provided. Furthermore, the use of a set target strength (tensile or compressive) for a material, as is the case for the New Zealand RE construction standards (1.3 MPa in NZS 4298:1998), should be avoided, as a material might have an acceptable strength under some conditions but not under others. Instead, standards should specify minimum strength requirements for given climatic conditions, in order to ensure that structures remain safe.

Water protection

If an RE wall is subjected to rainfall, water will run down the surface of the wall rather than soak into the material due to the presence of relatively small pores at the wall surface (the *overcoat effect*, Hall and Djerbib (2006)). However, prolonged exposure, either due to heavy rain or water pooling, results in water being absorbed by the material and so a reduced material strength. Therefore, prolonged exposure to water should be avoided; this is commonly achieved in construction, with good results, through the use of impermeable stem walls and large overhanging eaves (King, 1996; Walker et al., 2005; Easton, 2007), examples of which are shown in Figure 8.1. It is therefore recommended that this practice be continued for the use of unstabilised RE.

Putlogs

Traditional RE construction results in the formation of characteristic putlogs between the blocks, due to the use of formwork supports (see Figure 1.2). In modern construction, these putlogs are smaller or non-existent, due to the use of stronger materials for the formwork, and, if present, are filled after the removal of the formwork to prevent water or animal ingress and to improve the aesthetics of the finished wall surface. However, surviving structures show that these putlogs were not closed, despite being paths for water or ingress or animal access. Results found in Chapters 5 and 6 suggest that these putlogs were purposely left open in order to ensure that thick RE walls were able to dry throughout their width and not just at the surface, as might otherwise be the case, in order to improve their strength and potentially prevent uneven drying which might lead to cracking (although whether this was discovered by accident, through design or is simply the result of building traditions is unknown). Therefore, it is suggested that putlogs be left open during construction, rather than being sealed, and that their presence be incorporated into and not removed from the design of the structure.

Tension members and cracking

Results presented in Chapters 5 and 6 show that the tensile strength of RE is significantly less than its compressive strength for both of the tested soil mixes. Therefore, the use of RE in tension, for example in lintels, should be avoided unless it is otherwise supported (Walker, 2002). Furthermore, corners of overhanging features, for example above doorways, should be protected or be formed out of another material, for example fired brick, in order to prevent cracking.

Results presented in Chapter 7 showed that cracking occurs within the material on the application of a load to an RE structure. Therefore, sections of a structure that are likely to be loaded heavily should have good access for inspection and repair, if necessary. Furthermore, structures should be designed so that material cannot pile against entry or exit routes in the event of the material failing, for example in the event of an earthquake.

8.2.1.2 Construction

It is normal practice during construction of RE structures to wet the soil by spraying it with water. The water content of the material is then checked using the “drop test”; a fist-sized ball of soil is dropped from a height of roughly 1 m and the water content deemed acceptable if it breaks into several large pieces, as opposed to shattering or sticking to the ground. This is a highly subjective test and can lead to the over or underestimating of the water content, which results in reduced compacted densities for given compactive efforts, and so reduced strengths. If possible, it is therefore recommended that water contents be determined accurately in order to guarantee optimum compaction. Furthermore, RE materials are usually prepared to water contents above their optimum value in order to improve workability (and perhaps account for some drying which occurs prior to ramming) (Jaquin et al., 2009); as this also results in sub-optimal compaction, this practice should also be avoided.

Material compaction during construction uses either manual or mechanical rammers, depending on availability. It is therefore possible that different compactive efforts are used for different parts of a structure. Furthermore, as compaction is labour-intensive, there is a temptation for compaction to be hurried and left incomplete. As shown in Section 7.5.4, poorly-compacted material will suffer more cracking than well-compacted material for the same applied load. It is therefore recommended that the compaction process be closely supervised during construction. Related to this point is the common fault of over-compaction of samples for laboratory testing, in order to ensure favorable strengths. Again, this

practice can be prevented by supervising sample preparation so that results found in laboratory testing remain representative of the behaviour of the structure.

Results discussed in Chapter 7 show that the change in density with depth of a thin layer of RE is less than that of a thick layer. Therefore, care should be taken in relating optimum water contents and maximum bulk densities determined using laboratory samples to construction materials, as the use of thicker layers in construction will produce a less-dense layer for the same compactive effort. Therefore, samples prepared on site for testing in a laboratory should be compacted in layers as thick as those used during construction; the use of thinner layers will produce a more dense sample which will again lead to misleading results.

As discussed in the previous section, it was found in Chapter 5 that compacted materials with particle gradings within the limits proposed by Houben and Guillaud (1996) but with lower clay contents achieve higher compressive strengths than materials still within those limits but with higher clay contents for given temperature and humidity combinations. Therefore, materials with clay contents towards the lower values recommended by Houben and Guillaud (1996) should be considered for construction. As clay can be expensive to acquire and transport, this might reduce costs by reducing the amount of clay that needs to be added to a soil, if any, to make it acceptable for construction.

Results given in Section 6.4.5 show that the addition of dissolved ions to the pore water changes the behaviour of the clay particles and so the internal structure of the material. Therefore, if the use of water containing large amounts of dissolved ions, for example deep well or sea water, is required, tests should be conducted on the strength of the material wetted with that water, rather than the pure or deionised water used in the laboratory. Furthermore, a change from one water type to another during construction should be avoided in order to prevent unexpected changes in material strength. The addition of dissolved ions to soils might provide a method to improve a soil's suitability for RE construction; again, however, tests need to be conducted prior to construction in order to verify their effects. Results given in Section 6.4.5 suggest that dissolved ions have little effect on the tensile strength under equilibrium conditions for low S_r values, however tests on material under these conditions should also be conducted as the use of greater solution concentrations or different clay mineralogies might lead to significant changes in tensile strength compared to untreated material.

8.2.1.3 Conservation

RE structures made from high-clay soil mixes have smoother surface textures than those made from materials containing less clay, which grants them a greater resistance to surface damage than those with coarser surfaces. However, as results in Chapters 5 and 6 show, these materials are also weaker at equilibrium conditions than those containing less clay and so a compromise between durability and strength must be made.

Earth, lime-based and/or cement-based renders can be used to protect an RE structure from damage. Renders are desirable as they provide a smooth surface and can be moulded to form complex shapes, as shown in Figure 8.2, or painted. Earthen renders have very fine internal structures due to their very high clay content (King, 1996). Therefore, their equilibrium water content with a given temperature and humidity is quite high compared to the underlying material, so that the latter's water content might increase, thereby weakening it. Care must therefore be taken to ensure that the application of a render does not adversely affect the structure. The application of paint can also effectively seal the surface, preventing drying and again causing detrimental changes in material strength.

Lime-based renders can also be applied to surfaces for protection. The advantage of a lime-based render is that it is stronger than an earth render, providing greater durability. However, the use of lime can produce an even finer internal structure than the use of clay alone, depending on the materials the

lime is mixed with, potentially further increasing the water content of the underlying material.

Cement-based renders produce very durable surfaces which can easily be painted. However, their use is not recommended as cracking of and around the render, caused by natural movements of the wall, leads to water ingress and a build-up of water behind the render, causing the underlying material to weaken and fail. Therefore, more damage can potentially be caused to the structure than if the render were not present (Delgado and Guerrero, 2006).

8.2.2 Ancient structures

The conservation methods discussed in the previous section can be applied to both modern and ancient structures. A concern when conserving ancient structures is, however, that protective methods cannot be applied unless there is evidence of it being used during the structure's lifetime. However, it is recommended for the preservation of these structures that they be protected in some way, for example reconstructing roofs, applying renders or separating walls from the surrounding ground if debris has piled up over time. Methods for repairing ancient structures are equally applicable to modern structures, however more examples exist for ancient structures due to their longevity. Repair methods are often less in keeping with the original structure due to the need for immediate preservation, as well as the potential lack of similar materials or indeed funding for accurate restoration. Similar to the use of renders discussed in the previous section, repairs to RE structures can be made using earthen, lime or cement-based materials.

Damage to surfaces can be repaired through patching. Concrete patches are a common repair technique, where damaged sections of walls are dressed with concrete to restore the original lines of the building, as shown in Figure 8.3 (Delgado and Guerrero, 2006; Jaquin, 2008). As concrete is often readily available and easily mixed on site, repairs can be made quickly and without the need for skilled labour. However, as for cement renders, cracking and water ingress cause a build-up of water behind the patch, causing the underlying RE material to weaken and fail and the patch to become detached from the structure. The patch is subsequently re-patched, beginning the cycle of damage again. This effect is also possible if lime-based materials are used, although it is not as severe. It is therefore recommended that earthen materials be used for the repair of damaged structures. An example of this is shown in Figure 8.4; the repairs (lighter) are far more in keeping with the original structure and should age with time to achieve the same surface texture.

Results presented in Section 7.5.3 show that loaded RE material contains cracks, so that unloading the structure will not restore its former properties. Furthermore, removing only visibly-failed material prior to patching might not be sufficient to prevent further damage. It is therefore recommended that material around damaged areas also be removed.

Foundation settlement or other shifts in the structure can lead to the formation of large vertical tension cracks in RE structures, for example as shown in Figure 8.5(a) and (b). Cracks can be repaired either by filling the gap with material, as for patches, or through the use of staples. Staples are formed by cutting out a section of the wall either side of the crack and placing a strip of material across it, as shown in Figure 8.5(c). The advantage of stapling is that less material is required, however the material should be similar to that used for the main structure to provide a similar stiffness and strength, as shown by results presented in Chapters 5 and 6; a change in stiffness could cause the staple to detach from the structure, causing further damage (Jaquin, 2008). The disadvantage of stapling is that the majority of the crack remains open, so that the exposed material is still susceptible to damage. Furthermore, as discussed above, sufficiently large sections need to be removed from either side to avoid embedding the staple into already-cracked material, as the staple would simply detach causing further damage to the structure.

8.3 Further work

This section discusses topics for further work which have arisen from the investigations presented in this thesis.

8.3.1 Trapped pores and pore constriction

Work presented in Chapter 3 showed that the pore size distribution is closely linked to the water retention properties of a soil. However, it was found that both the combined capillary-adsorption (CCA) model and that used by Zhang and Li (2010) resulted in an over- and an under-estimation of the suction required to drain large and small pores respectively. This was attributed to changing material void ratio and the presence of trapped pores in the structure, due to the process of mercury intrusion. A suitable method for accounting for these trapped pores has not yet been developed; an extension to the CCA model would therefore be a method to account for these trapped pores so that the predicted retention curve would more closely match that found by experimentation.

8.3.2 Stratification and segregation

It was shown in Chapter 4 that a partial segregation of materials occurs if a mixture of sands is poured onto a surface, as occurs in the production of dry soil mixes for RE testing in a laboratory. However, the effect of the presence of clay in the soil mix was not investigated, although it was suggested that it might reduce the segregation effects. As clay is a key constituent of RE soil mixes, further work is required to determine the actual effect of clay on segregation in order to determine the structure of the material prior to compaction and to determine whether or not it is similar to natural RE.

8.3.3 Sources of strength in RE

Results presented in Chapters 5 and 6 show that RE materials gain strength with reducing water content and that their relative strengths depend on the material structure and generated suctions. However, as only two soil mixes were tested, the experiments conducted in those chapters should be extended to cover a wider range of soil types, in order to determine whether a specific soil type can be recommend for RE construction.

Results presented in Chapters 5 and 6 showed that suction is strongly linked to the unconfined compressive and tensile strength in RE materials. Further testing should be conducted using a range of suction measurement techniques in order to determine accurate retention properties for these materials in order to support estimated suction values used in these investigations.

The effect of the presence of dissolved ions on the strength of RE was investigated in Chapter 6 through the addition of CaCl_2 to the pore water. Ca^{2+} was selected as it is high in the lyotropic series and so is readily absorbed by clay minerals. The effect of ion addition on material structure should be extended by considering the effects of ions lower down the lyotropic series, for example K^+ , and different clay mineralogies. The experimental variation of results found for RE samples treated with CaCl_2 solutions was very high, making the effect of changing osmotic suction difficult to determine. An improved sample manufacturing and equilibration technique would reduce this variation and so allow the role of matric, osmotic and total suction in determining the tensile strength of RE to be more fully investigated.

It was found in Chapter 7 that the application of a load to an RE material results in the formation of cracks within the material. However, as cracking changes the internal structure of the material, it is likely that the equilibrium water contents of cracked materials are different (suggestibly lower due

to the presence of larger pores) to those for the same material prior to cracking, given results found in Chapters 5 and 6. Therefore, depending on the amount of cracking, the effect of loading an RE material might be an increase or a decrease in strength, in effect affording it a slight strength ‘buffer’ zone. The effects of cracking on the material strength should therefore be investigated in more detail, as they would enable the effects of damage in RE structures to be accurately assessed and addressed.

As the density of the material comprising an RE layer changes with depth, traditionally-used correction factors for sample size, determined for homogeneous material for example masonry, are not suitable for RE materials (Morel et al., 2007). Instead, it is recommended that layer thickness and maximum particle size be considered when accounting for sample size, in order to determine appropriate correction factors. The use of these correction factors would enable strengths recorded through laboratory testing to be modified to relate to full-scale structures.

8.3.4 Types of failure of RE

Results presented in Section 6.4.2.2 show that samples demonstrate ductile and brittle failure at high and low water contents respectively and it was suggested that the two conditions are separated by a critical suction value or pore size. Further work is required in order to investigate the significance of this suction value and to relate it to the material micro- and macrostructure; for example, it might correspond to the suction at which inter-aggregate pores empty so that water only resides in the intra-aggregate pores. If this were the case, then the brittle or ductile failure of samples would give important information concerning their microstructure. Related to the ductile or brittle failure of samples is the effect of deformation rates on strength, as investigated in Young and Mullins (1991) but called into question by results presented in Chapter 6. This is an important consideration for construction, as it might be that RE materials achieve greater strengths at lower than at higher deformation rates, which might correspond to long-term (e.g. settlement) and short-term (e.g. seismic) damage.

A consideration when designing RE structures is that material does not break into large sections on failure, as is the case in masonry structures, but instead crumbles (Walker et al., 2005). Work presented in Chapter 7 suggests that failure is due to the formation of cracks between the aggregates, however it is not known if a critical level of cracking exists for a given RE soil mix beyond which failure will occur. Again, an investigation into the properties of cracked RE would enable the effects of damage in RE structures to be properly assessed, as well as increasing confidence in its use.

It was necessary for multiple samples to be prepared and tested in Chapter 7, due to a restriction on the availability of the X-ray computed tomography (XRCT) scanner. Although results suggested that the application of a load results in the formation of cracks within the samples, this effect should be verified by testing a single sample at a range of applied loads, scanning the sample between each load iteration. Although XRCT allows the solid macrostructure of a material to be observed and objects larger than a certain resolution to be identified, it cannot easily distinguish between different material types. Furthermore, it does not yet have the resolution necessary to observe the smallest pores nor the distribution of water within them. Therefore, loaded samples should also be investigated using other imaging techniques, for example environmental scanning electron microscopy, in order to observe the associated changes in the microstructure.

8.3.5 RE structures

It was argued in Section 8.2.1.1 that the presence of putlogs might result in a stronger structure. Further work is therefore required to investigate the effect of these and other structural features on material strengths in order to determine whether they should be incorporated in modern RE design. The results

of these investigations would also be useful for the conservation of existing RE structures, as beneficial features could be restored or non-beneficial features removed.

It was found in Section 7.5.4 that the depth of a layer affects the density of the material, with thinner layers achieving more uniform densities throughout their depths than thicker ones. It is therefore suggested that a critical layer thickness exists, above which the compaction of the material will become insufficient to achieve the desired strength. The determination of this layer thickness would greatly aid RE design and increase confidence in its use by regimenting compaction procedures.

8.4 Concluding remarks

As stated at the beginning of this chapter, work presented in this thesis has demonstrated how various aspects of the behaviour of RE are governed by its internal structures. It is hoped that this initial work can provide a platform for future research into understanding the design, construction and conservation of RE as a geotechnical material so that designers, practitioners and clients can gain confidence in its use.

8.5 References

- Delgado, M. C. J., Guerrero, I. C., 2006. Earth building in Spain. *Construction and Building Materials* 20 (9), 679–690.
- Easton, D., 2007. *The Rammed Earth House, Completely Revised Edition*. Chelsea Green Publication Company, Vermont (USA).
- Hall, M., Djerbib, Y., 2006. Moisture ingress in rammed earth: Part 2 - the effect of soil particle-size distribution on the absorption of static pressure-driven water. *Construction and Building Materials* 20 (6), 374–383.
- Houben, H., Guillaud, H., 1996. *Earth construction - a comprehensive guide.*, Second Edition. Intermediate Technology Publications, London (UK).
- Jaquin, P. A., 2008. Study of historic rammed earth structures in Spain and India. *The Structural Engineer* 86 (2), 26–32.
- Jaquin, P. A., Augarde, C. E., Gallipoli, D., Toll, D. G., 2009. The strength of unstabilised rammed earth materials. *Géotechnique* 59 (5), 487–490.
- King, B., 1996. *Buildings of Earth and Straw: Structural Design for Rammed Earth and Straw-Bale Architecture*. Ecological Design Press, Sausalito, California (USA).
- Morel, J.-C., Pkla, A., Walker, P., 2007. Compressive strength testing of compressed earth blocks. *Construction and Building Materials* 21 (2), 303–309.
- Walker, P. (Ed.), 2002. *The Australian Earth Building Handbook*. SAI Global Ltd., Sydney, Australia.
- Walker, P., Keable, R., Martin, J., Maniatidis, V., 2005. *Rammed Earth: Design and Construction Guidelines*. BRE Bookshop, Watford (UK).
- Young, I. M., Mullins, C. E., 1991. Factors affecting the strength of undisturbed cores from soils with low structural stability. *European Journal of Soil Science* 42 (2), 205–217.
- Zhang, L. M., Li, X., 2010. Microporosity structure of coarse granular soils. *J. Geotech. and Geoenviron. Engrg.* 136 (10), 1425–1436.
-

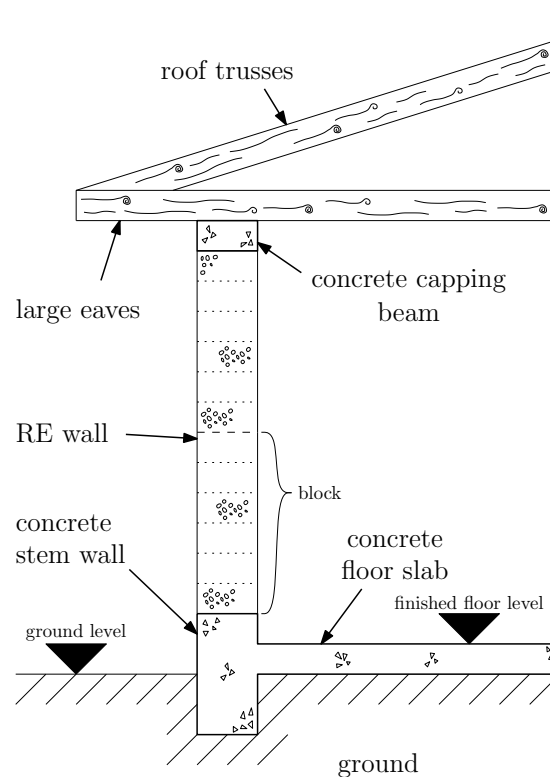


Figure 8.1: Simple detailing sketch of the use of a stem wall and overhanging eaves for RE wall protection. Note that additional details, for example roof and foundation detailing, are not shown.



Figure 8.2: Moulding of earthen render in Villafeliche, Zaragoza. Photographs by Paul A. Jaquin. Used with permission.

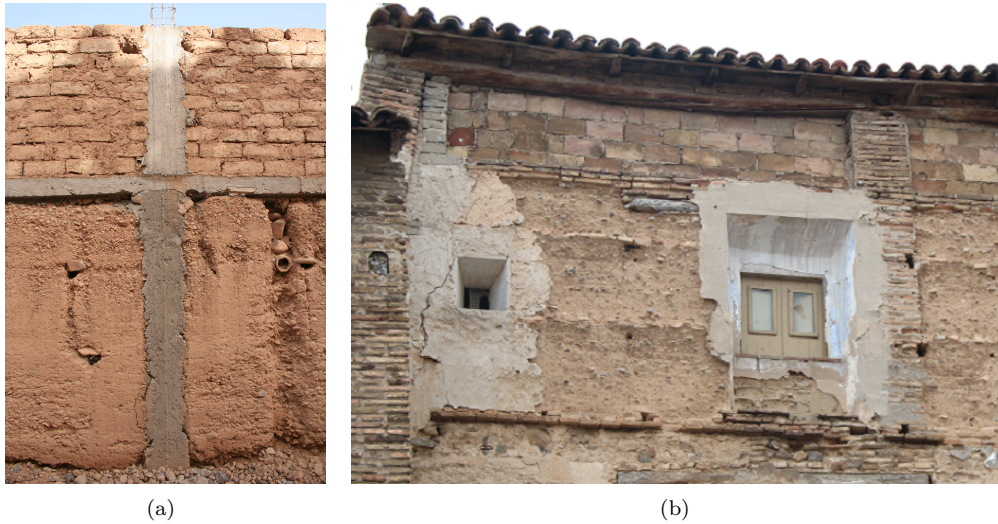


Figure 8.3: Concrete patches: a) the Asslim Kasbah, Morocco; b) Villafeliche, Zaragoza. Photographs by Paul A. Jaquin. Used with permission.



Figure 8.4: Earthen repairs made to Castillo Cox, Valencia. Photograph by Paul A. Jaquin. Used with permission.

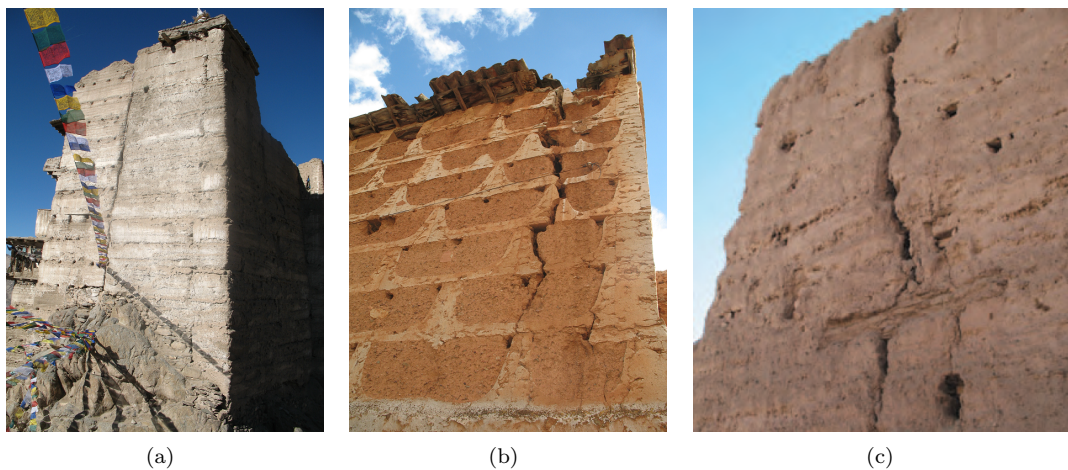


Figure 8.5: Tension cracks: a) watchtower in Namgyal Tsembo, Leh; b) Villafeliche, Zaragoza; c) crack repaired using an earthen staple, Basgo, Ladakh. Photographs by Paul A. Jaquin. Used with permission.

References

The following is a full list of references used in this thesis:

- Abdullah, W. S., Alshibli, K. A., Al-Zou'bi, M. S., 1999. Influence of pore water chemistry on the swelling behavior of compacted clays. *Applied Clay Science* 15 (5-6), 447–462.
- Acar, Y. B., Olivieri, I., 1990. Pore fluid effects on the fabric and hydraulic conductivity of laboratory-compacted clay. *Transportation Research Record* 1219, 144–159.
- Adrian, R., 1986. Multi-point optical measurements of simultaneous vectors in unsteady flow—a review. *International Journal of Heat and Fluid Flow* 7 (2), 127–145.
- Adrian, R. J., 1991. Particle imaging techniques for experimental fluid mechanics. *Annual Review of Fluid Mechanics* 23, 261–304.
- Ahmed, S., Lovell, C., Diamond, S., 1974. Pore sizes and strength of compacted clay. *ASCE J. Geotech Engng* 100(4), 407–425.
- Ahuja, L. R., Fiedler, F., Dunn, G. H., Benjamin, J. G., Garri-son, A., 1998. Changes in soil water retention curves due to tillage and natural reconsolidation. *Soil Science Society of America Journal* 62, 1228–1233.
- Ajaz, A., Parry, R. G. H., 1974. An unconfined direct tension test for compacted clays. *American Society for Testing and Materials Journal of Testing and Evaluation* 2 (3), 163–172.
- Ajaz, A., Parry, R. G. H., 1975a. Analysis of bending stresses in soil beams. *Géotechnique* 23 (3), 586–591.
- Ajaz, A., Parry, R. H. G., 1975b. Brazilian tensile test for soils: Discussion. *Canadian Geotechnical Journal* 12 (4), 542–544.
- Ajaz, A., Parry, R. H. G., 1975c. Stress-strain behaviour of two compacted clays in tension and compression. *Géotechnique* 25 (3), 495–512.
- Akbour, R. A., Douch, J., Hamdani, M., Schmitz, P., Sep 2002. Transport of kaolinite colloids through quartz sand: Influence of humic acid, Ca^{2+} , and trace metals. *Journal of Colloid and Interface Science* 253 (1), 1–8.
- Albrecht, W. A., 1940. Calcium-potassium-phosphorus relation as a possible factor in ecological array of plants. *Journal of the American Society of Agronomy* 32, 411–418.
- Allersma, H., 1982. Photo-elastic stress analysis and strains in simple shear. In: Vermeer, P. A., Luger, H. J. (Eds.), *Proc., IUTAM Symposium on Deformation and Failure of Granular Materials*. A. A. Balkema, Rotterdam, pp. 345–353.
- Allinson, D., Hall, M., 2010. Hygrothermal analysis of a stabilised rammed earth test building in the uk. *Energy and Buildings* 42, 845–852.
- Alonso, E., Gens, A., Hight, D. W., 1987. Special problems in soils. General report. In: *Proceedings of the 9th European Conference on Soil Mechanics*. Dublin, pp. 1087–1146.
- Alonso, E., Vaunat, J., Gens, A., 1999. Modelling the mechanical behaviour of expansive clays. *Engineering Geology* 54, 173–183.
- Alonso, E. E., Gens, A., Josa, A., 1990. A constitutive model for partially saturated soils. *Géotechnique* 40 (3), 405–430.
- Arifin, Y., Schanz, T., 2009. Osmotic suction of highly plastic clays. *Acta Geotechnica* 4, 177–191.
- Atkins, P., De Paula, J., 2006. *Physical Chemistry*, 8th Edition. Oxford University Press, New York (USA).
- Atkinson, B. K. (Ed.), 1987. *Fracture mechanics of rock*. Academic Press Inc., London (UK).
- Atzeni, C., Pia, G., Sanna, U., Spanu, N., 2008. A fractal model of the porous microstructure of earth-based materials. *Construction and Building Materials* 22 (8), 1607–1613.
- Aydin, A., Basu, A., 2006. The use of brazilian test as a quantitative measure of rock weathering. *Rock Mechanics and Rock Engineering* 39 (1), 77–85.
- Azmach, T. F., Sego, D. C., Arenson, L. U., Biggar, K. W., 2011. Tensile strength and stress-strain behaviour of devon silt under frozen fringe conditions. *Cold Regions Science and Technology* In Press, Corrected Proof, –.
- Baker, R., Frydman, S., 2009. Unsaturated soil mechanics: Critical review of physical foundations. *Engineering Geology* 106 (1-2), 26–39.
- Baltodano-Goulding, R., September 2010. Deformation behavior in unsaturated soils. In: Alonso, E., Gens, A. (Eds.), *Unsaturated Soils. Fifth International Conference on Unsaturated Soils*, CRC Press, pp. 181–185.
- Barden, L., McGown, A., Collins, K., 1973. The collapse mechanism in partly saturated soil. *Engineering Geology* 7 (1), 49–60.

- Barret, E. P., Joyner, L. G., Halenda, P. P., 1951. The determination of pore volume and area distributions in porous substances. *Journal of the American Chemical Society* 73, 373–380.
- Barzegar, A., November 1995. Structural stability and mechanical strength of salt-affected soils. PhD Thesis, The University of Adelaide.
- Barzegar, A., Murray, R., Churchman, G., Rengasamy, P., 1994a. The strength of remolded soils as affected by exchangeable cations and dispersible clay. *Australian Journal of Soil Research* 32 (2), 185–199.
- Barzegar, A. R., Oades, J. M., Rengasamy, P., 1996. Soil structure degradation and mellowing of compacted soils by saline sodic solutions. *Soil Science Society of America Journal* 60 (2), 583–588.
- Barzegar, A. R., Oades, J. M., Rengasamy, P., Giles, L., 1994b. Effect of sodicity and salinity on disaggregation and tensile strength of an alfisol under different cropping systems. *Soil & Tillage Research* 32 (4), 329–345.
- Barzegar, A. R., Oades, J. M., Rengasamy, P., Murray, R. S., 1995a. Tensile strength of dry, remoulded soils as affected by properties of the clay fraction. *Geoderma* 65 (1-2), 93–108.
- Barzegar, A. R., Rengasamy, P., Oades, J. M., 1995b. Effects of clay type and rate of wetting on the mellowing of compacted soils. *Geoderma* 68 (1-2), 39–49.
- Beckett, C. T. S., 2008. Cracking in rammed earth. MEng Dissertation, Durham University, Durham, UK.
- Betts, M. C., Miller, T. A. H., 1937. Rammed earth walls for buildings. *Farmers Bulletin No. 1500*. U.S. Department of Agriculture, Washington D.C. (U.S. Govt. Printing Office).
- Bhatia, S. K., Soliman, A. F., 1990. Frequency distribution of void ratio of granular materials determined by an image analyzer. *Soils and Foundations* 30 (1), 1–16.
- Bird, N., Bartoli, F., Dexter, A., 1996. Water retention models for fractal soil structures. *European Journal of Soil Science* 47, 1–6.
- Bird, N., Daz, M. C., Saa, A., Tarquis, A. M., 2006. Fractal and multifractal analysis of pore-scale images of soil. *Journal of Hydrology* 322 (1-4), 211–219.
- Blair, J. M., Falconer, R. E., Milne, A. C., Young, I. M., Crawford, J. W., 2007. Modeling three-dimensional microstructure in heterogeneous media. *Soil Science Society of America Journal* 71 (6), 1807–1812.
- Bolton, M., 1991. A guide to soil mechanics. M D & K Bolton.
- Bonala, M. V. S., Reddi, L. N., 1999. Fractal representation of soil cohesion. *Journal of Geotechnical and Geoenvironmental Engineering* 125 (10), 901–904.
- Boyd, A., 1962. Chinese architecture and town planning. Alec Tiranti Ltd, London (UK).
- Braunack, M. V., Hewitt, J. S., Dexter, A. R., 1979. Brittle fracture of soil aggregates and compaction of aggregate beds. *Journal of Soil Science* 30, 653–667.
- Brooks, R. H., Corey, A. T., 1964. Hydraulic properties of porous media. In: *Hydrology Paper No. 3*. Civil Engineering Dept., California State University, Fort Colins, Colorado.
- Brunauer, S., Emmett, P. H., Teller, E., 1938. Adsorption of gases in multimolecular layers. *Journal of the American Chemical Society* 60 (2), 309–319.
- BSI, 1990. BS 1377:1990. Methods of test for soils for civil engineering purposes.
- BSI, 2000. BS EN 772-2:2000 Methods of test for masonry units. Determination of compressive strength.
- BSI, 2002. BS EN 12390-3:2002. Testing hardened concrete. Compressive strength of test specimens.
- Buckingham, E., 1907. Studies on the movement of soil moisture. Vol. 38. United States Department of Agriculture Bureau of Soils.
- Bui, Q.-B., Morel, J.-C., 2009. Assessing the anisotropy of rammed earth. *Construction and Building Materials* 23 (9), 3005–3011.
- Buscarnera, G., Nova, R., September 2010. Saturation induced instability on bonded geomaterials. In: Alonso, E., Gens, A. (Eds.), *Unsaturated Soils*. Fifth International Conference on Unsaturated Soils, CRC Press, pp. 771–777.
- Butt, H.-J., 2008. Capillary forces: Influence of roughness and heterogeneity. *Langmuir* 24 (9), 4715–4721.
- Butt, H.-J., Kappl, M., 2009. Normal capillary forces. *Advances in Colloid and Interface Science* 146 (1-2), 48–60.
- Carneiro, F. L. L. E., Barcellos, A., 1953. Concrete tensile strength. *RILEM Bulletin Paris* 13.
- Casagrande, A., 1932. The structure of clay and its importance in foundation engineering. *Journal of the Boston Society Civil Engineers* 19 (4), 168–209.
- Causarano, H., 1993. Factors affecting the tensile strength of soil aggregates. *Soil & Tillage Research* 28 (1), 15–25.
- Chae, J., Kim, B., Park, S.-w., Kato, S., 2010. Effect of suction on unconfined compressive strength in partly saturated soils. *KSCE Journal of Civil Engineering* 14 (3), 281–290.
- Chambers, W., 1968. Design of Chinese buildings, furniture, dresses, machines and utensils. Benjamin Blom, Inc., New York (USA).

- Choquette, M., Brub, M.-A., Locat, J., 1987. Mineralogical and microtextural changes associated with lime stabilization of marine clays from eastern Canada. *Applied Clay Science* 2 (3), 215–232.
- Chorom, M., Regasamy, P., Murray, R. S., 1994. Clay dispersion as influenced by pH and net particle charge of sodic soils. *Australian Journal of Soil Research* 32 (6), 1243–1252.
- Cihan, A., Tyner, J. S., Perfect, E., 2009. Predicting relative permeability from water retention: A direct approach based on fractal geometry. *Water Resources Research* 45, 8.
- Cizeau, P., Makse, H. A., Stanley, H. E., 1999. Mechanisms of granular spontaneous stratification and segregation in two-dimensional silos. *Physical Review E* 59 (4), 4408–4421.
- Clever, H. L., 1985. Solubility of mercury. *Journal of Chemical Education* 62 (8), 720.
- Colliat-Dangus, J. L., Desrues, J., Foray, P., 1988. Triaxial testing of granular soil under elevated cell pressure. In: Donaghe, R. T., Chaney, R. C., Silver, M. L. (Eds.), *Proceedings of a conference on advanced triaxial testing for soil and rocks*. American Society for Testing and Materials, Philadelphia (USA), pp. 290–310.
- Collins, K., McGown, A., 1974. Form and function of microfabric features in a variety of natural soils. *Géotechnique* 24 (2), 223–254.
- Conti, A. P., 6–9 September 2009. Earth building today, a renewed use of an ancient technology. In: *Proceedings of the 11th International Conference on Non-Conventional Materials and Technologies (NOCMAT)*. Bath University.
- Cosenza, P., Tabbagh, A., 2004. Electromagnetic determination of clay water content: role of the microporosity. *Applied Clay Science* 26, 21–36.
- Coviello, A., Lagioia, R., Nova, R., 2005. On the measurement of the tensile strength of soft rocks. *Rock Mechanics and Rock Engineering* 38 (4), 251–273.
- Craig, R. F., 2004. *Soil Mechanics*, 7th Edition. Spon Press, London (UK).
- Crawford, C. B., 1968. Quick clays of eastern Canada. *Engineering Geology* 2 (4), 239–265.
- Croney, D., Coleman, J. D., Black, W. P. M., 1958. Movement and distribution of water in soil in relation to highway design and performance. *Highway Research Board Special Report* 40, 226–252.
- Cui, Y. J., 1993. Etude de comportement d'un limon compacté non saturé et sa modélisation dans un cadre élastoplastique. Ph.D. thesis, CERMES-ENPC.
- Dao, V. N. T., Morris, P. H., Dux, P. F., 2008. On equations for the total suction and its matric and osmotic components. *Cement and Concrete Research* 38 (11), 1302–1305.
- Dehandschutter, B., Vandycke, S., Sintubin, M., Vandenberghe, N., Gaviglio, P., Sizun, J. P., Wouters, L., 2004. Microfabric of fractured boom clay at depth: a case study of brittle-ductile transitional clay behaviour. *Applied Clay Science* 26 (1–4), 389–401.
- Dehandschutter, B., Vandycke, S., Sintubin, M., Vandenberghe, N., Wouters, L., 2005. Brittle fractures and ductile shear bands in argillaceous sediments: inferences from oligocene boom clay (belgium). *Journal of Structural Geology* 27 (6), 1095–1112.
- Delage, P., 2009. Discussion: Compaction behaviour of clay. *Géotechnique* 59 (1), 75–77.
- Delage, P., 2010. A microstructure approach to the sensitivity and compressibility of some eastern Canada sensitive clays. *Géotechnique* 60 (5), 353–368.
- Delage, P., Audiguier, M., Cui, Y. J., Howat, D., 1996. Microstructure of a compacted silt. *Canadian Geotechnical Journal* 33, 150–158.
- Delage, P., Lefebvre, G., 1984. Study of the structure of a sensitive Champlain clay and its evolution during consolidation. *Canadian Geotechnical Journal* 21 (1), 21–35.
- Delage, P., Marcial, D., Cui, Y. J., Ruiz, X., 2006. Ageing effects in a compacted bentonite: a microstructure approach. *Géotechnique* 56 (5), 291–304.
- Delage, P., Pellerin, F. M., 1984. Influence de la lyophilisation sur la structure d'une argile sensible du Québec. *Clay Minerals* 19 (2), 151–160.
- Delgado, M. C. J., Guerrero, I. C., 2006. Earth building in Spain. *Construction and Building Materials* 20 (9), 679–690.
- Desrues, J., Gioacchino, V., 2004. Strain localization in sand: an overview of the experimental results obtained in Grenoble using stereophotogrammetry. *International Journal for Numerical and Analytical Methods in Geomechanics* 28, 279–321.
- Dexter, A., 1988. Advances in characterization of soil structure. *Soil and Tillage Research* 11 (3–4), 199–238.
- Dexter, A. R., 1997. Physical properties of tilled soils. *Soil and Tillage Research* 43 (1–2), 41–63.
- Dexter, A. R., Chan, K. Y., 1991. Soil mechanical properties as influenced by exchangeable cations. *Journal of Soil Science* 42 (2), 219–226.
- Dexter, A. R., Kroesbergen, B., 1985. Methodology for determination of tensile strength of soil aggregates. *Journal of Agricultural Engineering Research* 31, 139–147.
- Diamond, S., 1970. Pore size distribution in clays. *Clays and Clay Minerals* 18, 7–23.
- Diamond, S., 1971. Microstructure and pore structure of impact-compacted clays. *Clays and Clay Minerals* 19, 239–249.

- Dodson, B., 1994. Weibull Analysis. ASQ Quality Press, Milwaukee (USA).
- Dow, 2008. Calcium chloride handbook: A guide to properties, forms, storage and handling. Dow Chemical Company (USA).
- d'Souzae, J. I., 2008. Mercury intrusion porosimetry: A tool for pharmaceutical particle characterisation. *Pharmainfo.net Latest Reviews* 6 (2).
- Easton, D., 2007. The Rammed Earth House, Completely Revised Edition. Chelsea Green Publication Company, Vermont (USA).
- Edlefsen, N. E., Anderson, A. B. C., 1943. The thermodynamics of soil moisture. *Hilgardia* 16, 31–299.
- Ersahin, S., Gunal, H., Kutlu, T., Yetgin, B., Coban, S., 2006. Estimating specific surface area and cation exchange capacity in soils using fractal dimension of particle-size distribution. *Geoderma* 136 (3–4), 588–597.
- Everett, D. H., 1972. Manual of symbols and terminology for physicochemical quantities and units, appendix ii: Definitions, terminology and symbols in colloid and surface chemistry. *Pure and Applied Chemistry* 31 (4), 577–638.
- Farrell, D. A., Greacen, E. L., Larson, W. E., 1967. The effect of water content on axial strain in a loam soil under tension and compression. *Soil Society of America Proceedings* 32, 445–450.
- Fisher, L. R., Israelachvili, J. N., 1979. Direct experimental verification of the Kelvin equation for capillary condensation. *Nature* 277 (5697), 548–549.
- Fisher, R. A., 1926. On the capillary forces in an ideal soil; correction of formulae given by W. B. Haines. *The Journal of Agricultural Science* 16 (03), 492–505.
- Foroutan-pour, K., Dutilleul, P., Smith, D. L., 1999. Advances in the implementation of the box-counting method of fractal dimension estimation. *Applied Mathematics and Computation* 105 (2–3), 195–210.
- Fredlund, D., Rahardjo, H., 1993. *Soil Mechanics for Unsaturated Soils*. John Wiley & Sons Inc., New York (USA).
- Fredlund, D. G., 2006. Unsaturated soil mechanics in engineering practice. *Journal of Geotechnical and Geoenvironmental Engineering* 132 (3), 286–321.
- Fredlund, D. G., Sheng, D., Zhao, J., 2011. Estimation of soil suction from the soil-water characteristic curve. *Canadian Geotechnical Journal* 48 (2), 186–198.
- Fredlund, D. G., Xing, A., 1994. Equations for the soil-water characteristic curve. *Canadian Geotechnical Journal* 31, 521–532.
- Fredlund, M., Gitirana, G., 2011. Probabilistic methods applied to unsaturated numerical modeling. *Geotechnical and Geological Engineering* 29, 217–223.
- Frydman, S., 1964. The applicability of the Brazilian (indirect tension) test to soils. *Australian Journal of Applied Science* 15, 335–343.
- Frydman, S., Baker, R., 2009. Theoretical soil-water characteristic curves based on adsorption, cavitation, and a double porosity model. *Int. J. Geomech.* 9 (6), 250–257.
- Gallipoli, D., Gens, A., Sharma, R., Vaunat, J., 2003. An elasto-plastic model for unsaturated soil incorporating the effects of suction and degree of saturation on mechanical behaviour. *Géotechnique* 53 (1), 123–135.
- Gelard, D., Fontaine, L., Maximilien, S., Olagnon, C., Laurent, J., Houben, H., Van Damme, H., 2007. When physics revisit earth construction: Recent advances in the understanding of the cohesion mechanisms of earthen materials. In: *Proc. International Symposium on Earthen Structures*, IIS Bangalore, 22–24 August 2007. pp. 294–302.
- Gens, A., 2010. Soil-environment interactions in geotechnical engineering. *Géotechnique* 60 (1), 3–74.
- Gens, A., Alonso, E. E., 1992. A framework for the behaviour of unsaturated expansive clays. *Canadian Geotechnical Journal* 29, 1013–1032.
- Gens, A., Alonso, E. E., Suriol, J., Lloret, A., 1995. Effect of structure on the volumetric behaviour of a compacted soil. In: *First International Conference on Unsaturated Soils. UNSAT '95*, Paris, France, pp. 83–88.
- Gens, A., Valleján, B., Sánchez, M., Imbert, C., Villar, M. V., Van Geet, M., 2011. Hydromechanical behaviour of a heterogeneous compacted soil: experimental observations and modelling. *Géotechnique* 61 (5), 367–386.
- Ghezzehei, T. A., Or, D., 2000. Dynamics of soil aggregate coalescence governed by capillary and rheological processes. *Water Resour. Res.* 36, 367–379.
- Gimenez, D., Perfect, E., Rawls, W. J., Pachepsky, Y., 1997. Fractal models for predicting soil hydraulic properties: a review. *Engineering Geology* 48 (3–4), 161–183.
- Gordon, J. E., 1991. *Structures: Or why things don't fall down*, eleventh Edition. Penguin Group, London (UK).
- Goyal, R. K., Tomassone, M. S., 2006. Power-law and exponential segregation in two-dimensional silos of granular mixtures. *Physical Review E* 74 (5), 10.
- Grant, C. D., Dexter, A. R., Oades, J. M., 1992. Residual effects of additions of calcium compounds on soil structure and strength. *Soil & Tillage Research* 22 (3–4), 283–297.
- Grasselli, Y., Herrmann, H., 1998. tude sur la forme d'un tas de billes dans un silo bidimensionnel. *Comptes Rendus de l'Académie des Sciences - Series IIB - Mechanics-Physics-Chemistry-Astronomy* 326 (1), 61–67.
- Grasselli, Y., Herrmann, H., 1999. Shapes of heaps and in silos. *The European Physical Journal B - Condensed Matter and Complex Systems* 10, 673–679.

- Grasselli, Y., Herrmann, H. J., 1997. On the angles of dry granular heaps. *Physica A: Statistical and Theoretical Physics* 246 (3-4), 301–312.
- Griffith, A. A., 1921. The phenomena of rupture and flow in solids. *Philosophical Transactions of the Royal Society of London. Series A, Containing Papers of a Mathematical or Physical Character* 221, pp. 163–198.
- Grof, Z., Lawrence, C. J., Stepnek, F., 2008. The strength of liquid bridges in random granular materials. *Journal of Colloid and Interface Science* 319 (1), 182–192.
- Guler, M., Edil, T. B., Bosscher, P. J., 1999. Measurement of particle movement in granular soils using image analysis. *Journal of Computing in Civil Engineering* 13 (2), 116–122.
- Hadeler, K. P., Kuttler, C., 1999. Dynamical models for granular matter. *Granular Matter* 2 (1), 9–18.
- Haines, W. B., 1930. Studies in the physical properties of soil. v. the hysteresis effect in capillary properties, and the modes of moisture distribution associated therewith. *The Journal of Agricultural Science* 20 (01), 97–116.
- Hajnos, M., Lipiec, J., Swieboda, R., Sokolowska, Z., Witkowska-Walczak, B., 2006. Complete characterization of pore size distribution of tilled and orchard soil using water retention curve, mercury porosimetry, nitrogen adsorption, and water desorption methods. *Geoderma* 135, 307–314, doi: DOI: 10.1016/j.geoderma.2006.01.010.
- Hall, M., Djerbib, Y., 2004. Rammed earth sample production: context, recommendations and consistency. *Construction and Building Materials* 18 (4), 281–286.
- Hall, M., Djerbib, Y., 2006a. Moisture ingress in rammed earth: Part 2 - the effect of soil particle-size distribution on the absorption of static pressure-driven water. *Construction and Building Materials* 20 (6), 374–383.
- Hall, M., Djerbib, Y., 2006b. Moisture ingress in rammed earth: Part 3 - sorptivity, surface receptiveness and surface inflow velocity. *Construction and Building Materials* 20 (6), 384–395.
- Hall, S. A., Bornert, M., Desrues, J., Pannier, Y., Lenoir, N., Viggiani, G., Bésuelle, P., 2010. Discrete and continuum analysis of localised deformation in sand using x-ray μ ct and volumetric digital image correlation. *Géotechnique* 60 (5), 315–322.
- Hallett, P. D., Dexter, A. R., Seville, J. P. K., 1995. Identification of pre-existing cracks on soil fracture surfaces using dye. *Soil and Tillage Research* 33 (3-4), 163–184.
- Hattab, M., Fleureau, J.-M., 2010. Experimental study of kaolin particle orientation mechanism. *Géotechnique* 60 (5), 323–331.
- Heath, A., Lawrence, M., Walker, P., Fourie, C., September 2009a. The compressive strength of modern earth masonry. In: *Proceedings of the 11th International Conference on Non-Conventional Materials and Technologies (NOCMAT)*. Bath University.
- Heath, A., Walker, P., Fourie, C., Lawrence, M., 2009b. Compressive strength of unfired clay masonry units. *Proceedings of the Institute of Civil Engineers: Construction Materials* 162 (3), 105–112.
- Heath, A. C., Pestana, J. M., Harvey, J. T., Bejerano, M. O., 2004. Normalizing behavior of unsaturated granular pavement materials. *Journal of Geotechnical and Geoenvironmental Engineering* 130, 896–904.
- Heathcote, K., Jankulovski, E., 1992. Aspect ratio correction factors for soilcrete blocks. *Australian civil engineering transactions CE34* (4: Australia: Institution of Engineers), 309–312.
- Herrmann, H. J., 1999. Shapes of granular surfaces. *Physica A: Statistical Mechanics and its Applications* 270 (1-2), 82–88.
- Herrmann, H. J., 2002. Granular matter. *Physica A: Statistical Mechanics and its Applications* 313 (1-2), 188–210.
- Hillel, D., 1998. *Environmental Soil Physics*. Academic Press, California (USA).
- Hillel, D., 2004. *Fundamentals of Soil Physics*. Academic Press, Inc., London (UK).
- Hirata, T., 1989. Fractal dimension of fault systems in Japan: Fractal structure in rock fracture geometry at various scales. *Pure and Applied Geophysics* 131, 157–170.
- Horn, R., Taubner, H., Wuttke, M., Baumgartl, T., 1994. Soil physical properties related to soil structure. *Soil and Tillage Research* 30 (2-4), 187–216.
- Houben, H., Guillaud, H., 1994. *Earthen architecture: A comprehensive guide*. Intermediate Technology Development Group, London (UK).
- Houben, H., Guillaud, H., 1996. *Earth construction - a comprehensive guide.*, Second Edition. Intermediate Technology Publications, London (UK).
- Hoyos, L. R., Pérez-Ruiz, D., Puppala, A. J., 2010. Constitutive modeling of unsaturated soil behavior using a refined suction-controlled true triaxial cell: Preliminary observations. In: Alonso, E., Gens, A. (Eds.), *Unsaturated Soils. Fifth International Conference on Unsaturated Soils*, CRC Press.
- Huang, G.-H., Zhang, R.-D., Huang, Q.-Z., 2006. Modeling soil water retention curve with a fractal method. *Pedosphere* 16, 137–146.
- Huang, H.-C., Tan, Y.-C., Liu, C.-W., Chen, C.-H., 2005. A novel hysteresis model in unsaturated soil. *Hydrological Processes* 19, 1653–1665.

- Hughes, J. M. O., Withers, N. J., 1974. Reinforcing of soft cohesive soils with stone columns. *Ground Engineering* 3, 42–49.
- Hyslip, J. P., Vallejo, L. E., 1997. Fractal analysis of the roughness and size distribution of granular materials. *Engineering Geology* 48 (3-4), 231–244.
- Ibarra, S. Y., McKyes, E., Broughton, R. S., 2005. Measurement of tensile strength of unsaturated sandy loam soil. *Soil and Tillage Research* 81 (1), 15–23.
- Irwin, G. R., 1957. Analysis of stresses and strains near the end of a crack traversing a plate. *Journal of Applied Mechanics* 24, 361–364.
- Iskander, M. G., Liu, J., Sadek, S., 2002. Transparent amorphous silica to model clay. *Journal of Geotechnical and Geoenvironmental Engineering* 128 (3), 262–273.
- Israelachvili, J. N., 2005. Importance of pico-scale topography of surfaces for adhesion, friction, and failure. *MRS Bulletin* 30 (7), 533–539.
- Iwamatsu, M., Horii, K., 1996. Capillary condensation and adhesion of two wetter surfaces. *Journal of Colloid and Interface Science* 182 (2), 400–406.
- Jaquin, P. A., 2008a. Analysis of historic rammed earth construction. PhD Thesis, Durham University.
- Jaquin, P. A., 2008b. Study of historic rammed earth structures in Spain and India. *The Structural Engineer* 86 (2), 26–32.
- Jaquin, P. A., 2010. How mud bricks work - using unsaturated soil mechanics principles to explain the material properties of earth buildings - a year of research. In: *From small steps to giant leaps - putting research into practice*.
- Jaquin, P. A., Augarde, C. E., Gallipoli, D., Toll, D. G., 2009. The strength of unstabilised rammed earth materials. *Géotechnique* 59 (5), 487–490.
- Jaquin, P. A., Augarde, C. E., Gerrard, C., 22-24 August 2007. Historic rammed earth structures in Spain, construction techniques and a preliminary classification. Bangalore: Interline Publishing.
- Jaquin, P. A., Augarde, C. E., Gerrard, C. M., 2008a. A chronological description of the spatial development of rammed earth techniques. *International Journal of Architectural Heritage: Conservation, Analysis and Restoration* 2 (4), 377–400.
- Jaquin, P. A., Augarde, C. E., Legrand, L., 2008b. Unsaturated characteristics of rammed earth. In: Toll, D. G. (Ed.), *First European Conference on Unsaturated Soils*. Durham University, Durham, England, pp. 417–422.
- Jaroniec, M., Gadkaree, K. P., Choma, J., 1996. Relation between adsorption potential distribution and pore volume distribution for microporous carbons. *Colloids and Surfaces A: Physicochemical and Engineering Aspects* 118 (3), 203–210.
- Jayasinghe, C., 2009. Structural design of earth buildings. Eco Ceylon Pvt. Ltd., Colombo.
- Jobmann, M., Billaux, D., 2010. Fractal model for permeability calculation from porosity and pore radius information and application to excavation damaged zones surrounding waste emplacement boreholes in Opalinus clay. *International Journal of Rock Mechanics and Mining Sciences* 47 (4), 583–589.
- Jommi, C., Sciotti, A., Sep 23-26 2003. A study of the microstructure to assess the reliability of laboratory compacted soils as reference material for earth constructions. In: Bontempi, F. (Ed.), *2nd International Conference on Structural and Construction Engineering*. A A Balkema Publishers, Rome, Italy, pp. 2409–2415.
- Jotisankasa, A., Coop, M., Ridley, A., 2009. The mechanical behaviour of an unsaturated compacted silty clay. *Géotechnique* 59 (5), 415–428.
- Jotisankasa, A., Ridley, A., Coop, M., 2007. Collapse behavior of compacted silty clay in suction-monitored oedometer apparatus. *Journal of Geotechnical and Geoenvironmental Engineering* 133 (7), 867–877.
- Kaufmann, J., 2009. Characterization of pore space of cement-based materials by combined mercury and wood's metal intrusion. *Mercury* 216 (1), 209–216.
- Kay, B. D., Dexter, A. R., 1992. The influence of dispersible clay and wetting drying cycles on the tensile-strength of a red-brown earth. *Australian Journal of Soil Research* 30 (3), 297–310.
- Keable, J., 1996. *Rammed earth structures: a code of practice*. Intermediate Technology Publications, London (UK).
- Keefe, L., 2005. *Earth Building: Methods and materials, repair and conservation*. Taylor & Francis, Oxford UK.
- Keller, A., 1998. High resolution, non-destructive measurement and characterization of fracture apertures. *International Journal of Rock Mechanics and Mining Sciences* 35 (8), 1037–1050.
- Ketcham, R. A., Carlson, W. D., 2001. Acquisition, optimization and interpretation of x-ray computed tomographic imagery: Applications to the geosciences. *Computers and Geosciences* 27, 381–400.
- Khaleel, R., Relyea, J. F., Conca, J. L., 1995. Evaluation of van Genuchten-Mualem relationships to estimate unsaturated hydraulic conductivity at low water contents. *Water Resour. Res.* 31, 2659–2668.
- Khoury, C. N., Miller, G. A., Hatami, K., Feb. 2010. Shear strength of unsaturated soil-geotextile interfaces. In: *ASCE Conf. Proc. Vol. 365*. ASCE, West Palm Beach, Florida, pp. 28–28.

- King, B., 1996. *Buildings of Earth and Straw: Structural Design for Rammed Earth and Straw-Bale Architecture*. Ecological Design Press, Sausalito, California (USA).
- Kirk, H., 2009. The behaviour of low plasticity rammed earth soils. Masters Thesis, Imperial College London.
- Klute, A. (Ed.), 1986. *Methods of Soil Analysis, Part 1. Physical and Mineralogical Methods*. ASA-SSSA Inc., Madison, Wisconsin, USA.
- Kohonen, M. M., Geromichalos, D., Scheel, M., Schier, C., Herminghaus, S., 2004. On capillary bridges in wet granular materials. *Physica A: Statistical Mechanics and its Applications* 339 (1-2), 7–15.
- Kravchenko, A., Zhang, R., 1998. Estimating the soil water retention from particle-size distributions: a fractal approach. *Soil Science* 163 (3), 171–179.
- Krefeld, 1938. Effect of shape of specimen on the apparent compressive strength of brick masonry. In: *Proceedings of the American Society of Materials*, Philadelphia, USA. pp. 363–369.
- Krishnayya, A. V. G., Eisenstein, Z., 1974. Brazilian tensile test for soils. *Canadian Geotechnical Journal* 11 (4), 632–642.
- Krishnayya, A. V. G., Eisenstein, Z., 1975. Brazilian tensile test for soils: second reply. *Canadian Geotechnical Journal* 12 (4), 544–545.
- Krishnayya, A. V. G., Eisenstein, Z., Morgenstern, N. R., 1974. Behaviour of compacted soil in tension. *Journal of the Geotechnical Engineering Division, Proceedings of the American Society of Civil Engineers* 100 (GT9), 1051–1061.
- Kruth, J., Bartscher, M., Carmignato, S., Schmitt, R., Chiffre, L. D., Weckenmann, A., 2011. Computed tomography for dimensional metrology. *CIRP Annals - Manufacturing Technology* 60 (2), 821 – 842.
- Kutilek, M., Jendele, L., Krejca, M., 2009. Comparison of empirical, semi-empirical and physically based models of soil hydraulic functions derived for bi-modal soils. *Journal of Contaminant Hydrology* 104 (1-4), 84–89.
- Lambe, T. W., 1960. A mechanistic picture of shear strength in clay. In: *Research Conference on the Shear Strength of Cohesive Soils*. ASCE, University of Boulder, Colorado (USA), pp. 555–580.
- Lang, A. R. G., 1967. Osmotic coefficients and water potentials of sodium chloride solutions from 0 to 40°C. *Australian Journal of Chemistry* 20, 2017–2023.
- Lange, D. A., Abell, A. B., Willis, K. L., Powell, S., 1998. Characterization of cement pore structure using wood's metal and mercury porosimetry. *Imaging Technologies*, 197–206.
- Lee, P., 2007. Francois Cointeraux and the school of "agriculture" in eighteenth-century France. *Journal of Architectural Education* 60 (4), 39–46.
- Lee, Y., Bassett, R., 2006. Application of a photogrammetric technique to a model tunnel. *Tunnelling and Underground Space Technology* 21 (1), 79–95.
- Leonards, G. A., Narain, J., 1963. Flexibility of clay and cracking of earth dams. *American Society of Civil Engineering Journal of Soil Mechanics and Foundation Engineering* 89 (SM2), 47–98.
- Likos, W. J., Jul 13-17 2009. Pore-scale model for water retention in unsaturated sand. *Amer Inst Physics*, Golden, CO, pp. 907–910.
- Lilley, D. M., Robinson, J., 1995. Ultimate strength of rammed earth walls with openings. *Proceedings of the Institution of Civil Engineers-Structures and Buildings* 110 (3), 278–287.
- Lipiec, J., Hatano, R., Slowinska-Jurkiewicz, A., 1998. The fractal dimension of pore distribution patterns in variously-compacted soil. *Soil and Tillage Research* 47 (1-2), 61–66.
- Liu, C. Y., Nylan, M., Barbieri-Low, A., 2005. *Recarving China's Past: Art, Archaeology, and Architecture of the 'Wu Family Shrines'*. Princeton University Art Museum, Princeton, New Jersey.
- Liu, J., Hu, R., Wang, R., Yang, L., 2010. Regeneration of vernacular architecture: new rammed earth houses on the upper reaches of the yangtze river. *Frontiers of Energy and Power Engineering in China* 4 (1), 93–99.
- Liu, J., Iskander, M. G., 2010. Modelling capacity of transparent soil. *Canadian Geotechnical Journal* 47, 451–460.
- Liu, Y., Zhao, C. G., Nov 04-07 2007. Modeling the hysteresis for soil-water characteristic curves. *China Communications Press*, Chongqing, China, pp. 383–392.
- Loureço, S. D. N., Gallipoli, D., Augarde, C. E., Toll, D., Evans, F., Medero, G., July 2008a. Studies of unsaturated soils by environmental scanning electron microscope using dynamic mode. In: Toll, D. G., Augarde, C. E., Gallipoli, D., Wheeler, S. J. (Eds.), *Unsaturated Soils: Advances in Geoengineering*. Proceedings of the 1st European Conference. First European Conference on Unsaturated Soils, Taylor & Francis.
- Loureço, S. D. N., Gallipoli, D., Augarde, C. E., Toll, D. G., Fisher, P. C., Congreve, A., in press. Formation and evolution of water menisci in unsaturated granular media. *Géotechnique*.
- Loureço, S. D. N., Gallipoli, D., Toll, D. G., Augarde, C. E., Evans, F. D., September 2010. Advances in tensiometer-based suction control systems. In: Alonso, E., Gens, A. (Eds.), *Unsaturated Soils*. Fifth International Conference on Unsaturated Soils, CRC Press, pp. 695–700.

- Lourenço, S. D. N., Toll, D. G., Augarde, C. E., Gallipoli, D., Congreve, A., Smart, T., Evans, F. D., July 2008b. Observations of unsaturated soils by environmental scanning electron microscopy in dynamic mode. In: Toll, D. G., Augarde, C. E., Gallipoli, D., Wheeler, S. J. (Eds.), *Unsaturated Soils: Advances in Geo-Engineering*. First European Conference on Unsaturated Soils, CRC Press.
- Love, J. P., Burd, H. J., Miligan, G. W. E., Houlby, G. T., 1987. Analytical and model studies of reinforcement of a layer of granular fill on a soft clay subgrade. *Canadian Geotechnical Journal* 24 (4), 611–622.
- Lu, N., Likos, W. J., 2004. *Unsaturated Soil Mechanics*. John Wiley & Sons, Inc., New Jersey (USA).
- Lu, N., Wu, B., Tan, C. P., 2007. Tensile strength characteristics of unsaturated sands. *Journal of Geotechnical and Geoenvironmental Engineering* 133 (2), 144–154.
- Makse, H. A., Ball, R. C., Stanley, H. E., Warr, S., 1998. Dynamics of granular stratification. *Physical Review E* 58 (3), 3357–3367.
- Makse, H. A., Havlin, S., King, P. R., Stanley, H. E., 1997. Spontaneous stratification in granular mixtures. *Nature* 386 (March), 379–381.
- Mandelbrot, B. B., 1967. How long is the coast of Great Britain? Statistical self-similarity and the fractional dimension. *Science* 156, 636–638.
- Maniatidis, V., Walker, P., 2003. *A Review of Rammed Earth Construction*. University of Bath.
- Maria, S., 2010. Methods for porosity measurement in lime-based mortars. *Construction and Building Materials* In Press, Corrected Proof, –.
- Maris, H., Balibar, S., 2000. Negative pressures and cavitation in liquid helium. *Physics Today* 53 (2), 29–34.
- Mason, G., Clark, W., 1965. Liquid bridges between spheres. *Chemical Engineering Science* 20 (10), 859–866.
- Mason, G., Morrow, N. R., 1991. Capillary behavior of a perfectly wetting liquid in irregular triangular tubes. *Journal of Colloid and Interface Science* 141 (1), 262–274.
- Mata, C., Romero, E., Ledesma, A., 2002. Hydro-chemical effects on water retention in bentonite-sand mixtures. In: Juco, J. F. T., De Campas, T. M. P., Marinho, F. A. M. (Eds.), *Proceedings of the 3rd International Conference on Unsaturated Soils*. Vol. 1. Swets and Zeitlinger, Rotterdam (NL), pp. 283–288.
- Mayer, R. P., Stowe, R. A., 2006. Packed uniform sphere model for solids: Interstitial access opening sizes and pressure deficiencies for wetting liquids with comparison to reported experimental results. *Journal of Colloid and Interface Science* 294 (1), 139–150.
- McKelvey, D., Sivakumar, V., Bell, A., Graham, J., 2004. Modelling vibrated stone columns in soft clay. *Proceedings of the Institution of Civil Engineers-Geotechnical Engineering* 157 (3), 137–149.
- Megias-Alguacil, D., Gauckler, L. J., 2010. Analysis of the capillary forces between two small solid spheres binded by a convex liquid bridge. *Powder Technology* 198 (2), 211–218.
- Meguid, M., Saada, O., Nunes, M., Mattar, J., 2008. Physical modeling of tunnels in soft ground: A review. *Tunnelling and Underground Space Technology* 23 (2), 185–198.
- Mehrotra, V., Sastry, K., 1980. Pendular bond strength between unequal-sized spherical particles. *Powder Technology* 25 (2), 203–214.
- Mendes, J., 2011. The impact of climate change on an instrumented embankment: an unsaturated soil mechanics approach. PhD. Thesis, Durham University, Durham.
- Middleton, G. F., 1953. *Build your house of earth*. Commonwealth Experimental Building Station, Melbourne, Australia.
- Millington, R. J., Quirk, J. P., 1961. Permeability of porous media. *Nature* 183, 387–388.
- Mitchell, J. K., 1991. Conduction phenomena: From theory to geotechnical practice. *Géotechnique* 41 (3), 299–340.
- Mitchell, J. K., Soga, K., 2005. *Fundamentals of Soil Behaviour*, Third Edition. John Wiley & Sons Inc., Hoboken, New Jersey (USA).
- Monroy, R., Zdravkovic, L., Ridley, A., 2010. Evolution of microstructure in compacted London clay during wetting and loading. *Géotechnique* 60, 105–199.
- Morel, J. C., Mesbah, A., Oggero, M., Walker, P., 2001. Building houses with local materials: means to drastically reduce the environmental impact of construction. *Building and Environment* 36 (10), 1119–1126.
- Morel, J.-C., Pkla, A., Walker, P., 2007. Compressive strength testing of compressed earth blocks. *Construction and Building Materials* 21 (2), 303–309.
- Morton, T., Stevenson, F., Taylor, B., Charlton Smith, N., 2005. Low cost earth brick construction, 2 Kirk Park, Dalguise: Monitoring and Evaluation. Tech. rep., Arc Architects, Auchtermuchty, Fife.
- Mu, F., Su, X., Dec. 2007. Analysis of liquid bridge between spherical particles. *China Particuology* 5 (6), 420–424.
- Mualem, Y., 1976. A new model for predicting the hydraulic conductivity of unsaturated porous media. *Water Resour. Res.* 12, –.
- Mullins, C. E., Panayiotopoulos, K. P., 1984. The strength of unsaturated mixtures of sand and kaolin and the concept of effective stress. *European Journal of Soil Science* 35 (3), 459–468.

- Munkholm, L. J., Schjønning, P., Kay, B. D., 2002. Tensile strength of soil cores in relation to aggregate strength, soil fragmentation and pore characteristics. *Soil and Tillage Research* 64 (1-2), 125–135.
- Murase, K., Mochida, T., Sagawa, Y., Sugama, H., 2008. Estimation on the strength of a liquid bridge adhered to three spheres. *Advanced Powder Technology* 19 (4), 349–367.
- Nahlawi, H., Chakrabarti, S., Kodikara, J., 2004. A direct tensile strength testing method for unsaturated geomaterials. *Geotechnical Testing Journal* 27 (4), 356–361.
- Ni, Q., Hird, C., Guymer, I., 2010. Physical modelling of pile penetration in clay using transparent soil and particle image velocimetry. *Géotechnique* 60 (2), 121–132.
- Nishimura, T., Fredlund, D. G., March 2002. Hysteresis effects resulting from drying and wetting under relatively dry conditions. In: Juça, de Campos, Marinho (Eds.), *Unsaturated Soils. Third International Conference on Unsaturated Soils*, Swets and Zeitlinger, Lisse, Recife, Brazil.
- Nowamooz, H., Chazallon, C., 2011. Finite element modelling of a rammed earth wall. *Construction and Building Materials* 25 (4), 2112–2121.
- Nowamooz, H., Masrouri, F., 2010. Relationships between soil fabric and suction cycles in compacted swelling soils. *Engineering Geology* 114 (3-4), 444–455.
- Nuth, M., Laloui, L., 2008. Advances in modelling hysteretic water retention curve in deformable soils. *Computers and Geotechnics* 35 (6), 835–844.
- NZS, 1998. NZS 4298:1998. Materials and workmanship for earth buildings incorporating amendment no. 1.
- Olivella, S., September 2010. Geotechnical and environmental models involving unsaturated soils and rocks. In: Alonso, E., Gens, A. (Eds.), *Unsaturated Soils. Fifth International Conference on Unsaturated Soils*, CRC Press.
- Or, D., Tuller, M., 1999. Liquid retention and interfacial area in variably saturated porous media: Upscaling from single-pore to sample-scale model. *Water Resour. Res.* 35, 3591–3605.
- Or, D., Tuller, M., 2002. Cavitation during desaturation of porous media under tension. *Water Resour. Res.* 38, 19–1–19–4.
- Or, D., Tuller, M., 2003. Capillarity. In: Hillel, D. (Ed.), *Encyclopedia of Soils in the Environment*. Vol. 1. Elsevier Ltd., Oxford, U.K., pp. 155–163.
- Ottino, J. M., Khakhar, D. V., 2001. Fundamental research in heaping, mixing, and segregation of granular materials: challenges and perspectives. *Powder Technology* 121 (2-3), 117–122.
- Ouhadi, V. R., Yong, R. N., 2008. Ettringite formation and behaviour in clayey soils. *Applied Clay Science* 42 (1-2), 258–265.
- Pachepsky, Y. A., Gimnez, D., Crawford, J. W., Rawls, W. J., 2000. Conventional and fractal geometry in soil science. In: Y. Pachepsky, J. C., Rawls, W. (Eds.), *Fractals in Soil Science*. Vol. Volume 27. Elsevier, pp. 7–18.
- Paikowsky, G., Xi, F., 2000. Particle motion tracking utilizing a high-resolution digital CCD camera. *Geotechnical Testing Journal* 23 (1), 123–134.
- Pan, B., Qian, K., Xie, H., Asundi, A., 2009. Two-dimensional digital image correlation for in-plane displacement and strain measurement: a review. *Measurement Science and Technology* 20 (6), 062001.
- Panayiotopoulos, K. P., 1996. The effect of matric suction on stress-strain relation and strength of three alfisols. *Soil and Tillage Research* 39 (1-2), 45–59.
- Park, S.-S., 2010. Effect of wetting on unconfined compressive strength of cemented sands. *J. Geotech. and Geoenviron. Engrg.* 136 (12), 1713–1720.
- Pedroso, D. M., Williams, D. J., 2011. Automatic calibration of soil-water characteristic curves using genetic algorithms. *Computers and Geotechnics* 38 (3), 330–340.
- Peel, M. C., Finlayson, B. L., McMahon, T. A., 2007. Updated world map of the Köppen-Geiger climate classification. *Hydrology and Earth System Sciences* 11, 1633–1644.
- Perfect, E., Rasiah, V., Kay, B. D., 1992. Fractal dimensions of soil aggregate-size distributions calculated by number and mass. *Journal of the Soil Science Society of America* 56, 1407–1409.
- Perrier, E. M. A., Bird, N. R. A., 2002. Modelling soil fragmentation: the pore solid fractal approach. *Soil & Tillage Research* 64, 91–99.
- Perrier, E. M. A., Bird, N. R. A., Rieu, M., 1999. Generalizing the fractal model of soil structure: the poresolid fractal approach. *Geoderma* 88, 137–164.
- Philip, J. R., 1977. Unitary approach to capillary condensation and adsorption. *Journal of Chemical Physics* 66, 5069–5075.
- Pietsch, W. B., 1968. Tensile strength of granular materials. *Nature* 217, 736–737.
- Pitois, O., Moucheron, P., Chateau, X., 2000. Liquid bridge between two moving spheres: An experimental study of viscosity effects. *Journal of Colloid and Interface Science* 231 (1), 26–31.
- Pitois, O., Moucheron, P., Chateau, X., 2001. Rupture energy of a pendular liquid bridge. *The European Physical Journal B - Condensed Matter and Complex Systems* 23 (1), 79–86.
- Powrie, W., 2008. *Soil Mechanics: Concepts and Applications*, 2nd Edition. Spon Press.

- Pradhan, B., Nagesh, M., Bhattacharjee, B., 2005. Prediction of the hydraulic diffusivity from pore size distribution of concrete. *Cement and Concrete Research* 35 (9), 1724–1733.
- Prashant, A., Penumadu, D., 2007. Effect of microfabric on mechanical behaviour of kaolin clay using cubical true tri-axial testing. *Journal of Geotechnical and Geoenvironmental Engineering* 133 (4), 433–444.
- Proctor, R. R., 1933. Fundamental principles of soil compaction. *Engineering News Record* 111 (9), 245–248.
- Quagliarini, E., Lenci, S., Iorio, M., 2010. Mechanical properties of adobe walls in a Roman republican domus at Suasa. *Journal of Cultural Heritage* 11 (2), 130–137.
- Rabinovich, Y. I., Esayanur, M. S., Moudgil, B. M., 2005. Capillary forces between two spheres with a fixed volume liquid bridge: Theory and experiment. *Langmuir* 21 (24), 10992–10997.
- Rahimi, H., Pazira, E., Tajik, F., 2000. Effect of soil organic matter, electrical conductivity and sodium adsorption ratio on tensile strength of aggregates. *Soil & Tillage Research* 54 (3–4), 145–153.
- Rao, S. M., Shivananda, P., 2005. Role of osmotic suction in swelling of salt-amended clays. *Canadian Geotechnical Journal* 42, 307–315.
- Rasband, W., 2002. NIH Image J.
URL <http://rsbweb.nih.gov/ij/index.html> (verified 02.08.2011)
- Reynolds, W. D., Drury, C. F., Tan, C. S., Fox, C. A., Yang, X. M., 2009. Use of indicators and pore volume-function characteristics to quantify soil physical quality. *Geoderma* 152 (3–4), 252–263.
- Ridler, T. W., Calvard, S., 1978. Picture thresholding using an iterative selection method. *Systems, Man and Cybernetics, IEEE Transactions on* 8 (8), 630–632.
- Rigby, S. P., Chigada, P. I., Wang, J., Wilkinson, S. K., Bateman, H., Al-Duri, B., Wood, J., Bakalis, S., Miri, T., 2011. Improving the interpretation of mercury porosimetry data using computerised x-ray tomography and mean-field dft. *Chemical Engineering Science* 66 (11), 2328–2339.
- Rodriguez, R., Candela, L., Lloret, A., Nov 2003. Experimental system for studying the hydromechanical behavior of porous media. *Soil Sci Soc Amer, Valladolid, Spain*, pp. 345–353.
- Rojas, E., Gallegos, G., Leal, J., September 2010. A porous model based on porosimetry to simulate retention curves. In: Alonso, E., Gens, A. (Eds.), *Unsaturated Soils. Fifth International Conference on Unsaturated Soils*, CRC Press, pp. 927–932.
- Rojas, E., Rojas, F., 2005. Modeling hysteresis of the soil-water characteristic curve. *Soils and Foundations* 45 (3), 135–145.
- Romero, E., 1999. Characterisation and thermo-hydro mechanical behaviour of unsaturated boom clay: an experimental study. Phd thesis, Universitat Politècnica de Catalunya, Barcelona, Spain.
- Romero, E., Gens, A., Lloret, A., 1999. Water permeability, water retention and microstructure of unsaturated compacted boom clay. *Engineering Geology* 54 (1–2), 117–127.
- Romero, E., Simms, P., 2008. Microstructure investigation in unsaturated soils: A review with special attention to contribution a mercury intrusion porosimetry and environmental scanning electron microscopy. *Geotechnical and Geological Engineering* 26, 705–727.
- Romero, E., Vaunat, J., Apr 10–12 2000. Retention curves of deformable clays. In: Tarantino, A., Mancuso, C. (Eds.), *Experimental Evidence and Theoretical Approaches in Unsaturated Soils*. A A Balkema Publishers, Trent, Italy, pp. 91–106.
- Rondeau, X., Affolter, C., Komunjer, L., Clausse, D., Guigon, P., 2003. Experimental determination of capillary forces by crushing strength measurements. *Powder Technology* 130 (1–3), 124–131.
- Roscoe, K. H., 1970. The influence of strains in soil mechanics. *Géotechnique* 20 (2), 129–170.
- Russell, A. R., 2010. Water retention characteristics of soils with double porosity. *European Journal of Soil Science* 61 (3), 412–424.
- Salem, H. S., Chilingarian, G. V., 1999. Determination of specific surface area and mean grain size from well-log data and their influence on the physical behavior of offshore reservoirs. *Journal of Petroleum Science and Engineering* 22 (4), 241–252.
- Samadani, A., Kudrolli, A., 2001. Angle of repose and segregation in cohesive granular matter. *Physical Review E* 6405 (5), 9.
- Samadani, A., Pradhan, A., Kudrolli, A., 1999. Size segregation of granular matter in silo discharges. *Physical Review E* 60 (6), 7203.
- Santamarina, J. C., Cho, G. C., March 2004. Soil behaviour: The role of particle shape. In: *Proceedings of the Skempton Conference*. London.
- Scholtès, L., Hicher, P., Nicot, F., Chareyre, B., Darve, F., 2009. On the capillary stress tensor in wet granular materials. *International Journal for Numerical and Analytical Methods in Geomechanics* 33 (10), 1289–1313.
- Shimokawa, M., Ohta, S., 2007. Dual stratification of a sand pile formed by trapped kink. *Physics Letters A* 366 (6), 591–595.

- Shinoda, M., Bathurst, R. J., 2004. Strain measurement of geogrids using a video-extensometer technique. *Geotechnical Testing Journal* 27 (5), 8p.
- Siemens, G., Peters, S., Take, W. A., 2010. Analysis of a drawdown test displaying the use of transparent soil in unsaturated flow applications. In: Alonso, E., Gens, A. (Eds.), *Unsaturated Soils. Fifth International Conference on Unsaturated Soils*, CRC Press.
- Simms, P. H., Yanful, E. K., 2001. Measurement and estimation of pore shrinkage and pore measurement in a clayey till during soil-water characteristic curve tests. *Canadian Geotechnical Journal* 38, 741–754.
- Simms, P. H., Yanful, E. K., 2004. Estimation of soil-water characteristic curve of clayey till using measured pore-size distributions. *Journal of Environmental Engineering-Asce* 130 (8), 847–854.
- Sivakumar, V., Tan, W. C., Murray, E. J., McKinley, J. D., 2006. Wetting, drying and compression characteristics of compacted clay. *Géotechnique* 56 (1), 57–62.
- Sivakumar, V., Wheeler, S., 2000. Influence of compaction procedure on the mechanical behaviour of an unsaturated compacted clay. part 1: Wetting and isotropic compression. *Géotechnique* 50 (4), 359–368.
- Slominski, C., Niedostatkiwicz, M., Tejchman, J., Apr. 2007. Application of particle image velocimetry (piv) for deformation measurement during granular silo flow. *Powder Technology* 173 (1), 1–18.
- SmartMeasurement, 2001. Conductivity of calcium chloride. Online, accessed 25.05.2009.
- Srebro, Y., Levine, D., 2003. Role of friction in compaction and segregation of granular materials. *Physical Review E* 68 (6), 9.
- Steinhardt, N. S., Xinian, F., Glahn, E., Throp, R. L., Juliano, A. L., 1984. *Chinese Traditional Architecture*. China Institute in America.
- Stevens, N., Ralston, J., Sedev, R., 2009. The uniform capillary model for packed beds and particle wettability. *Journal of Colloid and Interface Science* 337 (1), 162–169.
- Sun, D. A., Sheng, D. C., Cui, H. B., Sloan, S. W., 2007. A density-dependent elastoplastic hydro-mechanical model for unsaturated compacted soils. *International Journal for Numerical and Analytical Methods in Geomechanics* 31 (11), 1257–1279.
- Take, W. A., White, D. J., Bowers, K. H., Moss, N. A., Jun 15-17 2005. Remote real-time monitoring of tunnelling-induced settlement using image analysis. In: Bakker, K. J., Bezuijen, A., Broere, W., Kwast, E. A. (Eds.), *5th International Conference on Geotechnical Aspects of Underground Construction in Soft Ground*. Taylor & Francis Ltd, Amsterdam, pp. 771–777.
- Tamagnini, R., Apr 2004. An extended cam-clay model for unsaturated soils with hydraulic hysteresis. *Géotechnique* 54 (3), 223–228.
- Tamrakar, S. B., Mitachi, T., Toyosawa, Y., Mar 07-09 2007a. Factors affecting tensile strength measurement and modified tensile strength measuring apparatus for soil. Weimar, Germany, pp. 207–218.
- Tamrakar, S. B., Mitachi, T., Toyosawa, Y., 2007b. Measurement of soil tensile strength and factors affecting its measurements. *Soils and Foundations* 47 (5), 911–918.
- Tamrakar, S. B., Toyosawa, Y., Mitach, T., Itoh, K., 2005. Tensile strength of compacted and saturated soils using newly developed tensile strength measuring apparatus. *Soils and Foundations* 45 (6), 103–110.
- Tang, A.-M. e. a., 2005. Controlling suction by the vapour equilibrium technique at different temperatures and its application in determining the water retention properties of mx80 clay. *Canadian Geotechnical Journal* 42, 287–296.
- Tang, G. X., Graham, J., 2000. A method for testing tensile strength in unsaturated soils. *Geotechnical Testing Journal* 23 (3), 377–382.
- Tarantino, 2007. A possible critical stare framework for unsaturated compacted soils. *Géotechnique* 57 (4).
- Tarantino, A., 2009. A water retention model for deformable soils. *Géotechnique* 59 (9), 751–762.
- Tarantino, A., 2010. Unsaturated soils: compaction versus reconstituted states. In: Alonso, E., Gens, A. (Eds.), *Unsaturated soils. Fifth International Conference on Unsaturated Soils*, CRC Press, pp. 113–136.
- Tarantino, A., De Col, E., 2008. Compaction behaviour of clay. *Géotechnique* 58 (3), 199–213.
- Tarantino, A., Gallipoli, D., Augarde, C. E., de Gennaro, V., Gomez, R., Laloui, L., Mancuso, C., el Mountasir, G., Munoz, J. J., Pereira, J., Peron, H., Pisoni, G., Romero, E., Raveendraraj, A., Rojas, J. C., Toll, D. G., Tombolato, S., Wheeler, S., 2011. Benchmark of experimental techniques for measuring and controlling suction. *Géotechnique* 61 (4), 303–312.
- Tarantino, A., Tombolato, S., 2005. Coupling of hydraulic and mechanical behaviour in unsaturated compacted clay. *Géotechnique* 55 (4), 307–317.
- Taud, H., Martinez-Angeles, R., Parrot, J., Hernandez-Escobedo, L., 2005. Porosity estimation method by x-ray computed tomography. *Journal of Petroleum Science and Engineering* 47 (3–4), 209–217.
- Teh, K. L., Cassidy, M. J., Leung, C. F., Chow, Y. K., Randolph, M. F., Quah, C. K., 2008. Revealing the bearing capacity mechanisms of a penetrating spudcan through sand overlying clay. *Géotechnique* 58 (10), 793–804.

- Terzaghi, K., 1925. Principles of soil mechanics. *Engineering News Records* 95 (19, 742–746; 20, 796–800; 21, 832–836; 22, 874–878; 23, 912–915; 25, 987–990; 26, 1026–1029; 27, 1064–1068).
- Terzaghi, K., 1936. The shearing resistance of saturated soils and the angle between the planes of shear. In: *Proceedings of the First International Conference on Soil Mechanics*. Vol. 1. Cambridge, MA (USA), pp. 54–56.
- Thevanayagam, S., Nasarajah, S., 1998. Fractal model for flow through saturated soils. *Journal of Geotechnical and Geoenvironmental Engineering* 124 (1), 53–66.
- Thom, R., Sivakumar, R., Sivakumar, V., Murray, E. J., Mackinnon, P., 2007. Pore size distribution of unsaturated compacted kaolin: the initial states and final states following saturation. *Géotechnique* 57 (5), 469–474.
- Thompson, W., 1871. On the equilibrium of vapour at a curved surface of a liquid. *Phil. Mag.* 42(282).
- Tiwari, B., Ajmera, B., 2011. A new correlation relating the shear strength of reconstituted soil to the proportions of clay minerals and plasticity characteristics. *Applied Clay Science* 53 (1), 48–57.
- Toll, D. G., Mar 1990. A framework for unsaturated soil behaviour. *Géotechnique* 40 (1), 31–44.
- Toll, D. G., 1999. A data acquisition and control system for geotechnical testing. In: Toll, D. (Ed.), *Computing developments in civil and structural engineering*. Civil-Comp Press Ltd.
- Toll, D. G., Ong, B. H., 2003. Critical-state parameters for an unsaturated residual sandy clay. *Géotechnique* 53, 93–103.
- Tolle, C. R., Mcjunkin, T. R., J., G. D., 2003. Suboptimal minimum cluster volume cover-based method for measuring fractal dimension. In: *IEEE Transaction on Pattern Analysis and Machine Intelligence*. pp. 32–41.
- Tuller, M., Or, D., 2004. Retention of water in soil and the soil water characteristic curve. In: Hillel, D. (Ed.), *Encyclopedia of Soils in the Environment*. Vol. 4. Elsevier Ltd., Oxford, U.K., pp. 278–289.
- Tuller, M., Or, D., Dudley, L. M., 1999. Adsorption and capillary condensation in porous media: Liquid retention and interfacial configurations in angular pores. *Water Resour. Res.* 35 (7), 1949–1964.
- UCAR, 2002. Salinity - dissolved salts, measuring salinity. University Corporation for Atmospheric Research, Online, accessed 25.05.2009.
- Urso, M. E. D., Lawrence, C. J., Adams, M. J., 2002. A two-dimensional study of the rupture of funicular liquid bridges. *Chemical Engineering Science* 57 (4), 677–692.
- USDA, 1954. *Agriuculture handbook No. 60, Diagenesis and improvement of saline and alkali soils*. United States Salinity Laboratory, California (USA).
- Utomo, W. H., Dexter, A. R., 1981. Soil friability. *Journal of Soil Science* 32 (2), 203–213.
- Vallejo, L. E., 1996. Fractal analysis of the fabric changes in a consolidating clay. *Engineering Geology* 43 (4), 281–290.
- Vallejo, L. E., 2010. Compressive strength of unsaturated fissured clays. In: Alonso, E., Gens, A. (Eds.), *Unsaturated soils*. Fifth International Conference on Unsaturated Soils, CRC Press, pp. 387–390.
- Van Geet, M., Swennen, R., Wevers, M., 2000. Quantitative analysis of reservoir rocks by microfocus x-ray computerised tomography. *Sedimentary Geology* 132 (1-2), 25–36.
- Van Geet, M., Volckaert, G., Roels, S., 2005. The use of microfocus x-ray computed tomography in characterising the hydration of a clay pellet/powder mixture. *Applied Clay Science* 29 (2), 73–87.
- van Genuchten, M. T., 1980. A closed-form equation for predicting the hydraulic conductivity of unsaturated soils. *Soil Sci Soc Am J* 44 (5), 892–898.
- van Genuchten, M. T., Nielsen, D. R., 1985. On describing and predicting the hydraulic properties of unsaturated soil. *Annals of Geophysics* 3, 615–628.
- Vanapalli, S., Fredlund, D., 1997. Interpretation of undrained shear strength of unsaturated soils in terms of stress state variables. In: *3rd Brazilian Symposium on Unsaturated Soils*. pp. 278–289.
- Vanapalli, S. K., Fredlund, D. G., Pufahl, D. E., 1999. The influence of soil structure and stress history on the soil-water characteristics of a compacted till. *Géotechnique* 49 (2), 143–159.
- Vatsala, A., Srinivasa Murthy, B. R., 2001. Discussion: The influence of soil structure and stress history on the soil-water characteristics of a compacted till. *Géotechnique* 50 (0), 1–4.
- Venkatarama Reddy, B. V., Prasanna Kumar, P., 6-9 September 2009. Role of clay content and moisture on characteristics of cement stabilised rammed earth. In: *Proceedings of the 11th International Conference on Non-Conventional Materials and Technologies (NOCMAT)*. Bath University.
- Vesga, L., 2008. Equivalent effective stress and compressibility of unsaturated kaolinite clay subjected to drying. *Journal of Geotechnical and Geoenvironmental Engineering* 134 (3), 366–378.
- Volkwein, A., 1993. The capillary suction of water into concrete and the abnormal viscosity of the porewater. *Cement and Concrete Research* 23 (4), 843–852.
- Vomocil, J. A., Waldron, L. J., Chancellor, W. J., 1961. Soil tensile strength by centrifugation. *Soil Society of America Proceedings* 25, 176–180.

- Walker, P. (Ed.), 2002. The Australian Earth Building Handbook. SAI Global Ltd., Sydney, Australia.
- Walker, P., Keable, R., Martin, J., Maniatidis, V., 2005. Rammed Earth: Design and Construction Guidelines. BRE Bookshop, Watford (UK).
- Walker, P., Maniatidis, V., 2004. Rammed earth: a natural option for walling. Proceedings of the Institution of Civil Engineers-Civil Engineering 157 (1), 5–5.
- Wang, J. J., Zhu, J. G., Chiu, C. F., Zhang, H., 2007. Experimental study on fracture toughness and tensile strength of a clay. Engineering Geology 94 (1-2), 65–75.
- Washburn, E. W., 1921. The dynamics of capillary flow. Phys. Rev. 17 (3), 273–283.
- Webb, D. J., 1994. Stabilised soil and the built environment. Renewable Energy 5, 1066–1080.
- Webster, G., 1969. The Roman Imperial Army. A. and C. Black, London.
- Wellington, S. L., Vinegar, H. J., 1987. X-ray computerized tomography. Journal of Petroleum Technology, 885–898.
- Wheeler, S., Sivakumar, V., 1995. An elasto-plastic critical state framework for unsaturated soils. Géotechnique 45 (1), 35–53.
- Wheeler, S. J., Sharma, R. S., Buisson, M. S. R., 2003. Coupling of hydraulic hysteresis and stress-strain behaviour in unsaturated soils. Géotechnique 53 (1), 41–54.
- White, D. J., 2002. An investigation into the behaviour of pressed-in piles. Thesis, University of Cambridge, UK.
- White, D. J., Randolph, M. F., Thompson, B., 2005. An image-based deformation measurement system for the geotechnical centrifuge. International Journal of Physical Modelling in Geotechnics 5 (3), 1–12.
- White, D. J., Take, W. A., Bolton, M. D., 2003. Soil deformation measurement using particle image velocimetry (PIV) and photogrammetry. Géotechnique 53 (7), 619–631.
- Willis, K. L., Abell, A. B., Lange, D. A., 1998. Image-based characterization of cement pore structure using wood's metal intrusion. Cement and Concrete Research 28 (12), 1695–1705.
- Xu, Y. F., 2004a. Calculation of unsaturated hydraulic conductivity using a fractal model for the pore-size distribution. Computers and Geotechnics 31 (7), 549–557.
- Xu, Y. F., 2004b. Fractal approach to unsaturated shear strength. Journal of Geotechnical and Geoenvironmental Engineering 130 (3), 264–273.
- Xu, Y. F., Sun, D. A., 2002. A fractal model for soil pores and its application to determination of water permeability. Physica a-Statistical Mechanics and Its Applications 316 (1-4), 56–64.
- Yong, R. N., Ouhadi, V. R., 2007. Experimental study on instability of bases on natural and lime/cement-stabilized clayey soils. Applied Clay Science 35 (3-4), 238–249.
- Young, F. R., 1989. Cavitation. McGraw-Hill Book Company (UK) Ltd.
- Young, I. M., Mullins, C. E., 1991. Factors affecting the strength of undisturbed cores from soils with low structural stability. European Journal of Soil Science 42 (2), 205–217.
- Zeng, Y., Gantzer, C. J., Payton, R. L., Anderson, S. H., 1996. Fractal dimension and lacunarity of bulk density determined with X-ray computed tomography. Soil Science Society of America Journal 60 (6), 1718–1724.
- Zhang, G., Liang, D. F., Zhang, J. M., 2006. Image analysis measurement of soil particle movement during a soil-structure interface test. Computers and Geotechnics 33 (4-5), 248–259.
- Zhang, L. M., Li, X., 2010. Microporosity structure of coarse granular soils. J. Geotech. and Geoenviron. Engrg. 136 (10), 1425–1436.